

# Structure-Property Relations of Functional Materials Featuring a Perovskite Structure Motif

STEFAN BURGER

Vollständiger Abdruck der von der TUM School of Natural Sciences der Technischen Universität München zur Erlangung des akademischen Grades eines

Doktors der Naturwissenschaften (Dr. rer. nat.)

genehmigten Dissertation.

Vorsitz: Prof. Dr. Klaus Köhler

Prüfer\*innen der Dissertation:

1. Priv.-Doz. Dr. Gregor Kieslich
2. Priv.-Doz. Dr. Anthony Phillips
3. Prof. Dr. Tom Nilges

Die Dissertation wurde am 22.02.2023 bei der Technischen Universität München eingereicht und durch die TUM School of Natural Sciences am 09.05.2023 angenommen.



Die Forschungsarbeiten, die der vorliegenden Dissertationsschrift zugrunde liegen, wurden im Zeitraum von August 2017 bis Mai 2022 in der Nachwuchsgruppe „Structural Chemistry of Functional Materials“ am Lehrstuhl für Anorganische und Metallorganische Chemie der Technischen Universität München durchgeführt und durch ein Promotionsstipendium der Hans-Seidel Stiftung e.V. gefördert.

Einzelne Ergebnisse sowie Schlussfolgerungen aus der vorliegenden Arbeit mündeten in zwei genehmigten Anträgen für Forschungsprojekte bei der Deutschen Forschungsgemeinschaft und sind unter den Projektnummern 450070835 sowie 493871295 zu finden.



*Für alle, die immer an mich glauben und mich immer unterstützen.*



"Discere ne cessa, cura sapientia crescat: rara datur longo prudentia temporis usu."

*Disticha catonis 4,27*

"Science is beautiful when it makes simple explanations of phenomena or connections between different observations."

*Stephen Hawking*

"In den Wissenschaften ist viel Gewisses, sobald man sich von den Ausnahmen nicht irremachen läßt und die Probleme zu ehren weiß."

*Johann Wolfgang von Goethe*





# Acknowledgements

In the context of this doctoral thesis there are many people who have supported me to bringing it to a successful end and whom I would like to thank at this point from the bottom of my heart. However, this feels only like a drop in the ocean, as it is impossible to acknowledge the great support over many years in just a few sentences – it is undoubtedly impossible to put this in appropriate words.

My very special thanks goes first and foremost to **DR. GREGOR KIESLICH**, my doctoral advisor and mentor. GREGOR, it was a great honour for me to do my doctoral thesis with you and to be guided and supported by you during this time, both in terms of scientific assistance and as a friend. Thank you very much for all the trust you have placed in me and the many opportunities and freedom you have given me in my day-to-day research work - I have grown up a lot from this.

Furthermore, I would like to express my warmest gratitude to **PROF. DR. DR. PHIL. H.C. ROLAND A. FISCHER**, without whose support much would not have been possible. It is exceptional how junior research groups and their members receive such backing and I have always had the pleasure to feel like an integral part of the Chair of Inorganic and Metal-Organic Chemistry. No matter what questions or issues I had, you always had a listening ear – I really appreciate that.

I would like to thank **PROF. DR. SIR ANTHONY CHEETHAM** for agreeing to host me as a visiting scientist at the University of California in Santa Barbara for scheduled six months. I regret very much that this stay could not be realised in the end due to the pandemic situation – however I appreciate even more the fact that we maintained contact *via* digital channels.

I would like to express my deep thanks to the **HANNS-SEIDEL-STIFTUNG E.V.** for a doctoral scholarship I received as part of the "Institut für Begabtenförderung". Especially in the context of the conceptual support, I had the unique opportunity to improve my education beyond science itself and I have made many new contacts, some of which became really good friends. **MAX, GREGOR, MICHI, ANNE-MARIE, MAX** and **CARLO**, I will always remember all the experiences and impressions of this time with a big smile. Especially the foundation conference trips to Rome and Berlin have been absolute social milestones of my PhD time.

No dissertation project can be successfully realised without a properly running chair, in which many things are operated in the background, which may not always be appreciated in the day-to-day business, but which are of elemental importance. Therefore, I would like to emphasise my appreciation for both the scientific organisation and also the help with bureaucratic inconveniences. **GREGOR, CHRISTIAN, MIRZA, GABI, MARKUS, ALEX, DOMINIK, JULIEN** – our so-called "Mittelbau" – thank you for everything you have helped me with over the years. **MARTIN** and **DANA**, thank you for your support concerning the administration office.

Apart from the scientific environment, it is very important to also feel comfortable in the working environment. I would like to thank the entire AMC team for the great time we had over the last few years and all the fun and laughs we had during the many hours we spent together in the lab. Such a time as during the doctorate shapes you for life and I always like to remember back to great stories and events of that time. We also had a lot of fun outside the lab, either in cozy evenings or during the enjoyable annual group excursions.

I would like to particularly mention everyone from the "**KLEINGRUPPE KIESLICH**". Thank you for the great time and the beer garden evenings, which were always extremely amusing. But also the weekly seminars were a great experience! The combination of science and personal interest lectures put a smile on my face week after week.

**CARSTEN**, I would likewise sincerely thank you as well as the entire Makro chair. Although I moved camps after the master's thesis, you continued to give me "asylum" the whole time! Sometimes one forgets how important little things are to make such a long time, like the doctorate, worth living. The coffee kitchen, the beverage store, the social room - I was always allowed to continue using everything as if I were still one of yours! This cannot be appreciated highly enough.

Apart from that, I would just like to thank everyone from the AMC group who I have had the honour to work with. Each and every one has left a telling impression - sometimes in a good way, sometimes in a bad way. But this is also an important hands-on experience and a necessary part of a successful personality development and therefore a great input for future decisions we all have to make at some point.

Nevertheless, I would like to mention some people by name in the following, because they have especially shaped me in their own way and I will always remember them. I would like to express my heartfelt thanks to **DR. DAVE**, who, especially in the first few months of my dissertation, was always there to help and advise me and introduced me to the diligent skills of single crystal diffraction with infinite patience and passion.

I would like to thank **TOM** for his trusting nature and the true friendship that has been built up, starting already from baby shoes in Landshut-Münchnerau, which I hope will continue to tie us in the future.

Dear **SARAH**, thank you very much for the time you always had for me and the great chats in between. I have been with you since your first semester, so to speak, and it fills me with great pleasure to see how you have paved your way.

**PATRICIA** and **SEBASTIAN**, as our ways first crossed back then in the Makro chair, we have become good friends over time - many thanks for that, especially for funny moments during our "Neufahrn"-time. Hopefully we will celebrate many more great parties, visit "Dults" and play funny "Boßeln" tournaments in the future.

**LENA** and **FABIAN**, there is not much I can write within this ridiculously small paragraph that would even closely express what I would like to tell. We had a fantastic time, Fabi, starting at the macro chair and continuing then at the AMC chair, moving basically from a desk-to-desk environment into another floor to a desk-to-desk environment, where Lena joined the 4040/4039

corner. Without going into details of how you contributed to my successful doctorate (as this would certainly fill books itself), I just want to say thank you to both of you from the depths of my heart. I am absolutely sure we will continue our friendship in the future and share our time together.

I would have never been able to successfully complete my dissertation without the continued support of my family and friends outside of the university. This may sound a bit confusing at first, but it is of immense value to talk about issues or challenges (professional as well as psychological) with people who are not at all involved. Many thanks to my **MUM**, my **BROTHER**, my **SISTER** as well as my **GIRLFRIEND** and her family, who know exactly how I think and react and sometimes they get the heavy dose of bad mood on the days off and just stand it, because they know exactly that I need the support, even if I would never address it directly. Many thanks to all my friends and associations, where I can simply switch off mind to find distraction and recharge my batteries. In particular I want to mention the sports club "**EICHBAUM-OBERNDORFER EUGENBACH E.V.**" which gave me - besides the sports - endless funny and refreshing moments. It feels fantastic to be an integral part of such a solidarity. Furthermore, I am very thankful to my old friends from school, allied as team "**GRETLMÜHLE**", with whom there is still an extremely strong and trusting relationship and hopefully this will always be continued.



# Contents

<b>Nomenclature</b>	<b>vii</b>
<b>List of Figures</b>	<b>ix</b>
<b>List of Schemes</b>	<b>xiii</b>
<b>Abstract</b>	<b>xv</b>
<b>Zusammenfassung</b>	<b>xvii</b>
<b>1 MOTIVATION</b>	<b>1</b>
<b>2 CONTEXT OF PEROVSKITE-TYPE COORDINATION NETWORKS</b>	<b>3</b>
2.1 The Categorisation of Coordination Polymers . . . . .	3
2.2 The Development of Coordination Chemistry in Coordination Networks . . . . .	4
2.3 The Genesis of the Myth "Perovskite" as a Blueprint for Materials Structures . . . . .	8
2.4 The Perovskite Structure in Hybrid Materials . . . . .	11
2.4.1 Hybrid Perovskites . . . . .	11
2.4.2 Molecular Perovskites . . . . .	11
2.5 Mechanical Properties of Molecular Perovskites . . . . .	14
2.5.1 General Remarks on Expansion and Compression in Materials . . . . .	14
2.5.2 Insights into Stimuli-Dependent Material Response . . . . .	16
2.5.3 Impact of the Framework Structure in Coordination Polymers . . . . .	17
2.5.4 Order-Disorder Phase Transitions in Molecular Perovskites . . . . .	19
2.6 The Diversity of Molecular Perovskites . . . . .	23
2.7 Dicyanamide-Based Perovskite-Type Coordination Networks . . . . .	27
<b>3 OBJECTIVE</b>	<b>31</b>
<b>4 RESULTS AND DISCUSSION</b>	<b>33</b>
4.1 STUDY I: Tolerance Factors of Hybrid Organic-Inorganic Perovskites: Recent Improvements and Current State of Research . . . . .	33
4.2 STUDY II: A New Polar Perovskite Coordination Network with Azaspiroundecane as A-Site Cation . . . . .	43
4.3 STUDY III: Tilt and Shift Polymorphism in Molecular Perovskites . . . . .	49
4.4 STUDY IV: Tuning the Mechanical Properties of Dicyanamide-Based Molecular Perovskites . . . . .	59

4.5	STUDY V: Designing Geometric Degrees of Freedom in ReO <sub>3</sub> -Type Coordination Polymers . . . . .	67
<b>5</b>	<b>CONCLUSION</b>	<b>77</b>
<b>6</b>	<b>BIBLIOGRAPHY</b>	<b>81</b>
<b>7</b>	<b>METHODOLOGY</b>	<b>107</b>
7.1	Synthesis of Precursor Compounds and Crystalline Perovskite-Type Materials .	107
7.2	Characterisation of Crystalline Perovskite-Type Materials . . . . .	109
<b>8</b>	<b>SUPPLEMENTARY MATERIAL</b>	<b>115</b>
8.1	STUDY II: Supporting Information . . . . .	115
8.2	STUDY III: Electronic Supporting Information . . . . .	131
8.3	STUDY IV: Supplementary Information . . . . .	151
8.4	STUDY V: Supporting Information . . . . .	161
<b>9</b>	<b>APPENDIX</b>	<b>211</b>
A	List of Paper Publications . . . . .	211
B	List of Conference Contributions . . . . .	215
C	Reprint permissions . . . . .	217

# Nomenclature

1D	One-dimensional
2D	Two-dimensional
3D	Three-dimensional
<i>ad.</i>	Adiabatic
[ASU] <sup>+</sup>	6-azaspiro[5.5]undecanium
<i>B</i>	Bulk modulus
[BTea] <sup>+</sup>	Benzyltriethylammonium
CN	Coordination number
col.	Columnar
config.	Configurational
CP	Coordination polymer
[DAB] <sup>+</sup>	1,4-diazabicyclo[2.2.2]octane-1,4-dium
DAC	Diamond Anvil Cell
[dca] <sup>-</sup>	Dicyanamide
DESY	Deutsches Elektronen Synchrotron
DFT	Density Functional Theory
[DMA] <sup>+</sup>	Dimethylammonium
dpp	Dipyrido[3,2-a:2'3'-c]phenazine
DSC	Differential Scanning Calorimetry
DUT	Dresden University of Technology
<i>e.g.</i>	Exempli gratia
$\epsilon$	Strain
<i>esp.</i>	Especially
FT-IR	Fourier-transformed Infrared Spectroscopy
<i>G</i>	Free energy
GPa	Gigapascal
<i>H</i>	Enthalpy/Magnetic field
HKUST	Hong Kong University of Science and Technology
HOIP	Hybrid Organic-Inorganic Perovskite
<i>ib.</i>	Isobar
<i>i.e.</i>	Id est
<i>it.</i>	Isothermal
IUPAC	International Union of Pure and Applied Chemistry
<i>J</i>	Magnetic polarisation
K	Kelvin

kbar	Kilobar
LFSE	Ligand Field Stabilisation Energy
MIL	Matériaux de l'Institut Lavoisier
MK	Megakelvin
MOF	Metal-Organic Framework
NAC	Negative area compressibility
NLC	Negative linear compressibility
NLO	Non-linear optical effect
NMR	Nuclear Magnetic Resonance Spectroscopy
NTE	Negative thermal expansion
$\Omega$	Occupation states
$p$	Pressure
PBA	Prussian Blue Analogue
PCP	Porous Coordination Polymer
$p$ -DSC	Pressure DSC
[PPN] <sup>+</sup>	Bis(triphenylphosphine)iminium
PT	Phase transition
py	Pyridine
<i>resp.</i>	Respective
RUM	Rigid unit mode
$S$	Entropy
SBU	Secondary building unit
$\sigma$	Mechanical stress
SHG	Second-Harmonic Generation
$S_N2$	Substitution of second order
<i>spec.</i>	Specific
$T$	Temperature
TF	Tolerance Factor
TGA	Thermogravimetric analysis
TPa	Terapascal
$U$	Internal energy
UiO	Universitetet i Oslo
unconv.	Unconventional
$V$	Volume
ZIF	Zeolitic Imidazolate Framework



# List of Figures

- 2.1 Schematic of the structures of  $\text{Fe}_4[\text{Fe}(\text{CN})_6]_3$  (**a**) and  $\text{Ni}(\text{NH}_3)_2\text{Ni}(\text{CN})_4 \cdot 2\text{C}_6\text{H}_6$  (**b**) which illustrates the basic crystal structure of Prussian Blue and Hofmann clathrates.[17, 20] Note that in (**a**) incorporated water molecules and in (**b**) hydrogen atoms are omitted for clarity. Furthermore, for the structure in (**a**) possible vacant sites are randomly distributed and not explicitly shown. Colourcode: orange - Fe, dark gray - Ni, light gray - C, light blue - N, dark blue -  $\text{NH}_3$ . . . . . 6
- 2.2 The development from inorganic perovskites to hybrid and molecular perovskites. Shown is the cubic arrangement of the archetypical perovskite structure motif with the B-site cations painted in purple, the A-site cations in olive and the X-site anions in orange. On the left, the exchange of spherical A-site cations with molecules leads to hybrid perovskite structures, whereas on the right the evolution to molecular perovskites is achieved through the concomitant substitution of both A- and X-site ions with organic components. . . . . 12
- 2.3 Shown are the pseudocubic cells as structural diagram for  $\text{BaTiO}_3$  (**a**)[114] and  $[\text{BTea}]\text{Mn}(\text{C}_2\text{N}_3)_3$  (**b**)[115] with *BTea* = Benzyltriethylammonium. The stability of the perovskite motif is demonstrated as developed from the all-inorganic perovskite to the molecular one. Both phases can successfully be described by the Tolerance Factor approach. As molecular moieties in (**b**) introduce additional structural flexibility, various distortions lead to a symmetry lowering from cubic (left) to orthorhombic crystal system (right). Note that hydrogen atoms of the molecular structure are omitted for clarity. Colourcode: dark gray - Ti, purple - Mn, light gray - C, light blue - N, dark blue - Ba. . . . . 13
- 2.4 Cooperative rocking of the octahedra as rigid unit modes to explain negative thermal expansion behaviour in  $\text{ScF}_3$ . On heating, the bridging fluorine atoms show a large transverse component which in turn leads to a shortening of the Sc-Sc distance. Reprinted with permission from B. K. Greve, K. L. Martin, P. L. Lee, P. J. Chupas, K. W. Chapman, A. P. Wilkinson, *J. Am. Chem. Soc.* **2010**, 132, 44, 15496–15498. Copyright 2010 American Chemical Society. . . . . 16
- 2.5 Schematic representation of the deformation of a wine-rack type framework with a  $\beta$ -quartz-like network. The effect of elevated temperature is shown on the right (red), whereas an increase in pressure is illustrated on the left (blue). Note that the dotted lines are a guide to the eye to refer to the framework dimension at ambient conditions (middle panel). The design of the figure is inspired from ref. [182]. . . . . 18

- 2.6 Temperature-dependent structures for the different phases of  $[(\text{CH}_3)_3\text{NH}]\text{Mn}(\text{N}_3)_3$  with two phase transitions present from a monoclinic low-temperature to a rhombohedral high-temperature phase.[69] A sequential increase in disorder *i.e.* number of accessible microstates accounts for the larger configurational entropy. Note that the size ratio of the atoms shown are to emphasise on the A-cation and does not correspond to real atomic radii. Disordered positions are illustrated as half-filled. Colourcode: purple - Mn, gray - C, blue - N. . . . . 22
- 2.7 The development of order patterns along increasing degrees of freedom together with a structural diagram of a prototypical example with spherical ions in the simple  $\text{ReO}_3$ -structure (**a**) and in inorganic perovskites ( $\text{BaTiO}_3$ , **b**) to coordination networks with molecules on two positions as for  $[\text{DMA}]\text{Fe}(\text{HCOO})_3$  (*DMA* = dimethylammonium)[247] in **c** and finally the divalent cation/vacancy ordered  $[\text{DAB}]\text{Mn}_2(\text{H}_2\text{POO})_6$ [109] (**d**). . . . . 24
- 2.8 In **a**, 2D representations of molecular perovskite analogues are shown with a representative illustration of a columnar shift (left), an unconventional tilt (right) and the undistorted cubic aristotype (middle). In **b**, the three different possible binding modes for the coordination of formates and dicyanamides to metal centres, namely syn-syn, anti-anti and syn-anti, are displayed to emphasise on the different network geometries that are accessible when these type of linkers are used. The figures in **a** are inspired from schematics in ref.[132] . . . 25
- 2.9 The diversity of possible A-site and X-site ions to form molecular perovskites. In the top are structural diagrams for potential A-cations, whereas in the bottom all to date available X-anions are shown. Copyright 2020 Wiley. Used with permission from Li Wei, Alessandro Stroppa, Zhe-ming Wang, Song Gao, *Hybrid Organic-Inorganic Perovskites*, WILEY-VCH, Weinheim.[255] . . . . . 26
- 2.10 Schematic of the phase transition observed in  $[(\text{C}_3\text{H}_7)_4\text{N}]\text{Mn}(\text{C}_2\text{N}_3)_3$  at approx. 330 K.[278] The transformation from the low-temperature to the high-temperature phase is characterised by an increase in positional disorder on both the A- and X-site resulting in a large change of configurational entropy with a calculated value for the ratio of possible microstates of  $\Omega = 8$ . This eightfold order-disorder is accompanied with cationic displacement and columnar shifts in the low-symmetry phase, overall accounting for a large latent heat conversion during the phase transition. For simplicity reasons, all disordered positions are illustrated as filled, whereas hydrogen atoms are omitted. Colourcode: purple - Mn, gray - C, blue - N. . . . . 30
- 7.1 Precession images of a single crystal X-ray diffraction experiment for an exemplified monoclinic structure. Shown in **a**, **b** and **c** are the superimpositions in  $0kl$ ,  $h0l$  and  $hk0$  direction, respectively. The evaluation of the diffraction pattern ultimately provides a model for the postulated crystal structure of the investigated material. . . . . 110

- 
- 7.2 DSC curves of the molecular perovskite  $[(C_3H_7)_4N]Mn(C_2N_3)_3$  (top) and the polyether poly(oxyethylene)-1.000.000 (bottom) with emphasis on the thermal features at around 330 K. Despite the very similar temperature range, these signals correspond to different material properties. For both curves, the heat flow is shown as exo down. . . . . 111
- 7.3 In **(a)**, a diamond anvil cell with mounting bracket for use at the Diamond Light Source Ltd. extreme conditions beamline I15 is shown. Panel **(b)** displays a photograph of the experimental set-up for variable-temperature powder diffraction with capillaries including an attached cryosystem, taken at the powder diffraction beamline P02.1 of the Deutsches Elektronen-Synchrotron (DESY). . 112
- 7.4 2D diffractograms each recorded at a synchrotron facility. In **(a)**, the powder sample is investigated in a regular capillary set-up, whereas for **(b)** it is loaded into a plastic capillary for pressurisation experiments. Due to the fixed position of the sample in the pressure cell the resulting diffraction pattern (right) deviates from continuous rings. Note that the notch represents the beam stop and that the colour intensity from white to black resembles the intensity of the collected data. 113



# List of Schemes

7.1	Synthesis of quaternary ammonium salts <b>3</b> starting from ternary amines <b>1</b> and alky halides <b>2</b> with $R^x$ being alkyl moieties and $X$ representing a halide. . . . .	108
7.2	Synthesis of symmetric divalent quaternary ammonium salts <b>5</b> starting from ternary amines <b>1</b> and alky dihalides <b>4</b> with $R^x$ being alkyl moieties and $X^y$ representing halides. . . . .	108
7.3	Schematic of the mild-solution approach employed to synthesise dicyanamide-based molecular perovskites. Each precursor in aqueous solution is added to a batch vial which is then allowed to stand until crystalline material is formed. . .	109



# Abstract

Perovskite-type coordination networks have established themselves as an emerging material class in recent years. Formally, this material family represents a subclass of coordination polymers that follows the perovskite-type structure, in which molecular building blocks are incorporated both on the A- and the X-site. Thereby, a three-dimensional network is formed with an octahedral coordination of the metal centres, which are connected by ditopic molecular anions to span a void for accommodating a molecular cation for charge balancing. The large number of different possible combinations for the synthesis of a perovskite-type coordination network makes this class an interesting material platform, as small chemical changes can have large effects on the resulting material properties such as ferroelectrics, multiferroics or barocalorics amongst others, while the underlying perovskite topology remains untouched. The individual response of these different perovskite materials to external stimuli like pressure or temperature allows for a systematic study of the relationship of the structure and the respective property of the material. In addition, the common perovskite-type structural motif enables the application of concepts known from classical inorganic chemistry and facilitates their development towards these hybrid systems. The goal is to develop fundamental knowledge for design strategies towards targeted material properties. This doctoral thesis therefore deals with the subject of structure-property relations of perovskite-type coordination networks to crystal engineer these coordination polymers.

This dissertation gives in the beginning a review on the current status of different concepts to describe the stability of molecular perovskite-like phases (STUDY I). Then it is demonstrated that the chemical freedom of the molecular A-site cation can be exploited to specifically introduce target structural motifs into the perovskite-type coordination network, providing huge potential for the synthesis of manifold material structures (STUDY II). The incorporation of the customised cation 6-azaspiro[5.5]undecane ( $[ASU]^+$ ) produces the molecular perovskite  $[ASU]Cd(C_2N_3)_3$ , which crystallises in a polar space group at ambient conditions and exhibits an unusual irreversible phase transition when initially heated. Here, a special tilting mode in the structural framework is activated, which induces the polarity and results in a strong non-linear optical effect (NLO). By using the likewise new material series  $[(nPr)_3(CH_3)N]M(C_2N_3)_3$  with  $M = Mn^{2+}$ ,  $Co^{2+}$  and  $Ni^{2+}$ , in which the specifically prepared organic cation  $[(C_3H_7)(CH_3)N]^+$  is employed on the A-site (STUDY III), the existence of these irreversible phase transitions can be explained both with theoretical calculations and with experimental crystal structures. This leads to a new concept to describe tilt and shift polymorphs in molecular perovskites, which differ in the distortion pattern of the framework structure. After  $[(nPr)_3(CH_3)N]M(C_2N_3)_3$  goes through this phase transition, a reversible phase change behaviour is observed within the isostructural material series, with values for latent heat that show promising characteristics for

potential application as barocalorics. For this reason, further investigations use theoretical calculations based on density functional theory as well as experimental methods to provide an initial assessment of which extent the selection of the divalent metal cation affects the mechanical material properties, in particular the compressibility/bulk modulus (STUDY IV). It is shown that the bulk modulus depends on the phonon density of states of the  $[\text{MX}_3]^-$  framework with softer phonon modes correlating to lower bulk moduli. This could serve as a descriptor and parameter for potential application as barocaloric working medium when evaluating appropriate perovskite-type materials. The dissertation is complemented by the exploration of how synthetic freedom on the A-site can be applied to form materials beyond the  $\text{ABX}_3$  structure motif, and how these additional structural degrees of freedom in the perovskite material impact the response to external stimuli like pressure and temperature (STUDY V). By incorporating the divalent cations  $[\text{R}_3\text{N}(\text{CH}_2)_n\text{NR}_3]^{2+}$  ( $n = 4, 5$ ) as a template into a confining  $[\text{Mn}(\text{C}_2\text{N}_3)_3]^-$  framework, two adjacent coordination cages are chemically linked and act as a constrained unit, thereby installing new geometric degrees of freedom as herringbone or head-to-tail order pattern into the three-dimensional network. The resulting materials represent a new family of coordination polymers and are still formally derived from the perovskite structure, and demonstrate interesting mechanical properties such as linear negative thermal expansion (NTE) as well as negative linear compressibility (NLC).

The results of this thesis highlight the various opportunities for materials engineering in perovskite-type coordination networks. It is demonstrated how the chemical composition and structure determine the properties of the material. The molecular nature of the A-site cation is shown to offer great potential for the systematic investigation of the coordination networks as a material platform with regard to the response behaviour to external stimuli such as pressure and temperature. It is presented how mechanical properties such as phase transitions as well as expansion and compression behaviour can purposefully be manipulated. The doctoral thesis provides new findings in the field of coordination polymers and classifies them in structural concepts, enabling correlations of chemical and geometric degrees of freedom to material properties, which promotes the development of functional materials towards barocalorics or materials with exotic expansion characteristics.



# Zusammenfassung

Koordinationsnetzwerke vom Perowskit-Typ haben sich in letzter Zeit als eine aufstrebende Materialklasse etabliert. Diese Materialklasse leitet sich von der übergeordneten Klasse der Koordinationspolymere ab und ist gekennzeichnet durch das Perowskit-Strukturmotiv, bei dem auf der A- sowie auf der X-Seite molekulare Komponenten eingesetzt werden. Dadurch wird ein dreidimensionales Koordinationsnetzwerk erzeugt, in dem oktaedrisch koordinierte Metallzentren durch molekulare Anionen, die zwei Koordinationsstellen aufweisen, verbunden werden und in der entstehenden Lücke ein weiteres molekulares Kation zum Ladungsausgleich beheimatet wird. Aufgrund der großen Anzahl an verschiedenen Kombinationsmöglichkeiten zur erfolgreichen Synthese eines perowskitartigen Koordinationsnetzwerks stellt diese Klasse eine interessante Materialplattform dar, da kleine chemische Änderungen innerhalb der Zusammensetzung große Auswirkungen auf die Materialeigenschaften haben können, während die zugrundeliegende Topologie unverändert bleibt. Diese Modularität ist der Grund, weshalb "molekulare Perowskite" eine stark untersuchte Klasse an funktionalen Materialien darstellen, die großes Potenzial in diversen Anwendungsgebieten wie Ferroelektrika, Multiferroika oder Barokalorika neben anderen weiteren einstellbaren mechanischen Eigenschaften zeigen. Die individuelle strukturelle Antwort dieser verschiedenen Perowskit-Materialien auf äußere Einflüsse wie Druck oder Temperatur ermöglicht eine systematische Untersuchung der Beziehung zwischen der Struktur und der jeweiligen Eigenschaft des Materials. Darüber hinaus ermöglicht das gemeinsame Strukturmotiv die Anwendung von klassischen anorganischen Konzepten auf die Strukturchemie der Koordinationsnetzwerke und erleichtert deren Anpassung an diese hybridischen Systeme. Die Dissertation befasst sich daher mit dem Thema der Struktur-Eigenschafts-Beziehungen von Koordinationsnetzwerken mit Perowskit-Struktur.

Die Thesis gibt zunächst einen Überblick über den aktuellen Stand der verschiedenen Konzepte zur Beschreibung der Stabilität molekularer perowskitischer Phasen (STUDIE I). Anschließend wird gezeigt, dass die chemischen Freiheitsgrade des molekularen A-Kations ausgenutzt werden können, um gezielt strukturelle Motive in das Koordinationsnetzwerk einzubringen. Dies bietet enormes Potenzial für die Darstellung von vielfältigen Materialstrukturen (STUDIE II). Der Einbau des gezielt hergestellten Kations 6-azaspiro[5.5]undecan ( $[\text{ASU}]^+$ ) führt zu einer molekularen Perowskitphase  $[\text{ASU}]\text{Cd}(\text{C}_2\text{N}_3)_3$ , die bei Umgebungstemperatur in einer polaren Raumgruppe kristallisiert und beim erstmaligen Erhitzen einen ungewöhnlichen Phasenübergang irreversibler Natur zeigt. Dabei bewirkt die Aktivierung einer speziellen Verzerrungsmodi im Strukturgerüst die Polarität, die in einem starken nicht-linearen optischen Effekt (NLO) resultiert. Mithilfe des ebenfalls gezielt hergestellten organischen Kations  $[(\text{C}_3\text{H}_7)(\text{CH}_3)\text{N}]^+$ , das ebenso erfolgreich in ein perowskitartiges Koordinationsnetzwerk der Zusammensetzung  $[(n\text{Pr})_3(\text{CH}_3)\text{N}]\text{M}(\text{C}_2\text{N}_3)_3$  mit  $M = \text{Mn}^{2+}$ ,  $\text{Co}^{2+}$  und  $\text{Ni}^{2+}$  implementiert wird (STUDIE III),

kann die Existenz dieser irreversiblen Phasenübergänge sowohl durch theoretische Berechnungen, als auch anhand experimenteller Kristallstrukturen erklärt werden. Es wird darauf aufbauend ein neues Konzept zu Polymorphen in molekularen Perowskiten, die sich durch die Verzerrungsmuster der Gerüststruktur unterscheiden, eingeführt. Nach Durchlaufen dieses Übergangs für  $[(n\text{Pr})_3(\text{CH}_3)\text{N}]\text{M}(\text{C}_2\text{N}_3)_3$  bildet sich in den isostrukturellen Materialien ein reversibles Phasenwechselverhalten aus, dessen Kennwerte vielversprechende Einsatzmöglichkeiten als Barokalorika aufweisen. Daher wird in einer weiteren Untersuchung mit theoretischen Berechnungen, die auf der Dichtefunktionaltheorie basieren, sowie experimentellen Methoden eine erste Einschätzung abgegeben, inwieweit sich die Auswahl des zweiwertigen Metallkations auf die mechanischen Eigenschaften, insbesondere auf die Kompressibilität, auswirken (STUDIE IV). Es wird aufgezeigt, dass der Kompressionsmodul von der Zustandsdichte der Phononen des  $[\text{MX}_3]^-$ -Gerüsts abhängt, wobei weichere Phononenmoden zu einem niedrigeren Kompressionsmodul führen. Dieser könnte für zukünftige Fragestellungen im Bereich der Anwendung als barokalorisches Arbeitsmedium daher eine wichtige Kenngröße zur Evaluierung der Materialien darstellen. Ergänzt wird die Dissertation durch die Fragestellung, inwieweit die synthetischen Freiheitsgrade auf der molekularen A-Seite genutzt werden können, um Materialien jenseits des  $\text{ABX}_3$ -Strukturmotivs herzustellen und wie sich diese zusätzlichen geometrischen Freiheitsgrade innerhalb der Perowskit-Materialstruktur auf das Verhalten in Bezug auf Einflüsse wie Temperatur und Druck auswirken (STUDIE V). Durch Einbau der zweiwertigen Kationen  $[\text{R}_3\text{N}(\text{CH}_2)_n\text{NR}_3]^{2+}$  ( $n = 4, 5$ ) als Vorlage in ein umschließendes  $[\text{Mn}(\text{C}_2\text{N}_3)_3]^-$  Gerüst werden zwei benachbarte Koordinationskäfige chemisch verbunden und fungieren somit als Einheit, sodass neue geometrische Freiheitsgrade als Fischgräten- oder lamellenartiges Ordnungsmuster innerhalb des dreidimensionalen Netzwerks eingebaut werden. Die resultierenden Materialien stellen eine neue Familie von Koordinationspolymeren dar und leiten sich formal weiterhin von der Perowskit-Struktur ab. Sie zeigen interessante mechanische Eigenschaften wie uniaxiale negative thermische Expansion (NTE) sowie negative lineare Kompressibilität (NLC).

Die Ergebnisse dieser Arbeit behandeln die vielfältigen Möglichkeiten zur gezielten Materialherstellung in molekularen perowskitartigen Koordinationsnetzwerken. Dabei wird demonstriert, wie sich die chemische Zusammensetzung und damit einhergehend die Struktur auf die Eigenschaften der Materialien auswirken. Insbesondere die A-Kationen bieten großes Potenzial zur systematischen Untersuchung der Koordinationsnetzwerke als Materialplattform hinsichtlich des Antwortverhaltens auf äußere Einflüsse wie Druck und Temperatur. Zudem ist dargestellt, dass durch mechanische Eigenschaften wie z.B. Phasenübergänge, Expansion und Kompression das Materialverhalten gesteuert werden kann. Die Doktorarbeit liefert neuartige Ergebnisse im Bereich der Koordinationspolymere, ordnet diese in strukturelle Konzepte ein und gibt Einblicke in den Zusammenhang von chemischen und geometrischen Freiheitsgraden sowie den Materialeigenschaften, um funktionelle Materialien wie z.B. Barokalorika oder Materialien mit exotischem Ausdehnungsverhalten entwickeln zu können.

# 1 MOTIVATION

Research groups all around the world designate their field of work in one way or the other to research or engineering on "functional materials" with an emphasis on their synthesis and characterisation. In fact, this rather informal description of materials' research can be found in many different areas of modern chemistry research, and various classes of materials ranging from metals, ceramics or polymers to organic and pharmaceutical molecules with potential applications, *e.g.* in heterogeneous catalysis, polymer science, optoelectronics, ferroelectrics, energy storage or coatings and films can be included within this category. Therefore, a very general definition of the term "functional material" may be formulated as being any kind of substance that exhibits certain intrinsic properties for a particular application. One main goal in materials chemistry is to establish design principles towards functional materials with distinct properties and to look into substantial structure-property relationships, linking an identified material structure to a resulting material property. An important advantage of fundamental research in this context is the systematic identification of concepts and principles with the help of a predefined material platform, which might be applied across different material classes.

Vast examples exist to demonstrate that socio-political interests have a significant impact on the development of research priorities. Already back in ancient times, the most important discoveries that were made have steadily advanced the development of civilisation, for instance in the field of metallic alloys. As more robust utensils were needed, people started to look for ways to deliver stronger alloys. Even nowadays there is a direct correlation of technological challenges of society and inventions of materials science - new materials are the prerequisite for any technological progress. Today, however, aspects such as sustainability and recyclability play a very important role as well as in order to conserve natural resources like water, raw materials and energy, highly efficient production and fabrication procedures must be developed. Innovative novel materials are of particular importance here, because they are a key technology for achieving the ambitious objectives which have been set. In addition to energy conversion and storage materials, other important areas of current significance comprise medical advances and also microelectronics. Materials research therefore marks a decisive pacemaker to further develop important fields of technology. Seminal examples encompass for instance carbon fibres for lightweight construction, catalyst research for fuel cells and for the production of synthetic fuels, semiconducting materials for the conversion of solar energy to electricity, battery materials for high-performance mobile energy storage, as well as building materials for heavy-duty applications or sensor technology. Nevertheless, for all these ambitious goals, the daily job always begins in the laboratory. Fundamental research makes a major contribution to the principal investigation of a material's structure in order to be able to ultimately generate a functional material. It is through a deep understanding of the relationship of structure and

property, and clear guidelines and principles to establish these, that this knowledge can then be used to tackle coming research challenges.

The doctorate thesis picks up on this thoughts and aims to make a significant contribution to research on functional materials, in specific focusing on structure-property relationships in perovskite-type coordination networks. The work is motivated by the great capabilities that this material class shows for potential game change applications, *e.g.* with remarkable temperature- and pressure-driven tunable mechanical properties, as phase change materials in barocalorics or purposefully designed multiferroics among others. The document is structured that in chapter 2 an overview of the current state of theoretical background for the examined materials sheet is given, whereas chapter 3 leads into an accurate overview on the research questions and their motivation addressed in this thesis. In chapter 4, the research results are provided as original research papers and chapter 5 contains a final summary, evaluation and categorisation of the results.

# 2 CONTEXT OF PEROVSKITE-TYPE COORDINATION NETWORKS

## 2.1 The Categorisation of Coordination Polymers

The term "coordination polymer" describes a polymeric structure that has coordination sites as repeating units extending in 1, 2 or all 3 spatial dimensions.[1] Initially, the definition arises from the comparison of organic-inorganic polymeric compounds consisting of metal ions and coordinating ligands with organic polymers (macromolecules), *i.e.* the linking of organic repeating units by covalent bonds.[2] In doing so, some distinct differences should be pointed out. While, for example, the solid state structure of a coordination polymer is described as that of an infinite network, organic polymers have different chain lengths and are accordingly characterised on the basis of a molar mass distribution.[3] Therefore, coordination polymers are often crystalline materials with a long-range order, defined topology and distinct crystal structure, whereas organic polymers (when crystallised) are often referred to as "semi-crystalline", which is then determined by the degree of crystallinity.[2, 4] However, the crystalline nature of coordination polymers is not mandatory according to their IUPAC definition.[1] In contrast, in the liquid state coordination polymers are usually dissolved through dissociation into their individual building blocks, while dissolved polymers still consist of the solvated macromolecules. The classification of a compound as coordination polymer itself implies no information about its structural organisation beyond the coordinating character. There are many different types of structures with different connectivities that a coordination polymer can adopt. Therefore, in order to provide a conceptual overview of the development of coordination chemistry from rather simple coordination complexes towards more-dimensional coordination polymers or coordination networks, a few important milestones are presented below.<sup>§</sup> The results of this dissertation consider material structures whose underlying atomic arrangement follows the perovskite-type structure. Throughout the thesis, the addressed materials are henceforward denoted as "perovskite-type coordination networks", by default stating the three-dimensional character of the network structure. Synonymously, the phrase "molecular perovskite" may be used, which emphasises on the use of molecular building blocks both on the A- and X-site of the perovskite composition. In this way, the coordinating linker molecules act as bridges which

---

<sup>§</sup> Despite the fact that according to IUPAC a hierarchical terminology is available for the classification of coordination polymers,[1] these terms are sometimes used in a sloppy manner. In this way, the conceptual distinction between "coordination polymer" and "coordination network" often becomes blurred. In this thesis, for the materials discussed the term "coordination network" is used consistently in order to emphasise on the three-dimensional structural nature of these crystalline materials.

in turn results in coordination networks. Therefore, the focus of this introduction will later be on the perovskite structure-type with emphasis on its prototypical templating for network materials. In the course of the different sections, pioneering materials will also briefly be discussed with focus on material properties that will be of special relevance in the context of this doctoral thesis. In addition, occasional excursions will try to embed the matters of subject and scientific findings into the context of everyday life.

## 2.2 The Development of Coordination Chemistry in Coordination Networks

In the solid state, crystalline materials arrange in ordered arrays of their constituents and form distinct crystal structures. These periodic arrangements can be specified with the packing of the respective components, which concern atoms, molecules or ions.[5] Thereby, the array is organised in the way to arrange polyhedrally with the urge to reduce its overall lattice energy, usually through distributing in highest symmetry possible. In this way, various combinations of symmetry elements can be obtained, which are ordered in 230 space groups. This provides the basis of modern inorganic structural chemistry for the elucidation of crystal structures.[6]

In this manner, underlying differences in bonding between the components lead to distinct properties of the material. For instance, covalent network materials such as diamond exhibit different characteristics than metals, salts or molecular crystals, *e.g.* H<sub>2</sub>O in the solid state, which are due to diverse cohesive forces. When describing solid state materials, idealised bonding models are therefore usually applied to understand the crystal structures. In practice, the situation is often more complex, for example when considering the contribution of covalent bonding character in ionic arrangements.[7] However in the following the model of an ideal ionic crystal will be employed in order to introduce the structural chemistry of coordination polymers. Due to the wealth of possible ions with different ionic radii and charges, a large variety of different crystal structures with manifold coordination geometries and coordination numbers can result.[5] These structures provide then the basis for distinct lattice types like the sodium chloride structure (AB), the rutile structure (AB<sub>2</sub>) or the aluminum fluoride structure (AB<sub>3</sub>) among others, whose positional arrangement is adopted by many different known crystalline materials and minerals. As a consequence, the ratio of the ionic radii of the respective elements is crucial for the formation of specific structure types, as distortions decrease the symmetry of the crystal (PAULING'S rules).[8] The concept of the spatial arrangement of ionic constituents is not only limited to inorganic spherical atoms. Hence, even more sophisticated building blocks such as charged molecules and coordination compounds can substitute the position of atomic point charges within the crystal structure.

**Excursus 1: Alfred Werner - the first inorganic chemistry Nobel laureate**

Alfred Werner's research was rewarded with the Nobel Prize in Chemistry in 1913 "in recognition of his work on the linkage of atoms in molecules by which he has thrown new light on earlier investigations and opened up new fields of research especially in inorganic chemistry".[9]

Nowadays, the term "Werner-type complexes" became an eponym for octahedral transition metal complexes containing amines and simple anions. It became furthermore apparent that "chemical complexes" play a major role in almost all areas of chemistry, in particular also in the bioinorganic enzyme chemistry.[10]

Early examples of chemical compounds with complex ions are *e.g.* Prussian blue with the complex anion hexacyanidoferrate(II/III)[11] or ferric(III) thiocyanate[12] with the multiatomic  $\text{SCN}^-$  anion which were commonly used as colour pigments already in early times. Up to that time an unified and substantial model to comprehensively understand the nature of these materials with complex components was still lacking. In 1893, the Swiss chemist ALFRED WERNER laid the foundation for the "coordination theory", a concept that has guided the further development of the chemistry of coordination compounds.[13] According to his theory - thus later simply called "coordination chemistry" - large molecular complexes can form, which are held together by so-called "primary" and "secondary valences".[10] In this way, the concept of octahedral coordination geometry can be credited to him for explaining stoichiometry and isomerism in coordination compounds. A large number of chemical phenomena that could not be explained by classical structural theory until then suddenly had reasonable explanations. In turn, in terms of this model definition by Werner, chemical complexes are structurally described with a central atom as the coordination center and ligands bonded to this atom. Coordination polymers (CPs) are thus a subset of these coordination compounds, which are obtained when using building blocks that have more than one coordination site as ligands. In this way, two or even more central atoms may be linked by so-called bridging ligands, and as a result a polymeric chain constructed from coordination centers (nodes) and ligands (linkers) is realised. Thus, if these bridging ligands are chosen wisely, multidimensional extended networks can be formed in one-, two-, and three-dimensional directions.[14]

Looking back in history, it becomes apparent that "Prussian Blue" and also the "HOFMANN clathrates"[15] (see Figure 2.1) are historical examples of 3D coordination polymers whose structural composition could then be conceptually understood after Werner's pioneering studies.[16, 17] Moreover, the coordination nodes in coordination polymers can consist of polynuclear centers such as metal clusters like in  $\text{Zn}_4\text{O}(\text{C}_8\text{H}_4\text{O}_4)_3$ ,[18] thereby further increasing the structural diversity and hence complexity of coordination polymers by allowing both the choice of linkers and the choice of coordination nodes to define the structure of the resulting material. This also enables the manipulation of intramolecular chemical interactions between the linker molecules by introducing specific coordination modes through multitopic linkers, as demonstrated with carboxylates.[19] All of these manifold degrees of freedom contribute to

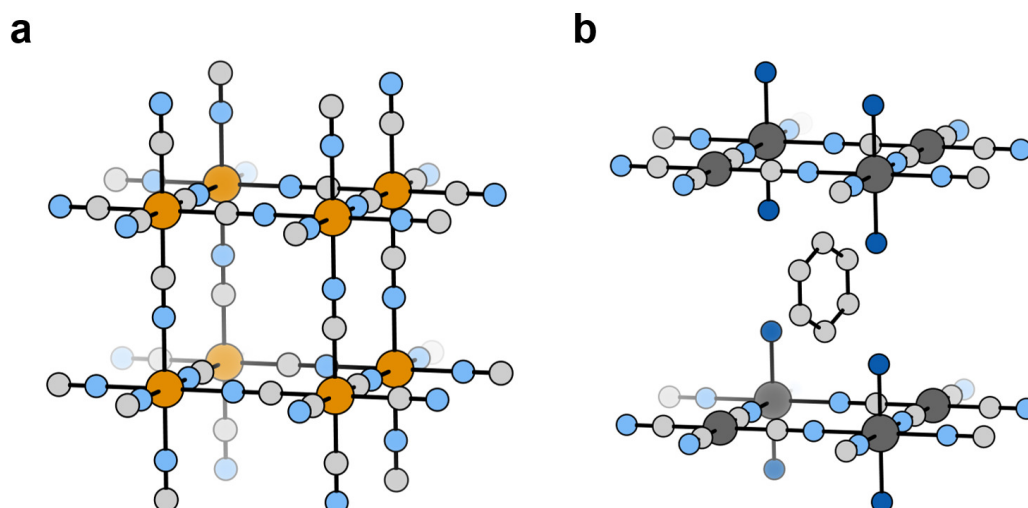


**Figure 2.1:** Schematic of the structures of  $\text{Fe}_4[\text{Fe}(\text{CN})_6]_3$  (a) and  $\text{Ni}(\text{NH}_3)_2\text{Ni}(\text{CN})_4 \cdot 2\text{C}_6\text{H}_6$  (b) which illustrates the basic crystal structure of Prussian Blue and Hofmann clathrates.[17, 20] Note that in (a) incorporated water molecules and in (b) hydrogen atoms are omitted for clarity. Furthermore, for the structure in (a) possible vacant sites are randomly distributed and not explicitly shown. Colourcode: orange - Fe, dark gray - Ni, light gray - C, light blue - N, dark blue -  $\text{NH}_3$ .

the many different material properties coordination polymers can exhibit, which can be readily engineered through linker and metal node chemistry.[21] In addition, the spatial arrangement of the coordination framework *resp.* the topology can have a decisive impact on macroscopic mechanical material properties.[22] Moreover, it should be emphasised that the stability of a cross-linked multidimensional framework can tolerate structural defects to a certain extent, which has led to the emergence of a research field specifically dedicated to the design of structural defects to study defect-induced properties of coordination polymers.[23–27] Despite the fact that most of the research on coordination polymers has been focusing on the crystalline state,[28] only very recently the applicability of coordination polymers has been extended even to the non-crystalline glassy state, an emerging research field of high scientific and technological relevance.[29] For instance, the formation of coordination polymer phases in the amorphous state has been demonstrated for materials such as  $\text{Zn}(\text{C}_3\text{H}_3\text{N}_2)$  (ZIF-4),[30, 31] the series  $[(\text{C}_3\text{H}_7)_4\text{N}]\text{M}(\text{C}_2\text{N}_3)_3$  (with  $M$  being  $\text{Mn}^{2+}$ ,  $\text{Fe}^{2+}$ ,  $\text{Co}^{2+}$ )[32] or the vacancy-rich  $\text{Cu}[\text{Fe}]_{2/3}$ ,[33] nicely illustrating the broad design possibilities that stem from the nature of coordination polymers. Therefore, arguably the most prominent subclasses of coordination polymers are metal-organic frameworks (MOFs),[34] Prussian blue analogues (PBAs),[35] and perovskite-type coordination networks.[36] While PBAs are mainly devoted to their propensity to exhibit low-energy dynamics towards interesting mechanical properties[37, 38] or to form vacancy arrangements,[39] MOFs represent porous coordination polymers (PCPs) which are characterised by the ability to be built from a large variety of different linkers and coordination nodes, the so-called secondary building units (SBU).[40, 41]



**Excursus 2: Metal-Organic Frameworks**

Metal-organic frameworks, a subclass of coordination polymers, are crystalline hybrid materials with potential voids *i.e.* porosity.[1] They are constructed from inorganic metal nodes and organic multitopic linker molecules, and show a high tailorability due to the nearly unlimited range of possible nodes and linkers, including options for post-synthetic modifications.[42] This leads to a portfolio of different MOF materials featuring large surface areas and therefore various material properties like gas storage or catalytic activity.

Prominent materials scientists such as RICHARD ROBSON,[43, 44] OMAR YAGHI,[45, 46] and SUSUMU KITAGAWA[47, 48] amongst others have been key contributors to the development of MOFs over the past three decades with topical structures like  $Zn_4O(bdc)_3$  (MOF-5),[18]  $Cu_3(btc)_2$  (HKUST-1)[49] or  $Cr(OH)(bdc)$  (MIL-53)[50] being seminal examples in the field. Further prevalent keywords that are pertinently associated with MOFs include "reticular synthesis", the assembly of rigid molecular building blocks into ordered structures,[51] and "structural flexibility".[52]

This can generate potential voids within the framework, which translates into a wealth of different network topologies and connectivity modes accessible with variable pore sizes of the structure, [53, 54] leading to research interests with potential applications in the field of gas storage,[55] separation,[56] sensing,[57] nonlinear optics[58, 59] or catalytic applications.[60] Perovskite-type coordination networks – hereinafter also referred to as molecular perovskites – in contrast all have in common that the underlying topology remains of the simple cubic  $\alpha$ -Po type, resulting in the basic connectivity of the metal center to the coordinating linker molecule being identical in all cases.[61] This gives a recurring structural motif that can be described by the general formula of the archetypical  $ABX_3$  perovskite structure-type, well-known from pristine inorganic perovskites.[62] Nevertheless, for perovskite-type coordination networks as for molecular frameworks, a large number of chemical and as a result structural degrees of freedom can be altered within this common structural motif.[63] In perovskite-type coordination networks this variability leads to a wide range of different materials properties such as (multi)ferroics,[64–66] improper ferroelectrics,[67] magnetic effects,[68, 69] or barocalorics.[70] Their chemical diversity resulting in manifold properties while maintaining a common building principle therefore provides the ideal precondition for a systematic study of potential structure-property relationships.

This dissertation hence focuses exclusively on perovskite-type coordination networks as a material platform in the following, with a brief introduction to the origin of perovskites as such and accompanied with a discussion of the many different possibilities for engineering perovskite-type network materials.

## 2.3 The Genesis of the Myth "Perovskite" as a Blueprint for Materials Structures

Crystalline materials with a perovskite architecture have already been known for over 150 years. In 1839 the German mineralogist GUSTAV ROSE described the mineral  $\text{CaTiO}_3$  for the first time,[71] found in the Ural Mountains, which he named after the Russian mineralogist LEV ALEKSEVICH VON PEROWSKI and which in the further history of mineralogical time became the eponym for the crystal structure classification "perovskite" with the original Strukturbericht designation "E2<sub>1</sub>". Curiously, the pristine mineral does actually not form the cubic perovskite structure that is nowadays well known, but instead crystallises in a distorted orthorhombic crystal system. An accurate structural determination however did not become possible until about 75 years later, when MAX VON LAUE and father and son BRAGG pioneered fundamental discoveries about the diffraction of X-rays on crystals in general and in detail established a methodology for appropriate elucidating crystalline structures.[72, 73] From this time, solid-state perovskite materials with the general composition  $\text{ABX}_3$  have significantly impacted the development of solid-state chemistry and condensed matter physics. In fact, there is hardly any other structural motif in today's materials science that combines such a variety of interesting phenomena as superconductivity,[74] dielectrics, ferroelectrics[75] or magnetoresistive effects[76] while preserving a unified underlying topology.[77] The success of this structure type is certainly also due to an increasing research interest as well as progress in synthetic methods in recent years towards the materials family of organic-inorganic perovskites, in which individual parts of the substantial framework, such as either the A- or X-ions or both, are replaced by organic molecular ions without altering the basic ionic connectivity.[78] Excitingly, these substitutions can have decisive impact on the properties of the resulting hybrid materials. However, before elaborating the special features of this emerging material class of organic-inorganic perovskites, it is reasonable to address the question first of why the class of perovskite materials itself actually has turned out to be such a successful blueprint for structural development.

From the pristine series of alkaline earth metal titanates, the geometric arrangement of an  $\text{ABX}_3$  perovskite can be generically described in terms of a basic skeletal structure derived from the related rhenium trioxide ( $\text{ReO}_3$ ) network structure, constructed from the B-site cations and the X-site anions. In this way, octahedra are formed consisting of a B-metal atom centre and six coordinating X-anions which are linked by their corner atoms in all three dimensions to span a three-dimensional framework. This framework shows the cubic primitive topology of the  $\alpha$ -polonium type and hosts the A-site cation in its cuboctahedral void generated by the parent B- and X-structure, which accounts for charge balancing to yield the overall neutral  $\text{ABX}_3$  material. In order to achieve charge neutrality for an  $\text{ABX}_3$  composition, many different permutations of elements are possible, so the charge distribution is not only limited to divalent anions as oxide combined with di- and tetravalent cations like in  $\text{CaTiO}_3$ . Instead, a large variety of compositions ranging from monovalent to pentavalent ions can be realised.

It is therefore important to emphasise that a perovskite structure consists of three ionic components which are in spatial relation through the two PLATONIC solids octahedron and cube. As a result, specific size ratios of the individual components must be maintained in order to generate a stable materials structure entity. Typically, the A-site positions are occupied by larger cations, while medium to smaller ones predominate on the B-site. In 1926, the Swedish mineralogist V. M. GOLDSCHMIDT studied the structure of inorganic perovskites and concluded that the sizes of the individual ions follow a specific relation.[79] This ratio is known as the "Tolerance Factor" and is defined as a quotient that relates the ionic radii of the different spherical elements to each other. More precisely, this corresponds to the ratio of the face diagonal to the  $\sqrt{2}$ -fold of the axial length of the respective unit cell, as shown in equation (2.1) below:

$$TF = \frac{r_A + r_X}{\sqrt{2} \cdot (r_B + r_X)} \quad (2.1)$$

Note that  $r_N$  symbolises the ionic radii of the respective parts A, B, C and TF refers to the Tolerance Factor. Examining all the inorganic perovskites known at that time, Goldschmidt concluded that the stability range of the aforementioned structure was primarily within a tolerance of  $0.8 < TF < 1.0$ , which demonstrates the remarkable compositional flexibility of the perovskite crystal structure. If the value of  $TF = 1.0$  is exceeded, the materials often tend to form hexagonal structures with one-dimensional chains, while for a value below 0.8, other structures of *e.g.* rhombohedral symmetry such as the Ilmenite- or Corundum-type, named after the minerals  $\text{FeTiO}_3$  and  $\text{Al}_2\text{O}_3$ , are generally observed.[79] In the further course of the development of solid-state chemistry, the Tolerance Factor concept proved to be the central mantra for the elemental composition of inorganic perovskites. It has been exploited not only to predict the existence of previously unknown perovskite materials, but also to explain specific distortions of the crystal structure of certain materials. For example, phases with a Tolerance Factor close to one mainly form a highly symmetric cubic structure, while phases with Tolerance Factors considerably smaller than one are usually found to have low-symmetric, orthorhombic structures with tilted octahedral building blocks. These possibilities for structural flexibility of the underlying perovskite motif account for the wealth of different properties found in inorganic perovskite materials.

As a model example, the discovery of the crystal structure and the intriguing dielectric and ferroelectric properties of  $\text{BaTiO}_3$  during the mid-20th century initiated the growing interest in inorganic perovskites research (see Figure 2.3(a) for an illustration of the structure).[80, 81] A dielectric is a material in which the charge carriers are hardly moveable, but can be polarised by an external electric field. Thus, the term describes a material in which there is no intrinsic electrical conductivity.[82]

**Excursus 3: Bariumtitanate – a ferroelectric ceramic material**

Ferroelectric materials induce electric dipoles below a characteristic CURIE temperature, resulting in a spontaneous polarisation that can be reversed by the application of an external electric field. The dependence of the polarisation on the applied electric field strength thereby follows a hysteresis loop.[83] Ferroelectricity has its origin in cooperative atomic displacements causing a structure in one of the 10 polar crystal classes and is in principle similar in nature to ferromagnetism.[75]

BaTiO<sub>3</sub> was the first polycrystalline ceramic material discovered to exhibit distinct ferroelectricity. Studies on BaTiO<sub>3</sub> received particular attention during World War II to be a key strategic material with high dielectric properties for various military technologies.[84] The origin of the ferroelectric property lies in its structural phase transition behaviour, which includes three distinct phase transitions from cubic to tetragonal, orthorhombic and finally rhombohedral symmetry. The cooperative displacive shift of the Ti<sup>4+</sup> and the O<sup>2-</sup> ions to off-center positions relative to the Ba<sup>2+</sup> ion is then accountable for the appearance of spontaneous polarisation.[85]

Ferroelectric materials are widely used as dielectrics in ferroelectric capacitors, sensor materials or as gate materials in field-effect transistors.[75]

Referring again to BaTiO<sub>3</sub> and CaTiO<sub>3</sub>, which in fact do not form an ideal cubic perovskite structure at ambient conditions, the importance of the Tolerance Factor concept is demonstrated, as it explains the appearance of the distorted structures, enabling the special materials properties.[86, 87] In more detail, the smaller A-site cation, which does not fit the cuboctahedral void ideally, causes a distortion at lower temperatures and thus induces a lowering of the crystal symmetry (to tetragonal or orthorhombic). In this context, another important concept describing the structure of perovskites was established by GLAZER in 1972[88] and improved by HOWARD and STOKES in the 1990s,[89] outlining the underlying mechanisms for cooperative tilting of the octahedra. This description served later on as a vital tool for the targeted development of structural distortions, which are, after all, the basis for explaining specific materials properties. The perovskite motif thus represents a robust geometric arrangement for which many different combinations lead to a stable material structure. The great advantage comes with the fact that the stability can be understood using simple and reliable principles such as the Tolerance Factor concept, the classification of different tilt systems or the octahedral factor.[90] Moreover, these correlations are equally applicable to the interpretation of related structures such as double perovskites, Ruddlesden-Popper or Dion-Jacobson phases, which underlines the importance of the perovskite motif in the development of structural chemistry.[91–94]

## 2.4 The Perovskite Structure in Hybrid Materials

### 2.4.1 Hybrid Perovskites

In the last decade, hybrid materials featuring the perovskite structure motif, *i.e.* organic-inorganic perovskites, have likewise gained exceptional attention in the materials community. In these materials, individual parts of the  $ABX_3$  structure are replaced by molecular building blocks.[36] In principle, staying in this terminology, any material that consists of organic and inorganic parts becomes a hybrid material.[95] In the context of perovskites, however, it has become common practice to refer to the term "hybrid perovskites" usually for materials which bear an organic molecule only on the A-site, while the X-site is occupied by a halide anion.[96] The phases  $[\text{CH}_3\text{NH}_3][\text{PbI}_3]$ [97] and  $[(\text{NH}_2)_2\text{CH}][\text{PbI}_3]$ [98, 99] have been known already since the 1970s but did not reach a major breakthrough until then.[100] These halide-based hybrid perovskites have led to breath-taking discoveries in optoelectronics amongst others, manifesting a new paradigm in solar cell research.[101, 102] A lot of effort has been put into research concerning the understanding of the stability of these systems together with a detailed elucidation of the origin of the optoelectronic properties. Current subjects deal with the issue of replacing the B-site atom lead with less problematic metals and to achieve an increased long-term stability of the phases.[103]

In this context it is worth mentioning the diverse use of the phrase "hybrid perovskite" in the literature.[104, 105] While, in general terms, this could in principle be understood as hybrid material of any kind of composition featuring a perovskite structure, it was primarily utilised to denote the semiconducting perovskite-derived materials like  $[\text{CH}_3\text{NH}_3][\text{PbI}_3]$ .[106]

### 2.4.2 Molecular Perovskites

When molecular components are incorporated both on the A-site and on the X-site at once, the term "molecular perovskite" or "perovskite-type coordination network" is being used.[62] It highlights the three-dimensional coordination network as a subset of coordination polymers and the structural chemistry within this network as being classical donor-acceptor complex chemistry in nature, see Figure 2.2 for a schematic of the evolution from inorganic to organic-inorganic hybrid and molecular perovskites. For instance, in molecular perovskites protonated amines can be used on the A-site, whereas for anions mainly formates, *i.e.* salts of formic acid,[107] or cyanides[108] are the molecules of choice. Nevertheless, hypophosphite[109] and dicyanamide[110, 111] molecules are also becoming particularly popular on the X-site. In 2014, the concept of the Tolerance Factor as a size match criterion was successfully applied to organic-inorganic perovskites as well.[112] By estimating effective molecular radii, various combinations of monovalent organic cations with divalent metal centres and molecules as anions could be evaluated to calculate Tolerance Factors analogous to the original concept. The key challenge thereby was to develop an easy-to-use method to determine the effective sizes

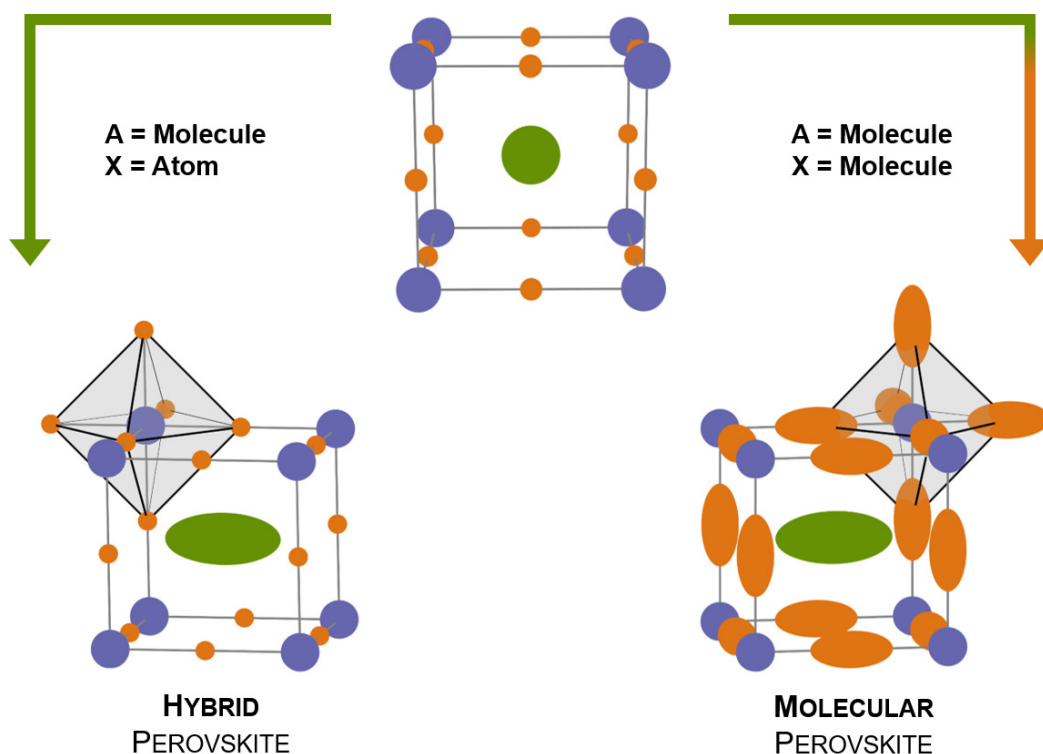


**Figure 2.2:** The development from inorganic perovskites to hybrid and molecular perovskites. Shown is the cubic arrangement of the archetypal perovskite structure motif with the B-site cations painted in purple, the A-site cations in olive and the X-site anions in orange. On the left, the exchange of spherical A-site cations with molecules leads to hybrid perovskite structures, whereas on the right the evolution to molecular perovskites is achieved through the concomitant substitution of both A- and X-site ions with organic components.

of cationic molecules such as methylammonium  $[\text{CH}_3\text{NH}_3]^+$  or formamidinium  $[(\text{NH}_2)_2\text{CH}]^+$  together with anisotropic anionic molecules such as formate  $[\text{HCOO}]^-$ , azide  $[\text{N}_3]^-$  or dicyanoaurate  $[\text{Au}(\text{CN})_2]^-$ . [113] It became evident that the stability criterion for the formation of the perovskite motif in molecular perovskites no longer applies as strictly as in the case of inorganic phases. Due to the increased structural flexibility of the multiatomic linker molecules, some arrangements are significantly distorted hence still form a stable perovskite phase. The concept therefore remains successful in predicting perovskite structure formation and trends in molecular perovskites. [111]

This is summarised in equation (2.2), for which the anisotropic nature of the molecules is taken into account as effective radii *resp.* height for cylindrically shaped anions:

$$TF_{ext.} = \frac{r_{A,eff.} + r_{X,eff.}}{\sqrt{2} \cdot (r_B + 0.5 \cdot h_{X,eff.})} \quad (2.2)$$

Following on from this extended approach, it was then feasible to screen the periodic table for new and promising A-B-X permutations that involve molecular building blocks, see Figure 2.3

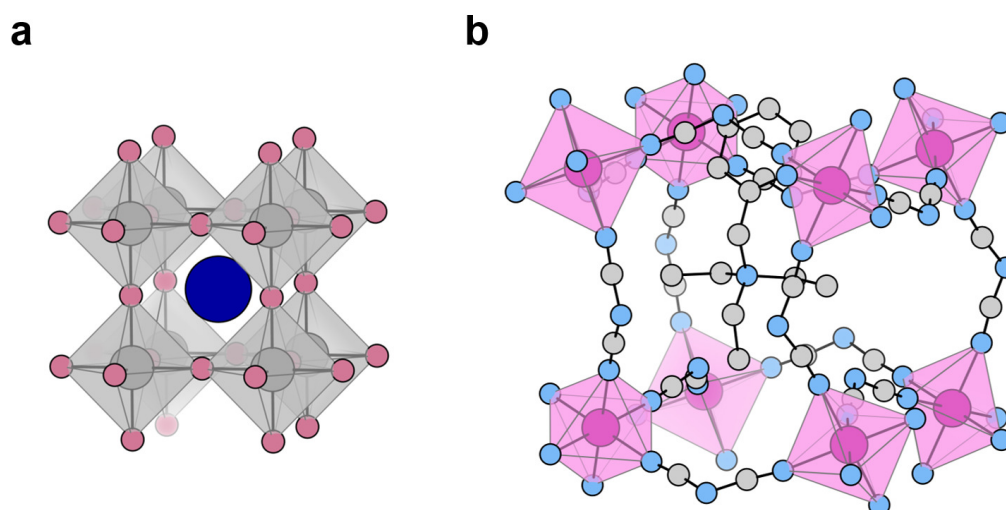


**Figure 2.3:** Shown are the pseudocubic cells as structural diagram for  $\text{BaTiO}_3$  **(a)**[114] and  $[\text{BTea}]\text{Mn}(\text{C}_2\text{N}_3)_3$  **(b)**[115] with *BTea* = Benzyltriethylammonium. The stability of the perovskite motif is demonstrated as developed from the all-inorganic perovskite to the molecular one. Both phases can successfully be described by the Tolerance Factor approach. As molecular moieties in **(b)** introduce additional structural flexibility, various distortions lead to a symmetry lowering from cubic (left) to orthorhombic crystal system (right). Note that hydrogen atoms of the molecular structure are omitted for clarity. Colourcode: dark gray - Ti, purple - Mn, light gray - C, light blue - N, dark blue - Ba.

for an illustration of a representative structural diagram for inorganic and molecular perovskite structures.[113] This resulted in a large number of contributions describing the discovery of novel perovskite phases that lie within the Tolerance Factor window for a stable perovskite structure.[116]

#### Excursus 4: Hybrid perovskites – a breakthrough in solar cell technology?

Hybrid perovskites, in particular elemental combinations based on lead as metal-cation and iodide as anion exhibit exceptional properties as photovoltaic absorbers for application as solar cell materials.[117, 118] The theoretical efficiency of such solar cells has been determined to be around 23%,[119, 120] challenging conventional cells based on silicon, which reach efficiencies up to 26%.[121] This demonstrates the enormous potential of these hybrid perovskites.[122, 123] When examining the origin of this phenomenon, the semiconducting behaviour of  $[\text{CH}_3\text{NH}_3][\text{PbI}_3]$  can be pinned down to the atomic connectivity within the perovskite structure, as the chemical bond linking the soft and diffuse iodide to the B-site cation shows a substantial covalent bond character.[124–126] In addition, the methylammonium cation is not spherical and larger than an atom, resulting in a polar moment due to the interaction with the anionic framework. This enables ferroelectric domains in  $[\text{CH}_3\text{NH}_3][\text{PbI}_3]$ , uniquely featured on the nature of the organic cation.[127]

In contrast to their all-inorganic counterparts, these organic-inorganic ones show intriguing properties like ferroelectric-to-paraelectric phase transitions or tunable mechanical response, as for example interactions of the molecular building blocks with the  $[BX_3]^-$  framework, *e.g.* hydrogen bonding caused by the presence of acidic protons of the molecular A-site cations, can have decisive impact on the resulting structure.[128–131] Altogether the accessible degrees of freedom are increased and structural flexibility is enhanced to activate symmetry-breaking distortions, possibly leading to a manifold phase transition behaviour.[132–135] The specifications behind these structural phase transitions, which account for the unique diversity of molecular perovskites, are discussed in more detail in the further course of this thesis.

## 2.5 Mechanical Properties of Molecular Perovskites

The mechanical properties of framework materials are usually studied in terms of their response towards external stimuli such as temperature and pressure. From a thermodynamic point of view, normally the system responds to a temperature decrease in an analogous way as to an (isotropic) pressure increase to counteract the change in GIBBS free energy caused by the external force.[136, 137] This is accomplished by structural adaptation of the material to minimise the total energy of the system, either in a flexible continuous way or by the aid of a structural phase transition. Often the same models are applied to describe the temperature- and pressure-dependent material response. In the majority the mechanistic explanation refers to the effect of temperature, which is also due to the fact that pressure-dependent studies are usually experimentally more demanding and require powerful radiation sources, whereas the systematic analysis of the temperature influence on a material can be realised in great detail with established methods.

### 2.5.1 General Remarks on Expansion and Compression in Materials

When a material is heated, the atoms begin to vibrate anharmonically around their equilibrium position *i.e.* levels of higher energy of the asymmetric potential well are excited, causing the distance between the atoms to be greater on average than in the original equilibrium state.[138] In the case of compression, the available volume becomes smaller and as a consequence the atoms come closer together.[139] Therefore, commonly an increase in temperature results in a volume expansion of the material, while an increase in isotropic (hydrostatic) pressure results in a volume shrinkage of the material. This is captured in equation (2.3) with  $\alpha_V$  representing the coefficient for volumetric thermal expansion at constant pressure (usually in  $\text{MK}^{-1}$ ),  $K_V$  the coefficient of volume compressibility at constant temperature (in  $\text{TPa}^{-1}$ ) and  $V$  ( $\text{\AA}^3$ ) the unit cell volume in relation to its  $T/p$ -dependant change  $\partial V$ . The bulk modulus  $B$  (denoted in GPa) is a further thermodynamic parameter to describe the mechanical response of a material towards hydrostatic pressure. Formally it is defined as the inverse of the compressibility  $K_V$  with



respect to the variation of pressure  $\partial p$  as a function of the cell volume change  $\partial V$  in relation to the ambient cell volume  $V_0$ . [140–142] It represents a property which ties the macroscopic behaviour with the microscopic structural arrangement in terms of the nature, organisation and strength of chemical bonds.

$$\alpha_V = \frac{1}{V} \cdot \left( \frac{\partial V}{\partial T} \right)_p \quad K_V = -\frac{1}{V} \cdot \left( \frac{\partial V}{\partial p} \right)_T \quad B = K_V^{-1} = -V_0 \cdot \left( \frac{\partial p}{\partial V} \right)_T \quad (2.3)$$

Likewise, the mechanical response of a solid can be decomposed to the three principal directions in space for their fractional component which in sum then account for total volume behaviour. For hydrostatic pressure, the force is applied uniformly from all three spatial directions. Consequently, a material always reduces its total volume, although in specific cases it is possible to observe an expansion in one or even two lateral directions. [140] Then this exotic material property is referred to as negative linear compressibility (NLC) or negative area compressibility (NAC). However, an increase in temperature can also cause volume contraction, which is then called negative thermal expansion (NTE). This can in principle involve all three principal axes, or it can propagate in only one or two lateral directions (uniaxial/biaxial NTE). [143] While volume shrinkage of a material with increasing temperature is possible, the mechanical stability criterion prevents overall volume expansion during hydrostatic compression. [140]

#### Excursus 5: NTE and NLC in a nutshell

Negative thermal expansion together with negative linear compressibility, *i.e.* materials contraction upon heating or expansion in one direction under equilateral compression, represent a counter-intuitive and therefore interesting material property. Thermal expansion, for example, plays a major role in the selection of construction materials or in the processing of materials, as different expansion coefficients in composite materials for example can cause stress cracking. In everyday life, this phenomenon is known from bridge construction, uneven temperature changes in brittle materials like glasses or dental care among other things, where expansion gap joints are purposefully installed to avoid stress cracks or glasses are altered in terms of their chemical composition to make them more robust. Negative compressibility is rapidly gaining interest, especially in recent years, since research on artificial muscle materials, for example, depends on how the materials used behave under contraction. Furthermore, materials with positive and negative expansion can be combined towards composites so that expansion and contraction compensate each other in the event of a change in temperature or pressure. Overall the composite material then does not change its volume at all or changes it in a precisely defined manner with respect to the external force.

Seminal examples of solid-state materials exhibiting NTE include ice at very low temperatures, [144]  $\beta$ -quartz at high temperatures [145] or scandium(III) fluoride  $\text{ScF}_3$ , [146] but probably the most prominent and well-studied example is zirconium tungstate  $\text{ZrW}_2\text{O}_8$ , [147] found in 1996, which from then on boosted research on NTE materials. The NLC effect was first found for the metal tellurium. [148]

## 2.5.2 Insights into Stimuli-Dependent Material Response

When looking for the microscopic origin of these phenomena and possibly comparing its absolute values, it should be emphasised that the magnitude of NTE and NLC effects is related to the proportionality of the  $V$ - to  $T(p)$ -data, which diverges discontinuously in case of a first order phase transition.[149] It is therefore crucial to differentiate if the effect is intrinsic to the structural motif, so to speak in the elastic regime,[150] or if it results from a reorientational phase change.[142] Whilst the model for the potential energy well of interatomic distances as mentioned above is suitable to rationalise positive thermal expansion, it cannot be employed to explain phase-specific negative expansion behaviour.[149] Instead, other ideas have been evolved to account for this NTE behaviour, which are generally either based on phonons, electronic transitions or framework hinging due to constrained mechanics.[140, 151, 152]

For example, low energy collective vibrations of polyhedra at certain frequencies as described through their phonon structures are assumed to be a potential origin of NTE.[153] Once atoms vibrate, vibration waves (phonons) travel through the lattice with the amplitude of the vibration increasing with increasing temperature. The occurrence of transverse vibration modes, which is the orthogonal displacement of bridging atoms, can then result in a contraction of two lattice atoms, if the underlying material structure is compatible so that the transversal modes dominate the longitudinal modes. This mechanism is sometimes referred to as the "guitar-string" or "tension" effect.[143] Especially in network materials *e.g.* zeolites,[154, 155] the introduction of rigid unit modes (RUM)[156] has proven to be a powerful tool for successfully explaining NTE and NLC effects, which also has its origin in (soft) phonon modes.[157] Originally established to understand displacive phase transitions in silicates,[156] the model also serves to explain NTE as well as NLC behaviour, as cooperative movement *resp.* correlated polyhedral tilts of undistorted rigid building blocks can be responsible for negative expansion and negative

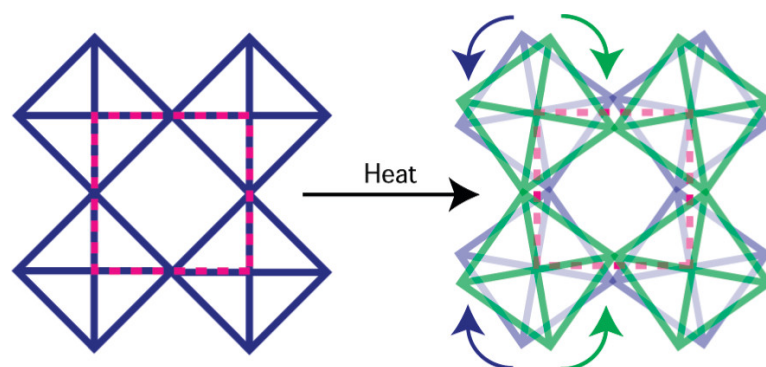


**Figure 2.4:** Cooperative rocking of the octahedra as rigid unit modes to explain negative thermal expansion behaviour in  $\text{ScF}_3$ . On heating, the bridging fluorine atoms show a large transverse component which in turn leads to a shortening of the Sc-Sc distance. Reprinted with permission from B. K. Greve, K. L. Martin, P. L. Lee, P. J. Chupas, K. W. Chapman, A. P. Wilkinson, *J. Am. Chem. Soc.* **2010**, 132, 44, 15496–15498. Copyright 2010 American Chemical Society.

compressibility, see Figure 2.4 for an illustration of the cooperative octahedral movement in  $\text{ScF}_3$  to be accountable for NTE.[146] It could be shown that this phonon-mediated behaviour for example causes the NTE effect in  $\text{ZrW}_2\text{O}_8$ , [158]  $\text{Zn}(\text{CN})_2$  [159] and many more oxide materials.[137] In general, it can potentially be applied to all kinds of flexible coordination networks and open framework materials that tolerate a coupled rotation of rigid units to generate transverse phonon modes.[160–164] Specifically to MOFs, it has been shown that in addition to collective phonon modes, local vibrations of the ligands contribute to the expansion behaviour by exploiting the available space of internal pore voids.[165]

Apart from these considerations based on phonons, further mechanisms involving electronic transitions like charge-transfer processes or magnetic coupling phenomena, can be attributed to be capable of explaining NTE effects.[142, 166] For instance, in materials which comprise different metal atoms like in  $\text{SrCu}_3\text{Fe}_4\text{O}_{12}$ , [167] temperature-dependent transitions involving changes in the metal valences by redistributing valence electrons can occur. This leads to a change in average bond lengths and potentially to an overall shrinkage or expansion of the cell volume.[168] In case of magnetostriction, [169] atypical changes in cell dimension are traced back to temperature-induced magnetic ordering with a competition of high-temperature states with large electronic entropy due to strong orbital overlap and magnetic low-temperature states with low electronic entropy as electrons are more localised.[170, 171] Typical materials that show this type of magnetostriction-driven NTE effect are phases from the family of manganese nitrides featuring the antiperovskite structure ( $\text{ANMn}_3$ ). [172, 173]

Especially in network materials and molecular crystals with a distinct mechanically constraining framework character, NTE and NLC behaviour can also be induced by the cooperative (re)arrangement of structural components and specific structural motifs itself.[139, 174] For instance, conformational changes, [175] geometric and structural flexibility, [176, 177] host-guest interactions [151] or rearrangement of packing motifs [140] can have a major impact on macroscopic materials properties.

### 2.5.3 Impact of the Framework Structure in Coordination Polymers

Perovskite-type coordination polymers with their pseudo-cubic coordination environment hold promising potential for exciting mechanical properties due to their multiatomic components embedded within the three-dimensional network structure, as properties can be tuned by the choice of different ingredients.[178, 179] The nature of these molecular building blocks provides accessible geometric degrees of freedom and as a result facilitates structural flexibility, while the underlying parent aristotype connectivity maintains the basic rigidity principles of the perovskite structure type.[61, 62] Given that organic X-anions generally do not have a perfect linear structure, the modular assembled 3D structure schemes are no longer following rectangular lattices. This results in a large number of examples of molecular perovskites deviating from the ideal cubic geometry through the formation of distorted structures by symmetry reduction.[132, 135] Furthermore, the encapsulated A-site molecule provides to some

extent independent structural freedom due to weak non-covalent interactions with the enclosing framework, which can lead to large (dis)order phenomena of the A-site molecule, thus providing a clear change in entropy-mediated driving force for potential structural phase transitions.[116] If however the adaptation to temperature or pressure occurs continuously within a flexible but constraining framework without a reorientational phase transition happening, the number of accessible structural response modes is limited. This can then lead to anisotropic stress-strain relations, continuous network distortions and structural disorder resulting in exciting macroscopic materials behaviour,[180, 181] characteristic for the respective phase, see Figure 2.5 for a mechanistic illustration of the effect of temperature and pressure on framework hinging. Common structural motifs in coordination polymers prone to exhibit these type of structural response resulting in NTE[183] and/or NLC[140] are for example the helical structure in bis(imidazolium) terephthalate,[184], hinging mechanisms attributed to the wine-rack type motif and the related honeycomb structure like in  $\text{Ag}_3[\text{Co}(\text{CN})_6]$ ,[185, 186]  $\text{Zn}[\text{Au}(\text{CN})_2]_2$ ,[187, 188]  $\text{InH}(\text{C}_8\text{O}_4\text{H}_4)_2$ [189] and the ammonium metal formates  $[\text{NH}_4][\text{M}(\text{HCOO})_3]$ ,[190, 191] or the herringbone motif such as in  $[\text{Fe}(\text{dpp})_2(\text{NCS})_2] \cdot \text{py}$  ( $\text{dpp}$  = dipyrido[3,2-a:2'3'-c]phenazine),  $\text{py}$  = pyridine)[192] and  $\text{Pd}(\text{C}_5\text{H}_6\text{O}_2)_2$ ,[193] all structure motifs that intrinsically bear directionality of elastic deformability. This is an usual behaviour of flexible framework materials and molecular crystals featuring a network structure predestined to component hinging and arises from the underlying shallow free energy landscape and the competitive nature of the hinge mechanism and the usual bond compression or expansion.[181, 194, 195] If this hinging force prevails, then NTE and NLC can occur. There are vast examples for temperature-

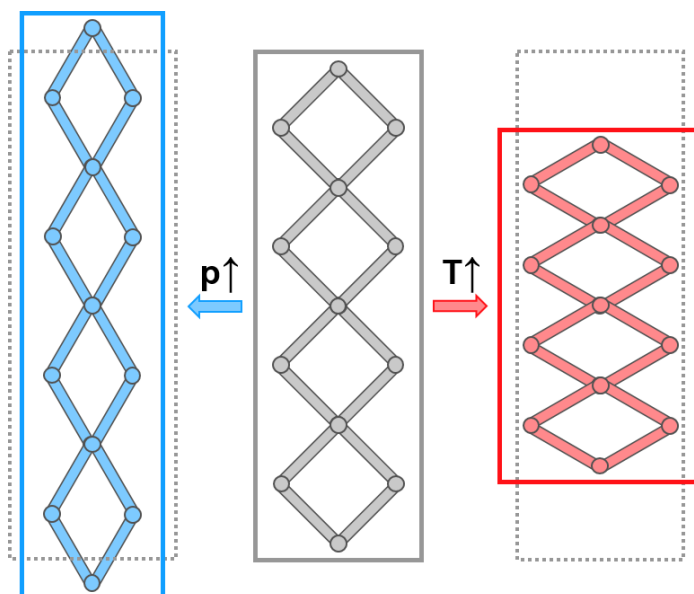


**Figure 2.5:** Schematic representation of the deformation of a wine-rack type framework with a  $\beta$ -quartz-like network. The effect of elevated temperature is shown on the right (red), whereas an increase in pressure is illustrated on the left (blue). Note that the dotted lines are a guide to the eye to refer to the framework dimension at ambient conditions (middle panel). The design of the figure is inspired from ref. [182].

and pressure-dependent studies in coordination polymers such as MOFs to study the role of topology or network geometry towards mechanical behaviour,[196–207] as well as studies that focus on the mechanical properties of perovskite-type coordination networks. For instance, in the series of alkylammonium metal formates  $[A][M(\text{HCOO})_3]$  with different B-site metals and A-site cations of different molecular anisotropy, a systematic analysis reveals the relationship of the asphericity of the organic cation and the framework flexibility towards hinging. Notably, the direction of framework response is determined by the A-site cation, as prolate and oblate shaped molecules constrain the framework hinging towards smaller or higher hinge angles upon temperature changes.[208] Besides that,  $[(\text{CH}_3)_4\text{N}]\text{Mn}(\text{N}_3)_3$  shows unusual thermal expansion when heated, as one principal axis evolves in terms of uniaxial negative expansion with coefficients that lie in similar range to formate-based perovskites.[209] Furthermore, despite pressure-dependent studies reveal only positive compressibilities, bulk moduli for selected formate-, [210–212] hypophospite-[213, 214] and dicyanamide-based [215, 216] molecular perovskites were experimentally determined and lie in the range of  $B = 24–27$  GPa for formates,  $B = 11–24$  GPa in case of hypophosphites and  $B = 6–8$  GPa for dicyanamides. These values are comparable to other crystalline coordination networks like MOFs, *c.f.*  $\text{Zr}_6\text{O}_4(\text{OH})_4(\text{ndc})_6$  (DUT-52,  $B = 17.0$  GPa), [217]  $\text{Al}(\text{NO}_2\text{-bdc})_2(\text{OH})$  (MIL-53(Al)<sub>NO<sub>2</sub></sub>,  $B = 7.3$  GPa) [218] or  $\text{Zr}_6\text{O}_4(\text{OH})_4(\text{NH}_2\text{-bdc})_6$  (UiO-66(Zr)-NH<sub>2</sub>,  $B = 25.2$  GPa) [219] and in general reflect the overall trend supported by chemical intuition that larger and thus more flexible coordination frameworks show less resistance to compression.[220]

#### 2.5.4 Order-Disorder Phase Transitions in Molecular Perovskites

In contrast to the above mentioned mechanical properties with regard to elastic rigid unit- and pattern-type movements, for properties related to a structural phase transition the origin of the transition lies in the difference of the free energy  $G$  of both phases. If the system is considered to be in thermodynamic equilibrium at the transition temperature, the phase with the lower free energy is more stable. This situation is described with the following equation (2.4):

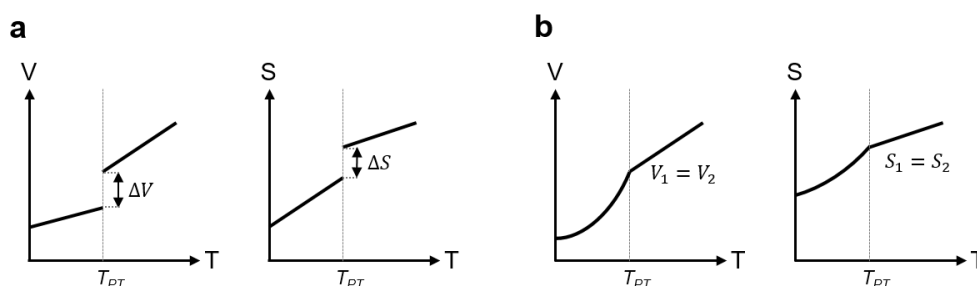
$$G = U - T \cdot S + p \cdot V - J \cdot H \cdot V - \sigma \cdot \varepsilon \cdot V \quad (2.4)$$

In this fundamental thermodynamic potential,  $U$  describes the internal energy,  $T$  the absolute temperature,  $S$  accounts for the entropy of the system,  $p$  denotes the external pressure and  $V$  the volume of the system. Additionally,  $J$  describes the magnetic polarisation,  $H$  the magnetic field,  $\sigma$  the mechanical stress and  $\varepsilon$  the strain.[221] The formula indicates that the free energy and with it the driving force of a phase transition may be manipulated not only by a change in temperature or pressure, but also by the application of a magnetic or electric field. For molecular perovskites, most of the structural phase transitions are a responsive behaviour to changes in temperature or pressure and are reversible in nature, as only a very few examples of irreversible perovskite-to-perovskite phase transitions are known to date.[109, 222]

**Excursus 6: Modern classification of phase transitions - short and crisp**

Phase transitions are ubiquitous phenomena in everyday life. Everyone is familiar with the states of matter "solid, liquid or gas" and their transformation sequence into each other, *e.g.* from ice to water and steam. Phase transitions are also commonly observed in solid-state physics, there usually occurring as solid-to-solid transformations related to symmetry changes of the structure. Hence, understanding the thermodynamics of these transitions is of great scientific interest, as oftentimes material properties can be attributed to the presence of phase transitions. In principle, there are two classes of transitions, which are categorised according to the way of how the state variables change at the transition point.

As can be seen in the schematic below (presented for a variation of temperature, the same accounts for pressure), for a phase transition of first order (panel **a**), the state variables such as  $V$  and  $S$  (and also  $H$ ) change discontinuously, *i.e.* the first derivatives become infinite at the transition point  $T_{PT}$ . Thereby latent heat is converted during the change of phase without a change in temperature. In daily life, this is known from the process of melting ice, as the temperature of ice-water does not change until all ice is melted. In case of a phase transition of second order (see panel **b** below), the state variables change homogeneously, so there is no difference in  $V$  or  $S$  (and  $H$ ) between the two phases at  $T_{PT}$ . Consequently, these transitions are continuous, a typical example being the reversible transition at the CURIE point in ferromagnetic materials.



Looking again at the fundamentals for the stability of a phase, the more common representation for the difference in free energy of the respective two phases at a distinct equilibrium, with the two intensive thermodynamic parameters temperature and pressure being constant at the transition, reduces therefore to:

$$\Delta G = \Delta U - T \cdot \Delta S + p \cdot \Delta V \quad (2.5)$$

From equation (2.5) it can be concluded that a change in free energy leading to a phase transition is associated with a pivotal change in the extensive properties of internal energy, entropy and volume. The initial empirical definition of a theory of phase transitions based on the Gibbs free energy as a function of thermodynamic parameters like temperature and pressure can be tracked back to the pioneering work of PAUL EHRENFEST.[223] Thereby, depending on the behaviour of the free energy and its derivatives with respect to specific thermodynamic quantities, phase transitions are classified into first order transitions (discontinuous) and second order transitions

(continuous). The mathematical representation for this second type of transitions is provided by the theory of LEV LANDAU,[224] in which based on symmetry changes the free energy is evolved by a TAYLOR expansion as a function of an order parameter. The value of the order parameter then indicates for the character of the phase transition.[225]

However, although most phase transitions in molecular perovskites, which are usually characterised by a change in symmetry and associated change in positional order (first-order transitions), can successfully be described by this theory, generally not all phase transitions in solids follow Ehrenfest's definition, such as the diverging behaviour of susceptibility in ferromagnetic transitions.[226, 227] Instead, particularly in the context of coordination polymers, the classification of phase transitions refers to the structural mechanism during the transition, which to some extent is certainly also reflected in the initial differentiation between first and second order transformations.[228] When only a slight displacement of atomic positions resulting in a distinct rearrangement of intramolecular interactions or small altering of bond lengths is responsible for a phase transition, it is referred to as "displacive phase transition".[229] Thereby, the change in symmetry of the two phases involved usually follows a group-subgroup relation derived from group-theoretical considerations.[89, 230] In contrast, if the transition requires a breaking and reformation of chemical bonds without a clear displacive pathway *i.e.* relies on a high activation energy, it is described as "reconstructive" in nature with no obvious symmetry relation between the phase structures.[231] As this kind typically comes with a change in topology and changes of atomic positions in the length scale of lattice parameters,[229] it is effectively not present in perovskite-type materials. Instead, most of the allotropic transformation of elements such as the transition from graphite to diamond[232] or from quartz to cristobalite[233] as well as selected transitions in various MOFs[31, 234–236] with a major reorganisation of the crystal structure are considered to be reconstructive.

The structural phase transitions in majority occurring in molecular perovskites maintain the topology of the perovskite-type network and are reversible,[116] which means they are characterised by distinct changes in latent heat and small hystereses (first order) *i.e.* positional displacements of atoms. In particular, the presence of hydrogen bonds as strong enthalpic interactions between the A-site cation and the negatively charged  $[BX]_3^-$  framework, unique to molecular components, is of special relevance in this context. Breaking these interactions causes a rearrangement on the atomic level in most cases, which usually results in a change of the crystal structure and the unit cell symmetry.[128, 131] This change in symmetry is reflected in a change of the contribution of configurational entropy to the total entropy of the system. Thus, the dynamics of a phase transition is characterised by the interplay of enthalpic and entropic factors. In addition, the incorporation of molecular building blocks into the  $ABX_3$  structure generates thermally accessible low energy lattice modes, which can further be altered through the variation of coordinated B-site metals *i.e.* the ligand field stabilisation energy (LFSE).[237, 238] These phonon modes provide a comparatively high lattice entropy which, together with configurational and rotational entropy, is then in balance with hydrogen bonding, if it is present.

This feature is intrinsic to the nature of molecular perovskites and therefore explicitly differentiates hybrid materials with a perovskite structure from inorganic ones.[239–241] This demonstrates the many possibilities that exist to manipulate the thermodynamics of structural phase transitions in molecular perovskites to systematically emphasise towards certain material properties, which in fact oftentimes have their origin in the presence and characteristics of the phase transition. In principle, enthalpic contributions can therefore be effectively influenced by the choice of appropriate building blocks, for example *via* implementing molecules with acidic protons as precondition for hydrogen bonding.[68, 128, 131] However, besides that clear structure-to-property correlations on how to specifically manipulate the thermodynamics of a phase transition towards large enthalpy differences (latent heat) are still lacking.

Nevertheless, a considerable entropic contribution to the total entropy and thus the free energy of a phase and its change during a transition is accessible by the chemical freedom of the A-site cation and to some extent also of the X-site anion. An increase in the number of possible occupation states of the molecule allows this proportion to be maximised, enabling the occurrence of different positional configurations of the A-site (or X-site) molecule within the perovskite cage geometry, a prerequisite to exhibit a large variety of order-disorder transitions.[64, 209, 242, 243] Hence, the larger the pseudocubic void of the perovskite host network, the larger the guest molecules that can be incorporated, so a high contribution to configurational entropy is usually accompanied by a high degree of structural complexity.[244, 245] This is reflected in equation

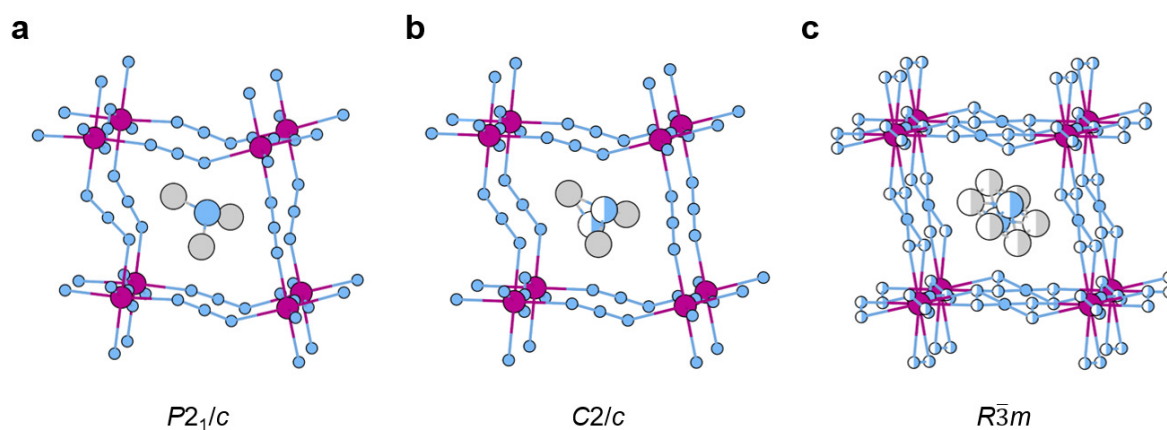


**Figure 2.6:** Temperature-dependent structures for the different phases of  $[(\text{CH}_3)_3\text{NH}]\text{Mn}(\text{N}_3)_3$  with two phase transitions present from a monoclinic low-temperature to a rhombohedral high-temperature phase.[69] A sequential increase in disorder *i.e.* number of accessible microstates accounts for the larger configurational entropy. Note that the size ratio of the atoms shown are to emphasise on the A-cation and does not correspond to real atomic radii. Disordered positions are illustrated as half-filled. Colourcode: purple - Mn, gray - C, blue - N.



(2.6), as the number of accessible microstates of a phase  $\Omega$  multiplied with the universal gas constant  $R$  estimates the configurational entropy  $S_{config.}$  of the system:

$$S_{config.} \approx R \cdot \ln(\Omega) \quad (2.6)$$

A representative example of a sequence of such order/disorder transitions in an azide-based molecular perovskite structure with a stepwise increase of the configurational entropy of the A- and X-site molecule is illustrated in Figure 2.6. Here,  $[(\text{CH}_3)_3\text{NH}]\text{Mn}(\text{N}_3)_3$  undergoes two distinct phase transitions from a low-temperature phase to an intermediate and then to a high-temperature phase.[69] Upon heating, the monoclinic structure in  $P2_1/c$  converts into an intermediate-temperature phase with  $C2/c$  symmetry at around 330 K, accompanied with a moderate increase in disorder at the A-site cation, see panel **a** and **b**. Further heating (at 360 K) then transforms the material into a rhombohedral structure with space-group  $R\bar{3}m$ , specified with pronounced disorder both at the A-site molecule as well as the azide linker, visualised in panel **c**. A potential driving force for the phase transitions is provided by the formation of  $\text{N}-\text{H} \cdots \text{N}$  hydrogen bonds between the guest molecule and the host network, which may be rearranged during the process of symmetry breaking. In this regard, the cation-dependent phase transition properties and magnetic orderings of this molecular perovskite family in the range from the small and acidic proton-enriched  $[\text{CH}_3\text{NH}_3]^+$  to the big and proton-deficient  $[(\text{CH}_3)_4\text{N}]^+$  could be probed, as the retaining flexible perovskite motif allows for different guest cations.[69] However, it should be emphasised that not all perovskite-type materials with hydrogen bonding interactions exhibit phase transitions. A detailed analysis of the two molecular perovskites  $[\text{C}(\text{NH}_2)_3]\text{Mn}(\text{HCOO})_3$  and  $[(\text{CH}_2)_3\text{NH}_2]\text{Mn}(\text{HCOO})_3$  for instance reveals six *resp.* four hydrogen bonds between the A-site cation and the anionic formate-framework with impacts on the thermal expansion and atomic displacement behaviour, but with no indications of any phase transitions present before thermal composition occurs.[128] So, ultimately it is the complex balance between entropic and enthalpic host-guest interactions to control and tune the mechanical properties and phase transition characteristics of perovskite-type coordination network materials.

As mentioned before, the size of the perovskite host network inherently correlates with the variety of potential A-site guest cations. Especially when seeking for compositions with designed phase transitions to enable a specific material property, a huge free energy difference between the phases is often desired. Therefore, a survey of the large diversity of the different molecular perovskite structures known to date is presented in the following.

## 2.6 The Diversity of Molecular Perovskites

In the previous chapters it has been comprehensively elaborated that perovskite-type coordination networks represent an important and versatile class of coordination polymer materials. Arguably the most outstanding feature of the perovskite structure is the great thermodynamic

stability of the topological arrangement of the individual components, while the actual crystal structure itself is flexible and thus dynamically unstable.[246] This modular building block concept therefore leaves plenty of room for a variety of different permutations with vast possibilities for directing the structural behaviour of the material and its resulting properties. In particular, the use of molecular building blocks in both the A- and X-positions offers numerous potential geometric degrees of freedom towards targeted material design, thereby generating a large chemical variability. For instance, when considering the structural ordering from the simple Rhenium trioxide structure towards the rather complex situation in perovskite-type coordination networks, the patterns of inorganic and molecular perovskites map milestones in its evolution with a sequential increase in structural diversity, as shown in Figure 2.7. For  $[\text{DAB}]\text{Mn}_2(\text{H}_2\text{POO})_6$  (panel **d**,  $\text{DAB} = 1,4\text{-diazabicyclo}[2.2.2]\text{octane-1,4-dium}$ ), a small divalent molecular cation occupies the position of the A-site, accompanied with an empty void to account for total charge balance within the host framework. This results in a double perovskite structure with a sequential ordering of cation and void, in which the pattern of vacancies describes the additional structural degree of freedom.[109]

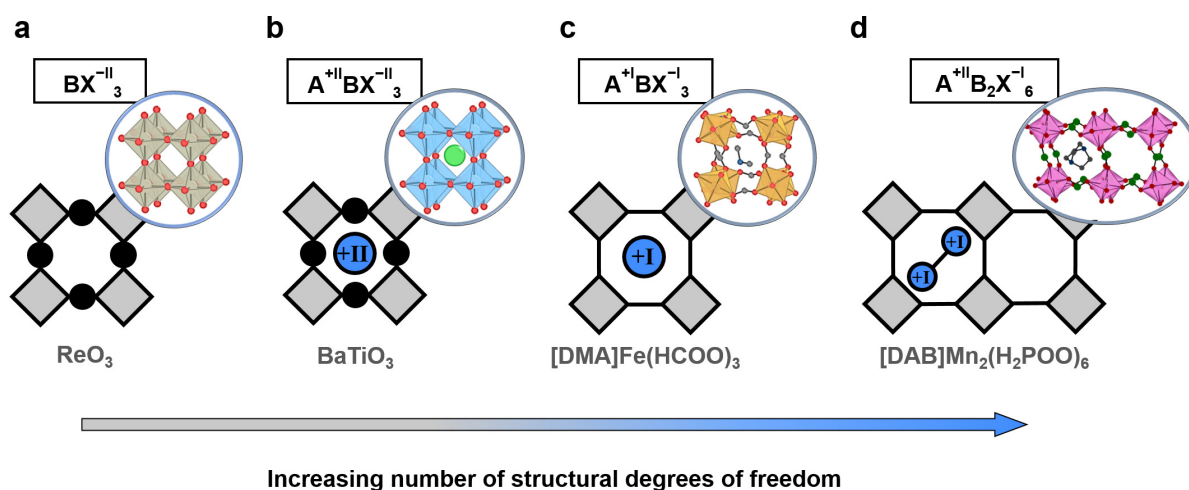


**Figure 2.7:** The development of order patterns along increasing degrees of freedom together with a structural diagram of a prototypical example with spherical ions in the simple  $\text{ReO}_3$ -structure (**a**) and in inorganic perovskites ( $\text{BaTiO}_3$ , **b**) to coordination networks with molecules on two positions as for  $[\text{DMA}]\text{Fe}(\text{HCOO})_3$  ( $\text{DMA} = \text{dimethylammonium}$ )[247] in **c** and finally the divalent cation/vacancy ordered  $[\text{DAB}]\text{Mn}_2(\text{H}_2\text{POO})_6$ [109] (**d**).

Formally, in perovskite-type coordination networks the incorporation of multiaatomic anions induces additional ways of geometric connectivity, since these molecules serve not anymore to link the octahedra in a corner-sharing, but in a corner-bridging fashion, and as such breach the limits of the cooperative tilting schemes as established for inorganic perovskites by Glazer.[88] This results in two different binding modes in "syn"- and "anti"-conformation of the linker coordinating to the metal atom.[68, 248] Moreover, it allows for unconventional and forbidden tilts and columnar shifts to appear within the three-dimensional material structure and provide

further structural ramifications that are not possible in inorganic perovskites, schematically displayed in Figure 2.8.[132, 135] These distortion factors can be exploited for the rational design of (improper) ferroelectrics amongst others.[67] As a consequence, it is rather difficult to systematically categorise the large number of molecular perovskite phases already reported in the literature, as structural features not necessarily correlate with material properties.

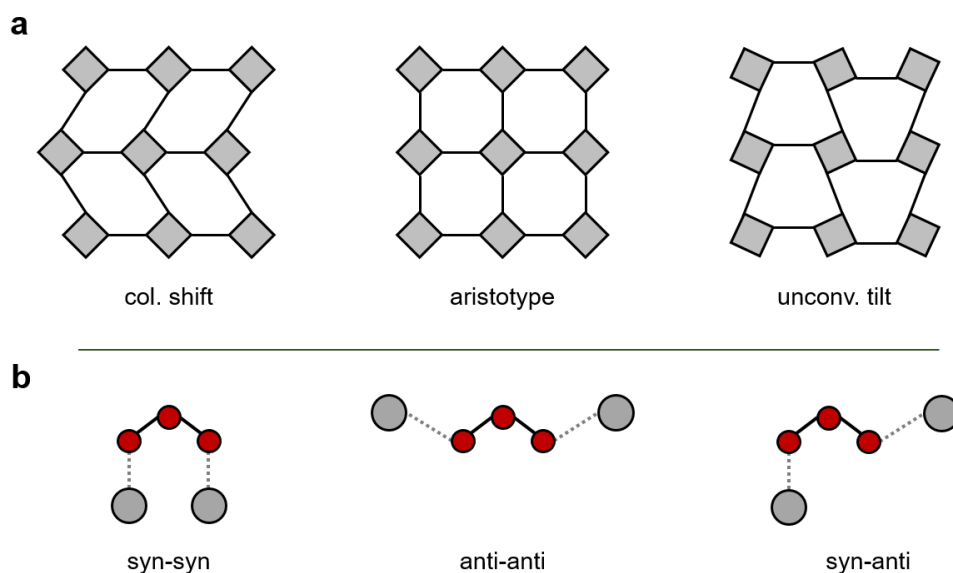


**Figure 2.8:** In **a**, 2D representations of molecular perovskite analogues are shown with a representative illustration of a columnar shift (left), an unconventional tilt (right) and the undistorted cubic aristotype (middle). In **b**, the three different possible binding modes for the coordination of formates and dicyanamides to metal centres, namely syn-syn, anti-anti and syn-anti, are displayed to emphasise on the different network geometries that are accessible when these type of linkers are used. The figures in **a** are inspired from schematics in ref.[132]

However, the wealth of perovskite-type coordination networks are typically divided into families according to the X-site anion respectively the size of the pseudocubic repeating units, whose void then accommodates A-site cations of different molecular sizes and symmetry. In this context, Figure 2.9 reviews all the building blocks known so far that have been used to form molecular perovskites of the  $ABX_3$  stoichiometry. Among the various X-site anions possible, currently formates, azides and dicyanamides represent the most intriguing perovskite families, with respectively interesting properties in the field of ferroelectrics[64, 249] and multiferroics[65, 250], ferroelastics[251] and magnetic ordering[69, 252] and tunable phase transition properties[242, 253], although hypophosphites and particularly cyanides are also receiving considerable attention. Molecular perovskites based on hypophosphite exhibit a wide range of unconventional tilts and shifts leading to unusual order patterns and distortion vectors, potentially paving the way to functional materials through distinct symmetry breaking mechanisms.[254]

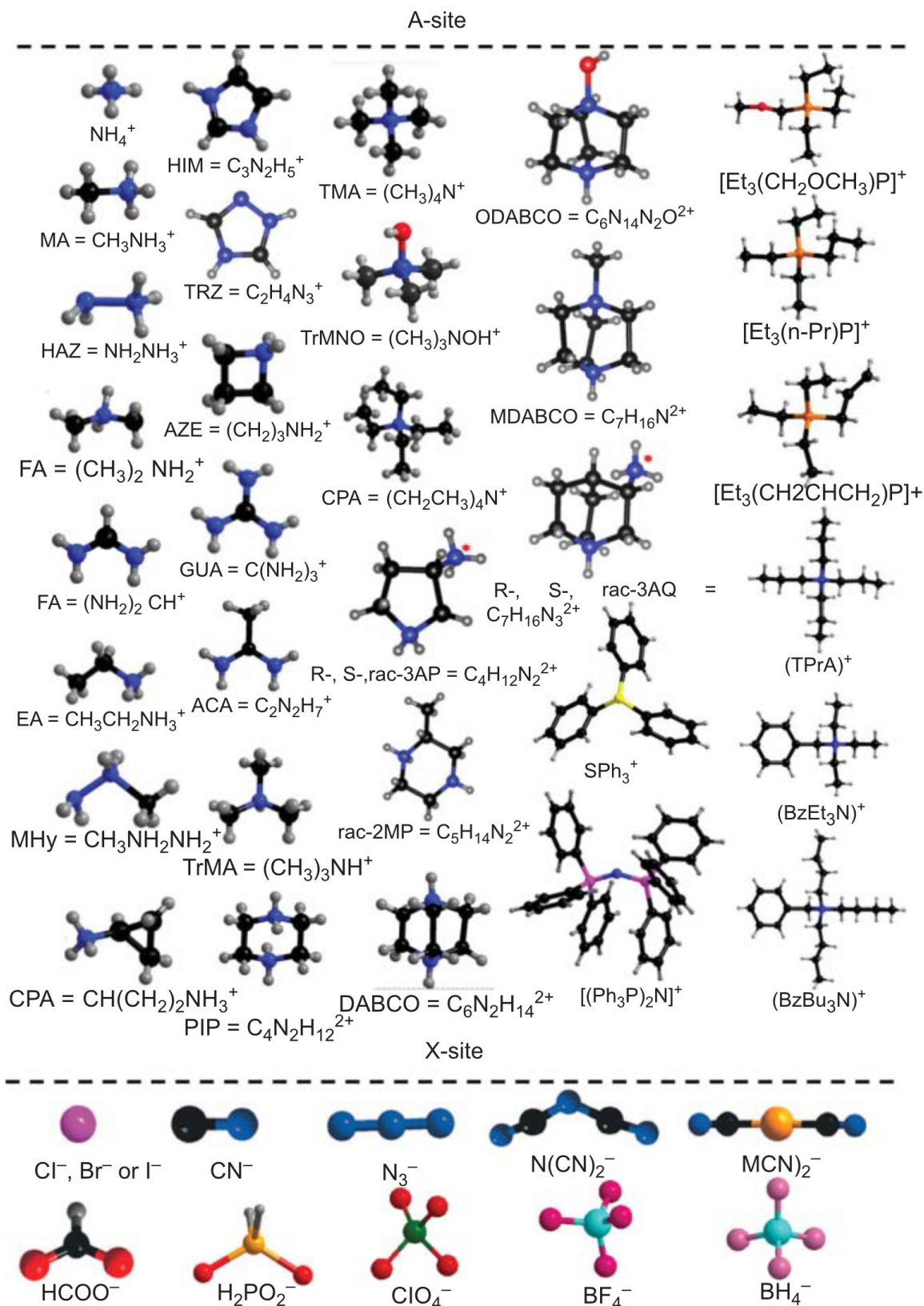


**Figure 2.9:** The diversity of possible A-site and X-site ions to form molecular perovskites. In the top are structural diagrams for potential A-cations, whereas in the bottom all to date available X-anions are shown. Copyright 2020 Wiley. Used with permission from Li Wei, Alessandro Stroppa, Zhe-ming Wang, Song Gao, *Hybrid Organic-Inorganic Perovskites*, WILEY-VCH, Weinheim.[255]

The ditopic nature of the cyanide anion enables the formation of double perovskites of the formula  $A_2BB'X_6$  with different cations, which further increases the diversity of available perovskite-type materials.[256–259] At the A-site position, mainly amines are employed, which vary in size depending on the linker and span from primary to quaternary ammonium cations.[255] The largest linker molecule known to form a pseudo-cube comprises dicyanoaurate  $Au(CN)_2^-$ , in which the metal-to-metal distance bridged by the linker already exceeds 10 Å.[260] In this way not only the implementation of huge and sterically demanding molecules such as PPN ( $PPN = \text{bis}(\text{triphenylphosphine})\text{iminium}$ ) or even the inclusion of potential solvent molecules next to the A-site cation can be realised, but it represents the border from a densely packed perovskite structure to a less dense structure that still follows an  $\alpha$ -Po topology such as MOF-5 and related coordination polymers, see section 2.2 for the context. Furthermore, in the series  $[A](NH_4)X_3$  it has recently been possible to even successfully replace the B-site metal atom towards all-organic perovskites, which demonstrate interesting ferroelectric properties.[261] Processing these materials towards sustainable metal-free high-performance ferroelectric applications is of ongoing research.[262] Nevertheless, for a detailed overview of all possible combinations of building blocks forming stable perovskite-type phases and their mechanical and material properties, the interested reader is referred to a number of seminal review articles in the literature that give an in-depth summary of the field.[36, 63, 78, 111, 255, 263]

In the further course of this paragraph, special emphasis will be given to dicyanamide-based perovskite-type network materials and their related properties, as the experimental work of this doctorate thesis focuses exclusively on these type of materials.

## 2.7 Dicyanamide-Based Perovskite-Type Coordination Networks

When the rather large, five-atomic molecular anion dicyanamide  $C_2N_3^-$  is used on the X-site (see Figure 2.9), accordingly large pseudocubic cavities are generated to accommodate bulky cations in the size dimension of tetra-*n*-propylammonium  $[(C_3H_7)_4N]^+$  or benzyltributylammonium  $[(C_7H_7)(C_4H_9)_3N]^+$ . [110, 115] In addition to ammonium cations, the perovskite void of dca-based coordination networks is equally suitable to incorporate sulfur- or phosphorus-containing cations such as triphenylsulfonium  $[(C_6H_5)_3S]^+$  and propyltriethylphosphonium  $[(C_3H_7)(C_2H_5)_3P]^+$ . [264, 265] There even exists a series of studies for the inclusion of organometallic sandwich complexes such as decamethylmetallocenes on the A-site, although this goes beyond the formal definition of an organic cation and is therefore not included in Figure 2.9.[266] The multitude of different guest molecules is a feature unique to this family of molecular perovskites, already hinting towards a pronounced flexibility of the underlying network geometry. Nevertheless, due to the size these molecules often deviate from the ideal

spherical shape, pushing the current approach to calculate Tolerance Factors to its limits. Supporting methodologies to properly determine ionic radii have accordingly been developed to take both the anisotropy of the guest and the flexibility of the host network into account.[267] For the B-site, so far the divalent cations of Cadmium, Manganese, Iron, Cobalt and Nickel are employed, which are bridged in an end-to-end fashion of the coordinating anion.[111]

Under certain conditions, however, due to the different possible coordination modes of dicyanamide, compounds with metal-coordination of the central nitrogen atom can also be formed ( $\mu$ -1,3 coordination), resulting in the formation of binary  $M(C_2N_3)_2$  salts.[268, 269] Moreover, hitherto no perovskite-type coordination network exists that comprise the combination of dicyanamide and Zinc as metal cation, since the formation of the stable  $Zn(dca)_2$  with tetrahedral coordination of the metal atom is highly preferred.[270]

The enhanced flexibility of the multiatomic linker molecule, which is substantially greater than that of *e.g.* formates or cyanides, allows for a large range of molecular perovskite structures with manifold properties. This not only enables some kind of templating effect of exotic A-site guest cations towards adapted host network structures of various symmetries, but provide an eminent platform for a rich phase transition behaviour, as in general less rigid frameworks are more susceptible towards external parameters like temperature or pressure. Thus, if carefully engineered, materials with transitions between different phases can be obtained, which may involve structural disorder at the A-site cation, the X-site anion as well as displacements, tilting and shifting of the B-site octahedra, a prerequisite for specific material properties towards highly functional materials.[132, 135]

For instance, in the family of  $[(C_3H_7)_4N]M(C_2N_3)_3$  a number of transitions are observed, which show isostructural phases at different temperature ranges depending on the size of the B-site metal cation. Generally, the quantity of different phases and inversely their transition temperature increases from  $M = Mn^{2+}$  to the smaller  $Fe^{2+}$ ,  $Co^{2+}$  and  $Ni^{2+}$ , while the analogue with  $M = Cd^{2+}$  deviates from this trend with again several phase transitions being known.[242, 253] It therefore seems that at least within this perovskite family the existence of its phase diversity is not merely a matter of internal structural stress induced by the size of the metal cation, but rather a result of additional parameters involving various distortion modes and intermolecular interactions.[111] Another example for the variety of dca-based molecular perovskites is the compound  $[(C_3H_7)(C_2H_5)_3P]Cd(C_2N_3)_3$ , as it crystallises in the non-centrosymmetric space group  $P2_12_12_1$  with pronounced nonlinear optical properties, which then can be exploited as second-harmonic generation (SHG) switch due to a temperature-dependent phase transition into a centrosymmetric space group.[271] Meanwhile, the representatives with halide-containing A-site cations like  $[(X(CH_2)_2)(C_2H_5)_3P]Mn(C_2N_3)_3$  ( $X = F, Cl$ ) exhibit phase transitions with interesting ferroelastic and switchable dielectric properties originating from distinct domain structures, and thus depict promising multiferroic materials.[272]

Arguably the most prominent feature of dicyanamide-containing molecular perovskites is the presence of pressure-induced phase transformations with a high sensitivity of the phase transition temperature towards the applied hydrostatic pressure.

**Excursus 7: The barocaloric effect**

The principle of a barocaloric cooler is based on the thermodynamic concept of converting work into heat by the compression of a medium followed by consecutive expansion, thereby generating a temperature difference. This change in heat is then withdrawn to feed a chiller or a heat pump.[273] If molecular perovskite materials are considered as solid-state working media, the crucial requirement for a barocaloric effect is a pressure-induced phase transition which is characterised by a significant change in latent heat. Furthermore, the transition should be accompanied with a large adiabatic change in temperature  $\Delta T_{ad.}$ , *i.e.* a high sensitivity of the phase transition temperature towards applied pressure and a considerable isothermal change in enthalpy  $\Delta H_{it.}$  and entropy  $\Delta S_{it.}$ [274]

For solid state materials, it has already been demonstrated that the simple and low-cost substances  $(\text{NH}_4)_2\text{SO}_4$ ,  $\text{NH}_4\text{I}$  and Neopentyl glycol show a large barocaloric effect.[195, 275, 276] The application of molecular perovskites as barocalorics is likewise promising in this regard due to their modular building principle to in-depth study composition-performance relations and the low working pressure required to activate the transition.[274] From a practical point of view, solid-state materials are easy to handle, while commonly used refrigerants in barocaloric machines rely on environmentally harmful or toxic liquids and gases like hydrohalocarbons. Competing technologies such as thermoelectric cooling, which exploits the PELTIER effect, are scientifically exciting but not yet mature, and most of them also rely on toxic and non-abundant elements.[277]

In  $[(\text{C}_3\text{H}_7)_4\text{N}]\text{Mn}(\text{C}_2\text{N}_3)_3$  and  $[(\text{C}_3\text{H}_7)_4\text{N}]\text{Cd}(\text{C}_2\text{N}_3)_3$  this structural change is characterised by a high degree of simultaneous order-disorder of the atomic positions of the organic cation as well as anion, resulting in a large change of configurational entropy. Figure 2.10 shows structural diagrams of this reversible transition with an emphasis of the change in disorder, which can be activated either by temperature or pressure changes. Since these phase transitions are of first-order in nature and therefore considered discontinuous (*c.f.* section 2.5), their change in state functions can be described by applying the CLAUSIUS-CLAPEYRON equation to quantify the dependency of the phase transition temperature  $T_{PT}$  to the applied pressure  $p$  in relation to the change in cell volume  $\Delta V$  and enthalpy  $\Delta H$ .

$$\frac{\partial T_{PT}}{\partial p} = \frac{T_{PT}}{\Delta H_{mol.}} \cdot \frac{\Delta V}{V} \cdot V_{mol.} \quad (2.7)$$

This equation was originally established for ideal gases, but with the aid of the MAXWELL relationship at constant pressures  $\left(\frac{\partial H}{\partial S}\right)_p = T$  it simplifies here for solids in terms of the specific cell volume  $\Delta V_{spec.}$  and the isothermal entropy change  $\Delta S_{it.}$  during the phase transition as follows:

$$\frac{\partial T_{PT}}{\partial p} = \frac{\Delta V_{spec.}}{\Delta S_{it.}} \quad (2.8)$$

This establishes a relationship between the pressure dependence of the phase transition temperature and the entropy *resp.* volume change during the transition and is called "indirect

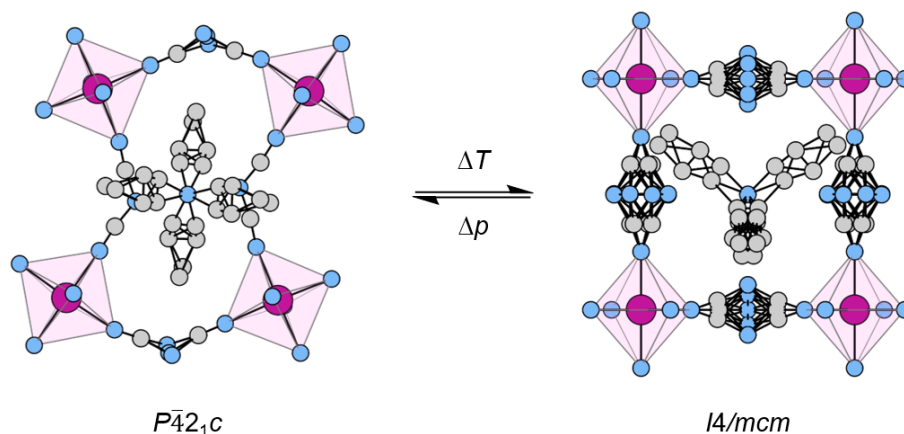


**Figure 2.10:** Schematic of the phase transition observed in  $[(C_3H_7)_4N]Mn(C_2N_3)_3$  at approx. 330 K.[278] The transformation from the low-temperature to the high-temperature phase is characterised by an increase in positional disorder on both the A- and X-site resulting in a large change of configurational entropy with a calculated value for the ratio of possible microstates of  $\Omega = 8$ . This eightfold order-disorder is accompanied with cationic displacement and columnar shifts in the low-symmetry phase, overall accounting for a large latent heat conversion during the phase transition. For simplicity reasons, all disordered positions are illustrated as filled, whereas hydrogen atoms are omitted. Colourcode: purple - Mn, gray - C, blue - N.

Clausius-Clapeyron method", as it results in a quantitative determination of an entropy change without actually conducting entropic studies. In the context of barocalorics, the ratio of the transition temperature to the applied pressure is also known as "barocaloric coefficient" and has emerged as an experimentally easily accessible figure of merit for potential barocaloric performance, as the susceptibility of the phase transition temperature towards pressure is a crucial requirement for molecular perovskites to be used in refrigeration processes. Another important feature with regard to the potential cooling capacity relates to the reversibility and associated hysteresis of the temperature of the complementary transformations during heating and cooling, which should ideally be as small as possible.[70] Current benchmark perovskite-type coordination networks are the two aforementioned  $[(C_3H_7)_4N]M(C_2N_3)_3$  comprising tetra-*n*-propylammonium with values for  $\frac{\partial T_{PT}}{\partial p} = 23.1 \text{ K}\cdot\text{kbar}^{-1}$  ( $M = Mn^{2+}$ ) and  $38.2 \text{ K}\cdot\text{kbar}^{-1}$  ( $M = Cd^{2+}$ ), respectively.[70, 242] Other recent barocaloric studies on molecular perovskites involve formate- and azide-analogues.[279, 280]



### 3 OBJECTIVE

Perovskite-type coordination networks represent an emerging class of hybrid materials with striking macroscopic properties originating from features of the crystal chemistry and are therefore attracting extraordinary attention within the materials science community. Their modular building principle creates a material platform which has one tremendous advantage: the capability to incorporate chemically diverse building blocks without affecting the underlying perovskite-type connectivity. Additionally, the structure motif can be susceptible to external factors such as temperature or pressure, resulting in structural phase transitions or structural entanglement behaviour with unexpected mechanical properties. As a result, the interpretation of the structure in relation to various chemical and structural degrees of freedom allows for a direct correlation between material structure and material properties. The design strategies thus benefit from the application of classical chemical principles during synthesis, while the prediction of temperature- and pressure-responsive behaviour is still very challenging, with clear "master profiles" being elusive. Current research aims for a fundamental understanding of the properties phenomena and mechanisms of materials response in perovskite-type coordination networks at the atomic level. This forms the basis for the central research idea upon which this thesis is constructed.

The overarching goal of the present dissertation is to establish clear correlations between structure and properties in perovskite-type coordination networks towards functional materials with targeted physical properties. By investigating the structure and behaviour of different crystalline phases in relation to thermodynamic parameters like temperature and pressure, design principles will be established to create microscopic characteristics and map them onto macroscopic features *esp.* mechanical properties, *e.g.* expansion behaviour and hardness, nonlinear optical properties, or barocalorics amongst others.

A number of milestones along this way are addressed and outlined below, which at first comprise a literature survey about prerequisites to form stable perovskite-type structures (STUDY I), with subsequent approaches for establishing new routes to extend current synthetic limits towards novel phases within the perovskite-type (STUDY II and III) and possibly beyond (STUDY V), and a discussion of the pressure-dependent mechanical properties of a molecular perovskite family based on theoretical calculations and experimental results (STUDY IV).

Most molecular ABX<sub>3</sub> perovskite materials known to date are based on commercially available building blocks. While this is well justified for the B- and X-sites through the inherent limitation of possible ions, the molecular nature of the A-site cation offers great freedom to systematically

vary the chemistry of the resulting perovskite phases by using different molecules. Hence, although the variety of different materials is restricted to the available size of the perovskite void, the exploitation of organic chemistry provides numerous ways to incorporate structural motifs with different functionalities such as asymmetries, chemical polarity or atomic packing through the dimension of the molecule, which can result in unprecedented properties. This raises the question *of which extent tailor-made or exotic structural motifs such as spiro compounds or specific functional groups can be incorporated into the perovskite-type host framework and how this directs the resulting material properties*. STUDY II addresses this thought and investigates the impact of a novel A-site motif on the material properties. It is worth noting that the nature of the A-site cation employed may not be exclusively accountable for the physical properties of the resulting material *per se*. It is known in literature that certain A-site molecules with specific structures also make a significant contribution to distortions within the host network.[254] The underlying question therefore is *to what extent the structural distortions of the framework affect the material as a subsidiary factor*, and if an overarching prescription can be formulated as to *how the organic ingredients systematically induce these framework distortions*, to which STUDY III provides an in-depth analysis with reference to key results from STUDY II. Structural phase transitions induced by changes in temperature often as well occur through the application of hydrostatic pressure. The crystal chemistry under high pressures reveals insights into the pressure-dependent elasticity of materials. In this context, barocalorics is an interesting material property of molecular perovskites that combines structural behaviour and elasticity upon compression. Apart from the conventional trial-and-error approach of generating pressure-susceptible phase transitions by varying the A-site chemistry, in STUDY IV it is investigated *to which degree the compressibility of a material can be considered as a descriptor to draw conclusions about barocaloric performance*. Theoretical calculations of the bulk moduli and their reliable experimental determination will be the first steps into this direction, with the aim to provide guidance on *how to use bulk moduli to systematically design materials with maximised barocaloric figure of merits*. Furthermore, the modular organisation of these coordination networks in principle allows for structural arrangements beyond the ABX<sub>3</sub> perovskite cage itself, as an increasing number of structural degrees of freedom can extend the A-site chemistry to multivalent cations. In this regard, STUDY V tackles the question *if it is possible to incorporate new degrees of structural freedom into these networks* by expanding the A-site cations of the molecular building blocks on the spatial dimension of linking adjacent perovskite-type cages. This might result in order patterns as known from related materials[140] and therefore can hint for unexpected temperature- and pressure-dependent material properties in molecular perovskites with respect to expansion and compression behaviour.

To narrow down the vast number of synthetic opportunities throughout the proposed research questions, the X-anion of choice is constricted to the multiatomic molecule dicyanamide in all studies. Furthermore, although different cations may be used for the B-site metal, the preferred candidate is manganese, which in previous literature studies has been proven to be extremely robust in the formation of perovskite phases.

# 4 RESULTS AND DISCUSSION

## 4.1 STUDY I: Tolerance Factors of Hybrid Organic-Inorganic Perovskites: Recent Improvements and Current State of Research

In this review article, the recent developments of different approaches to apply the Goldschmidt Tolerance Factor concept, originally established for inorganic perovskites, to the class of molecular perovskites is summarised. These molecular perovskites as a formal sub-class of coordination polymers represent organic-inorganic hybrid materials obeying the  $ABX_3$  structure type for which both the A-site and the X-site are occupied by molecular ions. Already in 2014, this Tolerance Factor concept was extended and applied to hybrid as well as molecular perovskites, which was back then set up solely based on empirical observations of different minerals, matching very well the stability criteria for most of the known A-B-X permutations that form perovskite-type materials. The article at hand takes on the improvements that have been made to develop the concept further to describe the stability of different perovskite phases even more accurately. This is, in addition to an updated method of determining atomic and molecular ionic radii for describing the size ratios of the respective ions more accurately, the introduction of an additional parameter to describe the structural stability. Furthermore, recent research examples are critically discussed for which the Tolerance Factor concept approach was used to assess the existence of perovskite phases.

This review was conceived and written by the author of this doctoral thesis together with Dr. Gregor Kieslich. The literature research and assessment was done by the author of this thesis together with Michael G. Ehrenreich and Dr. Gregor Kieslich.

Status: Published as a Review Article in Journal of Materials Chemistry A.

Reproduced from Ref. [281] with permission from the Royal Society of Chemistry, see APPENDIX, C Reprint permissions for details on the license agreement.

S. Burger, M. G. Ehrenreich and G. Kieslich, *Tolerance factors of hybrid organic–inorganic perovskites: recent improvements and current state of research*, *J. Mater. Chem. A*, 2018, **6**, 21785-21793, DOI: 10.1039/C8TA05794J.

Cite this: *J. Mater. Chem. A*, 2018, 6, 21785Received 17th June 2018  
Accepted 7th September 2018

DOI: 10.1039/c8ta05794j

rsc.li/materials-a

## Tolerance factors of hybrid organic–inorganic perovskites: recent improvements and current state of research

S. Burger, M. G. Ehrenreich and G. Kieslich \*

In 2014 we applied Goldschmidt's concept of ionic tolerance factors to the large family of hybrid organic–inorganic perovskites. Initially seen as a guiding concept for the discovery of new hybrid organic–inorganic perovskites, the tolerance factor concept has also proven to be a valuable tool for understanding and manipulating the phase stability and properties of existing phases. Since our initial report, there have been many research examples in which tolerance factors were used to understand the existence and stability of certain hybrid organic–inorganic perovskites, while the concept itself has been continuously improved. Here we give an update on the current state of the concept, reviewing the different improvements that have been made over the past few years and drawing on topical examples in which tolerance factors have played a major role.

### Introduction

Among the recent research directions in materials science, the research on organic–inorganic networks that adopt a perovskite motif is one of the fastest-moving areas. Materials such as  $[\text{CH}_3\text{NH}_3]\text{PbI}_3$ ,  $[(\text{NH}_2)_2\text{CH}]\text{PbI}_3$  and  $[\text{CH}_3\text{NH}_3]\text{PbBr}_3$  have led to breath-taking discoveries in optoelectronics, resulting in a new paradigm in solar cell research.<sup>1–6</sup> Likewise, related organic–inorganic perovskites such as  $[(\text{C}_3\text{H}_7)_4\text{N}]\text{Mn}(\text{C}_2\text{N}_3)_3$ ,  $[\text{NH}_3\text{NH}_2]\text{Zn}(\text{HCOO})_3$ ,  $[\text{C}_6\text{N}_2\text{H}_{14}](\text{NH}_4)\text{I}_3$  and  $[(\text{CH}_3)_3\text{NH}]\text{Cd}(\text{N}_3)_3$  show fascinating ferroelectric-to-paraelectric phase transitions and tuneable mechanical properties, and provide great opportunities as working media in mechanocalorics.<sup>7–11</sup> Having this collection of properties on hand, it is no surprise that much effort has recently been devoted to the discovery and synthesis of new hybrid  $\text{ABX}_3$  perovskite-type materials.

Like all-inorganic solid-state perovskites,  $\text{ABX}_3$  hybrid organic–inorganic perovskites adopt a three-dimensional  $\text{ReO}_3$ -type framework formed by the B-cation and X-anion with the A-site cation sitting in the open void of the network. Focusing on the connectivity of the  $\text{ReO}_3$ -network of different hybrid perovskites, it is possible to distinguish between  $\text{I}^3\text{O}^0$ -type and  $\text{I}^0\text{O}^3$ -type perovskites, following the nomenclature suggested by C. N. R. Rao and A. K. Cheetham for organic–inorganic (coordination) networks.<sup>12</sup> This classification highlights both the 3D connectivity of the  $\text{ReO}_3$ -type framework and the type of chemical bond involved with “I” in the nomenclature reflecting the dimensionality of the inorganic network and “O” reflecting the dimensionality of the coordination network. While

$\text{I}^3\text{O}^0$ -type perovskites can be described as materials with metal-cation–anion interactions in the 3D  $\text{ReO}_3$ -type network (Fig. 1a),<sup>13</sup>  $\text{I}^0\text{O}^3$ -type perovskites exhibit a framework composed of metal-cations and molecular anions (Fig. 1b–e),<sup>8,9,14,15</sup> or molecular cations and anion interactions (Fig. 1f).<sup>11</sup>

Such a separation into two sub-classes of three-dimensional hybrid perovskites with the general formula  $\text{ABX}_3$  is useful when focusing on the intrinsic properties that come from the nature of the  $[\text{BX}_3]^-$  framework. For instance, the semi-conducting behaviour of  $[\text{CH}_3\text{NH}_3]\text{PbI}_3$  originates from covalent lead iodide interactions,<sup>16</sup> whereas the insulating

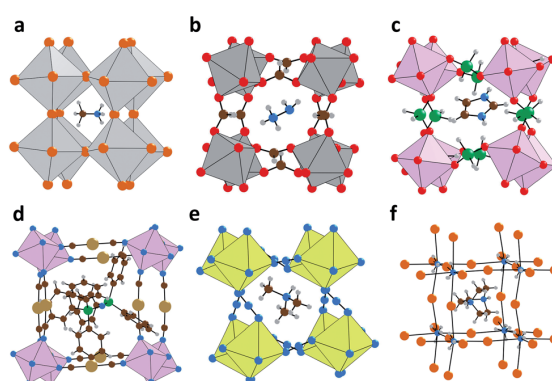


Fig. 1 Schematic representation of some typical hybrid perovskites: (a)  $[\text{CH}_3\text{NH}_3]\text{PbBr}_3$ , a representative of  $\text{I}^3\text{O}^0$  hybrid perovskites and (b)  $[\text{NH}_3\text{NH}_2]\text{Zn}(\text{HCOO})_3$ , (c)  $[\text{C}_3\text{N}_2\text{H}_5]\text{Mn}(\text{H}_2\text{POO})_3$ , (d)  $[\text{PPN}]\text{Mn}[\text{Au}(\text{CN})_2]_3$ , (e)  $[\text{NH}(\text{CH}_3)_3]\text{Cd}(\text{N}_3)_3$  and (f)  $[\text{H}_2\text{DABCO}](\text{NH}_4)\text{Br}_3$ , as representatives for the chemical flexibility of  $\text{I}^0\text{O}^3$  perovskites (DABCO = 1,4-di-azabicyclo [2.2.2]octane and PPN = bis(triphenylphosphine)iminium).

Department of Chemistry, Technical University of Munich, Lichtenbergstraße 4, 85748 Garching, Germany. E-mail: Gregor.Kieslich@tum.de

behaviour of  $[\text{CH}_3\text{NH}_3]\text{Mn}(\text{HCOO})_3$  is based on coordinative manganese oxygen bonds and in turn small energy band dispersion.<sup>17</sup> On the other hand, there are properties for which such a separation into two subclasses is less advantageous. For instance, it was shown that molecular building units on the A-site and/or X-site both lead to low energy lattice modes that are thermally accessible.<sup>18–20</sup> These lattice modes gain importance when phase transitions as a function of temperature and pressure are focused on. Particularly the propensity of the A-site cation to form strong hydrogen bonding interactions with the negatively charged framework has been revealed to be of outmost importance in this context.<sup>21,22</sup> For example, the temperature-driven order-disorder transitions in  $[\text{NH}_3\text{NH}_2]\text{Zn}(\text{HCOO})_3$  are directly related to hydrogen bonding interactions between the  $[\text{NH}_3\text{NH}_2]^+$  cation and the negatively charged  $[\text{Zn}(\text{HCOO})_3]^-$  framework.<sup>8</sup> Similarly, hydrogen bonding interactions have been identified to play a role in the low-temperature crystal chemistry of  $[\text{CH}_3\text{NH}_3]\text{PbI}_3$ .<sup>23</sup> It must be emphasized here that these hydrogen bonding interactions originate from the molecular nature of the A-site cation and are inherently absent in all-inorganic perovskites, drawing a clear line between hybrid perovskites and their all-inorganic analogues.<sup>24,25</sup> For a general overview that discusses the properties which come from the diversity of hybrid perovskites, we like to refer to some illuminating reviews that have appeared recently on this topic.<sup>26–29</sup>

When looking at more fundamental design principles towards new organic-inorganic frameworks that adopt a perovskite architecture, separation into subclasses becomes even less useful. In fact, the perovskite motif as such allows for applying the same geometrical considerations to  $\text{I}^3\text{O}^0$ - and  $\text{I}^0\text{O}^3$ -type perovskites. These geometrical considerations are at the heart of the guiding principle towards new (hybrid) perovskites: Goldschmidt's concept of ionic tolerance factors (TFs). Already in 2001, Mitzi considered applying Goldschmidt's concept to the family of lead halides, qualitatively estimating the available space for molecular A-cations.<sup>30</sup> It was then in 2014 when we applied Goldschmidt's concept to hybrid perovskites,<sup>31</sup> describing the size of molecular A-cations such as  $[\text{CH}_3\text{NH}_3]^+$  and  $[(\text{CH}_3)_2\text{NH}_2]^+$  based on a semi-empirical approach. Since our initial report, this concept has been continuously improved and widely used in the search for new hybrid perovskites. The purpose of this research update is to review the most important improvements in the tolerance factor concept for hybrid perovskites over the past few years, drawing on some topical research examples where TFs have been explicitly applied. We would further like to note that we have used the terminology hybrid perovskites throughout the manuscript, overarching both sub-classes,  $\text{I}^3\text{O}^0$  and  $\text{I}^0\text{O}^3$ , of organic-inorganic perovskite-type materials.

## The development of tolerance factors

In 1926, Goldschmidt formulated the tolerance factor concept for inorganic solid state perovskites; the relationship between the ionic radii of the A-site cation, B-site cation and X-site anion

obtained by applying simple trigonometry is given in eqn (1) and Fig. 2:<sup>32</sup>

$$\text{TF} = \frac{r_A + r_X}{\sqrt{2}(r_B + r_X)} \quad (1)$$

with  $r_A$  being the ionic radii of the A-site cation,  $r_B$  the ionic radii of the B-site cation and  $r_X$  the ionic radii of the X-site anion, respectively (Fig. 2). By treating all ions as hard spheres, Goldschmidt found that for TFs between 0.8 and 1, the perovskite structure is expected to form, with distorted structures usually observed when TFs decrease. This concept has played a central role in the development of oxide perovskites and is a Madelung-type equivalent for the perovskite structure – maximising enthalpic interactions through a high packing density. For all inorganic solid-state perovskites, this concept has been reviewed several times leading to an optimised TF window of approximately 0.87 and 1.<sup>33–36</sup> The success of the TF approach and its wide use comes from the manifold properties that can be found in different perovskite compounds and in turn the large interest of the materials science community in the synthesis and characterization of new and optimized perovskite-type materials. These properties evidently originate from the availability of manifold inorganic perovskite compounds with different compositions and properties that can be synthesised such as  $\text{PbZr}_x\text{Ti}_{1-x}\text{O}_3$ ,<sup>37</sup>  $\text{BaTiO}_3$ ,<sup>38,39</sup>  $\text{BiFeO}_3$ ,<sup>40</sup>  $\text{CsPbX}_3$ ,<sup>41</sup>  $\text{La}_x\text{Ca}_{1-x}\text{MnO}_3$ <sup>42</sup> or various metal-oxo perovskites for catalysis<sup>43</sup> to name just a few. Consequently, inorganic solid-state perovskites are one of the most important materials families in condensed matter physics and materials science.<sup>44,45</sup>

Motivated by the large interest of the materials science community in the search for new hybrid perovskite materials, we extended Goldschmidt's concept to hybrid perovskites in 2014.<sup>31</sup> The challenge was to find a simple and similarly applicable concept of describing the size of molecular cations such as  $[\text{CH}_3\text{NH}_3]^+$  or  $[(\text{NH}_2)_2\text{CH}]^+$ : what is the ionic radius of a molecular cation and which description is the most appropriate one? Furthermore, the anisotropy that comes with the use of molecular anions such as  $[\text{COO}]^-$ ,  $[\text{N}_3]^-$  or  $[\text{Au}(\text{CN})_2]^-$  was important to include. In this context a semi-empirical approach seemed to be the most elegant way, combining experimental inputs with reasonable simplifications: under the assumption of free rotation of the A-site molecule around the centre of mass together with experimental X-ray bond lengths,

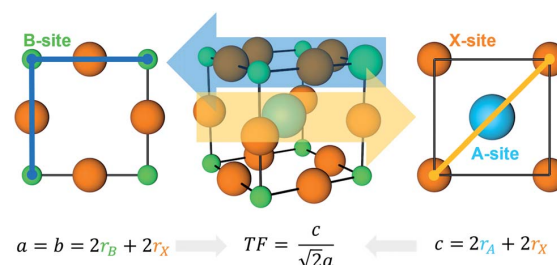


Fig. 2 Schematic of the perovskite structure (middle) and the trigonometric relationship of the ionic radii of the A-site, B-site and X-site that is used to derive the tolerance factor equation.

we estimated effective ionic radii  $r_{\text{eff,A}}$  for a series of molecular A-site cations. For instance, the effective radius  $r_{\text{eff,A}}$  of  $[\text{C}(\text{NH}_2)_3]^+$  (guanidinium) is obtained by identifying the centre of mass of the molecule (the C atom), and reported X-ray crystallographic data of a  $[\text{C}(\text{NH}_2)_3]^+$ -based perovskite was used to measure the distance from C to N – the non-hydrogen atom farthest away from C. To this distance, the Shannon reported radius of N is added to obtain the  $r_{\text{eff,A}}$  of  $[\text{C}(\text{NH}_2)_3]^+$ , presenting the largest possible spherical radius for a hypothetical fast rotating guanidinium cation. The simplification is clear: despite  $[\text{C}(\text{NH}_2)_3]^+$  being a planar cation, a spherical shape is approximated, and errors from X-ray crystallographic data must be considered. The anisotropy of molecular X-anions is taken into account by treating these as cylinders, assuming rotation around the main axis of the cylinder and the description of these with an effective height.<sup>14,31</sup> Based on the obtained set of effective ionic radii for molecular A-site cations (see Table 2, left column shows a selection of  $r_{\text{eff,A}}$  from our original work) and effective heights of molecular B-site anions, TFs of every A–B–X permutation can be calculated.<sup>46</sup> The applicability of TFs has been shown in our initial report,<sup>31</sup> where TFs for different hybrid Pb iodides and Mn formates have been calculated and compared to those of experimentally observed crystal structures. For TFs between 0.8 and 1.0, mainly hybrid perovskites were observed, whereas TFs > 1 or TFs < 0.8 predominantly led to low-dimensional structures (Fig. 3).

**Table 1** Improved ionic radii of a selection of B-site metal cations typically found in hybrid perovskites as given by Palgrave<sup>47</sup> compared to the radii reported by Shannon.<sup>48</sup> All values in Å. HS = high spin

Cation	Shannon	Palgrave <i>et al.</i>		
	Ionic radius	Iodides	Bromides	Chlorides
Pb <sup>2+</sup>	1.19	1.03	0.98	0.99
Mg <sup>2+</sup>	0.72	0.75	0.72	0.67
Ni <sup>2+</sup>	0.69	0.57	0.58	0.60
Mn <sub>(HS)</sub> <sup>2+</sup>	0.83	0.72	0.72	0.73
Yb <sup>2+</sup>	1.02	0.93	0.88	0.86

**Table 2** Ionic radii of typical A-site cations found in hybrid perovskites compared with radii reported by Kieslich *et al.*<sup>31</sup> and computationally derived radii as suggested by Becker *et al.*<sup>52</sup> All values in pm

A-site cation	Kieslich <i>et al.</i>	Becker <i>et al.</i>
	$r_{\text{eff,A}}$	$r_{\text{eff,A}}$
$[\text{NH}_4]^+$	146	170
$[\text{NH}_3\text{OH}]^+$	216	226
$[\text{CH}_3\text{NH}_3]^+$	217	238
$[\text{NH}_3\text{NH}_2]^+$	217	220
$[(\text{CH}_2)_3\text{NH}_2]^+$	250	284
$[(\text{NH}_2)_2\text{CH}]^+$	253	277
$[\text{C}_3\text{N}_2\text{H}_5]^+$	258	303
$[(\text{CH}_3)_2\text{NH}_2]^+$	272	296
$[\text{C}(\text{NH}_2)_3]^+$	278	280
$[(\text{CH}_3)_4\text{N}]^+$	292	301

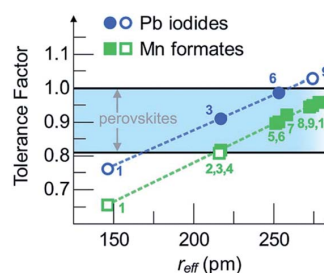


**Fig. 3** Showcasing the applicability of the TF concept for the series of hybrid lead iodides and manganese formates as reported in 2014.<sup>31</sup> For both families, a perovskite structure is experimentally observed for TFs between 0.8 and 1, using the effective radii as given in the initial publication. Open symbols indicate reported compounds with a nonperovskite structure.

When looking for the origin of the largest inaccuracies of the TF concept under the assumption that the formula itself is a reasonable approach, the attention is immediately drawn towards the question how accurate are the tabulated ionic radii? Consequently, the most important improvements that have been reported in the past few years concern the definition and description of effective ionic radii for the A-site and B-site cations. Following this thought, Palgrave and co-workers have made an important step forward in improving the concept for hybrid perovskites with X being a halide anion.<sup>47</sup> By recognising the different bonding situations of halides in comparison to ionic oxides and fluorides,<sup>48</sup> they have revised ionic radii of divalent metals when bound to different halides. For instance, they found that the  $r_{\text{B}}$  of  $\text{Pb}^{2+}$  in a hypothetical  $[\text{A}]\text{PbI}_3$  perovskite is better approximated with  $r_{\text{Pb}^{2+}} = 103$  pm, compared to the radius reported by Shannon ( $r_{\text{Pb}^{2+}} = 119$  pm), which was derived based on lead oxides. A similar conclusion can be drawn for bromides and chlorides, and the differences along the halide series to the Shannon radii are shown in Table 1. Additionally, Palgrave and co-workers suggested including the well-known octahedral factor  $\mu$  as an additional parameter when screening new hybrid perovskites.<sup>47,49</sup>  $\mu$  accounts for a possible size-mismatch between the B-cation and X-site, putting further constraints on the combination of B-site cations and X-site anions. In the context of ionic radii of halide-based systems, P. M. Woodward and co-workers recently reinvestigated Pb–X bond lengths in the solid solutions  $\text{Cs}_{1-x}\text{Rb}_x\text{PbBr}_3$  and  $\text{Cs}_{1-x}\text{Rb}_x\text{PbCl}_3$ , revising bond valence parameters<sup>50</sup> for the bond valence method and thus obtaining reasonable Pb–X bond lengths (with X being a halide) to determine revised tolerance factors.<sup>51</sup> The obtained trend of band-gap as a function of the tolerance factor for both series is remarkable, suggesting that the bond valence method is a suitable approach for all-inorganic halide perovskites. One key feature of this approach is the linear correlation of the calculated TFs with specific characteristics of the perovskite material, which in turn might uncover local structural deviations to explain interesting material behaviours. However, despite considering different classes of materials, hybrid and inorganic perovskites, respectively, the approaches by Palgrave and Woodward result in relatively

similar TFs, *e.g.* 0.92 and 0.953 for CsPbBr<sub>3</sub> and 0.93 and 0.948 for CsPbCl<sub>3</sub>, which are well within the TF window of ABO<sub>3</sub> perovskites as discussed by Woodward in 2001.<sup>33</sup>

Turning the attention to the A-site cation and the approaches to derive an effective radius for molecular A-cations, Becker *et al.* approached the challenge of obtaining more precise ionic radii of molecular cations computationally.<sup>52</sup> By looking at the total electron density of the gas phase energy-minimised states of several ions and taking the isocharge radius of [NH<sub>4</sub>]<sup>+</sup> as a reference, they calculated the effective ionic radii  $r_{\text{eff,A}}$  of 18 molecular cations. Their results are intrinsically consistent due to the applied method, showing a trend of larger effective ionic radii in comparison to our initially suggested  $r_{\text{eff,A}}$  (see Table 2 for comparison between  $r_{\text{eff,A}}$  from our initial approach and the computationally derived ionic radii by Becker and co-workers). In combination with the revised radii by Palgrave for the B-cation and the inclusion of the octahedral factor  $\mu$ , they obtained a shifted TF window, *i.e.*  $0.9 < \text{TF} < 1.12$ ,<sup>47</sup> which shows a general good agreement with our initial estimations. According to the authors, 93% of the already known stable 3D perovskites fit within their stated TF stability range which clearly indicates the powerful descriptive nature of this revised and similarly consistent concept, *e.g.* inaccuracies that might occur from experimental errors based on X-ray crystallographic data are absent in their computational approach. They suggested at this point 106 unknown compounds for which TFs fulfill the stability criteria for a 3D perovskite (see Fig. 4). It can therefore be concluded here that when calculating TFs, a consistent set of  $r_{\text{eff,A}}$  and the B-metal site should be used, of which the approach by Becker for A-site cations with the improvements made by Palgrave for B-site cations seems the most consistent approach at the current state.

Finally and only recently, the effective radii of A-site cations were further refined by explicitly taking into account the anisotropy of the molecular A-cation.<sup>53</sup> Saliba *et al.* introduced the globularity factor  $g = S/S_{\text{eq}}$  in which the actual surface  $S$  of

the molecular cation is related to the volume of the cation  $S_{\text{eq}}$  when treated as an ideal sphere. Notably, the “real” surface and respective volume have been derived computationally with [(NH<sub>2</sub>)<sub>2</sub>CH]PbI<sub>3</sub> as a reference with TF = 1. This approach seems useful when the molecular complexity and anisotropy of the A-cation are high, *e.g.* in the case of guanidinium, [C(NH<sub>2</sub>)<sub>3</sub>]<sup>+</sup> and formamidinium [(NH<sub>2</sub>)<sub>2</sub>CH]<sup>+</sup>. Importantly, however, this approach has only been validated for [C(NH<sub>2</sub>)<sub>3</sub>]<sup>+</sup> so far and requires further validation.

## Research examples

We now want to discuss a few selected research examples of the recent literature in which the TF concept has either been directly applied, leading to an understanding of the observed results or indicates the presence of a more complex underlying chemistry related to the thermodynamic landscape of the investigated material.

### Halide-based hybrid perovskites (I<sup>3</sup>O<sup>0</sup>)

Firstly, we would like to stay within the area of three-dimensional halide-based hybrid perovskites which have gained a large amount of research attention due to the outstanding properties of [CH<sub>3</sub>NH<sub>3</sub>]PbI<sub>3</sub> as a light absorber in thin film solar cells. The TF of the most studied compound [CH<sub>3</sub>NH<sub>3</sub>]PbI<sub>3</sub> lies well within the TF window of a stable perovskite phase in all the abovementioned approaches. Direct calorimetric measurements show, however, that [CH<sub>3</sub>NH<sub>3</sub>]PbI<sub>3</sub> is thermodynamically unstable with respect to its components, and consequently much research has been devoted to stabilizing [CH<sub>3</sub>NH<sub>3</sub>]PbI<sub>3</sub> chemically.<sup>54</sup> The use of [(NH<sub>2</sub>)<sub>2</sub>CH]<sup>+</sup> to form [(NH<sub>2</sub>)<sub>2</sub>CH]PbI<sub>3</sub> leads to a TF close to or slightly above 1 (depending on the concept used), and polymorphism is observed experimentally under ambient conditions. The [(NH<sub>2</sub>)<sub>2</sub>CH]PbI<sub>3</sub> perovskite phase is metastable leading to its transformation to a low-dimensional phase, visible by a change of colour from black (perovskite) to yellow (low-dimensional).<sup>16</sup> The transformation itself seems to be driven by a strain relaxation process which is caused by the size mismatch of the [(NH<sub>2</sub>)<sub>2</sub>CH]<sup>+</sup> cation and the void within the [PbI<sub>3</sub>]<sup>-</sup> lattice,<sup>55</sup> effects that are captured in the TF concept. It is therefore no surprise, however, that the perovskite phase can be stabilised by partial substitution with [CH<sub>3</sub>NH<sub>3</sub>]<sup>+</sup> on the A-site, or in other words, by moving the TF of the compounds into the stable regime. This approach was exploited by Zhu *et al.*<sup>56</sup> for the preparation of [(NH<sub>2</sub>)<sub>2</sub>CH]<sub>0.85</sub>Cs<sub>0.15</sub>PbI<sub>3</sub>, (see Fig. 5). Notably, both parent phases CsPbI<sub>3</sub> and [(NH<sub>2</sub>)<sub>2</sub>CH]PbI<sub>3</sub> exhibit TFs slightly too small (Cs<sup>+</sup>) and slightly too large ([C(NH<sub>2</sub>)<sub>3</sub>]<sup>+</sup>) to form a stable perovskite phase; however, averaging the radii leads to a TF within the stability criteria for [(NH<sub>2</sub>)<sub>2</sub>CH]<sub>0.85</sub>Cs<sub>0.15</sub>PbI<sub>3</sub>. This finding is fascinating by itself, suggesting a relatively flexible inorganic [PbI<sub>3</sub>]<sup>-</sup> framework in which lattice strain can be balanced by choosing the right A-site cations. Grätzel and co-workers<sup>57</sup> then continued the idea of tuning the stability by investigating triple cation perovskites consisting of [CH<sub>3</sub>NH<sub>3</sub>]<sup>+</sup>, [(NH<sub>2</sub>)<sub>2</sub>CH]<sup>+</sup> and Cs<sup>+</sup>, leading to a novel compositional strategy to develop

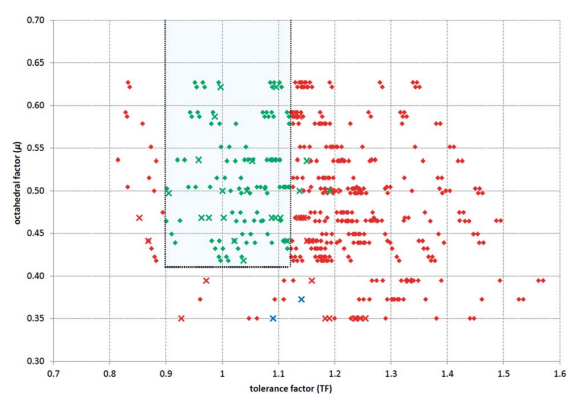


Fig. 4 2D mapping of octahedral factors and calculated TFs using the effective ionic radii as given by Becker *et al.* for which the empirical stability range is found to be  $0.9 < \text{TF} < 1.12$ . This plot suggests the existence of 106 hitherto unknown compounds (green crosses: reported 3D hybrid perovskites, red crosses: low dimensional phases, and unreported compounds: diamonds). Figure adapted from ref. 52.

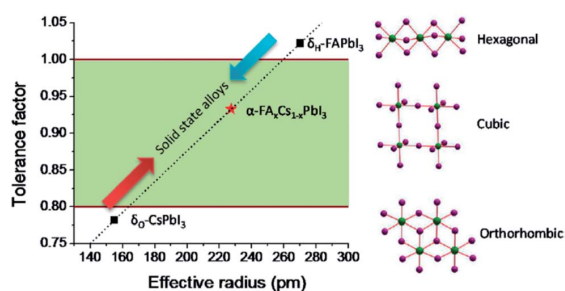


Fig. 5 Schematic showing how the stability criteria of TF can be used to stabilize the metastable phases of FAPbI<sub>3</sub> and CsPbI<sub>3</sub> by the formation of A-site solid solutions. Reprinted with permission from ref. 56. Copyright (2016) American Chemical Society.

perovskite solar cells bearing state-of-the-art performance characteristics. A possible explanation for the high turn-over efficiency of such phases could be the rigidification of the lattice, in turn decreasing carrier combination pathways. Shortly after, other researchers followed the idea of replacing the A-site cation with other molecular cations with different sizes to match the TF concept. For instance, Bakr *et al.* investigated the incorporation of ethylammonium [NH<sub>3</sub>C<sub>2</sub>H<sub>5</sub>]<sup>+</sup> into [CH<sub>3</sub>NH<sub>3</sub>]<sub>2</sub>PbI<sub>3</sub>.<sup>58</sup> They seemingly obtained materials with stoichiometries such as [NH<sub>3</sub>C<sub>2</sub>H<sub>5</sub>]<sub>0.17</sub>[CH<sub>3</sub>NH<sub>3</sub>]<sub>0.83</sub>PbI<sub>3</sub>, finding optimised optoelectronic properties based on increased carrier lifetimes. Similarly, the incorporation of large guanidinium [N(CH<sub>2</sub>)<sub>3</sub>]<sup>+</sup> cations was investigated, leading to improved materials stability paired with high turn-over efficiencies and averaged TFs within the stability window.<sup>59</sup> In the light of some recent discoveries, however, questions regarding the defect chemistry in such materials arise. For instance, Kanatzidis reported on the incorporation of ethylenediammonium [NH<sub>3</sub>C<sub>2</sub>H<sub>4</sub>NH<sub>3</sub>]<sup>2+</sup> enhancing the photovoltaic performance of the working materials.<sup>60</sup> Shortly after, they thoroughly studied the defect chemistry of such A-site solid solutions, revealing a complex defect chemistry behaviour related to materials series such as [CH<sub>3</sub>NH<sub>3</sub>]<sub>1-x</sub>[NH<sub>3</sub>C<sub>2</sub>H<sub>4</sub>NH<sub>3</sub>]<sub>x</sub>(Sn)<sub>1-0.7x</sub>(I)<sub>3-0.4x</sub> and [CH<sub>3</sub>NH<sub>3</sub>]<sub>1-x</sub>[NH<sub>3</sub>C<sub>2</sub>H<sub>4</sub>NH<sub>3</sub>]<sub>x</sub>(Pb)<sub>1-0.7x</sub>(I)<sub>3-0.4x</sub>,<sup>61</sup> with blue shifted band gaps (hollow perovskites). When further increasing the size of the A'-site cation in solid-solutions with the general stoichiometry A<sub>1-y</sub>A'<sub>y</sub>BX<sub>3</sub>, the formation of low dimensional structures is favoured. These low-dimensional structures depict the hybrid analogue of Ruddlesden-Popper and Dion-Jacobson-type phases.<sup>62,63</sup> It should be highlighted here that during the synthesis of such complex materials, particular care must be taken for the analysis of the crystal structure and composition. It was only recently realized that the decomposition reaction of dimethylformamide (DMF) into dimethylammonium (DMA) and the formate anion (DMF → DMA + HCOO<sup>-</sup>) plays a crucial role.<sup>64,65</sup> It seems that DMA can itself act as a molecular A-site cation for balancing the TF of the compound to fulfill the stability criteria. For instance, the perovskite phase of CsPbI<sub>3</sub> can potentially be stabilized by the incorporation of DMA, very similar to the approach schematically shown in Figure 4.<sup>66,67</sup>

Structural investigations must be performed with care, oftentimes a challenging task when only thin films are available. For instance, Xu *et al.* initially reported on increasing the moisture stability of [CH<sub>3</sub>NH<sub>3</sub>]<sub>2</sub>PbI<sub>3</sub> by the incorporation of two pseudohalide SCN<sup>-</sup> anions, thereby challenging the TF concept: the TF of a potential [CH<sub>3</sub>NH<sub>3</sub>]<sub>2</sub>PbI(SCN)<sub>2</sub> phase is significantly smaller than 0.8 due to the large size of the SCN<sup>-</sup> anions. However, structural characterisation remained challenging as suggested by the authors and shortly after, Hillebrecht and co-workers found that [CH<sub>3</sub>NH<sub>3</sub>]<sub>2</sub>PbI(SCN)<sub>2</sub> crystallises in the K<sub>2</sub>NiF<sub>4</sub>-type structure, again a hybrid representative of a Ruddlesden-Popper phase,<sup>68,69</sup> confirming the applicability of the TF concept. This on the one hand shows the increasing complexity of structural investigations when introducing structural complexity in the X-site by the use of molecular anions, but at the same time, underpins the importance of the TF concept in understanding crystal formation of different phases.<sup>70,71</sup>

Based on the current literature of hybrid perovskites of the type I<sup>3</sup>O<sup>0</sup>, TFs seem to be extremely useful in explaining stability criteria for existing and potentially new hybrid perovskite phases. Interestingly, the number of studies that explicitly use TFs for the study of Sn-based compounds which can be seen as less-toxic alternatives to Pb-based perovskites is limited.<sup>72</sup> This is not a big surprise, having in mind that TFs have mainly been applied to Pb-based perovskites for improving their stability by manipulating TFs thereby fulfilling size criteria for stability. The metastability of Sn<sup>2+</sup>-based materials, however, mainly originates from the low potential for the oxidation of Sn<sup>2+</sup> to Sn<sup>4+</sup> and not from size criteria. Similarly, TFs of double perovskites with the general formula A<sub>2</sub>BB'X<sub>6</sub> which present another way forward in the preparation of lead-free alternatives have not been in the broad focus of attention, and it is questionable if general applicable size criteria can be formulated in these cases. However, despite efforts in the synthesis of hybrid double perovskites,<sup>73,74</sup> it has been pointed out recently that orbital-symmetry requirements for the formation of direct band-gaps are difficult to fulfill in double perovskites.<sup>75,76</sup> When looking at more complex systems with semiconductive properties, it is important to realize that TFs also capture hybrid organic-inorganic Ruddlesden-Popper<sup>77</sup> and Dion-Jacobson<sup>78,79</sup> phases in which (2D) perovskite slabs are separated by interlayer motifs typically consisting of A'-cations that are too large to fit into the ReO<sub>3</sub>-cavity: while the 2D perovskite layers fulfill the TF stability criteria, the separation layers typically involve A'-cations with a relatively large organic backbone, *e.g.* [CH<sub>3</sub>(CH<sub>2</sub>)<sub>3</sub>NH<sub>3</sub>]<sub>2</sub> (*n*-butylammonium), that would lead to TFs significantly larger than 1.<sup>30,80,81</sup> For instance, Kanatzidis and co-workers reported on the successful preparation of [CH<sub>3</sub>(CH<sub>2</sub>)<sub>3</sub>NH<sub>3</sub>]<sub>2</sub>[CH<sub>3</sub>NH<sub>3</sub>]<sub>n-1</sub>Pb<sub>n</sub>I<sub>3n+1</sub> (*n* = 1, 2, 3, and 4) perovskite thin films, in which *n*-butylammonium as the very large A-cation separates perovskite layers which fulfill the TF criteria.<sup>63</sup>

Despite the high agreement of TFs with experimental observations, it is important to realize that in situations where [CH<sub>3</sub>NH<sub>3</sub>]<sup>+</sup> (or similarly [N(CH<sub>2</sub>)<sub>3</sub>]<sup>+</sup>) is replaced by intermediate-sized cations with different charges, [NH<sub>3</sub>C<sub>2</sub>H<sub>4</sub>NH<sub>3</sub>]<sup>2+</sup> (ethylenediammonium), the TF concept reaches its limitations. In these situations, *e.g.* the above-mentioned hollow perovskites,



the calculation and interpretation of TFs should be performed with care. These findings highlight the importance of in-depth structural studies on defective systems based on high resolution powder X-ray diffraction and X-ray total scattering experiments.<sup>53,82</sup> In fact, the complexity of the underlying thermodynamic landscape and in turn the impact of generally weak interactions are nicely seen when looking at the ternary system  $[\text{NH}_3\text{NH}_2]^+-\text{Pb}^{2+}-\text{I}^-$ , recently investigated by Miller and co-workers. The authors observe a range of different materials with different compositions such as  $[\text{NH}_3\text{NH}_2]_{15}\text{Pb}_3\text{I}_{21}$  and  $[\text{NH}_3\text{NH}_2]\text{PbI}_3$ .<sup>83</sup> Focusing on  $[\text{NH}_3\text{NH}_2]\text{PbI}_3$ , a low-dimensional structure is observed, despite a TF within the window at which a perovskite should be formed. In  $[\text{NH}_3\text{NH}_2]\text{PbI}_3$ , a low-dimensional structure is favoured due to a large number of hydrogen bonding interactions between neighbouring  $[\text{NH}_3\text{NH}_2]^+$  cations, which were observed in related materials.<sup>8</sup> Therefore it can be concluded that TFs seem to describe dominant interactions originating from the 3D  $\text{ReO}_3$ -like framework, *i.e.* ionic interactions, but the propensity of weak interactions originating from the molecular nature of the A-cations challenges this concept. From a chemical viewpoint, however, a seeming breakdown of the TF concept can be the start of interesting chemical interactions and sharpens the chemist's perception of the role of weak molecular interactions.

#### Hybrid perovskites of the type $\text{I}^0\text{O}^3$

We now want to discuss  $\text{I}^0\text{O}^3$ -type perovskites, in which the  $\text{ReO}_3$ -type framework is formed by molecular  $\text{X}^-$  anions, *e.g.*  $[\text{NH}_3\text{NH}_2]\text{Zn}(\text{HCOO})_3$ ,  $[\text{C}_3\text{N}_2\text{H}_5]\text{Mn}(\text{H}_2\text{POO})_3$  and  $[\text{PPN}]\text{-Mn}[\text{Au}(\text{CN})_2]_3$  (Fig. 1b–f). Due to the underlying coordination chemistry of the divalent metal cation and the X anion, such materials fall well within the large family of coordination polymers. As mentioned above, the difference in the underlying chemistry has large implications on the materials properties, with free lone pairs located at the molecular anions oftentimes acting as anchors for hydrogen bonding interactions.<sup>17,21,22,27</sup> Despite the chemical complexity coming from the molecular nature of the X-anion, it is fascinating to observe that the TF concept still holds good for the majority of these materials. For instance, materials families such as formates, azides, dicyanometallates and dicyanoamides form perovskite-type materials of which most of the materials exhibit TFs that fall within the window between 0.8 and 1 (see Fig. 3 for Mn-based formates).<sup>15,29,46,84</sup> An exciting finding of the recent literature in this context is the discovery of a new family of  $\text{I}^0\text{O}^3$ -type hybrid perovskites based on the hypophosphite  $[\text{H}_2\text{POO}]^-$  anion, extending the parameter space by establishing a new molecular X-anion.<sup>14</sup> Compounds such as  $[\text{N}(\text{CH}_2)_3]\text{Mn}(\text{H}_2\text{POO})_3$ ,  $[(\text{NH}_2)_2\text{CH}]\text{Mn}(\text{H}_2\text{POO})_3$  and  $[\text{C}_3\text{N}_2\text{H}_5]\text{Mn}(\text{H}_2\text{POO})_3$  highlight the applicability of the TF concept and at the same time, show the robustness of TFs towards cage distortions. To assess the distortions of the materials in more detail, the authors suggested the introduction of a distortion factor, enabling the comparison of the distortion of the different  $\text{ReO}_3$ -type 3D networks related to their observed volume. Such an analysis has been previously suggested qualitatively for formate-based

perovskites, leading to a classification in which large cage distortions and different binding situations of the formate anions are captured.<sup>85,86</sup> Importantly, such a classification also includes materials families in which monoatomic or very small A-cations are used as it is the case in perovskite-type materials such as  $\text{RbMn}(\text{HCOO})_3$  and  $(\text{NH}_4)\text{Cd}(\text{HCOO})_3$ . Very similar to the abovementioned halides, solid-solutions on the A-site can be used to tune dielectric properties, whilst staying within the TF window. Examples are the series  $[\text{NH}_3\text{NH}_2]_{1-x}[\text{CH}_3\text{NH}_3]_x\text{-Mn}(\text{HCOO})_3$  and  $[\text{NH}_3\text{NH}_2]_{1-x}[\text{NH}_3\text{OH}]_x\text{-Zn}(\text{HCOO})_3$  in which the temperature of the ferroelectric-to-paraelectric phase transition temperature can be tuned by varying  $x$ .<sup>87,88</sup> Interestingly, such solid-solutions offer the possibility to incorporate A-cations which do not form a perovskite-structure in their parent phase, *e.g.*  $[\text{NH}_3\text{OH}]^+$  in  $[\text{NH}_3\text{NH}_2]\text{Zn}(\text{HCOO})_3$ . The key behind the tuneable properties is the incorporation of small structural distortions, which directly achieves the balance between hydrogen-bonding interactions, and configurational and vibrational entropy – parameters that go beyond the TF concept. A similar conclusion can of course be drawn for related materials such as azides and dicyanamides.<sup>89,90</sup> Importantly and very similar to halide based perovskites, the energy landscape seems very shallow, and consequently, tuning the reaction temperature and solvent has a large impact on the obtained materials, again emphasizing the role of thermodynamic parameters. This was nicely shown by Mączka and co-workers, who investigated the effect of solvent, temperature and pressure within the family  $[\text{NH}_3\text{NH}_2]\text{M}(\text{HCOO})_3$  with  $\text{M} = \text{Mn}, \text{Zn}, \text{Co}$  and  $\text{Fe}$ .<sup>91</sup> For  $\text{M} = \text{Zn}$  and  $\text{Mn}$ , a perovskite structure is observed whilst  $\text{M} = \text{Co}$  and  $\text{Fe}$  lead to the formation of a low-dimensional structure, despite the TF concept suggesting the formation of perovskite-type phases for all divalent metals.<sup>8</sup> It was shown that for this family, vibrational entropy is an important parameter, flattening the energy landscape and in turn enabling experimentalists to assess polymorphism by changing reaction conditions.<sup>92</sup> Vibrational entropy in general has been identified as playing an important role in such materials, being the driving-force behind temperature driven phase transitions.<sup>19,93</sup> In the rigid body approach, the TF is not designed to capture such effects, and polymorphism in  $[\text{NH}_3\text{NH}_2]\text{Zn}(\text{HCOO})_3$  and potential phase transitions in general are tough to predict. Furthermore, comparisons can be drawn between the low dimensional structure of the  $[\text{NH}_3\text{NH}_2]\text{Zn}(\text{HCOO})_3$  polymorph and the abovementioned  $[\text{NH}_2\text{NH}_2]\text{PbI}_3$  phase, in which hydrogen bonding interactions between  $[\text{NH}_3\text{NH}_2]^+$  cations are observed. In general however, TFs are a very good guideline that gives experimentalists the first idea about the A–B–X permutation for which a perovskite-type structure is expected. The increased parameter space in  $\text{I}^0\text{O}^3$  hybrid perovskites, however, raises challenges in the targeted incorporation of distinct materials properties, while the balance of weak interactions such as dispersion interactions, hydrogen bonding interactions, and configurational and vibrational entropy together with the large library of molecular cations opens intriguing opportunities in caloric applications at the same time.<sup>10,94,95</sup>

Lastly, a fascinating class of hybrid perovskites moved into the focus of attention of the materials science community

that fall within the sub-class of  $I^0O^3$  hybrid perovskites: metal-free ferroelectric perovskites. In these materials, the three dimensional  $ReO_3$ -type framework is built of  $[NH_4]^+$  cations and  $X^-$ -anions such as  $Br^-$  and  $I^-$  and are charge balanced by divalent A-site cations such as  $[(CH_2)_6N_2(CH_3)H]^{2+}$ ,  $[(CH_2)_6N_2(OH)H]^{2+}$ ,  $[(CH_2)_3(CH)N_2H_5]^{2+}$  and  $[(CH_2)_5(CH)_2N_2H_4]^{2+}$ .<sup>11</sup> Some of these materials exhibit a complex structural behaviour as a function of temperature, with the rotation of the A-cation similar to the temperature activated disorder observed for  $[CH_3NH_3]^+$  in  $[CH_3NH_3]PbI_3$ . Initially reported in 2003 by Bremner and co-workers,<sup>96</sup> it was only recently found that large spontaneous polarization exists in  $[(CH_2)_6N_2(CH_3)H](NH_4)I_3$ , competing with the classical ferroelectric  $BaTiO_3$ . In these materials, the bonding situation within the network challenges the TF concept: whilst in some cases the TF concept is fulfilled, e.g. size criteria seem to dominate the energetic landscape, in other cases low dimensional, so-called hexagonal perovskites are preferred due to the possibility to form intermolecular interactions between A-site cations. It seems that due to the unusual bonding situation within the  $ReO_3$ -lattice, weaker interactions become even more important, and the TF concept should be carefully applied. However, for TFs > 0.9, mainly 3D perovskites are observed, pointing to the general applicability of the concept across various types of hybrid perovskites.

## A bright future?

After reviewing the most remarkable research examples that have been reported in the past three years, it is only natural to ask where can TFs take us in the future? When discussing this question, it is important to realise that the TF concept itself only depicts a broad guideline towards new hybrid perovskites and is far away from being a thermodynamic rule. As outlined above, the beauty of this guideline lies in its simplicity, making it possible to calculate TFs from available literature data within minutes. The abovementioned study by Becker and co-workers is only one study out of few in which TFs suggest the existence of many undiscovered phases.<sup>46,47,52,97,98</sup> At the same time, the concept sharpens our chemical intuition, not only for hybrid perovskites, but also for the complexity of organic-inorganic materials in general. For instance, when the TF of a hypothetical A-B-X permutation indicates the existence of a perovskite-type material but is experimentally not observed, or *vice versa*, it can be interesting to ask why? This can be the start of fascinating discoveries such as strong entropic effects or related phenomena.<sup>92-94</sup> In this regard, hybrid perovskites can remind us about the importance of lattice entropy in organic-inorganic materials. Following this thought, the TF concept is a rigid-body approach, intrinsically neglecting dynamic effects. In other words, rigid-body guidelines such as the TF concept (or similarly the reticular chemistry approach for metal-organic frameworks) provide a toolbox to understand and build network materials based on enthalpic interactions, whilst dynamic effects hidden in vibrational and configurational entropy are intrinsically neglected. The long-term goal might therefore be to find design principles, or at least common structural

anomalies, that allow for assessing entropic effects more generally. The first step towards this goal can be database assisted approaches that help screening for trends in symmetry-breaking phenomena. Similarly, in  $I^0O^3$  perovskites, tilts and shifts are observed that are not present in all inorganic perovskites, and despite inspiring studies, a broad overview of such effects is still missing.<sup>99,100</sup> Whether such studies will lead to further improvement of the TF concept is an open question for ongoing research, and it will be exciting to see how this development goes on. Therefore, when looking at the development of hybrid perovskites in the past few years, it can be summarised that the tolerance factor concept is an overarching guiding principle for chemists and physicists of different areas that can lead experimentalists in the right direction towards new hybrid perovskite materials, who should, however, always keep the limitations of such a concept in mind.

## Conflicts of interest

There are no conflicts to declare.

## Acknowledgements

GK and ME would like to thank the "Fonds der chemischen Industrie" for financial support through the Liebig Fellowship scheme. The authors are very grateful for insightful discussions with Ian Sharp and Anthony K. Cheetham.

## References

- 1 A. Kojima, K. Teshima, Y. Shirai and T. Miyasaka, *J. Am. Chem. Soc.*, 2009, **131**(17), 6050.
- 2 G. E. Eperon, S. D. Stranks, C. Menelaou, M. B. Johnston, L. M. Herz and H. J. Snaith, *Energy Environ. Sci.*, 2014, **7**(3), 982.
- 3 J.-W. Lee, D.-J. Seol, A.-N. Cho and N.-G. Park, *Adv. Mater.*, 2014, **26**(29), 4991.
- 4 X. Huang, Z. Zhao, L. Cao, Y. Chen, E. Zhu, Z. Lin, M. Li, A. Yan, A. Zettl, Y. M. Wang, X. Duan, T. Mueller and Y. Huang, *Science*, 2015, **348**(6240), 1230.
- 5 M. M. Lee, J. Teuscher, T. Miyasaka, T. N. Murakami and H. J. Snaith, *Science*, 2012, **338**(6107), 643.
- 6 B. V. Lotsch, *Angew. Chem., Int. Ed.*, 2014, **53**(3), 635.
- 7 J. M. Bermúdez-García, M. Sánchez-Andújar, S. Yáñez-Vilar, S. Castro-García, R. Artiaga, J. López-Becero, L. Botana, Á. Alegría and M. A. Señaris-Rodríguez, *Inorg. Chem.*, 2015, **54**(24), 11680.
- 8 S. Chen, R. Shang, K.-L. Hu, Z.-M. Wang and S. Gao, *Inorg. Chem. Front.*, 2014, **1**(1), 83.
- 9 Z.-Y. Du, Y.-Z. Sun, S.-L. Chen, B. Huang, Y.-J. Su, T.-T. Xu, W.-X. Zhang and X.-M. Chen, *Chem. Commun.*, 2015, **51**(86), 15641.
- 10 J. M. Bermúdez-García, M. Sánchez-Andújar and M. A. Señaris-Rodríguez, *J. Phys. Chem. Lett.*, 2017, **8**(18), 4419.

- 11 H.-Y. Ye, Y.-Y. Tang, P.-F. Li, W.-Q. Liao, J.-X. Gao, X.-N. Hua, H. Cai, P.-P. Shi, Y.-M. You and R.-G. Xiong, *Science*, 2018, **361**(6398), 151.
- 12 A. K. Cheetham, C. N. R. Rao and R. K. Feller, *Chem. Commun.*, 2006, (46), 4780.
- 13 K. Page, J. E. Siewenie, P. Quadrelli and L. Malavasi, *Angew. Chem., Int. Ed.*, 2016, **55**(46), 14320.
- 14 Y. Wu, S. Shaker, F. Brivio, R. Murugavel, P. D. Bristowe and A. K. Cheetham, *J. Am. Chem. Soc.*, 2017, **139**(47), 16999.
- 15 J. A. Hill, A. L. Thompson and A. L. Goodwin, *J. Am. Chem. Soc.*, 2016, **138**(18), 5886.
- 16 C. C. Stoumpos, C. D. Malliakas and M. G. Kanatzidis, *Inorg. Chem.*, 2013, **52**(15), 9019.
- 17 M. Mączka, A. Ciupa, A. Gağor, A. Sieradzki, A. Pikul, B. Macalik and M. Drozd, *Inorg. Chem.*, 2014, **53**(10), 5260.
- 18 C. Quarti, G. Grancini, E. Mosconi, P. Bruno, J. M. Ball, M. M. Lee, H. J. Snaith, A. Petrozza and F. de Angelis, *J. Phys. Chem. Lett.*, 2014, **5**(2), 279.
- 19 K. T. Butler, K. Svane, G. Kieslich, A. K. Cheetham and A. Walsh, *Phys. Rev. B*, 2016, **94**(18), 180103.
- 20 C. W. Myung, J. Yun, G. Lee and K. S. Kim, *Adv. Energy Mater.*, 2018, **8**(14), 1702898.
- 21 G. Kieslich, A. C. Forse, S. Sun, K. T. Butler, S. Kumagai, Y. Wu, M. R. Warren, A. Walsh, C. P. Grey and A. K. Cheetham, *Chem. Mater.*, 2016, **28**(1), 312.
- 22 K. L. Svane, A. C. Forse, C. P. Grey, G. Kieslich, A. K. Cheetham, A. Walsh and K. T. Butler, *J. Phys. Chem. Lett.*, 2017, **8**(24), 6154.
- 23 J.-H. Lee, N. C. Bristowe, P. D. Bristowe and A. K. Cheetham, *Chem. Commun.*, 2015, **51**(29), 6434.
- 24 G. Kieslich and A. L. Goodwin, *Mater. Horiz.*, 2017, **4**(3), 362.
- 25 F. El-Mellouhi, A. Marzouk, E. T. Bentría, S. N. Rashkeev, S. Kais and F. H. Alharbi, *ChemSusChem*, 2016, **9**(18), 2648.
- 26 J. Berry, T. Buonassisi, D. A. Egger, G. Hodes, L. Kronik, Y.-L. Loo, I. Lubomirsky, S. R. Marder, Y. Mastai, J. S. Miller, D. B. Mitzi, Y. Paz, A. M. Rappe, I. Riess, B. Rybtchinski, O. Stafsudd, V. Stevanovic, M. F. Toney, D. Zitoun, A. Kahn, D. Ginley and D. Cahen, *Adv. Mater.*, 2015, **27**(35), 5102.
- 27 W. Li, Z. Wang, F. Deschler, S. Gao, R. H. Friend and A. K. Cheetham, *Nat. Rev. Mater.*, 2017, **2**(3), 16099.
- 28 B. Saparov and D. B. Mitzi, *Chem. Rev.*, 2016, **116**(7), 4558.
- 29 W.-J. Xu, Z.-Y. Du, W.-X. Zhang and X.-M. Chen, *CrystEngComm*, 2016, **18**(41), 7915.
- 30 D. B. Mitzi, *J. Chem. Soc., Dalton Trans.*, 2001, **1**, 1.
- 31 G. Kieslich, S. Sun and A. K. Cheetham, *Chem. Sci.*, 2014, **5**(12), 4712.
- 32 V. M. Goldschmidt, *Naturwissenschaften*, 1926, **14**(21), 477.
- 33 M. W. Lufaso and P. M. Woodward, *Acta Crystallogr. B*, 2001, **57**(Pt 6), 725.
- 34 M. Kubicek, A. H. Bork and J. L. M. Rupp, *J. Mater. Chem. A*, 2017, **5**(24), 11983.
- 35 M. A. Peña and J. L. G. Fierro, *Chem. Rev.*, 2001, **101**(7), 1981.
- 36 J. B. Goodenough, *Rep. Prog. Phys.*, 2004, **67**(11), 1915.
- 37 C. Liu, B. Zou, A. J. Rondinone and Z. J. Zhang, *J. Am. Chem. Soc.*, 2001, **123**(18), 4344.
- 38 S. O'Brien, L. Brus and C. B. Murray, *J. Am. Chem. Soc.*, 2001, **123**(48), 12085.
- 39 A. von Hippel, R. G. Breckenridge, F. G. Chesley and L. Tisza, *Ind. Eng. Chem.*, 1946, **38**(11), 1097.
- 40 J. Wang, J. B. Neaton, H. Zheng, V. Nagarajan, S. B. Ogale, B. Liu, D. Viehland, V. Vaithyanathan, D. G. Schlom, U. V. Waghmare, N. A. Spaldin, K. M. Rabe, M. Wuttig and R. Ramesh, *Science*, 2003, **299**(5613), 1719.
- 41 C. K. MÖLLER, *Nature*, 1958, **182**, 1436.
- 42 S. Jin, T. H. Tiefel, M. McCormack, R. A. Fastnacht, R. Ramesh and L. H. Chen, *Science*, 1994, **264**(5157), 413.
- 43 J. Hwang, R. R. Rao, L. Giordano, Y. Katayama, Y. Yu and Y. Shao-Horn, *Science*, 2017, **358**(6364), 751.
- 44 A. K. Cheetham and C. N. R. Rao, *Science*, 2007, **318**(5847), 58.
- 45 S. Stølen, E. Bakken and C. E. Mohn, *Phys. Chem. Chem. Phys.*, 2006, **8**(4), 429.
- 46 G. Kieslich, S. Sun and A. K. Cheetham, *Chem. Sci.*, 2015, **6**(6), 3430.
- 47 W. Travis, E. N. K. Glover, H. Bronstein, D. O. Scanlon and R. G. Palgrave, *Chem. Sci.*, 2016, **7**(7), 4548.
- 48 R. D. Shannon, *Acta Crystallogr. A*, 1976, **32**(5), 751.
- 49 C. Li, X. Lu, W. Ding, L. Feng, Y. Gao and Z. Guo, *Acta Crystallogr. B*, 2008, **64**(Pt 6), 702.
- 50 R. M. Wood and G. J. Palenik, *Inorg. Chem.*, 1998, **37**(16), 4149.
- 51 M. R. Linaburg, E. T. McClure, J. D. Majher and P. M. Woodward, *Chem. Mater.*, 2017, **29**(8), 3507.
- 52 M. Becker, T. Klüner and M. Wark, *Dalton Trans.*, 2017, **46**(11), 3500.
- 53 S. Gholipour, A. M. Ali, J.-P. Correa-Baena, S.-H. Turren-Cruz, F. Tajabadi, W. Tress, N. Taghavinia, M. Grätzel, A. Abate, F. de Angelis, C. A. Gaggioli, E. Mosconi, A. Hagfeldt and M. Saliba, *Adv. Mater.*, 2017, **29**(38), 1702005.
- 54 G. P. Nagabhushana, R. Shivaramaiah and A. Navrotsky, *Proc. Natl. Acad. Sci. U. S. A.*, 2016, **113**(28), 7717.
- 55 X. Zheng, C. Wu, S. K. Jha, Z. Li, K. Zhu and S. Priya, *ACS Energy Lett.*, 2016, **1**(5), 1014.
- 56 Z. Li, M. Yang, J.-S. Park, S.-H. Wei, J. J. Berry and K. Zhu, *Chem. Mater.*, 2016, **28**(1), 284.
- 57 M. Saliba, T. Matsui, J.-Y. Seo, K. Domanski, J.-P. Correa-Baena, M. K. Nazeeruddin, S. M. Zakeeruddin, W. Tress, A. Abate, A. Hagfeldt and M. Grätzel, *Energy Environ. Sci.*, 2016, **9**(6), 1989.
- 58 W. Peng, X. Miao, V. Adinolfi, E. Alarousu, O. El Tall, A.-H. Emwas, C. Zhao, G. Walters, J. Liu, O. Ouellette, J. Pan, B. Murali, E. H. Sargent, O. F. Mohammed and O. M. Bakr, *Angew. Chem., Int. Ed.*, 2016, **55**(36), 10686.
- 59 A. D. Jodlowski, C. Roldán-Carmona, G. Grancini, M. Salado, M. Ralaiarisoa, S. Ahmad, N. Koch, L. Camacho, G. d. Miguel and M. K. Nazeeruddin, *Nat. Energy*, 2017, **2**(12), 972.
- 60 W. Ke, C. C. Stoumpos, M. Zhu, L. Mao, I. Spanopoulos, J. Liu, O. Y. Kontsevoi, M. Chen, D. Sarma, Y. Zhang,

- M. R. Wasielewski and M. G. Kanatzidis, *Sci. Adv.*, 2017, **3**(8), e1701293.
- 61 I. Spanopoulos, W. Ke, C. C. Stoumpos, E. C. Schueller, O. Y. Kontsevoi, R. Seshadri and M. G. Kanatzidis, *J. Am. Chem. Soc.*, 2018, **140**(17), 5728.
- 62 L. Mao, W. Ke, L. Pedesseau, Y. Wu, C. Katan, J. Even, M. R. Wasielewski, C. C. Stoumpos and M. G. Kanatzidis, *J. Am. Chem. Soc.*, 2018, **140**(10), 3775.
- 63 D. H. Cao, C. C. Stoumpos, O. K. Farha, J. T. Hupp and M. G. Kanatzidis, *J. Am. Chem. Soc.*, 2015, **137**(24), 7843.
- 64 N. K. Noel, M. Congiu, A. J. Ramadan, S. Fearn, D. P. McMeekin, J. B. Patel, M. B. Johnston, B. Wenger and H. J. Snaith, *Joule*, 2017, **1**(2), 328.
- 65 B. Dou, L. M. Wheeler, J. A. Christians, D. T. Moore, S. P. Harvey, J. J. Berry, F. S. Barnes, S. E. Shaheen and M. F. A. M. van Hest, *ACS Energy Lett.*, 2018, **3**(4), 979.
- 66 G. E. Eperon, G. M. Paternò, R. J. Sutton, A. Zampetti, A. A. Haghighirad, F. Cacialli and H. J. Snaith, *J. Mater. Chem. A*, 2015, **3**(39), 19688.
- 67 D. Liu, C. Yang and R. R. Lunt, *Joule*, 2018, **2**(9), 1827.
- 68 Q. Jiang, D. Rebolgar, J. Gong, E. L. Piacentino, C. Zheng and T. Xu, *Angew. Chem., Int. Ed.*, 2015, **54**(26), 7617.
- 69 M. Daub and H. Hillebrecht, *Angew. Chem., Int. Ed.*, 2015, **54**(38), 11016.
- 70 G. Tang, C. Yang, A. Stroppa, D. Fang and J. Hong, *J. Chem. Phys.*, 2017, **146**(22), 224702.
- 71 A. Halder, R. Chulliyil, A. S. Subbiah, T. Khan, S. Chattoraj, A. Chowdhury and S. K. Sarkar, *J. Phys. Chem. Lett.*, 2015, **6**(17), 3483.
- 72 S. F. Hoefler, G. Trimmel and T. Rath, *Monatsh. Chem.*, 2017, **148**(5), 795.
- 73 F. Wei, Z. Deng, S. Sun, F. Xie, G. Kieslich, D. M. Evans, M. A. Carpenter, P. D. Bristowe and A. K. Cheetham, *Mater. Horiz.*, 2016, **3**(4), 328.
- 74 Z. Deng, F. Wei, S. Sun, G. Kieslich, A. K. Cheetham and P. D. Bristowe, *J. Mater. Chem. A*, 2016, **4**(31), 12025.
- 75 C. N. Savory, A. Walsh and D. O. Scanlon, *ACS Energy Lett.*, 2016, **1**(5), 949.
- 76 T. T. Tran, J. R. Panella, J. R. Chamorro, J. R. Morey and T. M. McQueen, *Mater. Horiz.*, 2017, **4**(4), 688.
- 77 S. N. Ruddlesden and P. Popper, *Acta Crystallogr.*, 1957, **10**(8), 538.
- 78 M. Dion, M. Ganne and M. Tournoux, *Mater. Res. Bull.*, 1981, **16**(11), 1429.
- 79 A. J. Jacobson, J. W. Johnson and J. T. Lewandowski, *Inorg. Chem.*, 1985, **24**(23), 3727.
- 80 M. I. Saidaminov, O. F. Mohammed and O. M. Bakr, *ACS Energy Lett.*, 2017, **2**(4), 889.
- 81 J.-C. Blancon, A. V. Stier, H. Tsai, W. Nie, C. C. Stoumpos, B. Traoré, L. Pedesseau, M. Kepenekian, F. Katsutani, G. T. Noe, J. Kono, S. Tretiak, S. A. Crooker, C. Katan, M. G. Kanatzidis, J. J. Crochet, J. Even and A. D. Mohite, *Nat. Commun.*, 2018, **9**(1), 2254.
- 82 T. J. Jacobsson, S. Svanström, V. Andrei, J. P. H. Rivett, N. Kornienko, B. Philippe, U. B. Cappel, H. Rensmo, F. Deschler and G. Boschloo, *J. Phys. Chem. C*, 2018, **122**(25), 13548.
- 83 E. V. Campbell, B. Dick, A. L. Rheingold, C. Zhang, X. Liu, Z. V. Vardeny and J. S. Miller, *Chem.–Eur. J.*, 2018, **24**(1), 222.
- 84 M. Maćzka, A. Gaćgor, M. Ptak, W. Paraguassu, T. A. da Silva, A. Sieradzki and A. Pikul, *Chem. Mater.*, 2017, **29**(5), 2264.
- 85 L. C. Gómez-Aguirre, B. Pato-Doldán, A. Stroppa, S. Yáñez-Vilar, L. Bayarjargal, B. Winkler, S. Castro-García, J. Mira, M. Sánchez-Andújar and M. A. Señaris-Rodríguez, *Inorg. Chem.*, 2015, **54**(5), 2109.
- 86 S. M. Bovill and P. J. Saines, *CrystEngComm*, 2015, **17**(43), 8319.
- 87 G. Kieslich, S. Kumagai, A. C. Forse, S. Sun, S. Henke, M. Yamashita, C. P. Grey and A. K. Cheetham, *Chem. Sci.*, 2016, **7**(8), 5108.
- 88 S. Chen, R. Shang, B.-W. Wang, Z.-M. Wang and S. Gao, *Angew. Chem., Int. Ed.*, 2015, **54**(38), 11093.
- 89 X.-H. Zhao, X.-C. Huang, S.-L. Zhang, D. Shao, H.-Y. Wei and X.-Y. Wang, *J. Am. Chem. Soc.*, 2013, **135**(43), 16006.
- 90 J. M. Bermúdez-García, M. Sánchez-Andújar, S. Yáñez-Vilar, S. Castro-García, R. Artiaga, J. López-Beceiro, L. Botana, A. Alegria and M. A. Señaris-Rodríguez, *J. Mater. Chem. C*, 2016, **4**(22), 4889.
- 91 M. Maćzka, K. Pasińska, M. Ptak, W. Paraguassu, T. A. da Silva, A. Sieradzki and A. Pikul, *Phys. Chem. Chem. Phys.*, 2016, **18**(46), 31653.
- 92 G. Kieslich, S. Kumagai, K. T. Butler, T. Okamura, C. H. Hendon, S. Sun, M. Yamashita, A. Walsh and A. K. Cheetham, *Chem. Commun.*, 2015, **51**(85), 15538.
- 93 W. Wei, W. Li, K. T. Butler, G. Feng, C. J. Howard, M. A. Carpenter, P. Lu, A. Walsh and A. K. Cheetham, *Angew. Chem., Int. Ed.*, 2018, **57**(29), 8932.
- 94 K. T. Butler, A. Walsh, A. K. Cheetham and G. Kieslich, *Chem. Sci.*, 2016, **7**(10), 6316.
- 95 J. M. Bermúdez-García, M. Sánchez-Andújar, S. Castro-García, J. López-Beceiro, R. Artiaga and M. A. Señaris-Rodríguez, *Nat. Commun.*, 2017, **8**, 15715.
- 96 C. A. Bremner, M. Simpson and W. T. A. Harrison, *J. Am. Chem. Soc.*, 2002, **124**(37), 10960.
- 97 M. R. Filip and F. Giustino, *J. Phys. Chem. C*, 2016, **120**(1), 166.
- 98 J. I. Uribe, D. Ramirez, J. M. Osorio-Guillén, J. Osorio and F. Jaramillo, *J. Phys. Chem. C*, 2016, **120**(30), 16393.
- 99 H. L. B. Boström, J. A. Hill and A. L. Goodwin, *Phys. Chem. Chem. Phys.*, 2016, **18**(46), 31881.
- 100 Y. Wu, T. Binford, J. A. Hill, S. Shaker, J. Wang and A. K. Cheetham, *Chem. Commun.*, 2018, **54**(30), 3751.

## 4.2 STUDY II: A New Polar Perovskite Coordination Network with Azaspiroundecane as A-Site Cation

When staying within the appropriate size match criteria for A-B-X permutations as provided by the extended Tolerance Factor concept, many variations of stable perovskite-type coordination networks can be prepared. While for the B-site cations and X-site anions selection is rather limited, there is vast parameter space for a suitable A-site cation to be chosen. An intuitive approach therefore is to help oneself to the vast selection of commercially available molecular building blocks; however, when aiming to implement distinct structure motifs or functionalities, synthetic chemistry can be exploited to provide advanced precursor molecules.

In this work, the tailor-made molecular cation 6-azaspiro[5.5]undecane ( $[ASU]^+$ ) is synthesised to be implemented into a  $ReO_3$ -type coordination network consisting of cadmium(II) and the multiatomic anion dicyanamide (dca). The resulting molecular perovskite material not just features a novel ammonium cation but crystallises in a polar space group with a large nonlinear optical property and a rare combination of network deformations. These results are of high interest for the scientific community that focuses on accessing distinct structural degrees of freedom in network materials. The study presented here reveals one way to implement functionality and distortions into molecular perovskites and how they can be altered for a specific purpose.

This communication article was prepared as an integral part of the master thesis of Silva Kronawitter guided by the author of this doctorate thesis and Dr. Gregor Kieslich. The study itself was designed by the author of this thesis together with Dr. Gregor Kieslich, while the synthesis and characterisation of the materials as well as the interpretation of experimental results was performed by the author of this doctorate thesis in collaboration with Silva Kronawitter. The manuscript was essentially written by Silva Kronawitter as part of her master thesis together with the author of this doctorate thesis and Dr. Gregor Kieslich, who assisted in writing and interpretation of the results. The analysis of the different modes of network deformation was done by Hanna L. B. Boström, while Jan K. Zaręba performed the second-harmonic generation experiments. All co-authors critically reviewed and approved the manuscript.

Status: Published as a Communication in Dalton Transactions.

Reproduced from Ref. [282] with permission from the Royal Society of Chemistry, see APPENDIX, C Reprint permissions for terms and conditions of the license agreement.

S. Burger, S. Kronawitter, H. L. B. Boström, J. K. Zaręba and G. Kieslich, *A new polar perovskite coordination network with azaspiroundecane as A-site cation*, *Dalton Trans.*, 2020, **49**, 10740-10744, DOI: 10.1039/D0DT01968B.





## COMMUNICATION

View Article Online  
View Journal | View IssueCite this: *Dalton Trans.*, 2020, **49**, 10740Received 1st June 2020,  
Accepted 21st July 2020

DOI: 10.1039/d0dt01968b

rsc.li/dalton

## A new polar perovskite coordination network with azaspirodecane as A-site cation†

Stefan Burger, <sup>a</sup> Silva Kronawitter,<sup>a</sup> Hanna L. B. Boström, <sup>b</sup> Jan K. Zareba <sup>c</sup> and Gregor Kieslich <sup>\*a</sup>

**ABX<sub>3</sub> perovskite coordination networks are a rapidly growing subclass of crystalline coordination networks. At present, synthetic efforts in the field are dominated by the use of commercially available building blocks, leaving the potential for tuning properties via targeted compositional changes largely untouched. Here we apply a rational crystal engineering approach, using 6-azaspiro[5.5]undecane ([ASU]<sup>+</sup>) as A-site cation for the synthesis of the polar perovskite [ASU][Cd(C<sub>2</sub>N<sub>3</sub>)<sub>3</sub>].**

Dense and porous coordination networks offer a fascinating material platform in the search for new chemistries and physics. By combining inorganic coordination chemistry and organic linker chemistry, coordination networks provide experimentalists with access to intriguing crystal chemistries and the full range of chemical bond strength *via* composition.<sup>1,2</sup> In turn coordination networks exhibit many fundamentally interesting and scientifically relevant properties such as the recent discoveries of unusual elastic properties of cadmium halide polymeric chains<sup>3</sup> and [Cu(acac)<sub>2</sub>],<sup>4</sup> the colossal negative linear compressibility observed in Zn[Au(CN)<sub>2</sub>]<sub>2</sub>,<sup>5</sup> and the spin-crossover phenomena in a dicyanometallate-based perovskite-type coordination network<sup>6</sup> to name just a few.

Among the various existing dense coordination networks is the rapidly growing class of ABX<sub>3</sub> perovskite-type coordination networks which we refer to as molecular perovskites.<sup>7</sup> This nomenclature highlights the use of molecular building blocks on the A and X-site and draws a clear line to hybrid organic-inorganic perovskites such as [CH<sub>3</sub>NH<sub>3</sub>][PbI<sub>3</sub>] and [(NH<sub>2</sub>)<sub>2</sub>CH]

PbI<sub>3</sub>.<sup>8,9</sup> Similar to inorganic perovskites, molecular perovskites crystallise in an ABX<sub>3</sub> perovskite structure, with both the A-site and X-site occupied by molecular moieties. The molecular A-site cation sits in the void of the ReO<sub>3</sub>-type 3D [BX<sub>3</sub>]<sup>-</sup> network and can interact with the [BX<sub>3</sub>]-network *via* hydrogen bonds and dispersion interactions. The phase space of molecular perovskites appears to even exceed that of inorganic perovskites, and materials such as [(CH<sub>3</sub>)<sub>2</sub>NH<sub>2</sub>][M(HCOO)<sub>3</sub>] (M = Mn<sup>2+</sup>, Fe<sup>2+</sup>, Co<sup>2+</sup>, Ni<sup>2+</sup>, Zn<sup>2+</sup>, Cd<sup>2+</sup> and Na<sup>+</sup><sub>0.5</sub>Fe<sup>3+</sup><sub>0.5</sub>),<sup>10–13</sup> [(CH<sub>3</sub>)<sub>2</sub>NH<sub>2</sub>][M(N<sub>3</sub>)<sub>3</sub>] (M = Mn<sup>2+</sup>, Cd<sup>2+</sup>),<sup>14,15</sup> [TriBuMe][M(C<sub>2</sub>N<sub>3</sub>)<sub>3</sub>] (TriBuMe = tributylmethylammonium, M = Mn<sup>2+</sup>, Fe<sup>2+</sup>, Co<sup>2+</sup>, Ni<sup>2+</sup>),<sup>16</sup> [(CH<sub>3</sub>)<sub>2</sub>NH<sub>2</sub>][Mn(H<sub>2</sub>POO)<sub>3</sub>]<sup>17,18</sup> and [Btba][M(C<sub>2</sub>N<sub>3</sub>)<sub>3</sub>] (Btba = benzyltributylammonium, M = Mn<sup>2+</sup>, Co<sup>2+</sup>)<sup>19</sup> nicely demonstrate the chemical variability of molecular perovskites. Conceptually, this variability originates from the use of a molecular building block on the X-site which leads to an enlargement of the ReO<sub>3</sub>-type network and in turn to additional chemical freedom on the A-site, see Fig. 1. It is this chemical variability that in principle allows for studying and manipulating the physicochemical properties of molecular perovskites as a function of small chemical changes. In turn, molecular perovskites show a range of interesting properties such as promising barocaloric performances,<sup>20</sup> tuneable mechanical responses<sup>16</sup> and multiferroic properties.<sup>11,14</sup> Since the perovs-

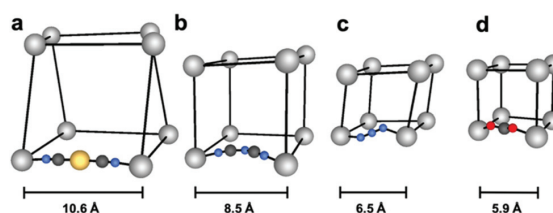


**Fig. 1** Illustrating the size dependence of the ReO<sub>3</sub>-type network in molecular perovskites as a function of the X-site anion with X = [Au(CN)<sub>2</sub>]<sup>-</sup> (a), [C<sub>2</sub>N<sub>3</sub>]<sup>-</sup> (b),<sup>16</sup> [N<sub>3</sub>]<sup>-</sup> (c)<sup>15</sup> and [HCOO]<sup>-</sup> (d).<sup>25</sup> For better visualisation, the A-site cation was deleted; colour code: Au – yellow, N – blue, C – dark grey, O – red and B-site cation in light grey.

<sup>a</sup>Technical University of Munich, Department of Chemistry, Lichtenbergstraße 4, 85748 Garching, Germany. E-mail: Gregor.Kieslich@tum.de

<sup>b</sup>Department of Inorganic Chemistry, Ångström Laboratory, Uppsala Universitet, Box 538, 751 21 Uppsala, Sweden

<sup>c</sup>Advanced Materials Engineering and Modelling Group, Wrocław University of Science and Technology, Wybrzeże Wyspiańskiego 27, 50-370 Wrocław, Poland

† Electronic supplementary information (ESI) available: Experimental, data analysis. CCDC 2006488 and 2006489. For ESI and crystallographic data in CIF or other electronic format see DOI: 10.1039/D0DT01968B

View Article Online

Dalton Transactions

Communication

kite building principle as structure motif is retained in molecular perovskites, the relative packing density as captured by the Goldschmidt's Tolerance Factor has proved to be an important tool in understanding the building principle of molecular perovskites.<sup>21–24</sup> When comparing molecular perovskites to inorganic perovskites, the use of molecular building units in molecular perovskites leads to chemical and structural degrees of freedom such as unconventional tilts and shifts when compared to the conventional tilt systems as captured by the Glazer notation,<sup>25,26</sup> the incorporation of (correlated) defects<sup>27</sup> and the manipulation of dynamic properties *via* A-site substitution amongst others.<sup>28,29</sup> Currently these additional degrees of freedom are mostly of scientific relevance although their role in design concepts based on tilt and shift engineering towards improper ferroelectrics has recently been highlighted.<sup>30,31</sup> These additional degrees of freedom nicely showcase the opportunities that come with the use of molecular building units and understanding their interplay and chemical origin can be considered as a milestone in the understanding of composition–structure–property relations in molecular perovskites.

In the pursuit to address these degrees of freedom synthetically current research efforts focus on the use of commercially available components.<sup>7,32</sup> In other words, one of the unique features of coordination networks—the *nearly unlimited chemical parameter space in the synthesis of tailor-made building blocks*—is broadly untouched, offering large opportunities for material tunability and for creating fundamental knowledge *via* systematic chemical manipulations. In this communication we follow on from this idea, presenting a route towards a new molecular perovskite with a tailor-made A-site cation which is based on the azaspiro motif. We show how to rationally select A–B–X permutations for the synthesis of a new molecular perovskite, reporting  $[\text{ASU}][\text{Cd}(\text{C}_2\text{N}_3)_3]$  as a new molecular perovskite with an unusual tilt system.

When looking for A-site cations with chemically interesting features, azaspiro compounds such as  $[\text{ASU}]^+$  (6-azaspiro[5.5]-undecane),  $[\text{ASD}]^+$  (5-azaspiro[4.5]decane) and  $[\text{ASN}]^+$  (5-azaspiro[4.4]nonane) are interesting candidates.<sup>33</sup> These molecular A-site cations seem to exhibit all ingredients that facilitate the discovery of interesting composition–symmetry–structure relations. They are accessible by standard organic substitution chemistry, the number of carbon atoms can be varied *via* the choice of the precursors, the synthesis of asymmetric azaspiro compounds such as ASD is possible and ring puckering<sup>34</sup> of incorporated azaspiro compounds with larger carbon rings can be expected. Therefore, azaspiro compounds are representing excellent candidates for studying the impact of size and symmetry on the formation and physicochemical properties of molecular perovskites. In this proof-of-principle study we focus on  $[\text{ASU}]^+$  as A-site cation for the synthesis of molecular perovskites.  $[\text{ASU}]^+$  can be prepared *via* nucleophilic substitution starting from piperidine and 1,5-dibromopentane, see Fig. 2a.<sup>33</sup> After A-site cation selection and synthesis, the Tolerance Factor concept can guide us in choosing a suitable A–B–X combination that is expected to form a perovskite-type structure. As for the X-site anion, the dicyanamide  $[\text{C}_2\text{N}_3]^-$

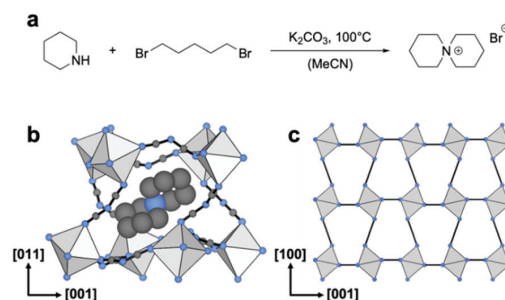


Fig. 2 (a) Synthetic scheme of  $[\text{ASU}]^+$  based on nucleophilic substitution. (b) shows the distorted 3D  $\text{ReO}_3$ -type network formed of  $\text{Cd}^{2+}$  and  $(\text{C}_2\text{N}_3)^-$  with  $[\text{ASU}]^+$  as the void-filling A-site cation. In (c) a 2D representation of the unconventional  $\text{M}_5^+$  tilt is shown. The tilt direction alternates along the axis of rotation, *i.e.* it is out of phase.

anion seems suitable.  $[\text{C}_2\text{N}_3]^-$  is a relatively large anion compared to other regularly used X-site anions such as  $[\text{N}_3]^-$ ,  $[\text{CN}]^-$  or  $[\text{HCOO}]^-$  (Fig. 1)<sup>35–37</sup> and allows for using A-site cations with more than four atoms. In the past,  $[\text{C}_2\text{N}_3]^-$  has proved robust for the synthesis of molecular perovskites with different A-site cations and metals such as  $[\text{Btba}][\text{Co}(\text{C}_2\text{N}_3)_3]$ ,<sup>19</sup>  $[\text{Et}_3(n\text{-Pr})\text{P}][\text{Cd}(\text{C}_2\text{N}_3)_3]$ <sup>38</sup> and  $[\text{TPrA}][\text{Mn}(\text{C}_2\text{N}_3)_3]$ ,<sup>39</sup> with  $\text{Et}_3(n\text{-Pr})\text{P}$  = propyltriethylphosphonium and  $\text{TPrA}$  = tetrapropylammonium. Together with a suitable divalent B-site cation, the size of the resulting three-dimensional  $[\text{B}(\text{C}_2\text{N}_3)_3]^-$  network is expected to be large enough to incorporate  $[\text{ASU}]^+$  for the formation of  $[\text{ASU}][\text{B}(\text{C}_2\text{N}_3)_3]$ . Following the idea of the Tolerance Factor approach, the B-site metal can be used to fine-tune the size of the  $[\text{B}(\text{C}_2\text{N}_3)_3]^-$  network, of which we tested  $\text{B} = \text{Cd}^{2+}$ ,  $\text{Mn}^{2+}$ ,  $\text{Co}^{2+}$  and  $\text{Ni}^{2+}$ . Along the series the Shannon ionic radius<sup>40</sup> decreases and hence the Tolerance Factor increases. Please note that due to the distorted 3D network we here use the Tolerance Factor as qualitative guideline rather than a strict concept. Finally, for the synthesis attempts of  $[\text{ASU}][\text{B}(\text{C}_2\text{N}_3)_3]$  with  $\text{B} = \text{Cd}^{2+}$ ,  $\text{Mn}^{2+}$ ,  $\text{Co}^{2+}$ , and  $\text{Ni}^{2+}$  a standard mild-solution route was chosen, following the successful synthesis of related dicyanamide-based molecular perovskites.<sup>41,42</sup> The synthetic approach involves the mixing of precursor salts in an aqueous solution mixture and single crystal formation at room temperature, see ESI† for experimental details.

The crystal structures of the materials were obtained by single crystal X-ray diffraction, see ESI† for details of the crystal structure solution. For the large second row divalent metal  $\text{B} = \text{Cd}^{2+}$  with a Shannon ionic radius of  $r_{\text{Cd}^{2+}} = 95$  pm we observe the formation of the perovskite coordination network  $[\text{ASU}][\text{Cd}(\text{C}_2\text{N}_3)_3]$ , whilst for the smaller cations  $\text{B} = \text{Mn}^{2+}$ ,  $\text{Ni}^{2+}$  and  $\text{Co}^{2+}$  (all  $r_{\text{M}^{2+}} < 84$  pm) a different network structure with the formula  $[\text{ASU}]_2[\text{B}_2(\text{C}_2\text{N}_3)_6] \cdot 2\text{H}_2\text{O}$  is obtained.<sup>40</sup> Therefore, the observed structures highlight once more the importance of size criteria in the formation step of crystalline molecular perovskites as captured by the Tolerance Factor approach and confirm the applied synthetic approach.

## Communication

As-synthesised crystals of  $[\text{ASU}][\text{Cd}(\text{C}_2\text{N}_3)_3]$  crystallise in the orthorhombic non-centrosymmetric polar space group  $Pna2_1$  with unit cell parameters  $a = 17.1022(9)$  Å,  $b = 10.7274(5)$  Å,  $c = 10.7037(5)$  Å,  $V = 1963.72(17)$  Å<sup>3</sup> at 100 K. To back-up the assignment of a polar space-group we performed a Kurtz-Perry powder test, confirming the absence of an inversion centre through the detection of a second harmonic generation signal (see ESI† for details). To the best of our knowledge, this is the first reported dicyanamide perovskite to crystallise in a polar space group<sup>30</sup> although examples with piezoelectric symmetries are known such as  $[\text{Et}_3(\text{CH}_2\text{CHCH}_2)\text{P}][\text{Mn}(\text{C}_2\text{N}_3)_3]$ <sup>43</sup> and  $[(\text{C}_3\text{H}_7)_4\text{N}][\text{Mn}(\text{C}_2\text{N}_3)_3]$ .<sup>44</sup> As expected for a molecular perovskite, each  $\text{Cd}^{2+}$  is octahedrally coordinated to its neighbouring Cd atoms *via* six  $\mu_{1,5}[\text{C}_2\text{N}_3]$ -bridges to form the 3D  $\text{ReO}_3$ -type  $[\text{Cd}(\text{C}_2\text{N}_3)_3]^-$  network, see Fig. 2b.  $[\text{ASU}]^+$  is sitting in the void of the pseudocubic  $\text{ReO}_3$ -type cavities of the resulting  $[\text{Cd}(\text{C}_2\text{N}_3)_3]^-$  network. Given the absence of any acidic hydrogen atoms in  $[\text{ASU}]^+$ , the cation can only interact through dispersion interactions with the 3D network. In turn, any structure-directing properties of the A-site cation are linked to its shape as it was discussed for the group of formate-based molecular perovskites.<sup>45</sup>

As highlighted previously, the use of molecular building units on the X-site leads to the availability of unconventional tilts and shifts within the  $\text{ReO}_3$ -type network which can be decomposed and described by group theory.<sup>46</sup> For  $[\text{ASU}][\text{Cd}(\text{C}_2\text{N}_3)_3]$ , such a decomposition shows that the symmetry is accounted for by three primary order parameters: a checkerboard shift (irrep  $\text{M}_2^-$ ), a conventional out-of-phase tilt ( $\text{R}_5^-$ ) and an unconventional tilt ( $\text{M}_5^+$ ). While the former two distortions are frequently found in dicyanamide perovskites, the  $\text{M}_5^+$  tilt is rare, see Fig. 2c.<sup>30</sup> So far, substantial activation of this mode has only been observed in two other molecular perovskites, the  $\text{ABX}_3$  solvate  $[\text{PPN}][\text{Cd}[\text{Ag}(\text{CN})_2]_3 \cdot 3\text{EtOH}]$ <sup>47</sup> and  $[(\text{CH}_3)_2\text{NH}_2][\text{Mn}(\text{N}_3)_3]$ ,<sup>45</sup> and a few A-site deficient systems.<sup>48</sup> Importantly, it is this distortion that in combination with the  $\text{M}_2^-$  shift leads to the polarity of  $[\text{ASU}][\text{Cd}(\text{C}_2\text{N}_3)_3]$  as previously suggested in a tilt and shift design concept towards molecular perovskites with improper ferroelectricity.<sup>31</sup> Having the prevalence of the  $\text{M}_2^-$  distortion in mind, incorporating the  $\text{M}_5^+$  tilt is an appealing strategy towards the development of additional polar dicyanamide perovskites, nicely demonstrating the benefit of using tailor-made cations in crystal structure engineering attempts.

Looking at the thermogravimetric analysis of the as-synthesised sample,  $[\text{ASU}][\text{Cd}(\text{C}_2\text{N}_3)_3]$  decomposes at approximately  $T = 323$  °C with no indication of any mass loss until decomposition (Fig. S6†). Calorimetry shows an irreversible heat event during the first heating cycle at approximately  $T = 55$  °C and a reversible heat event at  $T = 20$  °C (heating)/ $T = 22$  °C (cooling) during subsequent cycles (Fig. S5†). This behaviour is known from  $[\text{CH}_3\text{NH}_2\text{NH}_2][\text{Mn}(\text{HCOO})_3]$ <sup>49</sup> and  $[\text{TriBuMe}][\text{Mn}(\text{C}_2\text{N}_3)_3]$ <sup>16</sup> and presumably relates to an irreversible phase transition of  $[\text{ASU}][\text{Cd}(\text{C}_2\text{N}_3)_3]$  during the first heating step. The investigation of this phase transition which was previously understood as activation mechanism is cur-

rently under way and goes beyond the concept of this study which focuses on the incorporation and synthesis of molecular perovskites with a tailor-made A-site cation.

For the smaller divalent cations  $\text{B} = \text{Mn}^{2+}$ ,  $\text{Co}^{2+}$ , and  $\text{Ni}^{2+}$ , the 3D network decreases in size and a different structure is formed, which exhibits a diamond topology (see ESI†). It can be assumed that for smaller cations the void within the 3D  $\text{ReO}_3$ -type network is too small to host  $[\text{ASU}]^+$ , and hence, a different crystal structure becomes energetically more favourable. The  $\text{Mn}^{2+}$ ,  $\text{Co}^{2+}$  and  $\text{Ni}^{2+}$  compounds with the general formula  $[\text{ASU}]_2[\text{B}_2(\text{C}_2\text{N}_3)_6] \cdot 2\text{H}_2\text{O}$  crystallise in the monoclinic space-group  $P2_1/n$  and are isostructural, see ESI† for details. The structure consists of  $\text{MN}_5\text{O}$  octahedra where the divalent metal is coordinated by five terminal N-atoms of the  $[\text{C}_2\text{N}_3]^-$  ligands and one  $\text{H}_2\text{O}$  molecule. Only four of five  $[\text{C}_2\text{N}_3]^-$  anions are used as  $\mu_{1,5}[\text{C}_2\text{N}_3]$  linkers, and together with  $\text{H}_2\text{O}$ , only 4 of 6 ligands contribute to the connectivity of the 3D network. In total this leads to a diamond-type network connectivity with a ring of six linked octahedra as structure motif, see Fig. S11 and S12.† Notably, the  $[\text{ASU}]^+$  is disordered within this diamond network, whilst no disorder is observed in  $[\text{ASU}][\text{Cd}(\text{C}_2\text{N}_3)_3]$ .

In conclusion, we show how a new molecular perovskite with a rare tilt system can be synthesised by applying a crystal engineering approach based on the tailor-made A-site cation  $[\text{ASU}]^+$ . The size of the transition metal allows for fine tuning the size of the 3D  $[\text{B}(\text{C}_2\text{N}_3)_3]^-$  host network to a size that is suitable for incorporating the molecular A-site cation  $[\text{ASU}]^+$ . A detailed analysis of the structure *via* group theory reveals that polarity in  $[\text{ASU}][\text{Cd}(\text{C}_2\text{N}_3)_3]$  originates from the presence of an unconventional  $\text{M}_5^+$  tilt, nicely highlighting the opportunities of the large but still untouched chemical parameter space. The results and approach presented here offer a blueprint on how to access structural degrees of freedom within molecular perovskites *via* a crystal engineering based on chemical concepts and intuition. Looking forward, it will be interesting to see to which extent chemical and compositional changes can be used to alter and introduce distinct tilts and shifts. In this context, we would like to advocate that the analysis of the underlying tilt and shifts becomes standard for the report of new molecular perovskites, facilitating the identification of overarching composition-structure trends within molecular perovskites.

## Conflicts of interest

There are no conflicts to declare.

## Acknowledgements

SB acknowledges the Hanns-Seidel-foundation through a BMBF initiative for financial support. GK would like to thank the 'Fonds der Chemischen Industrie' for support through the Liebig Fellowship scheme. JKZ acknowledges financial support



from the Polish National Science Centre under “Maestro” DEC-2013/10/A/ST4/00114 grant.

## Notes and references

- C. Wang, D. Liu and W. Lin, *J. Am. Chem. Soc.*, 2013, **135**, 13222.
- Y. Cui, B. Li, H. He, W. Zhou, B. Chen and G. Qian, *Acc. Chem. Res.*, 2016, **49**, 483.
- M. Đaković, M. Borovina, M. Pisačić, C. B. Aakeröy, Ž. Soldin, B.-M. Kukovec and I. Kodrin, *Angew. Chem., Int. Ed.*, 2018, **57**, 14801.
- A. Worthy, A. Grosjean, M. C. Pfrunder, Y. Xu, C. Yan, G. Edwards, J. K. Clegg and J. C. McMurtrie, *Nat. Chem.*, 2018, **10**, 65.
- L. Wang, H. Luo, S. Deng, Y. Sun and C. Wang, *Inorg. Chem.*, 2017, **56**, 15101.
- W.-W. Wu, S.-G. Wu, Y.-C. Chen, G.-Z. Huang, B.-H. Lyu, Z.-P. Ni and M.-L. Tong, *Chem. Commun.*, 2020, **56**, 4551.
- W. Li, Z. Wang, F. Deschler, S. Gao, R. H. Friend and A. K. Cheetham, *Nat. Rev. Mater.*, 2017, **2**, 3.
- T. Baikie, Y. Fang, J. M. Kadro, M. Schreyer, F. Wei, S. G. Mhaisalkar, M. Graetzel and T. J. White, *J. Mater. Chem. A*, 2013, **1**, 5628.
- S. Sun, Z. Deng, Y. Wu, F. Wei, F. H. Isikgor, F. Brivio, M. W. Gaultois, J. Ouyang, P. D. Bristowe, A. K. Cheetham and G. Kieslich, *Chem. Commun.*, 2017, **53**, 7537.
- M. Mączka, A. Pietraszko, L. Macalik, A. Sieradzki, J. Trzmiel and A. Pikul, *Dalton Trans.*, 2014, **43**, 17075.
- P. Jain, N. S. Dalal, B. H. Toby, H. W. Kroto and A. K. Cheetham, *J. Am. Chem. Soc.*, 2008, **130**, 10450.
- P. Jain, V. Ramachandran, R. J. Clark, H. D. Zhou, B. H. Toby, N. S. Dalal, H. W. Kroto and A. K. Cheetham, *J. Am. Chem. Soc.*, 2009, **131**, 13625.
- M. Mączka, T. Almeida da Silva, W. Paraguassu and K. Pereira da Silva, *Spectrochim. Acta, Part A*, 2016, **156**, 112.
- M. Trzebiatowska, M. Mączka, M. Ptak, L. Giriunas, S. Balcianas, M. Simenas, D. Klose and J. Banys, *J. Phys. Chem. C*, 2019, **123**, 11840.
- X.-H. Zhao, X.-C. Huang, S.-L. Zhang, D. Shao, H.-Y. Wei and X.-Y. Wang, *J. Am. Chem. Soc.*, 2013, **135**, 16006.
- M. Mączka, A. Gagor, M. Ptak, D. Stefańska, L. Macalik, A. Pikul and A. Sieradzki, *Dalton Trans.*, 2019, **48**, 13006.
- Y. Wu, T. Binford, J. A. Hill, S. Shaker, J. Wang and A. K. Cheetham, *Chem. Commun.*, 2018, **54**, 3751.
- Y. Wu, S. Shaker, F. Brivio, R. Murugavel, P. D. Bristowe and A. K. Cheetham, *J. Am. Chem. Soc.*, 2017, **139**, 16999.
- M.-L. Tong, J. Ru, Y.-M. Wu, X.-M. Chen, H.-C. Chang, K. Mochizuki and S. Kitagawa, *New J. Chem.*, 2003, **27**, 779.
- J. M. Bermúdez-García, M. Sánchez-Andújar, S. Castro-García, J. López-Beceiro, R. Artiaga and M. A. Señaris-Rodríguez, *Nat. Commun.*, 2017, **8**, 15715.
- G. Kieslich, S. Sun and A. K. Cheetham, *Chem. Sci.*, 2015, **6**, 3430.
- W. Travis, E. N. K. Glover, H. Bronstein, D. O. Scanlon and R. G. Palgrave, *Chem. Sci.*, 2016, **7**, 4548.
- G. Kieslich and A. L. Goodwin, *Mater. Horiz.*, 2017, **4**, 362.
- S. Burger, M. G. Ehrenreich and G. Kieslich, *J. Mater. Chem. A*, 2018, **6**, 21785.
- H. L. B. Boström, J. A. Hill and A. L. Goodwin, *Phys. Chem. Chem. Phys.*, 2016, **18**, 31881.
- S. G. Duyker, J. A. Hill, C. J. Howard and A. L. Goodwin, *J. Am. Chem. Soc.*, 2016, **138**, 11121.
- H. L. B. Boström, J. Bruckmoser and A. L. Goodwin, *J. Am. Chem. Soc.*, 2019, **141**, 17978.
- G. Kieslich, S. Kumagai, A. C. Forse, S. Sun, S. Henke, M. Yamashita, C. P. Grey and A. K. Cheetham, *Chem. Sci.*, 2016, **7**, 5108.
- N. L. Evans, P. M. M. Thygesen, H. L. B. Boström, E. M. Reynolds, I. E. Collings, A. E. Phillips and A. L. Goodwin, *J. Am. Chem. Soc.*, 2016, **138**, 9393.
- H. L. B. Boström, *CrystEngComm*, 2020, **22**, 961.
- H. L. B. Boström, M. S. Senn and A. L. Goodwin, *Nat. Commun.*, 2018, **9**, 2380.
- W.-J. Xu, Z.-Y. Du, W.-X. Zhang and X.-M. Chen, *CrystEngComm*, 2016, **18**, 7915.
- M. G. Marino and K. D. Kreuer, *ChemSusChem*, 2015, **8**, 513.
- B. Zhou, Y. Imai, A. Kobayashi, Z.-M. Wang and H. Kobayashi, *Angew. Chem., Int. Ed.*, 2011, **50**, 11441.
- Z.-Y. Du, Y.-P. Zhao, C.-T. He, B.-Y. Wang, W. Xue, H.-L. Zhou, J. Bai, B. Huang, W.-X. Zhang and X.-M. Chen, *Cryst. Growth Des.*, 2014, **14**, 3903.
- W. Zhang, Y. Cai, R.-G. Xiong, H. Yoshikawa and K. Awaga, *Angew. Chem., Int. Ed.*, 2010, **49**, 6608.
- G. Kieslich, S. Sun and A. K. Cheetham, *Chem. Sci.*, 2014, **5**, 4712.
- L. Zhou, X. Zheng, P.-P. Shi, Z. Zafar, H.-Y. Ye, D.-W. Fu and Q. Ye, *Inorg. Chem.*, 2017, **56**, 3238.
- J. M. Bermúdez-García, M. Sánchez-Andújar, S. Yáñez-Vilar, S. Castro-García, R. Artiaga, J. López-Beceiro, L. Botana, Á. Alegría and M. A. Señaris-Rodríguez, *Inorg. Chem.*, 2015, **54**, 11680.
- R. D. Shannon, *Acta Crystallogr., Sect. A: Cryst. Phys., Diffraction, Theor. Gen. Crystallogr.*, 1976, **32**, 751.
- J. M. Bermúdez-García, M. Sánchez-Andújar, S. Yáñez-Vilar, S. Castro-García, R. Artiaga, J. López-Beceiro, L. Botana, A. Alegría and M. A. Señaris-Rodríguez, *J. Mater. Chem. C*, 2016, **4**, 4889.
- J. M. Bermúdez-García, S. Yáñez-Vilar, A. García-Fernández, M. Sánchez-Andújar, S. Castro-García, J. López-Beceiro, R. Artiaga, M. Dilshad, X. Moya and M. A. Señaris-Rodríguez, *J. Mater. Chem. C*, 2018, **6**, 9867.
- F.-J. Geng, L. Zhou, P.-P. Shi, X.-L. Wang, X. Zheng, Y. Zhang, D.-W. Fu and Q. Ye, *J. Mater. Chem. C*, 2017, **5**, 1529.
- J. A. Schlueter, J. L. Manson and U. Geiser, *Inorg. Chem.*, 2005, **44**, 3194.

### Communication

### Dalton Transactions

- 45 I. E. Collings, J. A. Hill, A. B. Cairns, R. I. Cooper, A. L. Thompson, J. E. Parker, C. C. Tang and A. L. Goodwin, *Dalton Trans.*, 2016, **45**, 4169.
- 46 B. J. Campbell, H. T. Stokes, D. E. Tanner and D. M. Hatch, *J. Appl. Crystallogr.*, 2006, **39**, 607.
- 47 J. A. Hill, A. L. Thompson and A. L. Goodwin, *J. Am. Chem. Soc.*, 2016, **138**, 5886.
- 48 H. A. Evans, Z. Deng, I. E. Collings, Y. Wu, J. L. Andrews, K. Pilar, J. M. Tuffnell, G. Wu, J. Wang, S. E. Dutton, P. D. Bristowe, R. Seshadri and A. K. Cheetham, *Chem. Commun.*, 2019, **55**, 2964.
- 49 M. Mączka, A. Gağor, M. Ptak, W. Paraguassu, T. A. da Silva, A. Sieradzki and A. Pikul, *Chem. Mater.*, 2017, **29**, 2264.

## 4.3 STUDY III: Tilt and Shift Polymorphism in Molecular Perovskites

The use of molecular moieties on the A- and X-site to form ABX<sub>3</sub> perovskite-type coordination polymers gives access to network distortion types which are intrinsically absent in inorganic perovskites. This additional synthetic freedom - when applied wisely - can translate to novel structural freedom such as order-disorder phase transitions and extensive network deformations to create functional materials with interesting and exotic properties.

In this work, a new concept in the materials class of molecular perovskites to describe "tilt and shift polymorphism" is discussed. The new materials [(C<sub>3</sub>H<sub>7</sub>)<sub>3</sub>CH<sub>3</sub>N]M[(C<sub>2</sub>N<sub>3</sub>)<sub>3</sub>] with  $M = \text{Mn}^{2+}, \text{Co}^{2+}, \text{Ni}^{2+}$  are presented, featuring two perovskite phases with the same composition at the same conditions but different tilt systems which can be transformed irreversibly into each other. This phenomenon was observed in prior studies,[109, 222, 282] however in this article the concept and driving force of the transformation is explained on an atomic level and is demonstrated for the first time by the aid of computational chemistry. The results of this study represent an important step to understand the crystal chemistry of molecular perovskites in greater detail and to elucidate the role of polymorphism in the science of perovskite-type coordination networks itself and will therefore impact on inorganic chemists research to design relations of structure and physiochemical properties towards targeted functional materials.

The study leading to this article was designed by the author of this doctorate thesis together with Dr. Gregor Kieslich. The author of this thesis conducted the experiments, analysed all experimental data and in collaboration with Dr. Gregor Kieslich compiled the data interpretation into a manuscript. Shivani Grover performed the respective DFT calculations guided by Dr. Keith T. Butler and Dr. Ricardo Grau-Crespo. Hanna L. B. Boström analysed the different tilting modes and contributed with expertise about network deformations in general to the study. All authors discussed the data and contributed to the manuscript. The issue front cover illustration for the article was prepared by Dr. Johannes Richers in consultation with the author of this doctorate thesis and Dr. Gregor Kieslich. The author of this thesis and Shivani Grover share first authorship for this article.

Status: Published as a Communication in Materials Horizons.

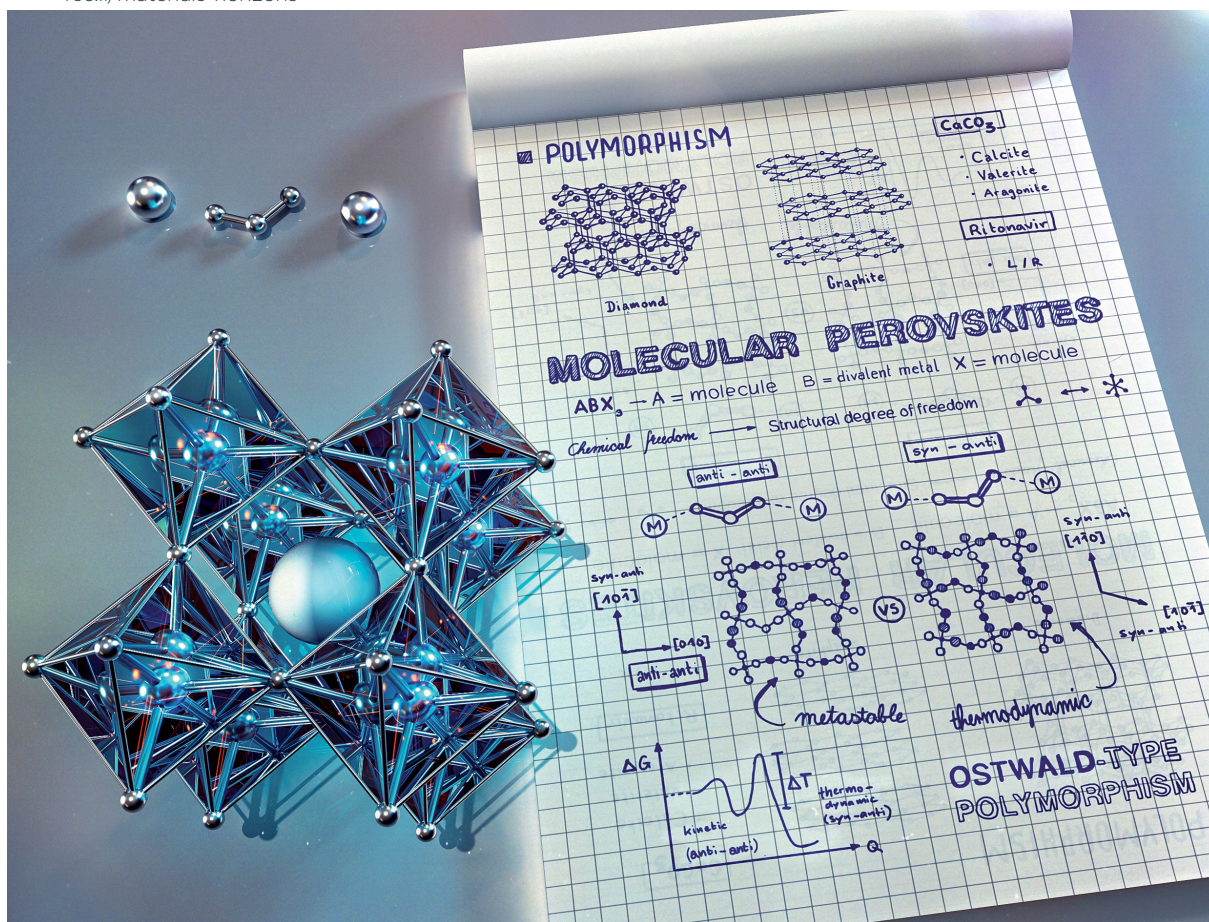
Reproduced from Ref. [283] with permission from the Royal Society of Chemistry. This article is licensed under a Creative Commons Attribution 3.0 Unported License with details of the agreement listed in APPENDIX, C Reprint permissions.

S. Burger, S. Grover, K. T. Butler, H. L. B. Boström, R. Grau-Crespo and G. Kieslich, *Tilt and shift polymorphism in molecular perovskites*, **Mater. Horiz.**, 2021, **8**, 2444-2450, DOI: 10.1039/D1MH00578B.

# Materials Horizons

Volume 8  
Number 9  
September 2021  
Pages 2345-2586

rsc.li/materials-horizons



ISSN 2051-6347



## Tilt and shift polymorphism in molecular perovskites†

Cite this: *Mater. Horiz.*, 2021, 8, 2444

Received 8th April 2021,  
Accepted 14th June 2021

DOI: 10.1039/d1mh00578b

rsc.li/materials-horizons

Stefan Burger,<sup>†</sup> Shivani Grover,<sup>‡</sup> Keith T. Butler,<sup>†</sup> Hanna L. B. Boström,<sup>d</sup>  
Ricardo Grau-Crespo<sup>†\*</sup> and Gregor Kieslich<sup>†\*</sup>

Molecular perovskites, *i.e.* ABX<sub>3</sub> coordination polymers with a perovskite structure, are a chemically diverse material platform for studying fundamental and applied materials properties such as barocalorics and improper ferroelectrics. Compared to inorganic perovskites, the use of molecular ions on the A- and X-site of molecular perovskites leads to new geometric and structural degrees of freedom. In this work we introduce the concept of tilt and shift polymorphism, categorising irreversible perovskite-to-perovskite phase transitions in molecular perovskites. As a model example we study the new molecular perovskite series [(*n*Pr)<sub>3</sub>(CH<sub>3</sub>)N]M(C<sub>2</sub>N<sub>3</sub>)<sub>3</sub> with M = Mn<sup>2+</sup>, Co<sup>2+</sup>, Ni<sup>2+</sup>, and *n*Pr = *n*-propyl, where different polymorphs crystallise in the perovskite structure but with different tilt systems depending on the synthetic conditions. Tilt and shift polymorphism is a direct ramification of the use of molecular building units in molecular perovskites and as such is unknown for inorganic perovskites. Given the role of polymorphism in materials science, medicine and mineralogy, and more generally the relation between physicochemical properties and structure, the concept introduced herein represents an important step in classifying the crystal chemistry of molecular perovskites and in maturing the field.

### New concepts

Polymorphic phases often show different physicochemical properties, making polymorphism an important concept in the chemistry and physics of condensed matter. Some canonical examples that showcase the discipline crossing nature of polymorphism are the 1D and 3D form of [(NH<sub>2</sub>)<sub>2</sub>CH]PbI<sub>3</sub>, the three different polymorphs of CaCO<sub>3</sub>, and the different forms of ritonavir. In this work, the concept of tilt and shift polymorphism is introduced, categorising irreversible perovskite-to-perovskite phase transitions in the emerging material class of molecular perovskites. Molecular perovskites have recently gained attention in the field of ferroelectrics, multiferroics and mechanocalorics. The incorporation of molecular building blocks in the 3D ReO<sub>3</sub>-type network of the perovskite structure leads to new geometric degrees of freedom, enabling the formation of polymorphic perovskite phases with different tilt and shift systems that are close in energy, *i.e.* tilt and shift polymorphs. Given the virtually unlimited chemical freedom to synthesise molecular perovskites of various kinds and the impact of structural details of the 3D network on the properties of molecular perovskites, tilt and shift polymorphism is an important new crystal chemistry principle.

## Introduction

Among dense coordination networks, the material class of ABX<sub>3</sub> coordination networks that crystallise in a perovskite structure

holds a unique place.<sup>1</sup> Here referred to as molecular perovskites, the existence of a common building principle for a whole material class means that composition–structure–property relations can be studied in great depth.<sup>2,3</sup> Research on molecular perovskites can seek inspiration from the literature on inorganic perovskites, and in a subsequent step, investigate how the use of molecular building units leads to new crystal chemistry principles.<sup>4</sup> Therefore, molecular perovskites combine one of the most important structural motifs in condensed matter chemistry and physics with the nearly unlimited chemical diversity of coordination polymers—an exciting material platform in the search for phenomena of technological and scientific relevance such as barocalorics and improper ferroelectrics.<sup>3,5–7</sup>

Akin to inorganic perovskites, ABX<sub>3</sub> molecular perovskites show a 3D [BX<sub>3</sub>]<sup>−</sup> network with **pcu** topology with the monovalent A-site cation sitting in the void of the network for charge balance.<sup>8</sup> The use of molecular X-site anions increases the size of the pseudocubic ReO<sub>3</sub>-type network, so that molecular A-site cations

<sup>a</sup> Department of Chemistry, Technical University of Munich, Lichtenbergstraße 4, 85748 Garching, Germany. E-mail: gregor.kieslich@tum.de

<sup>b</sup> Department of Chemistry, University of Reading, Whiteknights, Reading RG6 6DX, UK. E-mail: r.grau-crespo@reading.ac.uk

<sup>c</sup> Rutherford Appleton Laboratory, Scientific Computing Department (SciML), Didcot OX11 0QX, UK

<sup>d</sup> Max-Planck Institute for Solid State Research, Heisenbergstraße 1, 70569 Stuttgart, Germany

† Electronic supplementary information (ESI) available: Details on experimental data as well as DFT calculations. CCDC 2068712, 2068716 and 2068842–2068849. For ESI and crystallographic data in CIF or other electronic format see DOI: 10.1039/d1mh00578b

‡ S. B. and S. G. contributed equally to this work and share first authorship.

with varying chemistries and sizes can be used to form molecular perovskites such as  $[(\text{NH}_2)_3\text{C}]\text{M}(\text{HCOO})_3$ ,  $[(\text{CH}_3)_2\text{NH}_2]\text{M}(\text{N}_3)_3$ ,  $[(\text{C}_2\text{H}_5)_3(\text{C}_7\text{H}_7)\text{N}]\text{M}(\text{C}_2\text{N}_3)_3$  and  $[(\text{Ph}_3\text{P})_2\text{N}]\text{M}[\text{Au}(\text{CN})_2]_3$  with  $\text{M}^{2+}$  typically being  $\text{Mn}^{2+}$ ,  $\text{Co}^{2+}$ ,  $\text{Ni}^{2+}$  and  $\text{Zn}^{2+}$ .<sup>9–14</sup> More complex examples are the recently reported (defect-ordered) thiocyanate molecular perovskites,<sup>15</sup> A-site solid solutions,<sup>16,17</sup> molecular perovskites with mixed X-site anions,<sup>18,19</sup> and the conceptually related Prussian Blue Analogues.<sup>20,21</sup> The use of molecular moieties has important ramifications for the material properties, and formally, chemical (synthetic) freedom is translated to structural and geometric degrees of freedom.<sup>22</sup> For instance, molecular A-site cations enable temperature- and pressure-dependent order-disorder phase transitions related to the disorder of the molecular A-site cation,<sup>23,24</sup> and the integration of molecular X-site anions can lead to octahedral tilt patterns and columnar shifts that are intrinsically absent in inorganic perovskites.<sup>25</sup>

An important ramification of using molecular building units to form network materials is the introduction of weak chemical interactions such as dispersion interactions and hydrogen bonds. There are a number of research examples such as glass-type behaviour in  $[(\text{CH}_3)_2\text{NH}_2]\text{Zn}(\text{HCOO})_3$ ,<sup>26</sup> (defect-dependent) mechanical properties in  $[(\text{NH}_2)_3\text{C}]\text{Mn}(\text{HCOO})_3$ ,<sup>27</sup> temperature- and pressure-induced reversible  $[(\text{CH}_3)_2\text{NH}_2]\text{M}(\text{HCOO})_3$ <sup>28</sup> and irreversible  $[(n\text{Pr})_4\text{N}]\text{Cd}(\text{C}_2\text{N}_3)_3$ <sup>29</sup> phase transitions, and more generally, structural distortions that can be activated by temperature and pressure, that all together point at relatively shallow free energy landscapes.<sup>30</sup> The recent discovery of irreversible phase transitions in the perovskite materials  $[(\text{NH}_2)_3\text{C}]\text{Mn}(\text{H}_2\text{POO})_3$ ,  $[(\text{C}_5\text{H}_{10})_2\text{N}]\text{Cd}(\text{C}_2\text{N}_3)_3$  and  $[(\text{C}_4\text{H}_9)_3(\text{CH}_3)\text{N}]\text{Mn}(\text{C}_2\text{N}_3)_3$  is in full agreement with this perspective.<sup>31–33</sup> For instance, crystal structure analysis for  $[(\text{NH}_2)_3\text{C}]\text{Mn}(\text{H}_2\text{POO})_3$  has shown that the different polymorphs are related to different tilt systems, *i.e.* the detailed distortion arrangement within the  $[\text{Mn}(\text{H}_2\text{POO})_3]^-$  network, reminiscent of conformational polymorphism as observed for molecular crystals.<sup>34,35</sup>

Considering the property-determining role of conformational polymorphism in molecular crystals,<sup>36</sup> knowledge and control of polymorphism in molecular perovskites is important in advancing the field, with a rigorous categorisation of this phenomenon representing the first step. Here we introduce the concept of *tilt and shift polymorphism* for molecular perovskites, studying its structural and thermodynamic origin. We report the new molecular perovskite series  $[(n\text{Pr})_3(\text{CH}_3)\text{N}]\text{M}(\text{C}_2\text{N}_3)_3$  with  $\text{M} = \text{Mn}^{2+}$ ,  $\text{Co}^{2+}$ ,  $\text{Ni}^{2+}$ ,  $n\text{Pr} = n$ -propyl and  $\text{C}_2\text{N}_3^- =$  dicyanamide anion, which exhibits an irreversible perovskite-to-perovskite phase transition above room temperature. Depending on synthetic conditions, both polymorphs can be crystallised as single crystals. The series is used as a model example to establish the concept of tilt and shift polymorphism and to study its thermodynamic and structural nature by experiment and computation.

## Results and discussion

### Synthesis and structure determination

The series  $[(\text{C}_3\text{H}_7)_3(\text{CH}_3)\text{N}]\text{M}(\text{C}_2\text{N}_3)_3$  with  $\text{M} = \text{Mn}^{2+}$ ,  $\text{Co}^{2+}$  and  $\text{Ni}^{2+}$  was synthesised by applying an established mild-solution

crystallisation route, where the precursor materials methyltri-propylammonium chloride, sodium dicyanamide and the transition metal source were mixed at room temperature in an aqueous solution, see ESI,† for details. After two days, well-defined crystals suitable for single crystal X-ray diffraction formed. Within the series, all materials are isostructural and in the following discussion  $[(\text{C}_3\text{H}_7)_3(\text{CH}_3)\text{N}]\text{Ni}(\text{C}_2\text{N}_3)_3$  is used as representative but the same conclusions can be drawn for  $[(\text{C}_3\text{H}_7)_3(\text{CH}_3)\text{N}]\text{Mn}(\text{C}_2\text{N}_3)_3$  and  $[(\text{C}_3\text{H}_7)_3(\text{CH}_3)\text{N}]\text{Co}(\text{C}_2\text{N}_3)_3$ .

The structures of the as-synthesised materials were solved based on single-crystal X-ray diffraction (SCXRD) data recorded at 100 K.  $[(\text{C}_3\text{H}_7)_3(\text{CH}_3)\text{N}]\text{Ni}(\text{C}_2\text{N}_3)_3$  crystallises in the orthorhombic space group *Prma* with  $a = 9.8624(6)$  Å,  $b = 15.9509(9)$  Å and  $c = 12.6923(7)$  Å,  $V = 1996.7(2)$  Å<sup>3</sup>. We refer to the as-synthesised polymorph as **P(Ni)-I**. The material crystallises in a perovskite structure where each dicyanamide linker coordinates two metal centres in a  $\mu$ -1,5 fashion, spanning a three-dimensional  $[\text{Ni}(\text{C}_2\text{N}_3)_3]^-$  coordination network with metal centres in an octahedral coordination. The molecular A-site cation  $[(\text{C}_3\text{H}_7)_3(\text{CH}_3)\text{N}]^+$  sits in the void of the pseudocubic  $[\text{Ni}(\text{C}_2\text{N}_3)_3]^-$  network for charge balance. Positional disorder is observed for the A-site cation  $[(\text{C}_3\text{H}_7)_3(\text{CH}_3)\text{N}]^+$ , with each propyl and methyl group disordered over two sites.

Subsequently, differential scanning calorimetry (DSC) was performed to screen for phase transitions (Fig. 1a). In the first heating cycle, a heat event at approximately  $T = 365$  K was observed. Given the absence of a corresponding signal in the cooling cycle, this is an irreversible event. Material change due to the loss of solvent molecules is excluded *via* thermogravimetric analysis coupled with mass spectrometry,<sup>37</sup> see ESI,† Fig. S4 and S5. Together with temperature-dependent powder X-ray diffraction which confirms crystallinity until material decomposition at  $T > 530$  K, Fig. S11 (ESI†), we can conclude that the heat event at  $T = 365$  K represents an irreversible crystalline-to-crystalline phase transition from polymorph **P(Ni)-I** into a material which is referred to as **P(Ni)-Iib**. Along the series  $[(\text{C}_3\text{H}_7)_3(\text{CH}_3)\text{N}]\text{M}(\text{C}_2\text{N}_3)_3$  we find isostructural

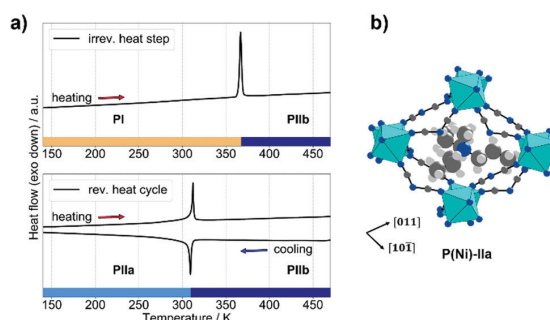


Fig. 1 (a) DSC traces of  $[(n\text{Pr})_3(\text{CH}_3)\text{N}]\text{Ni}(\text{C}_2\text{N}_3)_3$ . Shown are the heating step (top) and subsequent reversible cooling/heating cycle (bottom), highlighting the temperature range for the low-temperature and high-temperature phases with colour bars, respectively. (b) The pseudocubic coordination environment for the polymorph **P(Ni)-Iia**. Colour code: Ni – turquoise, N – dark blue, C – dark grey, H – light grey.

behaviour with increasing transition temperature from manganese to nickel, see Table S1 (ESI<sup>†</sup>) for an overview of thermodynamic parameters of the **P(M)-I**-to-**P(M)-IIb** phase transitions.

Such an irreversible phase transition was previously observed by us and others for  $[(\text{NH}_2)_3\text{C}]\text{Mn}(\text{H}_2\text{POO})_3$ ,  $[(\text{C}_4\text{H}_9)_3(\text{CH}_3)\text{N}]\text{Mn}(\text{C}_2\text{N}_3)_3$  and  $[(\text{C}_5\text{H}_{10})_2\text{N}]\text{Cd}(\text{C}_2\text{N}_3)_3$ . For  $[(\text{NH}_2)_3\text{C}]\text{Mn}(\text{H}_2\text{POO})_3$ , a single-crystal-to-single-crystal phase transition allowed for structure solution, showing an irreversible rearrangement of X-site molecules within the 3D  $[\text{Mn}(\text{H}_2\text{POO})_3]^-$  network as the underlying process.<sup>31</sup> Single crystals of **P(Ni)-I** break into a polycrystalline powder during the phase transition. To access structural details, we applied a high temperature crystallisation method at 370 K inspired by existing high-entropy nucleation routes.<sup>38</sup> After two days we obtained single crystals of **P(Ni)-IIb**, see ESI<sup>†</sup> for experimental details. SCXRD at 350 K shows that **P(Ni)-IIb** adopts the perovskite structure motif, crystallising in the rhombohedral space group  $R\bar{3}c$  with  $a = b = 12.5350(3)$  Å,  $c = 22.8074(12)$  Å and  $V = 3103.52(19)$  Å<sup>3</sup>. In **P(Ni)-IIb**, the A-site cation shows positional disorder, with all carbon atoms of the three propyl groups disordered over four positions and the methyl group disordered over two positions. Therefore, the phase transition from **P(Ni)-I** to **P(Ni)-IIb** represents an irreversible perovskite-to-perovskite phase transition. The two polymorphs **P(Ni)-I** and **P(Ni)-IIb** differ in the disorder of the A-site cation and, as will be established in the next section, in the chemical details of the tilt systems within the  $\text{ReO}_3$ -type network.

Following the traces of the DSC experiment, the irreversible heat event is followed by heat events that show the existence of a reversible phase transition. Therefore, **P(Ni)-IIb** represents a high-temperature phase of  $[(\text{C}_3\text{H}_7)_3(\text{CH}_3)\text{N}]\text{Ni}(\text{C}_2\text{N}_3)_3$  with a reversible phase-transition to a low-temperature phase that we call **P(Ni)-IIa**, see Fig. 1a (bottom). SCXRD experiments at 100 K show that **P(Ni)-IIa** crystallises in the polar space group  $R3c$  with  $a = b = 12.5883(8)$  Å,  $c = 21.5650(2)$  Å and  $V = 2959.5(4)$  Å<sup>3</sup>, see ESI<sup>†</sup> for details. For **P(Ni)-IIa** we find a fully ordered A-site cation, showing that the reversible phase transition **P(Ni)-IIa** to **P(Ni)-IIb** is an order-disorder phase transition related to the A-site cation. Such polar-to-nonpolar phase transitions, where A-site disorder introduces inversion symmetry, are well known for molecular perovskites.<sup>39,40</sup> Looking at the material metal series, phase transition temperatures correlate with size and ligand field stabilisation energy (LFSE) of the divalent metal, *i.e.*  $T_c(\text{P(M)-IIa to P(M)-IIb}) = 284$  K ( $\text{Mn}^{2+}$ ), 301 K ( $\text{Co}^{2+}$ ) and 312 K ( $\text{Ni}^{2+}$ ). The reversible phase transition shows analogies to phase transitions in  $[(\text{C}_3\text{H}_7)_4\text{N}]\text{Mn}(\text{C}_2\text{N}_3)_3$ <sup>41</sup> and  $[(\text{C}_3\text{H}_7)_4\text{N}]\text{Cd}(\text{C}_2\text{N}_3)_3$ ,<sup>42</sup> and thermodynamic data implies interesting barocaloric performances (Table S1, ESI<sup>†</sup>); however, such a characterisation goes beyond the scope of this work where the polymorphism between **P(Ni)-I** and **P(Ni)-II** is in the focus.

#### Tilt and shift polymorphism

Now we analyse the details of the structural differences between the polymorphs **P(M)-I** and **P(M)-II**, with focus on the structural details of the 3D  $[\text{M}(\text{C}_2\text{N}_3)_3]^-$  networks. The tilt distortions in

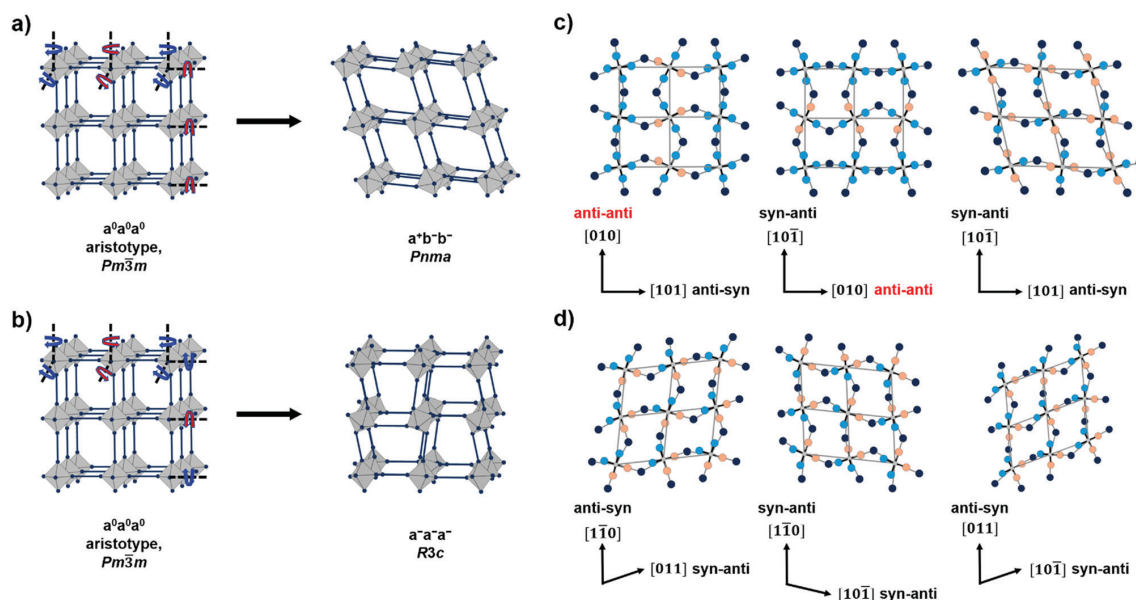


Fig. 2 (a and b) the tilt systems of the polymorphs **P(M)-I** and **P(M)-IIa** as derived from a hypothetical aristotype network with  $Pm\bar{3}m$  symmetry (schematic is inspired from ref. 47). Red arrows indicate clockwise and blue arrows indicate *anti*-clockwise tilts of octahedra; (c and d) show 2D projections of the pseudocubic  $\text{ReO}_3$ -type network with emphasis on *syn-anti* and *anti-anti* binding modes of the metal-dicyanamide-metal network connectivity for **P(M)-I** (c) and **P(M)-IIa** (d). Colour code for dicyanamide in (c and d): central N - dark blue, terminal N *syn* - salmon, terminal N *anti* - light blue. Grey lines are a guide to the eye and do not represent chemical bonds.

both polymorphs can be described with the Glazer notation as established for inorganic perovskites,<sup>40</sup> see Fig. 2(a) and (b). The tilt pattern of the orthorhombic polymorph **P(M)-I** shows one in-phase and two out-of-phase tilts ( $a^+b^-b^-$ ), while the rhombohedral polymorph only shows equilateral out-of-phase tilts ( $a^-a^-a^-$ ). These tilt patterns and related space groups are common for inorganic oxide perovskites and molecular perovskites.<sup>43–46</sup>

When looking for the origin of these tilt patterns and a potential way to transform them into each other, a binding mode analysis of bonds between the multiatomic dicyanamide linker and the metal is required.<sup>47</sup> For a  $\mu$ -1,5 coordination of the dicyanamide linker, three different binding modes are in principle possible: *syn-anti*, *syn-syn* and *anti-anti*.<sup>48,49</sup> For **P(M)-I** we observe binding modes that depend on the direction within the pseudocubic  $[\text{M}(\text{C}_2\text{N}_3)_3]^-$  framework. Along  $[10\bar{1}]$  and  $[101]$ , a *syn-anti* connectivity is observed, while an *anti-anti* connectivity is found along  $[010]$ . In contrast, only *syn-anti* binding modes are found for the polymorph **P(M)-IIa**, see Fig. 2(c) and (d). Details on the assignment of *syn*- and *anti*-binding modes, including torsion angles, can be found in the ESI,† Table S9. Therefore, the irreversible phase transition from **P(M)-I** to **P(M)-II** is related to a change of binding modes from an *anti-anti* to *syn-anti* connectivity of the  $[\text{C}_2\text{N}_3]^-$  anions, leaving the overall topology of the network unchanged. A change in X-site binding modes has been previously observed for the reversible pressure induced phase transition in  $[(\text{CH}_3)_2\text{NH}_2]\text{M}(\text{HCOO})_3$  ( $\text{M} = \text{Cu}^{2+}$ ,  $\text{Fe}^{2+}$  and  $\text{Mn}^{2+}$ ) and an irreversible non-perovskite to perovskite phase transition is known for  $[(n\text{Pr})_4\text{N}]\text{Cd}(\text{C}_2\text{N}_3)_3$ ; however, the here presented  $[(n\text{Pr})_3(\text{CH}_3)\text{N}]\text{M}(\text{C}_2\text{N}_3)_3$  series combines both phenomena in a perovskite-to-perovskite irreversible phase transition related to a change in the binding mode.

A group-theoretical analysis of group-subgroup relations between the  $Pnma$  and  $R\bar{3}c$  phases shows no obvious pathways for low-energy displacive phase transitions.<sup>50</sup> Any potential displacive phase transition would be expected to go through a high energy intermediate related to the arisotype in  $Pm\bar{3}m$  which can be expected for a metastable phase. Across the metal series  $\text{M} = \text{Mn}^{2+}$ ,  $\text{Co}^{2+}$  and  $\text{Ni}^{2+}$ , we observe a monotonic increase of the phase transition temperatures from **P(M)-I** to **P(M)-IIb**, which agrees with the trend of decreasing metal ion radius (and increasing LFSE), see ESI,† Table S1 for details. In other words, the ligand-to-metal bond strength seems to play a role in the transformation mechanism from an *anti-anti* to *syn-anti* connectivity of the  $(\text{C}_2\text{N}_3)^-$  X-site anions, arguably affecting the activation energy of the process. Since the network topology is maintained over the phase transition, describing this phase transition as ‘reconstructive’ seems inappropriate and a more detailed analysis is subject of future studies. Furthermore, we want to mention that the experimental, integrated phase transition enthalpies of this irreversible phase transition lie within the typical range,<sup>51</sup> but show no trends with metal radius, overall pointing towards a complex mechanism for the irreversible phase transition.

Following on from our results, and similar phenomena reported in the literature, we introduce the concept of tilt and shift polymorphism for molecular perovskites: tilt and shift polymorphism in molecular perovskites describes the existence of two molecular perovskites under the same conditions with the same composition, but with different underlying tilt systems and columnar shifts which may be transformed irreversibly into each other. While the presented examples only show Glazer-type (conventional) tilt polymorphism, we included the possibility of unconventional tilts and columnar shifts in this concept since preliminary results from us on  $[(\text{C}_5\text{H}_{10})_2\text{N}]\text{Cd}(\text{C}_2\text{N}_3)_3$  show that this type of polymorphism potentially includes unconventional tilts and columnar shifts.<sup>32</sup> We want to emphasise that this definition involves the existence of at least one metastable molecular perovskite phase, and therefore excludes reversible perovskite-to-perovskite phase transitions as a function of temperature or pressure.<sup>23,28,39</sup>

As such, tilt and shift polymorphism of molecular perovskites is closely related to conformational polymorphism as known from molecular crystals.<sup>35</sup> Akin conformational polymorphism, the term ‘tilt and shift polymorphism’ is descriptive in nature. The origin of tilt and shift polymorphism is the variable binding mode of dicyanamide, and at the current state we can only speculate which factors bring different binding modes and the resulting molecular perovskites close in energy. We hypothesise that large A-site cations provide a larger configurational space for creating two distinct structures close in energy. Likewise, A-site cations with acidic H-atoms with the propensity for the formation of hydrogen bond networks seem beneficial.<sup>28,30,31,52</sup> The challenge in identifying such factors, which relates to the challenge to understand the interplay between A-site cation chemistry and the 3D network, brings us back to the task of engineering chemical interactions and therewith the underlying free energy landscape; an interdisciplinary challenge across various fields of condensed matter research.<sup>53–55</sup>

#### Relative phase stabilities

To underpin experimental observations, we have used density functional theory (DFT) combined with lattice dynamic (LD) calculations, probing the relative stabilities of the different perovskite polymorphs. At 0 K, *i.e.* in the absence of any entropic contributions, a comparison of relative stabilities between rhombohedral and orthorhombic phases shows that the rhombohedral polymorph **P(M)-IIa** is the thermodynamically stable product when compared to **P(M)-I**, see Fig. 3a. Adding zero-point vibrational contributions to the energy difference reinforces the stability of the rhombohedral *vs.* the orthorhombic phase.

Since vibrational entropy can reverse thermodynamic stabilities at finite temperatures,<sup>30,56,57</sup> we calculated the vibrational free energy in the temperature range  $T = 0$ –400 K for all **P(M)-I** and **P(M)-IIa** phases. We would like to note that phonon dispersion curves show some imaginary frequencies which are normally associated with dynamic instabilities; however, a



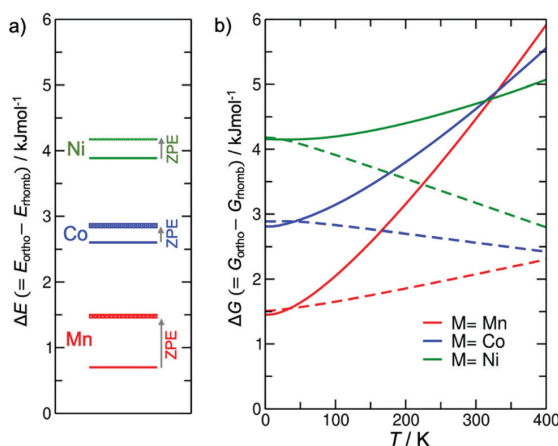


Fig. 3 (a) Energy differences between orthorhombic and rhombohedral phases for each composition, with and without zero-point energy (ZPE) corrections. (b) Vibrational free energy differences between the phases vs. temperature. The width of the ZPE-corrected lines in (a) and the two types of line in (b) reflect the different results from two ways of dealing with the (spurious) imaginary modes: ignoring the imaginary contributions (solid lines), or counting them as real contributions (dashed lines).

more in-depth analysis reveals that these imaginary frequencies are a numerical artefact from cell size effects for the LD simulations, see ESI.† In other words, both polymorphs are dynamically stable, and phase transitions between these phases are required to go through a high-energy intermediate rather than occurring *via* a simple displacive mechanism. Due to the spurious imaginary modes, which could not be re-normalised as we have done in previous studies,<sup>58</sup> we make two approximations for obtaining vibrational entropies: one to ignore the modes in the expression for free energy, the other to treat the negative modes as their positive inverse. These two approximations give extrema for how the free energy would evolve with temperature depending on the contribution of these modes. Fig. 3b shows unequivocally that the rhombohedral phase is more stable across the range of temperature of interest here, regardless of how we consider the contribution from the artificial imaginary modes. Therefore, we can here conclude that **P(M)-II** is the thermodynamically stable polymorph over the temperature range studied here, in excellent agreement with experimental observations, *i.e.* with the observation of crystallisation of this polymorph at higher temperatures.

Therefore, **P(M)-I** is the kinetic polymorph and its crystallisation seems to be kinetically favoured at ambient temperatures. Tilt and shift polymorphism for the here reported series  $[(n\text{Pr})_3(\text{CH}_3)\text{N}]\text{M}(\text{C}_2\text{N}_3)_3$  with  $\text{M} = \text{Mn}^{2+}$ ,  $\text{Co}^{2+}$ ,  $\text{Ni}^{2+}$  is therefore of Ostwald type. Whilst currently known examples of molecular perovskites that show tilt and shift polymorphism such as  $[(\text{NH}_2)_3\text{C}]\text{Mn}(\text{H}_2\text{POO})_3$ ,  $[(\text{C}_4\text{H}_9)_3(\text{CH}_3)\text{N}]\text{Mn}(\text{C}_2\text{N}_3)_3$  and  $[(\text{C}_5\text{H}_{10})_2\text{N}]\text{Cd}(\text{C}_2\text{N}_3)_3$  all seem to fulfil the Ostwald-rule of phase occurrences, there is no fundamental reason why this rule must be fulfilled at all times; in other words, it is likely that other molecular perovskites exist where altering the synthetic

conditions allows for obtaining tilt and shift polymorphism in molecular perovskites.

## Conclusion

In this work we introduce the concept of tilt and shift polymorphism for molecular perovskites, using the molecular perovskite series  $[(n\text{Pr})_3(\text{CH}_3)\text{N}]\text{M}(\text{C}_2\text{N}_3)_3$  with  $\text{M} = \text{Mn}^{2+}$ ,  $\text{Co}^{2+}$ ,  $\text{Ni}^{2+}$  as a blueprint for establishing the concept. Depending on the synthetic conditions, different perovskite polymorphs are obtained, and thermal treatment of the metastable polymorph **P(M)-I** leads to an irreversible perovskite-to-perovskite phase transition to **P(M)-II**. The **P(M)-II** polymorph exhibits a reversible order-disorder phase transition (**PIIa-PIIb**), which shows promising characteristics in terms of barocaloric properties. In-depth analysis reveals that structural differences between polymorphs are related to a subtle but important difference of the binding modes within the 3D  $[\text{M}(\text{C}_2\text{N}_3)_3]^-$  network, a mechanism intrinsically absent in inorganic perovskites. Density functional theory calculations show that for the whole stability temperature range the rhombohedral polymorph **P(M)-II** represents the thermodynamically more stable phase. The absence of real imaginary modes further suggests that the transformation goes through a high-energy transition state as underlying mechanism of the irreversible phase transition.

Tilt and shift polymorphism highlights the degrees of freedom, in this case, geometric degrees of freedom, that become accessible when moving from atomic to molecular building units. It underlines how little we have yet explored the vast chemical space of molecular perovskites, where subtle differences in the building principle can lead to different phases. The categorisation of tilt and shift polymorphism is important in developing the research area, helping us in the identification of degrees of freedom which have not yet been explored. When drawing comparisons to molecular crystals where properties such as optoelectronic properties and charge transport behaviour are tightly coupled to a distinct polymorph,<sup>59,60</sup> the necessity to understand and control tilt and shift polymorphism in molecular perovskites is apparent. For instance, the irreversible phase transition discussed here produces a molecular perovskite with promising phase transition thermodynamics for barocalorics, and the metastable form of  $[(\text{C}_5\text{H}_{10})_2\text{N}]\text{Cd}(\text{C}_2\text{N}_3)_3$  crystallises in a polar space group with a large second harmonic generation. More generally, it is exciting to see how the use of chemically more complex building units stimulates research to develop new strategies and concepts for material analysis and interpretation, and as such, molecular perovskites present a fascinating material platform for research of academic and applied purposes.

## Author contributions

S. B. and G. K. designed the study. S. B. synthesised the samples and performed sample analysis. H. L. B. B. contributed with expertise on the tilt and shift system analysis. S. G., K. T. B. and

R. G. C. carried out the DFT calculations. S. B., S. G., K. T. B., R. G. C. and G. K. interpreted experimental and computational results, and wrote the manuscript with revision by all authors.

## Conflicts of interest

There are no conflicts to declare.

## Acknowledgements

S. B. is grateful for holding a doctoral scholarship from the Hanns-Seidel Foundation. GK would like to thank the Fonds der Chemischen Industrie for support through the Liebig Fellowship scheme. S. G. is grateful for a doctoral studentship from the Felix Trust. H. L. B. gratefully acknowledges financial support from the Alexander von Humboldt Foundation. S. B. thanks David C. Mayer and Christian Jandl for assistance and service for single-crystal X-ray diffraction measurements due to lab access restrictions during the Corona pandemic. This work made use of ARCHER, the UK's national high-performance computing service, via the UK's HPC Materials Chemistry Consortium, which is funded by EPSRC (EP/R029431), and of the Young supercomputer, via the UK's Materials and Molecular Modelling Hub, which is partially funded by EPSRC (EP/T022213/1).

## Notes and references

- W. Li, Z. Wang, F. Deschler, S. Gao, R. H. Friend and A. K. Cheetham, *Nat. Rev. Mater.*, 2017, **2**, 16099.
- W. Wei, W. Li, K. T. Butler, G. Feng, C. J. Howard, M. A. Carpenter, P. Lu, A. Walsh and A. K. Cheetham, *Angew. Chem., Int. Ed.*, 2018, **57**, 8932.
- H. L. B. Boström, M. S. Senn and A. L. Goodwin, *Nat. Commun.*, 2018, **9**, 2380.
- G. Kieslich and A. L. Goodwin, *Mater. Horiz.*, 2017, **4**, 362.
- J. M. Bermúdez-García, M. Sánchez-Andújar and M. A. Señaris-Rodríguez, *J. Phys. Chem. Lett.*, 2017, **8**, 4419.
- J. M. Bermúdez-García, M. Sánchez-Andújar, S. Castro-García, J. López-Beceiro, R. Artiaga and M. A. Señaris-Rodríguez, *Nat. Commun.*, 2017, **8**, 15715.
- W.-J. Xu, Z.-Y. Du, W.-X. Zhang and X.-M. Chen, *CrystEngComm*, 2016, **18**, 7915.
- S. Burger, M. G. Ehrenreich and G. Kieslich, *J. Mater. Chem. A*, 2018, **6**, 21785.
- K.-L. Hu, M. Kurmoo, Z. Wang and S. Gao, *Chem. – Eur. J.*, 2009, **15**, 12050.
- X.-H. Zhao, X.-C. Huang, S.-L. Zhang, D. Shao, H.-Y. Wei and X.-Y. Wang, *J. Am. Chem. Soc.*, 2013, **135**, 16006.
- M.-L. Tong, J. Ru, Y.-M. Wu, X.-M. Chen, H.-C. Chang, K. Mochizuki and S. Kitagawa, *New J. Chem.*, 2003, **27**, 779.
- J. Lefebvre, D. Chartrand and D. B. Leznoff, *Polyhedron*, 2007, **26**, 2189.
- J. A. Hill, A. L. Thompson and A. L. Goodwin, *J. Am. Chem. Soc.*, 2016, **138**, 5886.
- Z.-Y. Du, T.-T. Xu, B. Huang, Y.-J. Su, W. Xue, C.-T. He, W.-X. Zhang and X.-M. Chen, *Angew. Chem., Int. Ed.*, 2015, **54**, 914.
- J. Y. Lee, S. Ling, S. P. Argent, M. S. Senn, L. Cañadillas-Delgado and M. J. Cliffe, *Chem. Sci.*, 2021, **9**, 2380.
- S. Chen, R. Shang, B.-W. Wang, Z.-M. Wang and S. Gao, *Angew. Chem.*, 2015, **54**, 11093.
- G. Kieslich, S. Kumagai, A. C. Forse, S. Sun, S. Henke, M. Yamashita, C. P. Grey and A. K. Cheetham, *Chem. Sci.*, 2016, **7**, 5108.
- Y. Wu, D. M. Halat, F. Wei, T. Binford, I. D. Seymour, M. W. Gaultois, S. Shaker, J. Wang, C. P. Grey and A. K. Cheetham, *Chem. – Eur. J.*, 2018, **24**, 11309.
- M. Mączka, A. Gağor, A. Pikul and D. Stefańska, *RSC Adv.*, 2020, **10**, 19020.
- A. Simonov, T. de Baerdemaeker, H. L. B. Boström, M. L. Ríos Gómez, H. J. Gray, D. Chernyshov, A. Bosak, H.-B. Bürgi and A. L. Goodwin, *Nature*, 2020, **578**, 256.
- A. E. Phillips and A. D. Fortes, *Angew. Chem., Int. Ed.*, 2017, **56**, 15950.
- H. L. B. Boström and A. L. Goodwin, *Acc. Chem. Res.*, 2021, **54**, 1288.
- W.-J. Xu, S.-L. Chen, Z.-T. Hu, R.-B. Lin, Y.-J. Su, W.-X. Zhang and X.-M. Chen, *Dalton Trans.*, 2016, **45**, 4224.
- M. Mączka, I. E. Collings, F. F. Leite and W. Paraguassu, *Dalton Trans.*, 2019, **48**, 9072.
- H. L. B. Boström, J. A. Hill and A. L. Goodwin, *Phys. Chem. Chem. Phys.*, 2016, **18**, 31881.
- T. Besara, P. Jain, N. S. Dalal, P. L. Kuhns, A. P. Reyes, H. W. Kroto and A. K. Cheetham, *Proc. Natl. Acad. Sci. U. S. A.*, 2011, **108**, 6828.
- H. L. B. Boström and G. Kieslich, *J. Phys. Chem. C*, 2021, **125**, 1467.
- I. E. Collings, M. Bykov, E. Bykova, M. Hanfland, S. van Smaalen, L. Dubrovinsky and N. Dubrovinskaja, *CrystEngComm*, 2018, **20**, 3512.
- M. Mączka, A. Gağor, M. Ptak, D. Stefańska and A. Sieradzki, *Phys. Chem. Chem. Phys.*, 2018, **20**, 29951.
- G. Kieslich, S. Kumagai, K. T. Butler, T. Okamura, C. H. Hendon, S. Sun, M. Yamashita, A. Walsh and A. K. Cheetham, *Chem. Commun.*, 2015, **51**, 15538.
- Y. Wu, S. Shaker, F. Brivio, R. Murugavel, P. D. Bristowe and A. K. Cheetham, *J. Am. Chem. Soc.*, 2017, **139**, 16999.
- S. Burger, S. Kronawitter, H. L. B. Boström, J. K. Zaręba and G. Kieslich, *Dalton Trans.*, 2020, **49**, 10740.
- M. Mączka, A. Gağor, M. Ptak, D. Stefańska, L. Macalik, A. Pikul and A. Sieradzki, *Dalton Trans.*, 2019, **48**, 13006.
- J. Bernstein and A. T. Hagler, *J. Am. Chem. Soc.*, 1978, **100**, 673.
- A. J. Cruz-Cabeza and J. Bernstein, *Chem. Rev.*, 2014, **114**, 2170.
- A. Nangia, *Acc. Chem. Res.*, 2008, **41**, 595.
- M. Mączka, A. Gağor, A. Stroppa, J. N. Gonçalves, J. K. Zaręba, D. Stefańska, A. Pikul, M. Drozd and A. Sieradzki, *J. Mater. Chem. C*, 2020, **8**, 11735.

- 38 S. Sobczak, P. Ratajczyk and A. S. Katrusiak, *Chem. – Eur. J.*, 2021, **27**, 7069.
- 39 M. Mączka, A. Gağor, M. Ptak, W. Paraguassu, T. A. da Silva, A. Sieradzki and A. Pikul, *Chem. Mater.*, 2017, **29**, 2264.
- 40 A. M. Glazer, *Acta Crystallogr., Sect. B: Struct. Crystallogr. Cryst. Chem.*, 1972, **28**, 3384.
- 41 J. M. Bermúdez-García, M. Sánchez-Andújar, S. Yáñez-Vilar, S. Castro-García, R. Artiaga, J. López-Beceiro, L. Botana, Á. Alegría and M. A. Señaris-Rodríguez, *Inorg. Chem.*, 2015, **54**, 11680.
- 42 J. M. Bermúdez-García, S. Yáñez-Vilar, A. García-Fernández, M. Sánchez-Andújar, S. Castro-García, J. López-Beceiro, R. Artiaga, M. Dilshad, X. Moya and M. A. Señaris-Rodríguez, *J. Mater. Chem. C*, 2018, **6**, 9867.
- 43 M. W. Lufaso and P. M. Woodward, *Acta Crystallogr., Sect. B: Struct. Sci.*, 2001, **57**, 725.
- 44 W. Li, Z. Zhang, E. G. Bithell, A. S. Batsanov, P. T. Barton, P. J. Saines, P. Jain, C. J. Howard, M. A. Carpenter and A. K. Cheetham, *Acta Mater.*, 2013, **61**, 4928.
- 45 P. Jain, V. Ramachandran, R. J. Clark, H. D. Zhou, B. H. Toby, N. S. Dalal, H. W. Kroto and A. K. Cheetham, *J. Am. Chem. Soc.*, 2009, **131**, 13625.
- 46 H. L. B. Boström, *CrystEngComm*, 2020, **22**, 961.
- 47 M. J. Cliffe, E. N. Keyzer, M. T. Dunstan, S. Ahmad, M. F. L. de Volder, F. Deschler, A. J. Morris and C. P. Grey, *Chem. Sci.*, 2019, **10**, 793.
- 48 X.-Y. Wang, Z.-M. Wang and S. Gao, *Chem. Commun.*, 2008, 281.
- 49 Z. Wang, K. Hu, S. Gao and H. Kobayashi, *Adv. Mater.*, 2010, **22**, 1526.
- 50 C. J. Howard and H. T. Stokes, *Acta Crystallogr., Sect. B: Struct. Sci.*, 1998, **54**, 782.
- 51 J. Nyman and G. M. Day, *CrystEngComm*, 2015, **17**, 5154.
- 52 I. E. Collings, R. S. Manna, A. A. Tsirlin, M. Bykov, E. Bykova, M. Hanfland, P. Gegenwart, S. van Smaalen, L. Dubrovinsky and N. Dubrovinskaia, *Phys. Chem. Chem. Phys.*, 2018, **20**, 24465.
- 53 A. P. Katsoulidis, D. Antypov, G. F. S. Whitehead, E. J. Carrington, D. J. Adams, N. G. Berry, G. R. Darling, M. S. Dyer and M. J. Rosseinsky, *Nature*, 2019, **565**, 213.
- 54 C. L. Hobday and G. Kieslich, *Dalton Trans.*, 2021, **50**, 3759.
- 55 A. D. Fortes, E. Suard and K. S. Knight, *Science*, 2011, **331**, 742.
- 56 K. T. Butler, P. Vervoorts, M. G. Ehrenreich, J. Armstrong, J. M. Skelton and G. Kieslich, *Chem. Mater.*, 2019, **31**, 8366.
- 57 K. T. Butler, K. Svane, G. Kieslich, A. K. Cheetham and A. Walsh, *Phys. Rev. B*, 2016, **94**, 180103.
- 58 G. Kieslich, J. M. Skelton, J. Armstrong, Y. Wu, F. Wei, K. L. Svane, A. Walsh and K. T. Butler, *Chem. Mater.*, 2018, **30**, 8782.
- 59 B. Huang, W.-C. Chen, Z. Li, J. Zhang, W. Zhao, Y. Feng, B. Z. Tang and C.-S. Lee, *Angew. Chem., Int. Ed.*, 2018, **57**, 12473.
- 60 T. Siegrist, C. Kloc, J. H. Schön, B. Batlogg, R. C. Haddon, S. Berg and G. A. Thomas, *Angew. Chem., Int. Ed.*, 2001, **40**, 1732.



## 4.4 STUDY IV: Tuning the Mechanical Properties of Dicyanamide-Based Molecular Perovskites

Perovskite-type coordination networks have in recent years attracted considerable attention as functional materials. Especially in the context of barocalorics, research effort aims to find perovskite-type materials with superior barocaloric coefficients as a result of large changes in entropy during structural phase transitions. To date, known materials exhibiting these kind of characteristics rely on the coincidental presence of a phase transition rather than on a systematic evaluation of mechanical properties towards the targeted application as barocalorics.

In this work, the theoretical assessment to derive the compressibility of perovskite-type materials is elaborated and the results are compared to experimentally obtained bulk moduli of the model material series  $[(C_3H_7)_3CH_3N]M[(C_2N_3)_3]$  with various divalent metals being calculated. The experimental bulk moduli for  $M = Mn^{2+}$ ,  $Co^{2+}$  and  $Ni^{2+}$  are extracted from high-pressure diffraction experiments and are compared to the data provided by computational chemistry. The understanding of relationships between geometric factors and the bulk moduli within these type of functional materials in terms of their mechanical properties agrees with chemical intuition and marks an important contribution towards establishing an accessible figure of merit descriptor for potential application as barocaloric materials.

The design of the study was mainly focused on theoretical calculations using density functional theory and was guided by Dr. Ricardo Grau-Crespo as principal investigator. Shivani Grover performed the theoretical calculations together with Dr. Ricardo Grau-Crespo and Dr. Keith T. Butler. Pia Vervoorts, Karina Hemmer and Dr. Gregor Kieslich together with the author of this doctorate thesis collected the high-pressure powder X-Ray diffraction data at Diamond Light Source Ltd., beamline I-15 during a scheduled beamtime. The author of this thesis analysed all experimental data and discussed the results with Dr. Gregor Kieslich. All authors contributed to the preparation of the manuscript. Shivani Grover and the author of this thesis share first authorship for this article with the responsibilities distributed to the theoretical and experimental contributions, respectively.

Status: Published as Research Paper in CrystEngComm.

Reproduced from Ref. [284] with permission from the Royal Society of Chemistry, see APPENDIX, C Reprint permissions for details on the license agreement.

S. Grover, S. Burger, K. T. Butler, K. Hemmer, P. Vervoorts, G. Kieslich and R. Grau-Crespo, *Tuning the mechanical properties of dicyanamide-based molecular perovskites*, *CrystEngComm*, 2023, **25**, 3439-3444, DOI: 10.1039/D3CE00009E.

Cite this: *CrystEngComm*, 2023, 25, 3439

## Tuning the mechanical properties of dicyanamide-based molecular perovskites†

 Shivani Grover,<sup>a</sup> Stefan Burger,<sup>b</sup> Keith T. Butler,<sup>c</sup> Karina Hemmer,<sup>b</sup> Pia Vervoorts,<sup>b</sup> Gregor Kieslich<sup>\*b</sup> and Ricardo Grau-Crespo<sup>id\*<sup>a</sup></sup>

ABX<sub>3</sub> molecular perovskites have recently gained attention in the field of ferroelectrics and barocalorics where the materials' mechanical properties such as mechanical stability, compressibility, hardness, and elasticity are important performance criteria. Akin to previous work on ceramic perovskites, research on molecular perovskites benefits from the modular building principle of the perovskite motif, enabling systematic studies to learn about the interplay of chemical composition, structure, and properties. Here we use the molecular perovskite series [(*n*Pr)<sub>3</sub>(CH<sub>3</sub>)N]M(C<sub>2</sub>N<sub>3</sub>)<sub>3</sub> (*n*Pr = -(C<sub>3</sub>H<sub>7</sub>) and M = Mn<sup>2+</sup>, Co<sup>2+</sup>, Fe<sup>2+</sup>, Ni<sup>2+</sup>, Zn<sup>2+</sup>, Cd<sup>2+</sup>, Ba<sup>2+</sup>, Sr<sup>2+</sup>, Ca<sup>2+</sup>, Hg<sup>2+</sup>, or Mg<sup>2+</sup>) as a model system to study the impact of the M<sup>2+</sup> metal species on the mechanical properties via lattice dynamic calculations and high-pressure powder X-ray diffraction. By using the bulk modulus as a proxy, we observe a relationship between geometric factors and mechanical properties that agree with chemical intuition. The results present a step forward for gradually refining our understanding of these materials, and contribute to the long-term goal, the design of materials with targeted macroscopic properties.

Received 3rd January 2023,  
Accepted 4th May 2023

DOI: 10.1039/d3ce00009e

rsc.li/crystengcomm

### Introduction

ABX<sub>3</sub> molecular perovskites, where A and/or X are molecular moieties, have attracted increased attention in recent years.<sup>1</sup> Research on molecular perovskites such as [(NH<sub>2</sub>)<sub>2</sub>CH]Mn(HCOO)<sub>3</sub>,<sup>2</sup> [N(CH<sub>3</sub>)<sub>4</sub>][Cd(N<sub>3</sub>)<sub>3</sub>],<sup>3</sup> and [(NH<sub>2</sub>)<sub>3</sub>C]Mn(H<sub>2</sub>POO)<sub>3</sub>,<sup>4</sup> has drawn inspiration from decades of research in the oxide perovskites, but with the additional benefit of the chemical space as offered by the inclusion of molecular units in the crystal structure,<sup>5</sup> as illustrated in Fig. 1a. Conceptually, the use of molecular A- and X-site species enhances the structural and chemical diversity in these perovskites, leading to new opportunities for tuning macroscopic material behaviour.<sup>6</sup> Examples are tilt-and-shift engineering to impart ferroelectric properties,<sup>7,8</sup> tunability of hydrogen bonding interactions<sup>9</sup> between the A-site cation and the 3D [BX<sub>3</sub>]<sup>-</sup> network with ramifications on the mechanical response,<sup>10,11</sup> adjustable phase transition thermodynamics,<sup>12,13</sup> and varying structural complexities<sup>14</sup> amongst others.

The mechanical properties of molecular perovskites have been demonstrated to be tuneable through different components of the material.<sup>15</sup> For instance, the larger elastic moduli and hardness of [C(NH<sub>2</sub>)<sub>3</sub>]Mn(HCOO)<sub>3</sub> compared to [(CH<sub>2</sub>)<sub>3</sub>NH<sub>2</sub>]Mn(HCOO)<sub>3</sub> have been attributed to the larger number of hydrogen bonding interactions,<sup>16</sup> and a similar conclusion can be drawn for the elastic moduli across the A-site solid solution series [NH<sub>3</sub>NH<sub>2</sub>]<sub>1-x</sub>[NH<sub>3</sub>OH]

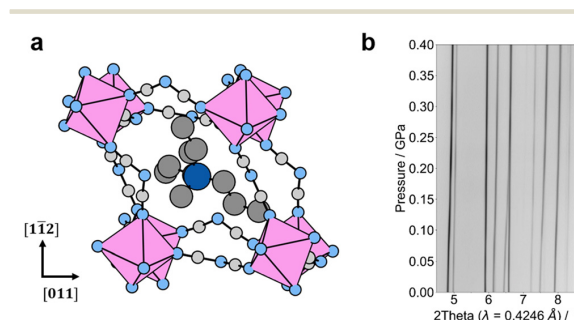


Fig. 1 (a) Crystal structure of [N(C<sub>3</sub>H<sub>7</sub>)<sub>3</sub>CH<sub>3</sub>]Mn(C<sub>2</sub>N<sub>3</sub>)<sub>3</sub> illustrating the 3D pseudo-cubic ReO<sub>3</sub>-type [M(C<sub>2</sub>N<sub>3</sub>)<sub>3</sub>]<sup>-</sup> network. In (b), HPPXRD pattern in the pressure range *p* = ambient – 0.4 GPa of [N(C<sub>3</sub>H<sub>7</sub>)<sub>3</sub>CH<sub>3</sub>]Mn(C<sub>2</sub>N<sub>3</sub>)<sub>3</sub> are shown as a contour plot and HPPXRD data of all materials including lattice parameters from Pawley profile fits are given in the ESI.† Colour scheme: C atoms of C<sub>2</sub>N<sub>3</sub><sup>-</sup> in light grey, C atoms of [N(C<sub>3</sub>H<sub>7</sub>)<sub>3</sub>CH<sub>3</sub>]<sup>+</sup> in dark grey, N atoms of C<sub>2</sub>N<sub>3</sub><sup>-</sup> in light blue, N atom of [N(C<sub>3</sub>H<sub>7</sub>)<sub>3</sub>CH<sub>3</sub>]<sup>+</sup> in dark blue, MnN<sub>6</sub> octahedra pink, and H atoms are omitted for clarity.

<sup>a</sup> Department of Chemistry, Food and Pharmacy, University of Reading, RG66DX, UK. E-mail: r.grau-crespo@reading.ac.uk

<sup>b</sup> Technical University of Munich, TUM School of Natural Sciences, Department of Chemistry, Lichtenbergstraße 4, 85748 Garching, Germany. E-mail: gregor.kieslich@tum.de

<sup>c</sup> Materials Research Institute, School of Engineering and Materials Science, Queen Mary University of London, Mile End Road, London E1 4NS, UK

† Electronic supplementary information (ESI) available. See DOI: <https://doi.org/10.1039/d3ce00009e>

‡ Shared contribution.

Zn(HCOO)<sub>3</sub>.<sup>17</sup> Looking at the impact of the metal ion, a linear correlation between the elastic moduli and the ligand field stabilisation energy has been observed for the series [(CH<sub>3</sub>)<sub>2</sub>NH<sub>2</sub>]<sub>3</sub>M(HCOO)<sub>3</sub> with M = Mn<sup>2+</sup>, Co<sup>2+</sup>, Ni<sup>2+</sup> and Zn<sup>2+</sup>.<sup>18</sup> Likewise, the bulk moduli of several molecular perovskites series, such as [(CH<sub>3</sub>)<sub>2</sub>NH<sub>2</sub>]<sub>3</sub>M(HCOO)<sub>3</sub> (M = Mn<sup>2+</sup>, Fe<sup>2+</sup> and Cu<sup>2+</sup>),<sup>19</sup> [(C<sub>3</sub>H<sub>7</sub>)<sub>4</sub>N]<sub>3</sub>M(C<sub>2</sub>N<sub>3</sub>)<sub>3</sub> (M = Mn<sup>2+</sup> and Cd<sup>2+</sup>),<sup>20,21</sup> [(NH<sub>2</sub>)<sub>3</sub>C]<sub>3</sub>M(HCOO)<sub>3</sub> (M = Mn<sup>2+</sup>, Co<sup>2+</sup> and Cd<sup>2+</sup>)<sup>22,23</sup> have been explored by high-pressure diffraction experiments on single crystals and powders. Some studies<sup>24,25</sup> have reported trends such as a relationship between size and chemistry of the divalent B-site metal and the bulk modulus, which agree with chemical intuition. Furthermore, the impact of B-site metal defects has been studied by comparing [C(NH<sub>2</sub>)<sub>3</sub>]<sub>3</sub>Mn(HCOO)<sub>3</sub> with its defective analogue [C(NH<sub>2</sub>)<sub>3</sub>]<sub>3</sub>Fe<sub>2/3</sub>□<sub>1/3</sub>(HCOO)<sub>3</sub>, (□ = vacancy), which exhibits a bulk modulus that is nearly 30% lower.<sup>26</sup> This body of work demonstrates the immense potential for tailoring the mechanical properties in hybrid and molecular perovskites, depending on a robust understanding of the chemical and physical principles that affect them.

More recently, molecular perovskites such as [(C<sub>3</sub>H<sub>7</sub>)<sub>4</sub>N]<sub>3</sub>Mn(C<sub>2</sub>N<sub>3</sub>)<sub>3</sub> and [(C<sub>3</sub>H<sub>7</sub>)<sub>4</sub>N]<sub>3</sub>Cd(C<sub>2</sub>N<sub>3</sub>)<sub>3</sub> have emerged as model systems in barocalorics, where their modular building principle enables the search for crystal chemistry factors that determine a material's performance in solid-state cooling.<sup>27,28</sup> A relation between compressibility and barocaloric performance has recently been implied,<sup>29</sup> an intuitive link when considering the barocaloric coefficient  $dT_c/dp$  as a proxy. A softer material is thus expected to exhibit a larger barocaloric coefficient, a rule which provides a useful guideline to manipulate barocaloric performance in the future. Therefore, the identification of crystal chemistry principles that determine a molecular perovskite's mechanical response, *i.e.* its structural response to pressure such as compressibility or similarly the bulk modulus, is an important step forward in the search for intuitive material design guidelines.

In the present work, we study the mechanical properties of the molecular perovskite series [(*n*Pr)<sub>3</sub>(CH<sub>3</sub>)N]<sub>3</sub>M(C<sub>2</sub>N<sub>3</sub>)<sub>3</sub>, (*n*Pr = -(C<sub>3</sub>H<sub>7</sub>) and M = Mn<sup>2+</sup>, Co<sup>2+</sup>, Fe<sup>2+</sup>, Ni<sup>2+</sup>, Zn<sup>2+</sup>, Cd<sup>2+</sup>, Ba<sup>2+</sup>, Sr<sup>2+</sup>, Ca<sup>2+</sup>, Hg<sup>2+</sup>, or Mg<sup>2+</sup>), combining density functional theory (DFT) simulations with high pressure powder X-ray diffraction (HPPXRD). Previously we have shown that [(*n*Pr)<sub>3</sub>(CH<sub>3</sub>)N]<sub>3</sub>M(C<sub>2</sub>N<sub>3</sub>)<sub>3</sub> can crystallise in two polymorphs, and in this work we focus on the thermodynamically stable rhombohedral compound, which exhibits an order-disorder phase transition related to [(*n*Pr)<sub>3</sub>(CH<sub>3</sub>)N]<sup>+</sup>. *Via* HPPXRD we determine the experimental bulk moduli for M = Mn<sup>2+</sup>, Co<sup>2+</sup> and Ni<sup>2+</sup> and apply DFT simulations to obtain the bulk modulus for an extended range of compositions. We find a strong trend relating the mechanical properties to the B-site Shannon radius and the B–X bond length. Our results agree with chemical intuition and with recently published barocaloric performances of related compounds such as [(C<sub>3</sub>H<sub>7</sub>)<sub>4</sub>N]<sub>3</sub>Mn(C<sub>2</sub>N<sub>3</sub>)<sub>3</sub> and [(C<sub>3</sub>H<sub>7</sub>)<sub>4</sub>N]<sub>3</sub>Cd(C<sub>2</sub>N<sub>3</sub>)<sub>3</sub>.<sup>27,28</sup>

## Results and discussion

We start by elucidating the experimental and computational bulk moduli of the molecular perovskite series [(*n*Pr)<sub>3</sub>(CH<sub>3</sub>)N]<sub>3</sub>M(C<sub>2</sub>N<sub>3</sub>)<sub>3</sub> (M = Mn<sup>2+</sup>, Co<sup>2+</sup>, Ni<sup>2+</sup>). The materials [(*n*Pr)<sub>3</sub>(CH<sub>3</sub>)N]<sub>3</sub>M(C<sub>2</sub>N<sub>3</sub>)<sub>3</sub> (M = Mn<sup>2+</sup>, Co<sup>2+</sup> and Ni<sup>2+</sup>) were synthesised according to the strategy established in our recent work.<sup>30</sup> In its low-temperature modification, the thermodynamic stable polymorph of [(*n*Pr)<sub>3</sub>(CH<sub>3</sub>)N]<sub>3</sub>M(C<sub>2</sub>N<sub>3</sub>)<sub>3</sub> crystallises in the space-group *R3c*. The divalent metal M<sup>2+</sup> is in an octahedral coordination from six nitrogen atoms forming a 3D ReO<sub>3</sub>-type [M(C<sub>2</sub>N<sub>3</sub>)<sub>3</sub>]<sup>−</sup> network, see Fig. 1a. The A-site cation [(*n*Pr)<sub>3</sub>(CH<sub>3</sub>)N]<sup>+</sup> sits in the void of the ReO<sub>3</sub>-network, forming the perovskite structure motif. At *T*<sub>c</sub> = 284 K (Mn<sup>2+</sup>), 301 K (Co<sup>2+</sup>) and 312 K (Ni<sup>2+</sup>), [(*n*Pr)<sub>3</sub>(CH<sub>3</sub>)N]<sub>3</sub>M(C<sub>2</sub>N<sub>3</sub>)<sub>3</sub> exhibits a temperature-driven order-disorder phase transition related to the A-site cation to the centrosymmetric space-group *R3c*. HPPXRD experiments were performed by using the “pressure jump cell”,<sup>31</sup> which enables the collection of HPPXRD data between ambient pressure and 0.4 GPa with a fine pressure resolution, see Fig. 1b for a representative contour plot and ESI† for further details. Lattice parameter and volume *V* as a function of pressure were extracted by Pawley profile fits to HPPXRD data, see Table 1 and ESI†. Given that HPPXRD experiments were performed at approximately 300 K, a pressure-driven phase transition from the high-temperature to the low-temperature polymorph can be expected for [(*n*Pr)<sub>3</sub>(CH<sub>3</sub>)N]<sub>3</sub>Mn(C<sub>2</sub>N<sub>3</sub>)<sub>3</sub> and [(*n*Pr)<sub>3</sub>(CH<sub>3</sub>)N]<sub>3</sub>Co(C<sub>2</sub>N<sub>3</sub>)<sub>3</sub> at low pressures,<sup>30</sup> however, due to the similarities between X-ray powder diffraction pattern of both phases, we used P-fplots to identify the onset of the phase transition, see ESI†. The bulk moduli of the high-pressure (low-temperature) phases were determined by fitting *V*(*p*) data to the Birch–Murnaghan equation of state (2nd order), and the results are shown in Table 2. We observe a decreasing unit cell volume and an increasing bulk modulus when going along the series Mn<sup>2+</sup>, Co<sup>2+</sup> and Ni<sup>2+</sup>. This trend agrees with chemical intuition: a higher packing density coming from a reduced metal radius leads to a higher bulk modulus, *i.e.* a lower compressibility.

In order to obtain bulk moduli *via* density functional theory (DFT), we used the low-temperature experimental structures as starting point for geometry optimisation, see ESI†. The obtained lattice parameters are in good agreement with the experimental values, with the inclusion of the Hubbard *U* correction improving the outcomes to errors below 2%. The bulk moduli were obtained by fitting DFT energy (*E*) vs. volume (*V*). For each point the structure was relaxed by optimising cell parameters and atomic coordinates at a fixed volume. The fitting of *E*(*V*) curves from DFT for [(*n*Pr)<sub>3</sub>(CH<sub>3</sub>)N]<sub>3</sub>M(C<sub>2</sub>N<sub>3</sub>)<sub>3</sub> compounds is shown in Fig. S1 in the ESI†. The bulk moduli obtained for M<sup>2+</sup> = Mn<sup>2+</sup>, Co<sup>2+</sup>, and Ni<sup>2+</sup> are listed in Table 2 and compared to experimental outcomes, showing that results from DFT calculations

**Table 1** Comparison of experimental and computationally obtained lattice parameters. Experimental values are taken from single crystal X-ray diffraction experiments at 100 K (ref. 30) whereas the calculations ignore vibrational effects and therefore are formally at 0 K (and without any zero-point contributions)

Parameter	M = Mn <sup>2+</sup>			M = Co <sup>2+</sup>			M = Ni <sup>2+</sup>		
	Exp.	Theory	Error	Exp.	Theory	Error	Exp.	Theory	Error
<i>a</i> /Å	10.36	10.28	-0.77%	10.26	10.19	-0.68%	10.22	10.16	-0.58%
$\alpha$ /deg	76.47	77.24	-1.0%	76.28	77.13	-1.11%	76.01	76.76	0.98%
<i>V</i> /Å <sup>3</sup>	1033.54	1017.39	-1.56%	1001.57	988.71	-1.28%	986.49	976.46	-1.02%

reproduce the trend of experimentally determined bulk moduli. The overestimation of absolute values of bulk moduli can be, at least partially, ascribed to the underestimation of lattice parameters within the level of theory employed, since more tightly packed structures show larger moduli. Table 1 shows that our DFT (GGA+U) calculations indeed predict slightly underestimated cell parameters (although note that experimental lattice parameters have been taken from structures at 100 K, while lattice parameters from DFT are formally at 0 K, ignoring also any zero-point vibrational effects).

The analysis above suggests a close relationship between crystal packing and mechanical properties. To further explore this effect and provide mechanistic insights, we have performed lattice dynamics calculations to obtain phonon spectra. The phonon density of states (pDoS) for the three compositions is shown in Fig. 2a. The pDoS has been decomposed into contributions from A-site cation, B-site metal cation and X-site linker anion by using Phonopy.<sup>32</sup> All three materials have qualitatively a similar pDoS, with the metal centre contribution only observed at low frequencies (up to 300 cm<sup>-1</sup>) which is related to the higher atomic mass of M<sup>2+</sup> compared to the other species in the material. From the zone-centre vibrational frequencies, a clear hardening of the soft optical modes  $\nu < 100$  cm<sup>-1</sup> is observed from Mn to Co and Ni, as shown in Fig. 2b. To better understand the origin of these differences, the contributions to the pDoS of the 3D [M(C<sub>2</sub>N<sub>3</sub>)<sub>3</sub>]<sup>-</sup> framework and A-site cation is calculated, see Fig. 2c. It is evident that the soft modes are dominated by the 3D framework only, where [(*n*Pr)<sub>3</sub>(CH<sub>3</sub>)N]Mn(C<sub>2</sub>N<sub>3</sub>)<sub>3</sub> has the greatest pDoS at low frequencies, followed by [(*n*Pr)<sub>3</sub>(CH<sub>3</sub>)N]Co(C<sub>2</sub>N<sub>3</sub>)<sub>3</sub> and then [(*n*Pr)<sub>3</sub>(CH<sub>3</sub>)N]Ni(C<sub>2</sub>N<sub>3</sub>)<sub>3</sub>. This trend in the low-frequency pDoS matches well with the trend in bulk modulus and supports the assertion that altering the framework by metal cation substitution provides a precise handle for tuning mechanical properties. This finding agrees with previous work on the effects of B–X

bonding on the mechanical properties of hybrid and molecular perovskites. It has been shown that stiffer B–X bonds achieved through greater ligand-field stabilisation<sup>18,33</sup> or through greater electronegativity differences properties<sup>11,34,35</sup> result in stiffer materials. The direct effect of B–X bonding on the bulk modulus suggests that it would be interesting to investigate how crystal chemistry can be

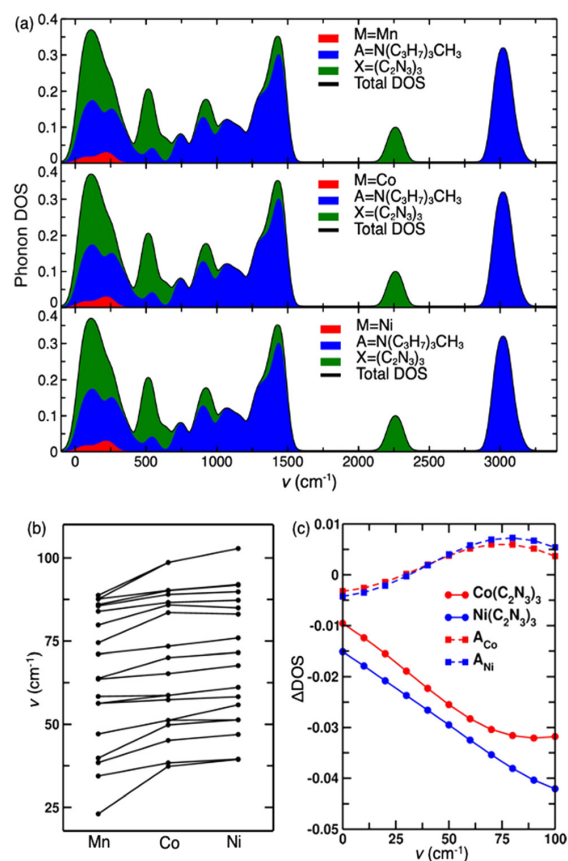


**Fig. 2** Vibrational properties of [N(C<sub>3</sub>H<sub>7</sub>)<sub>3</sub>CH<sub>3</sub>]M(C<sub>2</sub>N<sub>3</sub>)<sub>3</sub> perovskites (M = Mn<sup>2+</sup>, Co<sup>2+</sup> and Ni<sup>2+</sup>). (a) Phonon density of states, (b) zone-centre vibrational frequency of the soft modes for the three compositions, (c)  $\Delta$ DOS of the [Co(C<sub>2</sub>N<sub>3</sub>)<sub>3</sub>]<sup>-</sup> and [Ni(C<sub>2</sub>N<sub>3</sub>)<sub>3</sub>]<sup>-</sup> framework with [Mn(C<sub>2</sub>N<sub>3</sub>)<sub>3</sub>]<sup>-</sup> framework as reference and  $\Delta$ DOS from the A-site of Co and Ni substituted system with respect to Mn containing system.

**Table 2** Bulk modulus (*B*) for [N(C<sub>3</sub>H<sub>7</sub>)<sub>3</sub>CH<sub>3</sub>]M(C<sub>2</sub>N<sub>3</sub>)<sub>3</sub> as determined from theory and experiment. For M = Mn<sup>2+</sup> and Co<sup>2+</sup>, the bulk moduli were extracted from the high-pressure phase, *i.e.* the pressure regime *p* = 0.125–0.4 GPa (Mn<sup>2+</sup>) and 0.1–0.4 GPa (Co<sup>2+</sup>), see ESI† for more details

<i>B</i> /GPa	M = Mn <sup>2+</sup>	M = Co <sup>2+</sup>	M = Ni <sup>2+</sup>
Theory	11.0 ± 0.1	12.5 ± 0.1	13.4 ± 0.1
Experiment	7.08 ± 0.15	9.90 ± 0.30	10.85 ± 0.16



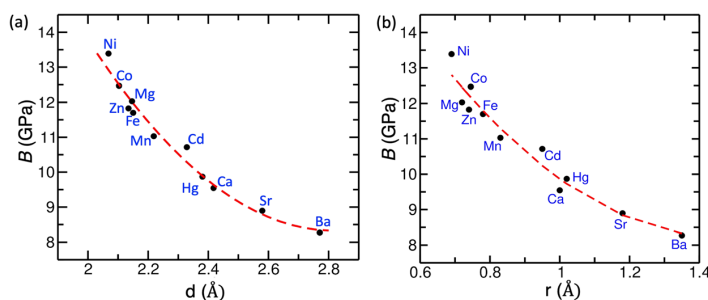


Fig. 3 Bulk modulus,  $B$ , as a function of (a) equilibrium metal-linker bond distance,  $d$ , and (b) Shannon radius,  $r$ , of  $M^{2+}$  cations for  $[N(C_2H_7)_3CH_3]M(C_2N_3)_3$  perovskites.

used to alter the mechanical properties across a range of different chemical environments.

Having established the importance of the nature of the metal cation in determining the mechanical and vibrational properties in these molecular perovskite systems, the next question is whether this trend extends to other metal species and if examining a wider range of compositions can allow us to draw stronger inferences about the origin of the effect. Therefore, we have explored a range of hypothetical  $[(nPr)_3(CH_3)N]M(C_2N_3)_3$  materials, where the mechanical properties can be modified by cation substitution at the M-site. We extend our computational simulations to systems containing other metals:  $Fe^{2+}$ ,  $Zn^{2+}$ ,  $Cd^{2+}$ ,  $Ba^{2+}$ ,  $Sr^{2+}$ ,  $Ca^{2+}$ ,  $Hg^{2+}$ , or  $Mg^{2+}$ , and determine their bulk modulus using DFT calculations. The calculated equilibrium cell parameters for all compositions at zero pressure and temperature, as well as the corresponding bulk moduli compressibilities, are listed in Table S1 of the ESI† These hypothetical structures are not necessarily stable experimentally, due to size and electron configuration effects. However, we can examine them computationally as we can constrain the symmetry of the system so that the metal forms an octahedral complex with  $C_2N_3^-$  linker anion to form the desired phase, as we are interested here in establishing the trend rather than in predicting real materials.

In Fig. 3 the variation in bulk modulus for various metal systems is shown. The Ba-containing system has the lowest bulk modulus (8.3 GPa), with the Ni-containing system having the highest value of 13.4 GPa among the systems of interest considered here. To examine the geometric factors determining the mechanical behaviour in this molecular perovskite series, we plot the variation in bulk modulus as a function of M–N bond length in  $MN_6$  octahedra (metal-linker bond distance),  $d$ . This shows that the larger the M–N bond distance, the smaller the bulk modulus (see Fig. 3a). This finding is similar to the situation in hybrid lead halide perovskites, where the stiffness, as measured by the Young modulus, decreases with the lead-to-halide bond length.<sup>34</sup> We further look at the variation in bulk modulus as a function of Shannon radius ( $r$ ) of the M cation, see Fig. 3b. Clearly, the Shannon radius is a good predictor of the bulk modulus in this series of compounds. The small differences between the relationships shown in Fig. 3a and b partially arise from deviations in the additivity rule of ionic radii due to

covalency effects (e.g. Co and Zn have similar ionic radii, but Co–N bonds can be expected to be slightly more covalent than Zn–N bonds because of the smaller electronegativity difference). The observation of the correlation of the bulk modulus with the Shannon radius is useful because Shannon radii are available *a priori*, without the need for a DFT optimisation.

## Conclusion

We have calculated the mechanical and vibrational properties of a molecular perovskite series, which are of importance for the potential application of these materials for barocaloric applications. We establish that the bulk modulus depends on the phonon density of states of the  $[MX_3]^-$  framework and specifically the metal-linker bond. Our analysis shows that the material with the softest phonon modes corresponds to the material with the lowest bulk modulus. Given the importance of the metal cation determining the vibrational and mechanical properties we extend our study to a series of hypothetical materials with other metals in oxidation state II: Fe, Zn, Cd, Ba, Sr, Ca, Hg, and Mg. These calculations reveal a clear relationship between the metal-linker bond length and the bulk modulus. Furthermore, we show that the Shannon radius of a metal, which can be known *a priori*, without calculations or experiments, is a good descriptor for how the bulk modulus will depend on composition.

The obtained dependence of the bulk modulus on the metal-to-nitrogen bond distance agrees with chemical intuition and provides a starting point for rational materials design of molecular perovskites with tailored mechanical properties. Other factors such as the preferred crystal structure, presence of defects, microstructure and vibrational properties will also contribute to the overall mechanical properties of the systems. However, to a first order it should be possible to carefully change the mechanical properties by metal substitution. We also emphasise that the metal does not need to be substituted completely; solid solutions are a powerful approach to continuously tailoring materials properties, and we expect that solid solutions could be a promising materials design strategy in these systems.

## Methods

### Computational details

Our calculations are based on density functional theory (DFT) as implemented in the Vienna *ab initio* simulation package (VASP).<sup>36,37</sup> The exchange–correlation energy of electrons is treated within the generalised gradient approximation (GGA) with the functional by Perdew, Burke, and Ernzerhof (PBE).<sup>38</sup> In order to account for the limitations of the GGA to describe the d orbitals of transition metals, we included Hubbard corrections for these orbitals (GGA+U), following the formalism introduced by Dudarev *et al.*,<sup>39</sup> where a single parameter ( $U_{\text{eff}}$ ) controls the strength of the correction. The  $U_{\text{eff}}$  parameters for Mn (4.0 eV), Co (3.3 eV), Fe (4 eV) and Ni (6.4 eV) were taken from the work by Wang *et al.*,<sup>40</sup> where they were fitted so that GGA+U could reproduce the experimental oxidation energies in transition metal oxides. We also included dispersion corrections following Grimme's D3 scheme.<sup>41</sup> The projector augmented wave (PAW) method<sup>42,43</sup> was used to describe the interactions between the valence electrons and the frozen cores, which consisted of 1s orbitals for C and N, and orbitals up to 3p for the transition metals. We used an energy cutoff of 520 eV to truncate the plane-wave expansion of the Kohn–Sham wavefunctions, which is 30% above the default cutoff for the employed PAW potentials, to minimise Pulay errors. Brillouin zone (BZ) integrations were performed by sampling the reciprocal space using a  $\Gamma$ -centred mesh of  $4 \times 4 \times 4$   $k$ -points with reference to rhombohedral unit cell. Spin polarisation was allowed in all calculations.

### Experimental methods

Samples were synthesised by applying a solution-based slow crystallisation method with details about precursors, concentrations, *etc.* in the ESI.† Pressure-dependent powder X-ray diffraction patterns in the range from ambient pressure to 0.4 GPa were collected using the pressure jump-cell,<sup>30</sup> a dedicated setup for exploring high pressure properties of soft materials.<sup>44</sup> Cell parameters for each pressure point were extracted by a Pawley profile fit analysis as implemented in TOPAS v6 (ref. 30) and  $V(p)$  data was fitted to a second-order Birch–Murnaghan equation of state by using the EoSFit7c software.<sup>45</sup>

## Author contributions

R. G.-C., K. T. B. and G. K. designed the study. S. G. carried out the DFT calculations. S. B. synthesised the samples and performed sample analysis. K. H. and P. V. assisted with synchrotron data collection. All authors contributed to the interpretation of experimental and computational results and to the writing of the manuscript.

## Conflicts of interest

There are no conflicts to declare.

## Acknowledgements

S. G. is grateful for a doctoral studentship from the Felix Trust. This work made use of ARCHER, the UK's national high-performance computing service, *via* the UK's HPC Materials Chemistry Consortium, which is funded by EPSRC (EP/R029431), and of the Young supercomputer, *via* the UK's Materials and Molecular Modelling Hub, which is partially funded by EPSRC (EP/T022213/1). S. B. is grateful for holding a doctoral scholarship from the Hanns-Seidel Foundation. K. H. thanks the 'Fonds der Chemischen Industrie' for a PhD fellowship. G. K. would also like to thank the 'Fonds der Chemischen Industrie' for support through the Liebig Fellowship scheme.

## References

- W. Li, Z. Wang, F. Deschler, S. Gao, R. H. Friend and A. K. Cheetham, *Nat. Rev. Mater.*, 2017, **2**, 16099.
- M. Maćzka, A. Ciupa, A. Gaćgor, A. Sieradzki, A. Pikul, B. Macalik and M. Drozd, *Inorg. Chem.*, 2014, **53**, 5260–5268.
- Z.-Y. Du, Y.-P. Zhao, W.-X. Zhang, H.-L. Zhou, C.-T. He, W. Xue, B.-Y. Wang and X.-M. Chen, *Chem. Commun.*, 2014, **50**, 1989–1991.
- Y. Wu, S. Shaker, F. Brivio, R. Murugavel, P. D. Bristowe and A. K. Cheetham, *J. Am. Chem. Soc.*, 2017, **139**, 16999–17002.
- G. Kieslich and A. L. Goodwin, *Mater. Horiz.*, 2017, **4**, 362–366.
- S. Burger, K. Hemmer, D. C. Mayer, P. Vervoorts, D. Daisenberger, J. K. Zaręba and G. Kieslich, *Adv. Funct. Mater.*, 2022, 2205343.
- H. L. B. Boström, M. S. Senn and A. L. Goodwin, *Nat. Commun.*, 2018, **9**, 2380.
- H. L. B. Boström, *CrystEngComm*, 2020, **22**, 961–968.
- K. L. Svane, A. C. Forse, C. P. Grey, G. Kieslich, A. K. Cheetham, A. Walsh and K. T. Butler, *J. Phys. Chem. Lett.*, 2017, **8**, 6154–6159.
- L.-J. Ji, S.-J. Sun, Y. Qin, K. Li and W. Li, *Coord. Chem. Rev.*, 2019, **391**, 15–29.
- J. Feng, *APL Mater.*, 2014, **2**, 081801.
- K. T. Butler, K. Svane, G. Kieslich, A. K. Cheetham and A. Walsh, *Phys. Rev. B*, 2016, **94**, 180103.
- G. Kieslich, J. M. Skelton, J. Armstrong, Y. Wu, F. Wei, K. L. Svane, A. Walsh and K. T. Butler, *Chem. Mater.*, 2018, **30**, 8782–8788.
- S. A. Hallweger, C. Kaufsler and G. Kieslich, *Phys. Chem. Chem. Phys.*, 2022, **24**, 9196–9202.
- W. Li, S. Henke and A. K. Cheetham, *APL Mater.*, 2014, **2**, 123902.
- W. Li, A. Thirumurugan, P. T. Barton, Z. Lin, S. Henke, H. H. M. Yeung, M. T. Wharmby, E. G. Bithell, C. J. Howard and A. K. Cheetham, *J. Am. Chem. Soc.*, 2014, **136**, 7801–7804.
- G. Kieslich, S. Kumagai, A. C. Forse, S. Sun, S. Henke, M. Yamashita, C. P. Grey and A. K. Cheetham, *Chem. Sci.*, 2016, **7**, 5108–5112.

- 18 J.-C. Tan, P. Jain and A. K. Cheetham, *Dalton Trans.*, 2012, **41**, 3949–3952.
- 19 I. E. Collings, M. Bykov, E. Bykova, M. Hanfland, S. van Smaalen, L. Dubrovinsky and N. Dubrovinskaia, *CrystEngComm*, 2018, **20**, 3512–3521.
- 20 M. Maćzka, I. E. Collings, F. F. Leite and W. Paraguassu, *Dalton Trans.*, 2019, **48**, 9072–9078.
- 21 M. Maćzka, M. Ptak, A. Gaćgor, A. Sieradzki, P. Peksa, G. Usevicius, M. Simenas, F. F. Leite and W. Paraguassu, *J. Mater. Chem. C*, 2019, **7**, 2408–2420.
- 22 H. Gao, C. Li, L. Li, W. Wei, Y. Tan and Y. Tang, *Dalton Trans.*, 2020, **49**, 7228–7233.
- 23 Z. Yang, G. Cai, C. L. Bull, M. G. Tucker, M. T. Dove, A. Friedrich and A. E. Phillips, *Philos. Trans. R. Soc., A*, 2019, **377**, 20180227.
- 24 M. Maćzka, M. Kryś, S. Sobczak, D. L. M. Vasconcelos, P. T. C. Freire and A. Katrusiak, *J. Phys. Chem. C*, 2021, **125**, 26958–26966.
- 25 M. Maćzka, S. Sobczak, M. Kryś, F. F. Leite, W. Paraguassu and A. Katrusiak, *J. Phys. Chem. C*, 2021, **125**, 10121–10129.
- 26 H. L. B. Boström and G. Kieslich, *J. Phys. Chem. C*, 2021, **125**, 1467–1471.
- 27 J. M. Bermúdez-García, M. Sánchez-Andújar and M. A. Señaris-Rodríguez, *J. Phys. Chem. Lett.*, 2017, **8**, 4419–4423.
- 28 J. M. Bermúdez-García, M. Sánchez-Andújar, S. Castro-García, J. López-Beceiro, R. Artiaga and M. A. Señaris-Rodríguez, *Nat. Commun.*, 2017, **8**, 15715.
- 29 B. Li, Y. Kawakita, S. Ohira-Kawamura, T. Sugahara, H. Wang, J. Wang, Y. Chen, S. I. Kawaguchi, S. Kawaguchi, K. Ohara, K. Li, D. Yu, R. Mole, T. Hattori, T. Kikuchi, S.-i. Yano, Z. Zhang, Z. Zhang, W. Ren, S. Lin, O. Sakata, K. Nakajima and Z. Zhang, *Nature*, 2019, **567**, 506–510.
- 30 S. Burger, S. Grover, K. T. Butler, H. L. B. Boström, R. Grau-Crespo and G. Kieslich, *Mater. Horiz.*, 2021, **8**, 2444–2450.
- 31 N. J. Brooks, B. L. L. E. Gauthe, N. J. Terrill, S. E. Rogers, R. H. Templer, O. Ces and J. M. Seddon, *Rev. Sci. Instrum.*, 2010, **81**, 064103.
- 32 A. Togo and I. Tanaka, *Scr. Mater.*, 2015, **108**, 1–5.
- 33 G. Feng, D. Gui and W. Li, *Cryst. Growth Des.*, 2018, **18**, 4890–4895.
- 34 S. Sun, F. H. Isikgor, Z. Deng, F. Wei, G. Kieslich, P. D. Bristowe, J. Ouyang and A. K. Cheetham, *ChemSusChem*, 2017, **10**, 3740–3745.
- 35 S. Sun, Y. Fang, G. Kieslich, T. J. White and A. K. Cheetham, *J. Mater. Chem. A*, 2015, **3**, 18450–18455.
- 36 G. Kresse and J. Furthmüller, *Phys. Rev. B: Condens. Matter Mater. Phys.*, 1996, **54**, 11169–11186.
- 37 G. Kresse and J. Furthmüller, *Comput. Mater. Sci.*, 1996, **6**, 15–50.
- 38 J. P. Perdew, K. Burke and M. Ernzerhof, *Phys. Rev. Lett.*, 1996, **77**, 3865–3868.
- 39 S. L. Dudarev, G. A. Botton, S. Y. Savrasov, C. J. Humphreys and A. P. Sutton, *Phys. Rev. B: Condens. Matter Mater. Phys.*, 1998, **57**, 1505–1509.
- 40 L. Wang, T. Maxisch and G. Ceder, *Phys. Rev. B: Condens. Matter Mater. Phys.*, 2006, **73**, 195107.
- 41 S. Grimme, J. Antony, S. Ehrlich and H. Krieg, *J. Chem. Phys.*, 2010, **132**, 154104.
- 42 P. E. Blöchl, *Phys. Rev. B: Condens. Matter Mater. Phys.*, 1994, **50**, 17953–17979.
- 43 G. Kresse and D. Joubert, *Phys. Rev. B: Condens. Matter Mater. Phys.*, 1999, **59**, 1758–1775.
- 44 P. Vervoorts, J. Stebani, A. S. J. Méndez and G. Kieslich, *ACS Mater. Lett.*, 2021, **3**, 1635–1651.
- 45 R. J. Angel, M. Alvaro and J. Gonzalez-Platas, *Z. Kristallogr. - Cryst. Mater.*, 2014, **229**, 405–419.



## 4.5 STUDY V: Designing Geometric Degrees of Freedom in ReO<sub>3</sub>-Type Coordination Polymers

In coordination polymers of the ABX<sub>3</sub> perovskite-type, an emerging subclass of dense crystalline, three-dimensional networks, properties of high scientific relevance and technologically important phenomena can be studied in great detail. The large range of different properties of this host-guest-type coordination networks originates from the modular building principle of the perovskite-motif and the numerous possible permutations of A-, B- and X-ions, enabling the chemical manipulation by tuning (multi-)atomic connectivity and intermolecular interactions within the framework. For these molecular perovskites, this allows intrinsically access to additional degrees of freedom when compared to classic inorganic or hybrid perovskites. However, so far all effort for tuning *e.g.* the mechanical properties through specific structural manipulation has been restricted to maintaining the ABX<sub>3</sub> perovskite motif itself. Thinking outside this box to extend the structural motif beyond the "classical" perovskite can even activate novel geometric degrees of freedom with the potential to enable hitherto unrevealed properties for this class of materials.

In the work presented here the synthesis of structurally organised A<sup>+II</sup>B<sub>2</sub><sup>+II</sup>X<sub>6</sub><sup>-I</sup> coordination networks is reported in which the spatial order of a molecular divalent A-site guest cation in a ReO<sub>3</sub>-type host network is introduced as a new geometric degree of freedom. The two materials [(C<sub>3</sub>H<sub>7</sub>)<sub>3</sub>N(CH<sub>2</sub>)<sub>n</sub>N(C<sub>3</sub>H<sub>7</sub>)<sub>3</sub>]Mn<sub>2</sub>(C<sub>2</sub>N<sub>3</sub>)<sub>6</sub> (*n* = 4,5) are introduced as the first member of a new material class where the divalent A-site cation bridges two ReO<sub>3</sub>-type [Mn(C<sub>2</sub>N<sub>3</sub>)<sub>3</sub>]<sup>-</sup> cages. The structural junction of two adjacent cuboctahedral cavities incorporates mechanical interlocking, creating an ideal prerequisite for interesting material properties. With the use of state-of-the-art synchrotron radiation and X-Ray diffraction methods, material properties such as linear negative thermal expansion and negative linear compressibility can be mapped onto the presence of a herringbone-type and a head-to-tail order pattern of the divalent A-site cations within the 3D host network. While both materials exhibit distinct uniaxial NTE, a property which is rather common for coordination networks, [(C<sub>3</sub>H<sub>7</sub>)<sub>3</sub>N(CH<sub>2</sub>)<sub>4</sub>N(C<sub>3</sub>H<sub>7</sub>)<sub>3</sub>]Mn<sub>2</sub>(C<sub>2</sub>N<sub>3</sub>)<sub>6</sub> shows a large NLC effect at its ambient phase, previously unknown for perovskite-type coordination networks.

The work highlights the power of crystal engineering approaches in the synthesis of new material families with new types of degrees of freedom and targeted stimuli-responsive behaviour and therefore opens a new avenue for scientists towards materials with interesting exotic material properties.

The article was written by the author of this doctorate thesis through contribution of Dr. Gregor Kieslich. The strategy and conceptional design was elaborated by the author of this thesis and critically discussed with Dr. Gregor Kieslich. David C. Mayer assisted with expertise on temperature-dependent single crystal X-Ray diffraction. K. Hemmer, P. Vervoorts, Dr. Dominik Daisenberger, Dr. Gregor Kieslich and the author of this thesis performed the high pressure

powder X-Ray diffraction experiments at Diamond Light Source Ltd., beamline I-15. The variable temperature powder X-Ray diffraction experiments were done by the author of this thesis and Dr. Gregor Kieslich at the Deutsches-Elektronen-Synchrotron, beamline P02.1. Jan K. Zaręba performed the second-harmonic generation measurements. All data were analysed and interpreted by the author of this doctorate thesis and discussed with the authors. All authors critically reviewed and approved the manuscript.

Status: Published as a Research Article in the journal "Advanced Functional Materials".

Reproduced from Ref. [285]. This is an open access article under the terms of the Creative Commons Attribution License, which permits use, distribution and reproduction in any medium, provided the original work is properly cited. The license details as well as terms and conditions for reprint can be found in the APPENDIX, C Reprint permissions.

S. Burger, K. Hemmer, D. C. Mayer, P. Vervoorts, D. Daisenberger, J. K. Zaręba and G. Kieslich, *Designing Geometric Degrees of Freedom in ReO<sub>3</sub>-Type Coordination Polymers*, **Adv. Funct. Mater.**, 2022, **32**, 2205343, DOI: 10.1002/adfm.202205343.

# Designing Geometric Degrees of Freedom in ReO<sub>3</sub>-Type Coordination Polymers

Stefan Burger, Karina Hemmer, David C. Mayer, Pia Vervoorts, Dominik Daisenberger, Jan K. Zaręba, and Gregor Kieslich\*

Engineering the interplay of structural degrees of freedom that couple to external stimuli such as temperature and pressure is a powerful approach for material design. New structural degrees of freedom expand the potential of the concept, and coordination polymers as a chemically versatile material platform offer fascinating possibilities to address this challenge. Here, we report a new class of perovskite-like AB<sub>2</sub>X<sub>6</sub> coordination polymers based on a [BX<sub>3</sub>]<sup>-</sup> ReO<sub>3</sub>-type host network ([Mn(C<sub>2</sub>N<sub>3</sub>)<sub>3</sub>]<sup>-</sup>), in which the spatial orientation of divalent A<sup>2+</sup> cations ([R<sub>3</sub>N(CH<sub>2</sub>)<sub>n</sub>NR<sub>3</sub>]<sup>2+</sup>) with separated charge centers that bridge adjacent ReO<sub>3</sub>-cavities is introduced as a new geometric degree of freedom. Herringbone and head-to-tail order pattern of [R<sub>3</sub>N(CH<sub>2</sub>)<sub>n</sub>NR<sub>3</sub>]<sup>2+</sup> cations are obtained by varying the separator length *n* and, together with distortions of the pseudocubic [BX<sub>3</sub>]<sup>-</sup> network, they determine the materials' stimuli-responsive behavior such as counterintuitive large negative compressibility and uniaxial negative thermal expansion. This new family of coordination polymers highlights the chemists' capabilities of designing matter on a molecular level to address macroscopic material functionality and underpins the opportunities of the design of structural degrees of freedom as a conceptual framework for rational material synthesis in the future.

## 1. Introduction


Dense and porous coordination polymers are a chemically versatile material platform and harbor a wealth of fascinating properties of academic and technological relevance. Recent examples are their application in next-generation water harvesting<sup>[1]</sup> and cooling technologies,<sup>[2]</sup> the observation of counter-intuitive material responses such as negative gas adsorption<sup>[3]</sup> and colossal negative linear compressibility<sup>[4]</sup> and negative thermal expansion,<sup>[5]</sup> enzyme-type molecular recognition<sup>[6]</sup> and their melting behavior as important intermediate state for the fabrication of functional glasses<sup>[7]</sup> amongst many more. These examples illustrate the importance of fundamental research related to the materials' stimuli-responsive behavior. It involves the study of material responsiveness for a knowledge-based improvement of existing material functionality, and provides the scientific basis for new material functions and potential next-generation technologies in the future.

In the pursuit to translate between synthetic chemistry and the underlying material's free energy surface which defines material responsiveness,<sup>[8,9]</sup> the decomposition of a material's structure in terms of available structural and electronic degrees of freedom has proved powerful.<sup>[10–12]</sup> In coordination polymers, the available structural degrees of freedom, that is, structural distortions that couple to external stimuli such as temperature and pressure, play the most prominent role due to relatively low densities and, when carefully engineered, can introduce new stimuli-responsive properties such as electric polarization that couples to an electric field.<sup>[13]</sup> The simple use of molecular scaffolds to synthesize 1D, 2D, or 3D coordination polymers introduces new unconventional structural degrees of freedom compared to solid-state inorganics. Examples are orientational degrees of freedom related to order–disorder phase transitions in the barocaloric [(C<sub>3</sub>H<sub>7</sub>)<sub>4</sub>N]Mn(C<sub>2</sub>N<sub>3</sub>)<sub>3</sub> and photovoltaic absorber [CH<sub>3</sub>NH<sub>3</sub>]<sub>2</sub>PbI<sub>3</sub>,<sup>[2,14]</sup> large translational network deformations in the flexible metal-organic frameworks (MOFs) CUK-1 and DMOF-1 derivatives<sup>[15,16]</sup> with potential in mechanical energy storage processes, and rotational molecular motions in amphidynamic MOFs<sup>[17]</sup> as a basis for coordination polymer-based molecular machines. The interpretation of a material's

S. Burger, K. Hemmer, D. C. Mayer, P. Vervoorts, G. Kieslich  
Department of Chemistry  
Technical University of Munich  
Lichtenbergstrasse 4, 85748 Garching, Germany  
E-mail: gregor.kieslich@tum.de

D. Daisenberger  
Diamond Light Source  
Harwell Science and Innovation Campus  
Didcot, Oxfordshire OX11 0DE, UK

J. K. Zaręba  
Institute of Advanced Materials  
Wrocław University of Science and Technology  
Wybrzeże Wyspiańskiego 27, Wrocław 50-370, Poland

 The ORCID identification number(s) for the author(s) of this article can be found under <https://doi.org/10.1002/adfm.202205343>.

© 2022 The Authors. Advanced Functional Materials published by Wiley-VCH GmbH. This is an open access article under the terms of the Creative Commons Attribution-NonCommercial-NoDerivs License, which permits use and distribution in any medium, provided the original work is properly cited, the use is non-commercial and no modifications or adaptations are made.

DOI: 10.1002/adfm.202205343

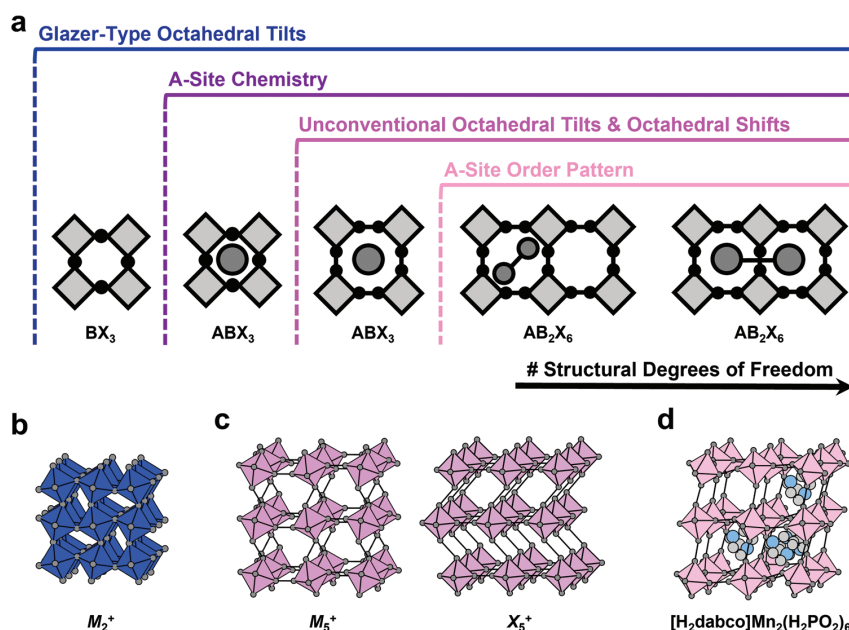


**Figure 1.** Structural degrees of freedom in  $ReO_3$ -type coordination polymers. a) In inorganic  $ReO_3$ -type materials and inorganic perovskites Glazer-type octahedral tilts can occur. The use of molecular X-site anions in molecular perovskites makes unconventional octahedral tilts and shifts accessible, and  $A^{2+}$  cations such as  $[H_2dabco]^{2+}$  in  $[H_2dabco]Mn_2(H_2PO_2)_6$  introduce the possibility of various A-site vacancy order pattern. In this work,  $A^{2+}$ -site cations with separated charges are used to form  $AB_2X_6$ -type materials, adding a new structural degree of freedom related to their spatial orientation within the  $ReO_3$ -type network. b) The  $M_2^+$  Glazer-type tilt. c) An unconventional tilt ( $M_5^+$ ) and shift ( $X_5^+$ ). d) The crystal structure of  $[H_2dabco]Mn_2(H_2PO_2)_6$  is shown with emphasis on the empty voids within the  $[Mn(H_2PO_2)_3]^-$  network. Note, for describing the distortion modes of the  $ReO_3$ -type network the Bradley–Cracknell notation ( $k_#^+$ ) is used and that phosphorus and hydrogen atoms are omitted in the structure of  $[H_2dabco]Mn_2(H_2PO_2)_6$  for clarity; color code: gray: C, light blue: N.

structure into structural degrees of freedom is capable of conceptualizing current and past research progress related to stimuli-responsive properties of coordination polymers in a concise framework, and in looking forward, engineering the interplay of several structural degrees of freedom shows large opportunities for designing materials with targeted and potentially new stimuli-responsive properties. Therefore, the search for new structural degrees of freedom and their synthetic integration to systematically direct material behavior is an active field of research, either explicitly or implicitly, and the chemical diversity of coordination polymers such as MOFs, Prussian blue analogues and  $ABX_3$  molecular perovskites offer exciting opportunities in this context. The discovery of hidden vacancy networks in Prussian Blue analogues,<sup>[18]</sup> the introduction of foldable nets<sup>[19]</sup> and geometry mismatch as concepts,<sup>[20]</sup> the synthesis of MOFs with frustrated metal-nodes and linker molecules with various internal conformations,<sup>[6,21]</sup> the categorization of unconventional tilts and shifts in molecular perovskites,<sup>[13]</sup> and the search for aperiodic MOFs<sup>[22]</sup> are a few important examples in this context.

$ABX_3$  molecular perovskites<sup>[23]</sup> such as  $[(NH_2)_2CH]Mn(H_2PO_2)_3$ ,<sup>[24]</sup>  $[(C_3H_7)_4N]Mn(C_2N_3)_3$ ,<sup>[25]</sup> and  $[(CH_3)_2NH_2]Zn(HCO_2)_3$ <sup>[26]</sup> are formally a subclass of coordination polymers and exhibit various unconventional structural degrees of freedom. Their structures are based on the well-known perovskite motif where the molecular A-site cation sits in the

void of a 3D  $[BX_3]^-$   $ReO_3$ -like network. Compared to inorganic perovskites, the use of molecular A- and/or X-site ions introduces unconventional octahedral tilts and shifts,<sup>[27]</sup> molecular order-disorder phase transitions as a function of temperature<sup>[28]</sup> and pressure,<sup>[29]</sup> complex structural phase transition behavior driven by collective changes in atomic vibration,<sup>[30]</sup> and polymorphism based on conformational isomerism of the B-X connectivity,<sup>[31]</sup> see **Figure 1**. Initially, unconventional degrees of freedom in molecular perovskites were in the center of fundamental research questions, but recent developments in the field of barocalorics,<sup>[32]</sup> multiferroics,<sup>[33]</sup> and improper ferroelectrics<sup>[13]</sup> highlight the possibilities of manipulating useful macroscopic properties through their targeted variation. When looking for synthetic strategies to integrate new structural degrees of freedom in molecular perovskites, it is important to emphasize that all current structural degrees of freedom originate from the use of molecular building units per sé rather than elaborate synthetic approaches.

Here we apply a crystal structure engineering strategy introducing novel geometric degrees of freedom in a  $ReO_3$ -type host network. The synthesis of  $AB_2X_6$  coordination polymers is reported, in which molecular  $A^{2+}$  cations with separated positive charges bridge two adjacent cavities of the host network, extending the structural chemistry of  $ReO_3$ -type networks with an additional geometric structural motif. The resulting  $AB_2X_6$ -materials are conceptually related to  $ABX_3$  molecular



perovskites which guides interpretation of their crystal chemistry. The A<sup>2+</sup> cations' order pattern depend on their chemical nature and act as property-directing factor, determining the materials' mechanical properties such as thermal expansion behavior and compressibility.

## 2. Results and Discussion

### 2.1. Crystal Structure Engineering Methodology

In the pursuit to introduce new geometric degrees of freedom in a ReO<sub>3</sub>-type network, the material [H<sub>2</sub>dabco]Mn<sub>2</sub>(H<sub>2</sub>PO<sub>4</sub>)<sub>6</sub> ([H<sub>2</sub>dabco]<sup>2+</sup> = 1,4-diazabicyclo[2.2.2]octane-1,4-dium) is an important starting point.<sup>[24]</sup> The use of the divalent cation [H<sub>2</sub>dabco]<sup>2+</sup> leads to a material in which half of the voids within the 3D ReO<sub>3</sub>-type [Mn(H<sub>2</sub>PO<sub>4</sub>)<sub>3</sub>]<sup>−</sup> cages are occupied, that is, a perovskite-type structure with ordered A-site vacancies, see Figure 1d. Inspired by this example, the use of a divalent A-site cation with separated charge centers, suitable to bridge two pseudocubic [BX<sub>3</sub>]<sup>−</sup> cages, can be envisaged, which introduces an additional geometric degree of freedom related to the spatial distribution of divalent A-site cations within the 3D [BX<sub>3</sub>]<sup>−</sup> host network.

The challenge in synthesizing an AB<sub>2</sub>X<sub>6</sub> coordination polymer where the divalent A-site cation bridges two [BX<sub>3</sub>]<sup>−</sup> type cages is the identification of a suitable A-B-X permutation. We use [C<sub>2</sub>N<sub>3</sub>]<sup>−</sup> as X-site anion and Mn<sup>2+</sup> as B-site divalent metal, a combination that has proved robust for the synthesis of various molecular perovskites with comparably large A-site cations such as [(C<sub>3</sub>H<sub>7</sub>)<sub>4</sub>N]Mn(C<sub>2</sub>N<sub>3</sub>)<sub>3</sub>,<sup>[25]</sup> [(C<sub>7</sub>H<sub>7</sub>)(C<sub>4</sub>H<sub>9</sub>)<sub>3</sub>N]Mn(C<sub>2</sub>N<sub>3</sub>)<sub>3</sub>,<sup>[34]</sup> and [(C<sub>3</sub>H<sub>7</sub>)<sub>3</sub>(CH<sub>3</sub>)N]Mn(C<sub>2</sub>N<sub>3</sub>)<sub>3</sub>.<sup>[31]</sup> On the A-site, a divalent cation must be chosen which exhibits two spatially separated positive charges that can bridge two ReO<sub>3</sub>-type [Mn(C<sub>2</sub>N<sub>3</sub>)<sub>3</sub>]<sup>−</sup> cages. A divalent A-site cation fulfilling these requirements is the cation [R<sub>3</sub>N(CH<sub>2</sub>)<sub>n</sub>NR'<sub>3</sub>]<sup>2+</sup>, where *n* determines the charge separation distance, and *R* and *R'* provide chemical control over the bulkiness of the cation through alkyl chain length, see Figure 2a. For the size of *R* and *R'*, a *n*-propyl group (*R* = −C<sub>3</sub>H<sub>7</sub>) seems suitable, resembling the situation in [(C<sub>3</sub>H<sub>7</sub>)<sub>4</sub>N]Mn(C<sub>2</sub>N<sub>3</sub>)<sub>3</sub>. Looking at the parameter *n*, a good separation between the charge centers is expected for *n* > 2. Therefore, [(C<sub>3</sub>H<sub>7</sub>)<sub>3</sub>N(CH<sub>2</sub>)<sub>4</sub>N(C<sub>3</sub>H<sub>7</sub>)<sub>3</sub>]<sup>2+</sup> (= TPC4TP<sup>2+</sup>) and [(C<sub>3</sub>H<sub>7</sub>)<sub>3</sub>N(CH<sub>2</sub>)<sub>5</sub>N(C<sub>3</sub>H<sub>7</sub>)<sub>3</sub>]<sup>2+</sup> (= TPC5TP<sup>2+</sup>) are promising divalent A-site cations which were synthesized by standard nucleophilic substitution strategies, see Figure S1, Supporting Information. Subsequently, the synthesis of the coordination polymers [TPC4TP]Mn<sub>2</sub>(C<sub>2</sub>N<sub>3</sub>)<sub>6</sub> and [TPC5TP]Mn<sub>2</sub>(C<sub>2</sub>N<sub>3</sub>)<sub>6</sub> was performed by following an established slow crystallization procedure. For instance, in a typical reaction the precursors [TPC4TP]Br<sub>2</sub>, Mn(NO<sub>3</sub>)<sub>2</sub>·4H<sub>2</sub>O and Na(C<sub>2</sub>N<sub>3</sub>) are mixed in a water/ethanol mixture. After several days, the formation of single crystals can be observed, see Figure S2, Supporting Information for details.

### 2.2. Structure and Pattern Analysis

Single crystal X-ray diffraction was used for structure solution, see Tables S2 and S3; Figures S11 and S12, Supporting

Information for details of data collection, full crystallographic data and details on structure model discussion. Both compounds crystallize in the monoclinic crystal system and [TPC4TP]Mn<sub>2</sub>(C<sub>2</sub>N<sub>3</sub>)<sub>6</sub> in a noncentrosymmetric space-group which was confirmed by second harmonic generation, see Figure S33, Supporting Information for experimental details. A combined TG/DSC analysis shows the absence of a phase transition over the whole stability range, see Figures S7 and S8, Supporting Information. Both materials adopt a 3D ReO<sub>3</sub>-type [Mn(C<sub>2</sub>N<sub>3</sub>)<sub>3</sub>]<sup>−</sup> coordination network where all Mn<sup>2+</sup> atoms are octahedrally coordinated by N atoms and linked to their neighbouring Mn<sup>2+</sup> atoms via six μ-1,5-[C<sub>2</sub>N<sub>3</sub>]<sup>−</sup> bridges. The A-site cations TPC4TP<sup>2+</sup> and TPC5TP<sup>2+</sup> are incorporated into the 3D network for charge balance, with one positive charge sitting in each void of a ReO<sub>3</sub>-type cage. Therefore, the divalent A-site cations bridge adjacent pseudocubic ReO<sub>3</sub>-type cages, see Figure 2b,d. Similar to molecular perovskites, active rigid unit modes in the ReO<sub>3</sub> network are possible and a distortion mode analysis of the 3D [Mn(C<sub>2</sub>N<sub>3</sub>)<sub>3</sub>]<sup>−</sup> network reveals the presence of primary order parameters distinctive for dicyanamide-based molecular perovskites,<sup>[27]</sup> see Supporting Information for full details of the mode analysis.

An intuitive description of both compounds starts from an ABX<sub>3</sub> molecular perovskite where −(CH<sub>2</sub>)<sub>*n*</sub>− is used to link two adjacent A-site cations. The introduction of such a −(CH<sub>2</sub>)<sub>*n*</sub>− link as a spacer introduces the spatial orientation of the A<sup>2+</sup> within the [Mn(C<sub>2</sub>N<sub>3</sub>)<sub>3</sub>]<sup>−</sup> network as a new structural degree of freedom which is geometric in nature. For [TPC4TP]Mn<sub>2</sub>(C<sub>2</sub>N<sub>3</sub>)<sub>6</sub> and [TPC5TP]Mn<sub>2</sub>(C<sub>2</sub>N<sub>3</sub>)<sub>6</sub> both A<sup>2+</sup> cations exhibit 2D order patterns within the 3D ReO<sub>3</sub>-type network, that is, they bridge [Mn(C<sub>2</sub>N<sub>3</sub>)<sub>3</sub>]<sup>−</sup> cages in two dimensions but not in the third. In [TPC4TP]Mn<sub>2</sub>(C<sub>2</sub>N<sub>3</sub>)<sub>6</sub> a herringbone-type order of TPC4TP<sup>2+</sup> is observed with an AB stacking of individual 2D layers, where B is shifted one pseudocubic unit along one dimension of the 2D layer. For the A-site cation in [TPC5TP]Mn<sub>2</sub>(C<sub>2</sub>N<sub>3</sub>)<sub>6</sub> an order pattern is found that we describe as head-to-tail, with head equal to tail, and a AA stacking sequence, see Figure 2c,e; Figures S13 and S15, Supporting Information. Therefore, A<sup>2+</sup> cations' order pattern and octahedral tilt pattern in [TPC4TP]Mn<sub>2</sub>(C<sub>2</sub>N<sub>3</sub>)<sub>6</sub> and [TPC5TP]Mn<sub>2</sub>(C<sub>2</sub>N<sub>3</sub>)<sub>6</sub> depend on the chemical identity of the [R<sub>3</sub>N(C<sub>*n*</sub>H<sub>2*n*</sub>)NR'<sub>3</sub>]<sup>2+</sup> cation.

The A<sup>2+</sup> cations' order pattern can be rationalized based on chemical intuition. For TPC4TP<sup>2+</sup> the length seems to perfectly match the available space within the [Mn(C<sub>2</sub>N<sub>3</sub>)<sub>3</sub>]<sup>−</sup> host network. This results in a 2D herringbone pattern where dispersion interactions between R of neighboring cations are presumably maximized. The AB stacking of different layers further suggests that this is achieved by placing one A<sup>2+</sup> cation in vicinity to a maximum number of other A<sup>2+</sup> cations. Adding another −CH<sub>2</sub>− unit significantly increases the length of the A<sup>2+</sup> cation, and the dominating factor that determines the order pattern is the reduction of adverse steric interactions between neighboring A<sup>2+</sup> cations. Due to the size of TPC5TP<sup>2+</sup> the herringbone pattern seems unfavorable since some of the propyl-chains reach into neighboring [BX<sub>3</sub>]<sup>−</sup>-cages. Instead, TPC5TP<sup>2+</sup> cations order parallel and lie skewed in the network to minimize unfavorable steric interactions with neighboring A-site cations which is not possible in the herringbone motif, see Figure 2. The distortion of the [B<sub>2</sub>X<sub>6</sub>]<sup>−</sup> cuboid along

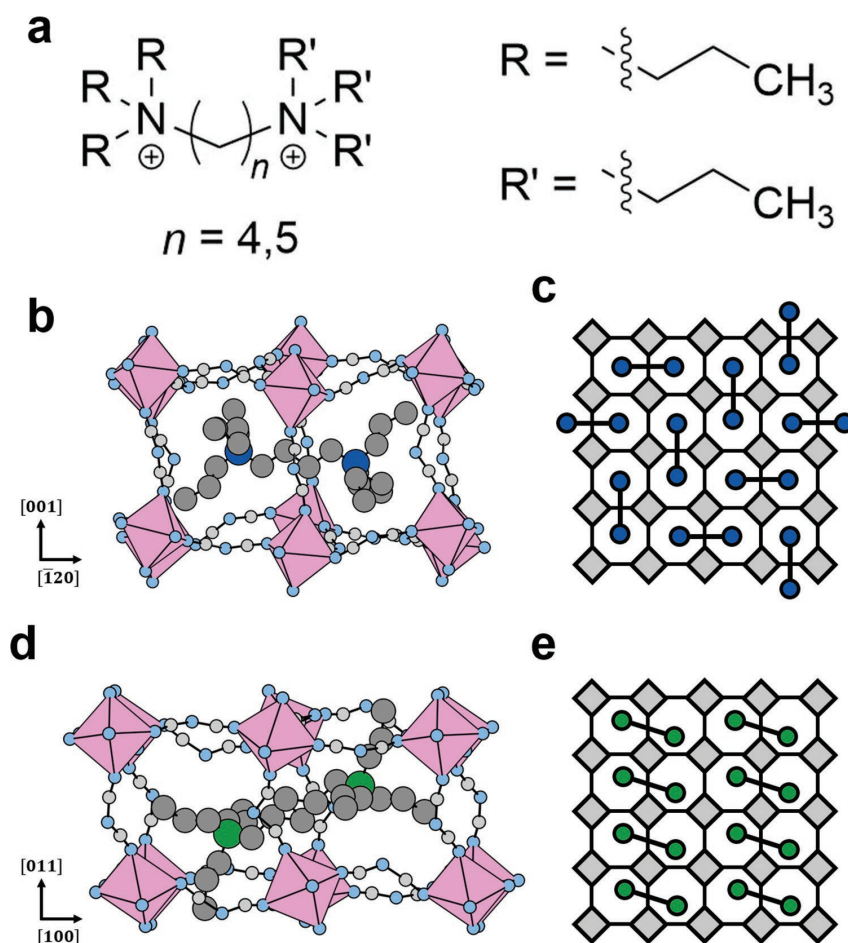


**Figure 2.** Crystal structures and  $A^{2+}$  cation order pattern in  $AB_2X_6$  materials. Shown are a) a structural diagram of the molecules employed on the A-site and b) the crystal structures of  $[TPC4TP]Mn_2(C_2N_3)_6$  and d)  $[TPC5TP]Mn_2(C_2N_3)_6$  with emphasis on how the divalent A-site cations bridge two pseudocubic  $Mn(C_2N_3)_3$  networks. c, e) For both materials a 2D order pattern of  $A^{2+}$  cations is observed. Depending on the separator length  $n$  of the  $[R_3N(C_nH_{2n})NR_3]^{2+}$  cation, we observe a herringbone pattern ( $n = 4$ , c) or a head-to-tail pattern ( $n = 5$ , e). The hydrogen atoms are not shown for clarity. Color code for crystal structures: green/dark blue: A-cation nitrogen, gray: carbon, light-blue: X-anion nitrogen, pink: manganese. For visualization purposes, the size of the A-site atoms was increased.

the space diagonal and the AA stacking which both target to reduce steric interactions agree with this interpretation. This adaptive interplay between  $A^{2+}$  cations, their order pattern and the  $[BX_3]^-$  network demonstrates the opportunities to synthetically engineer structural degrees of freedom in  $ReO_3$ -type coordination polymers to impart targeted responsive properties such as counterintuitive thermal and pressure responsive behavior and ferroelectricity.

### 2.3. Thermal Expansion Behavior and Compressibility

By drawing comparisons to materials with a herringbone motif and topologically related motifs such as  $Ag_3[Co(CN)_6]$ ,<sup>[35]</sup>  $KMn[Ag(CN)_2]_3$ ,<sup>[36]</sup>  $[Zn_2(fu-bdc)_2dabco]$ ,<sup>[37]</sup>  $[Fe(dpp)_2(NCS)_2] \cdot py$ ,<sup>[38]</sup>  $InH(bdc)_2$ ,<sup>[39]</sup> and  $MeOH \cdot H_2O$ ,<sup>[40]</sup> uniaxial negative

thermal expansion (NTE) and negative linear compressibility (NLC) based on molecular hinging and rhombic network deformations can be anticipated. Variable temperature powder X-ray diffraction ( $T = 100\text{--}400$  K) and high-pressure powder X-ray diffraction ( $p = \text{ambient--}0.4$  GPa) were performed to obtain thermal expansion coefficients ( $\alpha$ ) and compressibilities ( $\chi$ ) for both materials, see Figure S20– S29, Supporting Information for details. For comparison reasons, lattice parameters were transformed into principal axes  $X_1$ ,  $X_2$ , and  $X_3$ , see Table 1 and Tables S7, S9, S11, and S13, Supporting Information.  $\alpha$  and  $\chi$  of both materials are in a similar magnitude with  $[TPC4TP]Mn_2(C_2N_3)_6$  showing a slightly larger responsiveness toward temperature and pressure changes compared to  $[TPC5TP]Mn_2(C_2N_3)_6$ . This is ascribed to the lower packing density of  $[TPC4TP]Mn_2(C_2N_3)_6$  which agrees with the trend in bulk moduli and shifts of characteristic IR bands of the  $[C_2N_3]^-$

**Table 1.** Linear thermal expansion coefficients (MK<sup>-1</sup>), compressibilities (TPa<sup>-1</sup>) and calculated bulk moduli (GPa) of selected molecular framework materials in the ambient phase.

	$\alpha_{x1}$	$\alpha_{x2}$	$\alpha_{x3}$	$\chi_{x1}$	$\chi_{x2}$	$\chi_{x3}$	$B_0$	Ref.
[TPC4TP]Mn <sub>2</sub> (C <sub>2</sub> N <sub>3</sub> ) <sub>6</sub>	-72(3)	113(7)	130(2)	-12(1)	58(2)	69(3)	6.3(4)	This work
[TPC5TP]Mn <sub>2</sub> (C <sub>2</sub> N <sub>3</sub> ) <sub>6</sub>	-26(2)	69(2)	90(2)	6(1)	30(2)	53(1)	9.0(6)	This work
Ag <sub>3</sub> [Co(CN) <sub>6</sub> ] <sub>d</sub>	-126(1) <sup>a)</sup>	138(1) <sup>a)</sup>	138(1) <sup>a)</sup>	-76(9)	115(8)	115(8)	6.5(3)	[35,41]
KMn[Ag(CN) <sub>2</sub> ] <sub>3</sub>	61(2)	61(2)	-60(3)	-12(1)	33(1)	33(1)	12.7(11)	[36]
[Zn <sub>2</sub> (fu-L) <sub>2</sub> dabco] (np)	-94	373	5					[37]
[Fe(dpp) <sub>2</sub> (NCS) <sub>2</sub> ]·py	-85(1) <sup>a)</sup>	20(1) <sup>a)</sup>	231(1) <sup>a)</sup>	-10(2)	12(3)	53(4)	12.9(6)	[42,43]
InH(bdc) <sub>2</sub>	64(3)	64(3)	-35(2)	102	102	-62	6.8	[39,44]
MeOH·H <sub>2</sub> O	-19(1)	85(5)	230(19)	-3(2)	32(1)	108(1)	3.8(1)	[40]
[(C <sub>3</sub> H <sub>7</sub> ) <sub>4</sub> N]Mn(C <sub>2</sub> N <sub>3</sub> ) <sub>3</sub>				54(2)	54(2)	8(1)	8.1(11)	[45]
[C(NH <sub>2</sub> ) <sub>3</sub> ]Cd(HCOO) <sub>3</sub>	-17(1)	-17(1)	106(3)	3(1)	3(1)	21(1)	25.7(17)	[46,47]

Abbrev. fu = functionalized, L<sup>1</sup> = 2,5-bis(2-methoxyethoxy)benzene-1,4-dicarboxylate, np = narrow pore, dpp = dipyrido[3,2-*a*:2'-*c'*]phenazine, py = pyridine, bdc = benzene-1,4-dicarboxylate, <sup>a)</sup>recalculated from reported heating/compression lattice parameters using the software PASCAL.<sup>[48]</sup>

linker, see Table 1 and Figure S10 and Table S14, Supporting Information for details.

Looking at [TPC4TP]Mn<sub>2</sub>(C<sub>2</sub>N<sub>3</sub>)<sub>6</sub>, large uniaxial NTE and NLC behavior is observed along X<sub>1</sub> with  $\alpha_{x1} = -71.63 \pm 2.65$  MK<sup>-1</sup> and  $\chi_{x1} = -11.73 \pm 1.13$  TPa<sup>-1</sup>. X<sub>1</sub> points along [304] in the unit cell which is the space diagonal of a 2 × 2 × 2 [M(C<sub>2</sub>N<sub>3</sub>)<sub>3</sub>]<sup>-</sup> unit and the direction in which counter-intuitive material response based on a 3D hinging of A-site cations is expected, see Figure 3e and Figure S14, Supporting Information for a mechanistic illustration. For X<sub>2</sub> and X<sub>3</sub> uniaxial expansion and linear compressibility is observed, overall compensating for total framework deformation. This observation suggests that A-site hinging combined with a rhombic network distortion is suitable to rationalize uniaxial NTE and NLC behavior of [TPC4TP]Mn<sub>2</sub>(C<sub>2</sub>N<sub>3</sub>)<sub>6</sub>. To further support this interpretation, temperature-dependent single crystal X-ray diffraction for [TPC4TP]Mn<sub>2</sub>(C<sub>2</sub>N<sub>3</sub>)<sub>6</sub> at 100, 205, and 310 K was performed, see Table S3, Supporting Information. An increasing dihedral angle for two A-site cations ( $\angle_{100\text{K}} = 81.71(7)^\circ$  to  $\angle_{310\text{K}} = 83.8(3)^\circ$ ) and decreasing Mn-Mn distance along [304] are observed which corroborates the interpretation of thermal and pressure responsiveness of [TPC4TP]Mn<sub>2</sub>(C<sub>2</sub>N<sub>3</sub>)<sub>6</sub> based on a hinging mechanism. Importantly, it is the synergistic interplay of the A<sup>2+</sup> cations' herringbone order pattern and the constraining [BX<sub>3</sub>]<sup>-</sup> network that causes NTE and NLC based on a herringbone-based hinging mechanism in these framework materials. A herringbone motif alone is only an insufficient criteria as it was recently shown for the molecular crystals Cu(acac)<sub>2</sub> (acac<sup>2-</sup> = acetylacetonate)<sup>[49]</sup> and the series of linear acenes.<sup>[50]</sup> Comparing the sizes of  $\alpha_{x1}$  and  $\chi_{x1}$  of [TPC4TP]Mn<sub>2</sub>(C<sub>2</sub>N<sub>3</sub>)<sub>6</sub> with other molecular perovskites and coordination polymers (Table 1), the observed NLC coefficients and uniaxial NTE coefficients are large and to our knowledge [TPC4TP]Mn<sub>2</sub>(C<sub>2</sub>N<sub>3</sub>)<sub>6</sub> is the first ReO<sub>3</sub>-type coordination polymer with a large NLC coefficient of the ambient phase.

In contrast, for [TPC5TP]Mn<sub>2</sub>(C<sub>2</sub>N<sub>3</sub>)<sub>6</sub> we only find moderate uniaxial NTE along X<sub>1</sub> with  $\alpha_{x1} = -26.01 \pm 1.81$  MK<sup>-1</sup> and close to zero linear compressibility along X<sub>1</sub> which is approximately along the space-diagonal of a 1 × 2 × 2 pseudocubic [Mn(C<sub>2</sub>N<sub>3</sub>)<sub>3</sub>]<sup>-</sup> network. Therefore, uniaxial NTE propagates

perpendicular to the skewed head-to-tail arranged A-cations in [401] direction and is presumably based on a lamellar-type movement of the A-site molecules and a related rhombic distortion of the network. The absence of NLC behavior as a formally reversed structural distortion of uniaxial NTE is less clear; however, the different responses toward temperature and pressure changes illustrate that a clear mechanism that provides a well-defined minimum energy structural distortion is not provided by a head-to-tail arrangement of A-site cations when compared with a herringbone arrangement.

### 3. Conclusion

In conclusion, we introduce a new family of AB<sub>2</sub>X<sub>6</sub> coordination polymers based on a ReO<sub>3</sub>-type network. The synthesis of two representatives is reported in which the divalent A-site cation bridges two pseudocubic [BX<sub>3</sub>]<sup>-</sup> cages. This introduces the spatial orientation of divalent A<sup>2+</sup> cations as a geometric degree of freedom, while maintaining all structural degrees of freedom as known from molecular perovskites such as (unconventional) octahedral tilts and shifts, and a variable A-site cation chemistry. The type of A<sup>2+</sup> cation order pattern and its interplay with distortion modes of the 3D network are suitable to rationalize the mechanical properties of the materials. For [TPC4TP]Mn<sub>2</sub>(C<sub>2</sub>N<sub>3</sub>)<sub>6</sub>, the herringbone motif couples with structural distortions of the 3D network, providing a clear low-energy pathway for structural distortions as a function of temperature and pressure variation. In going forward, the chemical variability of divalent [R<sub>3</sub>N(CH<sub>2</sub>)<sub>n</sub>NR<sub>3</sub>]<sup>2+</sup> cations is promising to impart new, yet unknown A<sup>2+</sup> order pattern and therewith coupling schemes that determine the stimuli-responsive material properties. In particular, the use of nonsymmetric cations based on different R' and R functionalities is intriguing, where the use of R = -H and R' = -(C<sub>3</sub>H<sub>7</sub>) seems promising. Such an A-site cation incorporates one A-site end that is formally too small for forming a perovskite motif, which might introduce packing frustration coupled to extreme or counter-intuitive stimuli-responsive properties.

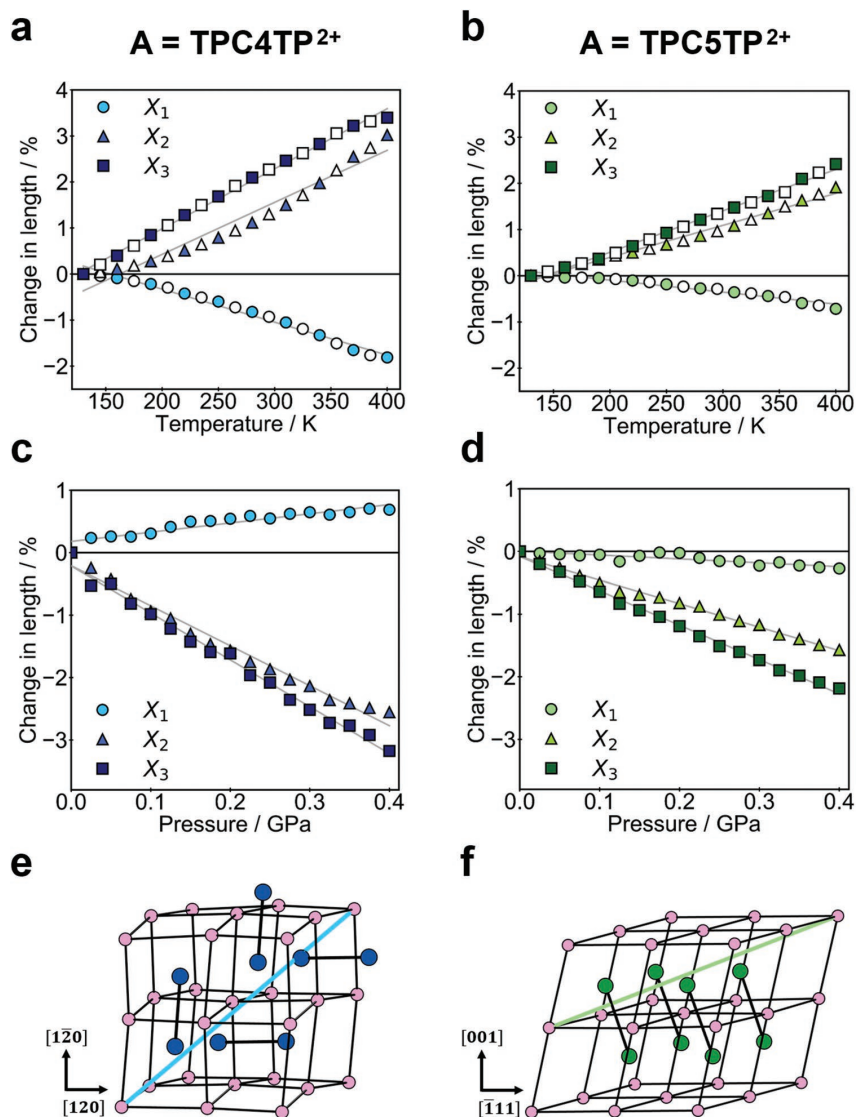


**Figure 3.** Temperature and pressure dependent structural behavior of  $AB_2X_6$  coordination polymers. Shown are the evolution of principal axes as a function of temperature and pressure. For  $A = TPC4TP^{2+}$ , uniaxial NTE and NLC along  $X_1$  is observed, whilst for  $A = TPC5TP^{2+}$  uniaxial NTE and positive compressibilities are found. For temperature-dependent data, filled and open symbols represent heating and cooling, respectively. e, f) show a  $2 \times 2 \times 2$  perovskite-type unit with the particular direction of propagation for the principal axis  $X_1$  illustrated, respectively. Color code: green/dark blue: A-cation N, pink: Mn. Note that the black lines are only a guide to the eye to indicate the perovskite-type connectivity and do not represent real chemical bonds.

The herein presented materials are conceptually related to the work by Telfer,<sup>[51]</sup> where geometric degrees of freedom were introduced by controlled interpenetration of MUF-9. This and many other examples highlight that decomposing a coordination networks' structure into (structural) degrees of freedom is a material class overarching conceptualization to rationalize stimuli-responsive material behavior, and in the future, may serve as a powerful design principle. As a concept, it represents a natural development of rigid-body guidelines such as the reticular chemistry approach<sup>[52]</sup> and the Goldschmidt tolerance

factor approach for (molecular) perovskites<sup>[53]</sup> to control responsive properties through crystal structure engineering. Importantly, when considering photoactive linker molecules or catalytically active structural entities in coordination polymers such as MOFs as chemical degrees of freedom, the combination of structural with chemical degrees of freedom seems intriguing to rationally synthesize multifunctional materials with potentially new properties. Research examples exist that can be understood within this framework such as switchable catalysts based on flexible MOFs,<sup>[54]</sup> energy transfer processes

in photoactive MOFs,<sup>[55]</sup> and the geometric arrangement of redox-active linker molecules in electrically conductive MOFs<sup>[56]</sup> amongst other examples. To advance this concept to a practically useful guideline, the identification of new structural degrees of freedom, learning about the design of their interplay, and impact on stimuli-responsive properties is key, to which this work provides an important step.

#### 4. Experimental Section

All experimental and analytical data including a detailed description of synthesis procedures for the precursor compounds as well as details on structure determination can be found in Supporting Information. This also includes experimental details for data collection at the synchrotron facilities Diamond Light Source Ltd., UK and DESY, Germany. The reported crystal structures are available through the Cambridge Crystallographic Database listed with the respective entry numbers as can be found in Supporting Information.

**Statistical Analysis:** All experimental data were evaluated with respect to relevant error calculations and measurement uncertainties and when appropriate, the results of error analysis are discussed in Supporting Information.

#### Supporting Information

Supporting Information is available from the Wiley Online Library or from the author.

#### Acknowledgements

S.B. would like to thank the Hanns-Seidel-Foundation for financial support through a Ph.D. fellowship. G.K. would like to thank the "Fonds der Chemischen Industrie" for support through the Liebig Fellowship scheme. K.H. thanks the "Fonds der Chemischen Industrie" for a Ph.D. fellowship. J.K.Z. acknowledges support from Academia Iuvenum, Wrocław University of Science and Technology. The authors would like to acknowledge beamtime at the Diamond Light Source Ltd., UK (experiment CY22477-2, beamline I15). The authors acknowledge DESY (Hamburg, Germany), a member of the Helmholtz Association HGF, for the provision of experimental facilities. Parts of this research were carried out at PETRA III (experiment I-20191507) and the authors would like to thank Martin Etter and Alexander Schökel for assistance in using beamline P02.1 for data collection. Additionally, the measurements at DESY leading to this results has been supported with travel reimbursement from DESY, for which the authors are grateful.

Open access funding enabled and organized by Projekt DEAL.

#### Conflict of Interest

The authors declare no conflict of interest.

#### Author Contributions Statement

S.B. and G.K. designed the study, analyzed experimental outcomes, and wrote the manuscript. K.H., P.V., and D.D. assisted in synchrotron data collection and interpretation of results. J.K.Z. conducted the SHG measurements and D.M. assisted with single crystal diffraction. In addition to continuous scientific exchange, all authors contributed to proof-reading and revisions of the manuscript.

#### Data Availability Statement

The data that support the findings of this study are available in the supplementary material of this article

#### Keywords

coordination polymers, materials chemistry, negative linear compressibility, structural degrees of freedom, uniaxial negative thermal expansion

Received: May 10, 2022

Revised: June 27, 2022

Published online: August 8, 2022

- [1] N. Hanikel, M. S. Prévot, O. M. Yaghi, *Nat. Nanotechnol.* **2020**, *15*, 348.
- [2] J. M. Bermúdez-García, M. Sánchez-Andújar, S. Castro-García, J. López-Beceiro, R. Artiaga, M. A. Señaris-Rodríguez, *Nat. Commun.* **2017**, *8*, 15715.
- [3] S. Krause, V. Bon, I. Senkovska, U. Stoeck, D. Wallacher, D. M. Töbrens, S. Zander, R. S. Pillai, G. Maurin, F.-X. Coudert, S. Kaskel, *Nature* **2016**, *532*, 348.
- [4] A. B. Cairns, J. Catafesta, C. Levelut, J. Rouquette, A. van der Lee, L. Peters, A. L. Thompson, V. Dmitriev, J. Haines, A. L. Goodwin, *Nat. Mater.* **2013**, *12*, 212.
- [5] N. C. Burtch, S. J. Baxter, J. Heinen, A. Bird, A. Schneemann, D. Dubbeldam, A. P. Wilkinson, *Adv. Funct. Mater.* **2019**, *29*, 1904669.
- [6] A. P. Katsoulidis, D. Antypov, G. F. S. Whitehead, E. J. Carrington, D. J. Adams, N. G. Berry, G. R. Darling, M. S. Dyer, M. J. Rosseinsky, *Nature* **2019**, *565*, 213.
- [7] S. Horike, S. S. Nagarkar, T. Ogawa, S. Kitagawa, *Angew. Chem., Int. Ed.* **2020**, *59*, 6652.
- [8] C. L. Hobday, G. Kieslich, *Dalton Trans.* **2021**, *50*, 3759.
- [9] S. Krause, N. Hosono, S. Kitagawa, *Angew. Chem., Int. Ed.* **2020**, *59*, 15325.
- [10] H. L. B. Boström, A. L. Goodwin, *Acc. Chem. Res.* **2021**, *54*, 1288.
- [11] M. J. Pitcher, P. Mandal, M. S. Dyer, J. Alaria, P. Borisov, H. Niu, J. B. Claridge, M. J. Rosseinsky, *Science* **2015**, *347*, 420.
- [12] J. H. Jung, Z. Fang, J. P. He, Y. Kaneko, Y. Okimoto, Y. Tokura, *Phys. Rev. Lett.* **2003**, *91*, 056403.
- [13] H. L. B. Boström, M. S. Senn, A. L. Goodwin, *Nat. Commun.* **2018**, *9*, 2380.
- [14] Q. Chen, H. Zhou, Z. Hong, S. Luo, H.-S. Duan, H.-H. Wang, Y. Liu, G. Li, Y. Yang, *J. Am. Chem. Soc.* **2014**, *136*, 622.
- [15] P. Iacomi, J. S. Lee, L. Vanduyfhuys, K. H. Cho, P. Fertey, J. Wierme, D. Granier, G. Maurin, V. van Speybroeck, J.-S. Chang, P. G. Yot, *Chem. Sci.* **2021**, *12*, 5682.
- [16] P. Vervoorts, J. Keupp, A. Schneemann, C. L. Hobday, D. Daisenberger, R. A. Fischer, R. Schmid, G. Kieslich, *Angew. Chem., Int. Ed.* **2021**, *60*, 787.
- [17] Y.-S. Su, E. S. Lamb, I. Liepuniute, A. Chronister, A. L. Stanton, P. Guzman, S. Pérez-Estrada, T. Y. Chang, K. N. Houk, M. A. Garcia-Garibay, S. E. Brown, *Nat. Chem.* **2021**, *13*, 278.
- [18] A. Simonov, T. de Baerdemaeker, H. L. B. Boström, M. L. Ríos Gómez, H. J. Gray, D. Chernyshov, A. Bosak, H.-B. Bürgi, A. L. Goodwin, *Nature* **2020**, *578*, 256.
- [19] F. M. Amombo Noa, E. Svensson Grape, S. M. Brülls, O. Cheung, P. Malmberg, A. K. Inge, C. J. McKenzie, J. Mårtensson, L. Öhrström, *J. Am. Chem. Soc.* **2020**, *142*, 9471.
- [20] V. Guillerm, D. Maspoch, *J. Am. Chem. Soc.* **2019**, *141*, 16517.

- [21] F. Haase, G. A. Craig, M. Bonneau, K. Sugimoto, S. Furukawa, *J. Am. Chem. Soc.* **2020**, *142*, 13839.
- [22] J. J. Oppenheim, G. Skorupskii, M. Dincă, *Chem. Sci.* **2020**, *11*, 11094.
- [23] W. Li, Z. Wang, F. Deschler, S. Gao, R. H. Friend, A. K. Cheetham, *Nat. Rev. Mater.* **2017**, *2*, 3.
- [24] Y. Wu, S. Shaker, F. Brivio, R. Murugavel, P. D. Bristowe, A. K. Cheetham, *J. Am. Chem. Soc.* **2017**, *139*, 16999.
- [25] J. A. Schlüter, J. L. Manson, U. Geiser, *Inorg. Chem.* **2005**, *44*, 3194.
- [26] P. Jain, N. S. Dalal, B. H. Toby, H. W. Kroto, A. K. Cheetham, *J. Am. Chem. Soc.* **2008**, *130*, 10450.
- [27] H. L. B. Boström, *CrystEngComm* **2020**, *22*, 961.
- [28] W.-J. Xu, S.-L. Chen, Z.-T. Hu, R.-B. Lin, Y.-J. Su, W.-X. Zhang, X.-M. Chen, *Dalton Trans.* **2016**, *45*, 4224.
- [29] I. E. Collings, M. Bykov, E. Bykova, M. Hanfland, S. van Smaalen, L. Dubrovinsky, N. Dubrovinskaia, *CrystEngComm* **2018**, *20*, 3512.
- [30] W. Wei, W. Li, K. T. Butler, G. Feng, C. J. Howard, M. A. Carpenter, P. Lu, A. Walsh, A. K. Cheetham, *Angew. Chem., Int. Ed.* **2018**, *57*, 8932.
- [31] S. Burger, S. Grover, K. T. Butler, H. L. B. Boström, R. Grau-Crespo, G. Kieslich, *Mater. Horiz.* **2021**, *8*, 2444.
- [32] J. M. Bermúdez-García, M. Sánchez-Andújar, M. A. Señaris-Rodríguez, *J. Phys. Chem. Lett.* **2017**, *8*, 4419.
- [33] L. Xin, Z. Zhang, M. A. Carpenter, M. Zhang, F. Jin, Q. Zhang, X. Wang, W. Tang, X. Lou, *Adv. Funct. Mater.* **2018**, *28*, 1806013.
- [34] M.-L. Tong, J. Ru, Y.-M. Wu, X.-M. Chen, H.-C. Chang, K. Mochizuki, S. Kitagawa, *New J. Chem.* **2003**, *27*, 779.
- [35] A. L. Goodwin, M. Calleja, M. J. Conterio, M. T. Dove, J. S. O. Evans, D. A. Keen, L. Peters, M. G. Tucker, *Science* **2008**, *319*, 794.
- [36] A. B. Cairns, A. L. Thompson, M. G. Tucker, J. Haines, A. L. Goodwin, *J. Am. Chem. Soc.* **2012**, *134*, 4454.
- [37] S. Henke, A. Schneemann, R. A. Fischer, *Adv. Funct. Mater.* **2013**, *23*, 5990.
- [38] H. J. Shepherd, T. Palamarciuc, P. Rosa, P. Guionneau, G. Molnár, J.-F. Létard, A. Bousseksou, *Angew. Chem., Int. Ed.* **2012**, *51*, 3910.
- [39] Q. Zeng, K. Wang, B. Zou, *J. Am. Chem. Soc.* **2017**, *139*, 15648.
- [40] A. D. Fortes, E. Suard, K. S. Knight, *Science* **2011**, *331*, 742.
- [41] A. L. Goodwin, D. A. Keen, M. G. Tucker, *Proc. Natl. Acad. Sci. USA* **2008**, *105*, 18708.
- [42] J. Kusz, M. Zubko, A. Fitch, P. Gütlisch, *Z. Kristallogr.* **2011**, *226*, 576.
- [43] J. N. Grima, R. Caruana-Gauci, D. Attard, R. Gatt, *Proc. R. Soc. A* **2012**, *468*, 3121.
- [44] I. E. Collings, M. G. Tucker, D. A. Keen, A. L. Goodwin, *CrystEngComm* **2014**, *16*, 3498.
- [45] M. Maćzka, I. E. Collings, F. F. Leite, W. Paraguassu, *Dalton Trans.* **2019**, *48*, 9072.
- [46] I. E. Collings, J. A. Hill, A. B. Cairns, R. I. Cooper, A. L. Thompson, J. E. Parker, C. C. Tang, A. L. Goodwin, *Dalton Trans.* **2016**, *45*, 4169.
- [47] H. Gao, C. Li, L. Li, W. Wei, Y. Tan, Y. Tang, *Dalton Trans.* **2020**, *49*, 7228.
- [48] M. J. Cliffe, A. L. Goodwin, *J. Appl. Cryst.* **2012**, *45*, 1321.
- [49] A. J. Brock, J. J. Whittaker, J. A. Powell, M. C. Pfrunder, A. Grosjean, S. Parsons, J. C. McMurtrie, J. K. Clegg, *Angew. Chem., Int. Ed.* **2018**, *57*, 11325.
- [50] S. Haas, B. Batlogg, C. Besnard, M. Schiltz, C. Kloc, T. Siegrist, *Phys. Rev. B* **2007**, *76*, 843.
- [51] A. Ferguson, L. Liu, S. J. Tapperwijn, D. Perl, F.-X. Coudert, S. van Cleuvenbergen, T. Verbiest, M. A. van der Veen, S. G. Telfer, *Nat. Chem.* **2016**, *8*, 250.
- [52] R. Freund, S. Canossa, S. M. Cohen, W. Yan, H. Deng, V. Guillermin, M. Eddaoudi, D. G. Madden, D. Fairen-Jimenez, H. Lyu, L. K. Macreadie, Z. Ji, Y. Zhang, B. Wang, F. Haase, C. Wöll, O. Zaremba, J. Andreo, S. Wuttke, C. S. Diercks, *Angew. Chem., Int. Ed.* **2021**, *60*, 23946.
- [53] G. Kieslich, S. Sun, A. K. Cheetham, *Chem. Sci.* **2014**, *5*, 4712.
- [54] S. Yuan, L. Zou, H. Li, Y.-P. Chen, J. Qin, Q. Zhang, W. Lu, M. B. Hall, H.-C. Zhou, *Angew. Chem., Int. Ed.* **2016**, *55*, 10776.
- [55] D. E. Williams, J. A. Rietman, J. M. Maier, R. Tan, A. B. Greytak, M. D. Smith, J. A. Krause, N. B. Shustova, *J. Am. Chem. Soc.* **2014**, *136*, 11886.
- [56] T. C. Narayan, T. Miyakai, S. Seki, M. Dincă, *J. Am. Chem. Soc.* **2012**, *134*, 12932.

## 5 CONCLUSION

Perovskite-like coordination networks as inherent representatives of coordination polymers represent an unique material platform to provide a detailed understanding of the relationship between a material's structure and its properties. In order to develop these relations, a comprehensive knowledge of the microscopic structural factors that are decisive for macroscopic physical properties is of fundamental importance. The presented dissertation contributes to filling this knowledge gap and elaborates important prerequisites for understanding the behaviour of these molecular perovskites. The key concept is to rationalise the composition of the coordination networks as a function of chemical and geometric degrees of freedom, thus establishing design principles to derive temperature- and pressure-dependent properties from structural features. Particularly the molecular A-site cation of the perovskite-type materials offers unique opportunities to systematically alter the material structure and investigate its impact on resulting properties. A review on the highlights of this thesis reflects two main research pillars discussed in detail. The concept of polymorphism in molecular perovskites categorises structural phase transitions in relation to active symmetry modes that are co-determined by the chemical degrees of freedom on the A-site and might serve as entry point for generating functional materials as barocalorics amongst others yet hidden. The crystal engineering approach of incorporating geometric degrees of freedom that go beyond the  $ABX_3$  perovskite structure concept itself introduces novel geometric constraints into perovskite-like host-guest coordination polymers and challenges previous A-site cation chemistry to ultimately enforce specific material properties. In more detail, as demonstrated in STUDY II, the material  $[ASU]Cd(C_2N_3)_3$  is one example of how to introduce distinct structural features into perovskite-type coordination networks. There, a new molecular perovskite material is characterised bearing a molecular A-site cation of specific shape. This azaspiro compound  $[ASU]^+$  induces a rare tilt system onto the host framework, which results in large non-linear optical properties of the resulting material. It is demonstrated that the polarity originates from an active unconventional tilt, a rigid unit mode exclusively present in perovskite-type materials if both the A- and the X-site are molecular in nature. It therefore demonstrates the vast opportunities that come with the various chemical degrees of freedom of the molecular A-site cation which have barely been touched as yet. In addition, the material exhibits an irreversible phase transition upon initial heating, a phenomenon that to this extent has been rarely seen before and might have its origin in the nature of the asymmetric cation as well. Following on from this, the results in STUDY III provide an interpretation of the presence of such irreversible phase transitions, introducing the concept of "tilt and shift polymorphism". In this context, a new series of isostructural materials with a perovskite architecture is presented, which also accommodates a customised molecular cation, that is methyltripropylammonium, and which also exhibits the aforementioned type of irreversible

phase transition. A detailed structural analysis of the resulting high-temperature phase reveals the structural differences being crucial to variations of the binding modes of the anion and the metal cation within the confining host framework. Once this transformation is completed, it remains irreversible, as theoretical calculations demonstrate the preferential stability compared to the initial phase. The shift in binding modes generates a material system which exhibits a reversible order-disorder phase transition with a large change in entropy and hence provides the precondition to serve as a functional material. As such, this example serves as a blueprint for the direct impact of synthetic freedom on available structural degrees of freedom to access previously unrecognised material properties. Along the metal series of the generated reversible phase transition, both the phase transition temperature and the change of configurational entropy vary monotonically from manganese and cobalt to nickel and therefore hint for interesting characteristics in terms of potential barocaloric properties. In anticipation of further experimental investigations, STUDY IV deals with the issue to access the compressibility of a material in a theoretical approach to use it as a figure of merit to ultimately estimate the suitability of a material for barocaloric applications before performing the time-consuming high-pressure experiments. The calculations reveal a dependence of the bulk modulus on the phonon density of states of the host network with emphasis on the metal-linker bonding. One important outcome implies that the softer phonon modes correspond to lower bulk moduli. As the metal cation and as a result the metal-linker bond length determines the vibrational properties, a clear correlation of the theoretical bulk modulus and the Shannon radius of the respective metal is demonstrated. The results are supported by an experimental determination of the bulk moduli of the three corresponding materials, which increase from manganese with  $B = 7.08$  GPa to nickel with  $B = 10.85$  GPa. This is in strong agreement with chemical intuition and highlights an important step forward towards *a priori* rational design of functional materials for potential barocaloric applications. The knowledge on the behaviour of perovskite-type coordination networks as a material platform acquired through the preceding studies culminate in STUDY V, in which a new family of  $AB_2X_6$  coordination polymers adapted from a  $ReO_3$ -type network is presented. Through the synthesis of divalent molecular A-site cations with separated charge centres and subsequent implementation into the perovskite-type framework, two adjacent  $[BX_3]^-$  cages are chemically bridged, adding additional entanglement of the guest site as a novel geometric degree of freedom into the material structure. Two different types of order pattern (herringbone and head-to-tail arrangement) are generated with a decisive impact on the resulting material properties. In this respect, the structure bearing the herringbone pattern marks the first representative of a material based on the perovskite-type architecture, which exhibits a pronounced NLC effect ( $\chi = -12(1)$  TPa $^{-1}$ ) and a NTE effect in its ambient phase. The highlight of this work lies in the systematic decomposition of a novel material structure into individual structural degrees of freedom based on the modular building block principle. This enables the specific assignment of macroscopic properties to microscopic structural elements. In particular, the incorporation of tailor-made (divalent) A-site motifs into a host BX-framework, the detailed mechanistic explanation of the occurrence of NTE and NLC as a result of novel geometric and structural degrees



---

of freedom, and insights into the relationship of phase transition characteristics, compressibility and barocaloric activity of molecular perovskites are key contributions and are a manifestation of modern scientific research capabilities.

In this dissertation a conceptual link is established between the chemical manipulation capabilities of the perovskite structure motif and the introduction of chemical and structural degrees of freedom towards novel structure families derived from the perovskite-type. Engineering molecular A-site cations can intentionally induce structural distortions of the enclosing framework with a decisive influence on the material properties. The activation of specific tilt and shift distortion modes can provide valuable strategies to evoke directed material properties by tilting. So far, the mechanism of the irreversible phase transformation is not yet clear. An *in situ* tracking of the crystallisation by means of total scattering and temperature-dependent diffraction experiments below and above the transition temperature could provide additional insights to understand and direct the synthesis of polymorphic phases and guide the development of design principles. The chemistry of the molecular A-site cation provides much more potential than the results of this dissertation could possibly cover, since for instance to date in dicyanamide-based perovskite-type coordination networks no molecular A-site cation is being known that carries X-H acidic protons for hydrogen-bonding between the guest and the host. The introduction of strong intermolecular forces *e.g.* through hydroxy groups might have a significant impact on network deformation to template the distortion of polymorphic crystalline phases originating from tailor-made cations. On this note, solid solutions within the ABX<sub>3</sub> structural family could reveal a great potential to induce unprecedented material properties *via* continuous dosing of a specific property derived from the pristine component. With extending the geometric degrees of freedom to multiple perovskite cages, this dissertation has opened the portal to an almost unrestricted number of possibilities for generating new material structures. The chemical variability of the A-site cation is not limited to the chemical linkage of two adjacent charge voids, but rather can expand to multivalent junctions with novel ordering patterns being imaginable. The nature of the guest-host interactions within the confining perovskite-like framework harbours a great power due to the highly robust matrix. It opens intriguing routes for developing material response schemes towards external stimuli, which can be accurately mapped onto coupling schemes of the A-site cation order patterns. As an example, the implementation of multivalent organic cations like alkylated 1,3-propanediamine as an additional geometric degree of freedom on the A-site of the photoabsorber material [CH<sub>3</sub>NH<sub>3</sub>]PbI<sub>3</sub> could be envisaged to overcome the severe disadvantage of the instability due to ion migration,[286, 287] thereby prevent migration by entanglement. Another great potential of these multivalent cations directs to the field of barocalorics. The chemical interlocking of individual A-cations can cause concise simultaneous order/disorder transitions with massive enthalpic and entropic changes, thus generating strong barocaloric effects. In a more abstract picture, the future development of the material class of molecular perovskites will depend on the progress in describing the structural response of the three-dimensional coordination networks. It necessitates a conceptualisation of the effects

that come with the exploitation of novel additional degrees of freedom only accessible due to the molecular nature. In general, conclusions to existing concepts that are already known from classical inorganic chemistry can be drawn, with a continuous adaption to meet the challenges of coordination networks with hybrid character. A paradigm in this regard is the advancement of the Glazer notation,[88] which was originally established for tilting systems in inorganic perovskites, towards molecular perovskites by incorporating the description of unconventional tilts and shifts.[135]

The scientific approach to decompose a materials structure into individual components as integral part of a modular system is a valuable method to study and to interpret the relationship between crystal structure and macroscopic properties and will be a key tool for the discovery of novel materials in the future, some of which have been introduced to the community with this dissertation.

## 6 BIBLIOGRAPHY

- [1] S. R. Batten, N. R. Champness, X.-M. Chen, J. Garcia-Martinez, S. Kitagawa, L. Öhrström, M. O’Keeffe, M. Paik Suh, J. Reedijk, “Terminology of metal–organic frameworks and coordination polymers (IUPAC Recommendations 2013)”, *Pure Appl. Chem.* **2013**, 85, 1715–1724, DOI 10.1351/PAC-REC-12-11-20.
- [2] K. M. Fromm, J. L. Sagué, L. Mirolo, “Coordination Polymer Networks: An Alternative to Classical Polymers?”, *Macromol. Symp.* **2010**, 291-292, 75–83, DOI 10.1002/masy.201050509.
- [3] R. F. T. Stepto, “Dispersity in polymer science (IUPAC Recommendations 2009)”, *Pure Appl. Chem.* **2009**, 81, 351–353, DOI 10.1351/PAC-REC-08-05-02.
- [4] A. KELLER, “Morphology of Crystallizing Polymers”, *Nature* **1952**, 169, 913–914, DOI 10.1038/169913a0.
- [5] E. Riedel, C. Janiak, *Anorganische Chemie: p. 69*, 7. Aufl., de Gruyter, Berlin, **2007**, DOI 10.1515/9783110189032.
- [6] M. Binnewies, M. Finze, M. Jäckel, P. Schmidt, H. Willner, G. Rayner-Canham, *Allgemeine und Anorganische Chemie*, 3. Aufl. 2016, Springer Berlin Heidelberg, Berlin, Heidelberg, **2016**.
- [7] C. E. Housecraft, Sharpe Alan G., *Inorganic Chemistry: p. 177*, 5. Auflage, Pearson Education Limited, Harlow, **2018**.
- [8] L. Pauling, “THE PRINCIPLES DETERMINING THE STRUCTURE OF COMPLEX IONIC CRYSTALS”, *J. Am. Chem. Soc.* **1929**, 51, 1010–1026, DOI 10.1021/ja01379a006.
- [9] The Nobel Prize in Chemistry 1913, NobelPrize.org, Nobel Prize Outreach AB 2022. Tue. 16 Aug 2022, <https://www.nobelprize.org/prizes/chemistry/1913/summary/>.
- [10] A. F. Holleman, N. Wiberg, E. Wiberg, *Lehrbuch der Anorganischen Chemie: p. 1316*, Walter de Gruyter, **2007**, DOI 10.1515/9783110206845.
- [11] A. Ludi, “Berliner Blau”, *Chem. Unserer Zeit* **1988**, 22, 123–127, DOI 10.1002/ciuz.19880220403.
- [12] A. F. Holleman, N. Wiberg, E. Wiberg, *Lehrbuch der Anorganischen Chemie: p. 1651*, Walter de Gruyter, **2007**, DOI 10.1515/9783110206845.
- [13] A. Werner, “Beitrag zur Konstitution anorganischer Verbindungen”, *Z. Anorg. Chem.* **1893**, 3, 267–330, DOI 10.1002/zaac.18930030136.

- [14] C. S. Diercks, M. J. Kalmutzki, N. J. Diercks, O. M. Yaghi, “Conceptual Advances from Werner Complexes to Metal-Organic Frameworks”, *ACS Cent. Sci.* **2018**, *4*, 1457–1464, DOI 10.1021/acscentsci.8b00677.
- [15] K. A. Hofmann, F. Küspert, “Verbindungen von Kohlenwasserstoffen mit Metallsalzen”, *Z. Anorg. Chem.* **1897**, *15*, 204–207, DOI 10.1002/zaac.18970150118.
- [16] R. Kuroda, Y. Sasaki, “The crystal structure of a Hofmann-type clathrate,  $\text{Mn}(\text{NH}_3)_2\text{Ni}(\text{NC})_4 \cdot 2\text{C}_6\text{H}_6$ ”, *Acta Cryst. B* **1974**, *30*, 687–690, DOI 10.1107/S0567740874003529.
- [17] H. J. Buser, D. Schwarzenbach, W. Petter, A. Ludi, “The crystal structure of Prussian Blue:  $\text{Fe}_4[\text{Fe}(\text{CN})_6]_3 \cdot x\text{H}_2\text{O}$ ”, *Inorg. Chem.* **1977**, *16*, 2704–2710, DOI 10.1021/ic50177a008.
- [18] H. Li, M. Eddaoudi, M. O’Keeffe, O. M. Yaghi, “Design and synthesis of an exceptionally stable and highly porous metal-organic framework”, *Nature* **1999**, *402*, 276–279, DOI 10.1038/46248.
- [19] N. Yoshinari, T. Konno, “Multitopic metal-organic carboxylates available as supramolecular building units”, *Coord. Chem. Rev.* **2023**, *474*, 214850, DOI 10.1016/j.ccr.2022.214850.
- [20] H. G. Büttner, G. J. Kearley, C. J. Howard, F. Fillaux, “Structure of the Hofmann clathrates  $\text{Ni}(\text{NH}_3)_2\text{Ni}(\text{CN})_4 \cdot 2\text{C}_6\text{D}_6$  and  $\text{Zn}(\text{NH}_3)_2\text{Ni}(\text{CN})_4 \cdot 2\text{C}_6\text{H}_6$ ”, *Acta Cryst. B* **1994**, *50*, 431–435, DOI 10.1107/S0108768193013539.
- [21] S. Kitagawa, R. Kitaura, S.-i. Noro, “Functional porous coordination polymers”, *Angew. Chem. Int. Ed.* **2004**, *43*, 2334–2375, DOI 10.1002/anie.200300610.
- [22] S. Horike, S. Shimomura, S. Kitagawa, “Soft porous crystals”, *Nat. Chem.* **2009**, *1*, 695–704, DOI 10.1038/nchem.444.
- [23] A. K. Cheetham, T. D. Bennett, F.-X. Coudert, A. L. Goodwin, “Defects and disorder in metal organic frameworks”, *Dalton Trans.* **2016**, *45*, 4113–4126, DOI 10.1039/c5dt04392a.
- [24] S. Dissegna, K. Epp, W. R. Heinz, G. Kieslich, R. A. Fischer, “Defective Metal-Organic Frameworks”, *Adv. Mater.* **2018**, DOI 10.1002/adma.201704501.
- [25] Z. Fan, J. Wang, W. Wang, S. Burger, Z. Wang, Y. Wang, C. Wöll, M. Cokoja, R. A. Fischer, “Defect Engineering of Copper Paddlewheel-Based Metal-Organic Frameworks of Type NOTT-100: Implementing Truncated Linkers and Its Effect on Catalytic Properties”, *ACS Appl. Mater. Interfaces* **2020**, *12*, 37993–38002, DOI 10.1021/acsaami.0c07249.
- [26] H. L. B. Boström, G. Kieslich, “Influence of Metal Defects on the Mechanical Properties of  $\text{ABX}_3$  Perovskite-Type Metal-formate Frameworks”, *J. Phys. Chem. C* **2021**, *125*, 1467–1471, DOI 10.1021/acs.jpcc.0c09796.

- 
- [27] D. Umeyama, A. Takai, K. Sonobe, “Postsynthetic Defect Formation in Three-Dimensional Hofmann-Type Coordination Polymers and Its Impact on Catalytic Activity”, *Inorg. Chem.* **2022**, *61*, 1697–1703, DOI 10.1021/acs.inorgchem.1c03560.
- [28] J. Fonseca, T. Gong, L. Jiao, H.-L. Jiang, “Metal–organic frameworks (MOFs) beyond crystallinity: amorphous MOFs, MOF liquids and MOF glasses”, *J. Mater. Chem. A* **2021**, *9*, 10562–10611, DOI 10.1039/D1TA01043C.
- [29] T. D. Bennett, S. Horike, “Liquid, glass and amorphous solid states of coordination polymers and metal–organic frameworks”, *Nat. Rev. Mater.* **2018**, *3*, 431–440, DOI 10.1038/s41578-018-0054-3.
- [30] K. S. Park, Z. Ni, A. P. Côté, J. Y. Choi, R. Huang, F. J. Uribe-Romo, H. K. Chae, M. O’Keeffe, O. M. Yaghi, “Exceptional chemical and thermal stability of zeolitic imidazolate frameworks”, *Proc. Natl. Acad. Sci. USA* **2006**, *103*, 10186–10191, DOI 10.1073/pnas.0602439103.
- [31] T. D. Bennett, A. L. Goodwin, M. T. Dove, D. A. Keen, M. G. Tucker, E. R. Barney, A. K. Soper, E. G. Bithell, J.-C. Tan, A. K. Cheetham, “Structure and properties of an amorphous metal-organic framework”, *Phys. Rev. Lett.* **2010**, *104*, 115503, DOI 10.1103/PhysRevLett.104.115503.
- [32] B. K. Shaw, A. R. Hughes, M. Ducamp, S. Moss, A. Debnath, A. F. Sapnik, M. F. Thorne, L. N. McHugh, A. Pugliese, D. S. Keeble, P. Chater, J. M. Bermudez-Garcia, X. Moya, S. K. Saha, D. A. Keen, F.-X. Coudert, F. Blanc, T. D. Bennett, “Melting of hybrid organic-inorganic perovskites”, *Nat. Chem.* **2021**, *13*, 778–785, DOI 10.1038/s41557-021-00681-7.
- [33] N. Ma, R. Ohtani, H. M. Le, S. S. Sørensen, R. Ishikawa, S. Kawata, S. Bureekaew, S. Kosasang, Y. Kawazoe, K. Ohara, M. M. Smedskjaer, S. Horike, “Exploration of glassy state in Prussian blue analogues”, *Nat. Commun.* **2022**, *13*, 4023, DOI 10.1038/s41467-022-31658-w.
- [34] H.-C. Zhou, J. R. Long, O. M. Yaghi, “Introduction to metal-organic frameworks”, *Chem. Rev.* **2012**, *112*, 673–674, DOI 10.1021/cr300014x.
- [35] S. S. Kaye, J. R. Long, “Hydrogen storage in the dehydrated prussian blue analogues  $M_3Co(CN)_6$  ( $M = Mn, Fe, Co, Ni, Cu, Zn$ )”, *J. Am. Chem. Soc.* **2005**, *127*, 6506–6507, DOI 10.1021/ja051168t.
- [36] W. Li, Z. Wang, F. Deschler, S. Gao, R. H. Friend, A. K. Cheetham, “Chemically diverse and multifunctional hybrid organic–inorganic perovskites”, *Nat. Rev. Mater.* **2017**, *2*, 16099, DOI 10.1038/natrevmats.2016.99.
- [37] A. L. Goodwin, C. J. Kepert, “Negative thermal expansion and low-frequency modes in cyanide-bridged framework materials”, *Phys. Rev. B* **2005**, *71*, 1, DOI 10.1103/PhysRevB.71.140301.

- [38] A. E. Phillips, A. D. Fortes, “Crossover between Tilt Families and Zero Area Thermal Expansion in Hybrid Prussian Blue Analogues”, *Angew. Chem. Int. Ed.* **2017**, *56*, 15950–15953, DOI 10.1002/anie.201708514.
- [39] A. Simonov, T. de Baerdemaeker, H. L. B. Boström, M. L. Ríos Gómez, H. J. Gray, D. Chernyshov, A. Bosak, H.-B. Bürgi, A. L. Goodwin, “Hidden diversity of vacancy networks in Prussian blue analogues”, *Nature* **2020**, *578*, 256–260, DOI 10.1038/s41586-020-1980-y.
- [40] M. Eddaoudi, D. B. Moler, H. Li, B. Chen, T. M. Reineke, M. O’Keeffe, O. M. Yaghi, “Modular chemistry: secondary building units as a basis for the design of highly porous and robust metal-organic carboxylate frameworks”, *Acc. Chem. Res.* **2001**, *34*, 319–330, DOI 10.1021/ar000034b.
- [41] D. J. Tranchemontagne, J. L. Mendoza-Cortés, M. O’Keeffe, O. M. Yaghi, “Secondary building units, nets and bonding in the chemistry of metal-organic frameworks”, *Chem. Soc. Rev.* **2009**, *38*, 1257–1283, DOI 10.1039/B817735J.
- [42] S. M. Cohen, “Postsynthetic methods for the functionalization of metal-organic frameworks”, *Chem. Rev.* **2012**, *112*, 970–1000, DOI 10.1021/cr200179u.
- [43] B. F. Hoskins, R. Robson, “Infinite polymeric frameworks consisting of three dimensionally linked rod-like segments”, *J. Am. Chem. Soc.* **1989**, *111*, 5962–5964, DOI 10.1021/ja00197a079.
- [44] B. F. Hoskins, R. Robson, “Design and construction of a new class of scaffolding-like materials comprising infinite polymeric frameworks of 3D-linked molecular rods. A reappraisal of the zinc cyanide and cadmium cyanide structures and the synthesis and structure of the diamond-related frameworks  $[\text{N}(\text{CH}_3)_4][\text{CuIZnII}(\text{CN})_4]$  and  $\text{CuI}[4,4',4'',4''']\text{-tetracyanotetraphenylmethane}[\text{BF}_4 \cdot x\text{C}_6\text{H}_5\text{NO}_2]$ ”, *J. Am. Chem. Soc.* **1990**, *112*, 1546–1554, DOI 10.1021/ja00160a038.
- [45] O. M. Yaghi, H. Li, “Hydrothermal Synthesis of a Metal-Organic Framework Containing Large Rectangular Channels”, *J. Am. Chem. Soc.* **1995**, *117*, 10401–10402, DOI 10.1021/ja00146a033.
- [46] O. M. Yaghi, G. Li, H. Li, “Selective binding and removal of guests in a microporous metal-organic framework”, *Nature* **1995**, *378*, 703–706, DOI 10.1038/378703a0.
- [47] M. Kondo, T. Yoshitomi, H. Matsuzaka, S. Kitagawa, K. Seki, “Three-Dimensional Framework with Channeling Cavities for Small Molecules:  $[\text{M}_2(4, 4'\text{-bpy})_3(\text{NO}_3)_4] \cdot x\text{H}_2\text{O}_n$  (M=Co, Ni, Zn)”, *Angew. Chem. Int. Ed.* **1997**, *36*, 1725–1727, DOI 10.1002/anie.199717251.
- [48] S. Kitagawa, M. Kondo, “Functional Micropore Chemistry of Crystalline Metal Complex-Assembled Compounds”, *Bull. Chem. Soc. Jpn.* **1998**, *71*, 1739–1753, DOI 10.1246/bcsj.71.1739.

- 
- [49] Chui, Lo Charmant, Orpen, Williams, “A chemically functionalizable nanoporous material”, *Science* **1999**, 283, 1148–1150, DOI 10.1126/science.283.5405.1148.
- [50] F. Millange, C. Serre, G. Férey, “Synthesis, structure determination and properties of MIL-53as and MIL-53ht: the first CrIII hybrid inorganic-organic microporous solids:  $\text{CrIII}(\text{OH})\cdot(\text{O}_2\text{C}-\text{C}_6\text{H}_4-\text{CO}_2)\cdot(\text{HO}_2\text{C}-\text{C}_6\text{H}_4-\text{CO}_2\text{H})_x$ ”, *Chem. Commun.* **2002**, 822–823, DOI 10.1039/B201381A.
- [51] O. M. Yaghi, M. O’Keeffe, N. W. Ockwig, H. K. Chae, M. Eddaoudi, J. Kim, “Reticular synthesis and the design of new materials”, *Nature* **2003**, 423, 705–714, DOI 10.1038/nature01650.
- [52] A. Schneemann, V. Bon, I. Schwedler, I. Senkovska, S. Kaskel, R. A. Fischer, “Flexible metal-organic frameworks”, *Chem. Soc. Rev.* **2014**, 43, 6062–6096, DOI 10.1039/C4CS00101J.
- [53] N. Stock, S. Biswas, “Synthesis of metal-organic frameworks (MOFs): routes to various MOF topologies, morphologies, and composites”, *Chem. Rev.* **2012**, 112, 933–969, DOI 10.1021/cr200304e.
- [54] S. Yuan, L. Huang, Z. Huang, Di Sun, J.-S. Qin, L. Feng, J. Li, X. Zou, T. Cagin, H.-C. Zhou, “Continuous Variation of Lattice Dimensions and Pore Sizes in Metal-Organic Frameworks”, *J. Am. Chem. Soc.* **2020**, 142, 4732–4738, DOI 10.1021/jacs.9b13072.
- [55] L. J. Murray, M. Dincă, J. R. Long, “Hydrogen storage in metal-organic frameworks”, *Chem. Soc. Rev.* **2009**, 38, 1294–1314, DOI 10.1039/B802256A.
- [56] Y.-S. Bae, R. Q. Snurr, “Development and evaluation of porous materials for carbon dioxide separation and capture”, *Angew. Chem. Int. Ed.* **2011**, 50, 11586–11596, DOI 10.1002/anie.201101891.
- [57] L. E. Kreno, K. Leong, O. K. Farha, M. Allendorf, R. P. van Duyne, J. T. Hupp, “Metal-organic framework materials as chemical sensors”, *Chem. Rev.* **2012**, 112, 1105–1125, DOI 10.1021/cr200324t.
- [58] R. Medishetty, J. K. Zareba, D. Mayer, M. Samoć, R. A. Fischer, “Nonlinear optical properties, upconversion and lasing in metal-organic frameworks”, *Chem. Soc. Rev.* **2017**, 46, 4976–5004, DOI 10.1039/C7CS00162B.
- [59] D. C. Mayer, A. Manzi, R. Medishetty, B. Winkler, C. Schneider, G. Kieslich, A. Pöthig, J. Feldmann, R. A. Fischer, “Controlling Multiphoton Absorption Efficiency by Chromophore Packing in Metal-Organic Frameworks”, *J. Am. Chem. Soc.* **2019**, 141, 11594–11602, DOI 10.1021/jacs.9b04213.
- [60] K. Hemmer, M. Cokoja, R. A. Fischer, “Exploitation of Intrinsic Confinement Effects of MOFs in Catalysis”, *ChemCatChem* **2021**, 13, 1683–1691, DOI 10.1002/cctc.202001606.

- [61] A. K. Cheetham, C. N. R. Rao, “There’s Room in the Middle”, *Science* **2007**, *318*, 58–59, DOI 10.1126/science.1147231.
- [62] G. Kieslich, A. L. Goodwin, “The same and not the same: Molecular perovskites and their solid-state analogues”, *Mater. Horiz.* **2017**, *4*, 362–366, DOI 10.1039/C7MH00107J.
- [63] H. L. B. Boström, A. L. Goodwin, “Hybrid Perovskites, Metal-Organic Frameworks, and Beyond: Unconventional Degrees of Freedom in Molecular Frameworks”, *Acc. Chem. Res.* **2021**, *54*, 1288–1297, DOI 10.1021/acs.accounts.0c00797.
- [64] P. Jain, N. S. Dalal, B. H. Toby, H. W. Kroto, A. K. Cheetham, “Order-disorder antiferroelectric phase transition in a hybrid inorganic-organic framework with the perovskite architecture”, *J. Am. Chem. Soc.* **2008**, *130*, 10450–10451, DOI 10.1021/ja801952e.
- [65] G. P. Nagabhushana, R. Shivaramaiah, A. Navrotsky, “Thermochemistry of Multiferroic Organic-Inorganic Hybrid Perovskites  $(\text{CH}_3)_2\text{NH}_2\text{M}(\text{HCOO})_3$  (M = Mn, Co, Ni, and Zn)”, *J. Am. Chem. Soc.* **2015**, *137*, 10351–10356, DOI 10.1021/jacs.5b06146.
- [66] L. Xin, Z. Zhang, M. A. Carpenter, M. Zhang, F. Jin, Q. Zhang, X. Wang, W. Tang, X. Lou, “Strain Coupling and Dynamic Relaxation in a Molecular Perovskite-Like Multiferroic Metal-Organic Framework”, *Adv. Funct. Mater.* **2018**, *28*, 1806013, DOI 10.1002/adfm.201806013.
- [67] H. L. B. Boström, M. S. Senn, A. L. Goodwin, “Recipes for improper ferroelectricity in molecular perovskites”, *Nat. Commun.* **2018**, *9*, 2380, DOI 10.1038/s41467-018-04764-x.
- [68] Z. Wang, K. Hu, S. Gao, H. Kobayashi, “Formate-based magnetic metal-organic frameworks templated by protonated amines”, *Adv. Mater.* **2010**, *22*, 1526–1533, DOI 10.1002/adma.200904438.
- [69] X.-H. Zhao, X.-C. Huang, S.-L. Zhang, D. Shao, H.-Y. Wei, X.-Y. Wang, “Cation-dependent magnetic ordering and room-temperature bistability in azido-bridged perovskite-type compounds”, *J. Am. Chem. Soc.* **2013**, *135*, 16006–16009, DOI 10.1021/ja407654n.
- [70] J. M. Bermúdez-García, M. Sánchez-Andújar, S. Castro-García, J. López-Beceiro, R. Artiaga, M. A. Señarís-Rodríguez, “Giant barocaloric effect in the ferroic organic-inorganic hybrid TPrAMn(dca)<sub>3</sub> perovskite under easily accessible pressures”, *Nat. Commun.* **2017**, *8*, 15715, DOI 10.1038/ncomms15715.
- [71] G. Rose, “Ueber einige neue Mineralien des Urals”, *J. prakt. Chem.* **1840**, *19*, 459–468, DOI 10.1002/prac.18400190179.
- [72] W. Friedrich, P. Knipping, M. Laue, “Interferenzerscheinungen bei Röntgenstrahlen”, *Ann. Phys.* **1913**, *346*, 971–988, DOI 10.1002/andp.19133461004.



- 
- [73] W. H. Bragg, W. L. Bragg, “The Reflection of X-rays by Crystals”, *Proc. Royal Soc. A* **1913**, 88, 428–438, DOI 10.1098/rspa.1913.0040.
- [74] J. G. Bednorz, K. A. Müller, “Possible highTc superconductivity in the Ba-La-Cu-O system”, *Z. Phys. B Con. Mat.* **1986**, 64, 189–193, DOI 10.1007/BF01303701.
- [75] W. Eerenstein, N. D. Mathur, J. F. Scott, “Multiferroic and magnetoelectric materials”, *Nature* **2006**, 442, 759–765, DOI 10.1038/nature05023.
- [76] G. H. Jonker, J. H. van Santen, “Ferromagnetic compounds of manganese with perovskite structure”, *Physica* **1950**, 16, 337–349, DOI 10.1016/0031-8914(50)90033-4.
- [77] J. M. D. Coey, M. Viret, S. von Molnár, “Mixed-valence manganites”, *Adv. Phys.* **1999**, 48, 167–293, DOI 10.1080/000187399243455.
- [78] B. Saparov, D. B. Mitzi, “Organic-Inorganic Perovskites: Structural Versatility for Functional Materials Design”, *Chem. Rev.* **2016**, 116, 4558–4596, DOI 10.1021/acs.chemrev.5b00715.
- [79] V. M. Goldschmidt, “Die Gesetze der Krystallochemie”, *Naturwissenschaften* **1926**, 14, 477–485, DOI 10.1007/BF01507527.
- [80] H. D. Megaw, “Crystal Structure of Barium Titanate”, *Nature* **1945**, 155, 484–485, DOI 10.1038/155484b0.
- [81] S. Miyake, R. Ueda, “On Polymorphic Change of BaTiO<sub>3</sub>”, *J. Phys. Soc. Jpn.* **1946**, 1, 32–33, DOI 10.1143/JPSJ.1.32.
- [82] G. H. Haertling, “Ferroelectric Ceramics: History and Technology”, *J. Am. Ceram. Soc.* **1999**, 82, 797–818, DOI 10.1111/j.1151-2916.1999.tb01840.x.
- [83] A. von Hippel, “Ferroelectricity, Domain Structure, and Phase Transitions of Barium Titanate”, *Rev. Mod. Phys.* **1950**, 22.
- [84] M. Acosta, N. Novak, V. Rojas, S. Patel, R. Vaish, J. Koruza, G. A. Rossetti, J. Rödel, “BaTiO<sub>3</sub>-based piezoelectrics: Fundamentals, current status, and perspectives”, *Appl. Phys. Rev.* **2017**, 4, 041305, DOI 10.1063/1.4990046.
- [85] H. F. Kay, P. Vousden, “XCV. Symmetry changes in barium titanate at low temperatures and their relation to its ferroelectric properties”, *Philos. Mag.* **1949**, 40, 1019–1040, DOI 10.1080/14786444908561371.
- [86] R. H. Buttner, E. N. Maslen, “Electron difference density and structural parameters in CaTiO<sub>3</sub>”, *Acta Cryst. B* **1992**, 48, 644–649, DOI 10.1107/S0108768192004592.
- [87] R. H. Buttner, E. N. Maslen, “Structural parameters and electron difference density in BaTiO<sub>3</sub>”, *Acta Cryst. B* **1992**, 48, 764–769, DOI 10.1107/S010876819200510X.
- [88] A. M. Glazer, “The classification of tilted octahedra in perovskites”, *Acta Cryst. B* **1972**, 28, 3384–3392, DOI 10.1107/S0567740872007976.

- [89] C. J. Howard, H. T. Stokes, “Group-Theoretical Analysis of Octahedral Tilting in Perovskites”, *Acta Cryst. B* **1998**, *54*, 782–789, DOI 10.1107/S0108768198004200.
- [90] M. Becker, T. Klüner, M. Wark, “Formation of hybrid ABX<sub>3</sub> perovskite compounds for solar cell application: First-principles calculations of effective ionic radii and determination of tolerance factors”, *Dalton Trans.* **2017**, *46*, 3500–3509, DOI 10.1039/c6dt04796c.
- [91] C. Liang, D. Zhao, Y. Li, X. Li, S. Peng, G. Shao, G. Xing, “Ruddlesden-Popper Perovskite for Stable Solar Cells”, *Energy Environ. Mater.* **2018**, *1*, 221–231, DOI 10.1002/eem2.12022.
- [92] F. Arabpour Roghabadi, M. Alidaei, S. M. Mousavi, T. Ashjari, A. S. Tehrani, V. Ahmadi, S. M. Sadrameli, “Stability progress of perovskite solar cells dependent on the crystalline structure: From 3D ABX<sub>3</sub> to 2D Ruddlesden–Popper perovskite absorbers”, *J. Mater. Chem. A* **2019**, *7*, 5898–5933, DOI 10.1039/C8TA10444A.
- [93] P. Huang, S. Kazim, M. Wang, S. Ahmad, “Toward Phase Stability: Dion–Jacobson Layered Perovskite for Solar Cells”, *ACS Energy Lett.* **2019**, *4*, 2960–2974, DOI 10.1021/acsenenergylett.9b02063.
- [94] A. E. Fedorovskiy, N. A. Drigo, M. K. Nazeeruddin, “The Role of Goldschmidt’s Tolerance Factor in the Formation of A<sub>2</sub>BX<sub>6</sub> Double Halide Perovskites and its Optimal Range”, *Small Methods* **2020**, *4*, 1900426, DOI 10.1002/smt.d.201900426.
- [95] *Hybrid materials: Synthesis, characterization, and applications*, 1. ed., 2. reprint, (Ed.: G. Kickelbick), Wiley-VCH, Weinheim, **2008**.
- [96] C. C. Stoumpos, M. G. Kanatzidis, “The Renaissance of Halide Perovskites and Their Evolution as Emerging Semiconductors”, *Acc. Chem. Res.* **2015**, *48*, 2791–2802, DOI 10.1021/acs.accounts.5b00229.
- [97] A. Kojima, K. Teshima, Y. Shirai, T. Miyasaka, “Organometal halide perovskites as visible-light sensitizers for photovoltaic cells”, *J. Am. Chem. Soc.* **2009**, *131*, 6050–6051, DOI 10.1021/ja809598r.
- [98] S. Pang, H. Hu, J. Zhang, S. Lv, Y. Yu, F. Wei, T. Qin, H. Xu, Z. Liu, G. Cui, “NH<sub>2</sub>CH=NH<sub>2</sub>PbI<sub>3</sub>: An Alternative Organolead Iodide Perovskite Sensitizer for Mesoscopic Solar Cells”, *Chem. Mater.* **2014**, *26*, 1485–1491, DOI 10.1021/cm404006p.
- [99] J.-W. Lee, D.-J. Seol, A.-N. Cho, N.-G. Park, “High-efficiency perovskite solar cells based on the black polymorph of HC(NH<sub>2</sub>)<sub>2</sub>PbI<sub>3</sub>”, *Adv. Mater.* **2014**, *26*, 4991–4998, DOI 10.1002/adma.201401137.
- [100] D. Weber, “CH<sub>3</sub>NH<sub>3</sub>PbX<sub>3</sub>, ein Pb(II)-System mit kubischer Perowskitstruktur”, *Z. Naturforsch. B* **1978**, *33*, 1443–1445, DOI 10.1515/znb-1978-1214.

- 
- [101] T. M. Brenner, D. A. Egger, L. Kronik, G. Hodes, D. Cahen, “Hybrid organic-inorganic perovskites: low-cost semiconductors with intriguing charge-transport properties”, *Nat. Rev. Mater.* **2016**, *1*, 4180, DOI 10.1038/natrevmats.2015.7.
- [102] C. W. Myung, J. Yun, G. Lee, K. S. Kim, “A New Perspective on the Role of A-Site Cations in Perovskite Solar Cells”, *Adv. Energy Mater.* **2018**, *8*, 1702898, DOI 10.1002/aenm.201702898.
- [103] K. Chen, S. Schünemann, S. Song, H. Tüysüz, “Structural effects on optoelectronic properties of halide perovskites”, *Chem. Soc. Rev.* **2018**, *47*, 7045–7077, DOI 10.1039/C8CS00212F.
- [104] J. Breternitz, S. Schorr, “What Defines a Perovskite?”, *Adv. Energy Mater.* **2018**, *8*, 1802366, DOI 10.1002/aenm.201802366.
- [105] N. Mercier, “Hybrid Halide Perovskites: Discussions on Terminology and Materials”, *Angew. Chem. Int. Ed.* **2019**, *58*, 17912–17917, DOI 10.1002/anie.201909601.
- [106] Q. A. Akkerman, L. Manna, “What Defines a Halide Perovskite?”, *ACS Energy Lett.* **2020**, *5*, 604–610, DOI 10.1021/acsenergylett.0c00039.
- [107] M. Maćzka, A. Ciupa, A. Gaĝor, A. Sieradzki, A. Pikul, B. Macalik, M. Drozd, “Perovskite metal formate framework of  $\text{NH}_2\text{-CH(+)NH}_2\text{Mn(HCOO)}_3$ : phase transition, magnetic, dielectric, and phonon properties”, *Inorg. Chem.* **2014**, *53*, 5260–5268, DOI 10.1021/ic500479e.
- [108] J.-H. Her, P. W. Stephens, C. M. Kareis, J. G. Moore, K. S. Min, J.-W. Park, G. Bali, B. S. Kennon, J. S. Miller, “Anomalous non-Prussian blue structures and magnetic ordering of  $\text{K}_2\text{Mn(II)Mn(II)(CN)}_6$  and  $\text{Rb}_2\text{Mn(II)Mn(II)(CN)}_6$ ”, *Inorg. Chem.* **2010**, *49*, 1524–1534, DOI 10.1021/ic901903f.
- [109] Y. Wu, S. Shaker, F. Brivio, R. Murugavel, P. D. Bristowe, A. K. Cheetham, “Am  $\text{Mn(H}_2\text{POO)}_3$ : A New Family of Hybrid Perovskites Based on the Hypophosphite Ligand”, *J. Am. Chem. Soc.* **2017**, *139*, 16999–17002, DOI 10.1021/jacs.7b09417.
- [110] J. A. Schlueter, J. L. Manson, U. Geiser, “Structural and magnetic diversity in tetraalkylammonium salts of anionic  $\text{M[N(CN)}_2\text{]}_3^-$  ( $\text{M} = \text{Mn}$  and  $\text{Ni}$ ) three-dimensional coordination polymers”, *Inorg. Chem.* **2005**, *44*, 3194–3202, DOI 10.1021/ic0484598.
- [111] J. García-Ben, L. N. McHugh, T. D. Bennett, J. M. Bermúdez-García, “Dicyanamide-perovskites at the edge of dense hybrid organic–inorganic materials”, *Coord. Chem. Rev.* **2022**, *455*, 214337, DOI 10.1016/j.ccr.2021.214337.
- [112] G. Kieslich, S. Sun, A. K. Cheetham, “Solid-state principles applied to organic–inorganic perovskites: New tricks for an old dog”, *Chem. Sci.* **2014**, *5*, 4712–4715, DOI 10.1039/C4SC02211D.

- [113] G. Kieslich, S. Sun, A. K. Cheetham, “An extended Tolerance Factor approach for organic-inorganic perovskites”, *Chem. Sci.* **2015**, *6*, 3430–3433, DOI 10.1039/c5sc00961h.
- [114] E. K. Al-Shakarchi, N. B. Mahmood, “Three Techniques Used to Produce BaTiO<sub>3</sub> Fine Powder”, *J. Mod. Phys.* **2011**, *02*, 1420–1428, DOI 10.4236/jmp.2011.211175.
- [115] M.-L. Tong, J. Ru, Y.-M. Wu, X.-M. Chen, H.-C. Chang, K. Mochizuki, S. Kitagawa, “Cation-templated construction of three-dimensional a-Po cubic-type [M(dca)<sub>3</sub>]-networks. Syntheses, structures and magnetic properties of A[M(dca)<sub>3</sub>] (dca = dicyanamide; for A = benzyltributylammonium, M = Mn<sup>2+</sup>, Co<sup>2+</sup>; for A = benzyltriethylammonium, M = Mn<sup>2+</sup>, Fe<sup>2+</sup>)”, *New J. Chem.* **2003**, *27*, 779–782, DOI 10.1039/B300760J.
- [116] W.-J. Xu, Z.-Y. Du, W.-X. Zhang, X.-M. Chen, “Structural phase transitions in perovskite compounds based on diatomic or multiatomic bridges”, *CrystEngComm* **2016**, *18*, 7915–7928, DOI 10.1039/C6CE01485B.
- [117] M. M. Lee, J. Teuscher, T. Miyasaka, T. N. Murakami, H. J. Snaith, “Efficient hybrid solar cells based on meso-superstructured organometal halide perovskites”, *Science* **2012**, *338*, 643–647, DOI 10.1126/science.1228604.
- [118] N. Pellet, P. Gao, G. Gregori, T.-Y. Yang, M. K. Nazeeruddin, J. Maier, M. Grätzel, “Mixed-organic-cation perovskite photovoltaics for enhanced solar-light harvesting”, *Angew. Chem. Int. Ed.* **2014**, *53*, 3151–3157, DOI 10.1002/anie.201309361.
- [119] M. Saliba, J.-P. Correa-Baena, M. Grätzel, A. Hagfeldt, A. Abate, “Perovskite Solar Cells: From the Atomic Level to Film Quality and Device Performance”, *Angew. Chem. Int. Ed.* **2018**, *57*, 2554–2569, DOI 10.1002/anie.201703226.
- [120] K. O. Brinkmann et al., “Perovskite-organic tandem solar cells with indium oxide interconnect”, *Nature* **2022**, *604*, 280–286, DOI 10.1038/s41586-022-04455-0.
- [121] K. Yoshikawa, H. Kawasaki, W. Yoshida, T. Irie, K. Konishi, K. Nakano, T. Uto, D. Adachi, M. Kanematsu, H. Uzu, K. Yamamoto, “Silicon heterojunction solar cell with interdigitated back contacts for a photoconversion efficiency over 26%”, *Nat. Energy* **2017**, *2*, 17032, DOI 10.1038/nenergy.2017.32.
- [122] J. Berry et al., “Hybrid Organic-Inorganic Perovskites (HOIPs): Opportunities and Challenges”, *Adv. Mater.* **2015**, *27*, 5102–5112, DOI 10.1002/adma.201502294.
- [123] D. A. Egger, A. M. Rappe, L. Kronik, “Hybrid Organic-Inorganic Perovskites on the Move”, *Acc. Chem. Res.* **2016**, *49*, 573–581, DOI 10.1021/acs.accounts.5b00540.
- [124] S. D. Stranks, G. E. Eperon, G. Grancini, C. Menelaou, M. J. P. Alcocer, T. Leijtens, L. M. Herz, A. Petrozza, H. J. Snaith, “Electron-hole diffusion lengths exceeding 1 micrometer in an organometal trihalide perovskite absorber”, *Science* **2013**, *342*, 341–344, DOI 10.1126/science.1243982.

- 
- [125] C. C. Stoumpos, C. D. Malliakas, M. G. Kanatzidis, “Semiconducting tin and lead iodide perovskites with organic cations: Phase transitions, high mobilities, and near-infrared photoluminescent properties”, *Inorg. Chem.* **2013**, *52*, 9019–9038, DOI 10.1021/ic401215x.
- [126] G. E. Eperon, S. D. Stranks, C. Menelaou, M. B. Johnston, L. M. Herz, H. J. Snaith, “Formamidinium lead trihalide: A broadly tunable perovskite for efficient planar heterojunction solar cells”, *Energy & Environmental Science* **2014**, *7*, 982, DOI 10.1039/c3ee43822h.
- [127] J. Breternitz, F. Lehmann, S. A. Barnett, H. Nowell, S. Schorr, “Role of the Iodide-Methylammonium Interaction in the Ferroelectricity of  $\text{CH}_3\text{NH}_3\text{PbI}_3$ ”, *Angew. Chem. Int. Ed.* **2020**, *59*, 424–428, DOI 10.1002/anie.201910599.
- [128] W. Li, A. Thirumurugan, P. T. Barton, Z. Lin, S. Henke, H. H.-M. Yeung, M. T. Wharmby, E. G. Bithell, C. J. Howard, A. K. Cheetham, “Mechanical tunability via hydrogen bonding in metal-organic frameworks with the perovskite architecture”, *J. Am. Chem. Soc.* **2014**, *136*, 7801–7804, DOI 10.1021/ja500618z.
- [129] F. El-Mellouhi, A. Marzouk, E. T. Bentría, S. N. Rashkeev, S. Kais, F. H. Alharbi, “Hydrogen Bonding and Stability of Hybrid Organic-Inorganic Perovskites”, *ChemSusChem* **2016**, *9*, 2648–2655, DOI 10.1002/cssc.201600864.
- [130] G. Kieslich, A. C. Forse, S. Sun, K. T. Butler, S. Kumagai, Y. Wu, M. R. Warren, A. Walsh, C. P. Grey, A. K. Cheetham, “Role of Amine–Cavity Interactions in Determining the Structure and Mechanical Properties of the Ferroelectric Hybrid Perovskite  $[\text{NH}_3\text{NH}_2]\text{Zn}(\text{HCOO})_3$ ”, *Chem. Mater.* **2016**, *28*, 312–317, DOI 10.1021/acs.chemmater.5b04143.
- [131] K. L. Svane, A. C. Forse, C. P. Grey, G. Kieslich, A. K. Cheetham, A. Walsh, K. T. Butler, “How Strong Is the Hydrogen Bond in Hybrid Perovskites?”, *J. Phys. Chem. Lett.* **2017**, *8*, 6154–6159, DOI 10.1021/acs.jpcclett.7b03106.
- [132] H. L. B. Boström, J. A. Hill, A. L. Goodwin, “Columnar shifts as symmetry-breaking degrees of freedom in molecular perovskites”, *Phys. Chem. Chem. Phys.* **2016**, *18*, 31881–31894, DOI 10.1039/c6cp05730f.
- [133] J.-H. Lee, N. C. Bristowe, J. H. Lee, S.-H. Lee, P. D. Bristowe, A. K. Cheetham, H. M. Jang, “Resolving the Physical Origin of Octahedral Tilting in Halide Perovskites”, *Chem. Mater.* **2016**, *28*, 4259–4266, DOI 10.1021/acs.chemmater.6b00968.
- [134] N. L. Evans, P. M. M. Thygesen, H. L. B. Boström, E. M. Reynolds, I. E. Collings, A. E. Phillips, A. L. Goodwin, “Control of Multipolar and Orbital Order in Perovskite-like  $\text{C}(\text{NH}_2)_3\text{CuxCd}_{1-x}(\text{HCOO})_3$  Metal-Organic Frameworks”, *J. Am. Chem. Soc.* **2016**, *138*, 9393–9396, DOI 10.1021/jacs.6b05208.
- [135] H. L. B. Boström, “Tilts and shifts in molecular perovskites”, *CrystEngComm* **2020**, *22*, 961–968, DOI 10.1039/C9CE01950B.

- [136] R. M. Hazen, L. W. Finger, *Comparative crystal chemistry. Temperature, pressure, composition and the variation of crystal structure*, John Wiley & Sons, Chichester, **1982**.
- [137] J. S. O. Evans, “Negative thermal expansion materials”, *J. Chem. Soc., Dalton Trans.* **1999**, 3317–3326, DOI 10.1039/A904297K.
- [138] J. Chen, L. Hu, J. Deng, X. Xing, “Negative thermal expansion in functional materials: controllable thermal expansion by chemical modifications”, *Chem. Soc. Rev.* **2015**, *44*, 3522–3567, DOI 10.1039/C4CS00461B.
- [139] Baughman, Stafstrom, Cui, Dantas, “Materials with negative compressibilities in one or more dimensions”, *Science* **1998**, *279*, 1522–1524, DOI 10.1126/science.279.5356.1522.
- [140] A. B. Cairns, A. L. Goodwin, “Negative linear compressibility”, *Phys. Chem. Chem. Phys.* **2015**, *17*, 20449–20465, DOI 10.1039/C5CP00442J.
- [141] C. Kittel, *Introduction to solid state physics*, 9th edition, Wiley, Hoboken, NJ, **2018**.
- [142] C. S. Coates, A. L. Goodwin, “How to quantify isotropic negative thermal expansion: magnitude, range, or both?”, *Mater. Horiz.* **2019**, *6*, 211–218, DOI 10.1039/C8MH01065J.
- [143] M. T. Dove, H. Fang, “Negative thermal expansion and associated anomalous physical properties: review of the lattice dynamics theoretical foundation”, *Rep. Prog. Phys.* **2016**, *79*, 066503, DOI 10.1088/0034-4885/79/6/066503.
- [144] K. Röttger, A. Endriss, J. Ihringer, S. Doyle, W. F. Kuhs, “Lattice constants and thermal expansion of H<sub>2</sub>O and D<sub>2</sub>O ice Ih between 10 and 265 K”, *Acta Cryst. B* **1994**, *50*, 644–648, DOI 10.1107/S0108768194004933.
- [145] L. Huang, J. Kieffer, “Structural origin of negative thermal expansion in high-temperature silica polymorphs”, *Phys. Rev. Lett.* **2005**, *95*, 215901, DOI 10.1103/PhysRevLett.95.215901.
- [146] B. K. Greve, K. L. Martin, P. L. Lee, P. J. Chupas, K. W. Chapman, A. P. Wilkinson, “Pronounced negative thermal expansion from a simple structure: cubic ScF<sub>3</sub>”, *J. Am. Chem. Soc.* **2010**, *132*, 15496–15498, DOI 10.1021/ja106711v.
- [147] T. A. Mary, J. S. O. Evans, T. Vogt, A. W. Sleight, “Negative Thermal Expansion from 0.3 to 1050 Kelvin in ZrW<sub>2</sub>O<sub>8</sub>”, *Science* **1996**, *272*, 90–92, DOI 10.1126/science.272.5258.90.
- [148] P. W. Bridgman, “The Compressibility of Metals at High Pressures”, *Proc. Natl. Acad. Sci. USA* **1922**, *8*, 361–365, DOI 10.1073/pnas.8.12.361.
- [149] K. Takenaka, “Negative thermal expansion materials: technological key for control of thermal expansion”, *Sci. Technol. Adv. Mater.* **2012**, *13*, 013001, DOI 10.1088/1468-6996/13/1/013001.

- 
- [150] F.-X. Coudert, “Responsive Metal–Organic Frameworks and Framework Materials: Under Pressure, Taking the Heat, in the Spotlight, with Friends”, *Chem. Mater.* **2015**, *27*, 1905–1916, DOI 10.1021/acs.chemmater.5b00046.
- [151] C. Schneider, D. Bodesheim, M. G. Ehrenreich, V. Crocellà, J. Mink, R. A. Fischer, K. T. Butler, G. Kieslich, “Tuning the Negative Thermal Expansion Behavior of the Metal–Organic Framework Cu<sub>3</sub>BTC<sub>2</sub> by Retrofitting”, *J. Am. Chem. Soc.* **2019**, *141*, 10504–10509, DOI 10.1021/jacs.9b04755.
- [152] C. Schneider, D. Bodesheim, J. Keupp, R. Schmid, G. Kieslich, “Retrofitting metal–organic frameworks”, *Nat. Commun.* **2019**, *10*, 4921, DOI 10.1038/s41467-019-12876-1.
- [153] W. Miller, C. W. Smith, D. S. Mackenzie, K. E. Evans, “Negative thermal expansion: a review”, *J. Mater. Sci.* **2009**, *44*, 5441–5451, DOI 10.1007/s10853-009-3692-4.
- [154] K. de Boer, Jansen, R. A. van Santen, “Structure-stability relationships for all-silica structures”, *Phys. Rev. B* **1995**, *52*, 12579–12590, DOI 10.1103/PhysRevB.52.12579.
- [155] G. D. Gatta, P. Lotti, G. Tabacchi, “The effect of pressure on open-framework silicates: elastic behaviour and crystal–fluid interaction”, *Phys. Chem. Minerals* **2018**, *45*, 115–138, DOI 10.1007/s00269-017-0916-z.
- [156] M. T. Dove, “Flexibility of network materials and the Rigid Unit Mode model: a personal perspective”, *Phil. Trans. R. Soc. A* **2019**, *377*, 20180222, DOI 10.1098/rsta.2018.0222.
- [157] A. P. Giddy, M. T. Dove, G. S. Pawley, V. Heine, “The determination of rigid-unit modes as potential soft modes for displacive phase transitions in framework crystal structures”, *Acta Cryst. A* **1993**, *49*, 697–703, DOI 10.1107/S0108767393002545.
- [158] J. Tao, A. Sleight, “The role of rigid unit modes in negative thermal expansion”, *J. Solid State Chem.* **2003**, *173*, 442–448, DOI 10.1016/S0022-4596(03)00140-3.
- [159] K. W. Chapman, P. J. Chupas, C. J. Kepert, “Direct observation of a transverse vibrational mechanism for negative thermal expansion in Zn(CN)<sub>2</sub>: an atomic pair distribution function analysis”, *J. Am. Chem. Soc.* **2005**, *127*, 15630–15636, DOI 10.1021/ja055197f.
- [160] D. Dubbeldam, K. S. Walton, D. E. Ellis, R. Q. Snurr, “Exceptional negative thermal expansion in isorecticular metal–organic frameworks”, *Angew. Chem. Int. Ed.* **2007**, *46*, 4496–4499, DOI 10.1002/anie.200700218.
- [161] S. S. Han, W. A. Goddard, “Metal–Organic Frameworks Provide Large Negative Thermal Expansion Behavior”, *J. Phys. Chem. C* **2007**, *111*, 15185–15191, DOI 10.1021/jp075389s.

- [162] Y. Wu, A. Kobayashi, G. J. Halder, V. K. Peterson, K. W. Chapman, N. Lock, P. D. Southon, C. J. Kepert, “Negative thermal expansion in the metal-organic framework material  $\text{Cu}_3(1,3,5\text{-benzenetricarboxylate})_2$ ”, *Angew. Chem. Int. Ed.* **2008**, *47*, 8929–8932, DOI 10.1002/anie.200803925.
- [163] N. Lock, Y. Wu, M. Christensen, L. J. Cameron, V. K. Peterson, A. J. Bridgeman, C. J. Kepert, B. B. Iversen, “Elucidating Negative Thermal Expansion in MOF-5”, *J. Phys. Chem. C* **2010**, *114*, 16181–16186, DOI 10.1021/jp103212z.
- [164] M. J. Cliffe, J. A. Hill, C. A. Murray, F.-X. Coudert, A. L. Goodwin, “Defect-dependent colossal negative thermal expansion in UiO-66(Hf) metal-organic framework”, *Phys. Chem. Chem. Phys.* **2015**, *17*, 11586–11592, DOI 10.1039/C5CP01307K.
- [165] J. D. Evans, J. P. Dürholt, S. Kaskel, R. Schmid, “Assessing negative thermal expansion in mesoporous metal–organic frameworks by molecular simulation”, *J. Mater. Chem. A* **2019**, *7*, 24019–24026, DOI 10.1039/C9TA06644F.
- [166] J. P. Attfield, “Mechanisms and Materials for NTE”, *Front. Chem.* **2018**, *6*, 371, DOI 10.3389/fchem.2018.00371.
- [167] I. Yamada, K. Tsuchida, K. Ohgushi, N. Hayashi, J. Kim, N. Tsuji, R. Takahashi, M. Matsushita, N. Nishiyama, T. Inoue, T. Irifune, K. Kato, M. Takata, M. Takano, “Giant negative thermal expansion in the iron perovskite  $\text{SrCu}_3\text{Fe}_4\text{O}_{12}$ ”, *Angew. Chem. Int. Ed.* **2011**, *50*, 6579–6582, DOI 10.1002/anie.201102228.
- [168] Y. W. Long, N. Hayashi, T. Saito, M. Azuma, S. Muranaka, Y. Shimakawa, “Temperature-induced A-B intersite charge transfer in an A-site-ordered  $\text{LaCu}_3\text{Fe}_4\text{O}_{12}$  perovskite”, *Nature* **2009**, *458*, 60–63, DOI 10.1038/nature07816.
- [169] G. Hausch, “Magnetovolume effects in invar alloys: Spontaneous and forced volume magnetostriction”, *Phys. Stat. Sol. (a)* **1973**, *18*, 735–740, DOI 10.1002/pssa.2210180236.
- [170] B. Y. Qu, B. C. Pan, “Nature of the negative thermal expansion in antiperovskite compound  $\text{Mn}_3\text{ZnN}$ ”, *J. Appl. Phys.* **2010**, *108*, 113920, DOI 10.1063/1.3517824.
- [171] K. Kodama, S. Iikubo, K. Takenaka, M. Takigawa, H. Takagi, S. Shamoto, “Gradual development of 5g antiferromagnetic moment in the giant negative thermal expansion material  $\text{Mn}_3\text{Cu}_{1-x}\text{GexN}$  ( $x\sim 0.5$ )”, *Phys. Rev. B* **2010**, *81*, 81, DOI 10.1103/PhysRevB.81.224419.
- [172] T. Hamada, K. Takenaka, “Giant negative thermal expansion in antiperovskite manganese nitrides”, *J. Appl. Phys.* **2011**, *109*, 07E309, DOI 10.1063/1.3540604.
- [173] Y. Sun, C. Wang, Q. Huang, Y. Guo, L. Chu, M. Arai, K. Yamaura, “Neutron diffraction study of unusual phase separation in the antiperovskite nitride  $\text{Mn}_3\text{ZnN}$ ”, *Inorg. Chem.* **2012**, *51*, 7232–7236, DOI 10.1021/ic300978x.



- 
- [174] Z. Liu, Q. Gao, J. Chen, J. Deng, K. Lin, X. Xing, “Negative thermal expansion in molecular materials”, *Chem. Commun.* **2018**, *54*, 5164–5176, DOI 10.1039/C8CC01153B.
- [175] P. Kuad, A. Miyawaki, Y. Takashima, H. Yamaguchi, A. Harada, “External stimulus-responsive supramolecular structures formed by a stilbene cyclodextrin dimer”, *J. Am. Chem. Soc.* **2007**, *129*, 12630–12631, DOI 10.1021/ja075139p.
- [176] S. Wannapaiboon, A. Schneemann, I. Hante, M. Tu, K. Epp, A. L. Semrau, C. Sterne-  
mann, M. Paulus, S. J. Baxter, G. Kieslich, R. A. Fischer, “Control of structural flexibility of layered-pillared metal-organic frameworks anchored at surfaces”, *Nat. Commun.* **2019**, *10*, 346, DOI 10.1038/s41467-018-08285-5.
- [177] P. Vervoorts, J. Keupp, A. Schneemann, C. L. Hobday, D. Daisenberger, R. A. Fischer, R. Schmid, G. Kieslich, “Configurational Entropy Driven High-Pressure Behaviour of a Flexible Metal-Organic Framework (MOF)”, *Angew. Chem. Int. Ed.* **2021**, *60*, 787–793, DOI 10.1002/anie.202011004.
- [178] J. C. Tan, A. K. Cheetham, “Mechanical properties of hybrid inorganic-organic framework materials: establishing fundamental structure-property relationships”, *Chem. Soc. Rev.* **2011**, *40*, 1059–1080, DOI 10.1039/C0CS00163E.
- [179] W. Li, S. Henke, A. K. Cheetham, “Research Update: Mechanical properties of metal-organic frameworks – Influence of structure and chemical bonding”, *APL Mater.* **2014**, *2*, 123902, DOI 10.1063/1.4904966.
- [180] A. B. Cairns, A. L. Goodwin, “Structural disorder in molecular framework materials”, *Chem. Soc. Rev.* **2013**, *42*, 4881–4893, DOI 10.1039/C3CS35524A.
- [181] C. L. Hobday, G. Kieslich, “Structural flexibility in crystalline coordination polymers: a journey along the underlying free energy landscape”, *Dalton Trans.* **2021**, *50*, 3759–3768, DOI 10.1039/D0DT04329J.
- [182] L. Wang, H. Luo, S. Deng, Y. Sun, C. Wang, “Uniaxial Negative Thermal Expansion, Negative Linear Compressibility, and Negative Poisson’s Ratio Induced by Specific Topology in ZnAu(CN)<sub>2</sub>”, *Inorg. Chem.* **2017**, *56*, 15101–15109, DOI 10.1021/acs.inorgchem.7b02416.
- [183] G. D. Barrera, J. A. O. Bruno, T. H. K. Barron, N. L. Allan, “Negative thermal expansion”, *J. Phys.: Condens. Matter* **2005**, *17*, R217–R252, DOI 10.1088/0953-8984/17/4/R03.
- [184] S. Zięba, A. Gzella, A. T. Dubis, A. Łapiński, “Combination of Negative, Positive, and Near-Zero Thermal Expansion in Bis(imidazolium) Terephthalate with a Helical Hydrogen-Bonded Network”, *Cryst. Growth Des.* **2021**, *21*, 3838–3849, DOI 10.1021/acs.cgd.1c00167.

- [185] A. L. Goodwin, D. A. Keen, M. G. Tucker, “Large negative linear compressibility of  $\text{Ag}_3\text{Co}(\text{CN})_6$ ”, *Proc. Natl. Acad. Sci. USA* **2008**, *105*, 18708–18713, DOI 10.1073/pnas.0804789105.
- [186] A. L. Goodwin, M. Calleja, M. J. Conterio, M. T. Dove, J. S. O. Evans, D. A. Keen, L. Peters, M. G. Tucker, “Colossal positive and negative thermal expansion in the framework material  $\text{Ag}_3\text{Co}(\text{CN})_6$ ”, *Science* **2008**, *319*, 794–797, DOI 10.1126/science.1151442.
- [187] A. L. Goodwin, B. J. Kennedy, C. J. Kepert, “Thermal expansion matching via framework flexibility in zinc dicyanometallates”, *J. Am. Chem. Soc.* **2009**, *131*, 6334–6335, DOI 10.1021/ja901355b.
- [188] A. B. Cairns, J. Catafesta, C. Levelut, J. Rouquette, A. van der Lee, L. Peters, A. L. Thompson, V. Dmitriev, J. Haines, A. L. Goodwin, “Giant negative linear compressibility in zinc dicyanoaurate”, *Nat. Mater.* **2013**, *12*, 212–216, DOI 10.1038/nmat3551.
- [189] Q. Zeng, K. Wang, B. Zou, “Large Negative Linear Compressibility in  $\text{InH}(\text{BDC})_2$  from Framework Hinging”, *J. Am. Chem. Soc.* **2017**, *139*, 15648–15651, DOI 10.1021/jacs.7b10292.
- [190] W. Li, M. R. Probert, M. Kosa, T. D. Bennett, A. Thirumurugan, R. P. Burwood, M. Parinello, J. A. K. Howard, A. K. Cheetham, “Negative linear compressibility of a metal-organic framework”, *J. Am. Chem. Soc.* **2012**, *134*, 11940–11943, DOI 10.1021/ja305196u.
- [191] I. E. Collings, M. Bykov, E. Bykova, M. G. Tucker, S. Petitgirard, M. Hanfland, K. Glazyrin, S. van Smaalen, A. L. Goodwin, L. Dubrovinsky, N. Dubrovinskaia, “Structural distortions in the high-pressure polar phases of ammonium metal formates”, *CrystEngComm* **2016**, *18*, 8849–8857, DOI 10.1039/C6CE01891B.
- [192] H. J. Shepherd, T. Palamarciuc, P. Rosa, P. Guionneau, G. Molnár, J.-F. Létard, A. Bousseksou, “Antagonism between extreme negative linear compression and spin crossover in  $\text{Fe}(\text{dpp})_2(\text{NCS})_2 \cdot \text{py}$ ”, *Angew. Chem. Int. Ed.* **2012**, *51*, 3910–3914, DOI 10.1002/anie.201108919.
- [193] L. Petters, S. Burger, S. Kronawitter, M. Drees, G. Kieslich, “Linear negative thermal expansion in  $\text{Pd}(\text{acac})_2$ ”, *CrystEngComm* **2021**, *23*, 5425–5429, DOI 10.1039/D1CE00534K.
- [194] L. Vanduyfhuys, S. M. J. Rogge, J. Wieme, S. Vandenbrande, G. Maurin, M. Waroquier, V. van Speybroeck, “Thermodynamic insight into stimuli-responsive behaviour of soft porous crystals”, *Nat. Commun.* **2018**, *9*, 204, DOI 10.1038/s41467-017-02666-y.
- [195] E. M. Reynolds, E. H. Wolpert, A. R. Overy, L. Mizzi, A. Simonov, J. N. Grima, S. Kaskel, A. L. Goodwin, “Function from configurational degeneracy in disordered framework materials”, *Faraday Discuss.* **2021**, *225*, 241–254, DOI 10.1039/D0FD00008F.

- 
- [196] T. D. Bennett, P. Simoncic, S. A. Moggach, F. Gozzo, P. Macchi, D. A. Keen, J.-C. Tan, A. K. Cheetham, “Reversible pressure-induced amorphization of a zeolitic imidazolate framework (ZIF-4)”, *Chem. Commun.* **2011**, 47, 7983–7985, DOI 10.1039/C1CC11985K.
- [197] W. Cai, A. Katrusiak, “Giant negative linear compression positively coupled to massive thermal expansion in a metal-organic framework”, *Nat. Commun.* **2014**, 5, 4337, DOI 10.1038/ncomms5337.
- [198] A. Clearfield, “Flexible MOFs under stress: pressure and temperature”, *Dalton Trans.* **2016**, 45, 4100–4112, DOI 10.1039/C5DT03228H.
- [199] A. J. Graham, D. R. Allan, A. Muszkiewicz, C. A. Morrison, S. A. Moggach, “The effect of high pressure on MOF-5: guest-induced modification of pore size and content at high pressure”, *Angew. Chem. Int. Ed.* **2011**, 50, 11138–11141, DOI 10.1002/anie.201104285.
- [200] I. Grobler, V. J. Smith, P. M. Bhatt, S. A. Herbert, L. J. Barbour, “Tunable anisotropic thermal expansion of a porous zinc(II) metal-organic framework”, *J. Am. Chem. Soc.* **2013**, 135, 6411–6414, DOI 10.1021/ja401671p.
- [201] S. A. Moggach, T. D. Bennett, A. K. Cheetham, “The effect of pressure on ZIF-8: increasing pore size with pressure and the formation of a high-pressure phase at 1.47 GPa”, *Angew. Chem. Int. Ed.* **2009**, 48, 7087–7089, DOI 10.1002/anie.200902643.
- [202] J. M. Ogborn, I. E. Collings, S. A. Moggach, A. L. Thompson, A. L. Goodwin, “Supramolecular mechanics in a metal–organic framework”, *Chem. Sci.* **2012**, 3, 3011, DOI 10.1039/C2SC20596C.
- [203] Y.-S. Wei, K.-J. Chen, P.-Q. Liao, B.-Y. Zhu, R.-B. Lin, H.-L. Zhou, B.-Y. Wang, W. Xue, J.-P. Zhang, X.-M. Chen, “Turning on the flexibility of isorecticular porous coordination frameworks for drastically tunable framework breathing and thermal expansion”, *Chem. Sci.* **2013**, 4, 1539, DOI 10.1039/C3SC22222E.
- [204] P. G. Yot, Q. Ma, J. Haines, Q. Yang, A. Ghoufi, T. Devic, C. Serre, V. Dmitriev, G. Férey, C. Zhong, G. Maurin, “Large breathing of the MOF MIL-47(VIV) under mechanical pressure: a joint experimental–modelling exploration”, *Chem. Sci.* **2012**, 3, 1100, DOI 10.1039/C2SC00745B.
- [205] S. Henke, A. Schneemann, R. A. Fischer, “Massive Anisotropic Thermal Expansion and Thermo-Responsive Breathing in Metal-Organic Frameworks Modulated by Linker Functionalization”, *Adv. Funct. Mater.* **2013**, 23, 5990–5996, DOI 10.1002/adfm.201301256.
- [206] S. J. Baxter, A. Schneemann, A. D. Ready, P. Wijeratne, A. P. Wilkinson, N. C. Burtch, “Tuning Thermal Expansion in Metal-Organic Frameworks Using a Mixed Linker Solid Solution Approach”, *J. Am. Chem. Soc.* **2019**, 141, 12849–12854, DOI 10.1021/jacs.9b06109.

- [207] P. Vervoorts, C. L. Hobday, M. G. Ehrenreich, D. Daisenberger, G. Kieslich, “The Zeolitic Imidazolate Framework ZIF-4 under Low Hydrostatic Pressures”, *Z. anorg. allg. Chem.* **2019**, *645*, 970–974, DOI 10.1002/zaac.201900046.
- [208] I. E. Collings, J. A. Hill, A. B. Cairns, R. I. Cooper, A. L. Thompson, J. E. Parker, C. C. Tang, A. L. Goodwin, “Compositional dependence of anomalous thermal expansion in perovskite-like ABX<sub>3</sub> formates”, *Dalton Trans.* **2016**, *45*, 4169–4178, DOI 10.1039/c5dt03263f.
- [209] L. C. Gómez-Aguirre, B. Pato-Doldán, A. Stroppa, L.-M. Yang, T. Frauenheim, J. Mira, S. Yáñez-Vilar, R. Artiaga, S. Castro-García, M. Sánchez-Andújar, M. A. Señarís-Rodríguez, “Coexistence of Three Ferroic Orders in the Multiferroic Compound (CH<sub>3</sub>)<sub>4</sub>NMn(N<sub>3</sub>)<sub>3</sub> with Perovskite-Like Structure”, *Chem. Eur. J.* **2016**, *22*, 7863–7870, DOI 10.1002/chem.201503445.
- [210] Z. Yang, G. Cai, C. L. Bull, M. G. Tucker, M. T. Dove, A. Friedrich, A. E. Phillips, “Hydrogen-bond-mediated structural variation of metal guanidinium formate hybrid perovskites under pressure”, *Phil. Trans. R. Soc. A* **2019**, *377*, 20180227, DOI 10.1098/rsta.2018.0227.
- [211] H. Gao, C. Li, L. Li, W. Wei, Y. Tan, Y. Tang, “High pressure and elastic properties of a guanidinium-formate hybrid perovskite”, *Dalton Trans.* **2020**, *49*, 7228–7233, DOI 10.1039/C9DT04805G.
- [212] I. E. Collings, M. Bykov, E. Bykova, M. Hanfland, S. van Smaalen, L. Dubrovinsky, N. Dubrovinskaia, “Disorder–order transitions in the perovskite metal–organic frameworks [(CH<sub>3</sub>)<sub>2</sub>NH<sub>2</sub>][M(HCOO)<sub>3</sub>] at high pressure”, *CrystEngComm* **2018**, *20*, 3512–3521, DOI 10.1039/C8CE00617B.
- [213] M. Mączka, M. Kryś, S. Sobczak, D. L. M. Vasconcelos, P. T. C. Freire, A. Katrusiak, “Evidence of Pressure-Induced Phase Transitions and Negative Linear Compressibility in Formamidinium Manganese-Hypophosphite Hybrid Perovskite”, *J. Phys. Chem. C* **2021**, *125*, 26958–26966, DOI 10.1021/acs.jpcc.1c08387.
- [214] M. Mączka, S. Sobczak, M. Kryś, F. F. Leite, W. Paraguassu, A. Katrusiak, “Mechanism of Pressure-Induced Phase Transitions and Structure–Property Relations in Methylhydrazinium Manganese Hypophosphite Perovskites”, *J. Phys. Chem. C* **2021**, *125*, 10121–10129, DOI 10.1021/acs.jpcc.1c01998.
- [215] M. Mączka, I. E. Collings, F. F. Leite, W. Paraguassu, “Raman and single-crystal X-ray diffraction evidence of pressure-induced phase transitions in a perovskite-like framework of (C<sub>3</sub>H<sub>7</sub>)<sub>4</sub>NMn(N(CN)<sub>2</sub>)<sub>3</sub>”, *Dalton Trans.* **2019**, *48*, 9072–9078, DOI 10.1039/c9dt01648a.

- 
- [216] M. Mączka, M. Ptak, A. Gaḡor, A. Sieradzki, P. Peksa, G. Usevicius, M. Simenas, F. F. Leite, W. Paraguassu, “Temperature- and pressure-dependent studies of a highly flexible and compressible perovskite-like cadmium dicyanamide framework templated with protonated tetrapropylamine”, *J. Mater. Chem. C* **2019**, *7*, 2408–2420, DOI 10.1039/C8TC06401F.
- [217] L. R. Redfern, L. Robison, M. C. Wasson, S. Goswami, J. Lyu, T. Islamoglu, K. W. Chapman, O. K. Farha, “Porosity Dependence of Compression and Lattice Rigidity in Metal–Organic Framework Series”, *J. Am. Chem. Soc.* **2019**, *141*, 4365–4371, DOI 10.1021/jacs.8b13009.
- [218] P. G. Yot, K. Yang, V. Guillerm, F. Ragon, V. Dmitriev, P. Parisiades, E. Elkaïm, T. Devic, P. Horcajada, C. Serre, N. Stock, J. P. S. Mowat, P. A. Wright, G. Férey, G. Maurin, “Impact of the Metal Centre and Functionalization on the Mechanical Behaviour of MIL–53 Metal–Organic Frameworks”, *Eur. J. Inorg. Chem.* **2016**, *2016*, 4424–4429, DOI 10.1002/ejic.201600263.
- [219] P. G. Yot, K. Yang, F. Ragon, V. Dmitriev, T. Devic, P. Horcajada, C. Serre, G. Maurin, “Exploration of the mechanical behavior of metal organic frameworks UiO-66(Zr) and MIL-125(Ti) and their NH<sub>2</sub> functionalized versions”, *Dalton Trans.* **2016**, *45*, 4283–4288, DOI 10.1039/C5DT03621F.
- [220] P. Vervoorts, J. Stebani, A. S. J. Méndez, G. Kieslich, “Structural Chemistry of Metal–Organic Frameworks under Hydrostatic Pressures”, *ACS Materials Lett.* **2021**, *3*, 1635–1651, DOI 10.1021/acsmaterialslett.1c00250.
- [221] M. M. Vopson, “Theory of giant-caloric effects in multiferroic materials”, *J. Phys. D: Appl. Phys.* **2013**, *46*, 345304, DOI 10.1088/0022-3727/46/34/345304.
- [222] M. Mączka, A. Gaḡor, M. Ptak, D. Stefańska, L. Macalik, A. Pikul, A. Sieradzki, “Structural, phonon, magnetic and optical properties of novel perovskite-like frameworks of TriBuMeM(dca)<sub>3</sub> (TriBuMe = tributylmethylammonium; dca = dicyanamide; M = Mn<sup>2+</sup>, Fe<sup>2+</sup>, Co<sup>2+</sup>, Ni<sup>2+</sup>)”, *Dalton Trans.* **2019**, *48*, 13006–13016, DOI 10.1039/c9dt02924a.
- [223] G. Jaeger, “The Ehrenfest Classification of Phase Transitions: Introduction and Evolution”, *Arch. Hist. Exact Sc.* **1998**, *53*, 51–81, DOI 10.1007/s004070050021.
- [224] P. C. Hohenberg, A. P. Krekhov, “An introduction to the Ginzburg–Landau theory of phase transitions and nonequilibrium patterns”, *Phys. Rep.* **2015**, *572*, 1–42, DOI 10.1016/j.physrep.2015.01.001.
- [225] R. A. Cowley, “Structural phase transitions I. Landau theory”, *Adv. Phys.* **1980**, *29*, 1–110, DOI 10.1080/00018738000101346.
- [226] E. Ising, “Beitrag zur Theorie des Ferromagnetismus”, *Z. Physik* **1925**, *31*, 253–258, DOI 10.1007/BF02980577.

- [227] L. Amico, R. Fazio, A. Osterloh, V. Vedral, “Entanglement in many-body systems”, *Rev. Mod. Phys.* **2008**, *80*, 517–576, DOI 10.1103/RevModPhys.80.517.
- [228] C. Rao, K. J. Rao, “Phase transformations in solids”, *Prog. Solid. State Ch.* **1967**, *4*, 131–185, DOI 10.1016/0079-6786(67)90007-6.
- [229] P. Tolédano, V. P. Dmitriev, *Reconstructive phase transitions in crystals and quasicrystals*, World Scientific, Singapore, **1996**.
- [230] H. T. Stokes, E. H. Kisi, D. M. Hatch, C. J. Howard, “Group-theoretical analysis of octahedral tilting in ferroelectric perovskites”, *Acta Cryst. B* **2002**, *58*, 934–938, DOI 10.1107/s0108768102015756.
- [231] H. T. Stokes, D. M. Hatch, J. Dong, J. P. Lewis, “Mechanisms for the reconstructive phase transition between the B1 and B2 structure types in NaCl and PbS”, *Phys. Rev. B* **2004**, *69*, 381, DOI 10.1103/PhysRevB.69.174111.
- [232] R. Z. Khaliullin, H. Eshet, T. D. Kühne, J. Behler, M. Parrinello, “Nucleation mechanism for the direct graphite-to-diamond phase transition”, *Nat. Mater.* **2011**, *10*, 693–697, DOI 10.1038/nmat3078.
- [233] A. C. D. CHAKLADER, A. L. ROBERTS, “Transformation of Quartz to Cristobalite”, *J. Am. Ceram. Soc.* **1961**, *44*, 35–41, DOI 10.1111/j.1151-2916.1961.tb15344.x.
- [234] J. Mart-Rujas, N. Islam, D. Hashizume, F. Izumi, M. Fujita, M. Kawano, “Dramatic structural rearrangements in porous coordination networks”, *J. Am. Chem. Soc.* **2011**, *133*, 5853–5860, DOI 10.1021/ja109160a.
- [235] H. Ohtsu, T. D. Bennett, T. Kojima, D. A. Keen, Y. Niwa, M. Kawano, “Amorphous-amorphous transition in a porous coordination polymer”, *Chem. Commun.* **2017**, *53*, 7060–7063, DOI 10.1039/C7CC03333H.
- [236] L. Longley, N. Li, F. Wei, T. D. Bennett, “Uncovering a reconstructive solid-solid phase transition in a metal-organic framework”, *R. Soc. open sci.* **2017**, *4*, 171355, DOI 10.1098/rsos.171355.
- [237] J.-C. Tan, P. Jain, A. K. Cheetham, “Influence of ligand field stabilization energy on the elastic properties of multiferroic MOFs with the perovskite architecture”, *Dalton Trans.* **2012**, *41*, 3949–3952, DOI 10.1039/C2DT12300B.
- [238] G. Feng, Di Gui, W. Li, “Structural and Chemical Bonding Dependence of Mechanical Properties in a Family of Metal-Formate Coordination Polymers”, *Cryst. Growth Des.* **2018**, *18*, 4890–4895, DOI 10.1021/acs.cgd.7b01768.
- [239] K. T. Butler, A. Walsh, A. K. Cheetham, G. Kieslich, “Organised chaos: Entropy in hybrid inorganic-organic systems and other materials”, *Chem. Sci.* **2016**, *7*, 6316–6324, DOI 10.1039/c6sc02199a.

- 
- [240] K. T. Butler, K. Svane, G. Kieslich, A. K. Cheetham, A. Walsh, “Microscopic origin of entropy-driven polymorphism in hybrid organic-inorganic perovskite materials”, *Phys. Rev. B* **2016**, *94*, DOI 10.1103/PhysRevB.94.180103.
- [241] G. Kieslich, J. M. Skelton, J. Armstrong, Y. Wu, F. Wei, K. L. Svane, A. Walsh, K. T. Butler, “Hydrogen Bonding versus Entropy: Revealing the Underlying Thermodynamics of the Hybrid Organic–Inorganic Perovskite [CH<sub>3</sub>NH<sub>3</sub>]PbBr<sub>3</sub>”, *Chem. Mater.* **2018**, *30*, 8782–8788, DOI 10.1021/acs.chemmater.8b03164.
- [242] J. M. Bermúdez-García, S. Yáñez-Vilar, A. García-Fernández, M. Sánchez-Andújar, S. Castro-García, J. López-Beceiro, R. Artiaga, M. Dilshad, X. Moya, M. A. Señarís-Rodríguez, “Giant barocaloric tunability in [(CH<sub>3</sub>CH<sub>2</sub>CH<sub>2</sub>)<sub>4</sub>N]Cd[N(CN)<sub>2</sub>]<sub>3</sub> hybrid perovskite”, *J. Mater. Chem. C* **2018**, *6*, 9867–9874, DOI 10.1039/C7TC03136J.
- [243] Z. Shi, Z. Fang, J. Wu, Y. Chen, Q. Mi, “Order-disorder transition of a rigid cage cation embedded in a cubic perovskite”, *Nat. Commun.* **2021**, *12*, 3548, DOI 10.1038/s41467-021-23917-z.
- [244] C. Kaußler, G. Kieslich, “crystIT: complexity and configurational entropy of crystal structures via information theory”, *J. Appl. Cryst.* **2021**, *54*, 306–316, DOI 10.1107/S1600576720016386.
- [245] S. A. Hallweger, C. Kaußler, G. Kieslich, “The structural complexity of perovskites”, *Phys. Chem. Chem. Phys.* **2022**, *24*, 9196–9202, DOI 10.1039/D2CP01123A.
- [246] E. K. H. Salje, “Characteristics of perovskite-related materials”, *Phil. Trans. Royal Soc.* **1989**, *328*, 409–416, DOI 10.1098/rsta.1989.0044.
- [247] P. Jain, V. Ramachandran, R. J. Clark, H. D. Zhou, B. H. Toby, N. S. Dalal, H. W. Kroto, A. K. Cheetham, “Multiferroic behavior associated with an order-disorder hydrogen bonding transition in metal-organic frameworks (MOFs) with the perovskite ABX<sub>3</sub> architecture”, *J. Am. Chem. Soc.* **2009**, *131*, 13625–13627, DOI 10.1021/ja904156s.
- [248] X.-Y. Wang, Z.-M. Wang, S. Gao, “Constructing magnetic molecular solids by employing three-atom ligands as bridges”, *Chem. Commun.* **2008**, 281–294, DOI 10.1039/B708122G.
- [249] M. Sánchez-Andújar, S. Presedo, S. Yáñez-Vilar, S. Castro-García, J. Shamir, M. A. Señarís-Rodríguez, “Characterization of the order-disorder dielectric transition in the hybrid organic-inorganic perovskite-like formate Mn(HCOO)(3)(CH(3))(2)NH(2)”, *Inorg. Chem.* **2010**, *49*, 1510–1516, DOI 10.1021/ic901872g.
- [250] L. C. Gómez-Aguirre, B. Pato-Doldán, J. Mira, S. Castro-García, M. A. Señarís-Rodríguez, M. Sánchez-Andújar, J. Singleton, V. S. Zapf, “Magnetic Ordering-Induced Multiferroic Behavior in CH<sub>3</sub>NH<sub>3</sub>Co(HCOO)<sub>3</sub> Metal-Organic Framework”, *J. Am. Chem. Soc.* **2016**, *138*, 1122–1125, DOI 10.1021/jacs.5b11688.

- [251] Z.-Y. Du, T.-T. Xu, B. Huang, Y.-J. Su, W. Xue, C.-T. He, W.-X. Zhang, X.-M. Chen, “Switchable guest molecular dynamics in a perovskite-like coordination polymer toward sensitive thermoresponsive dielectric materials”, *Angew. Chem. Int. Ed.* **2015**, *54*, 914–918, DOI 10.1002/anie.201408491.
- [252] Z.-Y. Du, Y.-Z. Sun, S.-L. Chen, B. Huang, Y.-J. Su, T.-T. Xu, W.-X. Zhang, X.-M. Chen, “Insight into the molecular dynamics of guest cations confined in deformable azido coordination frameworks”, *Chem. Commun.* **2015**, *51*, 15641–15644, DOI 10.1039/c5cc06863k.
- [253] J. M. Bermúdez-García, M. Sánchez-Andújar, S. Yáñez-Vilar, S. Castro-García, R. Artiaga, J. López-Beceiro, L. Botana, A. Alegría, M. A. Señarís-Rodríguez, “Multiple phase and dielectric transitions on a novel multi-sensitive [TPrA][M(dca)<sub>3</sub>] (M: Fe 2+, Co 2+ and Ni 2+) hybrid inorganic–organic perovskite family”, *J. Mater. Chem. C* **2016**, *4*, 4889–4898, DOI 10.1039/C6TC00723F.
- [254] Y. Wu, T. Binford, J. A. Hill, S. Shaker, J. Wang, A. K. Cheetham, “Hypophosphite hybrid perovskites: a platform for unconventional tilts and shifts”, *Chem. Commun.* **2018**, *54*, 3751–3754, DOI 10.1039/C8CC00907D.
- [255] W. Li, A. Stroppa, Z. Wang, S. Gao, *Hybrid organic-inorganic perovskites*, Wiley-VCH Verlag GmbH & Co. KGaA, Weinheim, **2020**, DOI 10.1002/9783527344338.
- [256] W. Zhang, H.-Y. Ye, R. Graf, H. W. Spiess, Y.-F. Yao, R.-Q. Zhu, R.-G. Xiong, “Tunable and switchable dielectric constant in an amphidynamic crystal”, *J. Am. Chem. Soc.* **2013**, *135*, 5230–5233, DOI 10.1021/ja3110335.
- [257] C. Shi, C.-H. Yu, W. Zhang, “Predicting and Screening Dielectric Transitions in a Series of Hybrid Organic-Inorganic Double Perovskites via an Extended Tolerance Factor Approach”, *Angew. Chem. Int. Ed.* **2016**, *55*, 5798–5802, DOI 10.1002/anie.201602028.
- [258] K. Qian, F. Shao, Z. Yan, J. Pang, X. Chen, C. Yang, “A perovskite-type cage compound as a temperature-triggered dielectric switchable material”, *CrystEngComm* **2016**, *18*, 7671–7674, DOI 10.1039/C6CE01421F.
- [259] W.-J. Xu, P.-F. Li, Y.-Y. Tang, W.-X. Zhang, R.-G. Xiong, X.-M. Chen, “A Molecular Perovskite with Switchable Coordination Bonds for High-Temperature Multiaxial Ferroelectrics”, *J. Am. Chem. Soc.* **2017**, *139*, 6369–6375, DOI 10.1021/jacs.7b01334.
- [260] J. A. Hill, A. L. Thompson, A. L. Goodwin, “Dicyanometallates as Model Extended Frameworks”, *J. Am. Chem. Soc.* **2016**, *138*, 5886–5896, DOI 10.1021/jacs.5b13446.
- [261] H.-Y. Ye, Y.-Y. Tang, P.-F. Li, W.-Q. Liao, J.-X. Gao, X.-N. Hua, H. Cai, P.-P. Shi, Y.-M. You, R.-G. Xiong, “Metal-free three-dimensional perovskite ferroelectrics”, *Science* **2018**, *361*, 151–155, DOI 10.1126/science.aas9330.



- 
- [262] A. L. Semrau, S. V. Dummert, C. Eckel, S. Mackewicz, R. T. Weitz, G. Kieslich, “Synthetic Approaches Targeting Metal-Free Perovskite [HMDABCO](NH<sub>4</sub>)I<sub>3</sub> Thin Films”, *Cryst. Growth Des.* **2022**, *22*, 406–413, DOI 10.1021/acs.cgd.1c01042.
- [263] C. Shi, X.-B. Han, W. Zhang, “Structural phase transition-associated dielectric transition and ferroelectricity in coordination compounds”, *Coord. Chem. Rev.* **2017**, DOI 10.1016/j.ccr.2017.09.020.
- [264] J. A. Schlueter, J. L. Manson, K. A. Hyzer, U. Geiser, “Spin canting in the 3D anionic dicyanamide structure (SPh<sub>3</sub>)Mn(dca)<sub>3</sub> (Ph = phenyl, dca = dicyanamide)”, *Inorg. Chem.* **2004**, *43*, 4100–4102, DOI 10.1021/ic035398p.
- [265] F.-J. Geng, L. Zhou, P.-P. Shi, X.-L. Wang, X. Zheng, Y. Zhang, D.-W. Fu, Q. Ye, “Perovskite-type organic–inorganic hybrid NLO switches tuned by guest cations”, *J. Mater. Chem. C* **2017**, *5*, 1529–1536, DOI 10.1039/C6TC05105G.
- [266] P. M. van der Werff, E. Martínez-Ferrero, S. R. Batten, P. Jensen, C. Ruiz-Pérez, M. Almeida, J. C. Waerenborgh, J. D. Cashion, B. Moubaraki, J. R. Galán-Mascarós, J. M. Martínez-Agudo, E. Coronado, K. S. Murray, “Hybrid materials containing organometallic cations and 3-D anionic metal dicyanamide networks of type Cp\*<sub>2</sub>MM'(dca)<sub>3</sub>”, *Dalton Trans.* **2005**, 285–290, DOI 10.1039/B415275A.
- [267] J. García-Ben, A. García-Fernández, P. Dafonte-Rodríguez, I. Delgado-Ferreiro, U. B. Cappel, S. Castro-García, M. Sánchez-Andújar, J. M. Bermúdez-García, M. A. Señarís-Rodríguez, “Narrowing the tolerance factor limits for hybrid organic-inorganic dicyanamide-perovskites”, *J. Solid State Chem.* **2022**, *316*, 123635, DOI 10.1016/j.jssc.2022.123635.
- [268] S. R. Batten, R. Robson, P. Jensen, B. Moubaraki, K. S. Murray, “Structure and molecular magnetism of the rutile-related compounds M(dca)<sub>2</sub>, M = CoII, NiII, CuII, dca = dicyanamide, N(CN)<sub>2</sub>–”, *Chem. Commun.* **1998**, 439–440, DOI 10.1039/A707264C.
- [269] S. R. Batten, K. S. Murray, “Structure and magnetism of coordination polymers containing dicyanamide and tricyanomethanide”, *Coord. Chem. Rev.* **2003**, *246*, 103–130, DOI 10.1016/S0010-8545(03)00119-X.
- [270] J. L. Manson, D. W. Lee, A. L. Rheingold, J. S. Miller, “Buckled-layered Structure of Zinc Dicyanamide, Zn(II)[N(CN)<sub>2</sub>]<sub>2</sub>”, *Inorg. Chem.* **1998**, *37*, 5966–5967, DOI 10.1021/ic980659u.
- [271] L. Zhou, X. Zheng, P.-P. Shi, Z. Zafar, H.-Y. Ye, D.-W. Fu, Q. Ye, “Switchable Nonlinear Optical and Tunable Luminescent Properties Triggered by Multiple Phase Transitions in a Perovskite-Like Compound”, *Inorg. Chem.* **2017**, *56*, 3238–3244, DOI 10.1021/acs.inorgchem.6b02508.

- [272] M.-M. Zhao, L. Zhou, P.-P. Shi, X. Zheng, X.-G. Chen, J.-X. Gao, L. He, Q. Ye, C.-M. Liu, D.-W. Fu, “3D Organic-Inorganic Perovskite Ferroelastic Materials with Two Ferroelastic Phases:  $\text{Et}_3\text{P}(\text{CH}_2)_2\text{FMn}(\text{dca})_3$  and  $\text{Et}_3\text{P}(\text{CH}_2)_2\text{ClMn}(\text{dca})_3$ ”, *Chem. Eur. J.* **2019**, *25*, 6447–6454, DOI 10.1002/chem.201900771.
- [273] N. A. de Oliveira, “Barocaloric effect and the pressure induced solid state refrigerator”, *J. Appl. Phys.* **2011**, *109*, 053515, DOI 10.1063/1.3556740.
- [274] J. M. Bermúdez-García, M. Sánchez-Andújar, M. A. Señarís-Rodríguez, “A New Playground for Organic-Inorganic Hybrids: Barocaloric Materials for Pressure-Induced Solid-State Cooling”, *J. Phys. Chem. Lett.* **2017**, *8*, 4419–4423, DOI 10.1021/acs.jpcllett.7b01845.
- [275] P. Lloveras, E. Stern-Taulats, M. Barrio, J.-L. Tamarit, S. Crossley, W. Li, V. Pomjakushin, A. Planes, L. Mañosa, N. D. Mathur, X. Moya, “Giant barocaloric effects at low pressure in ferroelectric ammonium sulphate”, *Nat. Commun.* **2015**, *6*, 8801, DOI 10.1038/ncomms9801.
- [276] P. Lloveras, A. Aznar, M. Barrio, P. Negrier, C. Popescu, A. Planes, L. Mañosa, E. Stern-Taulats, A. Avramenko, N. D. Mathur, X. Moya, J.-L. Tamarit, “Colossal barocaloric effects near room temperature in plastic crystals of neopentylglycol”, *Nat. Commun.* **2019**, *10*, 1803, DOI 10.1038/s41467-019-09730-9.
- [277] F. J. DiSalvo, “Thermoelectric Cooling and Power Generation”, *Science* **1999**, *285*, 703–706, DOI 10.1126/science.285.5428.703.
- [278] J. M. Bermúdez-García, M. Sánchez-Andújar, S. Yáñez-Vilar, S. Castro-García, R. Artiaga, J. López-Beceiro, L. Botana, Á. Alegría, M. A. Señarís-Rodríguez, “Role of Temperature and Pressure on the Multisensitive Multiferroic Dicyanamide Framework  $\text{TPrAMn}(\text{dca})_3$  with Perovskite-like Structure”, *Inorg. Chem.* **2015**, *54*, 11680–11687, DOI 10.1021/acs.inorgchem.5b01652.
- [279] M. Szafranski, W.-J. Wei, Z.-M. Wang, W. Li, A. Katrusiak, “Research Update: Tricritical point and large caloric effect in a hybrid organic-inorganic perovskite”, *APL Mater.* **2018**, *6*, 100701, DOI 10.1063/1.5049116.
- [280] J. Salgado-Beceiro, A. Nonato, R. X. Silva, A. García-Fernández, M. Sánchez-Andújar, S. Castro-García, E. Stern-Taulats, M. A. Señarís-Rodríguez, X. Moya, J. M. Bermúdez-García, “Near-room-temperature reversible giant barocaloric effects in  $[(\text{CH}_3)_4\text{N}]\text{Mn}[\text{N}_3]_3$  hybrid perovskite”, *Mater. Adv.* **2020**, *1*, 3167–3170, DOI 10.1039/D0MA00652A.
- [281] S. Burger, M. G. Ehrenreich, G. Kieslich, “Tolerance factors of hybrid organic-inorganic perovskites: recent improvements and current state of research”, *J. Mater. Chem. A* **2018**, *6*, 21785–21793, DOI 10.1039/C8TA05794J.
- [282] S. Burger, S. Kronawitter, H. L. B. Boström, J. K. Zaręba, G. Kieslich, “A new polar perovskite coordination network with azaspiroundecane as A-site cation”, *Dalton Trans.* **2020**, *49*, 10740–10744, DOI 10.1039/d0dt01968b.

- 
- [283] S. Burger, S. Grover, K. T. Butler, H. L. B. Boström, R. Grau-Crespo, G. Kieslich, “Tilt and shift polymorphism in molecular perovskites”, *Mater. Horiz.* **2021**, *8*, 2444–2450, DOI 10.1039/d1mh00578b.
- [284] S. Grover, S. Burger, K. T. Butler, K. Hemmer, P. Vervoorts, G. Kieslich, R. Grau-Crespo, “Tuning the mechanical properties of dicyanamide-based molecular perovskites”, *CrystEngComm* **2023**, *25*, 3439–3444, DOI 10.1039/D3CE00009E.
- [285] S. Burger, K. Hemmer, D. C. Mayer, P. Vervoorts, D. Daisenberger, J. K. Zaręba, G. Kieslich, “Designing Geometric Degrees of Freedom in ReO<sub>3</sub>-Type Coordination Polymers”, *Adv. Funct. Mater.* **2022**, *32*, 2205343, DOI 10.1002/adfm.202205343.
- [286] H. Yuan, E. Debroye, K. Janssen, H. Naiki, C. Steuwe, G. Lu, M. Moris, E. Orgiu, H. Uji-I, F. de Schryver, P. Samorì, J. Hofkens, M. Roeffaers, “Degradation of Methylammonium Lead Iodide Perovskite Structures through Light and Electron Beam Driven Ion Migration”, *J. Phys. Chem. Lett.* **2016**, *7*, 561–566, DOI 10.1021/acs.jpcllett.5b02828.
- [287] L. McGovern, M. H. Futscher, L. A. Muscarella, B. Ehrler, “Understanding the Stability of MAPbBr<sub>3</sub> versus MAPbI<sub>3</sub>: Suppression of Methylammonium Migration and Reduction of Halide Migration”, *J. Phys. Chem. Lett.* **2020**, *11*, 7127–7132, DOI 10.1021/acs.jpcllett.0c01822.
- [288] N. Menshutkin, “Beiträge zur Kenntnis der Affinitätskoeffizienten der Alkylhaloide und der organischen Amine”, *Z. Phys. Chem.* **1890**, *5U*, 589–600, DOI 10.1515/zpch-1890-0546.
- [289] N. Menshutkin, “Über die Affinitätskoeffizienten der Alkylhaloide und der Amine”, *Z. Phys. Chem.* **1890**, *6U*, 41–57, DOI 10.1515/zpch-1890-0607.
- [290] M. G. Marino, K. D. Kreuer, “Alkaline stability of quaternary ammonium cations for alkaline fuel cell membranes and ionic liquids”, *ChemSusChem* **2015**, *8*, 513–523, DOI 10.1002/cssc.201403022.
- [291] Z. J. Yu, US2008262194 (A1), **2008**.
- [292] R. Kuttan, A. N. Radhakrishnan, T. Spande, B. Witkop, “sym-Homospermidine, a naturally occurring polyamine”, *Biochemistry* **1971**, *10*, 361–365, DOI 10.1021/bi00779a001.
- [293] G. Coquerel, “Crystallization of molecular systems from solution: phase diagrams, supersaturation and other basic concepts”, *Chem. Soc. Rev.* **2014**, *43*, 2286–2300, DOI 10.1039/C3CS60359H.
- [294] O. V. Dolomanov, L. J. Bourhis, R. J. Gildea, J. A. K. Howard, H. Puschmann, “OLEX2 : a complete structure solution, refinement and analysis program”, *J. Appl. Cryst.* **2009**, *42*, 339–341, DOI 10.1107/S0021889808042726.

- [295] A. A. Coelho, “TOPAS and TOPAS-Academic : an optimization program integrating computer algebra and crystallographic objects written in C++”, *J. Appl. Cryst.* **2018**, *51*, 210–218, DOI 10.1107/S1600576718000183.
- [296] A. Jayaraman, “Diamond anvil cell and high-pressure physical investigations”, *Rev. Mod. Phys.* **1983**, *55*, 65–108, DOI 10.1103/RevModPhys.55.65.
- [297] N. J. Brooks, B. L. L. E. Gauthe, N. J. Terrill, S. E. Rogers, R. H. Templer, O. Ces, J. M. Seddon, “Automated high pressure cell for pressure jump x-ray diffraction”, *Rev. Sci. Instrum.* **2010**, *81*, 064103, DOI 10.1063/1.3449332.
- [298] S. Dissegna, P. Vervoorts, C. L. Hobday, T. Düren, D. Daisenberger, A. J. Smith, R. A. Fischer, G. Kieslich, “Tuning the Mechanical Response of Metal-Organic Frameworks by Defect Engineering”, *J. Am. Chem. Soc.* **2018**, *140*, 11581–11584, DOI 10.1021/jacs.8b07098.
- [299] G. Höhne, W. Dollhopf, K. Blankenhorn, P. U. Mayr, “On the pressure dependence of the heat of fusion and melting temperature of indium”, *Thermochim. Acta* **1996**, *273*, 17–24, DOI 10.1016/0040-6031(95)02686-X.

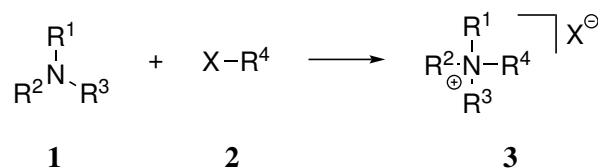
# 7 METHODOLOGY

The various studies from which this dissertation is compiled include a description of the synthesis and characterisation of several novel materials. For each of them the specific experimental instructions are concisely summarised in the respective Supporting Information of the research articles, see chapter 8. Nevertheless, the path to experimental success is usually more elaborate than the brief description of the mere synthetic instruction. Therefore, this chapter outlines the methodology and basic principles for the successful synthesis and characterisation of novel materials, such as those investigated in this doctorate thesis, as well as the interpretation of experimental data towards their structural and mechanical properties.

It is intended to provide an overview of conceptual insights into the routine laboratory procedures during the studies of this dissertation. Therefore, the focus is put on the central idea of how to successfully develop new materials and on the methodological approach to reasonable analysis techniques and what kind of conclusions can be drawn from each of them. For an in-depth description of the experimental set-up and the theoretical background of the individual measurement techniques, it is at this point referred to the appropriate textbook literature.

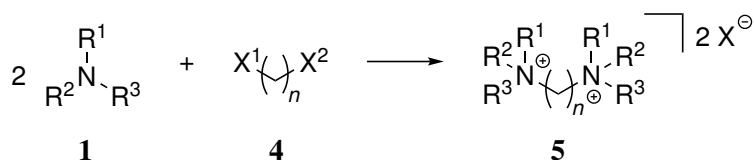
## 7.1 Synthesis of Precursor Compounds and Crystalline Perovskite-Type Materials

As the ammonium cation derivatives on the A-site of the molecular perovskite materials presented in this thesis are commercially not available, they are experimentally obtained by organic synthesis. This is usually done starting from a nucleophilic amine derivatised with alkyl substituents, which can either be purchased or has to be prepared beforehand. With this ternary amine, which still carries a lone pair, a *Menshutkin* reaction is conducted by means of alkylating agents such as alkyl halides to generate the desired corresponding quaternary ammonium salt in a concerted  $S_N2$ -type reaction.[288, 289] In this way, monovalent linear alkylammonium cations as well as cations bearing azaspiro units when starting from heterocyclic amines can be prepared.[290] Analogously, the formation of symmetric divalent alkyldiammonium cations is observed when alkyl dihalides are used. A general synthetic approach for the preparation of monovalent ammonium cations is illustrated in Scheme 7.1.



**Scheme 7.1:** Synthesis of quaternary ammonium salts **3** starting from ternary amines **1** and alkyl halides **2** with  $R^X$  being alkyl moieties and  $X$  representing a halide.

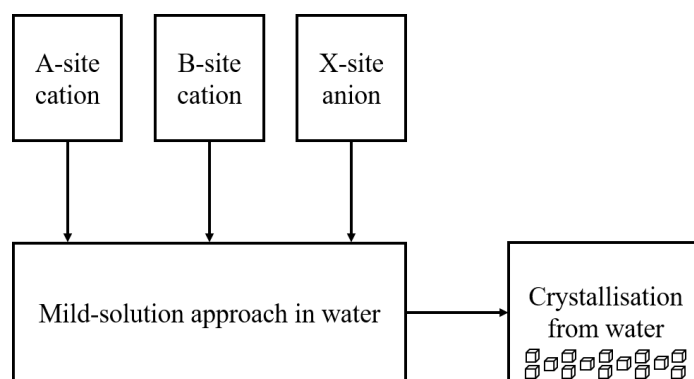
In Scheme 7.2 the general procedure to create symmetric divalent ammonium cations with chemically linked but separated charge centres is visualised. In principle, this approach can be extended to produce asymmetric or even larger polycationic ammonium derivatives.[291, 292]



**Scheme 7.2:** Synthesis of symmetric divalent quaternary ammonium salts **5** starting from ternary amines **1** and alkyl dihalides **4** with  $R^X$  being alkyl moieties and  $X^Y$  representing halides.

Afterwards, a regular organic work-up including extraction or recrystallisation usually yields the product as a colourless solid in high purity which is typically confirmed by  $^1\text{H-NMR}$  - and  $^{13}\text{C-NMR}$  -spectroscopy techniques.

With the tailor-made organic binary salt compound carrying the A-site cation of choice it is then attempted to form a crystalline three-dimensional coordination network that exhibits a perovskite structural motif. Throughout the thesis, various commercially available metal salts are used as source for the B-site metal, whereas only dicyanamide is used for the X-site anion, accessible as sodium dicyanamide. The experimental conditions to achieve this play an important role, as different synthetic environments can lead to different dimensionalities and connectivities of the resulting solid-state materials structure, very similar to the behaviour already long known for the synthesis of Metal-Organic Frameworks.[53] Usually this procedure is carried out as a "mild-solution approach", a batch reaction in the sense of a discontinuous one-pot synthesis in which all precursors are added as solution in an appropriate solvent, see Scheme 7.3 for a graphical illustration. While for formate-based perovskite materials this is practically always done in methanol, for molecular perovskites comprising dicyanamide as anionic linker molecule a synthetic protocol is usually suggested involving a mixture of ethanol and water as solvent. However, most of the molecular perovskite materials created within this thesis are synthesised in a slightly modified way which is from solutions in de-ionised water at ambient conditions or at refrigerator temperature.



**Scheme 7.3:** Schematic of the mild-solution approach employed to synthesise dicyanamide-based molecular perovskites. Each precursor in aqueous solution is added to a batch vial which is then allowed to stand until crystalline material is formed.

After mixing all ingredients together in the desired (ideally 1:1:3) stoichiometry, the solution is allowed to stand until the formation of crystalline material is observed in a self-organised fashion. The driving force for primary crystal nucleation thereby is the formation of a new stable thermodynamic phase resulting in a supersaturation of the solution with subsequent crystallisation and precipitation of the crystalline material.[293] With regard to the expected formation of materials of the perovskite-type structure, the influence of the concentration of the precursor solutions, the synthesis temperature and also the type of solvent must be considered and thoroughly investigated. In some cases, the separation of the product phase occurs particularly fast. This usually then does not result the product in single crystal quality, but rather as polycrystalline powder. Accordingly, after conducting various analytical procedures as described below, appropriate experimental modifications must be carried out if the intended material could not be prepared. This creates a dynamic feedback loop between material synthesis and material characterisation to elaborate all relevant correlations towards the targeted synthesis of functional perovskite-type materials.

## 7.2 Characterisation of Crystalline Perovskite-Type Materials

Crystalline substrate successfully prepared in this way is then recovered through multiple washing steps with a subsequent mild drying procedure. Hereinafter, the underlying atomic arrangement, the elemental composition as well as potential material properties are investigated. As the main focus lies on the synthesis of functional perovskite-type coordination networks, the first consideration is the elucidation of the crystal structure. For this purpose, a suitable crystal fragment is picked from the crude reaction vessel and is measured on a X-ray single-crystal diffractometer to determine the crystal structure from the analysis of the diffraction images. Since ultimately a reproducible and phase-pure synthesis of the targeted material is

desired, it is necessary to further investigate for phase purity of the bulk material. To do so, the recovered crystalline material is crushed, fine ground and prepared for analysis on a X-ray powder diffractometer. Based on the single-crystal structure solution together with the diffraction data of the polycrystalline sample, it can then be concluded if the synthesis procedure has resulted in the intended phase-pure material. Typical tools for that are analytical software like OLEX2 (for single-crystal structure refinement)[294] and DIFFRAC.TOPAS,[295] with which peak indexing, Pawley- and Rietveld refinements can be performed.

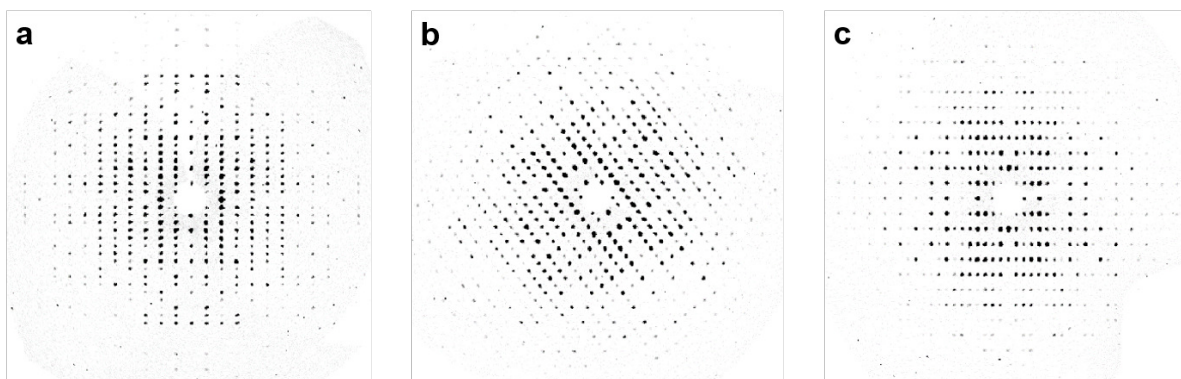


**Figure 7.1:** Precession images of a single crystal X-ray diffraction experiment for an exemplified monoclinic structure. Shown in **a**, **b** and **c** are the superimpositions in  $Ok_l$ ,  $hOl$  and  $hk0$  direction, respectively. The evaluation of the diffraction pattern ultimately provides a model for the postulated crystal structure of the investigated material.

In the absence of crystallites large enough to be analysed as single crystals, reasonable structure solution becomes much more difficult. Ab-initio Rietveld refinement of complex crystal structures solely relying on powder diffraction data is challenging and usually requires a suitable structural model as a starting template, either derived from an isostructural relationship of an analogous compound or from theoretical simulations. Complementary analysis with further evidence for structural features and the presence of functional groups include the Fourier-transform infrared spectroscopy (FT-IR), *i.e.* the excitation of chemical bond vibration with infrared radiation, or solid-state NMR spectroscopy. An elemental analysis after all confirms the purity of the compound.

The next stage consists of thermal analysis, which usually involves thermogravimetric analysis (TGA) and differential scanning calorimetry (DSC). With TGA experiments, the thermal decomposition of the substance caused by heat can be elucidated, which is done with a constant heating of the specimen while monitoring the sample mass. There are basically two measurement types available for this purpose, either under a flow of inert gas or in an oxidising atmosphere. However, typically these experiments are conducted through the first method, since the temperature of chemical decomposition is of primary interest. With knowledge about the decomposition process on hand, a DSC experiment with cyclic heating and cooling runs is then performed. In this technique, the sample is initially treated with a constant heating rate starting from a defined low to a high temperature, which is selected sufficiently below thermal



decomposition begins to ensure a non-destructive measurement. This allows for a controlled subsequent cooling to create a temperature-dependent measuring cycle, which can then be run several times to identify reversible phenomena. Therefore, if considering solid-state materials, only solid-to-solid transitions are monitored. During the temperature program, all heat flow to and from the sample is detected, which can be observed as a peak in the curve of heat flux versus temperature. It is important to note that in the first place a signal in the DSC curve does not provide enough distinct information about the transformation in the material itself, but rather gives hints for possible properties like phase transitions, crystallisation or melting events, or glass transition points amongst others. However, based on the shape and area of a peak as well as the direction of heat flux, which can be endothermic or exothermic, obvious conclusions about the nature of the investigated material property can be drawn. Furthermore it should be mentioned that the applied heating/cooling rate can have a crucial influence on the resulting shape of the peak and consequently the resolution of the signal and must be selected accordingly. As an example, Figure 7.2 shows two DSC curves with focus on the respective

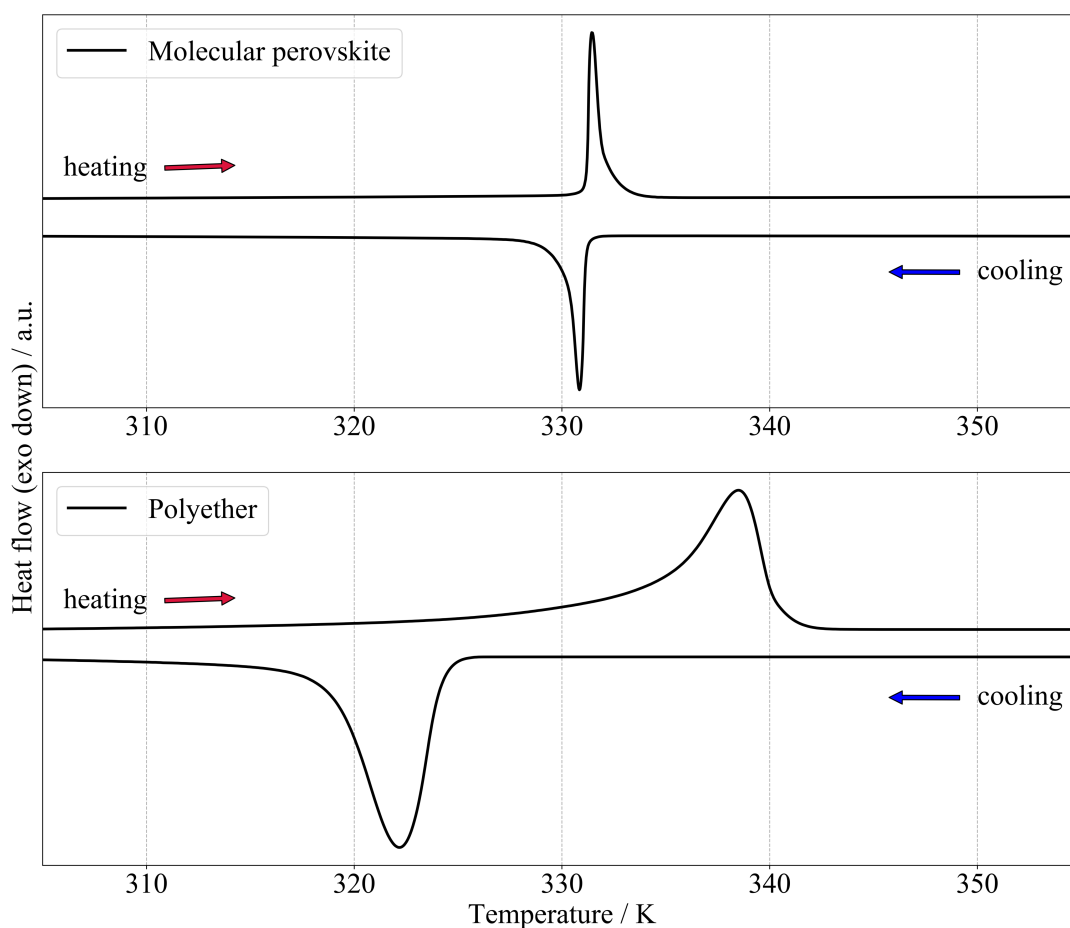


**Figure 7.2:** DSC curves of the molecular perovskite  $[(C_3H_7)_4N]Mn(C_2N_3)_3$  (top) and the polyether poly(oxyethylene)-1.000.000 (bottom) with emphasis on the thermal features at around 330 K. Despite the very similar temperature range, these signals correspond to different material properties. For both curves, the heat flow is shown as exo down.

thermal features, of which the one above represents the trace of a molecular perovskite material (here in particular  $[(C_3H_7)_4N]Mn(C_2N_3)_3$ ), [278] while at the bottom the profile of a semi-crystalline polymer is given (poly(oxyethylene)-1.000.000). For the molecular perovskite, the signals correspond to a structural order/disorder phase transition with a distinct change in symmetry. Such peaks typically have asymmetric shape and are characterised by a sharp onset (which marks the temperature of the transition) with subsequent tailing and a complementary inverted signal when the temperature profile is reversed. This is contrasted with the thermal response for melting and solidification of a semi-crystalline polymer, commonly indicated by a peak signal with fronting shape and a clear hysteresis between heating and cooling. Therefore, depending on the investigated material, different behaviour is already reflected in the shape of the detected signal.

In this thesis, cyclic DSC experiments were used exclusively to screen solid-state materials for the presence of structural phase transitions. Since for crystalline perovskite-type coordination networks these are typically first-order transformations with a reversible nature, as in detail discussed in section 2.5, the DSC analysis mostly revealed signals similar to the molecular perovskite example discussed above. If a relevant signal is detected, it is necessary to further investigate for the origin of the heat flux to eventually assign it to a structural transition. For this purpose, the diffraction methods previously described are employed to determine the crystal structure before and after the signal temperature. Furthermore, systematic temperature-dependent studies then allow for thermal expansion parameters and can give insights for a potential mechanism of the thermal material response. This is achieved by recording diffrac-

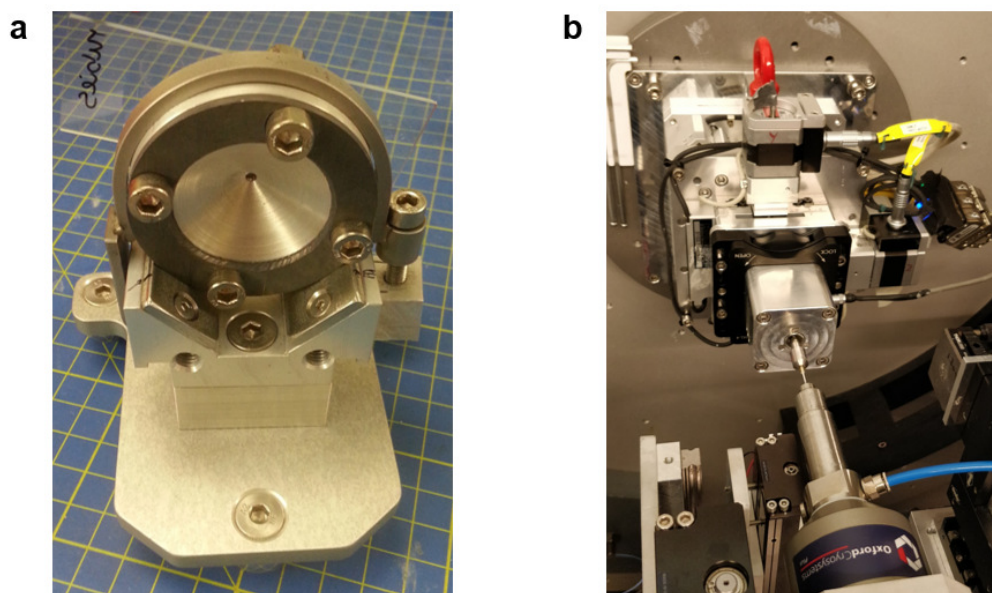


**Figure 7.3:** In (a), a diamond anvil cell with mounting bracket for use at the Diamond Light Source Ltd. extreme conditions beamline I15 is shown. Panel (b) displays a photograph of the experimental set-up for variable-temperature powder diffraction with capillaries including an attached cryosystem, taken at the powder diffraction beamline P02.1 of the Deutsches Elektronen-Synchrotron (DESY).

tograms at different temperatures and determining the cell parameters or structures for each point by means of the appropriate evaluation technique. Afterwards, these values can be put into relation with the corresponding temperature. The material behaviour can also be studied in terms of the variation of external pressure. This is done by using special pressure cells called diamond anvil cell (DAC), see Figure 7.3,[296] or customised pressure jump cell,[297, 298] in which the specimen is squeezed between two polished diamonds *resp.* a sealed plastic capillary surrounded with a pressure-transmitting medium. In the case of DACs, the pressure is applied by the aid of mechanical force built by screwing the diamonds together, while for the pressure jump cell this is done by an increase of water pressure within a cell with diamond windows. The recording of diffraction patterns as a function of applied hydrostatic pressure then enables the pressure-dependent material behaviour like compressibilities and bulk moduli to be investigated. Since these experiments usually require radiation of high intensity as well as brilliance, they are typically conducted at synchrotron facilities.

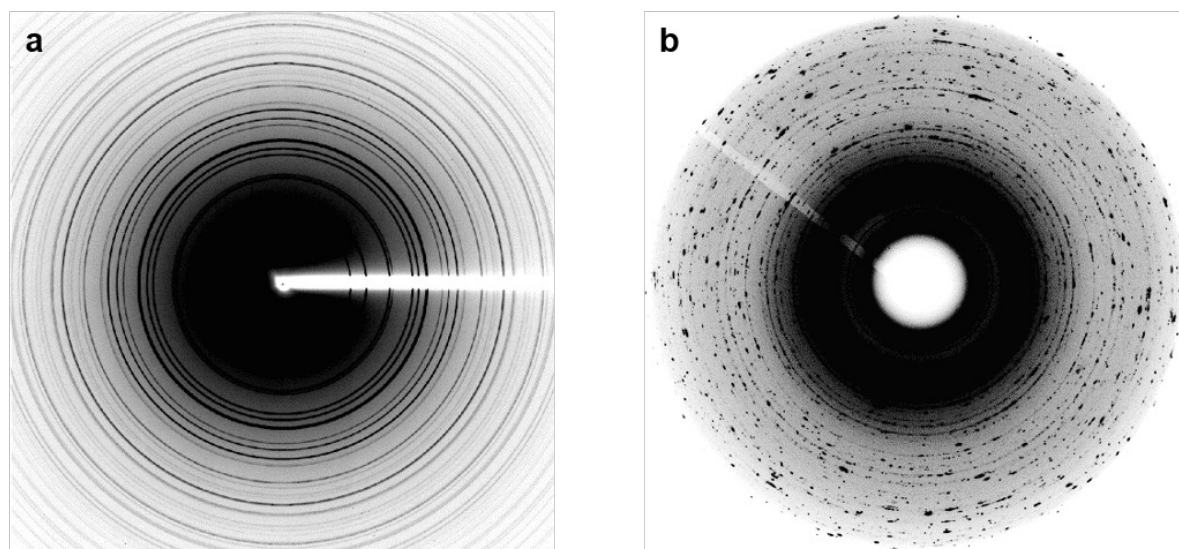


**Figure 7.4:** 2D diffractograms each recorded at a synchrotron facility. In (a), the powder sample is investigated in a regular capillary set-up, whereas for (b) it is loaded into a plastic capillary for pressurisation experiments. Due to the fixed position of the sample in the pressure cell the resulting diffraction pattern (right) deviates from continuous rings. Note that the notch represents the beam stop and that the colour intensity from white to black resembles the intensity of the collected data.

Figure 7.4 as an example shows diffraction patterns of the same powder sample recorded on 2D area detectors for a capillary measurement at ambient temperatures (left) and in a pressurised plastic capillary (right), both performed with synchrotron radiation. Due to the limitation of the pressure-dependent experiment to not spin the sample during radiation exposure, the homogeneity of the DEBYE-SCHERRER diffraction rings is significantly decreased. In the context of the experiment this is acceptable, as during processing the raw data are averaged and converted to 1D diffractograms (azimuthal integration). In consequence, the intensities are no longer characteristic for the crystal structure of the sample. For this reason, high-pressure data are

generally limited to the extraction of cell parameters. For those interested in further reading about high-pressure studies and the experimental gimmicks of the technique, however, it is at this point referred to the relevant literature.

To complete the brief overview in this paragraph of the most important methods employed in the studies of this doctorate thesis, a closer look on the application of the DSC method in the context of barocalorics will be given in the following. In these pressure-DSC measurements, the usual temperature-dependent DSC curves are run at different, in the course of the experiment constant pressures, which are applied pneumatically within a special pressure cell. Based on the relationship of the measured temperature of the recorded signal to the applied pressure, conclusions can then be drawn relative to the pressure susceptibility of the investigated sample, in particular the barocaloric coefficient as in detail described in Equation 2.7 and Equation 2.8. Certainly, several things have to be taken into account here: the gas flow must be regulated by appropriate inflow and outflow rates to ensure that the total pressure in the cell remains approximately constant over the entire temperature range. In addition, the set-up cell must be calibrated for each pressure point accordingly, since the required parameter of the reference material, *i.e.* the melting point of indium,[299] also varies depending on the applied pressure. In order to establish relationships to the barocaloric effect of a material in this way, the isothermal entropy change  $\Delta S_{it}$ , which means the exchange of energy (heat) triggered by external pressure, must be calculated. For this purpose, the isobaric entropy change  $\Delta S_{ib}$ , as a function of temperature at different pressures is experimentally determined. Afterwards,  $\Delta S_{it}$  is obtained as the difference of entropic data received at different pressures. If the experiments are conducted at uniform heating rates,  $H(p)$  describes the pressure-dependent experimental heat flux and  $T$  the temperature.[70]

$$\Delta S_{ib.(T)} = S(T, p) - S(T_0, p) = \int_{T_0}^T \frac{H(p)}{T} dT \quad (7.1)$$

$$\Delta S_{it., \Delta P} = \Delta S_{ib.(p \neq 1)} - \Delta S_{ib.(p = 1)} \quad (7.2)$$

As this procedure involves measurements at different constant pressures while changing the temperature, whereas the actual desired result (barocaloric effect) is a quantity that is intended to hold for a constant temperature with changes in pressures, it is also called "quasi-direct" method. If the isothermal entropy changes should be assessed in a direct way, the mode of operation of the p-DSC instrument needs to be adjusted. In this scenario, the specimen must be equilibrated to the temperature just after the phase transition event with subsequent application and release of hydrostatic pressure while monitoring the heat flux. Hereby it is ensured that the phase transition is triggered exclusively in a pressure-induced manner. Nevertheless, this procedure is experimentally very challenging, as hysteresis effects become particularly prominent during the reversible phase transition due to kinetic effects related to the rate of pressure change. Furthermore, temperature changes occur during compression and expansion of the pressure cell by the pneumatic medium, which can likewise significantly influence the results.

# 8 SUPPLEMENTARY MATERIAL

## 8.1 STUDY II: Supporting Information

Electronic Supplementary Material (ESI) for Dalton Transactions.  
This journal is © The Royal Society of Chemistry 2020

### Supporting Information

#### **A New Polar Perovskite Coordination Network with Azaspiroundecane as A-site Cation**

Stefan Burger,<sup>a</sup> Silva Kronawitter,<sup>a</sup> Hanna L. B. Boström,<sup>b</sup> Jan Zaręba<sup>c</sup> and Gregor Kieslich<sup>a</sup>

<sup>a</sup> Department of Chemistry, Technical University Munich, Lichtenbergstrasse 4, 85748 Garching, Germany.

<sup>b</sup> Department of Chemistry, Ångström Laboratory, Uppsala Universitet, Box 538, 751 21 Uppsala, Sweden.

<sup>c</sup> Advanced Materials Engineering and Modelling Group, Wrocław University of Science and Technology, Wybrzeże Wyspiańskiego 27, 50-370 Wrocław.

#### **Table of content:**

Synthetic procedures .....	2
NMR Spectroscopy of the A-site precursor [ASU]Br .....	3
Thermal analysis of the coordination networks .....	5
Powder X-ray diffraction data .....	7
Single crystal X-ray diffraction data .....	9
Group theoretical analysis .....	13
Second Harmonic Generation studies .....	14
References .....	15

## Synthetic procedures

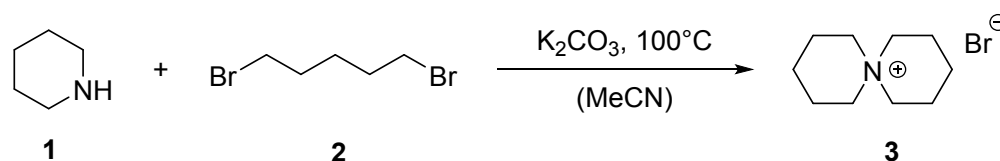
### Synthesis of 6-azaspiro[5.5]undecane bromide ([ASU]Br):

[ASU]Br was synthesised from commercially available 1,5-dibromopentane **2** and piperidine **1**. In a typical three-necked flask setup, the 1,5-dibromopentane (3.4 ml, 25 mmol) and potassium carbonate (4.15 g, 30 mmol) were mixed in acetonitrile (70 ml). After heating to reflux temperature, a solution of piperidine (2.5 ml, 25 mmol) in acetonitrile (10 ml) was added dropwise and stirred overnight, forming a white precipitate. After cooling down to room temperature, the solvent was removed under reduced pressure. The white precipitate was mixed with excess of ethanol (70 ml) and filtered to remove remaining  $K_2CO_3$ . The filtrate was concentrated in vacuo and precipitated in pure diethylether (80 ml) to yield a fine, white solid. This crude product was washed with diethylether (2 x 10 ml) and dried to constant weight, resulting in 3.9 g of pure product (67% yield) as a fine crystalline powder (see Figure S 3, 4).

**$^1H$ -NMR** (400 MHz, Deuterium Oxide):  $\delta$  [ppm] = 3.29 (t,  $J$  = 6.4 Hz, 8H), 1.89-1.67 (m, 8H), 1.58 (p,  $J$  = 6.4, 5.9 Hz, 4H).

**$^{13}C$ -NMR** (101 MHz, Deuterium Oxide):  $\delta$  [ppm] = 59.48, 21.13, 18.87.

**Figure S1:** Reaction scheme of [ASU]Br *via* a nucleophilic substitution mechanism. The route was adapted and modified from the literature.<sup>1</sup> The reaction is expected to also run under milder conditions and is flexible towards different di-haloalkanes which can be used to vary the carbon chain length in the resulting spiro compound.



### Synthesis of crystalline coordination networks:

For the preparation of the crystalline [ASU][Cd(C<sub>2</sub>N<sub>3</sub>)<sub>3</sub>] material and the other compounds for B = Mn<sup>2+</sup>, Co<sup>2+</sup>, and Ni<sup>2+</sup> commercially available Na(dca) (96%, Aldrich), Cd(Cl<sub>2</sub>)·H<sub>2</sub>O (98.5%, Alfa Aesar), Mn(NO<sub>3</sub>)<sub>4</sub>·4H<sub>2</sub>O (98%, Alfa Aesar), Co(NO<sub>3</sub>)<sub>6</sub>·6H<sub>2</sub>O (99%, abcr), Ni(NO<sub>3</sub>)<sub>2</sub>·6H<sub>2</sub>O (Alfa Aesar), millipore water and [ASU]Br were used. The synthesis of the coordination networks was approached *via* a mild solution chemistry procedure at ambient temperature. In a typical crystallisation approach, 0.25 ml water was placed at the bottom of a tube and then layered in order by 0.3 ml of an aqueous solution of Na(dca)

(2M), 0.5 ml of an aqueous  $M(\text{NO}_3/\text{Cl}_2) \cdot x\text{H}_2\text{O}$  solution (0.4M) and an aqueous solution of  $[\text{ASU}]\text{Br}$  (0.4M). Large block single crystals with sizes between 0.1 – 1 mm were collected after a couple of hours at ambient temperature and washed with the respective solvent.

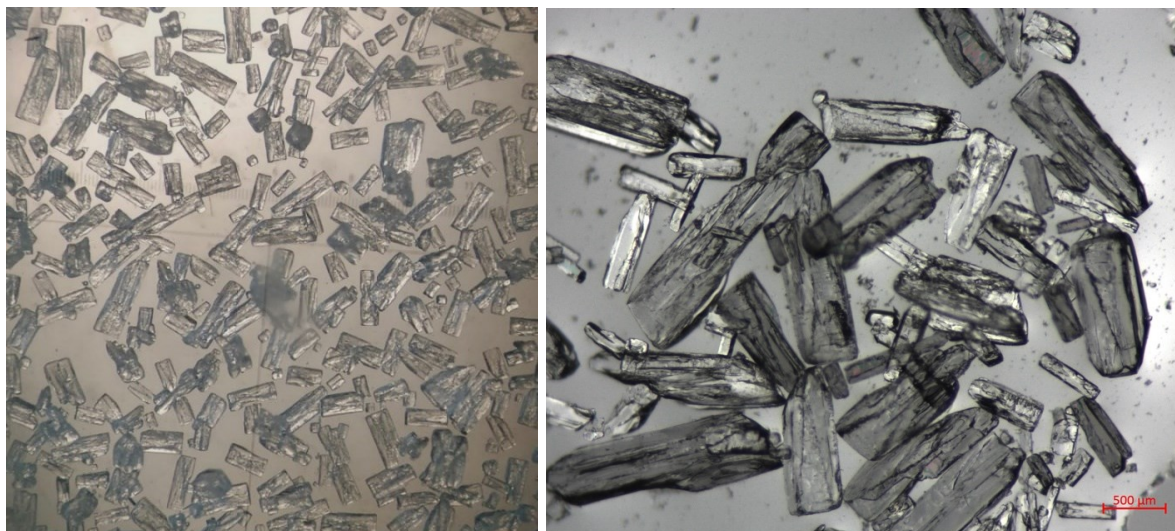


**Figure S2:** Photographs of the resulting crystals formed, exemplarily shown here for the colorless, large block crystals of the  $[\text{ASU}][\text{Cd}(\text{C}_2\text{N}_3)_3]$  material.

### NMR Spectroscopy of the A-site precursor $[\text{ASU}]\text{Br}$

The  $^1\text{H}$ - and  $^{13}\text{C}$ -NMR spectra were recorded on a *Bruker Avance III 400* spectrometer at room temperature (298 K). Chemical shifts are expressed as parts per million (ppm,  $\delta$ ). The following abbreviations t = triplet p = pentet and m = multiple are used to characterise all signals. All coupling constants are absolute values and are expressed in Hertz (Hz).<sup>2</sup>

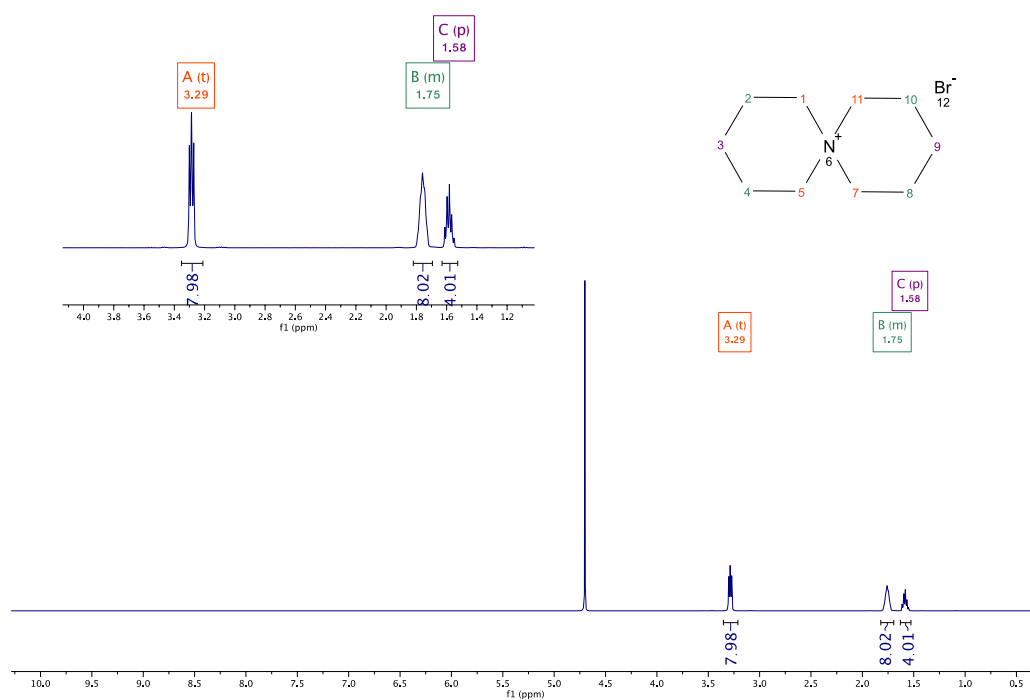


**Figure S3:**  $^1\text{H-NMR}$ -spectrum of [ASU]Br in Deuterium Oxide. All protons of the cyclic aliphatic amine could be assigned, confirming the purity of the compound.

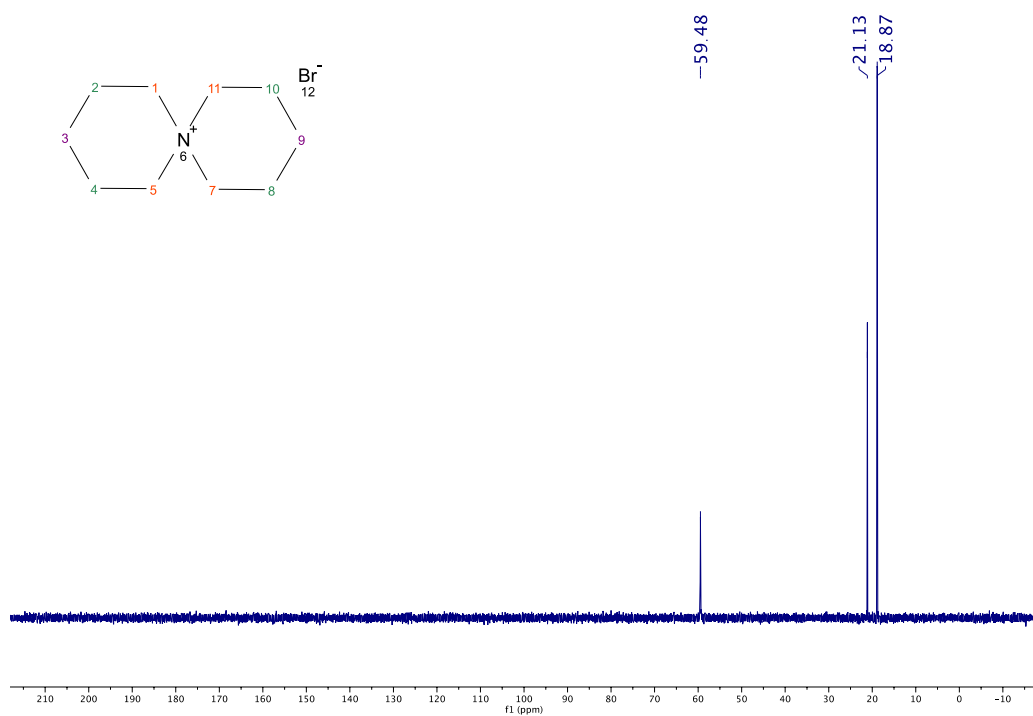


**Figure S4:**  $^{13}\text{C-NMR}$ -spectrum of [ASU]Br in Deuterium Oxide, showcasing only the three expected signals.



## Thermal analysis of the coordination networks

### Differential Scanning Calorimetry (DSC):

A DSC measurement was carried out on a DSC Q2000 from *TA instruments* with a heating rate of  $10 \text{ K min}^{-1}$  and a constant helium gas flow rate of  $25 \text{ ml min}^{-1}$ . A sample mass of  $6.7400 \text{ mg}$  was used for heating/cooling cycles. With regard to the decomposition temperature of the material, a temperature range between  $-150 \text{ }^\circ\text{C}$  and  $150 \text{ }^\circ\text{C}$  was chosen, using liquid nitrogen as cooling medium.

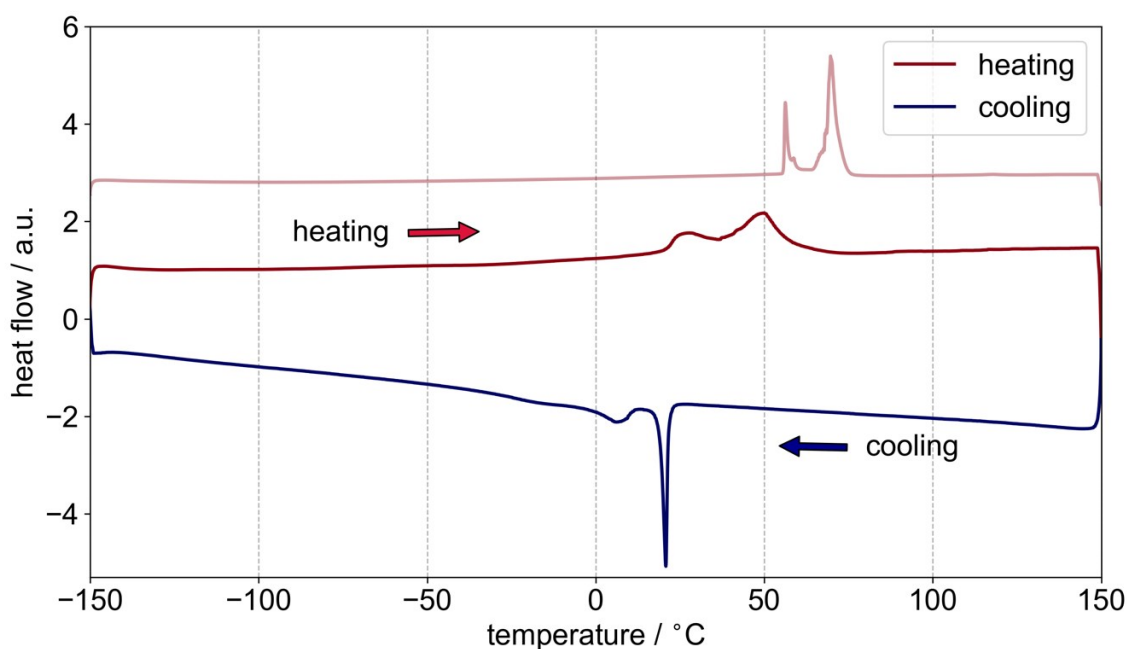


**Figure S5:** DSC curve as a function of temperature obtained by heating (red) and cooling (blue) the sample  $[\text{ASU}][\text{Cd}(\text{C}_2\text{N}_3)_3]$  at a rate of  $10 \text{ K min}^{-1}$  and a constant helium gas flow rate of  $25 \text{ ml min}^{-1}$ . An irreversible heat event during the first heating cycle at approximately  $55 \text{ }^\circ\text{C}$  is indicated by a feature, visualised by the upper light red line. During the subsequent cycles, a reproducible, reversible heat event at  $20 \text{ }^\circ\text{C}$  (heating) and  $22 \text{ }^\circ\text{C}$  (cooling) is observed. Please note, that these reversible heat event can be regarded as two distinct events, pointing at the possibility of two phase transitions with phase transition temperatures close to each other.

### Thermogravimetric analysis:

The determination of the thermal stability of the material was carried out with a *Netzsch STA 449F5* Jupiter machine using aluminum oxide pans with a sample mass of  $8.1540 \text{ mg}$ . The temperature of the oven cell was calibrated based on the melting points of the following metals: In, Sn, Bi and Zn. A baseline correction was performed by screening an empty sample pan with the respective temperature program prior to the experiment.

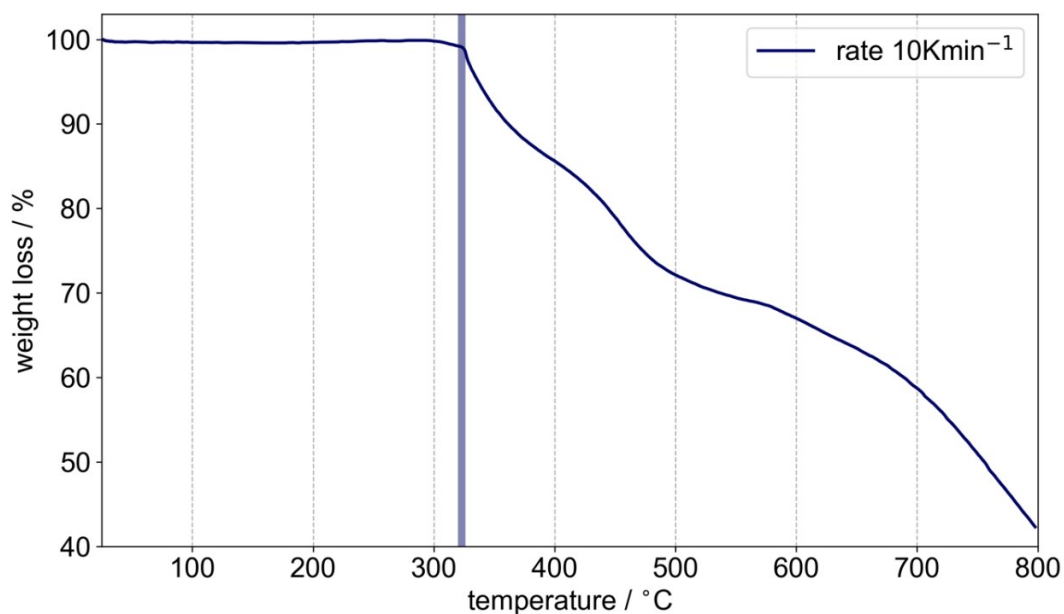


**Figure S6:** Thermal gravimetric analysis of [ASU][Cd(C<sub>2</sub>N<sub>3</sub>)<sub>3</sub>] from 25 °C to 800 °C with a rate of 10 K min<sup>-1</sup>. The vertical blue line indicates the point of decomposition around 323 °C.

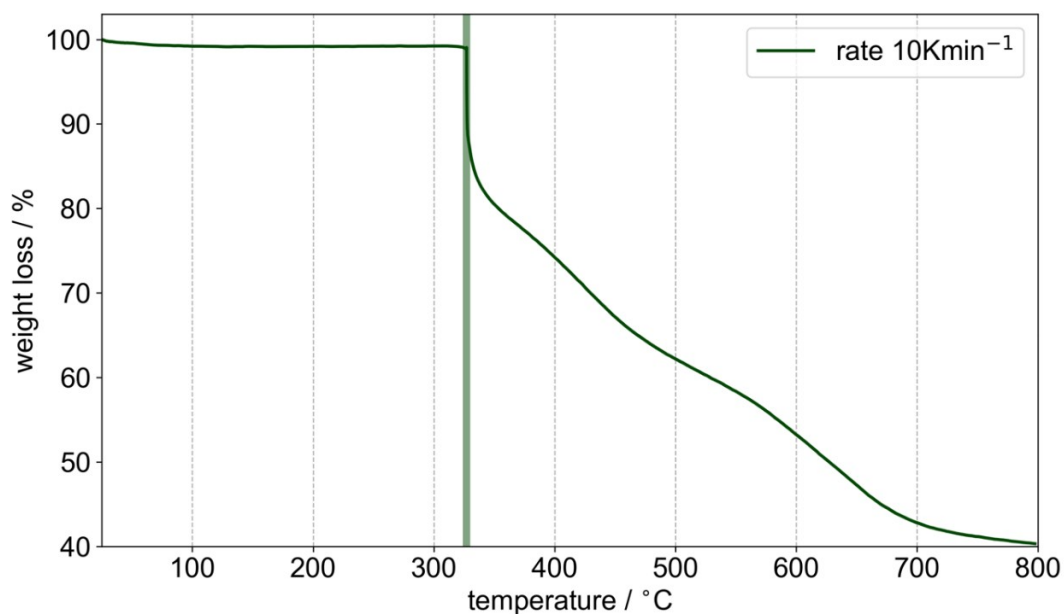


**Figure S7:** Thermal gravimetric analysis of [ASU]<sub>2</sub>[Ni<sub>2</sub>(C<sub>2</sub>N<sub>3</sub>)<sub>6</sub>]·2H<sub>2</sub>O from 25 °C to 800 °C with a rate of 10 K min<sup>-1</sup>. No sign for any weight loss that could potentially relate to a release of the coordinated water molecule can be observed. The vertical green line indicates the point of decomposition around 325 °C.

## Powder X-ray diffraction data

The PXRD measurements were performed using *Debye-Scherrer* geometry with borosilicate glass capillaries (0.5 mm in diameter) for the Cd perovskite compound and *Bragg-Brentano* geometry for the non-perovskite coordination networks in a PANalytical Empyrean diffractometer and a PANalytical PIXcel 1D detector with in-house Cu K<sub>α</sub> radiation ( $\lambda_1 = 1.5406 \text{ \AA}$ ,  $\lambda_2 = 1.5444 \text{ \AA}$ ,  $I_2/I_1 = 0.5$ ) operated at 45 kV (voltage) and 40 mA (intensity). A Ni-filter was used to remove the K<sub>β</sub> radiation. The measurement range was from 5.0° to 90° (2 $\theta$ ) for the Cd compound and from 5.0° to 50° (2 $\theta$ ) for the Mn, Co and Ni compounds with a minimum step size of 0.031° (2 $\theta$ ).

*Pawley* profile fit analysis was carried out for all patterns by using TOPAS v6. Standard deviations of all parameters were calculated and the use of "randomize\_on\_errors" ensured that the minimum of

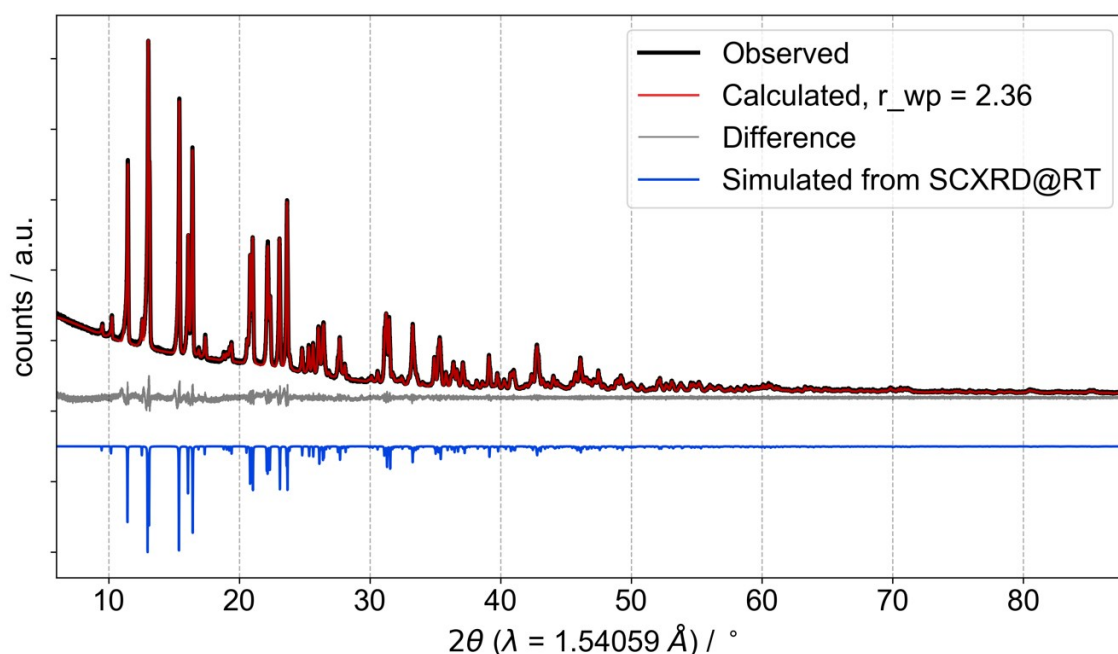


**Figure S8:** The Powder X-ray diffraction pattern of the obtained [ASU][Cd(C<sub>2</sub>N<sub>3</sub>)<sub>3</sub>] compound is shown in black, the simulated pattern from the single crystal structure at room temperature in blue and the calculated data from Pawley profile fit analysis in red, with  $r_{wp} = 2.36$ ,  $r_{exp} = 1.55$  and  $GOF = 1.52$ . The difference curve of the Pawley profile fit (grey) and the experimental data indicates the phase purity of the Cd compound.

refinement was achieved.

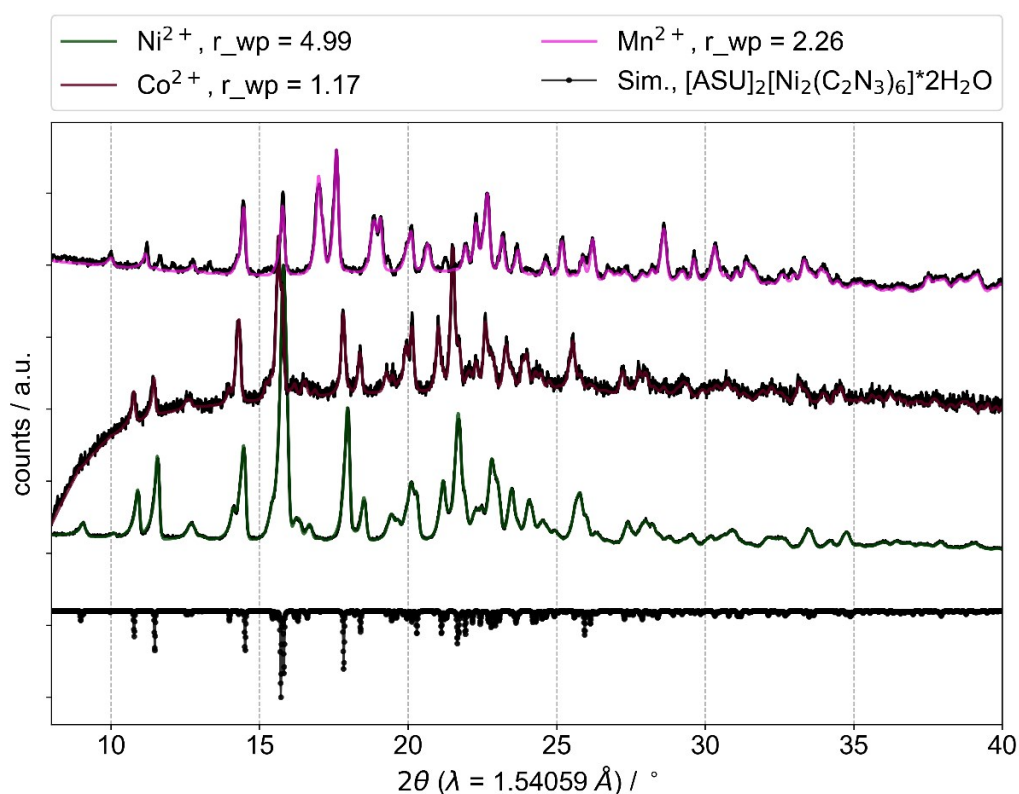


**Figure S9:** The Powder X-ray diffraction patterns of the isostructural  $[\text{ASU}]_2[\text{B}_2(\text{C}_2\text{N}_3)_6]\cdot 2\text{H}_2\text{O}$  ( $\text{B} = \text{Mn}^{2+}$ ,  $\text{Co}^{2+}$  and  $\text{Ni}^{2+}$ ) compounds are shown in pink ( $\text{B} = \text{Mn}^{2+}$ ), purple ( $\text{B} = \text{Co}^{2+}$ ) and green ( $\text{B} = \text{Ni}^{2+}$ ) and the simulated pattern from the single crystal structure of the Ni compound.

**Table S1:** Comparison of the crystallographic data of the coordination networks  $[\text{ASU}]_2[\text{B}_2(\text{C}_2\text{N}_3)_6]\cdot 2\text{H}_2\text{O}$  ( $\text{B} = \text{Mn}^{2+}$ ,  $\text{Co}^{2+}$  and  $\text{Ni}^{2+}$ ), extracted from the PXRD data.

$[\text{ASU}]_2[\text{M}_2(\text{C}_2\text{N}_3)_6]\cdot 2\text{H}_2\text{O}$	$\text{M} = \text{Mn}^{2+}$	$\text{M} = \text{Co}^{2+}$	$\text{M} = \text{Ni}^{2+}$
a (Å)	19.828(6)	20.628(6)	20.508(7)
b (Å)	10.187(3)	10.009(3)	9.971(4)
c (Å)	20.599(4)	20.900(5)	20.754(7)
Beta $\beta$ (°)	105.73(1)	106.19(1)	106.18(3)
Cellvolume V (Å <sup>3</sup> )	4005(2)	4144(2)	4076(2)
Space group	$P2_1/n$	$P2_1/n$	$P2_1/n$
r_wp	2.265	0.901	4.992
r_exp	1.569	1.010	1.414
GOF	1.443	0.892	3.530

## Single crystal X-ray diffraction data

Single crystal X-Ray diffraction intensity data were collected on a *Bruker* APEX-II CCD diffractometer equipped with a fine-focus tube with a Mo K $\alpha$  radiation source ( $\lambda = 0.71073 \text{ \AA}$ ), a *Triumph* monochromator, a CMOS plate detector and an *Oxford* Cryosystems cooling device by using the APEX III software package.<sup>3</sup> The crystals were fixed on the top of a microsampler, transferred to the diffractometer and frozen under a stream of cold nitrogen. A matrix scan was used to determine the initial lattice parameters. Reflections were merged and corrected for Lorentz and polarization effects, scan speed, and background using SAINT.<sup>4</sup> Absorption corrections, including odd and even ordered spherical harmonics were performed using SADABS.<sup>5</sup> Space group assignments were based upon systematic absences, E-statistics, and successful refinement of the structures. Data reduction was performed with APEX3 and structure solution was performed by using SHELX<sup>6</sup> as integrated in Olex2.<sup>7</sup> Structures were solved by direct methods with the aid of successive difference Fourier maps, and were refined against all data. Hydrogen atoms were placed in calculated positions and refined using a riding model.

**Table S2:** Crystallographic data from SCXRD for the [ASU][Cd(C<sub>2</sub>N<sub>3</sub>)<sub>3</sub>] compound at 100 K.

<b>Compound</b>	[ASU][Cd(C <sub>2</sub> N <sub>3</sub> ) <sub>3</sub> ]
<b>Chemical Formula</b>	C <sub>16</sub> H <sub>20</sub> CdN <sub>10</sub>
<b>Formula weight (g/mol)</b>	464.83
<b>Temperature (K)</b>	100
<b>Crystal system</b>	orthorhombic
<b>Space group</b>	<i>Pna</i> 2 <sub>1</sub>
<b>a (Å)</b>	17.1022(9)
<b>b (Å)</b>	10.7274(5)
<b>c (Å)</b>	10.7037(5)
<b><math>\alpha</math> (°)</b>	90
<b><math>\beta</math> (°)</b>	90
<b><math>\gamma</math> (°)</b>	90
<b>Volume (Å<sup>3</sup>)</b>	1963.72(17)
<b>Z</b>	4
<b><math>\rho_{\text{calc}}</math> (g/cm<sup>3</sup>)</b>	1.572
<b><math>\mu</math> (mm<sup>-1</sup>)</b>	1.135
<b>F (000)</b>	936

---

<b>Radiation</b>	MoK $\alpha$ ( $\lambda = 0.71073$ )
<b>2<math>\theta</math> range for data collection (°)</b>	4.482 to 54.196
<b>Index ranges</b>	$-21 \leq h \leq 21$ $-13 \leq k \leq 13$ $-13 \leq l \leq 13$
<b>Reflections collected</b>	63288
<b>Independent reflections</b>	4336 [ $R_{\text{int}} = 0.0421$ , $R_{\text{sigma}} = 0.0160$ ]
<b>Data/restraints/parameters</b>	4336/1/245
<b>Goodness of fit on <math>F^2</math></b>	1.125
<b>Final R indexes [<math>I &gt; 2\sigma(I)</math>]</b>	$R_1 = 0.0153$ , $wR_2 = 0.0355$
<b>Final R indexes [all data]</b>	$R_1 = 0.0175$ , $wR_2 = 0.0377$
<b>Largest diff. peak/hole/ (<math>\text{\AA}^{-3}</math>)</b>	0.24/-0.42
<b>Flack parameter</b>	0.09(2)
<b>CSD number</b>	2006488

---

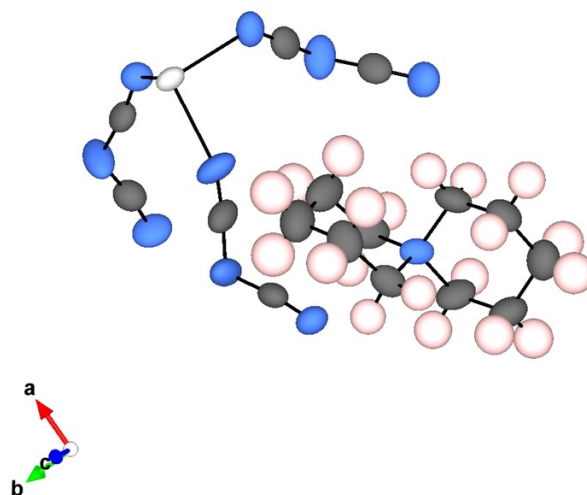


**Figure S10:** Structure of the  $ABX_3$  repetition unit of the  $[\text{ASU}][\text{Cd}(\text{C}_2\text{N}_3)_3]$  compound shown as displacement ellipsoids with 90% probability. The  $(\text{C}_2\text{N}_3)^-$  ligands act as bridges between the  $\text{Cd}^{2+}$  cations and the  $[\text{ASU}]^+$  cations are located in the void of the pseudocubic  $\text{ReO}_3$ -type cavities. Colour code: Cd – light grey, N – blue, C – dark grey, H – light pink.

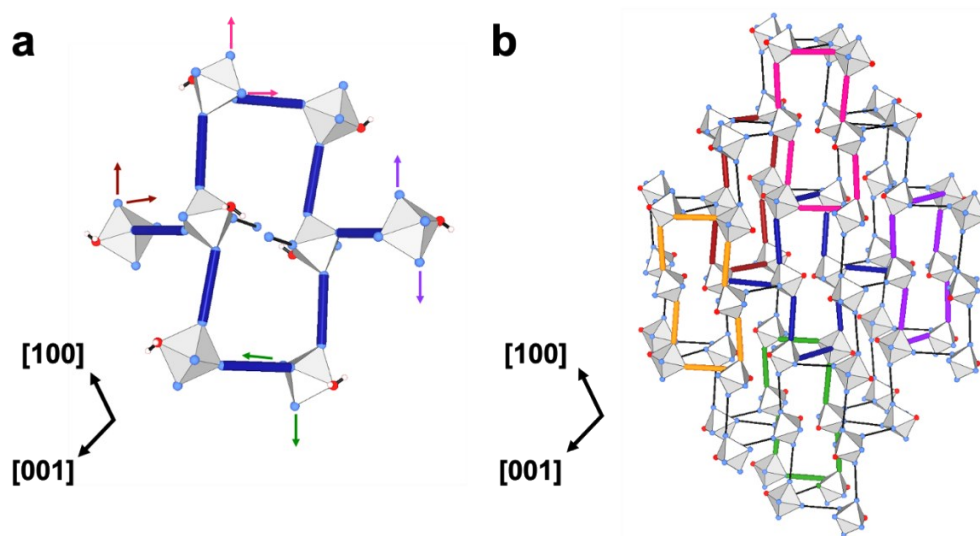
**Table S3:** Crystallographic data from SCXRD for the [ASU]<sub>2</sub>[Ni<sub>2</sub>(C<sub>2</sub>N<sub>3</sub>)<sub>6</sub>·2H<sub>2</sub>O compound at 100 K.

<b>Compound</b>	[ASU] <sub>2</sub> [Ni <sub>2</sub> (C <sub>2</sub> N <sub>3</sub> ) <sub>6</sub> ·2H <sub>2</sub> O
<b>Chemical Formula</b>	C <sub>32</sub> H <sub>44</sub> N <sub>20</sub> Ni <sub>2</sub> O <sub>2</sub>
<b>Formula weight (g/mol)</b>	858.29
<b>Temperature (K)</b>	100
<b>Crystal system</b>	monoclinic
<b>Space group</b>	<i>P</i> 2 <sub>1</sub> / <i>n</i>
<b>a (Å)</b>	20.3343(9)
<b>b (Å)</b>	9.9398(5)
<b>c (Å)</b>	20.5387(10)
<b>α (°)</b>	90
<b>β (°)</b>	106.735(2)
<b>γ (°)</b>	90
<b>Volume (Å<sup>3</sup>)</b>	3975.4(3)
<b>Z</b>	4
<b>ρ<sub>calc</sub> (g/cm<sup>3</sup>)</b>	1.434
<b>μ (mm<sup>-1</sup>)</b>	1.005
<b>F (000)</b>	1792.0
<b>Radiation</b>	MoK <sub>α</sub> (λ = 0.71073)
<b>2θ range for data collection (°)</b>	4.066 to 52.744
<b>Index ranges</b>	-25 ≤ <i>h</i> ≤ 25 -12 ≤ <i>k</i> ≤ 12 -25 ≤ <i>l</i> ≤ 25
<b>Reflections collected</b>	185958
<b>Independent reflections</b>	8144 [R <sub>int</sub> = 0.0626, R <sub>sigma</sub> = 0.0173]
<b>Data/restraints/parameters</b>	8144/0/491
<b>Goodness of fit on F<sup>2</sup></b>	1.080
<b>Final R indexes [I &gt; 2σ (I)]</b>	R <sub>1</sub> = 0.0477, wR <sub>2</sub> = 0.1030
<b>Final R indexes [all data]</b>	R <sub>1</sub> = 0.0588, wR <sub>2</sub> = 0.1130
<b>Largest diff. peak/hole/ (Å<sup>-3</sup>)</b>	0.69/-0.61
<b>CSD number</b>	2006489

**Single crystal structure of non-perovskite coordination networks:**

For the smaller divalent B-site cations ( $B = \text{Mn}^{2+}$ ,  $\text{Co}^{2+}$ , and  $\text{Ni}^{2+}$ ), isostructural diamond-type coordination networks with the general formula  $[\text{ASU}]_2[\text{B}_2(\text{C}_2\text{N}_3)_6] \cdot 2\text{H}_2\text{O}$  could be obtained. The  $\text{Mn}^{2+}$ ,  $\text{Co}^{2+}$  and  $\text{Ni}^{2+}$  compounds crystallise in the monoclinic centrosymmetric space-group  $P2_1/n$ . The underlying topology of the crystal structure was determined with TopCryst.<sup>8</sup>

**Figure S11:** The structure of the coordination networks  $[\text{ASU}]_2[\text{B}_2(\text{C}_2\text{N}_3)_6] \cdot 2\text{H}_2\text{O}$  ( $B = \text{Mn}^{2+}$ ,  $\text{Co}^{2+}$  and  $\text{Ni}^{2+}$ ) exemplary shown with the Ni compound. **(a)** shows the repeating motif formed of  $\text{B}^{2+}$  and  $(\text{C}_2\text{N}_3)^-$  bridging ligands. **(b)** The supercell  $2 \times 2 \times 2$  for a schematic representation of the unusual network connectivity. The repeating unit of **(a)** is shown in the middle (dark blue) and individual rings consists of six linked  $\text{BN}_5\text{O}$  octahedrons that display two corners at the same time.  $[\text{ASU}]^+$  cations, C atoms and H atoms in **(b)** were removed for better visualisation of the structure. Colour code: B – light grey, O – red, H – white, N – light blue.





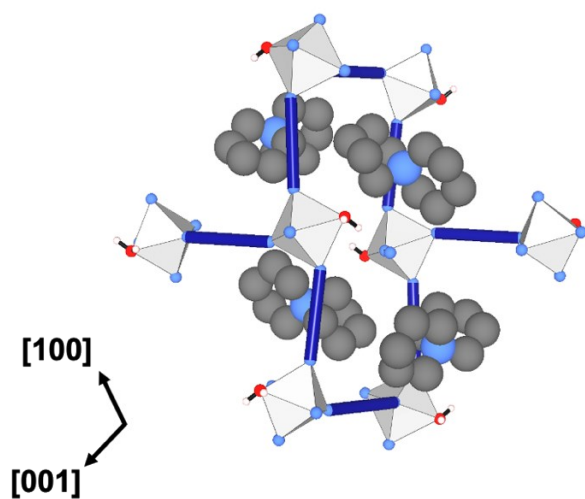


**Figure S12:** Visualisation of the dominating motif shown with the Ni compound and with [ASU]<sup>+</sup> cations for charge balance. For a better demonstration, the non-bridging  $\mu_{1,5}$ -dca linkers and the C atoms of the ligand were removed. Colour code: Ni – light grey, O – red, H – white, N – light blue, C – dark grey.

## Group theoretical analysis

Group-theoretical analysis was carried out by the web-based software ISODISTORT.<sup>9</sup> The structure was simplified by removing the A-site cation and the software FINDSYM<sup>10</sup> was used to verify that the omission of the cation did not change the symmetry. The modified structure was decomposed relative to a hypothetical parent perovskite structure with symmetry  $Pm\bar{3}m$  and linear linker. The origin was located on the A-site; note that the exact irrep label depends on the origin choice. Details of the results including magnitude are given in Table S4.

**Table S4:** Group theoretical analysis of  $[ASU][Cd(C_2N_3)_3]$ . The four strongest irreps are listed in order of decreasing magnitude. It shows the irrep, its relative magnitude, its order parameter direction, the space group it would give to if acting in isolation and a description. The primary order parameters (the set of distortions fully accounting for the symmetry) with largest magnitude are  $M_2^-$ ,  $R_5^-$  and  $M_5^+$ .

Irrep	Order parameter direction	Space group	Description
$M_2^-$	(a;0;0)	$P4/nmm$	Checkerboard shift
$R_5^-$	(0,a,a)	$Imma$	Out-of-phase conv. tilt
$X_5^+$	(0,0;0,0;a,a)	$Cmcm$	Dicyanamide bending
$M_5^+$	(a,-a;0,0;0,0)	$Pmna$	Unconventional tilts

## Second Harmonic Generation studies

Assessment of SHG efficiency of  $[\text{ASU}]\text{Cd}(\text{C}_2\text{N}_3)_3$  was performed with the use of Kurtz-Perry technique.

Generally, Kurtz-Perry technique requires the use of size-graded crystalline samples. Potassium dihydrogen phosphate (KDP) was used as a SHG reference.<sup>11,12</sup> Thus, prior to measurements, the single crystals of  $[\text{ASU}]\text{Cd}(\text{C}_2\text{N}_3)_3$  and KDP were crushed with spatula and sieved through a mini-sieve set (Aldrich), collecting a microcrystal size fraction of 88 - 125  $\mu\text{m}$ . Next, size-graded samples of  $[\text{ASU}]\text{Cd}(\text{C}_2\text{N}_3)_3$  and KDP were fixed between microscope glass slides forming tightly packed layers, sealed, and mounted to holder. Kurtz-Perry test was performed at 293K. As seen in Fig. S13, strong SHG signal at 400 nm was registered for  $[\text{ASU}]\text{Cd}(\text{C}_2\text{N}_3)_3$ , unequivocally confirming its non-centrosymmetric structure. Under identical irradiation conditions the SHG signal was collected from the KDP powder of the same particle size. The ratio of integral intensities of SHG signals demonstrates that the relative SHG efficiency of  $[\text{ASU}]\text{Cd}(\text{C}_2\text{N}_3)_3$  is equal to 0.21 that of KDP at 293K.

The laser radiation was delivered from a *Quantronix Integra-C* regenerative amplifier operating at 800 nm, pulse duration of 130 fs, and repetition rate of 1 kHz. The laser beam was passed through 5 mm aperture and was directed onto  $[\text{ASU}]\text{Cd}(\text{C}_2\text{N}_3)_3$  and KDP samples at 45 degrees. Laser beam was unfocused and its mean power was equal to 86 mW. Signal-collecting optics, mounted to the glass optical fiber, was placed perpendicularly to the plane of sample (backscattering geometry). Scattered pumping radiation was suppressed with the use of 700 nm shortpass dielectric filter (FESH0700, Thorlabs). The spectra of the diffused SHG were recorded by an *Ocean Optics Flame T fiber-coupled* CCD spectrograph (200  $\mu\text{m}$  entrance slit).

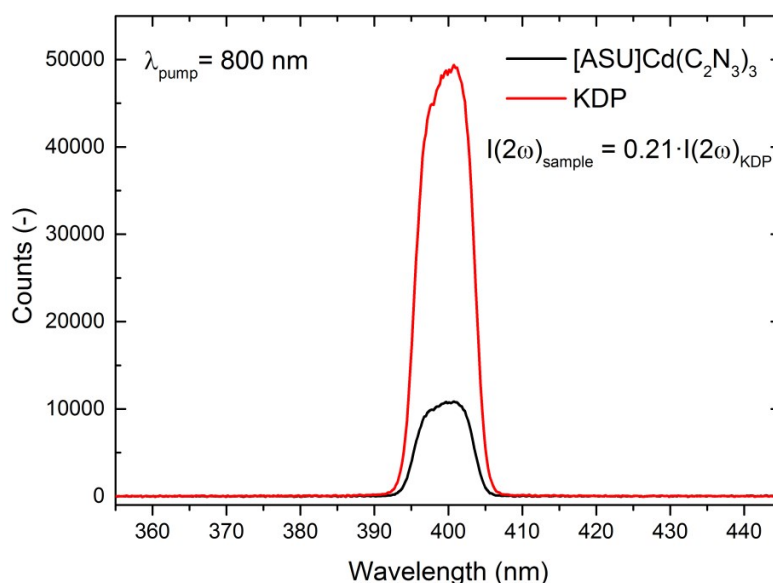


**Figure S13:** A comparison of SHG traces for  $[\text{ASU}]\text{Cd}(\text{C}_2\text{N}_3)_3$  (black) and that of KDP (red). The collection time of SHG signals for both,  $[\text{ASU}]\text{Cd}(\text{C}_2\text{N}_3)_3$  and KDP, was equal to 6000 ms. Powders of both compounds were sieved into 88 - 125  $\mu\text{m}$  particle size range.

**References**

1. M. G. Marino and K. D. Kreuer, *ChemSusChem*, 2015, **8**, 513.
2. G. R. Fulmer, A. J. M. Miller, N. H. Sherden, H. E. Gottlieb, A. Nudelman, B. M. Stoltz, J. E. Bercaw and K. I. Goldberg, *Organometallics*, 2010, **29**, 2176.
3. APEX suite of crystallographic software, *APEX 2 Version 2008.4*, Bruker AXS Inc., Madison, WI, USA, 2008.
4. SAINT, *Version 7.56a*, Bruker AXS Inc., Madison, WI, USA, 2008.
5. SADABS, *Version 2008/1*, Bruker AXS Inc., Madison, WI, USA, 2008.
6. G. M. Sheldrick, *Acta crystallographica. Section A, Foundations of crystallography*, 2008, **64**, 112.
7. O. V. Dolomanov, L. J. Bourhis, R. J. Gildea, J. A. K. Howard and H. Puschmann, *J Appl Crystallogr*, 2009, **42**, 339.
8. V. A. Blatov, A. P. Shevchenko and D. M. Proserpio, *Cryst. Growth Des.*, 2014, **14**, 3576.
9. B. J. Campbell, H. T. Stokes, D. E. Tanner and D. M. Hatch, *J. Appl. Crystallogr.*, 2006, **39**, 607.
10. H. T. Stokes and D. M. Hatch, *J. Appl. Crystallogr.*, 2005, **38**, 237.
11. S. K. Kurtz and T. T. Perry, *Journal of Applied Physics*, 1968, **39**, 3798.
12. A. Graja, *Phys. Stat. Sol. (b)*, 1968, **27**, K93-K97.

## 8.2 STUDY III: Electronic Supporting Information

Electronic Supplementary Material (ESI) for Materials Horizons.  
This journal is © The Royal Society of Chemistry 2021

### Electronic Supporting Information (ESI)

## Tilt and Shift Polymorphism in Molecular Perovskites

Stefan Burger,<sup>†a</sup> Shivani Grover,<sup>†b</sup> Keith T. Butler,<sup>c</sup> Hanna L. B. Boström,<sup>d</sup> Ricardo Grau-Crespo<sup>\*b</sup> and Gregor Kieslich<sup>\*a</sup>

† shared contribution.

\* gregor.kieslich@tum.de.

\* r.grau-crespo@reading.ac.uk.

### Contents

Experimental Procedures .....	2
Synthetic procedure for $(nPr)_3(CH_3)NCl$ .....	5
Elemental analysis for $[(C_3H_7)_3(CH_3)N]M(C_2N_3)_3$ ( $M = Mn^{2+}, Co^{2+}, Ni^{2+}$ ) .....	5
NMR data of the precursor compound $(nPr)_3(CH_3)NCl$ .....	6
Thermogravimetric analysis of $[(C_3H_7)_3(CH_3)N]M(C_2N_3)_3$ ( $M = Mn^{2+}, Co^{2+}, Ni^{2+}$ ) .....	7
Reversible Differential Scanning Calorimetry (DSC) of $[(C_3H_7)_3(CH_3)N]M(C_2N_3)_3$ ( $M = Mn^{2+}, Co^{2+}, Ni^{2+}$ ) .....	8
Fourier-transform Infrared spectroscopy (FT-IR) .....	9
Photographs of crystalline $[(C_3H_7)_3(CH_3)N]M(C_2N_3)_3$ ( $M = Mn^{2+}, Co^{2+}, Ni^{2+}$ ) .....	9
Powder X-Ray diffraction data .....	10
Single crystal X-Ray diffraction data .....	14
Quantum chemical calculations .....	19
References .....	20

## Experimental Procedures

### General information.

All chemicals used for the reactions were purchased from commercial suppliers (Sigma Aldrich, vwr) and were used without further purification. Solvents and millipore water for the syntheses and washing steps were in quality of reagent grade.

### Synthetic procedure for $(n\text{Pr})_3(\text{CH}_3)\text{NCl}$ .

The synthesis of  $\text{C}_{10}\text{H}_{24}\text{NI}$  was carried out following a standard nucleophilic substitution reaction protocol. Tri-*n*-propylamine 1 (14.33 g, 100 mmol, 1.0 eq.) was dissolved in 70 ml acetonitrile and stirred with dropwise added methyl iodide 2 (14.19 g, 100 mmol, 1.0 eq.) in 20 ml acetonitrile at room temperature for 3 hours. After solvent removal, the residual solid was recrystallised in ethyl acetate/acetonitrile (10:1) to yield a fine, colourless powder of  $\text{C}_{10}\text{H}_{24}\text{NI}$  3. By slowly rinsing an aqueous solution of  $\text{C}_{10}\text{H}_{24}\text{NI}$  over an ion exchange resin column with subsequent elution with diluted hydrochloric acid, the iodide salt was converted into the respective chloride salt recovering  $(n\text{Pr})_3(\text{CH}_3)\text{NCl}$  4 (18.02 g, 93.0 mmol, 93.0 %) as colourless powder after evaporation of the water under reduced pressure.

### Synthesis of $[(\text{C}_3\text{H}_7)_3(\text{CH}_3)\text{N}]\text{M}(\text{C}_2\text{N}_3)_3$ ( $\text{M} = \text{Mn}^{2+}, \text{Co}^{2+}, \text{Ni}^{2+}$ ).

In a representative experiment, solutions of  $(n\text{Pr})_3(\text{CH}_3)\text{NCl}$  4 (0.2 M, 1 eq.), sodium dicyanamide  $\text{Na}(\text{C}_2\text{N}_3)$  (2.0 M, 3 eq.) and the respective metal-salt precursor ( $\text{Mn}(\text{NO}_3)_2 \cdot 4\text{H}_2\text{O}$ ,  $\text{Co}(\text{NO}_3)_2 \cdot 6\text{H}_2\text{O}$  and  $\text{NiCl}_2 \cdot 6\text{H}_2\text{O}$ , 0.2 M, 1 eq.) in ultrapure water were prepared and mixed at ambient temperature and allowed to stand for two days until large cuboid block crystals with crystal sizes between 0.5 – 1 mm were observed. The crystals were collected and washed with ice-cold ultrapure water several times, dried at room temperature and stored under air for several months with no evidence for sample degradation, *i.e.* all obtained materials are stable under ambient conditions.

For the high temperature crystallisation, precursor solutions of the three components were mixed in the same way as for the mild-solution approach, but placed in a screw-cap-sealed, pressure-tight glass vial and were heated to 95°C by means of a temperature-controlled metal block. After two days, the presence of crystalline fragments was observed, which after washing with ice-cold ultrapure water were suitable for single-crystal diffraction experiments.

### NMR data of the precursor compound $(n\text{Pr})_3(\text{CH}_3)\text{NCl}$ .

$^1\text{H}$ -NMR and  $^{13}\text{C}$ -NMR spectra were recorded on a *Bruker Avance III 400* spectrometer at room temperature. Chemical shifts are expressed as parts per million (ppm,  $\delta$ ) downfield of tetramethylsilane (TMS) and are referenced to the residual solvent signal of acetonitrile.<sup>2</sup> The description of signals include: s = singlet, t = triplet and m = multiplet. All coupling constants are absolute values and are expressed in Hertz (Hz).  $^{13}\text{C}$ -NMR was measured as  $^1\text{H}$ -NMR decoupled. All signals were assigned to the respective nuclei based on common 2D experiments like COSY, HSQC and HMBC.

### Elemental analysis for $[(\text{C}_3\text{H}_7)_3(\text{CH}_3)\text{N}]\text{M}(\text{C}_2\text{N}_3)_3$ ( $\text{M} = \text{Mn}^{2+}, \text{Co}^{2+}, \text{Ni}^{2+}$ ).

The elemental analysis experiments were carried out by the Microanalytical Laboratory of the Technical University of Munich, on an Euroanalysis instrument by *HEKAtech via* flash combustion and subsequent chromatographic separation. The elemental composition was determined twice with both measurements being in excellent agreement with the calculated values. Weighted sample amounts were between 1-2 mg.

### Thermomechanical analysis of $[(\text{C}_3\text{H}_7)_3(\text{CH}_3)\text{N}]\text{M}(\text{C}_2\text{N}_3)_3$ ( $\text{M} = \text{Mn}^{2+}, \text{Co}^{2+}, \text{Ni}^{2+}$ ).

Thermal stability of the materials was determined with a *Netzsch STA449 F5 Jupiter* machine (70  $\mu\text{L}$  aluminum oxide pans with lid). Sample amounts of 5-10 mg were heated at 10  $\text{K min}^{-1}$  to 800°C under a constant flow of argon gas (20  $\text{mL min}^{-1}$ ). Temperature calibration of the oven cell was performed based on the melting point of the following metals: In, Sn, Bi, Zn, Al and Au. The baseline was corrected screening an empty sample pan with the respective measurement program prior to the experiment. Thermal gravimetric analysis coupled with mass spectrometry (TG-MS) was performed on a *Netzsch STA 409* with the same temperature and heat rate program as mentioned before and evaluated mass spectrometry signal of  $\text{H}_2\text{O}$  at  $m/z$  18, while data was smoothed using a Loess filter with a span of 0.03. The onset point of thermal decomposition was calculated with the point of intersection for the two tangents of the plateau without weight loss and inflection of maximised weight loss as listed in Table S1.

Differential scanning calorimetry was conducted in a *TA Instruments DSC Q2000* with a heating rate of 10  $\text{K min}^{-1}$  and a constant helium purging gas flow rate of 25  $\text{ml min}^{-1}$ . The temperature window was from -150°C to 200°C and was controlled with the use of liquid nitrogen as cooling medium. The temperature of the oven cell and the heat flow signal was calibrated with respect to the melting point of indium metal and verified by the internal calibration tools provided by *TA Instruments*. The heat flow signal is shown as exo down.

### Fourier-transform Infrared spectroscopy (FT-IR)

The FTIR spectra at room temperature were collected on a *Bruker* Vertex 70 FTIR machine using a *Bruker* Platinum ATR.

### Powder X-Ray diffraction data

Measurements for bulk material analysis were performed in transmission geometry in a *STOE* STADI P (Darmstadt, Germany) diffractometer equipped with Mo  $K_{\alpha}$  radiation ( $\lambda = 0.7093 \text{ \AA}$ ), a curved Ge(111) monochromator and a *DECTRIS* Mythen 1K detector. Voltage and intensity were 50 kV and 40 mA, respectively. The measurement range was from  $2.0^{\circ}$  to  $36.0^{\circ}$  ( $2\theta$ ), with samples being fixed between two adhesive strips.

Variable temperature powder X-ray diffraction was performed in capillary mode on the same instrument using an *Oxford* Habcryo-X Cryostream 700 Cobra for temperature control with steps of 15 K. Thermal expansion coefficients are given in the section below.

All obtained Powder X-Ray diffraction patterns were analysed by performing a Pawley profile fit analysis using TOPAS Academic v6 in combination with jEdit for creating the input files.<sup>3,4</sup> Standard deviations of all parameters were calculated, and by using "randomise\_on\_errors", it was ensured that the minimum of the refinement was reached.

### Single crystal X-Ray diffraction data

Single crystal X-Ray diffraction intensity data were collected on a *Bruker* diffractometer equipped with a TXS rotating anode with Mo- $K_{\alpha}$  radiation source ( $\lambda = 0.71073 \text{ \AA}$ ), or a *Bruker* "D8 Venture Duo IMS" diffractometer equipped with an IMS microsource anode for fine-focus with a Mo- $K_{\alpha}$  radiation source, a CMOS plate detector (*Bruker* APEX III,  $\kappa$ -CMOS) and Helios optics, or on a *Bruker* "D8 Kappa Apex II" with a fine-focus sealed tube and a *Triumph* monochromator. For temperature control, an *Oxford* Cryosystems cooling device was used. Machine control was enabled by using the APEX2 (D8 Kappa) or the APEX3 (TXS, IMS) software package.<sup>5</sup> Appropriate crystals were selected under a microscope in perfluorinated ether, fixed on top of a kapton micro sampler (*MiTeGen*), transferred to the diffractometer and frozen under a stream of cold nitrogen. A matrix scan was used to determine the initial lattice parameters. Reflections were merged and corrected for Lorentz and polarisation effects, scan speed, and background using SAINT.<sup>6</sup> Absorption corrections, including odd and even ordered spherical harmonics were performed using SADABS.<sup>7</sup> Space group assignments were based upon systematic absences, E-statistics, and successful refinement of the structures. Data reduction was performed with APEX3 and structure solution was performed by using SHELX as integrated in Olex2.<sup>8-10</sup> Structures were solved by direct methods with the aid of successive difference Fourier maps, and were refined against all data. Hydrogen atoms were placed in calculated positions and refined using a riding model. Non-hydrogen atoms were refined with anisotropic displacement parameters. Full-matrix least-squares refinements were carried out by minimising  $\sum_w(F_o^2 - F_c^2)^2$  with the SHELXL weighting scheme.<sup>8</sup> The visualisation of the crystal structures were generated using VESTA 3.4.0.<sup>11</sup>

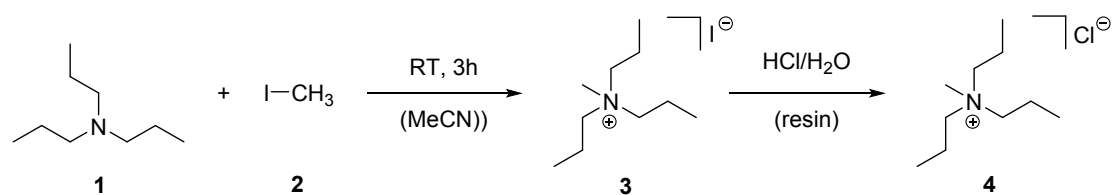
### Quantum chemical calculations

**Density functional theory simulations.** Our calculations are based on the density functional theory (DFT) as implemented in the Vienna Ab Initio Simulation Package (VASP).<sup>12,13</sup> The exchange-correlation energy of electrons is treated within the generalised gradient approximation (GGA) with the functional by Perdew, Burke and Ernzerhof (PBE).<sup>14</sup> In order to account for the limitations of the GGA to describe the d-orbitals of transition metals, we included Hubbard corrections for these orbitals (GGA+U), following the formalism introduced by Dudarev et al.,<sup>15</sup> where a single parameter ( $U_{\text{eff}}$ ) controls the strength of the correction. The  $U_{\text{eff}}$  parameters for Mn (4.0 eV), Co (3.3 eV), and Ni (6.4 eV) were taken from the work by Wang et al.,<sup>16</sup> where they were fitted so that GGA+U could reproduce the experimental oxidation energies in transition metal oxides. We also included dispersion corrections following Grimme's D3 scheme.<sup>17</sup> The projector augmented wave (PAW) method<sup>18,19</sup> was used to describe the interactions between the valence electrons and the frozen cores, which consisted of orbitals up to 1s for C and N, and up to 3p for the transition metals. We used an energy cut-off of 520 eV to truncate the planewave expansion of the Kohn-Sham wavefunctions, which was 30% above the default cut-off for the employed PAW potentials, to minimise Pulay errors. Brillouin zone (BZ) integrations were performed by sampling the reciprocal space using  $\Gamma$ -centred meshes of  $4 \times 3 \times 2$  k-points with reference to orthorhombic unit cell and of  $4 \times 4 \times 4$  k-points with reference to rhombohedral unit cell, which give similarly dense grids. Spin polarisation was allowed in all calculations to properly describe the magnetic transition metal cations.

**Phonon simulations.** Given the large size of the crystallographic unit cells, phonon dispersion curves were obtained from forces constants calculated by systematic displacements of ionic positions only within the unit cell, *via* the Phonopy code.<sup>20</sup> Representative phonon dispersion curves (in the case of the Mn compounds) for the orthorhombic and rhombohedral cells are shown in Fig. S13 a) and b). We are showing only the low-frequency region, but the phonon spectrum extends up to  $3200 \text{ cm}^{-1}$ .

The use of a single unit cell in the simulations, together with the softness of the low-frequency modes, led to numerical noise which translated into artificial imaginary modes in the phonon dispersion curves, away from the Brillouin centre. These imaginary frequencies could not be resolved by following the imaginary modes with ionic displacement in larger supercells (using the ModeMap code by Skelton et al.).<sup>21</sup> For example, the potential energy surfaces obtained by displacing the ions in the direction of eigenvectors for lowest-frequency bands at the F point for the rhombohedral phase, or for the U point for the orthorhombic phase, using appropriate supercells, showed normal convexity with a minimum at the optimised structures for both phases, Fig. S13 c). We therefore conclude that both structures are dynamically stable, representing local minima of the potential energy surface.

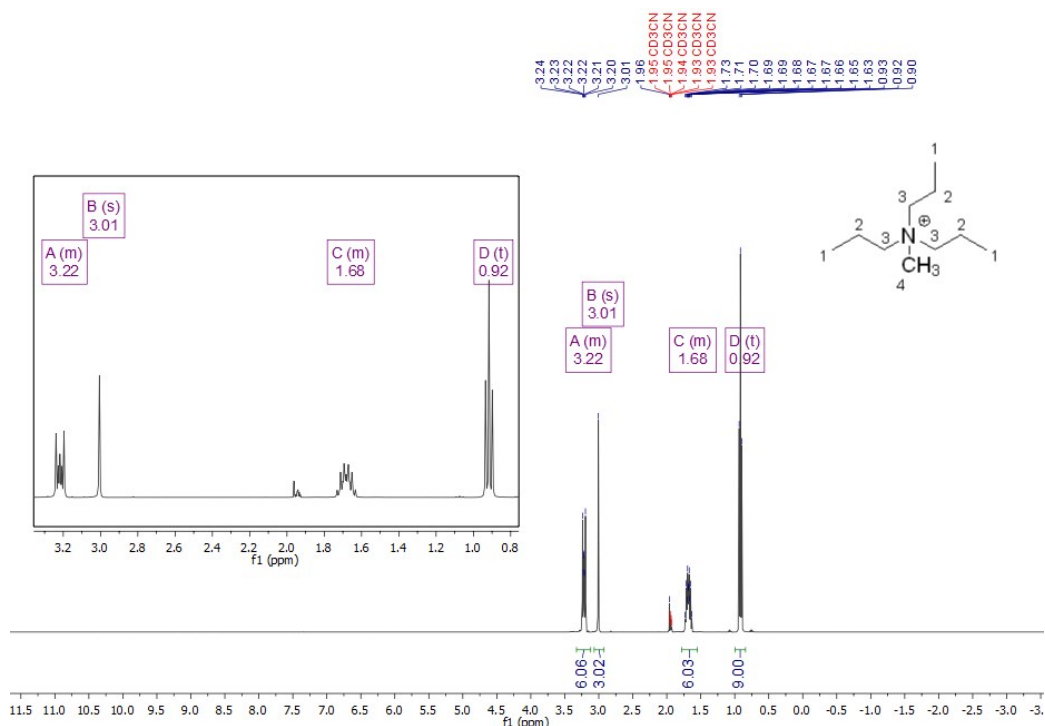
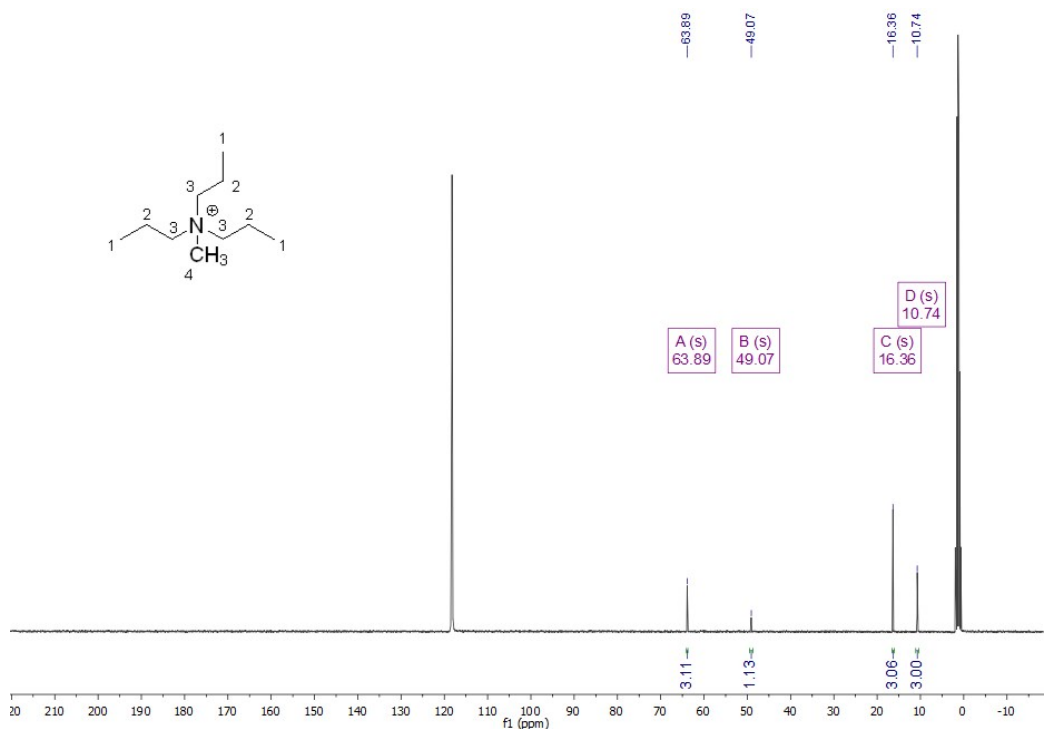


**Synthetic procedure for  $(nPr)_3(CH_3)NCl$ .****Fig. S1** Schematic of the synthesis route for  $(nPr)_3(CH_3)NCl$  following the Menshutkin reaction type.<sup>1</sup>**Elemental analysis for  $[(C_3H_7)_3(CH_3)N]M(C_2N_3)_3$  ( $M = Mn^{2+}, Co^{2+}, Ni^{2+}$ ).**

Elemental analysis calcd (%) for  $[(C_3H_7)_3(CH_3)N]Mn(C_2N_3)_3$ : C 46.72 H 5.88 N 34.05 Mn 13.35; found1 C 46.75 H 5.88 N 33.96, found2 C 46.85 H 5.90 N 34.06.

Elemental analysis calcd (%) for  $[(C_3H_7)_3(CH_3)N]Co(C_2N_3)_3$ : C 46.27 H 5.82 N 33.72 Co 14.19; found1 C 46.31 H 5.77 N 33.58, found2 C 46.35 H 5.80 N 33.64.

Elemental analysis calcd (%) for  $[(C_3H_7)_3(CH_3)N]Ni(C_2N_3)_3$ : C 46.29 H 5.83 N 33.74 Ni 14.14; found1 C 46.47 H 5.86 N 33.79, found2 C 46.58 H 5.87 N 33.87.

NMR data of the precursor compound  $(nPr)_3(CH_3)NCl$ .Fig. S2  $^1H$ -NMR spectrum of  $(nPr)_3(CH_3)NCl$  in acetonitrile- $d_3$ .Fig. S3  $^{13}C$ -NMR spectrum of  $(nPr)_3(CH_3)NCl$  in acetonitrile- $d_3$  with residual NMR solvent signals at  $\delta$  [ppm] = 118.26 (s) and 1.32 (hept).

$^1H$ -NMR (400 MHz, Acetonitrile- $d_3$ , 298 K):  $\delta$  [ppm] = 3.28 – 3.16 (m, 6H, C3-H), 3.01 (s, 3H, C4-H), 1.76 – 1.60 (m, 6H, C2-H), 0.92 (t,  $J$  = 7.3 Hz, 9H, C1-H).

$^{13}C$ -NMR (101 MHz, Acetonitrile- $d_3$ , 298 K):  $\delta$  [ppm] = 63.89 (C3), 49.07 (C4), 16.36 (C2), 10.74 (C1).

Thermogravimetric analysis of  $[(C_3H_7)_3(CH_3)N]M(C_2N_3)_3$  ( $M = Mn^{2+}, Co^{2+}, Ni^{2+}$ ).

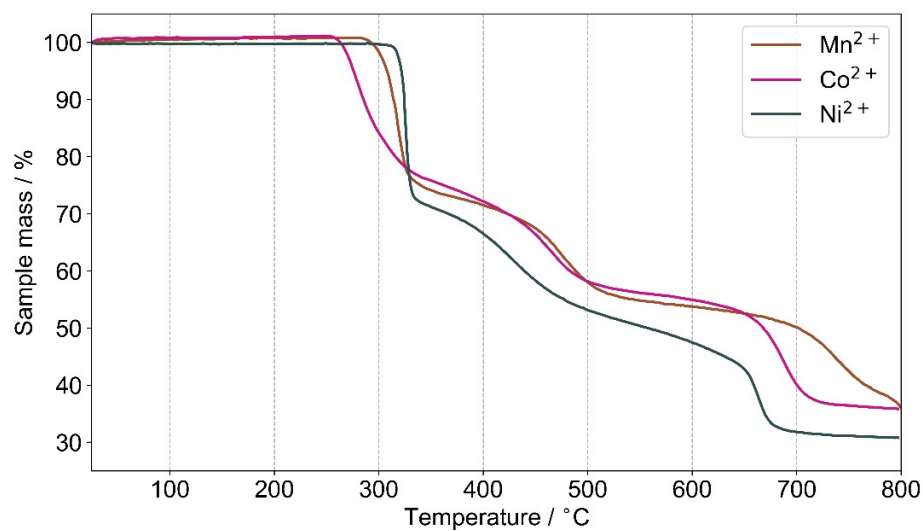


Fig. S4 TGA curves of  $[(C_3H_7)_3(CH_3)N]M(C_2N_3)_3$  with  $M$  being  $Mn^{2+}$  (brown),  $Co^{2+}$  (violet) and  $Ni^{2+}$  (dark green), indicating the thermal stability in an argon atmosphere.

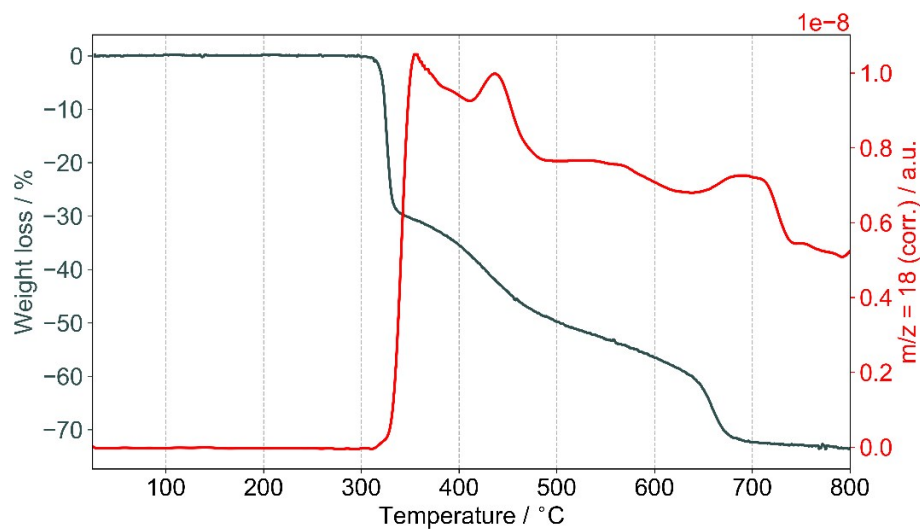


Fig. S5 Additional TGA curve (grey) coupled with mass spectrometry (red) for  $[(C_3H_7)_3(CH_3)N]Ni(C_2N_3)_3$ , showing no signs of weight loss during heating until the decomposition temperature.

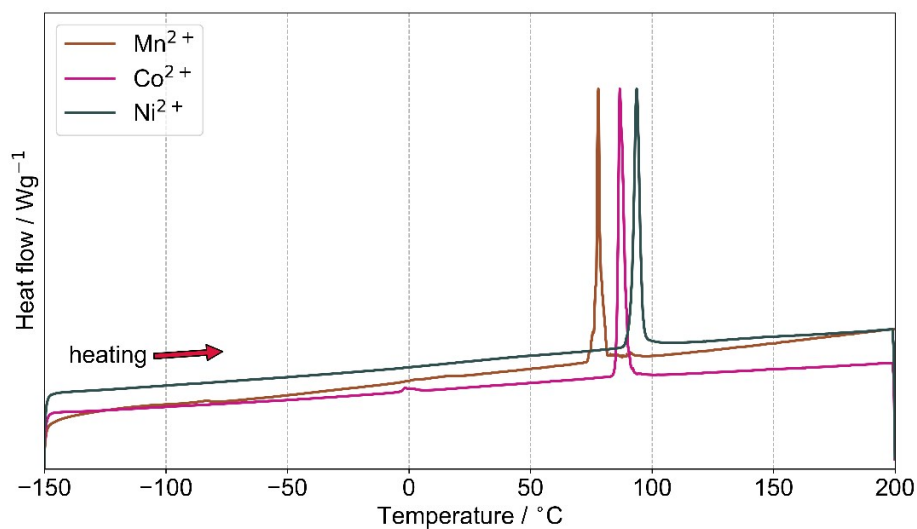
Reversible Differential Scanning Calorimetry (DSC) of  $[(C_3H_7)_3(CH_3)N]M(C_2N_3)_3$  ( $M = Mn^{2+}, Co^{2+}, Ni^{2+}$ ).

Fig. S6 Differential scanning calorimetry measurement for  $[(nPr)_3(CH_3)N]M(C_2N_3)_3$ . Shown is the curve for the first heating step of the as-synthesised materials from  $-150^\circ\text{C}$  to  $200^\circ\text{C}$ , highlighting the irreversible phase transition from the ambient  $Pnma$  phase to the high temperature  $R\bar{3}c$  phase. Colour code: brown -  $Mn^{2+}$ , violet -  $Co^{2+}$ , dark green -  $Ni^{2+}$ . Results including temperature of the phase transitions are summarised in Table S1.

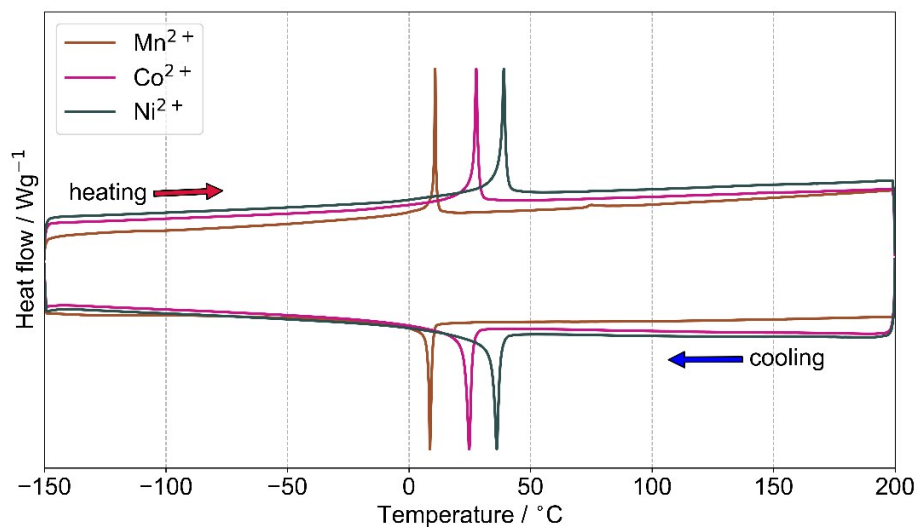


Fig. S7 Reversible differential scanning calorimetry measurement for  $[(nPr)_3(CH_3)N]M(C_2N_3)_3$ . Shown is the cyclic curve for the cooling with subsequent re-heating step of the materials after initial heat treatment, see Figure S6. Illustrated is the reversible rhombohedral-to-rhombohedral phase transition which is accessed when the as-synthesised samples are heated. Colour code: brown -  $Mn^{2+}$ , violet -  $Co^{2+}$ , dark green -  $Ni^{2+}$ . Thermodynamic characteristics for the phase transitions are summarised in Table S1.

Tab. S1 Phase transition characteristics for  $[(C_3H_7)_3(CH_3)N]M(C_2N_3)_3$  extracted from differential scanning calorimetry data with temperatures and enthalpies for the irreversible phase transition (Figure S6) as well as the reversible transition (Figure S7). Additionally, the decomposition temperature observed by TGA is listed.

M =	$T(\text{decomp.})^{[a]}$	$T_{PT}(\text{irrev.})^{[a]}$	$\Delta H_{PT}(\text{irrev.})^{[b]}$	$T_{PT}(\text{rev.})^{[a]}$	$\Delta H_{PT}(\text{rev.})^{[b]}$	$\Delta S_{PT}(\text{rev.})^{[c]}$
$Mn^{2+}$	304.8	76.9	7507.5	10.8	4932.3	17.4
$Co^{2+}$	263.6	85.4	8074.6	27.7	5324.9	17.7
$Ni^{2+}$	323.9	91.6	6629.5	39.0	5616.6	18.0

[a] in  $^\circ\text{C}$ . [b] in  $\text{J mol}^{-1}$ . [c] in  $\text{J (K mol)}^{-1}$ .

## Fourier-transform Infrared spectroscopy (FT-IR)

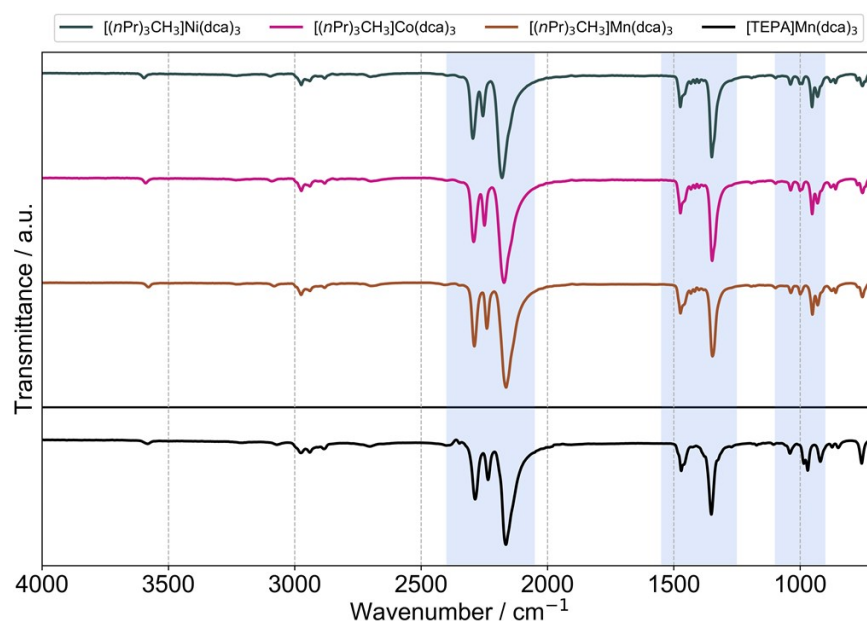


**Fig. S8** FT-IR spectra at room temperature for the as-synthesised series of  $[(C_3H_7)_3(CH_3)N]M(C_2N_3)_3$  with  $M$  being  $Mn^{2+}$  (brown),  $Co^{2+}$  (violet) and  $Ni^{2+}$  (dark green), indicating the isostructural nature of the three compounds. Additionally, the reference IR spectrum for  $[(C_3H_7)_4N]Mn(C_2N_3)_3$  (black) is shown, which shows the same signal arrangement as the  $[(C_3H_7)_3(CH_3)N]M(C_2N_3)_3$  series, typical for 3D dicyanamide-based molecular perovskites with  $\nu^- = 2300-2100\text{ cm}^{-1}$  (dca vibration modes),  $1500-1300\text{ cm}^{-1}$  ( $CH_x$  vibration modes) and  $1050-950\text{ cm}^{-1}$  (C-C and C-N-C vibrations). For a detailed assignment of all vibration modes to the respective signals/wavenumbers we would like to refer to ref. [23] where the authors assigned experimental IR modes for  $[(C_3H_7)_4N]Cd(C_2N_3)_3$ .

Photographs of crystalline  $[(C_3H_7)_3(CH_3)N]M(C_2N_3)_3$  ( $M = Mn^{2+}, Co^{2+}, Ni^{2+}$ ).

**Fig. S9** Batch photographs of crystalline material  $[(C_3H_7)_3(CH_3)N]M(C_2N_3)_3$  as synthesised in sample vials, with  $M$  being  $Mn^{2+}$  (left),  $Co^{2+}$  (middle) and  $Ni^{2+}$  (right). Crystallite sizes vary from 100 – 1000  $\mu\text{m}$ .

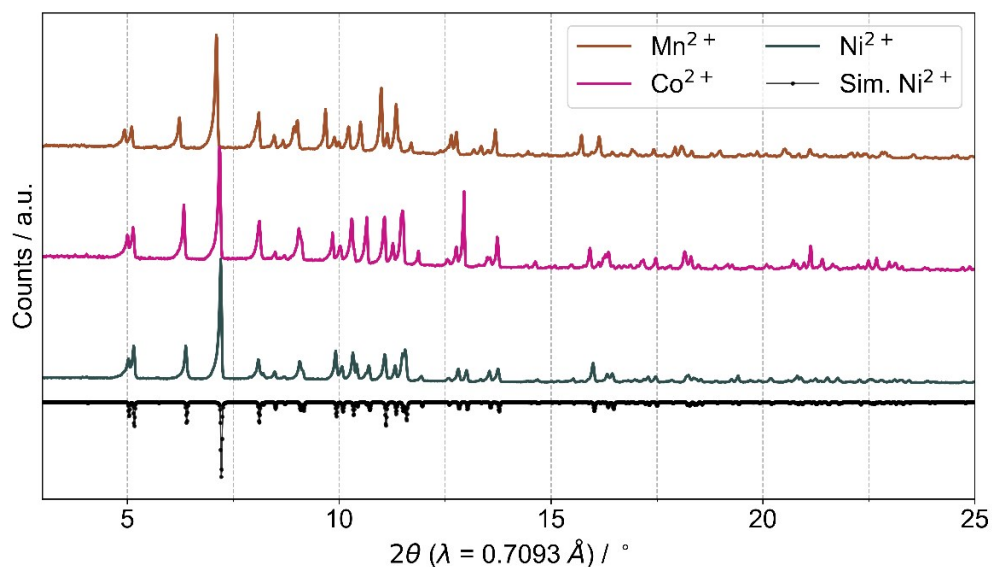
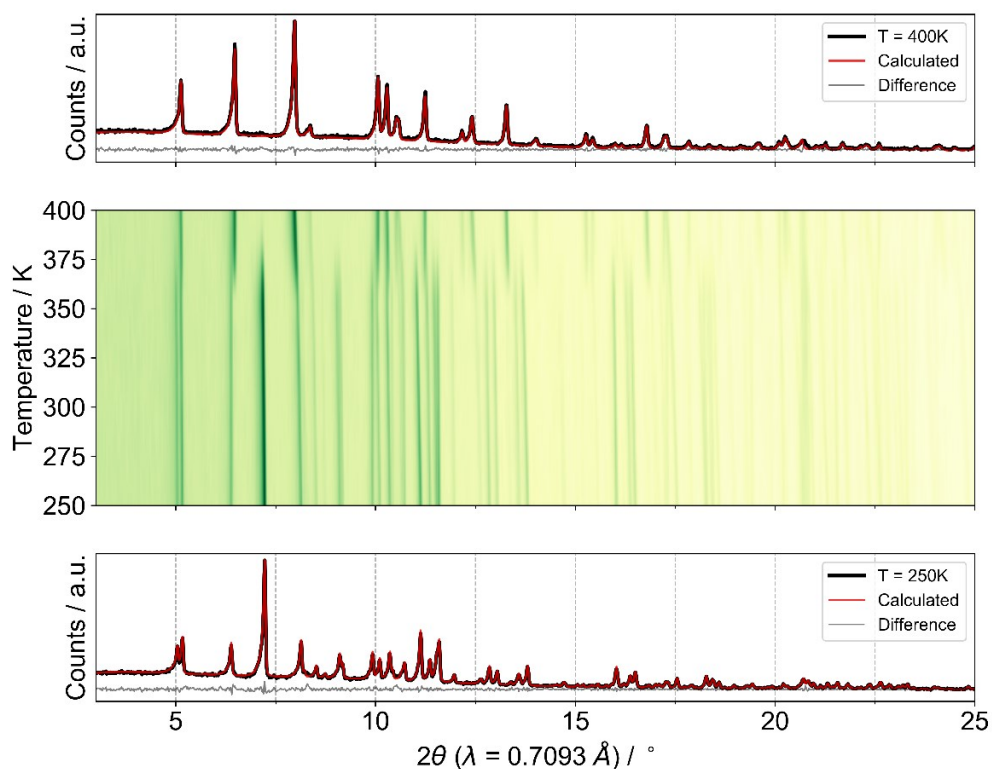


**Fig. S10** Powder X-ray diffraction patterns of the as-synthesised bulk materials of  $[(nPr)_3(CH_3)N]M(C_2N_3)_3$  based on an in-house ( $\lambda = 0.7093 \text{ \AA}$ ) molybdenum source device at room temperature. Shown in black at the bottom is the simulated powder pattern from crystal structure obtained *via* single crystal X-ray diffraction at room temperature for the  $Ni^{2+}$  containing compound, with the observed powder patterns for  $[(nPr)_3(CH_3)N]M(C_2N_3)_3$  with  $M$  being  $Ni^{2+}$  in dark green,  $Co^{2+}$  in violet and  $Mn^{2+}$  in brown, confirming the bulk phase purity and isostructural phase of the three samples.

#### Powder X-Ray diffraction data

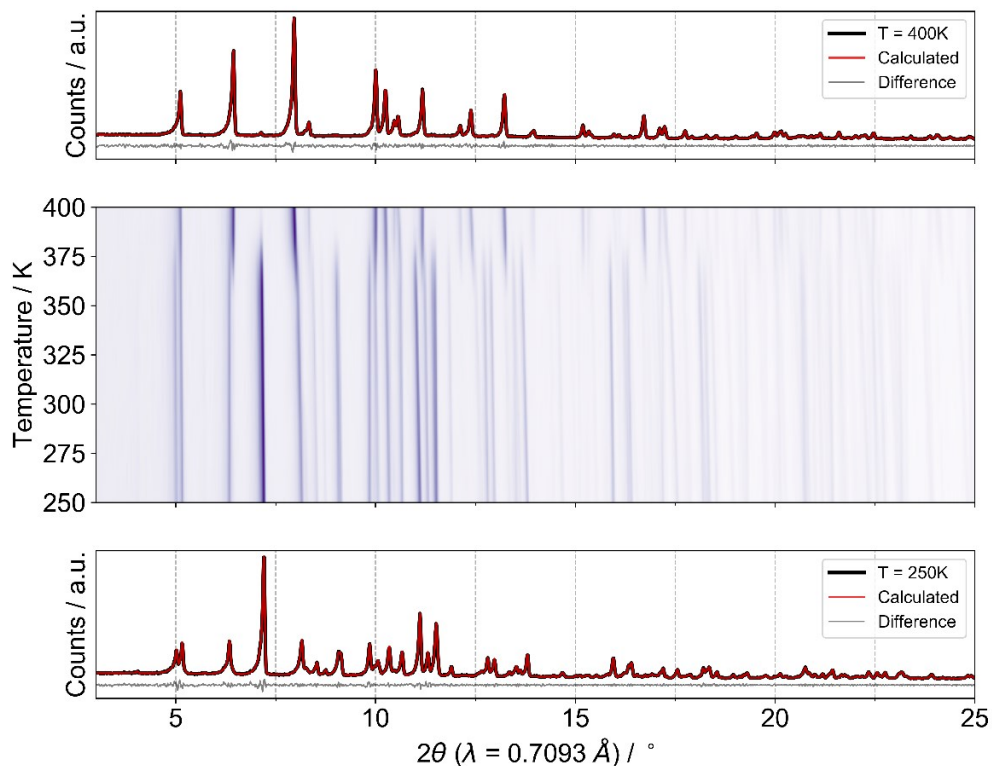


**Tab. S2** Refined cell parameters and deviations for  $[(n\text{Pr})_3(\text{CH}_3)\text{N}]\text{Ni}(\text{C}_2\text{N}_3)_3$  at temperatures from 250 K to 400 K, using the Pawley profile fit analysis method. Additionally, the output of PASCAL - principal axis strain calculations<sup>22</sup> with direction of projections of the three principal axes on the unit cell axes  $a$ ,  $b$  and  $c$  is shown. Listed are the resulting thermal expansion coefficients  $\alpha$  as well as the direction of propagation of the thermal response.

$T / \text{K}$	$r_{\text{wp}}$	$a / \text{\AA}$	$b / \text{\AA}$	$c / \text{\AA}$	$V / \text{\AA}^3$
250	4.1533	9.9842(6)	16.0860(10)	12.7032(9)	2040.2(2)
265	3.9511	9.9960(6)	16.0977(9)	12.7047(7)	2044.3(2)
280	3.8460	10.0108(6)	16.1134(9)	12.7033(7)	2049.2(2)
295	3.8132	10.0254(5)	16.1256(8)	12.7050(7)	2054.0(2)
310	3.6465	10.0400(5)	16.1410(8)	12.7036(7)	2058.7(2)
325	3.8173	10.0539(5)	16.1541(8)	12.7059(6)	2063.6(2)
340	3.6567	10.0707(4)	16.1696(7)	12.7050(6)	2068.9(2)
355	3.8018	10.0884(5)	16.1852(8)	12.7048(6)	2074.5(2)
370	3.2951	10.1044(16)	16.2011(21)	12.7063(12)	2080.0(5)

Axes	$\alpha / (\text{MK})^{-1}$	$\sigma\alpha / (\text{MK})^{-1}$	$a$	$b$	$c$
$X_1$	0.8203	0.5042	0.0000	0.0000	1.0000
$X_2$	59.3014	1.0540	0.0000	1.0000	0.0000
$X_3$	100.4661	2.0829	-1.0000	0.0000	0.0000
$V$	161.7253	3.5036			



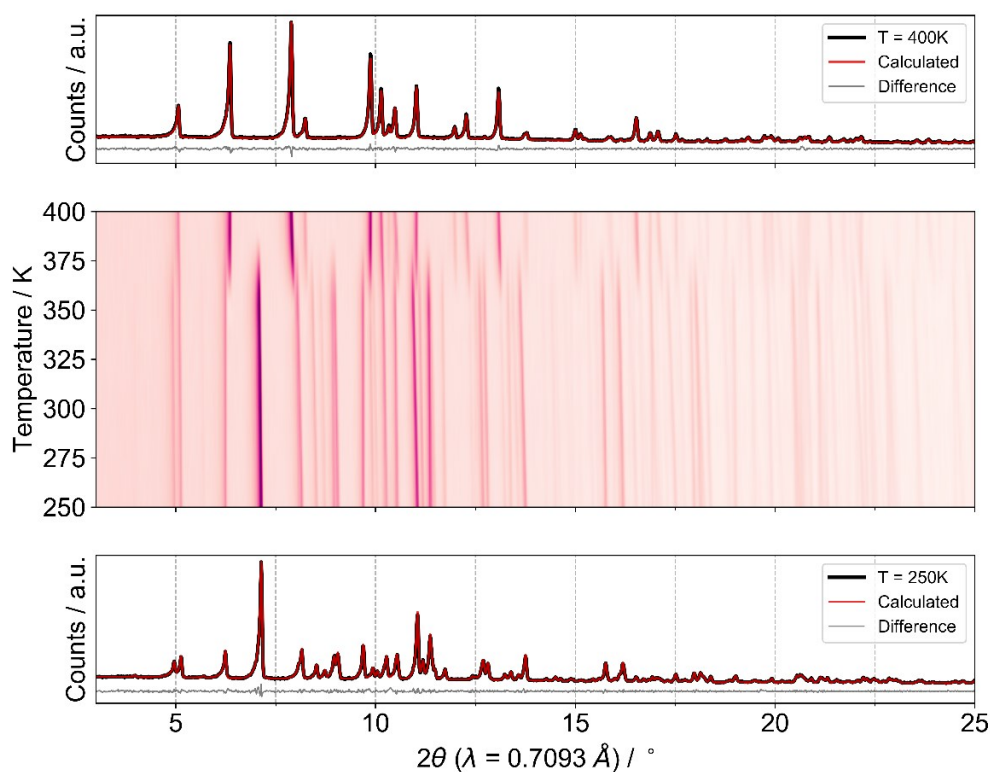
**Fig. S12** Variable-temperature powder XRD patterns of  $[(n\text{Pr})_3(\text{CH}_3)\text{N}]\text{Co}(\text{C}_2\text{N}_3)_3$  for the as-prepared orthorhombic phase. The bottom panel shows the Pawley profile fit outcome of the pattern at 250 K, serving as the starting point for sequenced analysis of the respective temperature points till 400 K for which the profile fit is shown on top of the plot. In the middle of the plot are the experimental data of variable temperature experiments illustrated as heat map with deeper colour corresponding to a higher intensity in the respective Bragg reflection.

**Tab. S3** Refined cell parameters and deviations for  $[(n\text{Pr})_3(\text{CH}_3)\text{N}]\text{Co}(\text{C}_2\text{N}_3)_3$  at temperatures from 250 K to 400 K, using the Pawley profile fit analysis method. Additionally, the output of PASCAL - principal axis strain calculations with direction of projections of the three principal axes on the unit cell axes  $a$ ,  $b$  and  $c$  is shown. Listed are the resulting thermal expansion coefficients  $\alpha$  as well as the direction of propagation of the thermal response.

$T / \text{K}$	$r_{\text{wp}}$	$a / \text{\AA}$	$b / \text{\AA}$	$c / \text{\AA}$	$V / \text{\AA}^3$
250	3.2877	9.9721(4)	16.1778(7)	12.8061(6)	2066.0(1)
265	3.3928	9.9865(3)	16.1919(5)	12.8066(5)	2070.8(1)
280	3.5148	10.0011(3)	16.2055(6)	12.8065(5)	2075.6(1)
295	3.3842	10.0159(3)	16.2212(6)	12.8067(5)	2080.7(1)
310	3.4712	10.0306(4)	16.2353(5)	12.8075(5)	2085.7(1)
325	3.2966	10.0474(4)	16.2499(5)	12.8063(5)	2090.9(1)
340	3.4113	10.0626(4)	16.2659(6)	12.8072(5)	2096.2(1)
355	3.3138	10.0805(4)	16.2809(6)	12.8063(4)	2101.8(1)
370	3.1826	10.0998(6)	16.2956(9)	12.8052(6)	2107.5(2)

Axes	$\alpha / (\text{MK})^{-1}$	$\sigma\alpha / (\text{MK})^{-1}$	$a$	$b$	$c$
$X_1$	-0.4676	0.3846	0.0000	0.0000	1.0000
$X_2$	60.6959	0.4817	0.0000	1.0000	0.0000
$X_3$	105.4286	2.0554	-1.0000	0.0000	0.0000
$V$	166.5718	2.1850			



**Fig. S13** Variable-temperature powder XRD patterns of  $[(n\text{Pr})_3(\text{CH}_3)\text{N}]\text{Mn}(\text{C}_2\text{N}_3)_3$  for the as-prepared orthorhombic phase. The bottom panel shows the Pawley profile fit outcome of the pattern at 250 K, serving as the starting point for sequenced analysis of the respective temperature points till 400 K for which the profile fit is shown on top of the plot. In the middle of the plot are the experimental data of variable temperature experiments illustrated as heat map with deeper colour corresponding to a higher intensity in the respective Bragg reflection.



**Tab. S4** Refined cell parameters and deviations for  $[(nPr)_3(CH_3)N]M(C_2N_3)_3$  at temperatures from 250 K to 400 K, using the Pawley profile fit analysis method. Additionally, the output of PASCAL - principal axis strain calculations with direction of projections of the three principal axes on the unit cell axes  $a$ ,  $b$  and  $c$  is shown. Listed are the resulting thermal expansion coefficients  $\alpha$  as well as the direction of propagation of the thermal response.

$T / K$	$r_{wp}$	$a / \text{\AA}$	$b / \text{\AA}$	$c / \text{\AA}$	$V / \text{\AA}^3$
250	3.4619	9.9727(3)	16.3817(6)	13.0213(4)	2127.3(1)
265	3.5507	9.9877(3)	16.3962(6)	13.0226(4)	2132.6(1)
280	3.1339	10.0046(3)	16.4135(5)	13.0237(4)	2138.6(1)
295	3.2508	10.0210(3)	16.4294(5)	13.0232(4)	2144.1(1)
310	3.1952	10.0387(3)	16.4474(5)	13.0246(4)	2150.5(1)
325	3.3884	10.0543(3)	16.4633(6)	13.0255(5)	2156.1(1)
340	3.4424	10.0732(3)	16.4816(6)	13.0275(5)	2162.9(1)
355	3.5132	10.0921(3)	16.4984(6)	13.0270(5)	2169.1(1)

Axes	$\alpha / (\text{MK})^{-1}$	$\alpha\alpha / (\text{MK})^{-1}$	$a$	$b$	$c$
$X_1$	-4.4959	2.2322	0.0000	0.0000	1.0000
$X_2$	69.6802	0.7471	0.0000	1.0000	0.0000
$X_3$	107.4559	0.9771	-1.0000	0.0000	0.0000
$V$	174.3908	2.4237			

**Tab. S5** Summary of cell and refinement parameters for the material series  $[(nPr)_3(CH_3)N]M(C_2N_3)_3$  at 250 K for the as-synthesised polymorph P(M)-I and for the transformed polymorph P(M)-IIb at 400 K which served as starting and end point for the sequential analysis of the variable temperature powder diffraction experiments.

$M$	$a / \text{\AA}$	$b / \text{\AA}$	$c / \text{\AA}$	$\alpha, \beta, \gamma / ^\circ$	$r_{wp}$	$r_{exp}$	GOF
250 K, space group $Pnma$							
$Mn^{2+}$	9.9747(3)	16.3853(7)	13.0237(5)	90, 90, 90	3.4116	3.4606	0.986
$Co^{2+}$	9.9721(4)	16.1778(7)	12.8061(6)	90, 90, 90	3.2877	3.1628	1.039
$Ni^{2+}$	9.9842(6)	16.0860(10)	12.7032(9)	90, 90, 90	4.1533	3.8669	1.074

$M$	$a / \text{\AA}$	$c / \text{\AA}$	$\alpha, \beta, \gamma / ^\circ$	$r_{wp}$	$r_{exp}$	GOF
400 K, space group $R\bar{3}c$						
$Mn^{2+}$	12.7867(2)	23.2773(5)	90, 90, 120	3.7574	4.0794	0.921
$Co^{2+}$	12.6107(2)	23.0957(7)	90, 90, 120	3.0832	3.1515	0.978
$Ni^{2+}$	12.5288(3)	23.0607(9)	90, 90, 120	4.6015	4.5611	1.009

Comment to the thermal expansion behaviour of  $[(nPr)_3(CH_3)N]M(C_2N_3)_3$ :

We observe an anisotropic thermal expansion behaviour for the as-synthesised phase P(M)-I with no or little uniaxial negative thermal expansion in  $X_1$  direction and strong positive thermal expansion in  $X_3$  direction. The anisotropic behaviour increases from  $Ni^{2+}$  to  $Mn^{2+}$ . This leads to an overall positive thermal volume expansion, which lies in the range of magnitude of the related molecular perovskite series  $[(C_3H_7)_4N]M(C_2N_3)_3$ .<sup>23</sup>

## Single crystal X-Ray diffraction data

Tab. S6 Summary of crystallographic data of  $[(nPr)_3CH_3]M(C_2N_3)_3$  for the as-synthesised orthorhombic P(M)-I phases.

Compound	$[(nPr)_3CH_3]Ni(C_2N_3)_3$	$[(nPr)_3CH_3]Ni(C_2N_3)_3$	$[(nPr)_3CH_3]Co(C_2N_3)_3$	$[(nPr)_3CH_3]Mn(C_2N_3)_3$
Empirical formula	$C_{16}H_{24}N_{10}Ni$	$C_{16}H_{24}N_{10}Ni$	$C_{16}H_{24}N_{10}Co$	$C_{16}H_{24}N_{10}Mn$
Formula weight / (g mol) <sup>-1</sup>	415.16	415.16	415.38	411.39
Temperature / K	100.0	300.0	298.0	298.0
Crystal system	orthorhombic	orthorhombic	orthorhombic	orthorhombic
Space group	<i>Pnma</i>	<i>Pnma</i>	<i>Pnma</i>	<i>Pnma</i>
<i>a</i> / Å	9.8624(6)	10.0232(3)	10.0138(2)	10.0193(5)
<i>b</i> / Å	15.9509(9)	16.1193(5)	16.2151(4)	16.4215(10)
<i>c</i> / Å	12.6923(7)	12.6992(4)	12.7967(3)	13.0125(7)
$\alpha$ / °	90	90	90	90
$\beta$ / °	90	90	90	90
$\gamma$ / °	90	90	90	90
Volume / Å <sup>3</sup>	1996.7(2)	2051.77(11)	2077.86(8)	2141.0(2)
Z	4	4	4	4
$\rho_{calc}$ / g cm <sup>-3</sup>	1.381	1.344	1.328	1.276
$\mu$ / mm <sup>-1</sup>	0.995	0.968	0.848	0.638
F (000)	872.0	872.0	868.0	860.0
Crystal size / mm <sup>-3</sup>	0.307 × 0.202 × 0.169	0.261 × 0.219 × 0.179	0.384 × 0.305 × 0.226	0.285 × 0.278 × 0.27
Radiation	MoK $\alpha$ ( $\lambda$ = 0.71073)	MoK $\alpha$ ( $\lambda$ = 0.71073)	MoK $\alpha$ ( $\lambda$ = 0.71073)	MoK $\alpha$ ( $\lambda$ = 0.71073)
2 $\theta$ range for data collection / °	4.102 to 59.146	5.054 to 57.398	4.054 to 52.736	3.994 to 52.742
Index ranges	-13 ≤ <i>h</i> ≤ 13 -22 ≤ <i>k</i> ≤ 22 -17 ≤ <i>l</i> ≤ 17	-13 ≤ <i>h</i> ≤ 13 -21 ≤ <i>k</i> ≤ 21 -16 ≤ <i>l</i> ≤ 17	-12 ≤ <i>h</i> ≤ 12 -20 ≤ <i>k</i> ≤ 20 -15 ≤ <i>l</i> ≤ 15	-12 ≤ <i>h</i> ≤ 12 -20 ≤ <i>k</i> ≤ 20 -16 ≤ <i>l</i> ≤ 16
Reflections collected	116055	77417	100185	28206
Independent reflections	2893 $R_{int}$ = 0.0482 $R_{sigma}$ = 0.0141	2734 $R_{int}$ = 0.0379 $R_{sigma}$ = 0.0094	2206 $R_{int}$ = 0.0250 $R_{sigma}$ = 0.0079	2271 $R_{int}$ = 0.0374 $R_{sigma}$ = 0.0183
Data/restraints/parameters	2893/0/189	2734/0/177	2206/0/183	2271/0/170
Goodness of fit on F <sup>2</sup>	1.197	1.051	1.071	1.020
Final R indexes [ <i>I</i> > 2 $\sigma$ ( <i>I</i> )]	$R_1$ = 0.0385 $wR_2$ = 0.0985	$R_1$ = 0.0283 $wR_2$ = 0.0738	$R_1$ = 0.0252 $wR_2$ = 0.0758	$R_1$ = 0.0294 $wR_2$ = 0.0779
Final R indexes [all data]	$R_1$ = 0.0427 $wR_2$ = 0.1008	$R_1$ = 0.0390 $wR_2$ = 0.0805	$R_1$ = 0.0270 $wR_2$ = 0.0780	$R_1$ = 0.0462 $wR_2$ = 0.0888
Largest diff. peak/hole / eÅ <sup>-3</sup>	0.43/-0.46	0.28/-0.34	0.25/-0.33	0.21/-0.26
Flack parameter <sup>24</sup>	---	---	---	---
CCDC number	2068712	2068716	2068842	2068843

**Tab. S7** Summary of crystallographic data of  $[(nPr)_3(CH_3)N]M(C_2N_3)_3$  for the rhombohedral P(M)-IIa phases.

Compound	$[(nPr)_3CH_3]Ni(C_2N_3)_3$	$[(nPr)_3CH_3]Co(C_2N_3)_3$	$[(nPr)_3CH_3]Mn(C_2N_3)_3$
Empirical formula	$C_{16}H_{24}N_{10}Ni$	$C_{16}H_{24}N_{10}Co$	$C_{16}H_{24}N_{10}Mn$
Formula weight / $(g\text{mol})^{-1}$	415.16	415.38	411.39
Temperature / K	100.0	100.0	100.0
Crystal system	trigonal	trigonal	trigonal
Space group	$R\bar{3}c$	$R\bar{3}c$	$R\bar{3}c$
$a / \text{\AA}$	12.5883(8)	12.6783(16)	12.8301(13)
$b / \text{\AA}$	12.5883(8)	12.6783(16)	12.8301(13)
$c / \text{\AA}$	21.565(2)	21.585(5)	21.750(3)
$\alpha / ^\circ$	90	90	90
$\beta / ^\circ$	90	90	90
$\gamma / ^\circ$	120	120	120
Volume / $\text{\AA}^3$	2959.5(5)	3004.7(10)	3100.7(8)
Z	6	6	6
$\rho_{\text{calc}} / g\text{cm}^{-3}$	1.398	1.377	1.322
$\mu / \text{mm}^{-1}$	1.007	0.880	0.661
F (000)	1308.0	1302.0	1290.0
Crystal size / $\text{mm}^{-3}$	$0.314 \times 0.277 \times 0.16$	$0.246 \times 0.204 \times 0.18$	$0.176 \times 0.122 \times 0.107$
Radiation	$\text{MoK}\alpha$ ( $\lambda = 0.71073$ )	$\text{MoK}\alpha$ ( $\lambda = 0.71073$ )	$\text{MoK}\alpha$ ( $\lambda = 0.71073$ )
2 $\theta$ range for data collection / $^\circ$	5.314 to 59.15	5.292 to 56.554	5.242 to 55.728
Index ranges	$-16 \leq h \leq 17$ $-16 \leq k \leq 17$ $-29 \leq l \leq 29$	$-16 \leq h \leq 15$ $-16 \leq k \leq 16$ $-28 \leq l \leq 26$	$-16 \leq h \leq 16$ $-16 \leq k \leq 16$ $-28 \leq l \leq 28$
Reflections collected	16219	15254	14822
Independent reflections	1840 $R_{\text{int}} = 0.0266$ $R_{\text{sigma}} = 0.0165$	1650 $R_{\text{int}} = 0.0252$ $R_{\text{sigma}} = 0.0148$	1650 $R_{\text{int}} = 0.0675$ $R_{\text{sigma}} = 0.0377$
Data/restraints/parameters	1840/1/87	1650/1/87	1650/1/87
Goodness of fit on $F^2$	1.047	1.090	1.082
Final R indexes [ $I > 2\sigma(I)$ ]	$R_1 = 0.0161$ $wR_2 = 0.0401$	$R_1 = 0.0166$ $wR_2 = 0.0410$	$R_1 = 0.0396$ $wR_2 = 0.0983$
Final R indexes [all data]	$R_1 = 0.0173$ $wR_2 = 0.0408$	$R_1 = 0.0183$ $wR_2 = 0.0429$	$R_1 = 0.0480$ $wR_2 = 0.1039$
Largest diff. peak/hole / $e\text{\AA}^{-3}$	0.20/-0.24	0.17/-0.17	0.86/-0.46
Flack parameter <sup>24</sup>	0.443(15)	0.448(19)	0.36(5)
Flack parameter_s.u.	0.015	0.019	0.050
CCDC number	2068844	2068846	2068848

Tab. S8 Summary of crystallographic data of  $[(nPr)_3(CH_3)N]M(C_2N_3)_3$  for the rhombohedral P(M)-IIb phases.

Compound	$[(nPr)_3CH_3]Ni(C_2N_3)_3$	$[(nPr)_3CH_3]Co(C_2N_3)_3$	$[(nPr)_3CH_3]Mn(C_2N_3)_3$
Empirical formula	$C_{16}H_{24}N_{10}Ni$	$C_{16}H_{24}N_{10}Co$	$C_{16}H_{24}N_{10}Mn$
Formula weight / (g mol) <sup>-1</sup>	415.16	415.38	411.39
Temperature / K	350.0	350.0	350.0
Crystal system	trigonal	trigonal	trigonal
Space group	$R\bar{3}c$	$R\bar{3}c$	$R\bar{3}c$
$a / \text{Å}$	12.5350(3)	12.6131(2)	12.7694(5)
$b / \text{Å}$	12.5350(3)	12.6131(2)	12.7694(5)
$c / \text{Å}$	22.8074(12)	22.8639(6)	23.0222(13)
$\alpha / ^\circ$	90	90	90
$\beta / ^\circ$	90	90	90
$\gamma / ^\circ$	120	120	120
Volume / Å <sup>3</sup>	3103.5(2)	3150.10(13)	3251.0(3)
Z	6	6	6
$\rho_{\text{calc}} / \text{g cm}^{-3}$	1.333	1.314	1.261
$\mu / \text{mm}^{-1}$	0.960	0.839	0.630
F (000)	1308.0	1302.0	1290.0
Crystal size / mm <sup>-3</sup>	0.314 × 0.277 × 0.16	0.218 × 0.157 × 0.142	0.185 × 0.169 × 0.12
Radiation	MoK $\alpha$ ( $\lambda = 0.71073$ )	MoK $\alpha$ ( $\lambda = 0.71073$ )	MoK $\alpha$ ( $\lambda = 0.71073$ )
2 $\theta$ range for data collection / °	5.18 to 55.736	5.158 to 57.378	5.108 to 59.12
Index ranges	-16 ≤ h ≤ 15 -16 ≤ k ≤ 16 -29 ≤ l ≤ 30	-16 ≤ h ≤ 15 -17 ≤ k ≤ 16 -30 ≤ l ≤ 30	-17 ≤ h ≤ 17 -17 ≤ k ≤ 17 -31 ≤ l ≤ 31
Reflections collected	17980	17146	57844
Independent reflections	830 $R_{\text{int}} = 0.0199$ $R_{\text{sigma}} = 0.0079$	907 $R_{\text{int}} = 0.0219$ $R_{\text{sigma}} = 0.0084$	1025 $R_{\text{int}} = 0.0359$ $R_{\text{sigma}} = 0.0124$
Data/restraints/parameters	830/84/103	907/60/94	1025/63/94
Goodness of fit on F <sup>2</sup>	1.107	1.133	1.095
Final R indexes [ $I > 2\sigma(I)$ ]	$R_1 = 0.0234$ $wR_2 = 0.0656$	$R_1 = 0.0249$ $wR_2 = 0.0691$	$R_1 = 0.0391$ $wR_2 = 0.1197$
Final R indexes [all data]	$R_1 = 0.0261$ $wR_2 = 0.0691$	$R_1 = 0.0312$ $wR_2 = 0.0749$	$R_1 = 0.0513$ $wR_2 = 0.1317$
Largest diff. peak/hole / eÅ <sup>-3</sup>	0.16/-0.47	0.13/-0.22	0.16/-0.29
Flack parameter <sup>24</sup>	---	---	---
CCDC number	2068845	2068847	2068849

**Tab. S9** Torsion angles for the two polymorphs **P-(Ni)-I** and **P(Ni)-IIa** at 100 K. The torsion angle belongs to the metal atom and the respective dicyanamide molecule as bent linker. The two terminal and the central N atoms of dicyanamide are used to determine the angle. This defines the torsion angles as follows:  $\alpha(1) = \text{Ni}(1)\text{-N}(1)\text{-N}(3)\text{-N}(5)$  and  $\alpha(2) = \text{N}(1)\text{-N}(3)\text{-N}(5)\text{-Ni}(2)$  and results in the respective binding mode geometry with  $\alpha < 90^\circ$  representing **syn** geometry and  $\alpha > 90^\circ$  being **anti** geometry. Additionally, the crystallographic directions are given in analogy to Figure 2 of the manuscript.

Direction	Atom number	Torsion angle / °	Binding mode
<i>P(Ni)-I, orthorhombic <math>Pnma</math></i>			
[010]	Ni1-N3-N5-N3	99.2(8)	<b>anti</b>
	N3-N5-N3-Ni1	99.2(8)	<b>anti</b>
[101]	Ni1-N4-N6-N7	108.3(3)	anti
	N4-N6-N7-Ni1	87.8(3)	syn
[10 $\bar{1}$ ]	Ni1-N7-N6-N4	87.8(3)	syn
	N7-N6-N4-Ni1	108.3(3)	anti
<i>P(Ni)-IIa, rhombohedral <math>R3c</math></i>			
[1 $\bar{1}$ 0]	Ni1-N2-N5-N3	117.67(18)	anti
	N2-N5-N3-Ni1	86.6(8)	syn
[011]	Ni1-N3-N5-N2	86.6(8)	syn
	N3-N5-N2-Ni1	117.67(18)	anti
[10 $\bar{1}$ ]	Ni1-N3-N5-N2	86.6(8)	syn
	N3-N5-N2-Ni1	117.67(18)	anti

Statement on the absolute structure determination of the polymorph phases P(M)-IIa; here exemplarily based on the Ni-compound, however, this applies to the isostructural Co- and Mn- analogues in the same manner as they show the same checkCIF comment:

Output of the (IUCr) checkCIF procedure for  $[(n\text{Pr})_3\text{CH}_3]\text{Ni}(\text{C}_2\text{N}_3)_3$ :

STRVA01\_ALERT\_4\_C: Flack test results are ambiguous.

From the CIF: `_refine_ls_abs_structure_Flack` 0.443.

From the CIF: `_refine_ls_abs_structure_Flack_su` 0.015.

PURPOSE: To check that `_refine_ls_abs_structure_flack` is within expected limits.

*“The correct absolute structure has been defined by the atomic coordinates if `_refine_ls_abs_structure_flack` is close to 0.0 (and the s.u. is sufficiently small).*

*In cases of intermediate values of `_refine_ls_abs_structure_flack`, a merohedral twin or a partial mix of enantiomers may be present and this fact should be discussed in the manuscript. However, intermediate values might also be obtained when the absolute structure parameter is essentially meaningless because the compound is a weak anomalous scatterer.”*

It is known for rhombohedral symmetry and non-centrosymmetric space groups that (merohedral) twinning of single crystals is prone to occur which may be solved using the twin law (0 1 0 1 0 0 0 -1).<sup>25</sup> Treatment of the diffraction data with this law delivers the same structural model. However, since this twin matrix corresponds to the inverted symmetry operation of the non-centrosymmetric Laue group of the crystal structure, the presented diffraction data are treated with the inversion operator which is a common method for absolute structure determination with Flack parameters.<sup>24</sup>

Since the `_refine_ls_abs_structure_Flack_s.u.` values for all three compounds with  $\text{Ni}^{2+}$ ,  $\text{Co}^{2+}$  and  $\text{Mn}^{2+}$  are close to 0.0 after refinement and the Flack parameters are close to  $x = 0.5$  (which would mean racemic or twinned), we believe our structure determination treating the data as inversion twin gives a reliable model for the absolute crystal structure.

E-statistics  $|E^2-1|$  for the rhombohedral structural models (0.736: non-centrosymmetric; 0.968: centrosymmetric):

$[(n\text{Pr})_3\text{CH}_3]\text{Mn}(\text{C}_2\text{N}_3)_3$ : 0.795 (100 K), 0.990 (350 K)

$[(n\text{Pr})_3\text{CH}_3]\text{Co}(\text{C}_2\text{N}_3)_3$ : 0.843 (100 K), 0.974 (350 K)

$[(n\text{Pr})_3\text{CH}_3]\text{Ni}(\text{C}_2\text{N}_3)_3$ : 0.826 (100 K), 0.943 (350 K)

To confirm the ordered structure in polar  $R3c$ , we tried to refine the low-temperature data in the centrosymmetric space group  $R\bar{3}c$ . However, as we were not able to refine a reliable structural model in  $R\bar{3}c$  for the ordered structures, we state the structural model in the polar, non-centrosymmetric space group  $R3c$  being appropriate, in addition to the information given by the E-statistics which confirms our assumption.

## Quantum chemical calculations

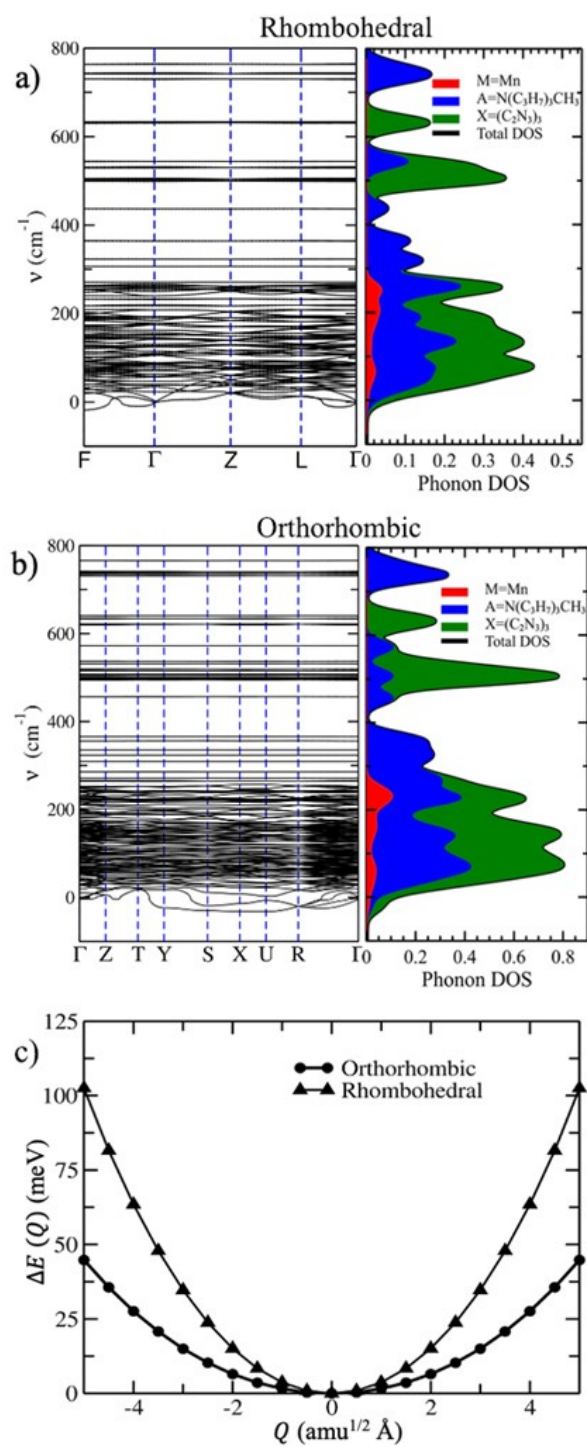


**Fig. S14** Phonon dispersion curves and partial density of states in the low-frequency region for the Mn-containing materials in a) the rhombohedral and b) the orthorhombic phase, calculated using a unit cell; c) Potential energy surfaces in the direction of eigenvectors for lowest-frequency bands at the F point for the rhombohedral phase, and U point for the orthorhombic phase, using appropriate supercells.

## References

- 1 N. Menshutkin, *Z. Phys. Chem.*, 1890, **5U**.
- 2 G. R. Fulmer, A. J. M. Miller, N. H. Sherden, H. E. Gottlieb, A. Nudelman, B. M. Stoltz, J. E. Bercaw and K. I. Goldberg, *Organometallics*, 2010, **29**, 2176.
- 3 G. S. Pawley, *J. Appl. Cryst.*, 1981, **14**, 357.
- 4 A. A. Coelho, *J. Appl. Cryst.*, 2018, **51**, 210.
- 5 APEX3 suite of crystallographic software, *Bruker AXS Inc. Madison Wisconsin USA*, **2015**, Version 5.2.
- 6 SAINT, *Bruker AXS Inc., Madison, Wisconsin, USA*, **2014**, Version 8.34A.
- 7 SADABS, *Bruker AXS Inc., Madison, Wisconsin, USA*, **2014**, Version 2014/5.
- 8 G. M. Sheldrick, *Acta Crystallogr. Sect. C*, 2015, **71**, 3.
- 9 G. M. Sheldrick, *Acta Crystallogr. Sect. A*, 2015, **71**, 3.
- 10 O. V. Dolomanov, L. J. Bourhis, R. J. Gildea, J. A. K. Howard and H. Puschmann, *J. Appl. Crystallogr.*, 2009, **42**, 339.
- 11 K. Momma and F. Izumi, *J. Appl. Cryst.*, 2011, **44**, 1272.
- 12 G. Kresse and J. Furthmüller, *Comput. Mater. Sci.*, 1996, **6**, 15.
- 13 Kresse and Furthmüller, *Phys. Rev. B Condens. Matter*, 1996, **54**, 11169.
- 14 Perdew, Burke and Ernzerhof, *Proc. Natl. Acad. Sci. USA*, 1996, **77**, 3865.
- 15 S. L. Dudarev, G. A. Botton, S. Y. Savrasov, C. J. Humphreys and A. P. Sutton, *Phys. Rev. B Condens. Matter*, 1998, **57**, 1505.
- 16 L. Wang, T. Maxisch and G. Ceder, *Phys. Rev. B*, 2006, **73**, 603.
- 17 S. Grimme, J. Antony, S. Ehrlich and H. Krieg, *J. Chem. Phys.*, 2010, **132**, 154104.
- 18 Blöchl, *Phys. Rev. B Condens. Matter*, 1994, **50**, 17953.
- 19 G. Kresse and D. Joubert, *Phys. Rev. B Condens. Matter*, 1999, **59**, 1758.
- 20 A. Togo and I. Tanaka, *Scr. Mater.*, 2015, **108**, 1.
- 21 J. M. Skelton, L. A. Burton, S. C. Parker, A. Walsh, C.-E. Kim, A. Soon, J. Buckeridge, A. A. Sokol, C. R. A. Catlow, A. Togo and I. Tanaka, *Phys. Rev. Lett.*, 2016, **117**, 75502.
- 22 M. J. Cliffe and A. L. Goodwin, *J. Appl. Cryst.*, 2012, **45**, 1321.
- 23 J. M. Bermúdez-García, M. Sánchez-Andújar, S. Yáñez-Vilar, S. Castro-García, R. Artiaga, J. López-Beceiro, L. Botana, Á. Alegría and M. A. Señarís-Rodríguez, *Inorg. Chem.*, 2015, **54**, 11680.
- 24 H. D. Flack, *Acta Cryst. A*, 1983, **39**, 876.
- 25 S. Parsons, *Acta Cryst. D*, 2003, **59**, 1995.



## 8.3 STUDY IV: Supplementary Information

Electronic Supplementary Material (ESI) for CrystEngComm.  
This journal is © The Royal Society of Chemistry 2023

### Supplementary Information

# Tuning the Mechanical Properties of Dicyanamide-Based Molecular Perovskites

Shivani Grover,<sup>‡a</sup> Stefan Burger,<sup>‡b</sup> Keith T. Butler,<sup>c</sup> Karina Hemmer,<sup>b</sup> Pia Vervoorts,<sup>b</sup> Gregor Kieslich<sup>\*b</sup> and Ricardo Grau-Crespo<sup>\*a</sup>

<sup>a</sup> *Department of Chemistry, Food and Pharmacy, University of Reading, United Kingdom, RG66DX, UK.*

<sup>b</sup> *Department of Chemistry, Technical University of Munich, Lichtenbergstraße 4, 85748 Garching, GER.*

<sup>c</sup> *Materials Research Institute, School of Engineering and Materials Science, Queen Mary University of London, Mile End Road, London E1 4NS, UK.*

<sup>‡</sup> Shared contribution

#### AUTHOR INFORMATION

Corresponding Authors

\*[r.grau-crespo@reading.ac.uk](mailto:r.grau-crespo@reading.ac.uk)

\*[gregor.kieslich@tum.de](mailto:gregor.kieslich@tum.de)

## Theoretical calculations

### Bulk Modulus - Birch-Murnaghan equation of state.

We use a third-order Birch-Murnaghan equation of state [1, 2] with energy  $E$  as function of volume  $V$ :

$$E(V) = E_0 + \frac{9V_0B}{16} \left\{ \left[ \left( \frac{V_0}{V} \right)^{\frac{2}{3}} - 1 \right]^3 B' + \left[ \left( \frac{V_0}{V} \right)^{\frac{2}{3}} - 1 \right]^2 \left[ 6 - 4 \left( \frac{V_0}{V} \right)^{\frac{2}{3}} \right] \right\}$$

where  $V_0$  is the equilibrium volume,  $B$  is the bulk modulus,  $B'$  is the derivative of the bulk modulus with respect to pressure, and  $E_0$  is the energy at the equilibrium volume. The bulk moduli is computed by fitting the DFT energy ( $E$ ) vs. volume ( $V$ ) points to the above equation. For each point the structure was relaxed by optimising cell parameters and ionic coordinates at a fixed volume. We found that the fitting was largely insensitive to the value of pressure derivative, so we fixed it at  $B' = 4.0$  for all compositions, which is equivalent to using a second-order equation of state. The fitted energy vs. volume curves are shown in Figure S-1. The employed equation of state describes the energy variation adequately.

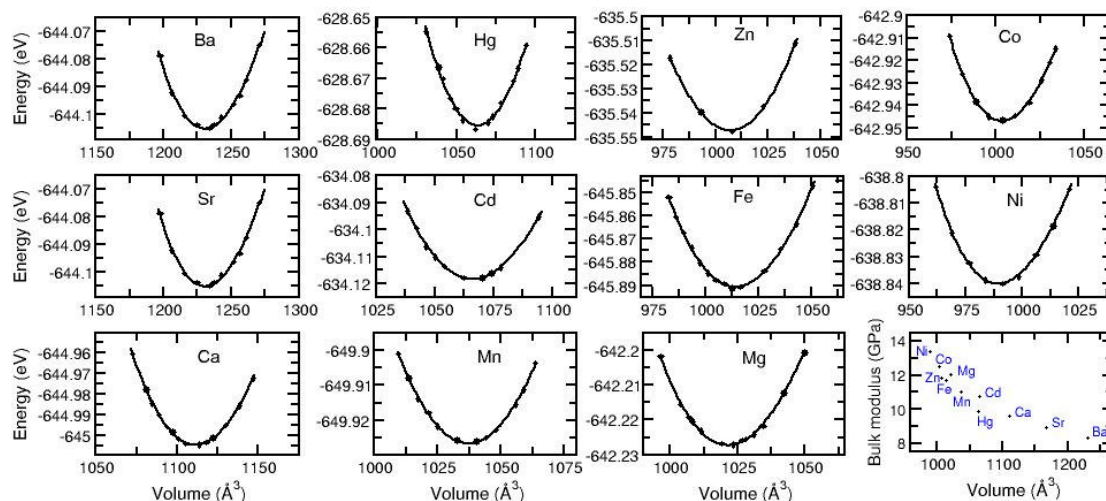


**Figure S-1.** Fitted energy-volume curves from DFT calculations for  $[N(C_3H_7)_3CH_3]M(C_2N_3)_3$  perovskites. The final frame represents the bulk moduli vs. the equilibrium volume in each case.

Table S-1 shows the equilibrium cell parameters at zero pressure and temperature, together with the bulk moduli ( $B$ ) and the linear ( $K$ ) and volumetric ( $K_V$ ) compressibilities obtained from the DFT simulations:

$$K = -\frac{1}{a_0} \frac{\partial a}{\partial p}$$

$$K_V = -\frac{1}{V_0} \frac{\partial V}{\partial p}$$

**Tab. S-1.** Equilibrium cell parameters ( $a_0$ ,  $\alpha_0$ ) and volume ( $V_0$ ) at zero pressure and temperature, as calculated from DFT; and the corresponding bulk moduli ( $B$ ) and linear and volumetric ( $K_V$ ) compressibilities.

Metal M	$a_0 / \text{\AA}$	$\alpha_0 / \text{degrees}$	$V_0 / \text{\AA}^3$	$B / \text{GPa}$	$K / \text{TPa}^{-1}$	$K_V (\text{TPa}^{-1})$
Ni	10.21	76.76	989.5	13.4	25.3	75.9
Co	10.24	77.13	1003.5	12.5	26.7	80.0
Zn	10.26	76.91	1007.3	11.8	28.0	84.1
Fe	10.27	77.24	1014.2	11.7	28.5	85.6
Mg	10.31	77.00	1021.5	12.0	27.7	83.1
Mn	10.35	77.25	1037.3	11.0	30.2	90.5
Cd	10.44	77.49	1065.8	10.7	30.8	92.4
Hg	10.44	77.16	1063.6	9.9	33.8	101.2
Ca	10.56	78.23	1111.5	9.5	34.3	102.7
Sr	10.71	78.98	1167.6	8.9	36.7	109.9
Ba	10.87	79.75	1230.8	8.3	40.7	122.1

## Experimental Procedures

### General information.

The molecular perovskite materials were synthesised according to a strategy established in our labs, as described in the literature[3].

### Powder diffraction data using Synchrotron radiation.

High-pressure powder X-ray (HPPXRD) data were collected at the Diamond Light Source (beamline I15) within beamtime CY22477-2 using an X-ray energy of 29.2 keV ( $\lambda = 0.4246 \text{ \AA}$ ) and a 2D PerkinElmer area detector for data collection. A high pressure cell was used to apply hydrostatic pressure to the sample during data collection, which is described in detail at <https://www.imperial.ac.uk/pressurecell/> and refs [4-6]. The pestled samples were loaded into a PTFE plastic capillary (inside diameter 1.8 mm) together with Silicone oil AP 100 as pressure transmitting medium (which is known to keep hydrostatic conditions up to pressure of 0.9 GPa) and sealed with Araldyte-2014-1 glue. In total, 17 HPPXRD patterns were collected between  $p = \text{ambient}$  and  $p = 0.40 \text{ GPa}$  including one after releasing the pressure to prove reversibility. For all samples reversibility of compression was confirmed. The step size was chosen to be  $\Delta p = 0.025 \text{ GPa}$ .

All obtained Powder X-Ray diffraction patterns were analysed by performing a Pawley profile fit analysis using TOPAS Academic v6 in combination with jEdit for creating the input files [7, 8]. Standard deviations of all parameters were calculated, and by using "randomise\_on\_errors", it was ensured that the minimum of the refinement was reached.

### Bulk Modulus - Birch-Murnaghan equation of state

For extraction of the bulk moduli  $K$  of the materials, the obtained cell volume data from the powder diffraction experiments were plotted against the applied pressure and fitted with a 2<sup>nd</sup>-order Birch-Murnaghan equation of state (BM EoS). Standard deviations of the lattice parameters and volumes which were obtained during the Pawley profile analysis were included in the fitting process of the  $V(p)$  data with the software EoSFIT-7c [9]. For the applied pressure a standard deviation of  $\sigma p = 0.002 \text{ GPa}$  was included in the calculation. As indicated in the norm. pressure  $F$  to strain  $f$  plots, a phase transition for the Mn- and Co-containing material can be anticipated. Therefore, the bulk moduli were calculated with the appropriate pressure points for the high-pressure/low-temperature phase.

The functionality of the pressure cell set-up throughout the allocated beamtime was verified by determining the bulk moduli of two known reference materials, KBr and NiDMG. The calculated bulk moduli match the literature values very well and the procedure is described in detail in reference[4].

### Powder X-Ray diffraction data

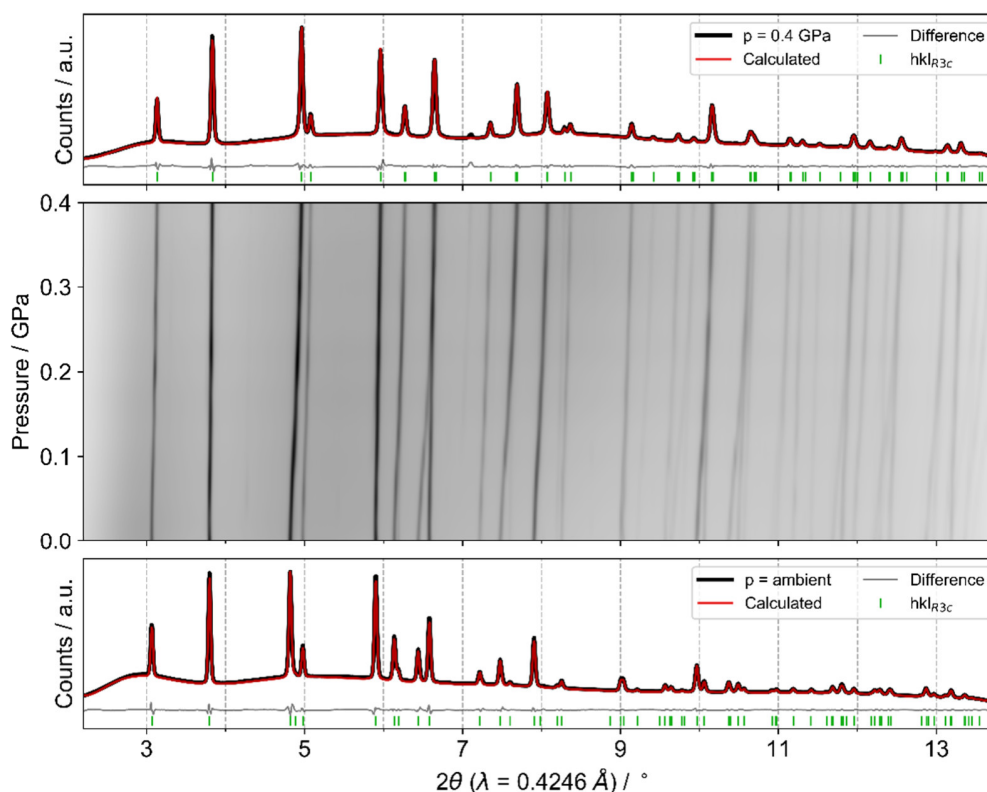
All three materials  $[(n\text{Pr})_3(\text{CH}_3)\text{N}]M(\text{C}_2\text{N}_3)_3$  ( $M = \text{Mn}^{2+}, \text{Co}^{2+}, \text{Ni}^{2+}$ ) were thermally converted from the as-synthesised orthorhombic polymorph ( $Pnma$ ) into the rhombohedral polymorph ( $R3c$ ) prior to the diffraction experiment, as it is well described in the literature[3]. In case of the Cobalt- and the Nickel analogous, residual traces of the orthorhombic phase could be identified in the powder diffraction pattern, which was considered during the Pawley profile fitting process. The following tables only show cell parameters for the rhombohedral phase; however, the contour plots visualise  $hkl$  indices for both phases, where appropriate, to ensure that all reflections in the experimental pattern are assigned to the respective phase.

**Tab. S-2.** Pawley profile fit outcome of refined cell parameters and deviations for  $[(n\text{Pr})_3(\text{CH}_3\text{N})\text{Mn}(\text{C}_2\text{N}_3)_3]$  at different pressures, ranging from ambient to  $p = 0.4$  GPa. At the bottom, output data of PASCAL - principal axis strain calculations [10] with direction of projections of the three principal axes on the unit cell axes  $a$ ,  $b$  and  $c$  is shown. Reported are the median compressibilities  $K$  with respective errors  $\sigma K$ .

$p$ / GPa	$r_{\text{wp}}$	$a$ / Å	$c$ / Å	$v$ / Å <sup>3</sup>
0.0001	1.26702	12.8110(1)	22.6791(4)	3223.45(8)
0.0250	1.39462	12.8121(2)	22.6259(4)	3216.45(10)
0.0500	1.48570	12.8052(2)	22.5755(4)	3205.83(9)
0.0750	1.23549	12.7975(1)	22.5207(3)	3194.21(8)
0.1000	1.30935	12.7842(1)	22.4444(4)	3176.76(8)
0.1250	1.29589	12.7750(1)	22.3711(4)	3161.83(9)
0.1500	1.17781	12.7674(1)	22.3050(4)	3148.75(9)
0.1750	1.24627	12.7648(1)	22.2593(6)	3141.00(11)
0.2000	1.29082	12.7509(2)	22.2032(6)	3126.26(11)
0.2250	1.45353	12.7434(2)	22.1566(8)	3116.03(13)
0.2500	1.23468	12.7358(2)	22.1176(10)	3106.84(16)
0.2750	1.41414	12.7281(2)	22.0942(16)	3099.82(24)
0.3000	1.39222	12.7196(2)	22.0459(17)	3088.92(26)
0.3250	1.33689	12.7130(2)	22.0008(15)	3079.38(22)
0.3500	1.29175	12.7050(2)	21.9697(14)	3071.19(21)
0.3750	1.32574	12.6988(2)	21.9389(10)	3063.88(17)
0.4000	1.45667	12.6900(2)	21.9162(14)	3056.45(21)

Axes	$K$ / (TPa) <sup>-1</sup>	$\sigma K$ / (TPa) <sup>-1</sup>	$a$	$b$	$c$
$X_1$	80.3727	2.8871	0.0000	0.0000	1.0000
$X_2$	25.6881	0.7233	-0.7071	-0.7071	0.0000
$X_3$	25.6881	0.7233	0.7071	-0.7071	0.0000
$V$	136.1786	3.4448			



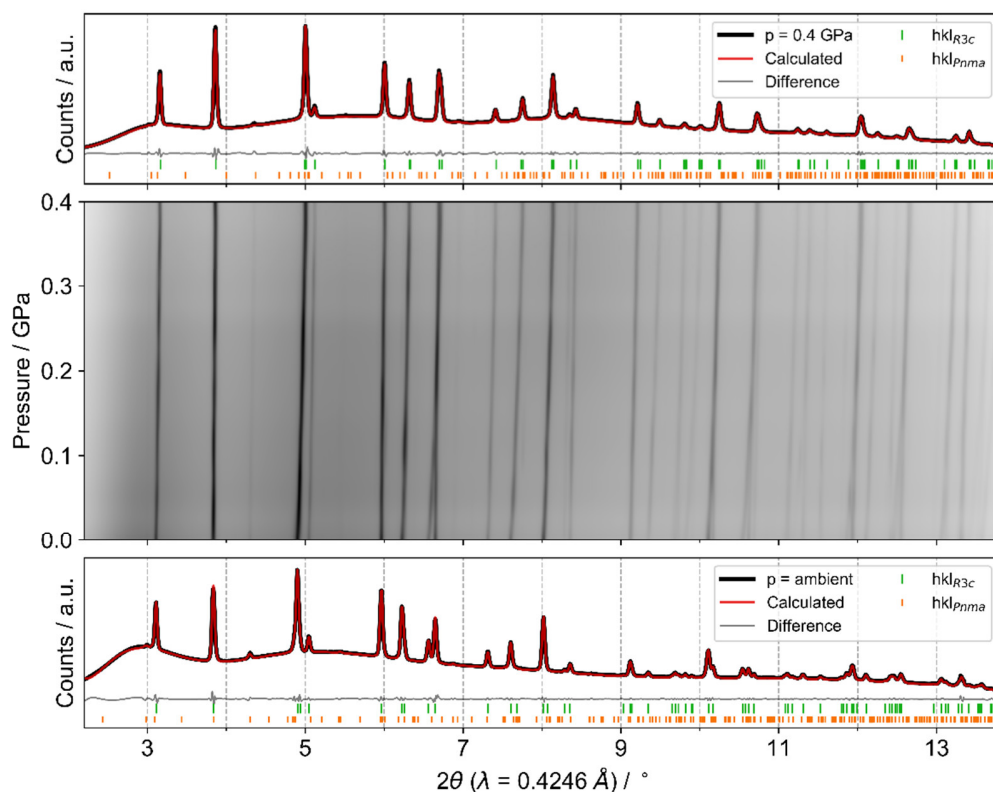
**Figure S-2.** HPPXRD analysis of  $[(n\text{Pr})_3(\text{CH}_3\text{N})\text{Mn}(\text{C}_2\text{N}_3)_3]$  from ambient pressures to 0.4 GPa. The middle shows a contour plot of the pressure dependent diffraction patterns with intense colour corresponding to a strong reflection. Additionally, a Pawley profile fit of the patterns at ambient conditions as well as at the final pressure is shown to prove for phase purity.

**Tab. S-3.** Pawley profile fit outcome of refined cell parameters and deviations for  $[(n\text{Pr})_3(\text{CH}_3)\text{N}]\text{Co}(\text{C}_2\text{N}_3)_3$  at different pressures, ranging from ambient to  $p = 0.4$  GPa. At the bottom, output data of PASCAL - principal axis strain calculations[10] with direction of projections of the three principal axes on the unit cell axes  $a$ ,  $b$  and  $c$  is shown. Reported are the median compressibilities  $K$  with respective errors  $\sigma K$ .

$p$ / GPa	$r_{\text{wp}}$	$a$ / Å	$c$ / Å	$V$ / Å <sup>3</sup>
0.0001	1.24116	12.6783(3)	22.2548(7)	3097.94(16)
0.0250	0.86059	12.6752(2)	22.1793(7)	3085.95(15)
0.0500	0.73018	12.6724(3)	22.1311(6)	3077.88(14)
0.0750	0.67945	12.6650(2)	22.0888(6)	3068.43(13)
0.1000	0.83940	12.6667(3)	22.0575(8)	3064.85(17)
0.1250	0.68913	12.6598(2)	22.0303(8)	3057.76(14)
0.1500	0.64338	12.6496(2)	21.9890(11)	3047.12(18)
0.1750	0.66756	12.6449(2)	21.9491(13)	3039.35(21)
0.2000	0.77087	12.6358(3)	21.9179(14)	3030.63(24)
0.2250	0.70785	12.6309(2)	21.8913(14)	3024.60(22)
0.2500	0.75586	12.6279(3)	21.8517(14)	3017.73(22)
0.2750	0.66911	12.6227(2)	21.8309(10)	3012.34(17)
0.3000	0.69694	12.6169(2)	21.8033(12)	3005.80(19)
0.3250	0.74042	12.6099(2)	21.7811(12)	2999.37(20)
0.3500	0.76696	12.6021(2)	21.7475(8)	2991.05(15)
0.3750	0.75124	12.5958(2)	21.7268(8)	2985.24(14)
0.4000	0.83585	12.5993(2)	21.7229(8)	2986.33(14)

Axes	$K$ / (TPa) <sup>-1</sup>	$\sigma K$ / (TPa) <sup>-1</sup>	$a$	$b$	$c$
$X_1$	52.9545	0.9249	0.0000	0.0000	1.0000
$X_2$	17.5806	0.6632	-0.0005	1.0000	0.0000
$X_3$	17.5806	0.6633	0.8943	0.4475	0.0000
$V$	93.2264	2.5061			



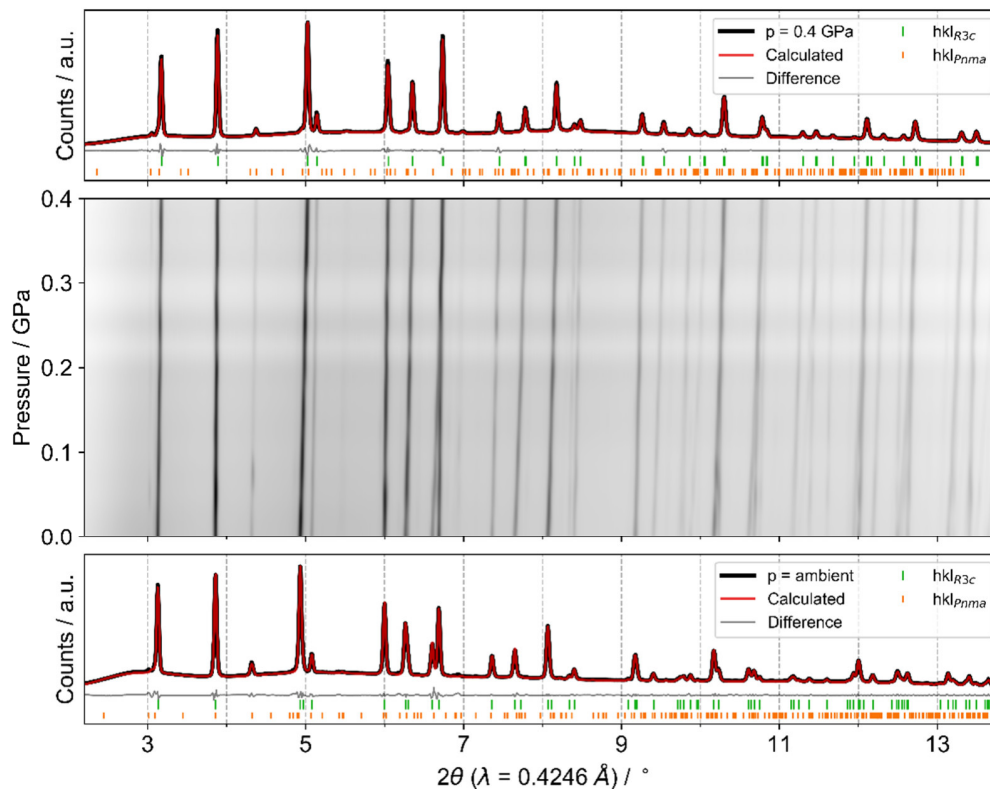
**Figure S-3.** HPPXRD analysis of  $[(n\text{Pr})_3(\text{CH}_3)\text{N}]\text{Co}(\text{C}_2\text{N}_3)_3$  from ambient pressures to 0.4 GPa. The middle shows a contour plot of the pressure dependent diffraction patterns with intense colour corresponding to a strong reflection. Additionally, a Pawley profile fit of the patterns at ambient conditions as well as at the final pressure is shown to prove for phase purity.

**Tab. S-4.** Pawley profile fit outcome of refined cell parameters and deviations for  $[(n\text{Pr})_3(\text{CH}_3)\text{N}]\text{Ni}(\text{C}_2\text{N}_3)_3$  at different pressures, ranging from ambient to  $p = 0.4$  GPa. At the bottom, output data of PASCAL - principal axis strain calculations[10] with direction of projections of the three principal axes on the unit cell axes  $a$ ,  $b$  and  $c$  is shown. Reported are the median compressibilities  $K$  with respective errors  $\sigma K$ .

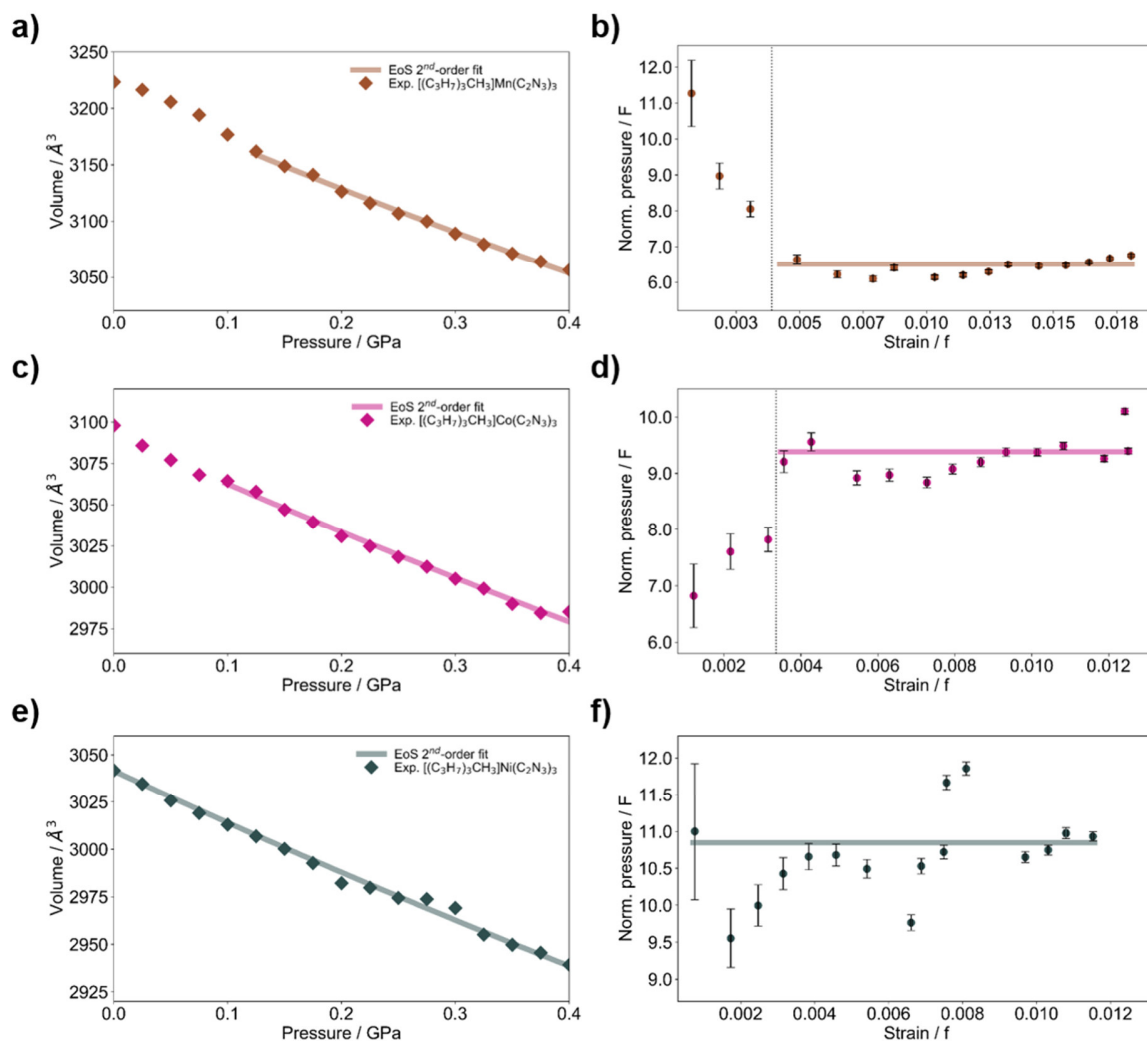
$p$ / GPa	$r_{\text{wp}}$	$a$ / Å	$c$ / Å	$v$ / Å <sup>3</sup>
0.0001	1.55532	12.6035(2)	22.1114(6)	3041.77(12)
0.0250	1.47999	12.5989(2)	22.0755(6)	3034.63(13)
0.0500	1.57006	12.5908(2)	22.0420(7)	3026.13(13)
0.0750	1.37025	12.5846(2)	22.0066(6)	3018.30(12)
0.1000	1.23712	12.5838(1)	21.9709(5)	3013.00(09)
0.1250	1.27594	12.5789(2)	21.9435(7)	3006.91(12)
0.1500	1.17245	12.5749(2)	21.9084(7)	3000.21(13)
0.1750	1.19148	12.5676(2)	21.8795(5)	2992.74(11)
0.2000	1.30097	12.5566(2)	21.8424(6)	2982.45(13)
0.2250	1.57405	12.5570(3)	21.8221(10)	2979.88(19)
0.2500	1.17840	12.5498(3)	21.8072(9)	2974.44(17)
0.2750	1.78251	12.5503(2)	21.7838(11)	2971.46(19)
0.3000	1.81037	12.5464(3)	21.7721(14)	2968.04(25)
0.3250	1.43181	12.5320(3)	21.7307(13)	2955.58(21)
0.3500	1.32149	12.5262(3)	21.7057(10)	2949.45(18)
0.3750	1.62886	12.5202(7)	21.7079(15)	2946.96(38)
0.4000	1.78734	12.5106(8)	21.6882(18)	2939.76(45)

Axes	$K$ / (TPa) <sup>-1</sup>	$\sigma K$ / (TPa) <sup>-1</sup>	$a$	$b$	$c$
$X_1$	43.7922	1.1561	0.0000	0.0000	1.0000
$X_2$	17.7272	1.3559	-0.9907	-0.1362	0.0000
$X_3$	17.7250	1.3592	0.3628	0.9319	0.0000
$V$	82.8543	1.4220			



**Figure S-4.** HPPXRD analysis of  $[(n\text{Pr})_3(\text{CH}_3)\text{N}]\text{Ni}(\text{C}_2\text{N}_3)_3$  from ambient pressures to 0.4 GPa. The middle shows a contour plot of the pressure dependent diffraction patterns with intense colour corresponding to a strong reflection. Additionally, a Pawley profile fit of the patterns at ambient conditions as well as at the final pressure is shown to prove for phase purity.



**Figure S-5.** Panels a) to f) show the Birch-Murnaghan equation of state of second order for the three materials, respectively, fitted to p-V data from the HPPXRD experiments with the norm. pressure to strain plots to ensure feasibility of the bulk modulus analysis. For  $M = \text{Mn}^{2+}$  and  $\text{Co}^{2+}$  the high-pressure phase transition is proposed to resemble the temperature induced phase transition which agrees with the analysis of HPPXRD pattern. The phase transitions are most visible in the Ff-plots and are indicated with a dotted line for b) and d), for which the analysis was carried out only for the high-pressure data points. Colour code: Mn – brown, Co – pink, Ni – grey.

**Tab. S-5.** Overview of calculated bulk moduli  $B$ ,  $B'$  and refined  $V_0$  including the estimated standard deviation obtained from pressure-dependent diffraction data of  $[(n\text{Pr})_3(\text{CH}_3)\text{N}]M(\text{C}_2\text{N}_3)_3$  with  $M$  being Manganese, Cobalt and Nickel. For  $M = \text{Mn}^{2+}$  and  $\text{Co}^{2+}$ , the bulk moduli were extracted from the high-pressure phase as indicated in b) and d) in Figure S-5. The phase transition occurs at  $p = 0.125$  GPa ( $\text{Mn}^{2+}$ ) and 0.1 GPa ( $\text{Co}^{2+}$ ). For  $M = \text{Ni}^{2+}$  no indication of a phase transition is evident in the Ff-Plot, despite a clear peak movement in the contour plots, and therefore, the full HPPXRD dataset was used to derive the bulk modulus.

$[(n\text{Pr})_3(\text{CH}_3)\text{N}]M(\text{C}_2\text{N}_3)_3$	$M = \text{Mn}^{2+}$	$M = \text{Co}^{2+}$	$M = \text{Ni}^{2+}$
$B$ / GPa	7.08	9.90	10.85
$\sigma_B$ / GPa	0.15	0.30	0.16
$B'$	4.00	4.00	4.00
$V_0$ / $\text{\AA}^3$	3213.4(22)	3092.9(23)	3041.5(6)



## References

1. Murnaghan, F.D. Proceedings of the National Academy of Sciences, 1944. **30**(9): p. 244-247.
2. Birch, F. Physical Review, 1947. **71**(11): p. 809-824.
3. Burger, S., S. Grover, K.T. Butler, H.L.B. Boström, R. Grau-Crespo, and G. Kieslich. Materials Horizons, 2021. **8**(9): p. 2444-2450.
4. Vervoorts, P., J. Keupp, A. Schneemann, C.L. Hobday, D. Daisenberger, R.A. Fischer, R. Schmid, and G. Kieslich. Angewandte Chemie International Edition, 2021. **60**(2): p. 787-793.
5. Dissegna, S., P. Vervoorts, C.L. Hobday, T. Düren, D. Daisenberger, A.J. Smith, R.A. Fischer, and G. Kieslich. Journal of the American Chemical Society, 2018. **140**(37): p. 11581-11584.
6. Brooks, N.J., B.L.L.E. Gauthe, N.J. Terrill, S.E. Rogers, R.H. Templer, O. Ces, and J.M. Seddon. Review of Scientific Instruments, 2010. **81**(6): p. 064103.
7. Pawley, G.S. Journal of Applied Crystallography, 1981. **14**(6): p. 357-361.
8. Coelho, A. Journal of Applied Crystallography, 2018. **51**(1): p. 210-218.
9. Angel, R.J., M. Alvaro, and J. Gonzalez-Platas. 2014. **229**(5): p. 405-419.
10. Cliffe, M.J. and A.L. Goodwin. Journal of Applied Crystallography, 2012. **45**(6): p. 1321-1329.



## 8.4 STUDY V: Supporting Information

**ADVANCED  
FUNCTIONAL  
MATERIALS**

### Supporting Information

for *Adv. Funct. Mater.*, DOI: 10.1002/adfm.202205343

Designing Geometric Degrees of Freedom in ReO<sub>3</sub>-Type  
Coordination Polymers

*Stefan Burger, Karina Hemmer, David C. Mayer, Pia  
Vervoorts, Dominik Daisenberger, Jan K. Zaręba, and  
Gregor Kieslich\**

## Supporting Information

### **Designing Geometric Degrees of Freedom in ReO<sub>3</sub>-Type Coordination Polymers**

Stefan Burger,<sup>[1]</sup> Karina Hemmer,<sup>[1]</sup> David C. Mayer,<sup>[1]</sup> Pia Vervoorts,<sup>[1]</sup> Dominik Daisenberger,<sup>[2]</sup> Jan K. Zaręba,<sup>[3]</sup> and Gregor Kieslich\*<sup>[1]</sup>

<sup>1</sup>Department of Chemistry, Technical University of Munich, Lichtenbergstraße 4, 85748 Garching, GER.

<sup>2</sup>Diamond Lightsource, Harwell Science and Innovation Campus, Didcot OX11 0DE, Oxfordshire, UK.

<sup>3</sup>Advanced Materials Engineering and Modelling Group, Wrocław University of Science and Technology, Wybrzeże Wyspiańskiego 27, 50-370 Wrocław, POL.

\* E-mail: Gregor.Kieslich@tum.de

## Table of content

Synthesis procedures .....	3
Synthesis of the precursors N,N-Hexapropylalkyl-diaminiumbromide $\text{ABr}_2$ . .....	3
Synthesis of the $\text{AB}_2\text{X}_6$ materials $[\text{TPC4TP}]\text{Mn}_2(\text{C}_2\text{N}_3)_6$ and $[\text{TPC5TP}]\text{Mn}_2(\text{C}_2\text{N}_3)_6$ . .....	4
Analytical NMR data of the precursor compounds $[\text{A}]\text{Br}_2$ .....	5
Thermal analysis of $[\text{TPC4TP}]\text{Mn}_2(\text{C}_2\text{N}_3)_6$ and $[\text{TPC5TP}]\text{Mn}_2(\text{C}_2\text{N}_3)_6$ .....	8
Thermogravimetric analysis .....	8
Differential Scanning Calorimetry at low temperatures .....	9
Fourier-transform-Infrared-Spectroscopy (FT-IR) .....	11
Structural models for $[\text{TPC4TP}]\text{Mn}_2(\text{C}_2\text{N}_3)_6$ and $[\text{TPC5TP}]\text{Mn}_2(\text{C}_2\text{N}_3)_6$ .....	13
Single crystal X-Ray diffraction data for $[\text{TPC4TP}]\text{Mn}_2(\text{C}_2\text{N}_3)_6$ and $[\text{TPC5TP}]\text{Mn}_2(\text{C}_2\text{N}_3)_6$ ..	13
Variable-temperature single crystal X-ray diffraction for $[\text{TPC4TP}]\text{Mn}_2(\text{C}_2\text{N}_3)_6$ .....	16
Discussion of structural model for $[\text{TPC5TP}]\text{Mn}_2(\text{C}_2\text{N}_3)_6$ .....	21
Distortion mode analysis .....	23
Powder X-Ray diffraction data .....	25
Lab-source PXRD data of bulk sample .....	25
High-resolution powder XRD data at variable temperatures .....	27
Pressure dependent high-resolution powder XRD data .....	33
Bulk Modulus - Birch-Murnaghan equation of state .....	41
KBr as reference material for pressure cell and analysis .....	43
Second Harmonic Generation studies .....	46
References .....	48

## Synthesis procedures

All used chemicals were purchased from commercial suppliers (Sigma Aldrich, vwr) and were used without further purification. Solvents and millipore water for the syntheses and washing steps were in quality of reagent grade.

Synthesis of the precursors *N,N*-Hexapropylalkyl-diaminiumbromide  $\text{ABr}_2$ .

In a typical experiment, a solution of 1,4-dibromoalkane or 1,5-dibromoalkane **2** in acetonitrile (100 ml) was prepared. Tri-*n*-propyl amine **1** (4 eq.) was slowly added at room temperature and the mixture was stirred at reflux temperature of acetonitrile for 48 hours. After a colorless precipitation was formed, the reaction mixture was cooled down, filtered and washed several times with ethyl acetate. Recrystallisation in ethyl acetate/acetonitrile led to the crystallization of large, colorless needles, yielding the pure product **3**.

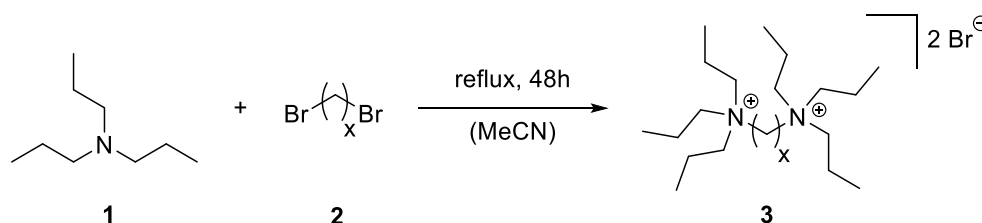


**Figure S-1:** Schematic of the synthesis route for  $[\text{TPC4TP}]\text{Br}_2$  and  $[\text{TPC5TP}]\text{Br}_2$ . The route was adapted and slightly modified from the literature.<sup>[1]</sup>

$X = 4$ : ***N,N*-hexapropylbutane-1,4-diaminiumbromide  $[\text{TPC4TP}]\text{Br}_2$ :**

Starting material: 1,4-dibromobutane (5.40 g, 25 mmol, 1 eq.), product yield 80.6% (10.13 g, 20.16 mmol).

$X = 5$ : ***N,N*-hexapropylpentyl-1,5-diaminiumbromide  $[\text{TPC5TP}]\text{Br}_2$ :**

Starting material: 1,5-dibromopentane (5.75 g, 25 mmol, 1 eq.), product yield 45.8% (5.91 g, 11.45 mmol).

### Synthesis of the $AB_2X_6$ materials $[TPC4TP]Mn_2(C_2N_3)_6$ and $[TPC5TP]Mn_2(C_2N_3)_6$ .

Samples of the composition  $[A]Mn_2(C_2N_3)_6$  were synthesized *via* a mild solution approach route followed by slow crystallization of the desired materials. In a representative experiment, a solution of  $[TPC4TP]Br_2$  in ultrapure water (0.4 M, 1 eq.) was mixed with a solution of manganese chloride tetrahydrate (Sigma-Aldrich) in absolute ethanol (0.2 M, 2 eq.) and a solution of sodium dicyanamide ( $Na(C_2N_3)$ , Sigma-Aldrich) in ultrapure water (2.0 M, 6 eq.). The obtained solution was allowed to stand at 2 °C for 4 days, until colorless, large cuboid block crystals were observed. The crystals were collected and washed with ice-cold ultrapure water several times and dried at room temperature.

**EA**  $[TPC4TP]Mn_2(C_2N_3)_6$ : calc. C 48.11 H 5.94 N 33.00 Mn 12.95, found C 48.19 H 6.01 N 33.28

**EA**  $[TPC5TP]Mn_2(C_2N_3)_6$ : calc. C 48.72 H 6.07 N 32.47 Mn 12.73, found C 48.87 H 6.02 N 32.60

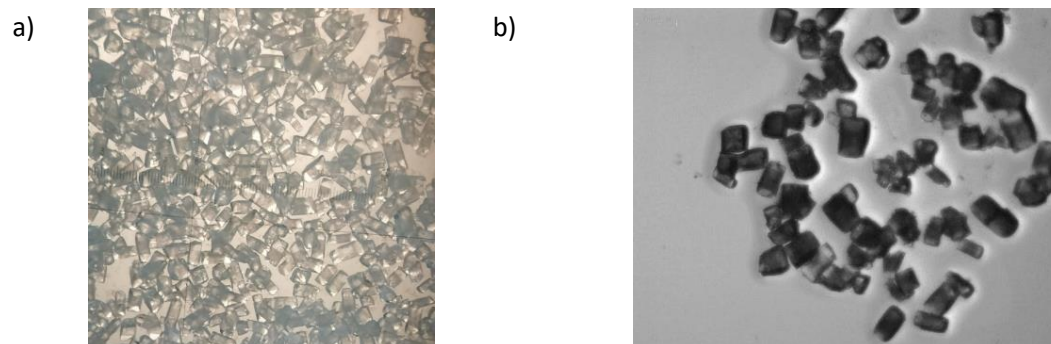


**Figure S-2:** Photographs of crystallised samples with the composition  $[TPC4TP]Mn_2(C_2N_3)_6$  representing homogeneously shaped block crystals. Picture on the right (b) indicates an approximate crystal size of 500x300  $\mu m$ .

## Analytical NMR data of the precursor compounds [A]Br<sub>2</sub>

<sup>1</sup>H-NMR and <sup>13</sup>C-NMR spectra were recorded on a *Bruker* Avance III 400 spectrometer at room temperature. Chemical shifts are expressed as parts per million (ppm,  $\delta$ ) downfield of tetramethylsilane (TMS) and are referenced to the residual solvent signal of deuterium oxide.<sup>[2]</sup> The description of signals include: s = singlet, t = triplet and m = multiplet. All coupling constants are absolute values and are expressed in Hertz (Hz). <sup>13</sup>C-NMR was measured as <sup>1</sup>H-NMR decoupled. All signals were assigned to the respective nuclei based on common 2D experiments like COSY, HSQC and HMBC.

### [TPC4TP]Br<sub>2</sub>:

<sup>1</sup>H-NMR (400 MHz, D<sub>2</sub>O, 298 K):  $\delta$  [ppm] = 3.32 (t,  $J$  = 7.3 Hz, 4H, C4-H), 3.28 – 3.12 (m, 12H, C3-H), 1.87 – 1.61 (m, 16H, C2-H, C5-H), 0.97 (t,  $J$  = 7.2 Hz, 18H, C1-H).

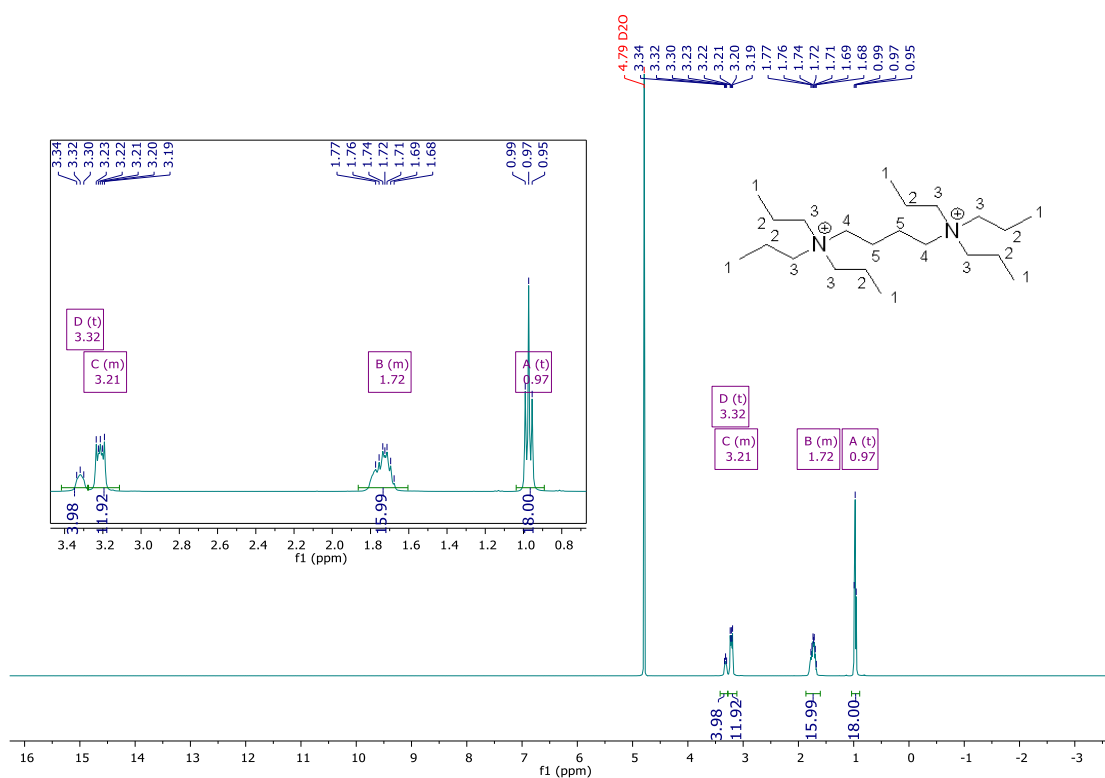
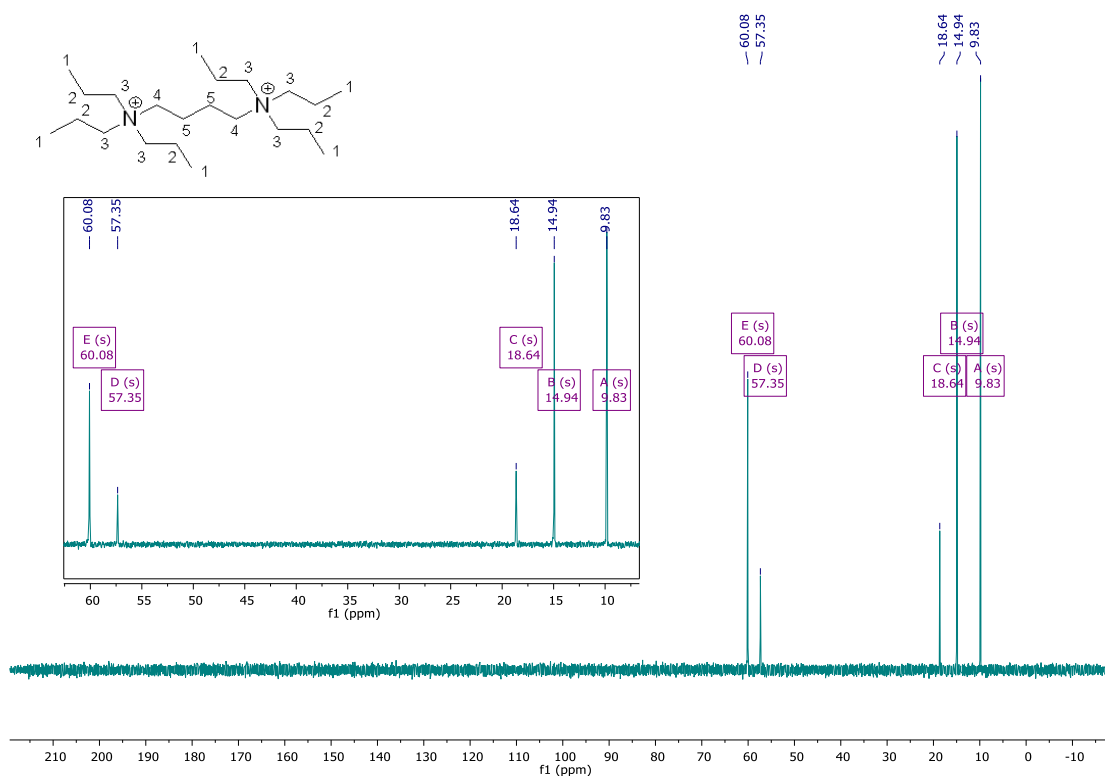
<sup>13</sup>C-NMR (101 MHz, D<sub>2</sub>O, 298 K):  $\delta$  [ppm] = 60.08 (C3), 57.35 (C4), 18.64 (C5), 14.94 (C2), 9.83 (C1).

### [TPC5TP]Br<sub>2</sub>:

<sup>1</sup>H-NMR (400 MHz, D<sub>2</sub>O, 298 K):  $\delta$  [ppm] = 3.33 – 3.02 (m, 16H, C3-H), 1.88 – 1.62 (m, 16H, C2-H), 1.42 (p,  $J$  = 7.7 Hz, 2H, C4-H), 0.98 (t,  $J$  = 7.3 Hz, 18H, C1-H).

<sup>13</sup>C-NMR (101 MHz, D<sub>2</sub>O, 298 K):  $\delta$  [ppm] = 59.98 (C3), 57.99 (C4), 22.77 (C6), 21.06 (C5), 14.93 (C2), 9.90 (C1).



Figure S-3:  $^1\text{H-NMR}$  spectrum of  $[\text{TPC4TP}]\text{Br}_2$  in deuterium oxide.Figure S-4:  $^{13}\text{C-NMR}$  spectrum of  $[\text{TPC4TP}]\text{Br}_2$  in deuterium oxide.

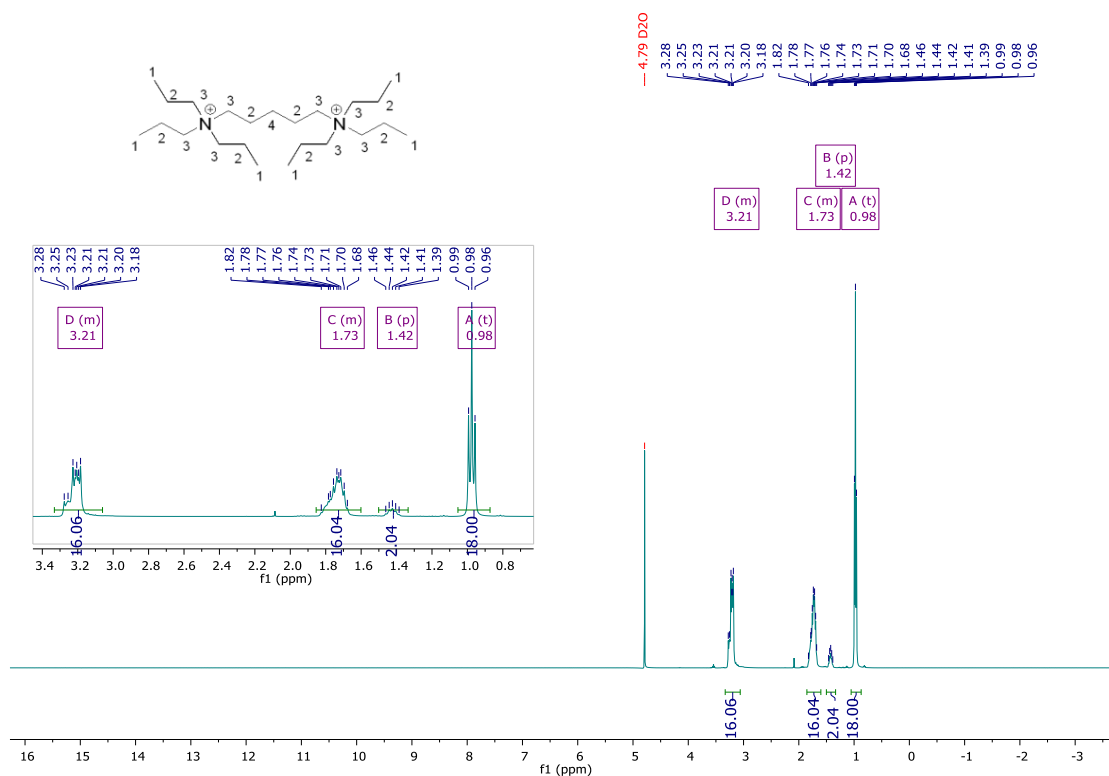


Figure S-5: <sup>1</sup>H-NMR spectrum of [TPC5TP]Br<sub>2</sub> in deuterium oxide.

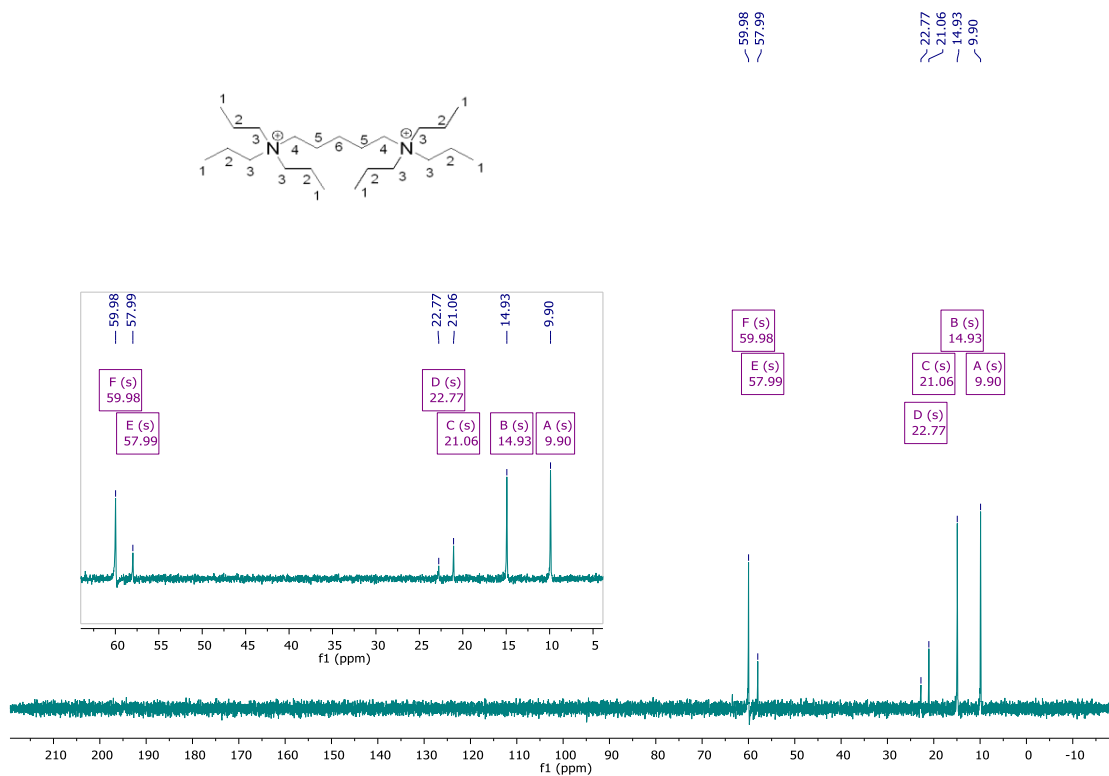
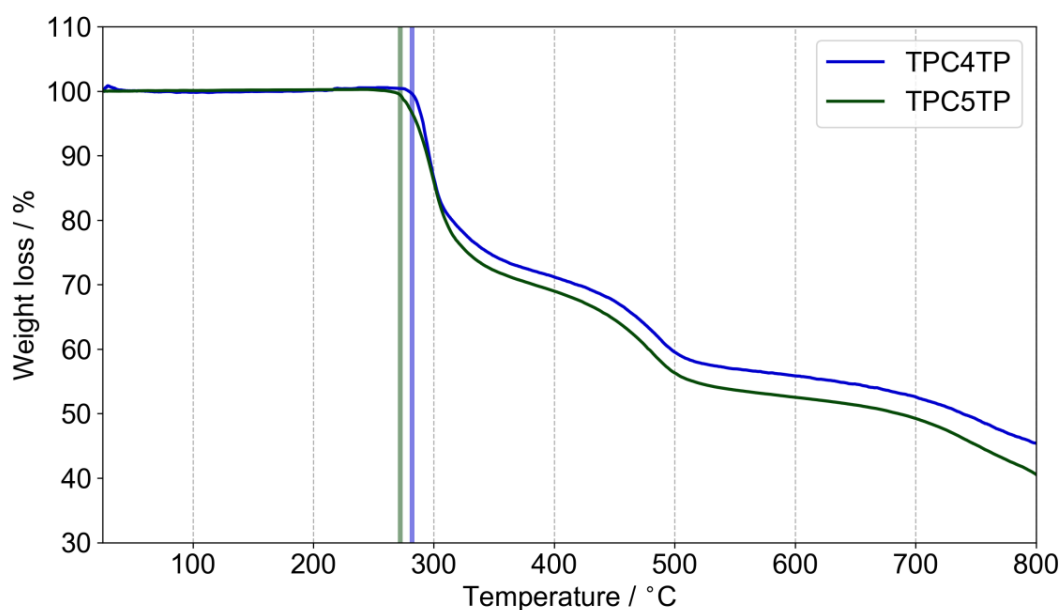


Figure S-6: <sup>13</sup>C-NMR spectrum of [TPC5TP]Br<sub>2</sub> in deuterium oxide.

Thermal analysis of  $[\text{TPC4TP}]\text{Mn}_2(\text{C}_2\text{N}_3)_6$  and  $[\text{TPC5TP}]\text{Mn}_2(\text{C}_2\text{N}_3)_6$ 

## Thermogravimetric analysis

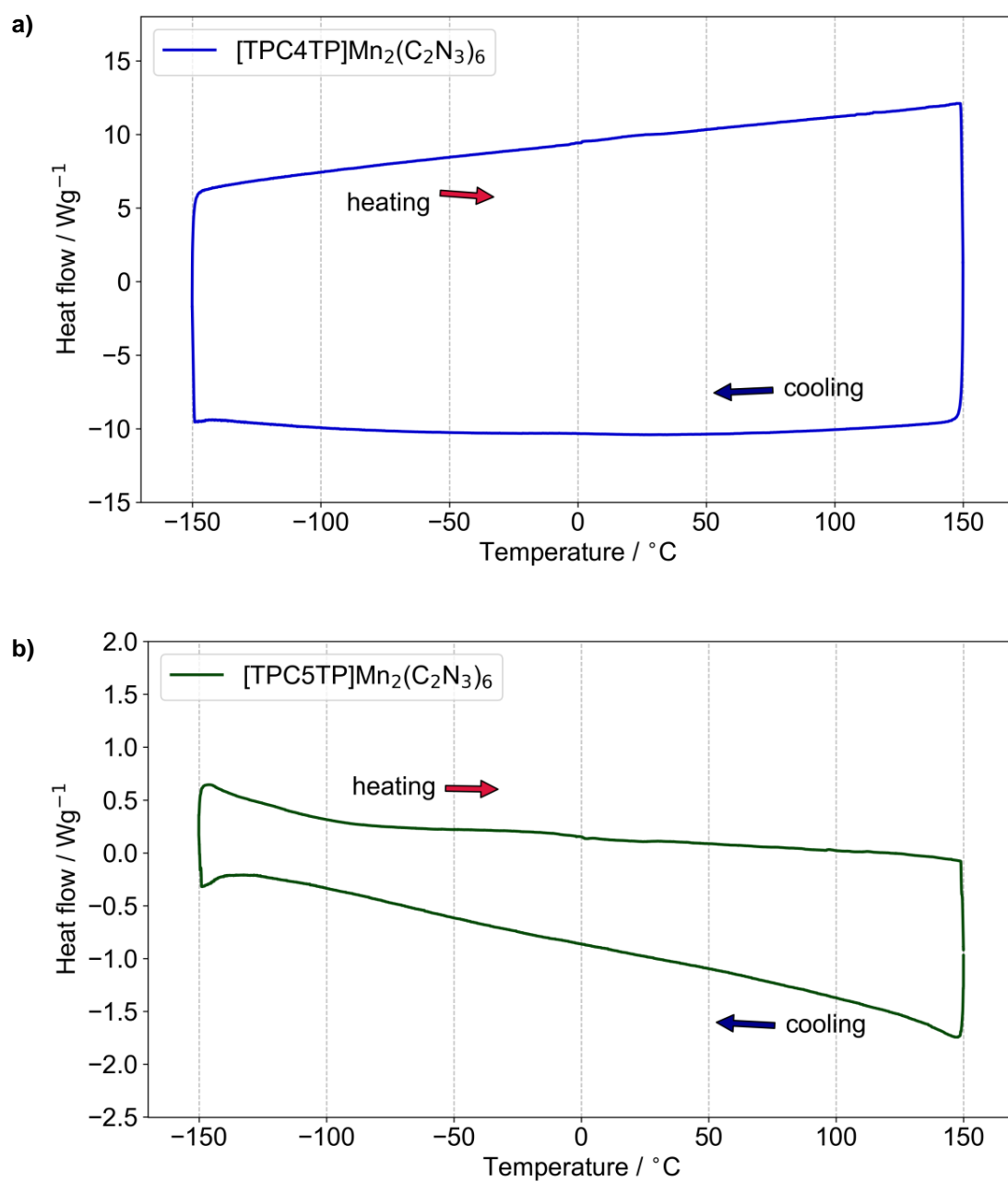
Thermal stability of the material was determined with a *NETZSCH* STA449 F5 Jupiter machine using aluminum oxide pans ( $70 \mu\text{L}$  with lid) with sample amount of 3.5680 mg for  $[\text{TPC4TP}]\text{Mn}_2(\text{C}_2\text{N}_3)_6$  and 13.5405 mg for  $[\text{TPC5TP}]\text{Mn}_2(\text{C}_2\text{N}_3)_6$ . The sample mass and the heat flow signal using an empty reference pan were recorded simultaneously. The heat flow signal did not show any feature that would point towards a phase transition and is therefore left out for clarity. Temperature calibration of the oven cell was performed based on the melting point of the following metals: In, Sn, Bi, Zn, Al and Au. The baseline was corrected screening an empty sample pan with the respective measurement program prior to the experiment. The following thermal program was applied using argon gas ( $20\text{mLmin}^{-1}$ ) for purging: At  $27^\circ\text{C}$  isothermal equilibration (30min), ramp from  $27^\circ\text{C}$  to  $800^\circ\text{C}$  with  $10\text{Kmin}^{-1}$ , isothermal equilibrium for 5 minutes.



**Figure S-7:** TGA curves of the solids  $[\text{TPC4TP}]\text{Mn}_2(\text{C}_2\text{N}_3)_6$  (shown in red) and  $[\text{TPC5TP}]\text{Mn}_2(\text{C}_2\text{N}_3)_6$  (visualised in darkgreen) indicating thermal stability up to a temperature of onset  $282^\circ\text{C}$  for  $[\text{TPC4TP}]\text{Mn}_2(\text{C}_2\text{N}_3)_6$  and  $272^\circ\text{C}$  for  $[\text{TPC5TP}]\text{Mn}_2(\text{C}_2\text{N}_3)_6$  without any loss of weight, respectively.

### Differential Scanning Calorimetry at low temperatures

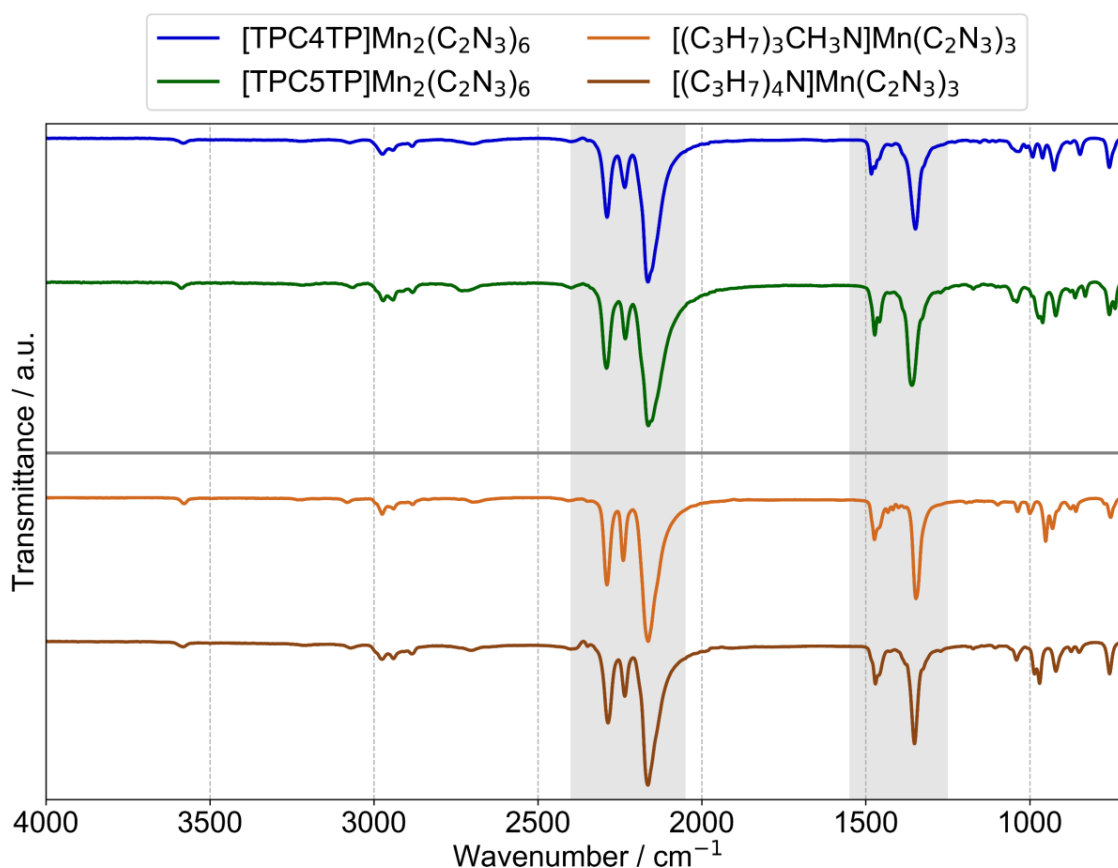
A DSC measurement was carried out on a DSC Q2000 from *TA Instruments* with a heating rate of  $10\text{Kmin}^{-1}$  and a constant helium purging gas flow rate of  $25\text{mlmin}^{-1}$ . The temperature window ranges from  $-150\text{ }^{\circ}\text{C}$  to  $150\text{ }^{\circ}\text{C}$  with respect to the decomposition of the investigated sample and was controlled with the use of liquid nitrogen as cooling medium. The temperature of the oven cell and the heat flow signal was calibrated with respect to the melting point of indium metal and verified by the internal calibration tools provided by *TA Instruments*. For  $[\text{TPC4TP}]\text{Mn}_2(\text{C}_2\text{N}_3)_6$ , a sample mass of 4.2240 mg, for  $[\text{TPC5TP}]\text{Mn}_2(\text{C}_2\text{N}_3)_6$  4.066 mg was used, following a heat/cool/heat cycle. As typical for DSC techniques, the first heating step was discarded to compensate inhomogeneities in the sample. The heat flow signal is shown as exo down.



**Figure S-8:** Cyclic differential scanning calorimetry (DSC) measurement curves for a cooling/heating cycle from +150 °C to -150 °C visualising no feature that could point towards a phase transition, confirming the stability of the *Pc* phase of [TPC4TP]Mn<sub>2</sub>(C<sub>2</sub>N<sub>3</sub>)<sub>6</sub> (red curve, upper plot a) as well as the *P2<sub>1</sub>/c* phase of [TPC5TP]Mn<sub>2</sub>(C<sub>2</sub>N<sub>3</sub>)<sub>6</sub> (darkgreen curve, lower graph b) for the whole temperature range.

## Fourier-transform-Infrared-Spectroscopy (FT-IR)

The FTIR spectra for both materials were collected at room temperature on a Bruker Vertex 70 FTIR machine using a Bruker Platinum ATR. The detector was cooled down with liquid nitrogen until a stable background signal was reached.

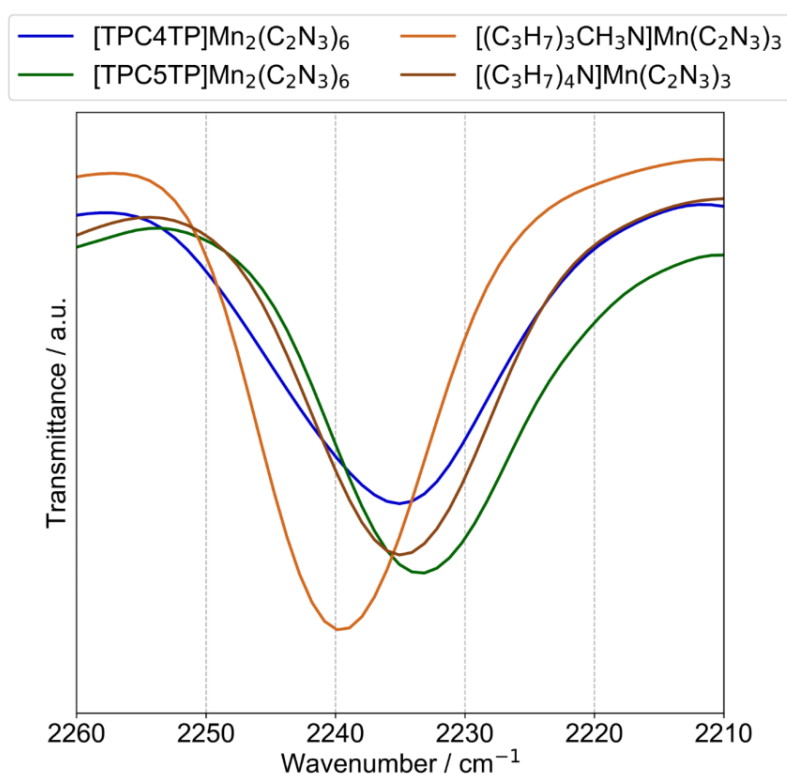


**Figure S-9:** FT-IR spectra for [TPC4TP] $Mn_2(C_2N_3)_6$  (blue) and [TPC5TP] $Mn_2(C_2N_3)_6$  (green) as well as spectra of  $[(C_3H_7)_3CH_3N]Mn(C_2N_3)_3$  (light brown) and  $[(C_3H_7)_4N]Mn(C_2N_3)_3$  (brown) for comparison,<sup>[3]</sup> collected at room temperature. As discussed, both  $AB_2X_6$  materials behave as 3D molecular perovskites, indicated by the same kind of signal arrangement in the IR spectra compared to the  $ABX_3$  analog which is typical for 3D perovskite coordination networks with dicyanamide linkers.<sup>[4]</sup> Highlighted in grey color are the regions typical for  $\mu$ -1,5-coordination of dicyanamide to metal to form octahedra with  $\tilde{\nu} = 2300\text{-}2100\text{ cm}^{-1}$  (dca vibration modes) and for the A-site cation at  $1500\text{-}1300\text{ cm}^{-1}$  ( $CH_x$  vibration modes).

Analysis of the wavenumber region between  $\tilde{\nu} = 2300\text{-}2100\text{ cm}^{-1}$  for which stretching modes of the dicyanamide triple bond can be assigned, in detail the vibration band at  $\tilde{\nu} = 2245\text{-}2225\text{ cm}^{-1}$  for  $\tilde{\nu}_s (C \equiv N)$ ,<sup>[4]</sup> reveals the same wavenumbers for [TPC4TP] $Mn_2(C_2N_3)_6$  and  $[(C_3H_7)_4N]Mn(C_2N_3)_3$ , underpinning the close structural relationship of the 3D  $[Mn(C_2N_3)_3]^-$ -network of the here introduced materials and existing molecular perovskites. Additionally, the stretching mode for [TPC5TP] $Mn_2(C_2N_3)_6$  shifts the IR band towards a smaller wavenumber, whereas for  $[(C_3H_7)_3CH_3N]Mn(C_2N_3)_3$  it is shifted to a higher wavenumber value, see table S-1 and figure S-10 for details.

**Table S-1:** Wavenumber  $\tilde{\nu}$  of one specific IR band of the C≡N stretching mode, as illustrated in figure S-10.

	$\tilde{\nu}_s$
[TPC4TP]Mn <sub>2</sub> (C <sub>2</sub> N <sub>3</sub> ) <sub>6</sub>	2235
[(C <sub>3</sub> H <sub>7</sub> ) <sub>4</sub> N]Mn(C <sub>2</sub> N <sub>3</sub> ) <sub>3</sub>	2235
[TPC5TP]Mn <sub>2</sub> (C <sub>2</sub> N <sub>3</sub> ) <sub>6</sub>	2232
[(C <sub>3</sub> H <sub>7</sub> ) <sub>3</sub> CH <sub>3</sub> N]Mn(C <sub>2</sub> N <sub>3</sub> ) <sub>3</sub>	2239

**Figure S-10:** Zoom-in of the FT-IR spectra for [TPC4TP]Mn<sub>2</sub>(C<sub>2</sub>N<sub>3</sub>)<sub>6</sub> (blue), [TPC5TP]Mn<sub>2</sub>(C<sub>2</sub>N<sub>3</sub>)<sub>6</sub> (green), [(C<sub>3</sub>H<sub>7</sub>)<sub>3</sub>CH<sub>3</sub>N]Mn(C<sub>2</sub>N<sub>3</sub>)<sub>3</sub> (light brown) and [(C<sub>3</sub>H<sub>7</sub>)<sub>4</sub>N]Mn(C<sub>2</sub>N<sub>3</sub>)<sub>3</sub> (brown), collected at room temperature. For the IR band around 2240-2230 cm<sup>-1</sup>, corresponding to a stretching mode of the C≡N bond of the dicyanamide molecule, a shift of the signal for [TPC5TP]Mn<sub>2</sub>(C<sub>2</sub>N<sub>3</sub>)<sub>6</sub> and [(C<sub>3</sub>H<sub>7</sub>)<sub>3</sub>CH<sub>3</sub>N]Mn(C<sub>2</sub>N<sub>3</sub>)<sub>3</sub> is observed.

As the vibrational frequency corresponds to the strength of a bond with an active vibration

mode following the relation  $\tilde{\nu} = \frac{1}{2\pi} * \sqrt{\frac{k}{\mu}}$  (with  $k$  being the spring constant for the bond and  $\mu$

being the reduced mass), a shift to higher wavenumbers generally implies a stronger bond *i.e.* a shortening of the C≡N bond. Therefore, the flexible 3D metal-dicyanamide host framework adapts for smaller A-site cations such as [(C<sub>3</sub>H<sub>7</sub>)<sub>3</sub>CH<sub>3</sub>N]<sup>+</sup> compared to [(C<sub>3</sub>H<sub>7</sub>)<sub>4</sub>N]<sup>+</sup> towards a more compact confinement while being able to stretch for guests like TPC5TP<sup>2+</sup> compared to TPC4TP<sup>2+</sup> to enclose also larger A-site cations.

Structural models for [TPC4TP]Mn<sub>2</sub>(C<sub>2</sub>N<sub>3</sub>)<sub>6</sub> and [TPC5TP]Mn<sub>2</sub>(C<sub>2</sub>N<sub>3</sub>)<sub>6</sub>Single crystal X-Ray diffraction data for [TPC4TP]Mn<sub>2</sub>(C<sub>2</sub>N<sub>3</sub>)<sub>6</sub> and [TPC5TP]Mn<sub>2</sub>(C<sub>2</sub>N<sub>3</sub>)<sub>6</sub>

Single crystal X-Ray diffraction intensity data were collected on a *Bruker* diffractometer equipped with a TXS rotating anode with Mo-K $\alpha$  radiation source ( $\lambda = 0.71073 \text{ \AA}$ ), a CMOS plate detector (*Bruker* APEX III,  $\kappa$ -CMOS) and a Helios optics and a “D8 Venture Duo IMS” diffractometer with IMS microsource anode for fine-focus with Mo-K $\alpha$  radiation source,  $\kappa$ -geometry, PhotonII hybrid pixel detector and Helios optics coupled with an Oxford Cryosystems cooling device by using the APEX3 software package.<sup>[5]</sup> Appropriate crystals were selected in perfluorinated ether, fixed on top of a kapton micro sampler, transferred to the diffractometer and frozen under a stream of cold nitrogen. A matrix scan was used to determine the initial lattice parameters. Reflections were merged and corrected for Lorentz and polarization effects, scan speed, and background using SAINT.<sup>[6]</sup> Absorption corrections, including odd and even ordered spherical harmonics were performed using SADABS.<sup>[7]</sup> Space group assignments were based upon systematic absences, E-statistics, and successful refinement of the structures. Data reduction was performed with APEX3 and structure solution was performed by using SHELX as integrated in Olex2.<sup>[8,9]</sup> Structures were solved by direct methods with the aid of successive difference Fourier maps, and were refined against all data. Hydrogen atoms were placed in calculated positions and refined using a riding model. Non-hydrogen atoms were refined with anisotropic displacement parameters. Full-matrix least-squares refinements were carried out by minimizing  $\sum w(F_o^2 - F_c^2)^2$  with the SHELXL weighting scheme.<sup>[9]</sup> The images of the crystal structures were generated using VESTA 3.4.0.<sup>[10]</sup>

**Table S-2:** Crystallographic data of [TPC4TP]Mn<sub>2</sub>(C<sub>2</sub>N<sub>3</sub>)<sub>6</sub>, collected at 100 K, and [TPC5TP]Mn<sub>2</sub>(C<sub>2</sub>N<sub>3</sub>)<sub>6</sub>, collected at 220 K.

Compound	[TPC4TP]Mn <sub>2</sub> (C <sub>2</sub> N <sub>3</sub> ) <sub>6</sub>	[TPC5TP]Mn <sub>2</sub> (C <sub>2</sub> N <sub>3</sub> ) <sub>6</sub>
<b>Empirical formula</b>	C <sub>68</sub> H <sub>100</sub> Mn <sub>4</sub> N <sub>40</sub>	C <sub>35</sub> H <sub>52</sub> Mn <sub>2</sub> N <sub>20</sub>
<b>Formula weight / gmol<sup>-1</sup></b>	1697.63	862.84
<b>Temperature / K</b>	100.0	220.13
<b>Crystal system</b>	monoclinic	monoclinic
<b>Space group</b>	<i>Pc</i>	<i>P21/c</i>
<b>a / Å</b>	11.6995(6)	14.1287(7)
<b>b / Å</b>	21.4227(12)	9.6632(6)
<b>c / Å</b>	17.2448(10)	32.9504(16)



$\alpha / ^\circ$	90	90
$\beta / ^\circ$	92.264(2)	98.031(2)
$\gamma / ^\circ$	90	90
Volume / $\text{\AA}^3$	4318.8(4)	4454.5(4)
Z	2	4
$\rho_{\text{calc}} / \text{gcm}^{-3}$	1.305	1.287
$\mu / \text{mm}^{-1}$	0.635	0.617
$F(000)$	1776.0	1808.0
Crystal size / $\text{mm}^{-3}$	0.248 × 0.15 × 0.136	0.242 × 0.149 × 0.148
Radiation	MoK $_{\alpha}$ ( $\lambda = 0.71073 \text{ \AA}$ )	MoK $_{\alpha}$ ( $\lambda = 0.71073 \text{ \AA}$ )
$2\theta$ range for data collection / $^\circ$	3.802 to 57.398	3.56 to 51.358
Index ranges	-15 ≤ h ≤ 15 -28 ≤ k ≤ 28 -23 ≤ l ≤ 23	-17 ≤ h ≤ 15 -11 ≤ k ≤ 11 -40 ≤ l ≤ 40
Reflections collected	293242	62172
Independent reflections	22313 [ $R_{\text{int}} = 0.0514$ , $R_{\text{sigma}} = 0.0237$ ]	8463 [ $R_{\text{int}} = 0.0621$ , $R_{\text{sigma}} = 0.0318$ ]
Data/restraints/parameters	22313/2/1040	8463/0/541
Goodness of fit on $F^2$	1.062	1.033
Final R indexes [ $I > 2\sigma(I)$ ]	$R_1 = 0.0330$ , $wR_2 = 0.0812$	$R_1 = 0.0533$ , $wR_2 = 0.1408$
Final R indexes [all data]	$R_1 = 0.0375$ , $wR_2 = 0.0837$	$R_1 = 0.0834$ , $wR_2 = 0.1709$
Largest diff. peak/hole / $e \text{ \AA}^{-3}$	0.43/-0.53	0.72/-0.35
Flack parameter <sup>[11]</sup>	0.149(11)	--
CCDC number	2059110	2059111

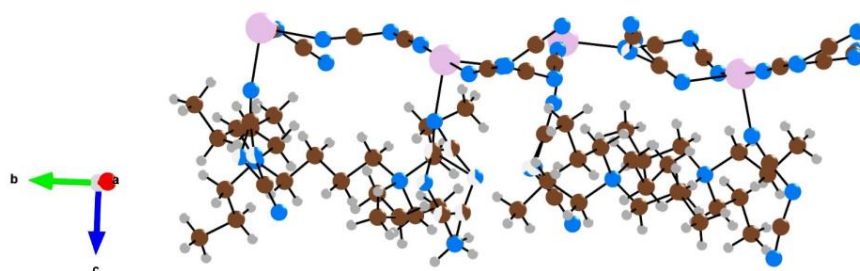


**Figure S-11:** Asymmetric unit of [TPC4TP]Mn<sub>2</sub>(C<sub>2</sub>N<sub>3</sub>)<sub>6</sub> shown as ball and stick model. The (C<sub>2</sub>N<sub>3</sub>)-ligands connect the Mn<sup>2+</sup> cations to form a three-dimensional coordination network with pseudocubic ReO<sub>3</sub>-type voids. Colour code: Mn – rosy, N – blue, C – brown, H – grey.

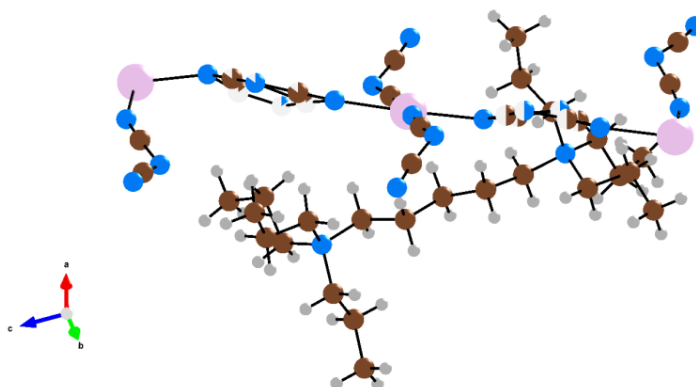


**Figure S-12:** Asymmetric unit of [TPC5TP]Mn<sub>2</sub>(C<sub>2</sub>N<sub>3</sub>)<sub>6</sub> shown as ball and stick model. The (C<sub>2</sub>N<sub>3</sub>)-ligands connect the Mn<sup>2+</sup> cations to form a three-dimensional coordination network with pseudocubic ReO<sub>3</sub>-type voids. Colour code: Mn – rosy, N – blue, C – brown, H – grey.

Interestingly, we find strong anisotropic thermal ellipsoids refined as positional disorder for the central atoms of the dicyanamide linker molecule perpendicular to the A-cations plane for both [TPC4TP]Mn<sub>2</sub>(C<sub>2</sub>N<sub>3</sub>)<sub>6</sub> and [TPC5TP]Mn<sub>2</sub>(C<sub>2</sub>N<sub>3</sub>)<sub>6</sub>, indicating translational atomic displacement and thus underpinning the synergistic interaction of the highly adaptive 3D host network to embed bulky divalent guest molecules.

Statement on alerts of the checkcif procedures for the single crystal X-Ray structures:

[TPC4TP]Mn<sub>2</sub>(C<sub>2</sub>N<sub>3</sub>)<sub>6</sub>: no alerts to take special care of (only alerts level G).

[TPC5TP]Mn<sub>2</sub>(C<sub>2</sub>N<sub>3</sub>)<sub>6</sub>:

ALERT level C

PLAT094\_ALERT\_2\_C Ratio of Maximum / Minimum Residual Density ....., 2.09 Report

PLAT241\_ALERT\_2\_C High 'MainMol' Ueq as Compared to Neighbors of N4 Check  
And 9 other PLAT241 Alerts

PLAT242\_ALERT\_2\_C Low 'MainMol' Ueq as Compared to Neighbors of Mn1 Check  
And 9 other PLAT242 Alerts

PLAT905\_ALERT\_3\_C Negative K value in the Analysis of Variance ... -1.312 Report

PLAT911\_ALERT\_3\_C Missing FCF Refl Between Thmin & STh/L= 0.600 2 Report

These alerts were carefully inspected and do not impair the absolute structure determination for [TPC5TP]Mn<sub>2</sub>(C<sub>2</sub>N<sub>3</sub>)<sub>6</sub>. It corresponds to a few missing reflections behind the beamstop at very low diffracting angles. High/low 'MainMol' Ueq alerts rely on the values of the anisotropic displacement parameters and can be assigned to the diffraction measurement at elevated temperatures which results in higher Ueq values especially for the lighter atoms.

Variable-temperature single crystal X-ray diffraction for [TPC4TP]Mn<sub>2</sub>(C<sub>2</sub>N<sub>3</sub>)<sub>6</sub>

Additionally, variable temperature single crystal X-Ray diffraction of [TPC4TP]Mn<sub>2</sub>(C<sub>2</sub>N<sub>3</sub>)<sub>6</sub> was performed at 100 K, 205 K and 310 K. For comparison reasons, the measurement at 100 K was repeated for consistency in the data collection strategy, same crystal fragment and exposure time. The measurement strategy was programmed for a monoclinic symmetry to optimize the total data collection time for each temperature point.

**Table S-3:** Variable temperature crystallographic data of [TPC4TP]Mn<sub>2</sub>(C<sub>2</sub>N<sub>3</sub>)<sub>6</sub>, collected at 100 K, 205 K and 310 K.

Compound	[TPC4TP]Mn <sub>2</sub> (C <sub>2</sub> N <sub>3</sub> ) <sub>6</sub>		
Empirical formula	C <sub>68</sub> H <sub>100</sub> Mn <sub>4</sub> N <sub>40</sub>		
Formula weight / gmol <sup>-1</sup>	1697.63		
Temperature / K	99.99	204.68	310.11
Crystal system	monoclinic	monoclinic	monoclinic
Space group	<i>Pc</i>	<i>Pc</i>	<i>Pc</i>
<i>a</i> / Å	11.7043(3)	11.8592(3)	11.966(2)
<i>b</i> / Å	21.3769(4)	21.4664(4)	21.703(4)
<i>c</i> / Å	17.2578(4)	17.2561(4)	17.223(4)
$\alpha$ / °	90	90	90
$\beta$ / °	92.1820(10)	93.2090(10)	94.208(7)
$\gamma$ / °	90	90	90
Volume / Å <sup>3</sup>	4314.80(17)	4386.07(17)	4460.6(15)
<i>Z</i>	2	2	2
$\rho_{\text{calc}}$ / gcm <sup>-3</sup>	1.307	1.285	1.264
$\mu$ / mm <sup>-1</sup>	0.635	0.625	0.615
<i>F</i> (000)	1776.0	1776.0	1776.0
Crystal size /mm <sup>-3</sup>	0.2 × 0.2 × 0.2	0.2 × 0.2 × 0.2	0.2 × 0.2 × 0.2
Radiation	MoK $\alpha$ ( $\lambda$ = 0.71073 Å)		
2 $\theta$ range for data collection / °	1.906 to 54.202	1.898 to 54.206	1.876 to 50.054
Index ranges	-15 ≤ <i>h</i> ≤ 15	-15 ≤ <i>h</i> ≤ 15	-14 ≤ <i>h</i> ≤ 14
	-27 ≤ <i>k</i> ≤ 27	-27 ≤ <i>k</i> ≤ 26	-25 ≤ <i>k</i> ≤ 25
	-22 ≤ <i>l</i> ≤ 22	-22 ≤ <i>l</i> ≤ 22	-14 ≤ <i>l</i> ≤ 20
Reflections collected	66762	68218	28450

<b>Independent reflections</b>	18375 [ $R_{\text{int}} = 0.0511$ $R_{\text{sigma}} = 0.0483$ ]	19093 [ $R_{\text{int}} = 0.0596$ $R_{\text{sigma}} = 0.0554$ ]	13174 [ $R_{\text{int}} = 0.0600$ $R_{\text{sigma}} = 0.0746$ ]
<b>Data/restraints/parameters</b>	18375/2/1040	19093/2/1028	13174/2/956
<b>Goodness of fit on <math>F^2</math></b>	1.032	1.067	1.018
<b>Final R indexes [<math>I &gt; 2\sigma(I)</math>]</b>	$R_1 = 0.0349$ , $wR_2 = 0.0748$	$R_1 = 0.0463$ , $wR_2 = 0.1044$	$R_1 = 0.0648$ , $wR_2 = 0.1610$
<b>Final R indexes [all data]</b>	$R_1 = 0.0456$ , $wR_2 = 0.0827$	$R_1 = 0.0789$ , $wR_2 = 0.1284$	$R_1 = 0.1128$ , $wR_2 = 0.2008$
<b>Largest diff. peak/hole / e <math>\text{\AA}^{-3}</math></b>	0.51/-0.46	0.44/-0.37	0.42/-0.31
<b>Flack parameter<sup>[11]</sup></b>	0.001(7)	-0.018(10)	0.06(2)
<b>CCDC number</b>	2149988	2149989	2149990

Statement on alerts of the checkcif procedures for the VT experiments:

**100 K:**

ALERT level C

PLAT911\_ALERT\_3\_C *Missing FCF Refl Between Thmin & STh/L= 0.600; 10 Report*

PLAT913\_ALERT\_3\_C *Missing # of Very Strong Reflections in FCF ....; 7 Note*

**205 K:**

ALERT level C

PLAT241\_ALERT\_2\_C *High 'MainMol' Ueq as Compared to Neighbors of N9; Check*

PLAT242\_ALERT\_2\_C *Low 'MainMol' Ueq as Compared to Neighbors of Mn1; Check*

PLAT341\_ALERT\_3\_C *Low Bond Precision on C-C Bonds; 0.00957 Ang.*

PLAT905\_ALERT\_3\_C *Negative K value in the Analysis of Variance -0.071; Report*

PLAT911\_ALERT\_3\_C *Missing FCF Refl Between Thmin & STh/L= 0.600; 11 Report*

PLAT913\_ALERT\_3\_C *Missing # of Very Strong Reflections in FCF ....; 9 Note*

**310 K:**

ALERT level B

PLAT341\_ALERT\_3\_B *Low Bond Precision on C-C Bonds; 0.0193 Ang.*

ALERT level C

PLAT241\_ALERT\_2\_C *High 'MainMol' Ueq as Compared to Neighbors of N6; Check*

PLAT242\_ALERT\_2\_C *Low 'MainMol' Ueq as Compared to Neighbors of Mn1; Check*

PLAT360\_ALERT\_2\_C *Short C(sp3)-C(sp3) Bond C18 - C19; 1.39 Ang.*

PLAT361\_ALERT\_2\_C *Long C(sp3)-C(sp3) Bond C17 - C18; 1.65 Ang.*

PLAT911\_ALERT\_3\_C *Missing FCF Refl Between Thmin & STh/L= 0.600; 11 Report*

PLAT913\_ALERT\_3\_C *Missing # of Very Strong Reflections in FCF ....; 9 Note*

*PLAT918\_ALERT\_3\_C Reflection(s) with I(obs) much Smaller I(calc); 1 Check*

These alerts are due to some missing reflections masked behind the beamstop and the data collection strategy being monoclinic P for a non-centrosymmetric monoclinic symmetry which results in less data redundancy and reduced mean I/s. High/low 'MainMol' Ueq and sporadic low bond precision are caused by measurements at elevated temperatures which naturally results in higher values for atomic displacement parameters. All this is reasonable for rather short temperature-dependent measurements and does not change the general statement about the unit cell and the relative position of the atoms to each other, so the quality of the obtained results is more than sufficient for the required pattern analysis.

From the crystal structures at different temperatures, the uniaxial negative thermal expansion behavior of [TPC4TP]Mn<sub>2</sub>(C<sub>2</sub>N<sub>3</sub>)<sub>6</sub> can be followed. As shown in table S-4, the Mn-Mn distance along [304] decreases with increasing temperature, compensated by an increase of the Mn-Mn distance along [010] and  $\bar{3}01$ . Mechanistically, a hinging mechanism of the A-site cations results in uniaxial NTE (and NLC), resulting in a decreasing dihedral angle of the respective N-atoms of the two corresponding molecules.

**Table S-4:** Temperature-dependent Mn-Mn distances for  $[\text{TPC4TP}]\text{Mn}_2(\text{C}_2\text{N}_3)_6$  in  $[304] \equiv X_1$  (NTE)-,  $[010] \equiv X_2$  (PTE)- and  $[\bar{3}01] \equiv X_3$  (PTE)-direction at 100 K, 205 K and 310 K, respectively (in Å). Additionally, the dihedral angle of a  $\text{A}^{2+}$ -hinge for each of the temperature is listed (in °).

	100 K	205 K	310 K
Mn-Mn ( $X_1$ )	28.5488(6)	28.5397(6)	28.441(5)
$\Phi(\text{N1-N2-N2-N1})$	81.71(7)	82.31(11)	83.8(3)
Mn-Mn ( $X_2$ )	21.3769(5)	21.4664(5)	21.703(5)
Mn-Mn ( $X_3$ )	11.7043(3)	11.8592(3)	11.966(3)

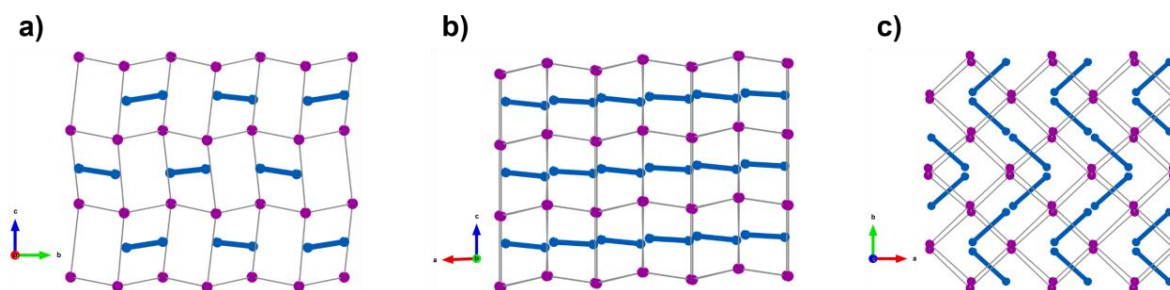


**Figure S-13:** View along the crystallographic a-, b- and c-axes for the crystal structure of  $[\text{TPC4TP}]\text{Mn}_2(\text{C}_2\text{N}_3)_6$ . Along the b-axis (b) it is evident that A-site cations are located within the ab-plane, stacking along the c-axis, thus a 2D arrangement is present within the 3D host network. Along the c-axis in (c), it is shown that the A-site cations form a herringbone-type zigzag order pattern with two A-site cation hinging. Colour code: Mn atoms – rosy, N atoms – blue. Blue sticks depict schematically a divalent molecule, whereas grey lines indicate the perovskite-type 3D connectivity and are only a guidance to the eye, as dicyanamide linkers are omitted for simplicity.

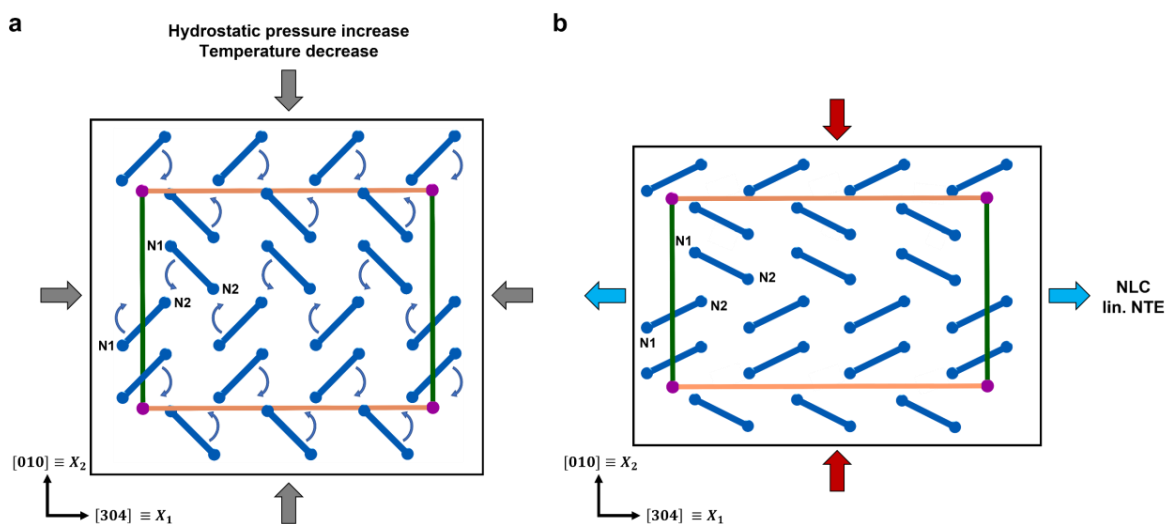


**Figure S-14:** 2D herringbone-type order pattern facilitates uniaxial NTE and NLC behavior. The direction of propagation for these effects lies along the backbone ( $[304]$ ) of the herring as shown in (a). In (b), simultaneous motion of the herring bone in  $[\text{TPC4TP}]\text{Mn}_2(\text{C}_2\text{N}_3)_6$  leads to an elongation along  $X_1$ . Shown are the Mn-Mn distances along the NLC & lin. NTE direction ( $X_1$ ) in orange and corresponding PLC and PTE direction ( $X_2$ ) in green, resulting in an anisotropic structural response.

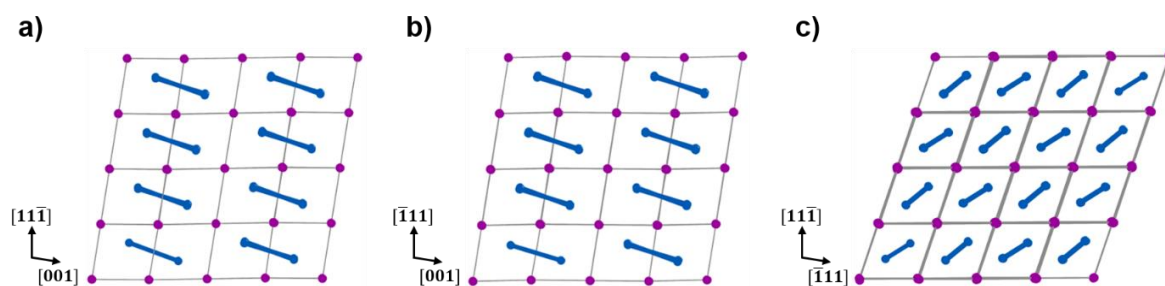


**Figure S-15:** View along the three pseudocubic axes of the ReO<sub>3</sub>-type host network for the crystal structure of [TPC5TP]Mn<sub>2</sub>(C<sub>2</sub>N<sub>3</sub>)<sub>6</sub>. In (a) and (b) it is evident that A-site cations are located within two adjacent pseudocubic voids to be linked within a 2D plane and form a head-to-tail arrangement, stacking along the third direction, thus a 2D arrangement is present within the 3D host network. In c), it is shown that along the direction of bridged A-site cations within the two connected pseudocubes, no chemical bonds are present in the two other directions, which confirms the head-to-tail order pattern of the A-site cations in two dimensions stacking lamellae-like. Colour code: Mn atoms – rosy, N atoms – blue. Blue sticks depict schematically a divalent molecule, whereas grey lines indicate the perovskite-type 3D connectivity and are only a guidance to the eye, as dicyanamide linkers are omitted for simplicity.

Discussion of structural model for [TPC5TP]Mn<sub>2</sub>(C<sub>2</sub>N<sub>3</sub>)<sub>6</sub>

For [TPC5TP]Mn<sub>2</sub>(C<sub>2</sub>N<sub>3</sub>)<sub>6</sub>, ordinary data processing of single crystal X-Ray diffraction with harvesting spots with a minimum ratio of  $I/\sigma I = 10$  for unit cell determination leads to an indexed cell with  $c$  being half of the unit cell axis reported in Table S-2. Data reduction based on this found cell and subsequent structure solution yields a structure model with distinct disorder-like electron density clearly visible for the atoms of the molecular guest cation. From a chemical point of view, this disorder is counterintuitive and leaves crystallographers sceptical to investigate this phenomenon in more detail as it might hint for a complex twinning issue. Indeed, an analysis of the raw data using the program *CELL\_NOW* as implemented in the APEX3 software package<sup>[5]</sup> yields two detwinned sets of diffraction peaks with distinct domains allocatable, for which the following orientation matrix could be determined with the initial cell found to be  $a = 14.191$ ,  $b = 9.545$ ,  $c = 17.161$ ,  $\alpha = 90.35$ ,  $\beta = 107.95$  and  $\gamma = 89.15$ :

$$\text{Orientation matrix: } \begin{pmatrix} 0.02766822 & -0.02790610 & 0.05882717 \\ -0.01545002 & 0.09578081 & 0.01707149 \\ -0.06695888 & -0.03204518 & -0.00051820 \end{pmatrix}$$

Rotating the second domain by 179.8°, which would give rise to a pseudo-merohedral twinning phenomenon, about the

$$\text{reciprocal axis } \begin{pmatrix} -0.014 \\ 0.002 \\ 1.000 \end{pmatrix} \text{ and the real axis } \begin{pmatrix} 0.354 \\ 0.009 \\ 1.000 \end{pmatrix}$$

generates a possible twin law to convert the  $hkl$  from the second domain to the first domain:

$$\text{Transformation matrix: } \begin{pmatrix} -1.011 & 0.004 & -0.030 \\ 0.001 & -1.000 & 0.008 \\ 0.709 & 0.028 & 1.011 \end{pmatrix}.$$

However, neither data reduction based on the two detwinned domains nor refinement of twinned data using the identified twin law results in an appropriate structural model.

Furthermore, variation of the detector distance from a small to very large distance or changing of the X-ray wavelength from a Mo-source to a Cu-source did not improve the quality of the recorded data, see Fig. S-14 and S-15 for visualization of diffraction data.



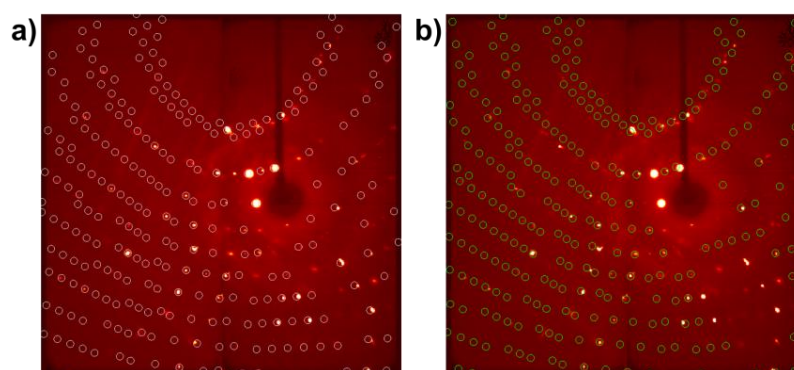


**Figure S-16:** a) and b) shows the overlay of expected reflections for the two found twin domains, respectively, with a clear distinction between the two patterns with overlapping and non-overlapping reflections.

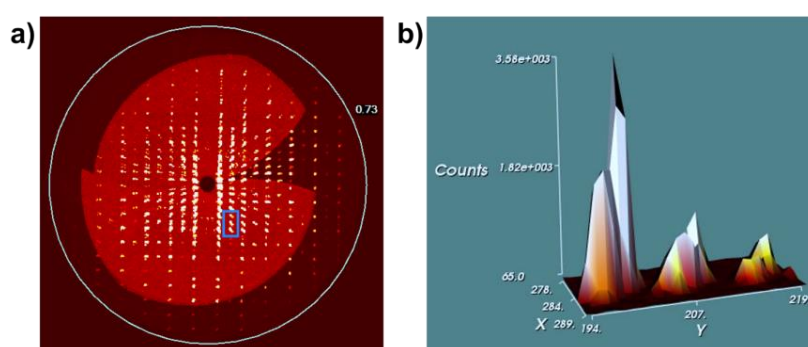


**Figure S-17:** a) shows the precession image of the  $1kl$  plane with the presence of at least two interpenetrating reflection patterns clearly visible. In b), a 3D peak profile view is shown, showcasing a twin domain arising additionally to the main crystal domain.

As we are confident that any disorder refined when treating the data as a non-twinned domain originates from a twinning or related phenomenon rather than from actual positional disorder, we decided to search for a different cell, inspired by *Richard E. Marsh* about the critical assessment of choosing correct space groups in crystal structure determination.<sup>[12]</sup>

When considering also very weak reflections in initial spot harvesting, a unit cell with a  $c$ -axis of  $\sim 33 \text{ \AA}$  is found. Data processing and structure solution based on this unit cell leads to a structure model with doubled volume cell as compared to the one when only considering strong reflections for unit cell determination. Structure refinement then yields an absolute crystal structure model for  $[\text{TPC5TP}]\text{Mn}_2(\text{C}_2\text{N}_3)_6$  as reported in Table S-2 with no residual electron density of positional disorder nor evidence for twinning present.

## Distortion mode analysis

For the analysis of the distortion modes present in the crystal structures of [TPC4TP]Mn<sub>2</sub>(C<sub>2</sub>N<sub>3</sub>)<sub>6</sub> and [TPC5TP]Mn<sub>2</sub>(C<sub>2</sub>N<sub>3</sub>)<sub>6</sub>, the software tool ISODISTORT<sup>[13]</sup> was used. To prepare the crystallographic information file, the atoms of the A-site cation were removed to generate a structure file consisting only of the atoms of the manganese-dicyanamide framework. During the analysis, the structure is decomposed relative to a hypothetical parent perovskite aristotype in cubic  $Pm\bar{3}m$  symmetry with a potential A-site cation located at the origin (0,0,0). As for the decomposition of a structure with bent linkers like dicyanamide into symmetry modes of a parent structure only the displacive distortions of the N atoms coordinating to the metal center are considered, it is sufficient to generate the cubic aristotype from two atom sites with a cell length approximately matching the octahedra distance in the target structure, thus assuming a linear linker geometry. As there are in total 9 distortion modes possible for molecular perovskites,<sup>[14]</sup> the decomposed distortion modes after analysis are assigned to the respective group of irreducible representations for conventional and unconventional tilting as well as for columnar shifts.

Structure of the parent phase input .cif-file:

```
_cell_length_a 8.0
_cell_length_b 8.0
_cell_length_c 8.0
_cell_angle_alpha 90
_cell_angle_beta 90
_cell_angle_gamma 90
_space_group_name 'P m -3 m'
_space_group_IT_number 221

Mn1  1.0  0.500000  0.500000  0.500000  Biso 1.00 Mn
N1   1.0  0.250000  0.500000  0.500000  Biso 1.00 N
```

[TPC4TP]Mn<sub>2</sub>(C<sub>2</sub>N<sub>3</sub>)<sub>6</sub>

Distorted structure: Space group: 7 *Pc* Cs-2, Lattice parameters:  $a = 11.69950$ ,  $b = 21.42270$ ,  $c = 17.24480$ ,  $\alpha = 90.00000$ ,  $\beta = 92.26400$ ,  $\gamma = 90.00000$ .

Subgroup: 7 *Pc*, basis =  $\left\{ \begin{pmatrix} 1 \\ -1 \\ 0 \end{pmatrix}, \begin{pmatrix} 2 \\ 2 \\ 0 \end{pmatrix}, \begin{pmatrix} 0 \\ 0 \\ 2 \end{pmatrix} \right\}$ , origin = (-0.09863, 0.09863, -0.99665),  $s = 8$ ,

$i = 192$ .

Active  $k$ -vectors:  $(0, 0, 0)$ ,  $(\frac{1}{4}, \frac{1}{4}, 0)$ ,  $(\frac{1}{2}, \frac{1}{2}, \frac{1}{2})$ ,  $(0, 0, \frac{1}{2})$ ,  $(\frac{1}{2}, \frac{1}{2}, 0)$ ,  $(\frac{1}{4}, \frac{1}{4}, \frac{1}{2})$ .

All possible active distortion modes:

$\Gamma_1^+, \Gamma_3^+, \Gamma_4^+, \Gamma_5^+, \Gamma_4^-, \Gamma_5^-, R_4^+, R_5^+, R_3^-, R_4^-, R_5^-, X_2^+, X_5^+, X_1^-, X_4^-, X_5^-, M_1^+, M_4^+, M_5^+, M_2^-, M_5^-$   
SM1, SM2, SM3, SM4, S1, S2, S3, S4.

Conventional tilting:  $R_5^-$ .

Unconventional tilting:  $\Gamma_4^+, X_5^-, M_5^+, X_1^-$ .

Columnar shift:  $\Gamma_5^+, X_5^+, M_2^-$ .

[TPC5TP]Mn<sub>2</sub>(C<sub>2</sub>N<sub>3</sub>)<sub>6</sub> (Note: the cell length of the arisotype was set to  $a = 8.5$ )

Distorted structure: Space group: 14  $P2_1/c$  C2h-5, Lattice parameters:  $a = 14.12870$ ,  
 $b = 9.66320$ ,  $c = 32.95040$ ,  $\alpha = 90.00000$ ,  $\beta = 98.03100$ ,  $\gamma = 90.00000$ .

Subgroup: 14  $P2_1/c$ , basis =  $\left\{ \begin{pmatrix} 2 \\ 0 \\ 0 \end{pmatrix}, \begin{pmatrix} 0 \\ 1 \\ 1 \end{pmatrix}, \begin{pmatrix} 0 \\ -1 \\ 1 \end{pmatrix} \right\}$ , origin =  $\left( \frac{1}{2}, \frac{1}{2}, \frac{1}{2} \right)$ ,  $s = 4$ ,  $i = 48$ .

Active  $k$ -vectors:  $(0, 0, 0)$ ,  $\left( \frac{1}{2}, \frac{1}{2}, \frac{1}{2} \right)$ ,  $\left( \frac{1}{2}, 0, 0 \right)$ ,  $\left( 0, \frac{1}{2}, \frac{1}{2} \right)$ .

All possible active distortion modes:  $\Gamma_1^+, \Gamma_3^+, \Gamma_4^+, \Gamma_5^+, R_3^-, R_4^-, R_5^-, X_2^-, X_3^-, X_5^-, M_2^+, M_3^+, M_5^+$ .

Conventional tilting:  $R_5^-, M_2^+$ .

Unconventional tilting:  $\Gamma_4^+, X_5^-, M_5^+$ .

Columnar shift:  $\Gamma_5^+$ .

Primary order parameters:  $R_5^-, M_5^+$ .

So for [TPC4TP]Mn<sub>2</sub>(C<sub>2</sub>N<sub>3</sub>)<sub>6</sub> the crystallographic description leads to two independent A-site cations resulting in A<sub>2</sub>B<sub>4</sub>X<sub>12</sub> as asymmetric unit, whereas in the case of  $n = 5$ , a two-one screw axis symmetry operation induces an inversion center, reducing the crystallographic description to one independent A-site cation. This indicates a more complex structural description for [TPC4TP]Mn<sub>2</sub>(C<sub>2</sub>N<sub>3</sub>)<sub>6</sub> as captured by the resulting active distortion modes, for which all possible unconventional tilting and columnar shift modes are possible, whereas [TPC5TP]Mn<sub>2</sub>(C<sub>2</sub>N<sub>3</sub>)<sub>6</sub> shows only one columnar shift and three unconventional tilting modes but more distinct conventional tilting.

## Powder X-Ray diffraction data

All obtained Powder X-Ray diffraction patterns were analysed by performing a Pawley profile fit analysis or a Rietveld refinement using TOPAS Academic v6 in combination with jEdit for creating the input files.<sup>[15]</sup> Standard deviations of all parameters were calculated, and by using “randomize\_on\_errors”, it was ensured that the minimum of the refinement was reached.

### Lab-source PXRD data of bulk sample

Powder X-ray diffraction measurements were performed using Bragg-Brentano geometry in a PANalytical Empyrean diffractometer equipped with a PANalytical PIXcel 1D detector. X-ray Cu K $\alpha$  radiation ( $\lambda_1 = 1.5406 \text{ \AA}$ ,  $\lambda_2 = 1.5444 \text{ \AA}$ ,  $I_2/I_1 = 0.5$ ) was used for the measurements. K $\beta$  radiation was removed with a Ni-filter. Voltage and intensity were 45 kV and 40 mA, respectively. The measurement range was from 5.0° to 50.0° ( $2\theta$ ) with a step size of 0.031° ( $2\theta$ ) and 30 minutes acquisition time in total.

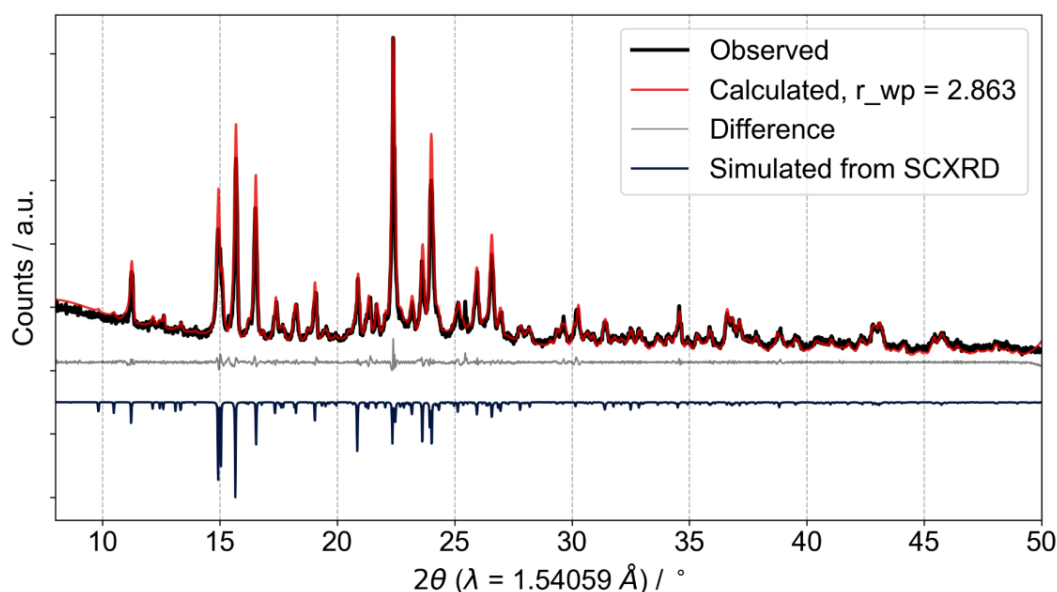


**Figure S-18:** Result of the Pawley profile fit refinement of [TPC4TP]Mn<sub>2</sub>(C<sub>2</sub>N<sub>3</sub>)<sub>6</sub> based on an in-house ( $\lambda = 1.540596 \text{ \AA}$ ) copper source device at room temperature. Observed data is shown in black, whereas the outcome of profile fit analysis is depicted in red. The grey line indicates the difference of experimental and calculated data with figure of merits  $r_{wp} = 2.863$ ,  $r_{exp} = 1.246$  and  $GOF = 2.298$ , confirming phase purity of the bulk material.

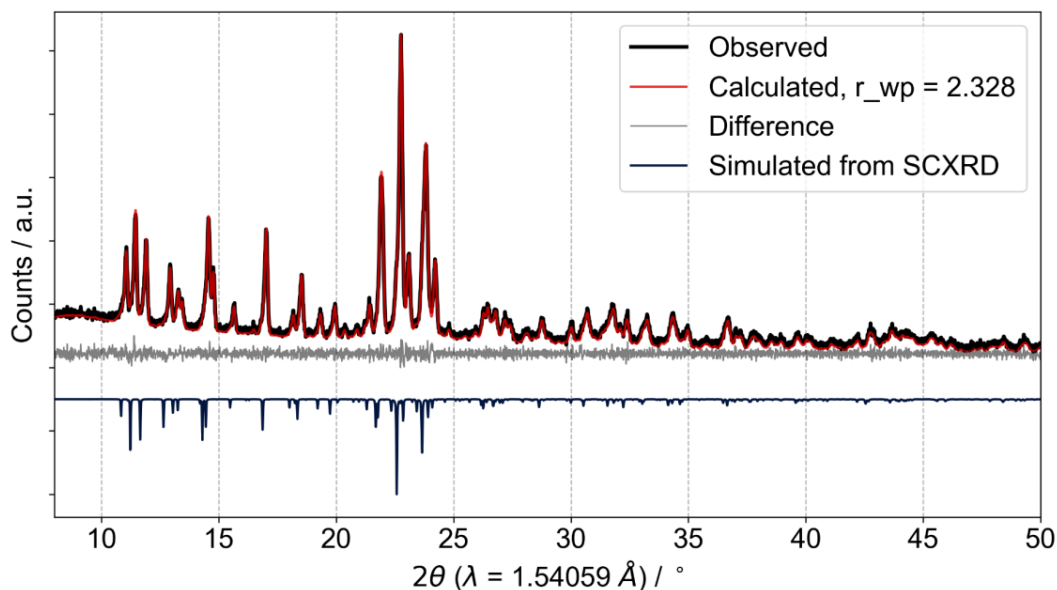


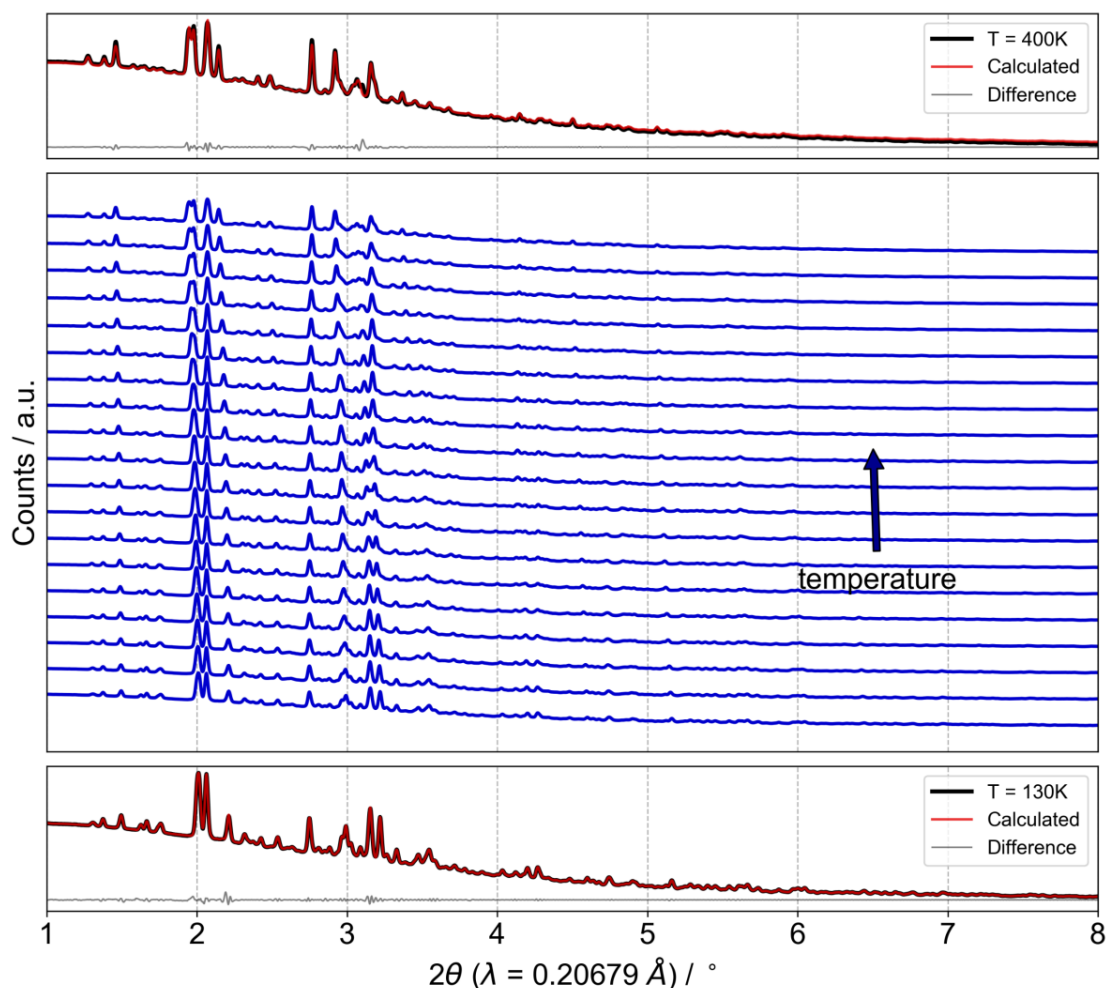
**Figure S-19:** Result of the Pawley profile fit refinement of  $[\text{TPC5TP}]\text{Mn}_2(\text{C}_2\text{N}_3)_6$  based on an in-house ( $\lambda = 1.540596 \text{ \AA}$ ) copper source device at room temperature. Observed data is shown in black, whereas the outcome of profile fit analysis is depicted in darkgreen. The grey line indicates the difference of experimental and calculated data with figure of merits  $r_{\text{wp}} = 2.328$ ,  $r_{\text{exp}} = 1.952$  and  $\text{GOF} = 1.193$ , confirming phase purity of the bulk material.

**Table S-5:** Cell parameters and deviations of the coordination networks  $[\text{TPC4TP}]\text{Mn}_2(\text{C}_2\text{N}_3)_6$  and  $[\text{TPC5TP}]\text{Mn}_2(\text{C}_2\text{N}_3)_6$ , extracted from the lab-source PXRD data.

$[\text{A}][\text{Mn}_2(\text{C}_2\text{N}_3)_6]$	$\text{A} = \text{TPC4TP}^{2+}$	$\text{A} = \text{TPC5TP}^{2+}$
$a / \text{\AA}$	11.908(2)	14.120(2)
$b / \text{\AA}$	21.692(2)	9.703(1)
$c / \text{\AA}$	17.206(3)	33.120(5)
$\beta / ^\circ$	94.17(2)	98.60(1)
$V / \text{\AA}^3$	4433(1)	4486(1)
Space group	$Pc$	$P2_1/c$
$r_{\text{wp}}$	2.863	2.328
$r_{\text{exp}}$	1.246	1.952
GOF	2.298	1.192

## High-resolution powder XRD data at variable temperatures

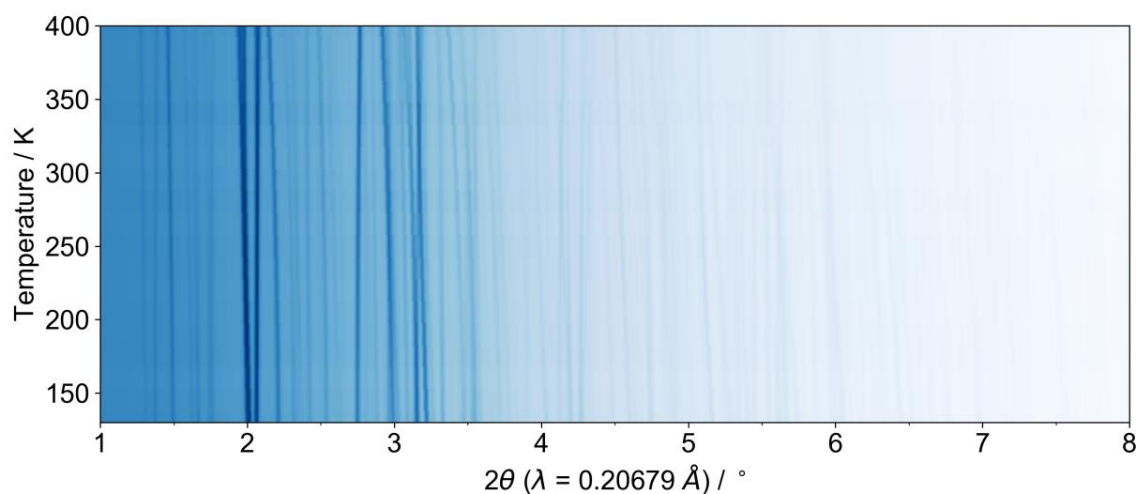
Temperature dependent high-resolution synchrotron radiation diffraction data were collected at the P02.1 beamline at the DESY:PETRAIII Light-source, Hamburg, Germany (experiment number I-20191507). The beamline operates with a fixed energy of 60 keV ( $\lambda = 0.20679 \text{ \AA}$ ) with data collected in the temperature range of 130 K to 400 K in steps of 15 K, equipped with a Perkin Elmer 1621EN detector with a collecting step size of 0.0029118 in  $2\theta$ . For temperature control the Habcryo-X Cryostream from Oxford Cryosystems Ltd. was used to ensure a stable temperature at the sample. Data were collected with 100 seconds of acquisition time per temperature step.



**Figure S-20:** Variable temperature powder XRD patterns of  $[\text{TPC4TP}]\text{Mn}_2(\text{C}_2\text{N}_3)_6$ . Shown in blue is a stack plot of the pattern at each temperature point, ranging from 130 K to 400 K with step size of 15 K each, upwards from low to high temperatures. Depicted at the bottom is the Pawley profile fit analysis of the pattern at 130 K, serving as the starting point for sequenced analysis of the temperature points, respectively. Shown there are the observed, calculated and differenced data with figure of merits  $r_{\text{wp}} = 0.349$ ,  $r_{\text{exp}} = 1.023$  and cell parameters  $a = 11.76894$ ,  $b = 21.44131$ ,  $c = 17.26491$ ,  $\beta = 92.64507^\circ$ , space-group  $Pc$ .

**Table S-6:** Refined cell parameters and deviations of [TPC4TP]Mn<sub>2</sub>(C<sub>2</sub>N<sub>3</sub>)<sub>6</sub> at variable temperatures, using the Pawley profile fit analysis method.

<i>T</i> / K	<i>r</i> <sub>wp</sub>	<i>a</i> / Å	<i>b</i> / Å	<i>c</i> / Å	<i>β</i> / °	<i>V</i> / Å <sup>3</sup>
130	0.34856	11.7689(8)	21.4413(9)	17.2649(8)	92.645(7)	4352.0(4)
145	0.35623	11.7876(8)	21.4502(10)	17.2676(9)	92.758(7)	4361.0(4)
160	0.36821	11.8050(8)	21.4650(10)	17.2685(12)	92.869(8)	4370.3(5)
175	0.36272	11.8243(8)	21.4805(10)	17.2691(16)	93.001(9)	4380.2(5)
190	0.35779	11.8452(7)	21.5006(9)	17.2694(20)	93.135(11)	4391.5(6)
205	0.34862	11.8642(8)	21.5251(8)	17.2670(23)	93.269(11)	4402.4(7)
220	0.34209	11.8831(7)	21.5509(7)	17.2586(26)	93.429(11)	4411.8(7)
235	0.31236	11.9009(7)	21.5794(7)	17.2573(23)	93.574(12)	4423.3(7)
250	0.31925	11.9159(7)	21.6108(6)	17.2552(17)	93.711(10)	4434.1(5)
265	0.27967	11.9331(4)	21.6439(5)	17.2514(7)	93.889(5)	4445.4(3)
280	0.26408	11.9470(4)	21.6801(5)	17.2482(6)	94.028(5)	4456.5(2)
295	0.23847	11.9601(4)	21.7201(4)	17.2438(5)	94.167(4)	4467.7(2)
310	0.26285	11.9736(4)	21.7628(5)	17.2395(11)	94.328(7)	4479.5(3)
325	0.30358	11.9847(5)	21.8091(6)	17.2312(8)	94.479(5)	4490.0(3)
340	0.54218	11.9986(10)	21.8646(11)	17.2273(12)	94.658(7)	4504.2(6)
355	0.82695	12.0124(21)	21.9247(22)	17.2151(23)	94.870(12)	4518.8(10)
370	1.07216	12.0212(40)	21.9876(45)	17.2151(23)	95.039(15)	4532.7(19)
385	1.03226	12.0261(54)	22.0292(48)	17.2082(29)	95.149(13)	4540.5(24)
400	1.18792	12.0296(60)	22.0888(66)	17.2112(41)	95.227(14)	4554.3(29)

**Figure S-21:** Shown is the contour plot of experimental data of [TPC4TP]Mn<sub>2</sub>(C<sub>2</sub>N<sub>3</sub>)<sub>6</sub> at variable temperatures with a darker colour corresponding to a higher intensity in the bragg peaks, respectively.

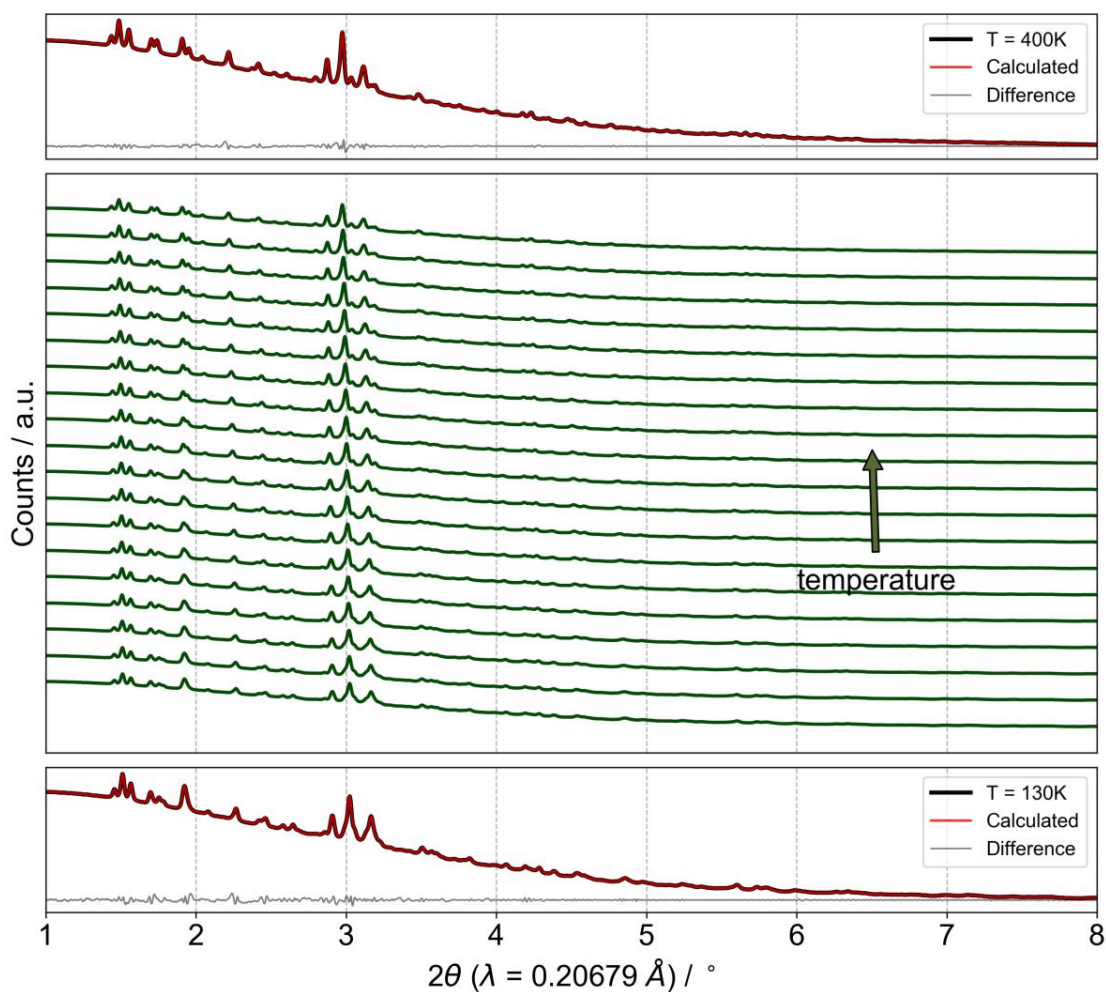
**Table S-7:** Output of PASCAL - principal axis strain calculations with direction of projections of  $X$  on the unit cell axes  $a$ ,  $b$  and  $c$  for  $[\text{TPC4TP}]\text{Mn}_2(\text{C}_2\text{N}_3)_6$  at variable temperatures. Listed are the resulting principal axes  $X_n$  with thermal expansion coefficients  $\alpha$  and the changes of length for  $X_1$ ,  $X_2$ ,  $X_3$  and  $V$ , respectively.

Axes	$\alpha$ / MK-1	$\sigma\alpha$ / MK-1	$a$	$b$	$c$
$X_1$	-71.6349	2.6511	-0.6219	0.0000	-0.7831
$X_2$	113.0519	6.5100	0.0000	1.0000	-0.0000
$X_3$	130.4539	2.4771	-0.9451	0.0000	0.3269
$V$	173.8351	2.2412			

$T$ / K	$X_1$ / %	$X_2$ / %	$X_3$ / %	$V$ / $\text{\AA}^3$	$V_{\text{in}}$ / $\text{\AA}^3$
130	0.0000	0.0000	0.0000	4352.0115	4346.0981
145	-0.0399	0.0416	0.2046	4360.9927	4357.4461
160	-0.0886	0.1106	0.3971	4370.2702	4368.7941
175	-0.1514	0.1828	0.6154	4380.2007	4380.1421
190	-0.2152	0.2767	0.8451	4391.5462	4391.4900
205	-0.2949	0.3906	1.0597	4402.4328	4402.8380
220	-0.4227	0.5110	1.2824	4411.8402	4414.1860
235	-0.5088	0.6442	1.4973	4423.3222	4425.5340
250	-0.5977	0.7904	1.6859	4434.1171	4436.8820
265	-0.7239	0.9448	1.9149	4445.4060	4448.2300
280	-0.8221	1.1138	2.0958	4456.4764	4459.5780
295	-0.9283	1.3003	2.2696	4467.6542	4470.9259
310	-1.0515	1.4992	2.4619	4479.4572	4482.2739
325	-1.1903	1.7151	2.6254	4490.0385	4493.6219
340	-1.3286	1.9743	2.8257	4504.2041	4504.9699
355	-1.5068	2.2544	3.0556	4518.8383	4516.3179
370	-1.6507	2.5480	3.2201	4532.6997	4527.6659
385	-1.7633	2.7420	3.3166	4540.5238	4539.0139
400	-1.8106	3.0198	3.3979	4554.3376	4550.3618

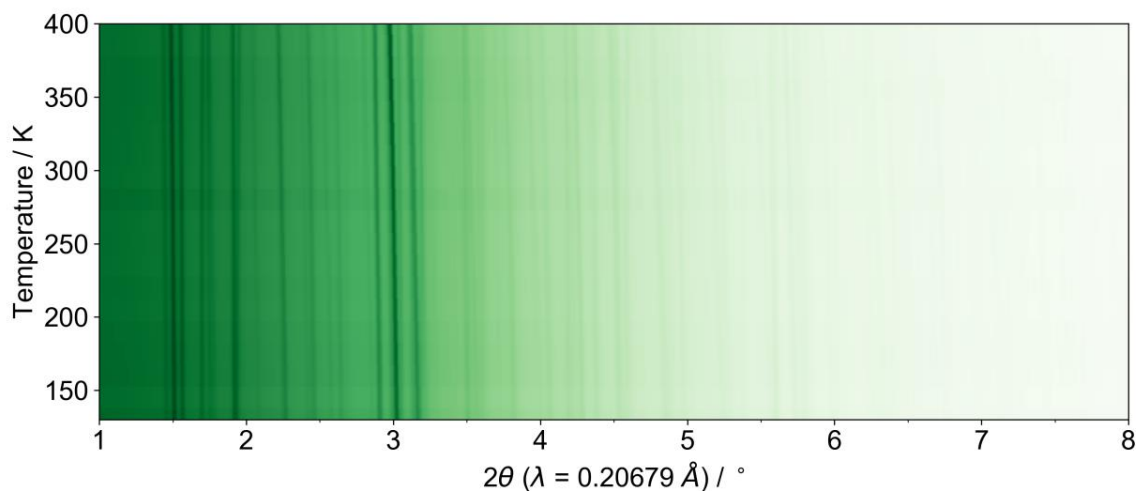




**Figure S-22:** Variable temperature powder XRD patterns of  $[\text{TPC5TP}]\text{Mn}_2(\text{C}_2\text{N}_3)_6$ . Shown in darkgreen is a stack plot of the pattern at each temperature point, ranging from 130 K to 400 K with step size of 15 K each, upwards from low to high temperatures. Depicted at the bottom is the Pawley profile fit analysis of the pattern at 130 K, serving as the starting point for sequenced analysis of the temperature points, respectively. Shown there are the observed, calculated and differenced data with figure of merits  $r_{\text{wp}} = 0.165$ ,  $r_{\text{exp}} = 1.316$  and cell parameters  $a = 14.06566$ ,  $b = 9.60864$ ,  $c = 32.77211$ ,  $\beta = 97.83929^\circ$ , space-group  $P2_1/c$ .

**Table S-8:** Refined cell parameters and deviations of [TPC5TP]Mn<sub>2</sub>(C<sub>2</sub>N<sub>3</sub>)<sub>6</sub> at variable temperatures, using the Pawley profile fit analysis method.

T / K	r_wp	a / Å	b / Å	c / Å	β / °	V / Å <sup>3</sup>
130	0.16497	14.0657(11)	9.6086(7)	32.7721(36)	97.839(11)	4387.82(68)
145	0.16237	14.0682(11)	9.6174(6)	32.7909(32)	97.885(9)	4394.64(62)
160	0.14175	14.0690(9)	9.6262(6)	32.8164(29)	97.940(7)	4401.72(56)
175	0.15721	14.0724(10)	9.6345(6)	32.8390(30)	97.982(8)	4409.19(57)
190	0.15332	14.0754(11)	9.6425(7)	32.8695(31)	98.035(8)	4417.32(62)
205	0.15681	14.0778(10)	9.6507(6)	32.9046(30)	98.104(7)	4425.79(58)
220	0.15384	14.0822(10)	9.6568(6)	32.9387(31)	98.196(7)	4433.57(59)
235	0.16816	14.0870(10)	9.6650(7)	32.9722(32)	98.292(8)	4442.27(62)
250	0.17379	14.0893(11)	9.6735(7)	33.0050(34)	98.387(9)	4450.23(66)
265	0.17322	14.0909(10)	9.6816(7)	33.0374(34)	98.478(10)	4457.80(67)
280	0.15194	14.0925(10)	9.6916(7)	33.0770(30)	98.565(9)	4467.25(60)
295	0.15938	14.0958(9)	9.7013(7)	33.1128(31)	98.625(8)	4476.85(59)
310	0.16806	14.0950(10)	9.7128(8)	33.1452(32)	98.728(8)	4485.09(66)
325	0.1616	14.0963(10)	9.7255(7)	33.1752(32)	98.787(8)	4494.73(63)
340	0.17108	14.0972(13)	9.7386(8)	33.2089(33)	98.884(8)	4504.43(72)
355	0.19252	14.1005(14)	9.7528(10)	33.2258(35)	98.942(8)	4513.65(80)
370	0.1402	14.0957(12)	9.7653(7)	33.3055(27)	99.123(6)	4526.47(63)
385	0.16866	14.0983(16)	9.7780(9)	33.3358(31)	99.220(7)	4536.08(78)
400	0.17834	14.1010(22)	9.7926(11)	33.3783(35)	99.348(8)	4547.9(10)

**Figure S-23:** Shown is the contour plot of experimental data of [TPC5TP]Mn<sub>2</sub>(C<sub>2</sub>N<sub>3</sub>)<sub>6</sub> at variable temperatures with a darker colour corresponding to a higher intensity in the Bragg peaks, respectively.

**Table S-9:** Output of PASCAL - principal axis strain calculations with direction of projections of  $X$  on the unit cell axes  $a$ ,  $b$  and  $c$  for  $[\text{TPC5TP}]\text{Mn}_2(\text{C}_2\text{N}_3)_6$  at variable temperatures. Listed are the resulting principal axes  $X_n$  with thermal expansion coefficients  $\alpha$  and the changes of length for  $X_1$ ,  $X_2$ ,  $X_3$  and  $V$ , respectively.

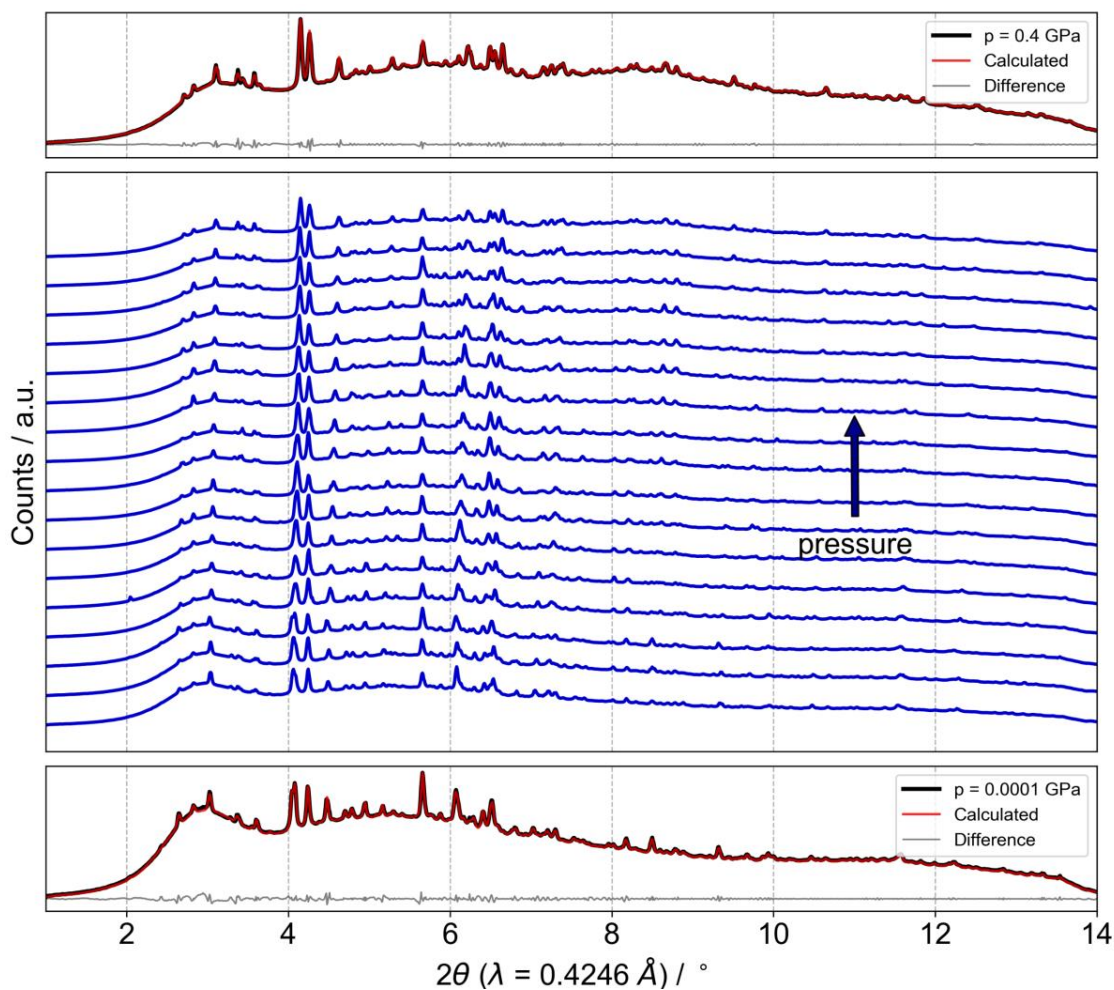
Axes	$\alpha$ / MK-1	$\sigma\alpha$ / MK-1	$a$	$b$	$c$
$X_1$	-26.0064	1.8093	0.9652	-0.0000	0.2614
$X_2$	69.2198	2.1085	0.0000	-1.0000	0.0000
$X_3$	89.6281	2.2472	-0.7836	0.0000	0.6213
$V$	134.4522	2.5277			

$T$ / K	$X_1$ / %	$X_2$ / %	$X_3$ / %	$V$ / Å <sup>3</sup>	$V_{\text{in}}$ / Å <sup>3</sup>
130	0.0000	0.0000	0.0000	4387.8187	4382.0803
145	-0.0125	0.0770	0.0909	4394.6403	4390.9295
160	-0.0385	0.1726	0.1826	4401.7262	4399.7788
175	-0.0395	0.2571	0.2688	4409.1884	4408.6281
190	-0.0478	0.3524	0.3667	4417.3231	4417.4774
205	-0.0706	0.4377	0.4964	4425.7928	4426.3267
220	-0.1028	0.5014	0.6412	4433.5694	4435.1759
235	-0.1373	0.5866	0.7876	4442.2683	4444.0252
250	-0.1851	0.6748	0.9274	4450.2297	4452.8745
265	-0.2338	0.7591	1.0630	4457.7957	4461.7238
280	-0.2736	0.8634	1.2123	4467.2516	4470.5731
295	-0.2842	0.9638	1.3391	4476.8465	4479.4223
310	-0.3565	1.0837	1.4776	4485.0900	4488.2716
325	-0.3806	1.2160	1.5867	4494.7258	4497.1209
340	-0.4386	1.3521	1.7273	4504.4283	4505.9702
355	-0.4612	1.5000	1.8093	4513.6503	4514.8195
370	-0.5923	1.6304	2.0991	4526.4653	4523.6687
385	-0.6441	1.7628	2.2345	4536.0815	4532.5180
400	-0.7153	1.9147	2.4182	4547.8601	4541.3673

### Pressure dependent high-resolution powder XRD data

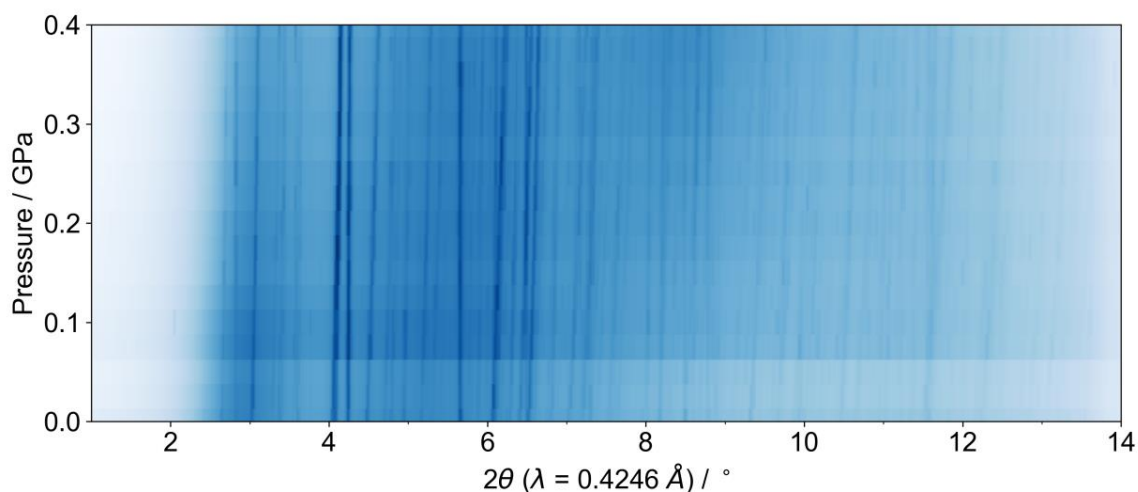
High-pressure powder X-ray (HPPXRD) data were collected at the Diamond Light Source (beamline I15) within beamtime CY22477-2 using an X-ray energy of 29.2 keV ( $\lambda = 0.4246 \text{ \AA}$ ) and a 2D PerkinElmer area detector for data collection. The applied high-pressure cell is described in detail at <https://www.imperial.ac.uk/pressurecell/> and refs<sup>[16]</sup>. The homogeneously ground samples ([TPC4TP]Mn<sub>2</sub>(C<sub>2</sub>N<sub>3</sub>)<sub>6</sub> and [TPC5TP]Mn<sub>2</sub>(C<sub>2</sub>N<sub>3</sub>)<sub>6</sub>) were filled together with Silicone oil AP 100 as pressure transmitting medium into a PTFE plastic capillary (inside diameter 1.8 mm) and then sealed with Araldyte-2014-1 glue. For the chosen silicone oil, it is expected to maintain hydrostatic conditions up to pressures of  $p = 0.9 \text{ GPa}$ . The plastic capillary was loaded into the water filled sample chamber. The pressure on the sample is adjusted by increasing or decreasing the water pressure in the sample chamber using a hydraulic gauge pump system equipped with three pressure transducers to control the applied pressure precisely. HPPXRD is performed through two diamond windows in the sample chamber. In total, 17 HPPXRD patterns were collected between  $p = \text{ambient}$  and 0.40 GPa including one after releasing the pressure to prove reversibility. The step size was chosen to be  $\Delta p = 0.025 \text{ GPa}$ .



**Figure S-24:** Pressure dependent HPPXRD patterns of  $[\text{TPC4TP}]\text{Mn}_2(\text{C}_2\text{N}_3)_6$ . Shown in blue is a stack plot of the pattern at each pressure point, upwards from ambient to high pressures. Depicted at the bottom is the Pawley profile fit analysis of the pattern at ambient conditions, serving as the starting point for sequenced analysis of the pressure points, respectively. Shown there are the observed, calculated and differenced data with cell parameters  $a = 11.940832$ ,  $b = 21.705501$ ,  $c = 17.230456$ ,  $\beta = 94.09478^\circ$ , space-group  $Pc$ .

**Table S-10:** Overview of the refined cell parameters and deviations of [TPC4TP]Mn<sub>2</sub>(C<sub>2</sub>N<sub>3</sub>)<sub>6</sub> at different pressures, using the Pawley profile fit analysis method.

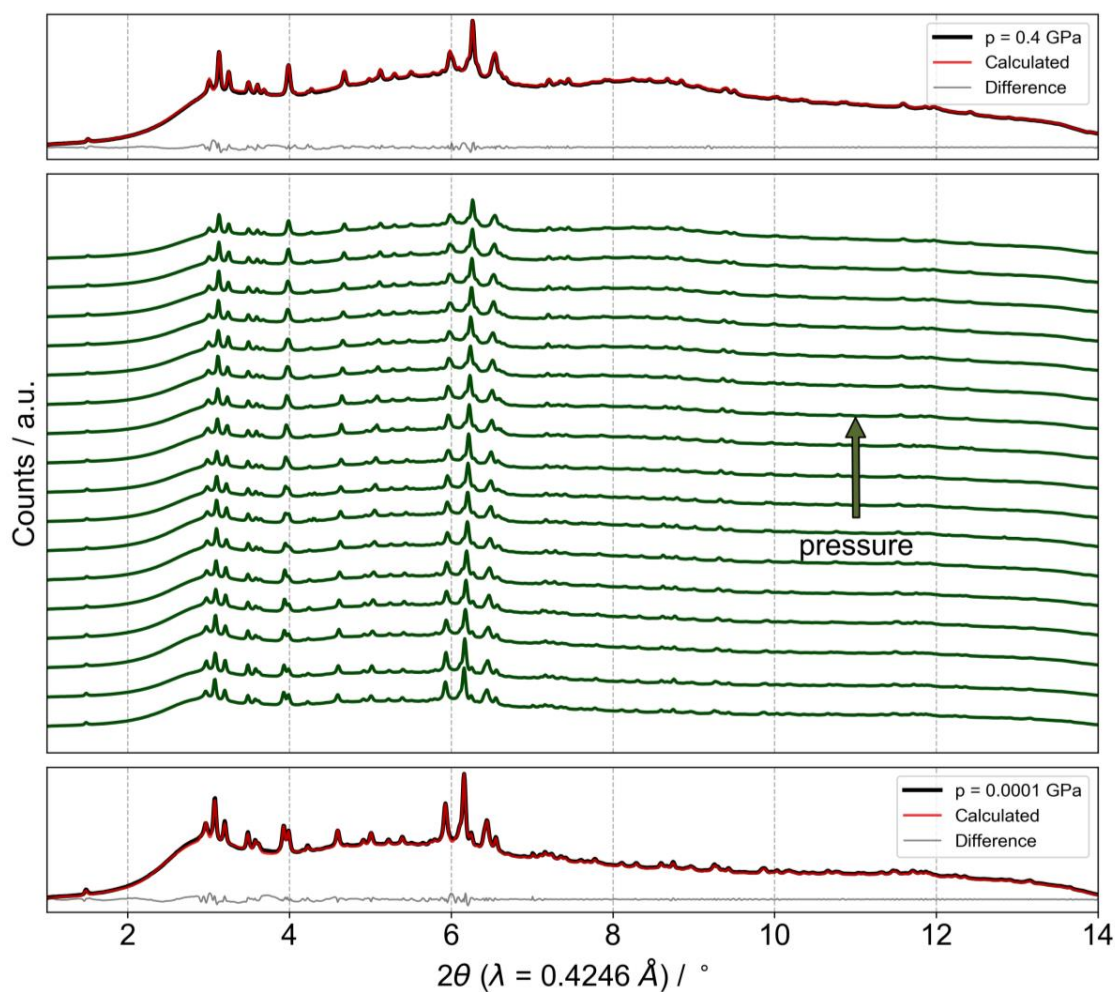
$p / \text{GPa}$	$r_{\text{wp}}$	$a / \text{\AA}$	$b / \text{\AA}$	$c / \text{\AA}$	$\beta / ^\circ$	$V / \text{\AA}^3$
0.0001	0.70414	11.9429(15)	21.7063(25)	17.2324(27)	94.110(21)	4455.8(10)
0.025	0.75586	11.8998(41)	21.6531(34)	17.2362(21)	93.732(21)	4431.8(17)
0.050	0.63443	11.9057(31)	21.6141(30)	17.2372(34)	93.724(22)	4426.3(16)
0.075	0.72441	11.8816(31)	21.5294(28)	17.2268(86)	93.609(45)	4398.0(25)
0.100	0.63807	11.8644(22)	21.4931(33)	17.2246(57)	93.489(30)	4384.2(18)
0.125	0.59661	11.8549(25)	21.4425(32)	17.2350(40)	93.391(29)	4373.5(15)
0.150	0.60998	11.8346(17)	21.3976(25)	17.2336(20)	93.222(23)	4357.2(9)
0.175	0.64357	11.8206(17)	21.3612(42)	17.2252(18)	93.129(26)	4342.9(12)
0.200	0.60633	11.8073(25)	21.3561(12)	17.2329(16)	93.090(24)	4339.1(10)
0.225	0.61376	11.7974(31)	21.2803(60)	17.2207(16)	92.939(19)	4317.6(17)
0.250	0.69323	11.7852(29)	21.2550(70)	17.2106(17)	92.903(29)	4305.7(18)
0.275	0.57882	11.7692(25)	21.1948(53)	17.2165(12)	92.798(18)	4289.5(15)
0.300	0.59434	11.7634(28)	21.1602(50)	17.2100(15)	92.714(21)	4279.0(15)
0.325	0.57792	11.7380(28)	21.1143(32)	17.2005(20)	92.643(22)	4258.4(13)
0.350	0.61998	11.7352(33)	21.1053(39)	17.2018(20)	92.592(23)	4256.1(15)
0.375	0.63674	11.7270(38)	21.0724(30)	17.2098(37)	92.543(26)	4248.6(18)
0.400	0.75205	11.7281(47)	21.0168(36)	17.1928(45)	92.472(28)	4233.9(21)

**Figure S-25:** Results of high-pressure powder X-ray diffraction experiments shown as contour plot of experimental data of [TPC4TP]Mn<sub>2</sub>(C<sub>2</sub>N<sub>3</sub>)<sub>6</sub> from ambient pressure to 0.4 GPa. A darker colour corresponds to a higher intensity in the respective bragg peaks.

**Table S-11:** Output of PASCAL - principal axis strain calculations with direction of projections of  $X$  on the unit cell axes  $a$ ,  $b$  and  $c$  for  $[\text{TPC4TP}]\text{Mn}_2(\text{C}_2\text{N}_3)_6$  at high pressures. Listed are the resulting principal axes  $X_n$  with median compressibility coefficients  $K$  and the changes of length for  $X_1$ ,  $X_2$ ,  $X_3$  and  $V$ , respectively.

Axes	$K / \text{TPa}^{-1}$	$\sigma K / \text{TPa}^{-1}$	$a$	$b$	$c$	$\epsilon_0$	$\lambda$	$P_c$	$\nu$
$X_1$	-11.7338	1.1315	-0.6395	0.0000	-0.7688	-2.5952e-04	1.1363e-02	-0.0002	0.4654
$X_2$	58.4423	1.5506	-0.9394	0.0000	0.3427	8.0320e-04	-5.3860e-02	-0.0035	0.7479
$X_3$	68.8050	2.3821	0.0000	1.0000	-0.0000	5.1248e-10	-6.3684e-02	0.0001	0.7912
$V$	123.7388	3.4154							

$p / \text{GPa}$	$X_1 / \%$	$X_2 / \%$	$X_3 / \%$	$V / \text{\AA}^3$	$K_1$	$K_2$	$K_3$
0.0001	0.0000	0.0000	0.0000	4455.7880	-405.89	166.26	4756.70
0.025	0.2353	-0.2450	-0.5290	4431.8117	-37.84	98.76	108.95
0.050	0.2588	-0.4249	-0.4972	4426.2744	-26.18	84.27	94.23
0.075	0.2558	-0.7427	-0.8150	4397.9636	-21.09	76.51	86.56
0.100	0.3065	-0.9378	-0.9824	4384.1722	-18.09	71.36	81.51
0.125	0.4117	-1.0516	-1.2156	4373.4527	-16.06	67.57	77.80
0.150	0.4978	-1.2992	-1.4224	4357.2053	-14.57	64.61	74.89
0.175	0.5060	-1.4648	-1.5899	4342.9238	-13.42	62.20	72.51
0.200	0.5436	-1.5659	-1.6135	4339.0764	-12.50	60.17	70.52
0.225	0.5885	-1.7502	-1.9626	4317.6227	-11.73	58.44	68.81
0.250	0.5474	-1.8668	-2.0790	4305.6501	-11.09	56.93	67.31
0.275	0.6221	-2.0328	-2.3564	4289.4675	-10.54	55.60	65.98
0.300	0.6479	-2.1378	-2.5158	4279.0452	-10.06	54.41	64.79
0.325	0.6081	-2.3606	-2.7274	4258.4305	-9.64	53.33	63.72
0.350	0.6484	-2.4123	-2.7690	4256.1095	-9.27	52.35	62.74
0.375	0.7053	-2.4879	-2.9207	4248.6365	-8.93	51.46	61.84
0.400	0.6886	-2.5556	-3.1766	4233.8606	-8.63	50.64	61.01

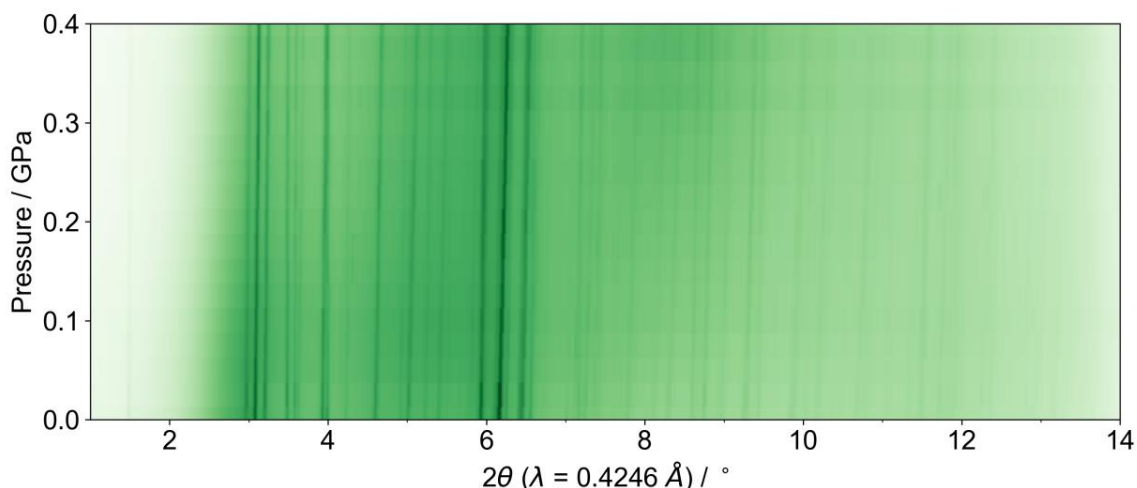


**Figure S-26:** Pressure dependent HPPXRD patterns of  $[\text{TPC5TP}]\text{Mn}_2(\text{C}_2\text{N}_3)_6$ . Shown in darkgreen is a stack plot of the pattern at each pressure point, upwards from ambient to high pressures. Depicted at the bottom is the Pawley profile fit analysis of the pattern at ambient conditions, serving as the starting point for sequenced analysis of the pressure points, respectively. Shown there are the observed, calculated and differenced data with cell parameters  $a = 17.01056$ ,  $b = 9.70711$ ,  $c = 14.10749$ ,  $\beta = 105.56538^\circ$ , space-group  $P2_1/c$ .



**Table S-12:** Overview of the refined cell parameters and deviations of  $[\text{TPC5TP}]\text{Mn}_2(\text{C}_2\text{N}_3)_6$  at different pressures, using the Pawley profile fit analysis method.

$p / \text{GPa}$	$r_{\text{wp}}$	$a / \text{\AA}$	$b / \text{\AA}$	$c / \text{\AA}$	$\beta / ^\circ$	$V / \text{\AA}^3$
0.0001	0.69793	14.1104(21)	9.7051(15)	33.1386(63)	98.625(17)	4486.8(13)
0.025	0.66916	14.1014(15)	9.6899(13)	33.0773(47)	98.557(15)	4469.4(10)
0.050	0.59452	14.1007(21)	9.6735(17)	33.0549(63)	98.564(19)	4458.5(13)
0.075	0.54597	14.0971(22)	9.6587(14)	33.0115(60)	98.545(17)	4444.9(13)
0.100	0.5527	14.0949(22)	9.6429(14)	32.9779(60)	98.485(16)	4433.1(13)
0.125	0.50718	14.0815(20)	9.6243(14)	32.9278(58)	98.502(19)	4413.5(12)
0.150	0.51765	14.0923(20)	9.6143(14)	32.9152(60)	98.465(18)	4411.0(12)
0.175	0.53035	14.0948(19)	9.6041(13)	32.9061(55)	98.400(18)	4406.7(11)
0.200	0.52352	14.0915(19)	9.5897(11)	32.8794(50)	98.366(15)	4395.8(10)
0.225	0.54759	14.0833(19)	9.5738(12)	32.8573(50)	98.399(15)	4382.7(11)
0.250	0.5273	14.0778(19)	9.5586(11)	32.8114(54)	98.409(17)	4367.7(11)
0.275	0.51857	14.0730(20)	9.5496(12)	32.7820(54)	98.350(22)	4358.9(11)
0.300	0.52372	14.0647(18)	9.5369(12)	32.7600(52)	98.365(18)	4347.5(11)
0.325	0.56938	14.0687(21)	9.5210(11)	32.7114(59)	98.304(23)	4335.7(11)
0.350	0.58321	14.0608(22)	9.5126(11)	32.6883(52)	98.294(22)	4326.5(11)
0.375	0.56829	14.0569(23)	9.5021(11)	32.6562(52)	98.288(22)	4316.3(11)
0.400	0.56274	14.0523(21)	9.4928(11)	32.6325(50)	98.258(21)	4307.9(11)

**Figure S-27:** Results of high-pressure powder X-ray diffraction experiments shown as contour plot of experimental data of  $[\text{TPC5TP}]\text{Mn}_2(\text{C}_2\text{N}_3)_6$  from ambient pressure to 0.4 GPa. A darker colour corresponds to a higher intensity in the respective bragg peaks.

**Table S-13:** Output of PASCAL - principal axis strain calculations with direction of projections of  $X$  on the unit cell axes  $a$ ,  $b$  and  $c$  for  $[\text{TPC5TP}]\text{Mn}_2(\text{C}_2\text{N}_3)_6$  at high pressures. Listed are the resulting principal axes  $X_i$  with median compressibility coefficients  $K$  and the changes of length for  $X_1$ ,  $X_2$ ,  $X_3$  and  $V$ , respectively.

Axes	$K/\text{TPa}^{-1}$	$\sigma K/\text{TPa}^{-1}$	$a$	$b$	$c$	$\varepsilon_0$	$\lambda$	$P_c$	$v$
$X_1$	6.3428	1.3530	-0.9873	0.0000	-0.1591	8.3374e-05	-6.9353e-03	-0.0241	1.1886
$X_2$	30.2044	2.1080	-0.4947	-0.0000	0.8691	4.2765e-05	-2.7564e-02	0.0000	0.6874
$X_3$	52.5545	0.7121	0.0000	-1.0000	-0.0000	1.9149e-05	-4.9927e-02	-0.0000	0.8796
$V$	97.9263	1.6251							

$p/\text{GPa}$	$X_1/\%$	$X_2/\%$	$X_3/\%$	$V/\text{\AA}^3$	$K_1$	$K_2$	$K_3$
0.0001	0.0000	0.0000	0.0000	4486.7964	4.09	359.12	128.88
0.025	-0.0298	-0.1570	-0.2012	4469.4067	4.67	60.05	68.46
0.050	-0.0456	-0.2602	-0.3258	4458.5057	5.05	48.34	62.98
0.075	-0.0663	-0.3907	-0.4785	4444.9297	5.33	42.58	59.98
0.100	-0.0532	-0.5052	-0.6413	4433.1437	5.56	38.92	57.94
0.125	-0.1611	-0.6477	-0.8332	4413.4749	5.76	36.30	56.41
0.150	-0.0705	-0.6901	-0.9355	4411.0395	5.93	34.29	55.18
0.175	-0.0185	-0.7351	-1.0408	4406.6517	6.08	32.67	54.17
0.200	-0.0259	-0.8234	-1.1897	4395.7889	6.22	31.34	53.30
0.225	-0.1047	-0.8778	-1.3529	4382.6577	6.34	30.20	52.55
0.250	-0.1547	-1.0078	-1.5101	4367.7433	6.46	29.23	51.89
0.275	-0.1593	-1.1108	-1.6029	4358.8996	6.57	28.37	51.30
0.300	-0.2272	-1.1717	-1.7337	4347.4582	6.67	27.61	50.77
0.325	-0.1757	-1.3265	-1.8969	4335.6857	6.76	26.92	50.28
0.350	-0.2263	-1.3984	-1.9833	4326.5202	6.85	26.31	49.83
0.375	-0.2555	-1.4929	-2.0915	4316.3369	6.93	25.75	49.42
0.400	-0.2738	-1.5710	-2.1882	4307.8686	7.01	25.23	49.04

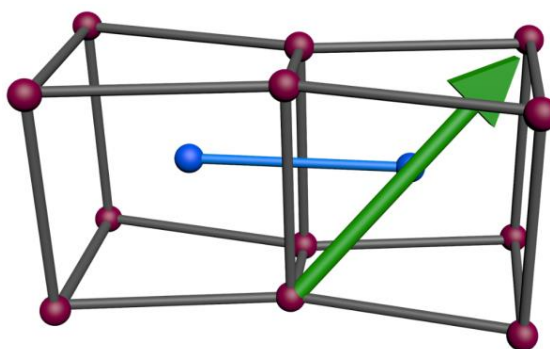


**Figure S-28:** Orthonormal projection of the principal axis of the crystallographic direction [304] showing uniaxial NTE and NLC for [TPC4TP] $\text{Mn}_2(\text{C}_2\text{N}_3)_6$ , indicated by the green arrow. Both NTE and NLC progress in the same direction that is the approximate space diagonal of a representative  $[\text{MX}]_3$  cuboid. Please note that more precisely it resembles the space diagonal of a representative  $2 \times 2$  block of an  $\text{AB}_2\text{X}_6$  unit, as defined by the herringbone-type order pattern of the A-site cation. The figure was created with *Autodesk 3ds Max free student license*.

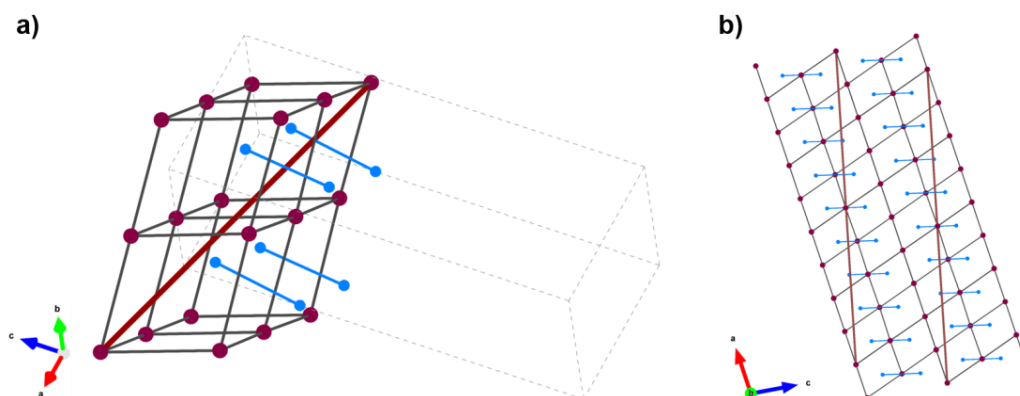


**Figure S-29:** Orthonormal projection of the principal axis  $X_1$  for [TPC5TP] $\text{Mn}_2(\text{C}_2\text{N}_3)_6$  showing the smallest compressibility coefficient  $K_1$  and uniaxial NTE along the [401] direction, approximately showcased with the brownish vector, representing the space diagonal of a  $1 \times 2$   $(\text{M}_2\text{X}_6)^-$  cuboid as seen in (a). In (b), it is illustrated that the vector of uniaxial NTE and smallest compressibility propagates orthogonal to the A-site cations which are lamellae-like stacked. The figures were created with *VESTA 3.4.0*.

## Bulk Modulus - Birch-Murnaghan equation of state

The bulk moduli  $K$  of the materials  $[\text{TPC4TP}]\text{Mn}_2(\text{C}_2\text{N}_3)_6$  and  $[\text{TPC5TP}]\text{Mn}_2(\text{C}_2\text{N}_3)_6$  were obtained by fitting a 3<sup>rd</sup>-order Birch-Murnaghan equation of state (BM EoS) to the extracted, pressure dependent cell volume data. Standard deviations of the lattice parameters and volumes which were obtained during the Pawley profile analysis were included in the fitting process of the  $V(p)$  data with the software EoSFIT-7c<sup>[17]</sup>. For the applied pressure a standard deviation of  $\sigma p = 0.002$  GPa was included in the calculation. The extracted bulk moduli are  $K_0([\text{TPC4TP}]\text{Mn}_2(\text{C}_2\text{N}_3)_6) = 6.26 \pm 0.38$  GPa and  $K_0([\text{TPC5TP}]\text{Mn}_2(\text{C}_2\text{N}_3)_6) = 8.96 \pm 0.58$  GPa.

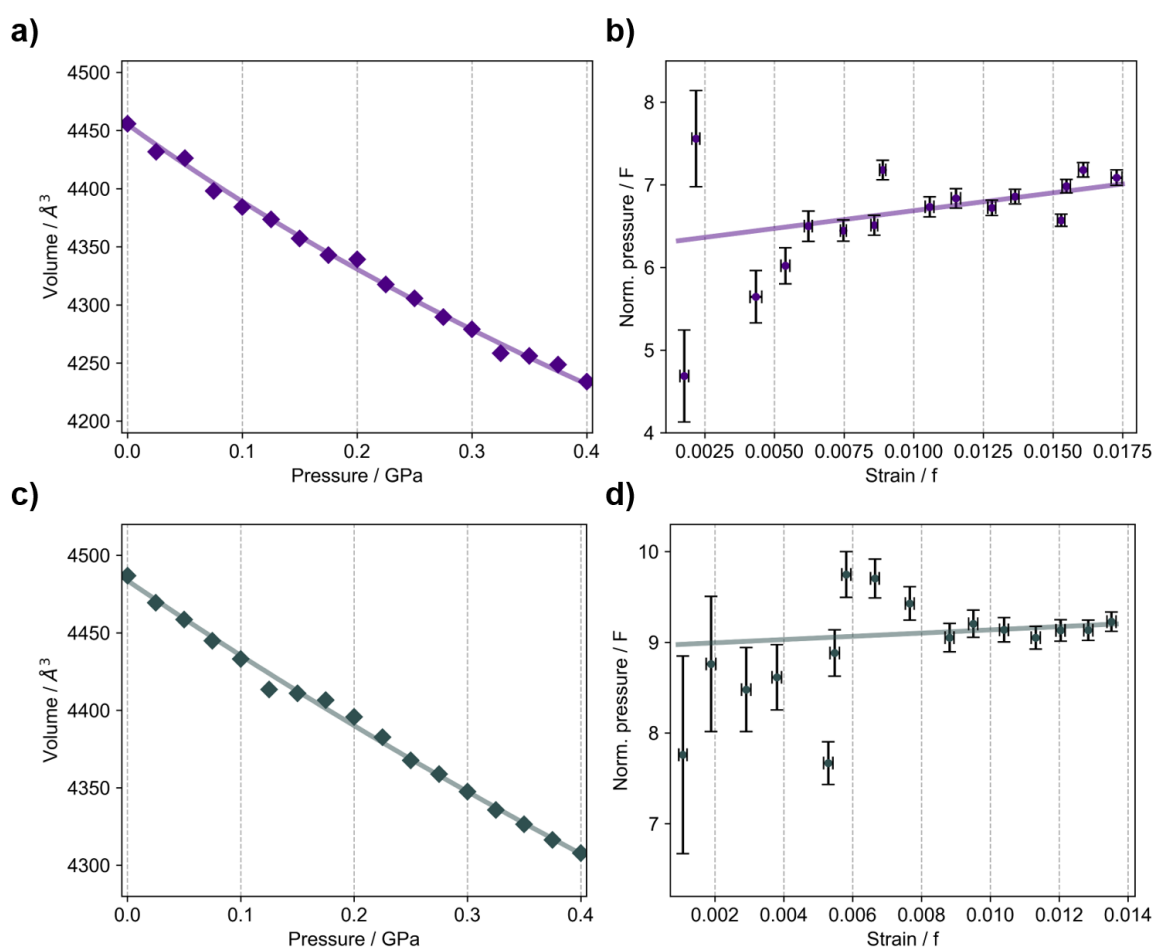


**Figure S-30:**  $p$ - $V$  data and the equation of state fits for both  $[\text{TPC4TP}]\text{Mn}_2(\text{C}_2\text{N}_3)_6$  (a, b) and  $[\text{TPC5TP}]\text{Mn}_2(\text{C}_2\text{N}_3)_6$  (c, d) as well as the norm. pressure  $F$  vs strain  $f$  plots, confirming the applicability of the BM 3<sup>rd</sup>-order EoS fit to derive the bulk moduli.

**Table S-14:** Overview of extracted bulk moduli  $K_0$ ,  $K_p$  and fitted  $V_0$  for the unit cell volume at ambient pressures, respectively.

[A][Mn <sub>2</sub> (C <sub>2</sub> N <sub>3</sub> ) <sub>6</sub> ]	A = TPC4TP <sup>2+</sup>	A = TPC5TP <sup>2+</sup>
$K_0$ / GPa	6.26(38)	8.96(58)
$K_p$	8.60(27)	5.32(31)
$V_0$ / Å <sup>3</sup>	4455.3(24)	4483.7(25)

Additionally, Table S-17 shows the calculations outcome of the bulk modulus values (2<sup>nd</sup> and 3<sup>rd</sup> order) using the principal axis strain calculations program PASCAL<sup>[18]</sup>, verifying the Equation of state fits using EoSFIT-7c.

**Table S-15:** Birch-Murnaghan Coefficients of [TPC4TP]Mn<sub>2</sub>(C<sub>2</sub>N<sub>3</sub>)<sub>6</sub> and [TPC5TP]Mn<sub>2</sub>(C<sub>2</sub>N<sub>3</sub>)<sub>6</sub>, extracted from the high-pressure powder X-ray HPPXRD data using PASCAL. Note that the bulk moduli and derivative are indexed as  $B_0$  for the bulk modulus and  $B'$  for derivation. Additionally, the fitted  $V_0$  for the unit cell volume including deviation at ambient pressures is listed.

[TPC4TP]Mn <sub>2</sub> (C <sub>2</sub> N <sub>3</sub> ) <sub>6</sub>							
	$B_0$ / GPa	$\sigma B_0$ / GPa	$V_0$ / Å <sup>3</sup>	$\sigma V_0$ / Å <sup>3</sup>	$B'$	$\sigma B'$	$P_c$ / GPa
2 <sup>nd</sup>	7.1380	0.1443	4449.2582	2.6554	4	n/a	0
3 <sup>rd</sup>	6.2474	0.5271	4453.9910	4.1184	9.2379	3.2540	0

[TPC5TP]Mn <sub>2</sub> (C <sub>2</sub> N <sub>3</sub> ) <sub>6</sub>							
	$B_0$ / GPa	$\sigma B_0$ / GPa	$V_0$ / Å <sup>3</sup>	$\sigma V_0$ / Å <sup>3</sup>	$B'$	$\sigma B'$	$P_c$ / GPa
2 <sup>nd</sup>	9.2344	0.1655	4482.4969	1.8763	4	n/a	0
3 <sup>rd</sup>	9.0319	0.6236	4483.1381	2.7668	5.0684	3.2077	0

Given the higher bond energy per volume unit of [TPC5TP]Mn<sub>2</sub>(C<sub>2</sub>N<sub>3</sub>)<sub>6</sub> due to the additional -CH<sub>2</sub>- group in the A-site cation, this trend is reasonable as a higher packing density results in a less compressible material. These values are comparable with those from other dicyanamide based perovskite coordination networks such as [(C<sub>3</sub>H<sub>7</sub>)<sub>4</sub>N]Mn(C<sub>2</sub>N<sub>3</sub>)<sub>3</sub> or [(C<sub>3</sub>H<sub>7</sub>)<sub>4</sub>N]Cd(C<sub>2</sub>N<sub>3</sub>)<sub>3</sub>, for which a bulk modulus  $B_0$  (Mn) = 8.1(11) GPa<sup>[19]</sup> and  $B_0$  (Cd) = 6.2(6) GPa<sup>[4]</sup> was determined, matching well the compressibility behavior of three-dimensional perovskite-type frameworks.

## KBr as reference material for pressure cell and analysis

To verify the cell setup and the pressure applied, potassium bromide KBr was used as a reference material with very well documented high-pressure behaviour, see ref [20]. The capillary was prepared in the same way as the samples before. In total, 22 HPPXRD patterns were collected between  $p = \text{ambient}$  and 0.40 GPa including one after releasing the pressure. The step size was  $\Delta p = 0.02$  GPa.

KBr powder diffraction data was successfully indexed and refined in the cubic space group  $Fm\bar{3}m$  with ambient cell parameters  $a = b = c = 6.59717(3)$  and  $V = 287.126(4) \text{ \AA}^3$  as reported previously.<sup>[21]</sup> A complete list with all refined cell parameters and their standard deviations can be found in Table S-12. The bulk modulus was calculated in the exact same way as for the samples and was determined to be  $K_0(\text{KBr}) = 14.10 \pm 0.30$  GPa which is in great accordance with the bulk modulus reported by Mezouar et al. ( $K = 14.2$  GPa).<sup>[20]</sup>

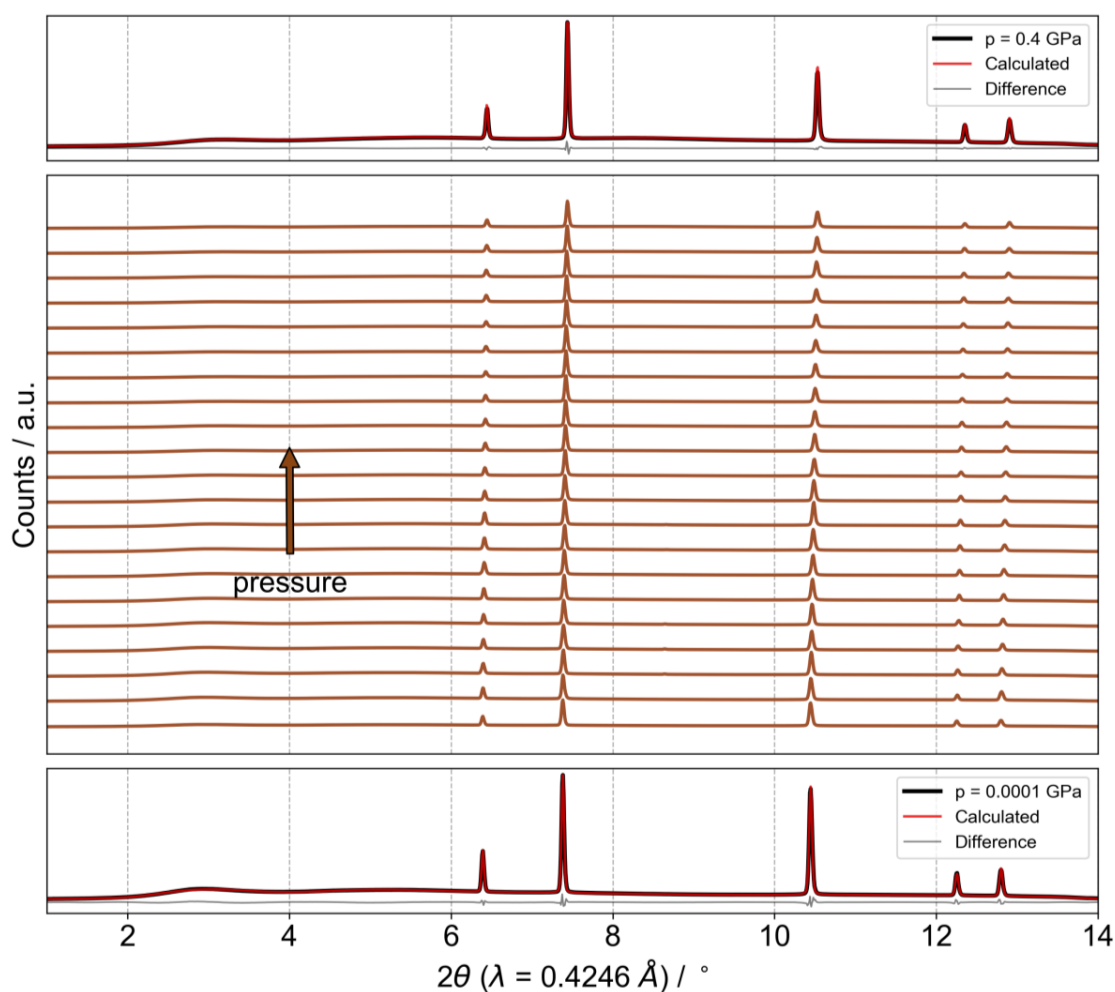


**Figure S-31:** Pressure dependent HPPXRD patterns of KBr. Shown in brown is a stack plot of the pattern at each pressure point, upwards from ambient to high pressures. Depicted at the bottom is the Pawley profile fit analysis of the pattern at ambient conditions, serving as the starting point for sequenced analysis of the pressure points, respectively.

**Table S-16:** Overview of the refined cell parameters and deviations of KBr at different pressures, using the Pawley profile fit analysis method.

<b><math>p</math> / GPa</b>	<b><math>r_{wp}</math></b>	<b><math>a</math> / Å</b>	<b><math>V</math> / Å<sup>3</sup></b>
0.0001	2.09580	6.59717(3)	287.126(4)
0.02	2.07053	6.59429(4)	286.750(5)
0.04	1.66727	6.59152(3)	286.390(4)
0.06	1.89154	6.58865(4)	286.016(5)
0.08	1.84404	6.58559(4)	285.617(5)
0.10	1.67652	6.58219(3)	285.175(4)
0.12	1.99093	6.57876(4)	284.729(5)
0.14	1.87701	6.57619(3)	284.395(4)
0.16	1.86156	6.57349(3)	284.045(4)
0.18	2.17171	6.57169(4)	283.813(5)
0.20	2.19611	6.56934(4)	283.507(5)
0.22	1.99750	6.56572(3)	283.039(4)
0.24	2.41846	6.56387(4)	282.800(5)
0.26	2.57715	6.56169(4)	282.519(5)
0.28	2.82356	6.55968(4)	282.259(5)
0.30	3.06817	6.55729(4)	281.951(5)
0.32	2.64092	6.55458(4)	281.601(5)
0.34	3.01573	6.55311(4)	281.412(6)
0.36	3.06517	6.55158(4)	281.215(6)
0.38	2.56768	6.54715(4)	280.644(5)
0.40	2.15067	6.54447(3)	280.300(4)

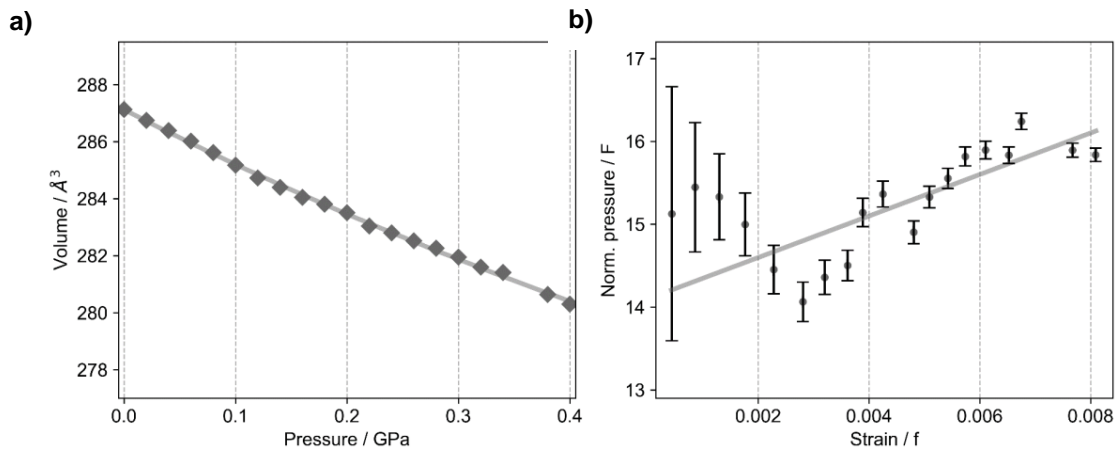


**Figure S-32:**  $p$ - $V$  data and the equation of state fit for KBr (a) as well as the norm. pressure  $F$  vs strain  $f$  plot (b), confirming the applicability of the BM 3<sup>rd</sup>-order EoS fit to derive the bulk modulus.



## Second Harmonic Generation studies

Assessment of SHG efficiency of  $[\text{TPC4TP}]\text{Mn}_2(\text{C}_2\text{N}_3)_6$  and  $[\text{TPC5TP}]\text{Mn}_2(\text{C}_2\text{N}_3)_6$  was performed with the use of Kurtz-Perry technique. Potassium dihydrogen phosphate (KDP) was used as a SHG reference.<sup>[22]</sup> Prior to measurements, crystalline powders of  $[\text{TPC4TP}]\text{Mn}_2(\text{C}_2\text{N}_3)_6$  and  $[\text{TPC5TP}]\text{Mn}_2(\text{C}_2\text{N}_3)_6$  and KDP were sieved through a mini-sieve set (Aldrich), collecting a microcrystal size fraction smaller than  $63\ \mu\text{m}$ . Next, size-graded samples of  $[\text{TPC4TP}]\text{Mn}_2(\text{C}_2\text{N}_3)_6$ ,  $[\text{TPC5TP}]\text{Mn}_2(\text{C}_2\text{N}_3)_6$  and KDP were fixed between microscope glass slides forming tightly packed layers, sealed, and mounted to the holder. Kurtz-Perry test was performed at 293K.

The laser radiation was delivered from a Quantronix Integra-C regenerative amplifier operating at 800 nm, pulse duration of 130 fs, and repetition rate of 1 kHz. The laser beam was directed onto  $[\text{TPC4TP}]\text{Mn}_2(\text{C}_2\text{N}_3)_6$ ,  $[\text{TPC5TP}]\text{Mn}_2(\text{C}_2\text{N}_3)_6$  and KDP samples at 45 degrees. Signal-collecting optics, mounted to the glass optical fiber, was placed perpendicularly to the plane of sample (backscattering geometry). For each sample the same signal collection geometry was employed, and the average power of laser beam was constant (820 mW). Scattered pumping radiation was suppressed with the use of 700 nm shortpass dielectric filter (FESH0700, Thorlabs). The spectra of the diffused SHG were recorded by an Ocean Optics QEPro fiber-coupled CCD spectrograph. The signal collection time for  $[\text{TPC4TP}]\text{Mn}_2(\text{C}_2\text{N}_3)_6$  and  $[\text{TPC5TP}]\text{Mn}_2(\text{C}_2\text{N}_3)_6$  was set to 6000 ms, whereas for KDP it was equal to 600 ms.

*CAUTION. Work with the high-power laser brings danger to the eyes, especially in spectral range in which the beam is invisible. Adequate eye protection should be applied during measurements.*

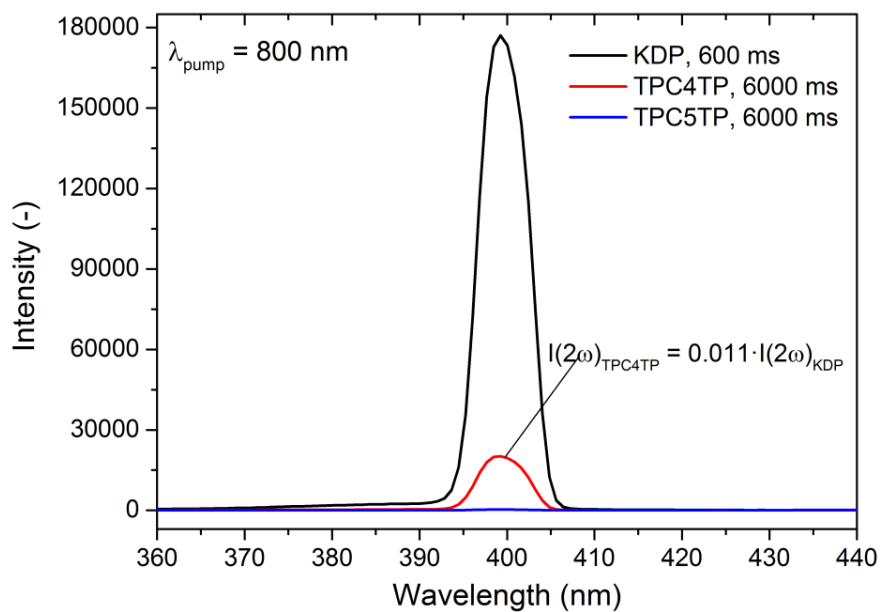


**Figure S-33:** A comparison of SHG traces for [TPC4TP] $\text{Mn}_2(\text{C}_2\text{N}_3)_6$  (red), [TPC5TP] $\text{Mn}_2(\text{C}_2\text{N}_3)_6$  (blue) and for KDP (black). The collection time differed from 600 ms for KDP as reference to 6000 ms for the two sample materials.

## References

- [1] K. Yang, M. Tyagi, J. S. Moore, Y. Zhang, *J. Am. Chem. Soc.* **2014**, *136*, 1268.
- [2] G. R. Fulmer, A. J. M. Miller, N. H. Sherden, H. E. Gottlieb, A. Nudelman, B. M. Stoltz, J. E. Bercaw, K. I. Goldberg, *Organometallics* **2010**, *29*, 2176.
- [3] S. Burger, S. Grover, K. T. Butler, H. L. B. Boström, R. Grau-Crespo, G. Kieslich, *Mater. Horiz.* **2021**, *8*, 2444.
- [4] M. Mączka, M. Ptak, A. Gągor, A. Sieradzki, P. Peksa, G. Usevicius, M. Simenas, F. F. Leite, W. Paraguassu, *J. Mater. Chem. C* **2019**, *7*, 2408.
- [5] Bruker AXS Inc., Madison, Wisconsin, USA, *APEX suite of crystallographic software* **2015**, *APEX 3*, Version 2015-5.2.
- [6] Bruker AXS Inc., Madison, Wisconsin, USA, *APEX suite of crystallographic software* **2014**, *SAINT*, Version 8.34A.
- [7] Bruker AXS Inc., Madison, Wisconsin, USA, *APEX suite of crystallographic software* **2014**, *SADABS*, Version 2014/5.
- [8] a) G. M. Sheldrick, *Acta Crystallogr. Sect. C* **2015**, *71*, 3; b) O. V. Dolomanov, L. J. Bourhis, R. J. Gildea, J. A. K. Howard, H. Puschmann, *J. Appl. Cryst.* **2009**, *42*, 339.
- [9] G. M. Sheldrick, *Acta Crystallogr. Sect. A* **2015**, *71*, 3.
- [10] K. Momma, F. Izumi, *J. Appl. Cryst.* **2011**, *44*, 1272.
- [11] H. D. Flack, *Acta Cryst. A* **1983**, *39*, 876.
- [12] R. E. Marsh, *Acta Cryst.* **1995**, *51*, 897.
- [13] B. J. Campbell, H. T. Stokes, D. E. Tanner, D. M. Hatch, *J. Appl. Cryst.* **2006**, *39*, 607.
- [14] a) H. L. B. Boström, *CrystEngComm* **2020**, *22*, 961; b) H. L. B. Boström, M. S. Senn, A. L. Goodwin, *Nat. Commun.* **2018**, *9*, 2380.
- [15] a) G. S. Pawley, *J. Appl. Cryst.* **1981**, *14*, 357; b) A. A. Coelho, *J. Appl. Cryst.* **2018**, *51*, 210.
- [16] a) N. J. Brooks, B. L. L. E. Gauthe, N. J. Terrill, S. E. Rogers, R. H. Templer, O. Ces, J. M. Seddon, *Rev. Sci. Instrum.* **2010**, *81*, 64103; b) S. Dissegna, P. Vervoorts, C. L. Hobday, T. Düren, D. Daisenberger, A. J. Smith, R. A. Fischer, G. Kieslich, *J. Am. Chem. Soc.* **2018**, *140*, 11581.
- [17] R. J. Angel, M. Alvaro, J. Gonzalez-Platas, *Z. Kristallogr. Cryst. Mater.* **2014**, 229.
- [18] M. J. Cliffe, A. L. Goodwin, *J. Appl. Cryst.* **2012**, *45*, 1321.
- [19] M. Mączka, I. E. Collings, F. F. Leite, W. Paraguassu, *Dalton Trans.* **2019**, *48*, 9072.
- [20] A. Dewaele, A. B. Belonoshko, G. Garbarino, F. Occelli, P. Bouvier, M. Hanfland, M. Mezouar, *Phys. Rev. B* **2012**, *85*, 805.
- [21] V. Meisalo, O. Inkinen, *Acta Cryst.* **1967**, *22*, 58.
- [22] a) S. K. Kurtz, T. T. Perry, *J. Appl. Phys.* **1968**, *39*, 3798; b) A. Graja, *Phys. Status Solidi B* **1968**, *27*, K93-K97.



# 9 APPENDIX

## A List of Paper Publications

### I Publications as first author integrated in this doctorate thesis

- "Tolerance factors of hybrid organic–inorganic perovskites: recent improvements and current state of research."  
**S. Burger**, M. G. Ehrenreich and G. Kieslich, *J. Mater. Chem. A*, 2018, 6, 21785-21793 (STUDY I).
- "A new polar perovskite coordination network with azaspiroundecane as A-site cation."  
**S. Burger**, S. Kronawitter, H. L. B. Boström, J. K. Zaręba and G. Kieslich, *Dalton Trans.*, 2020, 49, 10740-10744 (STUDY II).
- "Tilt and shift polymorphism in molecular perovskites."  
**S. Burger**,<sup>‡</sup> S. Grover,<sup>‡</sup> K. T. Butler, H. L. B. Boström, R. Grau-Crespo and G. Kieslich, *Mater. Horiz.*, 2021, 8, 2444-2450 (STUDY III).
- "Tuning the mechanical properties of dicyanamide-based molecular perovskites."  
S. Grover,<sup>‡</sup> **S. Burger**,<sup>‡</sup> K. T. Butler, K. Hemmer, P. Vervoorts, G. Kieslich and R. Grau-Crespo, *CrystEngComm*, 2023, 25, 3439-3444 (STUDY IV).
- "Designing Geometric Degrees of Freedom in ReO<sub>3</sub>-Type Coordination Polymers."  
**S. Burger**, K. Hemmer, D. C. Mayer, P. Vervoorts, D. Daisenberger, J. K. Zaręba and G. Kieslich, *Adv. Funct. Mater.*, 2022, 2205343 (STUDY V).

---

<sup>‡</sup> These authors contributed equally to this work.

## II Publications as co-author originated from collaborations within this doctorate project<sup>†</sup>

- "Flexible and Ultrasoft Inorganic 1D Semiconductor and Heterostructure Systems Based on SnIP."  
C. Ott, F. Reiter, M. Baumgartner, M. Pielmeier, A. Vogel, P. Walke, **S. Burger**, M. Ehrenreich, G. Kieslich, D. Daisenberger, J. Armstrong, U. K. Thakur, P. Kumar, S. Chen, D. Donadio, L. S. Walter, R. T. Weitz, K. Shankar and T. Nilges, *Adv. Funct. Mater.*, 2019, 29, 1900233.

Contributed with high-pressure powder X-ray diffraction measurements at Diamond Light Source Ltd. and revisions of the manuscript.

- "Mechanical properties of the ferroelectric metal-free perovskite MDABCO(NH<sub>4</sub>)I<sub>3</sub>."  
M. G. Ehrenreich, Z. Zeng, **S. Burger**, M. R. Warren, M. W. Gaultois, J.-C. Tan and G. Kieslich, *Chem. Commun.*, 2019, 55, 3911.

Contributed with high-pressure single crystal X-ray diffraction measurements at Diamond Light Source Ltd. and revisions of the manuscript.

- "Defect Engineering of Copper Paddlewheel-Based Metal–Organic Frameworks of Type NOTT-100: Implementing Truncated Linkers and Its Effect on Catalytic Properties."  
Z. Fan, J. Wang, W. Wang, **S. Burger**, Z. Wang, Y. Wang, C. Wöll, M. Cokoja and R. A. Fischer, *ACS Appl. Mater. Interfaces*, 2020, 34, 37993–38002.

Contributed with expertise on powder X-ray diffraction, performing all the Pawley profile fit analyses on powder pattern relevant for the study as well as preparation of the Supporting Information.

- "Revisiting the High-Pressure Properties of the Metal-Organic Frameworks ZIF-8 and ZIF-67."  
P. Vervoorts, **S. Burger**, K. Hemmer and G. Kieslich, *ChemRxiv*, 2020, DOI: 10.26434/chemrxiv.13146278.

Contributed with low high-pressure powder X-ray diffraction measurements at the Diamond Light Source Ltd. and revisions of the manuscript.

---

<sup>†</sup> Contribution to each publication is listed below.

- "Linear negative thermal expansion in Pd(acac)<sub>2</sub>."  
L. Petters, **S. Burger**, S. Kronawitter, M. Drees and G. Kieslich, *CrystEngComm*, 2021, 23, 5425-5429.

Contributed with expertise on Rietveld refinement based on powder X-ray diffraction, variable temperature powder X-ray diffraction measurements at the Deutsches Elektronen-Synchrotron and revisions of the manuscript.





## B List of Conference Contributions

### I Oral presentations

- "Functional materials as novel and sustainable refrigerants."  
**S. Burger**, Plenary lecture, Doctoral students conference, 2021, Kloster Banz, Hanns-Seidel Stiftung e.V.

## II Poster presentations

- "Crystal chemistry of functional organic-inorganic perovskites."  
**S. Burger**, M. G. Ehrenreich and G. Kieslich, Bulk Scattering in Condensed Matter Physics and Chemistry (CMPC) workshop, 2018, Hamburg.
- "Crystal chemistry of functional organic-inorganic perovskites."  
**S. Burger**, M. G. Ehrenreich and G. Kieslich, PCG Intensive School in Physical Crystallography summer school, 2018, Abingdon, UK.
- "Molecular perovskites under extreme conditions - response of dense coordination networks to temperature and hydrostatic pressures."  
**S. Burger**, M. G. Ehrenreich and G. Kieslich, 14<sup>th</sup> International conference on materials chemistry (MC 14), 2019, Birmingham, UK.

## C Reprint permissions

### STUDY I: Tolerance Factors of Hybrid Organic-Inorganic Perovskites: Recent Improvements and Current State of Research



This is a License Agreement between Stefan Burger ("User") and Copyright Clearance Center, Inc. ("CCC") on behalf of the Rightsholder identified in the order details below. The license consists of the order details, the Marketplace Order General Terms and Conditions below, and any Rightsholder Terms and Conditions which are included below. All payments must be made in full to CCC in accordance with the Marketplace Order General Terms and Conditions below.

Order Date	28-Jul-2022	Type of Use	Republish in a thesis/dissertation
Order License ID	1252397-1	Publisher Portion	Royal Society of Chemistry Chapter/article
ISSN	2050-7496		

#### LICENSED CONTENT

Publication Title	Journal of materials chemistry. A, Materials for energy and sustainability	Publication Type	e-Journal
Article Title	Tolerance Factors of hybrid perovskites: recent improvements and current state of research	Start Page	21785
Author/Editor	Royal Society of Chemistry (Great Britain)	End Page	21793
Date	01/01/2013	Issue	44
Language	English	Volume	6
Country	United Kingdom of Great Britain and Northern Ireland	URL	<a href="http://pubs.rsc.org/en/journals/journalissues/ta">http://pubs.rsc.org/en/journals/journalissues/ta</a>
Rightsholder	Royal Society of Chemistry		

#### REQUEST DETAILS

Portion Type	Chapter/article	Rights Requested	Main product and any product related to main product
Page range(s)	21785-21793	Distribution	Worldwide
Total number of pages	9	Translation	Original language of publication
Format (select all that apply)	Print, Electronic	Copies for the disabled?	No
Who will republish the content?	Author of requested content	Minor editing privileges?	No
Duration of Use	Life of current edition	Incidental promotional use?	No
Lifetime Unit Quantity	Up to 499	Currency	EUR

**NEW WORK DETAILS**

---

Title	PhD Thesis	Institution name	Technical University of Munich
Instructor name	Stefan Burger	Expected presentation date	2022-09-19

**ADDITIONAL DETAILS**

---

Order reference number	N/A	The requesting person / organization to appear on the license	Stefan Burger
------------------------	-----	---	---------------

**REUSE CONTENT DETAILS**

---

Title, description or numeric reference of the portion(s)	Tolerance Factors of hybrid perovskites: recent improvements and current state of research	Title of the article/chapter the portion is from	Tolerance Factors of hybrid perovskites: recent improvements and current state of research
Editor of portion(s)	Burger, Stefan; Ehrenreich, Michael; Kieslich, Gregor	Author of portion(s)	Burger, Stefan; Ehrenreich, Michael; Kieslich, Gregor
Volume of serial or monograph	6	Issue, if republishing an article from a serial	44
Page or page range of portion	21785-21793	Publication date of portion	2018-01-01

## STUDY II: A New Polar Perovskite Coordination Network with Azaspiroundecane as A-Site Cation



This is a License Agreement between Stefan Burger ("User") and Copyright Clearance Center, Inc. ("CCC") on behalf of the Rightsholder identified in the order details below. The license consists of the order details, the Marketplace Order General Terms and Conditions below, and any Rightsholder Terms and Conditions which are included below. All payments must be made in full to CCC in accordance with the Marketplace Order General Terms and Conditions below.

Order Date	28-Jul-2022	Type of Use	Republish in a thesis/dissertation
Order License ID	1252397-2	Publisher	ROYAL SOCIETY OF CHEMISTRY
ISSN	1477-9234	Portion	Chapter/article

### LICENSED CONTENT

Publication Title	Dalton transactions	Rightsholder	Royal Society of Chemistry
Article Title	A new polar perovskite coordination network with azaspiroundecane as A-site cation.	Publication Type	e-Journal
		Start Page	10740
		End Page	10744
Author/Editor	Royal Society of Chemistry (Great Britain)	Issue	31
		Volume	49
Date	01/01/2003		
Language	English		
Country	United Kingdom of Great Britain and Northern Ireland		

### REQUEST DETAILS

Portion Type	Chapter/article	Rights Requested	Main product and any product related to main product
Page range(s)	10740-10744	Distribution	Worldwide
Total number of pages	5	Translation	Original language of publication
Format (select all that apply)	Print, Electronic	Copies for the disabled?	No
Who will republish the content?	Author of requested content	Minor editing privileges?	No
Duration of Use	Life of current edition	Incidental promotional use?	No
Lifetime Unit Quantity	Up to 499	Currency	EUR

### NEW WORK DETAILS

Title	PhD Thesis	Institution name	Technical University of Munich
Instructor name	Stefan Burger	Expected presentation date	2022-09-19

ADDITIONAL DETAILS

---

Order reference number	N/A	The requesting person / organization to appear on the license	Stefan Burger
------------------------	-----	---	---------------

REUSE CONTENT DETAILS

---

Title, description or numeric reference of the portion(s)	A new polar perovskite coordination network with azaspiroundecane as A-site cation.	Title of the article/chapter the portion is from	A new polar perovskite coordination network with azaspiroundecane as A-site cation.
Editor of portion(s)	Burger, Stefan; Kronawitter, Silva; Boström, Hanna; Zaręba, Jan Kazimierz; Kieslich, Gregor	Author of portion(s)	Burger, Stefan; Kronawitter, Silva; Boström, Hanna; Zaręba, Jan Kazimierz; Kieslich, Gregor
Volume of serial or monograph	49	Issue, if republishing an article from a serial	31
Page or page range of portion	10740-10744 	Publication date of portion	2020-08-11

## **STUDY III: Tilt and Shift Polymorphism in Molecular Perovskites**

"This article is licensed under a Creative Commons Attribution 3.0 Unported Licence. The material from this article can be used in other publications without requesting further permissions from the RSC, provided that the correct acknowledgement is given."

"Tilt and shift polymorphism in molecular perovskites" by Stefan Burger, Shivani Grover, Keith T. Butler, Hanna L. B. Boström, Ricardo Grau-Crespo, Gregor Kieslich (<https://doi.org/10.1039/D1MH00578B>) is licensed under a Creative Commons Attribution 3.0 Unported Licence (<https://creativecommons.org/licenses/by/3.0/>).

## STUDY IV: Tuning the Mechanical Properties of Dicyanamide-Based Molecular Perovskites



This is a License Agreement between Stefan Burger ("User") and Copyright Clearance Center, Inc. ("CCC") on behalf of the Rightsholder identified in the order details below. The license consists of the order details, the Marketplace Permissions General Terms and Conditions below, and any Rightsholder Terms and Conditions which are included below.

All payments must be made in full to CCC in accordance with the Marketplace Permissions General Terms and Conditions below.

Order Date	14-Jun-2023	Type of Use	Republish in a thesis/dissertation
Order License ID	1365649-1	Publisher	ROYAL SOCIETY OF CHEMISTRY
ISSN	1466-8033	Portion	Chapter/article

### LICENSED CONTENT

Publication Title	CrystEngComm	Country	United Kingdom of Great Britain and Northern Ireland
Article Title	Tuning the Mechanical Properties of Dicyanamide-Based Molecular Perovskites	Rightsholder	Royal Society of Chemistry
Author/Editor	Royal Society of Chemistry (Great Britain)	Publication Type	e-Journal
Date	01/01/1999	URL	<a href="http://www.rsc.org/Publishing/Journals/ce/index.asp">http://www.rsc.org/Publishing/Journals/ce/index.asp</a>
Language	English		

### REQUEST DETAILS

Portion Type	Chapter/article	Rights Requested	Main product and any product related to main product
Page Range(s)	3439-3444	Distribution	Worldwide
Total Number of Pages	6	Translation	Original language of publication
Format (select all that apply)	Electronic	Copies for the Disabled?	No
Who Will Republish the Content?	Author of requested content	Minor Editing Privileges?	No
Duration of Use	Life of current edition	Incidental Promotional Use?	No
Lifetime Unit Quantity	Up to 499	Currency	EUR

### NEW WORK DETAILS

Title	PhD Thesis	Institution Name	Technical University of Munich
Instructor Name	Stefan Burger	Expected Presentation Date	2023-06-18



## ADDITIONAL DETAILS

Order Reference Number	N/A	The Requesting Person/Organization to Appear on the License	Stefan Burger
------------------------	-----	---	---------------

## REQUESTED CONTENT DETAILS

Title, Description or Numeric Reference of the Portion(s)	Tuning the mechanical properties of dicyanamide- based molecular perovskites	Title of the Article/Chapter the Portion Is From	Tuning the Mechanical Properties of Dicyanamide-Based Molecular Perovskites
Editor of Portion(s)	Grover, Shivani; Burger, Stefan; Butler, Keith; Hemmer, Karina; Vervoorts, Pia; Kieslich, Gregor; Grau-Crespo, Ricardo	Author of Portion(s)	Grover, Shivani; Burger, Stefan; Butler, Keith; Hemmer, Karina; Vervoorts, Pia; Kieslich, Gregor; Grau-Crespo, Ricardo
Volume / Edition	25	Issue, if Republishing an Article From a Serial	N/A
Page or Page Range of Portion	3439–3444	Publication Date of Portion	2023-06-12

## General Terms and Conditions - Royal Society of Chemistry

### Marketplace Order General Terms and Conditions

The following terms and conditions ("General Terms"), together with any applicable Publisher Terms and Conditions, govern User's use of Works pursuant to the Licenses granted by Copyright Clearance Center, Inc. ("CCC") on behalf of the applicable Rightsholders of such Works through CCC's applicable Marketplace transactional licensing services (each, a "Service").

1) Definitions. For purposes of these General Terms, the following definitions apply:

"License" is the licensed use the User obtains via the Marketplace platform in a particular licensing transaction, as set forth in the Order Confirmation.

"Order Confirmation" is the confirmation CCC provides to the User at the conclusion of each Marketplace transaction. "Order Confirmation Terms" are additional terms set forth on specific Order Confirmations not set forth in the General Terms that can include terms applicable to a particular CCC transactional licensing service and/or any Rightsholder-specific terms.

"Rightsholder(s)" are the holders of copyright rights in the Works for which a User obtains licenses via the Marketplace platform, which are displayed on specific Order Confirmations.

"Terms" means the terms and conditions set forth in these General Terms and any additional Order Confirmation Terms collectively.

"User" or "you" is the person or entity making the use granted under the relevant License. Where the person accepting the Terms on behalf of a User is a freelancer or other third party who the User authorized to accept the General Terms on the User's behalf, such person shall be deemed jointly a User for purposes of such Terms.

"Work(s)" are the copyright protected works described in relevant Order Confirmations.

2) Description of Service. CCC's Marketplace enables Users to obtain Licenses to use one or more Works in accordance with all relevant Terms. CCC grants Licenses as an agent on behalf of the copyright rightsholder identified in the relevant Order Confirmation.

3) Applicability of Terms. The Terms govern User's use of Works in connection with the relevant License. In the event of any conflict between General Terms and Order Confirmation Terms, the latter shall govern. User acknowledges that Rightsholders have complete discretion whether to grant any permission, and whether to place any limitations on any grant, and that CCC has no right to supersede or to modify any such discretionary act by a Rightsholder.

4) Representations; Acceptance. By using the Service, User represents and warrants that User has been duly authorized

by the User to accept, and hereby does accept, all Terms.

5) Scope of License; Limitations and Obligations. All Works and all rights therein, including copyright rights, remain the sole and exclusive property of the Rightsholder. The License provides only those rights expressly set forth in the terms and conveys no other rights in any Works

6) General Payment Terms. User may pay at time of checkout by credit card or choose to be invoiced. If the User chooses to be invoiced, the User shall: (i) remit payments in the manner identified on specific invoices, (ii) unless otherwise specifically stated in an Order Confirmation or separate written agreement, Users shall remit payments upon receipt of the relevant invoice from CCC, either by delivery or notification of availability of the invoice via the Marketplace platform, and (iii) if the User does not pay the invoice within 30 days of receipt, the User may incur a service charge of 1.5% per month or the maximum rate allowed by applicable law, whichever is less. While User may exercise the rights in the License immediately upon receiving the Order Confirmation, the License is automatically revoked and is null and void, as if it had never been issued, if CCC does not receive complete payment on a timely basis.

7) General Limits on Use. Unless otherwise provided in the Order Confirmation, any grant of rights to User (i) involves only the rights set forth in the Terms and does not include subsequent or additional uses, (ii) is non-exclusive and non-transferable, and (iii) is subject to any and all limitations and restrictions (such as, but not limited to, limitations on duration of use or circulation) included in the Terms. Upon completion of the licensed use as set forth in the Order Confirmation, User shall either secure a new permission for further use of the Work(s) or immediately cease any new use of the Work(s) and shall render inaccessible (such as by deleting or by removing or severing links or other locators) any further copies of the Work. User may only make alterations to the Work if and as expressly set forth in the Order Confirmation. No Work may be used in any way that is defamatory, violates the rights of third parties (including such third parties' rights of copyright, privacy, publicity, or other tangible or intangible property), or is otherwise illegal, sexually explicit, or obscene. In addition, User may not conjoin a Work with any other material that may result in damage to the reputation of the Rightsholder. User agrees to inform CCC if it becomes aware of any infringement of any rights in a Work and to cooperate with any reasonable request of CCC or the Rightsholder in connection therewith.

8) Third Party Materials. In the event that the material for which a License is sought includes third party materials (such as photographs, illustrations, graphs, inserts and similar materials) that are identified in such material as having been used by permission (or a similar indicator), User is responsible for identifying, and seeking separate licenses (under this Service, if available, or otherwise) for any of such third party materials; without a separate license, User may not use such third party materials via the License.

9) Copyright Notice. Use of proper copyright notice for a Work is required as a condition of any License granted under the Service. Unless otherwise provided in the Order Confirmation, a proper copyright notice will read substantially as follows: "Used with permission of [Rightsholder's name], from [Work's title, author, volume, edition number and year of copyright]; permission conveyed through Copyright Clearance Center, Inc." Such notice must be provided in a reasonably legible font size and must be placed either on a cover page or in another location that any person, upon gaining access to the material which is the subject of a permission, shall see, or in the case of republication Licenses, immediately adjacent to the Work as used (for example, as part of a by-line or footnote) or in the place where substantially all other credits or notices for the new work containing the republished Work are located. Failure to include the required notice results in loss to the Rightsholder and CCC, and the User shall be liable to pay liquidated damages for each such failure equal to twice the use fee specified in the Order Confirmation, in addition to the use fee itself and any other fees and charges specified.

10) Indemnity. User hereby indemnifies and agrees to defend the Rightsholder and CCC, and their respective employees and directors, against all claims, liability, damages, costs, and expenses, including legal fees and expenses, arising out of any use of a Work beyond the scope of the rights granted herein and in the Order Confirmation, or any use of a Work which has been altered in any unauthorized way by User, including claims of defamation or infringement of rights of copyright, publicity, privacy, or other tangible or intangible property.

11) Limitation of Liability. UNDER NO CIRCUMSTANCES WILL CCC OR THE RIGHTSHOLDER BE LIABLE FOR ANY DIRECT, INDIRECT, CONSEQUENTIAL, OR INCIDENTAL DAMAGES (INCLUDING WITHOUT LIMITATION DAMAGES FOR LOSS OF BUSINESS PROFITS OR INFORMATION, OR FOR BUSINESS INTERRUPTION) ARISING OUT OF THE USE OR INABILITY TO USE A WORK, EVEN IF ONE OR BOTH OF THEM HAS BEEN ADVISED OF THE POSSIBILITY OF SUCH DAMAGES. In any event, the total liability of the Rightsholder and CCC (including their respective employees and directors) shall not exceed the total amount actually paid by User for the relevant License. User assumes full liability for the actions and omissions of its principals, employees, agents, affiliates, successors, and assigns.

12) Limited Warranties. THE WORK(S) AND RIGHT(S) ARE PROVIDED "AS IS." CCC HAS THE RIGHT TO GRANT TO USER THE RIGHTS GRANTED IN THE ORDER CONFIRMATION DOCUMENT. CCC AND THE RIGHTSHOLDER DISCLAIM ALL OTHER

WARRANTIES RELATING TO THE WORK(S) AND RIGHT(S), EITHER EXPRESS OR IMPLIED, INCLUDING WITHOUT LIMITATION IMPLIED WARRANTIES OF MERCHANTABILITY OR FITNESS FOR A PARTICULAR PURPOSE. ADDITIONAL RIGHTS MAY BE REQUIRED TO USE ILLUSTRATIONS, GRAPHS, PHOTOGRAPHS, ABSTRACTS, INSERTS, OR OTHER PORTIONS OF THE WORK (AS OPPOSED TO THE ENTIRE WORK) IN A MANNER CONTEMPLATED BY USER; USER UNDERSTANDS AND AGREES THAT NEITHER CCC NOR THE RIGHTSHOLDER MAY HAVE SUCH ADDITIONAL RIGHTS TO GRANT.

13) Effect of Breach. Any failure by User to pay any amount when due, or any use by User of a Work beyond the scope of the License set forth in the Order Confirmation and/or the Terms, shall be a material breach of such License. Any breach not cured within 10 days of written notice thereof shall result in immediate termination of such License without further notice. Any unauthorized (but licensable) use of a Work that is terminated immediately upon notice thereof may be liquidated by payment of the Rightsholder's ordinary license price therefor; any unauthorized (and unlicensable) use that is not terminated immediately for any reason (including, for example, because materials containing the Work cannot reasonably be recalled) will be subject to all remedies available at law or in equity, but in no event to a payment of less than three times the Rightsholder's ordinary license price for the most closely analogous licensable use plus Rightsholder's and/or CCC's costs and expenses incurred in collecting such payment.

14) Additional Terms for Specific Products and Services. If a User is making one of the uses described in this Section 14, the additional terms and conditions apply:

a) *Print Uses of Academic Course Content and Materials (photocopies for academic coursepacks or classroom handouts).* For photocopies for academic coursepacks or classroom handouts the following additional terms apply:

i) The copies and anthologies created under this License may be made and assembled by faculty members individually or at their request by on-campus bookstores or copy centers, or by off-campus copy shops and other similar entities.

ii) No License granted shall in any way: (i) include any right by User to create a substantively non-identical copy of the Work or to edit or in any other way modify the Work (except by means of deleting material immediately preceding or following the entire portion of the Work copied) (ii) permit "publishing ventures" where any particular anthology would be systematically marketed at multiple institutions.

iii) Subject to any Publisher Terms (and notwithstanding any apparent contradiction in the Order Confirmation arising from data provided by User), any use authorized under the academic pay-per-use service is limited as follows:

A) any License granted shall apply to only one class (bearing a unique identifier as assigned by the institution, and thereby including all sections or other subparts of the class) at one institution;

B) use is limited to not more than 25% of the text of a book or of the items in a published collection of essays, poems or articles;

C) use is limited to no more than the greater of (a) 25% of the text of an issue of a journal or other periodical or (b) two articles from such an issue;

D) no User may sell or distribute any particular anthology, whether photocopied or electronic, at more than one institution of learning;

E) in the case of a photocopy permission, no materials may be entered into electronic memory by User except in order to produce an identical copy of a Work before or during the academic term (or analogous period) as to which any particular permission is granted. In the event that User shall choose to retain materials that are the subject of a photocopy permission in electronic memory for purposes of producing identical copies more than one day after such retention (but still within the scope of any permission granted), User must notify CCC of such fact in the applicable permission request and such retention shall constitute one copy actually sold for purposes of calculating permission fees due; and

F) any permission granted shall expire at the end of the class. No permission granted shall in any way include any right by User to create a substantively non-identical copy of the Work or to edit or in any other way modify the Work (except by means of deleting material immediately preceding or following the entire portion of the Work copied).

iv) Books and Records; Right to Audit. As to each permission granted under the academic pay-per-use Service, User shall maintain for at least four full calendar years books and records sufficient for CCC to determine the numbers

of copies made by User under such permission. CCC and any representatives it may designate shall have the right to audit such books and records at any time during User's ordinary business hours, upon two days' prior notice. If any such audit shall determine that User shall have underpaid for, or underreported, any photocopies sold or by three percent (3%) or more, then User shall bear all the costs of any such audit; otherwise, CCC shall bear the costs of any such audit. Any amount determined by such audit to have been underpaid by User shall immediately be paid to CCC by User, together with interest thereon at the rate of 10% per annum from the date such amount was originally due. The provisions of this paragraph shall survive the termination of this License for any reason.

b) *Digital Pay-Per-Uses of Academic Course Content and Materials (e-coursepacks, electronic reserves, learning management systems, academic institution intranets).* For uses in e-coursepacks, posts in electronic reserves, posts in learning management systems, or posts on academic institution intranets, the following additional terms apply:

i) The pay-per-uses subject to this Section 14(b) include:

A) Posting e-reserves, course management systems, e-coursepacks for text-based content, which grants authorizations to import requested material in electronic format, and allows electronic access to this material to members of a designated college or university class, under the direction of an instructor designated by the college or university, accessible only under appropriate electronic controls (e.g., password);

B) Posting e-reserves, course management systems, e-coursepacks for material consisting of photographs or other still images not embedded in text, which grants not only the authorizations described in Section 14(b)(i)(A) above, but also the following authorization: to include the requested material in course materials for use consistent with Section 14(b)(i)(A) above, including any necessary resizing, reformatting or modification of the resolution of such requested material (provided that such modification does not alter the underlying editorial content or meaning of the requested material, and provided that the resulting modified content is used solely within the scope of, and in a manner consistent with, the particular authorization described in the Order Confirmation and the Terms), but not including any other form of manipulation, alteration or editing of the requested material;

C) Posting e-reserves, course management systems, e-coursepacks or other academic distribution for audiovisual content, which grants not only the authorizations described in Section 14(b)(i)(A) above, but also the following authorizations: (i) to include the requested material in course materials for use consistent with Section 14(b)(i)(A) above; (ii) to display and perform the requested material to such members of such class in the physical classroom or remotely by means of streaming media or other video formats; and (iii) to "clip" or reformat the requested material for purposes of time or content management or ease of delivery, provided that such "clipping" or reformatting does not alter the underlying editorial content or meaning of the requested material and that the resulting material is used solely within the scope of, and in a manner consistent with, the particular authorization described in the Order Confirmation and the Terms. Unless expressly set forth in the relevant Order Confirmation, the License does not authorize any other form of manipulation, alteration or editing of the requested material.

ii) Unless expressly set forth in the relevant Order Confirmation, no License granted shall in any way: (i) include any right by User to create a substantively non-identical copy of the Work or to edit or in any other way modify the Work (except by means of deleting material immediately preceding or following the entire portion of the Work copied or, in the case of Works subject to Sections 14(b)(1)(B) or (C) above, as described in such Sections) (ii) permit "publishing ventures" where any particular course materials would be systematically marketed at multiple institutions.

iii) Subject to any further limitations determined in the Rightsholder Terms (and notwithstanding any apparent contradiction in the Order Confirmation arising from data provided by User), any use authorized under the electronic course content pay-per-use service is limited as follows:

A) any License granted shall apply to only one class (bearing a unique identifier as assigned by the institution, and thereby including all sections or other subparts of the class) at one institution;

B) use is limited to not more than 25% of the text of a book or of the items in a published collection of essays, poems or articles;

C) use is limited to not more than the greater of (a) 25% of the text of an issue of a journal or other periodical or (b) two articles from such an issue;

D) no User may sell or distribute any particular materials, whether photocopied or electronic, at more than

one institution of learning;

E) electronic access to material which is the subject of an electronic-use permission must be limited by means of electronic password, student identification or other control permitting access solely to students and instructors in the class;

F) User must ensure (through use of an electronic cover page or other appropriate means) that any person, upon gaining electronic access to the material, which is the subject of a permission, shall see:

- a proper copyright notice, identifying the Rightsholder in whose name CCC has granted permission,
- a statement to the effect that such copy was made pursuant to permission,
- a statement identifying the class to which the material applies and notifying the reader that the material has been made available electronically solely for use in the class, and
- a statement to the effect that the material may not be further distributed to any person outside the class, whether by copying or by transmission and whether electronically or in paper form, and User must also ensure that such cover page or other means will print out in the event that the person accessing the material chooses to print out the material or any part thereof.

G) any permission granted shall expire at the end of the class and, absent some other form of authorization, User is thereupon required to delete the applicable material from any electronic storage or to block electronic access to the applicable material.

iv) Uses of separate portions of a Work, even if they are to be included in the same course material or the same university or college class, require separate permissions under the electronic course content pay-per-use Service. Unless otherwise provided in the Order Confirmation, any grant of rights to User is limited to use completed no later than the end of the academic term (or analogous period) as to which any particular permission is granted.

v) Books and Records; Right to Audit. As to each permission granted under the electronic course content Service, User shall maintain for at least four full calendar years books and records sufficient for CCC to determine the numbers of copies made by User under such permission. CCC and any representatives it may designate shall have the right to audit such books and records at any time during User's ordinary business hours, upon two days' prior notice. If any such audit shall determine that User shall have underpaid for, or underreported, any electronic copies used by three percent (3%) or more, then User shall bear all the costs of any such audit; otherwise, CCC shall bear the costs of any such audit. Any amount determined by such audit to have been underpaid by User shall immediately be paid to CCC by User, together with interest thereon at the rate of 10% per annum from the date such amount was originally due. The provisions of this paragraph shall survive the termination of this license for any reason.

c) *Pay-Per-Use Permissions for Certain Reproductions (Academic photocopies for library reserves and interlibrary loan reporting) (Non-academic internal/external business uses and commercial document delivery).* The License expressly excludes the uses listed in Section (c)(i)-(v) below (which must be subject to separate license from the applicable Rightsholder) for: academic photocopies for library reserves and interlibrary loan reporting; and non-academic internal/external business uses and commercial document delivery.

- i) electronic storage of any reproduction (whether in plain-text, PDF, or any other format) other than on a transitory basis;
- ii) the input of Works or reproductions thereof into any computerized database;
- iii) reproduction of an entire Work (cover-to-cover copying) except where the Work is a single article;
- iv) reproduction for resale to anyone other than a specific customer of User;
- v) republication in any different form. Please obtain authorizations for these uses through other CCC services or directly from the rightsholder.

Any license granted is further limited as set forth in any restrictions included in the Order Confirmation and/or in these Terms.

d) *Electronic Reproductions in Online Environments (Non-Academic-email, intranet, internet and extranet)*. For "electronic reproductions", which generally includes e-mail use (including instant messaging or other electronic transmission to a defined group of recipients) or posting on an intranet, extranet or Intranet site (including any display or performance incidental thereto), the following additional terms apply:

i) Unless otherwise set forth in the Order Confirmation, the License is limited to use completed within 30 days for any use on the Internet, 60 days for any use on an intranet or extranet and one year for any other use, all as measured from the "republishing date" as identified in the Order Confirmation, if any, and otherwise from the date of the Order Confirmation.

ii) User may not make or permit any alterations to the Work, unless expressly set forth in the Order Confirmation (after request by User and approval by Rightsholder); provided, however, that a Work consisting of photographs or other still images not embedded in text may, if necessary, be resized, reformatted or have its resolution modified without additional express permission, and a Work consisting of audiovisual content may, if necessary, be "clipped" or reformatted for purposes of time or content management or ease of delivery (provided that any such resizing, reformatting, resolution modification or "clipping" does not alter the underlying editorial content or meaning of the Work used, and that the resulting material is used solely within the scope of, and in a manner consistent with, the particular License described in the Order Confirmation and the Terms.

15) Miscellaneous.

a) User acknowledges that CCC may, from time to time, make changes or additions to the Service or to the Terms, and that Rightsholder may make changes or additions to the Rightsholder Terms. Such updated Terms will replace the prior terms and conditions in the order workflow and shall be effective as to any subsequent Licenses but shall not apply to Licenses already granted and paid for under a prior set of terms.

b) Use of User-related information collected through the Service is governed by CCC's privacy policy, available online at [www.copyright.com/about/privacy-policy/](http://www.copyright.com/about/privacy-policy/).

c) The License is personal to User. Therefore, User may not assign or transfer to any other person (whether a natural person or an organization of any kind) the License or any rights granted thereunder; provided, however, that, where applicable, User may assign such License in its entirety on written notice to CCC in the event of a transfer of all or substantially all of User's rights in any new material which includes the Work(s) licensed under this Service.

d) No amendment or waiver of any Terms is binding unless set forth in writing and signed by the appropriate parties, including, where applicable, the Rightsholder. The Rightsholder and CCC hereby object to any terms contained in any writing prepared by or on behalf of the User or its principals, employees, agents or affiliates and purporting to govern or otherwise relate to the License described in the Order Confirmation, which terms are in any way inconsistent with any Terms set forth in the Order Confirmation, and/or in CCC's standard operating procedures, whether such writing is prepared prior to, simultaneously with or subsequent to the Order Confirmation, and whether such writing appears on a copy of the Order Confirmation or in a separate instrument.

e) The License described in the Order Confirmation shall be governed by and construed under the law of the State of New York, USA, without regard to the principles thereof of conflicts of law. Any case, controversy, suit, action, or proceeding arising out of, in connection with, or related to such License shall be brought, at CCC's sole discretion, in any federal or state court located in the County of New York, State of New York, USA, or in any federal or state court whose geographical jurisdiction covers the location of the Rightsholder set forth in the Order Confirmation. The parties expressly submit to the personal jurisdiction and venue of each such federal or state court.

## STUDY V: Designing Geometric Degrees of Freedom in ReO<sub>3</sub>-Type Coordination Polymers

JOHN WILEY AND SONS LICENSE  
TERMS AND CONDITIONS

Aug 16, 2022

---

---

This Agreement between Technical University of Munich -- Stefan Burger ("You") and John Wiley and Sons ("John Wiley and Sons") consists of your license details and the terms and conditions provided by John Wiley and Sons and Copyright Clearance Center.

License Number 5370770345606

License date Aug 16, 2022

Licensed Content Publisher John Wiley and Sons

Licensed Content Publication Advanced Functional Materials

Licensed Content Title Designing Geometric Degrees of Freedom in ReO<sub>3</sub>-Type Coordination Polymers

Licensed Content Author Stefan Burger, Karina Hemmer, David C. Mayer, et al

Licensed Content Date Aug 8, 2022

Licensed Content Volume 0

Licensed Content Issue 0

Licensed Content Pages 8

Type of use Dissertation/Thesis

Requestor type Author of this Wiley article



---

Format	Print and electronic
Portion	Full article
Will you be translating?	No
Title	PhD Thesis
Institution name	Technical University of Munich
Expected presentation date	Sep 2022
Requestor Location	Technical University of Munich Lichtenbergstraße 4 Garching, 85748 Germany Attn: Technical University of Munich
Publisher Tax ID	EU826007151
Total	0.00 EUR
Terms and Conditions	

#### **TERMS AND CONDITIONS**

This copyrighted material is owned by or exclusively licensed to John Wiley & Sons, Inc. or one of its group companies (each a "Wiley Company") or handled on behalf of a society with which a Wiley Company has exclusive publishing rights in relation to a particular work (collectively "WILEY"). By clicking "accept" in connection with completing this licensing transaction, you agree that the following terms and conditions apply to this transaction (along with the billing and payment terms and conditions established by the Copyright Clearance Center Inc., ("CCC's Billing and Payment terms and conditions"), at the time that you opened your RightsLink account (these are available at any time at <http://myaccount.copyright.com>).

#### **Terms and Conditions**

- The materials you have requested permission to reproduce or reuse (the "Wiley Materials") are protected by copyright.
- You are hereby granted a personal, non-exclusive, non-sub licensable (on a stand-alone basis), non-transferable, worldwide, limited license to reproduce the Wiley Materials for the purpose specified in the licensing process. This license, **and any CONTENT (PDF or image file) purchased as part of your order**, is for a one-time use only and limited to any maximum distribution number specified in the license. The first instance of republication or reuse granted by this license must be completed within two years of the date of the grant of this license (although copies prepared before the end date may be distributed thereafter). The Wiley Materials shall not be used in any other manner or for any other purpose, beyond what is granted in the license. Permission is granted subject to an appropriate acknowledgement given to the author, title of the material/book/journal and the publisher. You shall also duplicate the copyright notice that appears in the Wiley publication in your use of the Wiley Material. Permission is also granted on the understanding that nowhere in the text is a previously published source acknowledged for all or part of this Wiley Material. Any third party content is expressly excluded from this permission.
- With respect to the Wiley Materials, all rights are reserved. Except as expressly granted by the terms of the license, no part of the Wiley Materials may be copied, modified, adapted (except for minor reformatting required by the new Publication), translated, reproduced, transferred or distributed, in any form or by any means, and no derivative works may be made based on the Wiley Materials without the prior permission of the respective copyright owner. **For STM Signatory Publishers clearing permission under the terms of the [STM Permissions Guidelines](#) only, the terms of the license are extended to include subsequent editions and for editions in other languages, provided such editions are for the work as a whole in situ and does not involve the separate exploitation of the permitted figures or extracts**, You may not alter, remove or suppress in any manner any copyright, trademark or other notices displayed by the Wiley Materials. You may not license, rent, sell, loan, lease, pledge, offer as security, transfer or assign the Wiley Materials on a stand-alone basis, or any of the rights granted to you hereunder to any other person.
- The Wiley Materials and all of the intellectual property rights therein shall at all times remain the exclusive property of John Wiley & Sons Inc, the Wiley Companies, or their respective licensors, and your interest therein is only that of having possession of and the right to reproduce the Wiley Materials pursuant to Section 2 herein during the continuance of this Agreement. You agree that you own no right, title or interest in or to the Wiley Materials or any of the intellectual property rights therein. You shall have no rights hereunder other than the license as provided for above in Section 2. No right, license or interest to any trademark, trade name, service mark or other branding ("Marks") of WILEY or its licensors is granted hereunder, and you agree that you shall not assert any such right, license or interest with respect thereto
- NEITHER WILEY NOR ITS LICENSORS MAKES ANY WARRANTY OR REPRESENTATION OF ANY KIND TO YOU OR ANY THIRD PARTY, EXPRESS, IMPLIED OR STATUTORY, WITH RESPECT TO THE MATERIALS OR THE ACCURACY OF ANY INFORMATION CONTAINED IN THE MATERIALS, INCLUDING, WITHOUT LIMITATION, ANY IMPLIED

WARRANTY OF MERCHANTABILITY, ACCURACY, SATISFACTORY QUALITY, FITNESS FOR A PARTICULAR PURPOSE, USABILITY, INTEGRATION OR NON-INFRINGEMENT AND ALL SUCH WARRANTIES ARE HEREBY EXCLUDED BY WILEY AND ITS LICENSORS AND WAIVED BY YOU.

- WILEY shall have the right to terminate this Agreement immediately upon breach of this Agreement by you.
- You shall indemnify, defend and hold harmless WILEY, its Licensors and their respective directors, officers, agents and employees, from and against any actual or threatened claims, demands, causes of action or proceedings arising from any breach of this Agreement by you.
- IN NO EVENT SHALL WILEY OR ITS LICENSORS BE LIABLE TO YOU OR ANY OTHER PARTY OR ANY OTHER PERSON OR ENTITY FOR ANY SPECIAL, CONSEQUENTIAL, INCIDENTAL, INDIRECT, EXEMPLARY OR PUNITIVE DAMAGES, HOWEVER CAUSED, ARISING OUT OF OR IN CONNECTION WITH THE DOWNLOADING, PROVISIONING, VIEWING OR USE OF THE MATERIALS REGARDLESS OF THE FORM OF ACTION, WHETHER FOR BREACH OF CONTRACT, BREACH OF WARRANTY, TORT, NEGLIGENCE, INFRINGEMENT OR OTHERWISE (INCLUDING, WITHOUT LIMITATION, DAMAGES BASED ON LOSS OF PROFITS, DATA, FILES, USE, BUSINESS OPPORTUNITY OR CLAIMS OF THIRD PARTIES), AND WHETHER OR NOT THE PARTY HAS BEEN ADVISED OF THE POSSIBILITY OF SUCH DAMAGES. THIS LIMITATION SHALL APPLY NOTWITHSTANDING ANY FAILURE OF ESSENTIAL PURPOSE OF ANY LIMITED REMEDY PROVIDED HEREIN.
- Should any provision of this Agreement be held by a court of competent jurisdiction to be illegal, invalid, or unenforceable, that provision shall be deemed amended to achieve as nearly as possible the same economic effect as the original provision, and the legality, validity and enforceability of the remaining provisions of this Agreement shall not be affected or impaired thereby.
- The failure of either party to enforce any term or condition of this Agreement shall not constitute a waiver of either party's right to enforce each and every term and condition of this Agreement. No breach under this agreement shall be deemed waived or excused by either party unless such waiver or consent is in writing signed by the party granting such waiver or consent. The waiver by or consent of a party to a breach of any provision of this Agreement shall not operate or be construed as a waiver of or consent to any other or subsequent breach by such other party.
- This Agreement may not be assigned (including by operation of law or otherwise) by you without WILEY's prior written consent.
- Any fee required for this permission shall be non-refundable after thirty (30) days from receipt by the CCC.
- These terms and conditions together with CCC's Billing and Payment terms and conditions (which are incorporated herein) form the entire agreement between you and

WILEY concerning this licensing transaction and (in the absence of fraud) supersedes all prior agreements and representations of the parties, oral or written. This Agreement may not be amended except in writing signed by both parties. This Agreement shall be binding upon and inure to the benefit of the parties' successors, legal representatives, and authorized assigns.

- In the event of any conflict between your obligations established by these terms and conditions and those established by CCC's Billing and Payment terms and conditions, these terms and conditions shall prevail.
- WILEY expressly reserves all rights not specifically granted in the combination of (i) the license details provided by you and accepted in the course of this licensing transaction, (ii) these terms and conditions and (iii) CCC's Billing and Payment terms and conditions.
- This Agreement will be void if the Type of Use, Format, Circulation, or Requestor Type was misrepresented during the licensing process.
- This Agreement shall be governed by and construed in accordance with the laws of the State of New York, USA, without regards to such state's conflict of law rules. Any legal action, suit or proceeding arising out of or relating to these Terms and Conditions or the breach thereof shall be instituted in a court of competent jurisdiction in New York County in the State of New York in the United States of America and each party hereby consents and submits to the personal jurisdiction of such court, waives any objection to venue in such court and consents to service of process by registered or certified mail, return receipt requested, at the last known address of such party.

## **WILEY OPEN ACCESS TERMS AND CONDITIONS**

Wiley Publishes Open Access Articles in fully Open Access Journals and in Subscription journals offering Online Open. Although most of the fully Open Access journals publish open access articles under the terms of the Creative Commons Attribution (CC BY) License only, the subscription journals and a few of the Open Access Journals offer a choice of Creative Commons Licenses. The license type is clearly identified on the article.

### **The Creative Commons Attribution License**

The [Creative Commons Attribution License \(CC-BY\)](#) allows users to copy, distribute and transmit an article, adapt the article and make commercial use of the article. The CC-BY license permits commercial and non-

### **Creative Commons Attribution Non-Commercial License**

The [Creative Commons Attribution Non-Commercial \(CC-BY-NC\) License](#) permits use, distribution and reproduction in any medium, provided the original work is properly cited and is not used for commercial purposes.(see below)

### **Creative Commons Attribution-Non-Commercial-NoDerivs License**

The [Creative Commons Attribution Non-Commercial-NoDerivs License](#) (CC-BY-NC-ND)

permits use, distribution and reproduction in any medium, provided the original work is properly cited, is not used for commercial purposes and no modifications or adaptations are made. (see below)

**Use by commercial "for-profit" organizations**

Use of Wiley Open Access articles for commercial, promotional, or marketing purposes requires further explicit permission from Wiley and will be subject to a fee.

Further details can be found on Wiley Online Library <http://olabout.wiley.com/WileyCDA/Section/id-410895.html>

**Other Terms and Conditions:**


**v1.10 Last updated September 2015**

Questions? [customercare@copyright.com](mailto:customercare@copyright.com) or +1-855-239-3415 (toll free in the US) or +1-978-646-2777.



## Permissions for figures reprinted in this thesis

Reprint permission for Figure 2.4:

Home ? Help Live Chat Stefan Burger

**Pronounced Negative Thermal Expansion from a Simple Structure: Cubic ScF3**

Author: Benjamin K. Greve, Kenneth L. Martin, Peter L. Lee, et al  
Publication: Journal of the American Chemical Society  
Publisher: American Chemical Society  
Date: Nov 1, 2010

*Copyright © 2010, American Chemical Society*

**PERMISSION/LICENSE IS GRANTED FOR YOUR ORDER AT NO CHARGE**

This type of permission/license, instead of the standard Terms and Conditions, is sent to you because no fee is being charged for your order. Please note the following:

- Permission is granted for your request in both print and electronic formats, and translations.
- If figures and/or tables were requested, they may be adapted or used in part.
- Please print this page for your records and send a copy of it to your publisher/graduate school.
- Appropriate credit for the requested material should be given as follows: "Reprinted (adapted) with permission from {COMPLETE REFERENCE CITATION}. Copyright {YEAR} American Chemical Society." Insert appropriate information in place of the capitalized words.
- One-time permission is granted only for the use specified in your RightsLink request. No additional uses are granted (such as derivative works or other editions). For any uses, please submit a new request.

If credit is given to another source for the material you requested from RightsLink, permission must be obtained from that source.

[BACK](#) [CLOSE WINDOW](#)

© 2022 Copyright - All Rights Reserved | [Copyright Clearance Center, Inc.](#) | [Privacy statement](#) | [Data Security and Privacy](#)  
| [For California Residents](#) | [Terms and Conditions](#)Comments? We would like to hear from you. E-mail us at [customercare@copyright.com](mailto:customercare@copyright.com)

Reprint permission for Figure 2.9:

JOHN WILEY AND SONS LICENSE  
TERMS AND CONDITIONS

Sep 19, 2022

---

---

This Agreement between Technical University of Munich -- Stefan Burger ("You") and John Wiley and Sons ("John Wiley and Sons") consists of your license details and the terms and conditions provided by John Wiley and Sons and Copyright Clearance Center.

License Number	5392681191617
License date	Sep 19, 2022
Licensed Content Publisher	John Wiley and Sons
Licensed Content Publication	Wiley Books
Licensed Content Title	Hybrid Organic-Inorganic Perovskites
Licensed Content Author	Alessandro Stroppa Li Wei Song Gao Zhe-ming Wang
Licensed Content Date	Oct 1, 2020
Licensed Content Pages	1
Type of use	Dissertation/Thesis
Requestor type	University/Academic
Format	Print and electronic
Portion	Figure/table

Number of figures/tables	1
Will you be translating?	No
Title	PhD Thesis
Institution name	Technical University of Munich
Expected presentation date	Sep 2022
Portions	Figure 1.5
Requestor Location	Technical University of Munich Lichtenbergstraße 4  Garching, 85748 Germany Attn: Technical University of Munich
Publisher Tax ID	EU826007151
Total	0.00 EUR

Terms and Conditions

### TERMS AND CONDITIONS

This copyrighted material is owned by or exclusively licensed to John Wiley & Sons, Inc. or one of its group companies (each a "Wiley Company") or handled on behalf of a society with which a Wiley Company has exclusive publishing rights in relation to a particular work (collectively "WILEY"). By clicking "accept" in connection with completing this licensing transaction, you agree that the following terms and conditions apply to this transaction (along with the billing and payment terms and conditions established by the Copyright Clearance Center Inc., ("CCC's Billing and Payment terms and conditions"), at the time that you opened your RightsLink account (these are available at any time at <http://myaccount.copyright.com>).

#### Terms and Conditions



- The materials you have requested permission to reproduce or reuse (the "Wiley Materials") are protected by copyright.
- You are hereby granted a personal, non-exclusive, non-sub licensable (on a stand-alone basis), non-transferable, worldwide, limited license to reproduce the Wiley Materials for the purpose specified in the licensing process. This license, **and any CONTENT (PDF or image file) purchased as part of your order**, is for a one-time use only and limited to any maximum distribution number specified in the license. The first instance of republication or reuse granted by this license must be completed within two years of the date of the grant of this license (although copies prepared before the end date may be distributed thereafter). The Wiley Materials shall not be used in any other manner or for any other purpose, beyond what is granted in the license. Permission is granted subject to an appropriate acknowledgement given to the author, title of the material/book/journal and the publisher. You shall also duplicate the copyright notice that appears in the Wiley publication in your use of the Wiley Material. Permission is also granted on the understanding that nowhere in the text is a previously published source acknowledged for all or part of this Wiley Material. Any third party content is expressly excluded from this permission.
- With respect to the Wiley Materials, all rights are reserved. Except as expressly granted by the terms of the license, no part of the Wiley Materials may be copied, modified, adapted (except for minor reformatting required by the new Publication), translated, reproduced, transferred or distributed, in any form or by any means, and no derivative works may be made based on the Wiley Materials without the prior permission of the respective copyright owner. **For STM Signatory Publishers clearing permission under the terms of the [STM Permissions Guidelines](#) only, the terms of the license are extended to include subsequent editions and for editions in other languages, provided such editions are for the work as a whole in situ and does not involve the separate exploitation of the permitted figures or extracts**, You may not alter, remove or suppress in any manner any copyright, trademark or other notices displayed by the Wiley Materials. You may not license, rent, sell, loan, lease, pledge, offer as security, transfer or assign the Wiley Materials on a stand-alone basis, or any of the rights granted to you hereunder to any other person.
- The Wiley Materials and all of the intellectual property rights therein shall at all times remain the exclusive property of John Wiley & Sons Inc, the Wiley Companies, or their respective licensors, and your interest therein is only that of having possession of and the right to reproduce the Wiley Materials pursuant to Section 2 herein during the continuance of this Agreement. You agree that you own no right, title or interest in or to the Wiley Materials or any of the intellectual property rights therein. You shall have no rights hereunder other than the license as provided for above in Section 2. No right, license or interest to any trademark, trade name, service mark or other branding ("Marks") of WILEY or its licensors is granted hereunder, and you agree that you shall not assert any such right, license or interest with respect thereto
- NEITHER WILEY NOR ITS LICENSORS MAKES ANY WARRANTY OR REPRESENTATION OF ANY KIND TO YOU OR ANY THIRD PARTY, EXPRESS, IMPLIED OR STATUTORY, WITH RESPECT TO THE MATERIALS OR THE ACCURACY OF ANY INFORMATION CONTAINED IN THE MATERIALS, INCLUDING, WITHOUT LIMITATION, ANY IMPLIED

WARRANTY OF MERCHANTABILITY, ACCURACY, SATISFACTORY QUALITY, FITNESS FOR A PARTICULAR PURPOSE, USABILITY, INTEGRATION OR NON-INFRINGEMENT AND ALL SUCH WARRANTIES ARE HEREBY EXCLUDED BY WILEY AND ITS LICENSORS AND WAIVED BY YOU.

- WILEY shall have the right to terminate this Agreement immediately upon breach of this Agreement by you.
- You shall indemnify, defend and hold harmless WILEY, its Licensors and their respective directors, officers, agents and employees, from and against any actual or threatened claims, demands, causes of action or proceedings arising from any breach of this Agreement by you.
- IN NO EVENT SHALL WILEY OR ITS LICENSORS BE LIABLE TO YOU OR ANY OTHER PARTY OR ANY OTHER PERSON OR ENTITY FOR ANY SPECIAL, CONSEQUENTIAL, INCIDENTAL, INDIRECT, EXEMPLARY OR PUNITIVE DAMAGES, HOWEVER CAUSED, ARISING OUT OF OR IN CONNECTION WITH THE DOWNLOADING, PROVISIONING, VIEWING OR USE OF THE MATERIALS REGARDLESS OF THE FORM OF ACTION, WHETHER FOR BREACH OF CONTRACT, BREACH OF WARRANTY, TORT, NEGLIGENCE, INFRINGEMENT OR OTHERWISE (INCLUDING, WITHOUT LIMITATION, DAMAGES BASED ON LOSS OF PROFITS, DATA, FILES, USE, BUSINESS OPPORTUNITY OR CLAIMS OF THIRD PARTIES), AND WHETHER OR NOT THE PARTY HAS BEEN ADVISED OF THE POSSIBILITY OF SUCH DAMAGES. THIS LIMITATION SHALL APPLY NOTWITHSTANDING ANY FAILURE OF ESSENTIAL PURPOSE OF ANY LIMITED REMEDY PROVIDED HEREIN.
- Should any provision of this Agreement be held by a court of competent jurisdiction to be illegal, invalid, or unenforceable, that provision shall be deemed amended to achieve as nearly as possible the same economic effect as the original provision, and the legality, validity and enforceability of the remaining provisions of this Agreement shall not be affected or impaired thereby.
- The failure of either party to enforce any term or condition of this Agreement shall not constitute a waiver of either party's right to enforce each and every term and condition of this Agreement. No breach under this agreement shall be deemed waived or excused by either party unless such waiver or consent is in writing signed by the party granting such waiver or consent. The waiver by or consent of a party to a breach of any provision of this Agreement shall not operate or be construed as a waiver of or consent to any other or subsequent breach by such other party.
- This Agreement may not be assigned (including by operation of law or otherwise) by you without WILEY's prior written consent.
- Any fee required for this permission shall be non-refundable after thirty (30) days from receipt by the CCC.
- These terms and conditions together with CCC's Billing and Payment terms and conditions (which are incorporated herein) form the entire agreement between you and

WILEY concerning this licensing transaction and (in the absence of fraud) supersedes all prior agreements and representations of the parties, oral or written. This Agreement may not be amended except in writing signed by both parties. This Agreement shall be binding upon and inure to the benefit of the parties' successors, legal representatives, and authorized assigns.

- In the event of any conflict between your obligations established by these terms and conditions and those established by CCC's Billing and Payment terms and conditions, these terms and conditions shall prevail.
- WILEY expressly reserves all rights not specifically granted in the combination of (i) the license details provided by you and accepted in the course of this licensing transaction, (ii) these terms and conditions and (iii) CCC's Billing and Payment terms and conditions.
- This Agreement will be void if the Type of Use, Format, Circulation, or Requestor Type was misrepresented during the licensing process.
- This Agreement shall be governed by and construed in accordance with the laws of the State of New York, USA, without regards to such state's conflict of law rules. Any legal action, suit or proceeding arising out of or relating to these Terms and Conditions or the breach thereof shall be instituted in a court of competent jurisdiction in New York County in the State of New York in the United States of America and each party hereby consents and submits to the personal jurisdiction of such court, waives any objection to venue in such court and consents to service of process by registered or certified mail, return receipt requested, at the last known address of such party.

## **WILEY OPEN ACCESS TERMS AND CONDITIONS**

Wiley Publishes Open Access Articles in fully Open Access Journals and in Subscription journals offering Online Open. Although most of the fully Open Access journals publish open access articles under the terms of the Creative Commons Attribution (CC BY) License only, the subscription journals and a few of the Open Access Journals offer a choice of Creative Commons Licenses. The license type is clearly identified on the article.

### **The Creative Commons Attribution License**

The [Creative Commons Attribution License \(CC-BY\)](#) allows users to copy, distribute and transmit an article, adapt the article and make commercial use of the article. The CC-BY license permits commercial and non-

### **Creative Commons Attribution Non-Commercial License**

The [Creative Commons Attribution Non-Commercial \(CC-BY-NC\) License](#) permits use, distribution and reproduction in any medium, provided the original work is properly cited and is not used for commercial purposes.(see below)

### **Creative Commons Attribution-Non-Commercial-NoDerivs License**

The [Creative Commons Attribution Non-Commercial-NoDerivs License \(CC-BY-NC-ND\)](#)

permits use, distribution and reproduction in any medium, provided the original work is properly cited, is not used for commercial purposes and no modifications or adaptations are made. (see below)

**Use by commercial "for-profit" organizations**

Use of Wiley Open Access articles for commercial, promotional, or marketing purposes requires further explicit permission from Wiley and will be subject to a fee.

Further details can be found on Wiley Online Library <http://olabout.wiley.com/WileyCDA/Section/id-410895.html>

**Other Terms and Conditions:**

**v1.10 Last updated September 2015**

**Questions? [customercare@copyright.com](mailto:customercare@copyright.com) or +1-855-239-3415 (toll free in the US) or +1-978-646-2777.**

---

---

"Detailreiche und fundierte Arbeit braucht Weile, denn peripher kann's jeder; irgendwann muss aber ein Schlusstrich gezogen werden. Und das ist auch gut so."

*Ich, Stefan Burger, niederbayerischer Hobby-Philosoph*

